DOCTORAL THESIS

INTUMESCENT COATINGS ON STEEL STRUCTURES EXPOSED TO NATURAL FIRES

Leibniz University Hannover, Germany
2022

Dipl.-Ing.
Waldemar Weisheim

DOI: http://dx.doi.org/10.15488/11732
URL: https://www.repo.uni-hannover.de/handle/123456789/11825

Intumescent Coatings on Steel Structures Exposed to Natural Fires

Von der Fakultät für Bauingenieurwesen und Geodäsie
der Gottfried Wilhelm Leibniz Universität Hannover
zur Erlangung des akademischen Grades

Doktor-Ingenieur
- Dr.-Ing. -

genehmigte Dissertation
von

Dipl.-Ing. Waldemar Weisheim

Erscheinungsjahr: 2022

Promotionskommission:

Hauptreferent:	**Prof. Dr.-Ing. Peter Schaumann** Institut für Stahlbau, Leibniz Universität Hannover
Korreferent:	**Prof. Dr.-Ing. Jochen Zehfuß** Institut für Baustoffe, Massivbau und Brandschutz, Technische Universität Braunschweig
Kommissionsmitglied:	**Prof. Dr.-Ing. Nabil A. Fouad** Institut für Bauphysik, Leibniz Universität Hannover
Vorsitzender:	**Prof. Dr.-Ing. Udo Nackenhorst** Institut für Baumechanik und Numerische Mechanik Leibniz Universität Hannover
Tag der Promotion:	24.09.2021

Intumescent Coatings on Steel Structures Exposed to Natural Fires

Short abstract:

The main objective of this thesis is to evaluate the thermal and mechanical behaviour of intumescent coatings (also known as reactive fire protection materials) that are used to protect steel structures from a fire exposure due to natural fires. As the intumescence process of currently available coatings deemed to be highly dependent on the heating regime, comprehensive experimental investigations are performed to understand the correlation between the heating as well as the cooling regime and the thermomechanical performance of intumescent coatings. Due to differences in sensitivity, a solvent-borne and a waterborne intumescent coating are investigated by, among others, evaluating their insulation efficiency.
Based on the experimental data, a thermomechanical material model is developed. This material model enables two- and three-dimensional finite element simulations of the intumescent coatings applied on steel structures. As natural fires can show arbitrary regimes characterised by various heating and cooling rates, the material model is formulated universally by taking the heating and cooling rate-dependent behaviour of the intumescent coatings into account.
Additionally to the finite element modelling, a MATLAB-based calculation approach is developed, aiming to reduce the computational effort and, thus, providing a design procedure for the dry film thickness of intumescent coatings for any desired fire exposure that is covered by the examined parameter range. As no other approach exists yet, this is the first scientifically-based method for the determination of the required dry film thickness of intumescent coatings to protect steel structures when being exposed to natural fires.

Keywords: intumescent coatings, natural fire, heating, cooling, thermal conductivity, morphology, expansion, finite element simulation, MATLAB-based calculation, design, dry film thickness

Abstract

Intumescent coatings (ICs) are used whenever filigree and architecturally attractive steel structures are requested in combination with fire resistance requirements. The application of intumescent coatings combines both the maintenance of the architectural appearance of steel structures and the required fire resistance. Despite their thin layer thicknesses, intumescent coatings are designed to protect steel structures in fire due to their particular behaviour. When being exposed to heat, the inert coating expands multiple times the original thickness to form a highly insulating char with low thermal conductivity that protects the underlying steel structure from rapid heating.
As intumescent coatings are non-standardised products, the introduction to the German market is regulated by general technical approvals (abZ, *German:* allgemeine bauaufsichtliche Zulassung), general design certifications (aBG, *German:* allgemeine Bauartgenehmigung) or European Technical Assessments (ETAs).
The insulating efficiency of intumescent coatings is verified during the national and European approvals by small-scale fire tests. Within these fire tests coated steel plates are exposed to the ISO standard fire. Fire tests on loaded and unloaded beams and columns, which are also part of the approval procedure underlie the same fire exposure. As the dry film thickness of intumescent coatings is derived from these tests as a function of section factor, design temperature and fire resistance rating (currently 30 to 120 minutes), the values for the dry film thickness are solely related to the ISO standard fire.

Due to the increasing use of performance-based design methods for steel structures in fire, it becomes more and more important to assess the fire protection performance of intumescent coatings in case of natural fires. As coatings are nowadays only assessed for the fire exposure according to the ISO standard fire, there is a lack of scientific evidence regarding the thermomechanical performance of intumescent coatings for fire scenarios, which deviate from the standard fire.
Therefore, the main objective of this thesis is to evaluate the thermal performance of intumescent coatings in natural fires and to identify the relevant parameters for the description of the temperature and heating rate-dependent behaviour of intumescent coatings.

The objective was achieved in the first step by a comprehensive literature review, where the latest research developments were analysed with regard to the thermal performance of intumescent coatings in natural fires. The focus was on both the intumescent coatings themselves and their ingredients. In this way the reason for the heating rate-dependent behaviour of intumescent coatings could be identified. With respect to own experimental investigations, thermoanalytical methods, known in literature, were additionally evaluated to ensure reliable and reproducible studies.

In the second step, own experimental investigations on the thermal performance of intumescent coatings were performed. Due to differences in sensitivity, a solvent-borne and a waterborne intumescent coating were selected.
A total of 113 small-scale fire tests on the heating behaviour of coated steel plates were performed to evaluate the fire protection performance of the investigated coatings due to constant heating rates and selected natural fires. To achieve this, a newly developed experimental setup was used to measure both the steel plate temperature and the temperature development inside the expanded char. The results of the performed tests showed a significant influence of heating rates on the thermal performance of the investigated coatings, especially for the solvent-borne product. Best fire protection performances were mainly observed for high heating rates.
Following the results of the small-scale fire tests, further 52 laboratory tests on the expansion behaviour of the intumescent coatings for various heating and cooling rates of natural fires were performed. With the help of these, a clear correlation between the maximum temperature and the expansion as well as between the heating rates and the expansion could be identified.
To complement the laboratory tests, thermoanalytical (DSC and TGA) and morphological analyses (digital microscopy) were carried out to investigate the pore size and structure of the formed char due to changes in heating rates and reaction stages. It was found out that especially the results of the morphological analyses provide important information for the physical description of the temperature and heating rate-dependent behaviour of intumescent coatings in case of fire.
As the crucial findings regarding the thermomechanical behaviour of intumescent coatings were achieved by small-scale tests, a large-scale fire test was finally performed to investigate both the scale effect and the effect of shape and stress-induced cracks in the foamed char on the heating behaviour of loaded and unloaded beams and columns in case of a selected natural fire.

With the aim to extend the parameter range, the results of the performed laboratory tests were used to develop a finite element based modelling approach to describe the high-temperature behaviour of intumescent coatings in case of natural fires. This was achieved by, among others, the development of a thermal conductivity model for intumescent coatings in the heating and cooling phase of natural fires and a subroutine-based description of the expansion behaviour.
The numerical models were validated against own small- and large-scale fire tests. The obtained results showed a very good agreement for the simulated temperatures (of the steel components and the foamed chars) and the expanded char thicknesses with respect to the investigated parameter range.

In the last step, the results obtained from the experimental and numerical investigations were used to develop a design method for the dry film thickness of intumescent coating in natural fires.
Due to the variety of natural fires, a design method solely based on tests could not be realised due to the outlay of time and expense. Therefore, a MATLAB-

based calculation approach was developed. This approach is based on the thermal conductivity model that was developed for the numerical simulations and needs only the expansion and morphology data as input parameters. In addition to the design of the dry film thickness, the MATLAB method is developed to calculate the temperature development of any coated steel profile due to any desired natural fire. Due to its efficient and accurate calculation, the method is a great alternative to the numerical simulations. This is proven by appropriate validation results.
Since the MATLAB method is provided as open source code (download at: www.stahlbau.uni-hannover.de) the functions and data of the approach can be extended at any time by the user. Currently, the calculation method provides a material database for a waterborne intumescent coating and numerous steel profiles that are in common use in steel constructions.

Taken as a whole, the present doctoral thesis provides fundamental findings on the thermomechanical performance of intumescent coatings in natural fires, presents new methods for the experimental investigation of the heating rate-dependent behaviour of intumescent coatings and introduces a new material model to reliably describe the expansion and heating behaviour of intumescent coatings in natural fires for both numerical simulations and simplified calculations.

Keywords: intumescent coatings, natural fire, heating, cooling, thermal conductivity, morphology, expansion, finite element simulation, MATLAB-based calculation, design, dry film thickness

---

Kurzfassung

Reaktive Brandschutzsysteme finden in der Regel Anwendung, wenn das schlanke und architektonisch ansprechende Erscheinungsbild eines Stahltragwerks bei gleichzeitiger Sicherstellung eines ausreichenden Feuerwiderstandes gewahrt werden soll. Aufgrund ihrer geringen Trockenschichtdicken sind reaktive Brandschutzsysteme kaum von herkömmlichen (Korrosions-) Anstrichen zu unterscheiden. Die Besonderheit der reaktiven Brandschutzsysteme liegt in ihrer Funktionsweise, da sie erst im Brandfall ihre thermische Schutzwirkung entfalten. Einer Brandeinwirkung ausgesetzt, expandieren reaktive Brandschutzsysteme um das Vielfache ihrer Trockenschichtdicke. Dabei bilden Sie ein feinporiges Kohlenstoffgerüst aus, dessen geringe Wärmeleitfähigkeit das Erwärmungsverhalten der darunter liegenden Stahlbauteile zeitlich verzögert. Da reaktive Brandschutzsysteme zu den nicht normativ geregelten Bauprodukten zählen, werden sie derzeit in Deutschland auf der Grundlage von allgemeinen bauaufsichtlichen Zulassungen (abZ) bzw. allgemeinen Bauartgenehmigungen (aBG) sowie Europäisch Technischen Bewertungen (ETA, *engl.:* European Technical Assessment) bauaufsichtlich eingeführt.
Die thermische Schutzwirkung von reaktiven Brandschutzsystemen wird im Rahmen des nationalen und europäischen Zulassungsverfahrens anhand von Laborbrandversuchen bewertet. Bei diesen Versuchen werden beschichtete Stahlplatten einer Temperaturbeanspruchung gemäß der Einheits-Temperaturzeitkurve ausgesetzt. Auch die in diesem Zusammenhang durchgeführten Brandversuche an belasteten und unbelasteten Stützen und Trägern werden ebenfalls unter der Zugrundlegung der Einheits-Temperaturzeitkurve durchgeführt. Die daraus abgeleiteten Trockenschichtdicken der Brandschutzsysteme, die in Abhängigkeit des Profilfaktors, der kritischen Bauteiltemperatur und der Feuerwiderstandsdauer (derzeit 30 bis 120 Minuten) definiert werden, basieren daher ausschließlich auf der thermischen Einwirkung der Normbrandkurve.
Mit der zunehmenden Etablierung der objektorientierten Bemessung von Stahltragwerken im Brandfall rückt die Bewertung der Leistungsfähigkeit von reaktiven Brandschutzsystemen bei Naturbrandeinwirkungen zunehmend in den Fokus. Da die Brandschutzsysteme derzeit ausschließlich auf der Grundlage der Einheits-Temperaturzeitkurve bewertet werden, ist ihr thermisches Verhalten bei Naturbrandeinwirkungen nicht hinreichend bekannt.
Das Ziel dieser Dissertation ist daher die Bewertung der thermischen Schutzwirkung von reaktiven Brandschutzsystemen bei Naturbränden sowie die Identifikation relevanter Kenngrößen für die physikalische Beschreibung des temperatur- und heizratenabhängigen Verhaltens reaktiver Brandschutzsysteme.

Zur Erreichung des Ziels wurde im ersten Schritt eine umfangreiche Literaturstudie durchgeführt und der aktuelle Stand der Forschung in Hinblick auf das thermische Verhalten von reaktiven Brandschutzsystemen bei Naturbrandeinwirkungen analysiert. Hierbei wurde der Fokus sowohl auf die Brandschutzsysteme selbst als auch

auf ihre Einzelbestandteile gelegt. Auf diese Weise konnte die Ursache für das heizratenabhängige Verhalten reaktiver Brandschutzsysteme bei Naturbränden identifiziert werden. In Hinblick auf die Durchführung eigener Untersuchungen wurden zudem literaturbekannte Analysemethoden recherchiert und auf ihre Eignung sowie Reproduzierbarkeit hin bewertet.

Im zweiten Schritt wurden experimentelle Untersuchungen zur thermischen Leistungsfähigkeit reaktiver Brandschutzsysteme durchgeführt. Aufgrund ihres unterschiedlichen Verhaltens wurden hierbei ein wasserbasiertes sowie ein lösemittelhaltiges reaktives Brandschutzsystem ausgewählt.
In insgesamt 113 kleinmaßstäblichen Erwärmungsversuchen an beschichteten Stahlplatten wurde zunächst die thermische Schutzwirkung der untersuchten Brandschutzsysteme in Abhängigkeit konstanter Aufheizgeschwindigkeiten sowie ausgewählter Naturbrände analysiert. Hierzu wurde ein eigens entwickelter Versuchsaufbau verwendet, der neben der Messung der Stahlplattentemperatur vor allem die Analyse der Temperaturentwicklung innerhalb des expandierenden Brandschutzsystems ermöglicht. Hierdurch konnte gezeigt werden, dass das lösemittelhaltige Brandschutzsystem deutlich sensitiver auf variierende Aufheizgeschwindigkeiten reagiert und beide Brandschutzsysteme bei hohen Aufheizgeschwindigkeiten ihre größte thermische Schutzwirkung entfalten.
Aufbauend auf den Erwärmungsversuchen wurde in insgesamt 52 Laborversuchen eine systematische Analyse des Expansionsverhaltens bei variierenden Aufheiz- und Abkühlgeschwindigkeiten von Naturbränden durchgeführt. Ein entsprechend temperatur- und heizratenabhängiges Expansionsverhalten konnte hierbei identifiziert werden.
Komplementiert wurden die Laboruntersuchungen durch thermoanalytische (DSC und TGA) sowie morphologische Analysen (Digitalmikroskopie) der Porenstruktur und Porengrößenverteilung in Abhängigkeit der Aufheizgeschwindigkeiten und der Reaktionszustände der Brandschutzsysteme. Vor allem die Ergebnisse der morphologischen Untersuchungen liefern wichtige Erkenntnisse für die Formulierung eines temperatur- und heizratenabhängigen Materialmodells reaktiver Brandschutzsysteme.
In einem großmaßstäblichen Brandversuch an einem belasteten und unbelasteten Träger sowie einer unbelasteten Stütze wurde abschließend der Maßstabseinfluss auf das Materialverhalten der reaktiven Brandschutzsysteme untersucht und der Einfluss von geometriebedingten und mechanisch induzierten Rissen im Brandschutzsystem auf das Erwärmungsverhalten der untersuchten Bauteile im Zuge eines ausgewählten Naturbrandes analysiert und bewertet.

Mit dem Ziel den Parameterbereich der Untersuchungen zu erweitern, wurden die Ergebnisse der durchgeführten Laboruntersuchungen dazu verwendet, um einen numerischen Modellierungsansatz zur Beschreibung des Hochtemperaturverhaltens von reaktiven Brandschutzsystemen bei Naturbränden zu entwickeln. Realisiert wurde dies u.a. durch die Entwicklung eines Materialmodells für die Wärmeleitfähigkeit von reaktiven Brandschutzsystemen für die Aufheiz- und

Abkühlphasen von Naturbränden sowie durch eine subroutinenbasierte Beschreibung des Expansionsverhaltens.
Die Validierung der numerischen Modelle erfolgte anhand von klein- und großmaßstäblichen Erwärmungs- und Brandversuchen. Insgesamt konnte eine sehr gute Übereinstimmung zwischen den simulierten und gemessenen Temperaturen (an den Stahlbauteilen und in den Brandschutzsystemen) und der Ausbildung der expandierten Schichtdicken für den untersuchten Parameterbereich erzielt werden.
Die Erkenntnisse aus den experimentellen und numerischen Untersuchungen wurden in einem letzten Schritt dazu genutzt, um erstmalig eine Dimensionierungsmethode für die Trockenschichtdicke von reaktiven Brandschutzsystemen bei Naturbränden zu entwickeln.
Da die Vielzahl an möglichen Naturbränden eine rein versuchsbasierte Dimensionierung der Trockenschichtdicke, wie sie im Falle der aktuellen Zulassungspraxis erfolgt, erschwert, wurde eine MATLAB-basierte Berechnungsmethode entwickelt. Diese Methode basiert auf dem Wärmeleitfähigkeitsmodell, das für die numerischen Simulationen entwickelt wurde, und bedarf lediglich der Kenntnis des Expansionsverhaltens sowie der Morphologie der reaktiven Brandschutzsysteme. Das MATLAB-Programm kann zusätzlich für die Berechnung der Stahltemperaturen beliebiger Profile, Naturbrände sowie Brandschutzsysteme verwendet werden und stellt somit eine effiziente und zuverlässige Alternative zu den numerischen Simulationen dar. Dies belegen entsprechende Validierungsergebnisse. Aufgrund der freien Zugänglichkeit (Download unter: `www.stahlbau.uni-hannover.de`) ist eine beliebige Erweiterung des Programms möglich. Derzeit liegt dem Programm eine Datenbank von Materialkennwerten eines wasserbasierten Brandschutzsystems sowie stahlbauüblicher Profile zugrunde.

Die vorliegende Dissertation liefert insgesamt grundlegende Erkenntnisse über das thermomechanische Verhalten reaktiver Brandschutzsysteme bei Naturbrandeinwirkungen, präsentiert neue Methoden für die experimentelle Untersuchung des heizratenabhängigen Verhaltens von reaktiven Brandschutzsystemen und stellt neue Materialmodelle für eine zuverlässige Beschreibung des Expansions- und Erwärmungsverhaltens von reaktiven Brandschutzsystemen bei Naturbränden in numerischen Simulationen und vereinfachten Berechnungen bereit.

Schlagworte: Reaktive Brandschutzsysteme, Naturbrand, Aufheizphase, Abkühlphase, Wärmeleitfähigkeit, Morphologie, Expansion, Finite-Elemente Simulation, MATLAB-Berechnung, Dimensionierung, Trockenschichtdicke

---

Preface

This thesis was submitted to the Faculty of Civil Engineering and Geodetic Science, Leibniz University Hannover (Germany), as a partial fulfillment of the requirements to obtain the Doctoral degree (Dr.-Ing.). The work presented was carried out in the years 2015 - 2019 in the laboratory at the Institute for Steel Construction under the supervision of Prof. Dr.-Ing. Peter Schaumann.

Thesis objective

The objective of the work reported in this thesis is primarily to evaluate the thermal and mechanical performance of intumescent coatings in natural fires and to ensure a reliable design of the dry film thickness of the coatings in order to enable steel structures to withstand any exposure to fire.

Acknowledgement

The successful completion of my doctoral thesis marks the end of an important chapter in my life, which was dominated by many ups and only a few downs. I am extremely grateful for that. However, the fact that I was able to complete my doctoral thesis in such a successful way is not only my credit, but the result of the great support I received during my professional and private life.

Prof. Dr.-Ing. Peter Schaumann, head of the Institute for Steel Construction at the Leibniz University Hannover, is largely responsible for my successful development as a scientist. He encouraged me to work as research assistant at his institute while I was a student. I would like to thank him most sincerely for his deep trust, his unremitting support, his warm-hearted manner and for many years of great collaboration as doctorate supervisor. Even though my time as assistant has now come to an end, I will always be connected with the Institute for Steel Construction and the Leibniz University Hannover.
Working in science means, first of all, working together in a team. I am therefore very grateful to have been part of the team that worked on the IGF research

project 19176 N. Under the leadership of Prof. Dr.-Ing. Jochen Zehfuß, head of the Fire Safety Division at the Institute of Building Materials, Concrete Construction and Fire Safety at the Technical University of Braunschweig, we have been able to gather important knowledge about the behaviour of different fire protection materials in natural fires. Crucial to the success of the project was the excellent cooperation between the two institutes. Therefore, I would like to thank Prof. Dr.-Ing. Jochen Zehfuß not only for the great collaboration in the research project but also for taking over the co-authoring of my doctoral thesis.
The IGF research project 19176 N could only be initiated thanks to the funding from the Federal Ministry for Economic Affairs and Energy (BMWi) through the Arbeitsgemeinschaft industrieller Forschungsvereinigungen Otto von Guericke e.V. (AiF) and the Deutscher Ausschuß für Stahlbau e.V. (DASt). A further decisive reason for the success of the research project was the generous donation of materials from industry. I would like to express my sincere thanks to GOLDBECK Bauelemente Bielefeld SE, Rudolf Hensel GmbH and Sika Deutschland GmbH for their great support.
In addition, I would like to thank Prof. Dr.-Ing. Udo Nackenhorst, head of the Institute of Mechanics and Computational Mechanics, and Prof. Dr.-Ing. Nabil Fouad, head of the Institute of Building Physics, not only for chairing my doctoral examination and for being a member of the doctoral committee, but also for their shaping influence during the first semesters of my studies. I had the opportunity to learn a lot from them.
Behind every institute and its director there is usually a powerful team of scientists, technicians, laboratory assistants and administrative staff. This was also the case during my time at the Institute for Steel Construction. I enjoyed working with my colleagues very much and I am grateful that I was able to learn a lot from them. I would like to thank two colleagues in particular at this point. One of them is Dr.-Ing. Florian Tabeling. He already supported and encouraged me during my studies and gave me the opportunity to prove my abilities during my diploma thesis. Secondly, I would like to thank M.Sc. Maximilian Mund for proofreading my thesis and the numerous expert exchanges and discussions.

I would also like to express my sincere thanks to my brother, Dr. rer. nat. Eugen Weisheim. He has not only proofread my work, but has always offered me advice and support as my brother, my best friend and my greatest critic. Thank you very much!
Finally, I would like to thank two of the most important people in my life, my parents Tatjana and Viktor Weisheim. In 1996, they made the decision to leave their home country and come to Germany to offer my brother and me a better future. It was not easy for any of us. But as a family we succeeded. The fact that my brother and I have come so far is a great credit to our parents. Therefore, I dedicate this work to my parents and thank them from the bottom of my heart for their support and courage.

List of Symbols and Abbreviations

Latin Symbols

A_i	temperature-independent pre-exponential factor (1/s)
A_m/V	section factor of the unprotected steel member (m^{-1})
$A_p(\theta)/V$	section factor of the protected steel member (m^{-1})
c_a	temperature-dependent heat capacity of steel (J/(kgK))
$c_p(\theta)$	specific heat capacity (kJ/(kgK))
d_p	dry film thickness (m)
$E_{fi,d}$	design effect of actions including effects of thermal expansion
E_i	activation energy (J/mol)
f_β	current values of the predefined field variables (-)
f_β^I	initial values of the predefined field variables (-)
k_i	reaction rate constant (1/s)
k_{sh}	correction factor for the shadow effect (-)
L	foam thickness (m)
n	x, y or z-direction in Cartesian coordinates (-)
n	number of elements discretising the char thickness (-)
R	universal gas constant (8.314 J/(K· mol))
$R_{fi,d,t}$	corresponding design resistance in the fire situation
T	absolute temperature (K)
t_0	dry film thickness at ambient temperature (mm)
$t(\theta)$	char thickness at char temperature θ (mm)
t_i	char thickness of a single element at char temperature θ (mm)
$t_p(\theta)$	char thickness of the coating (m)
V/A_p	reciprocal of the section factor (m)
V^{gas}	volume of gas trapped inside the char (mm^3)
V^{tot}	total volume of the formed char (mm^3)

Greek Symbols

α	thermal expansion coefficient at char temperature θ (1/K)
$\alpha(\theta, f_\beta)$:	thermal expansion coefficient (1/K)
$\alpha(\theta)$	degree of conversion (-)
α_c	convective heat transfer coefficient ($\mathrm{W/(m^2K)}$)
α_i	thermal expansion coefficient at increment i (1/K)
$\boldsymbol{\alpha_{T,n}}$	vector of thermal elongation coefficients (1/K)
β	extinction coefficient (m^{-1})
$\Delta\theta_\mathrm{a,t}$	change of steel temperature (°C)
$\Delta\theta_a$	temperature increase of the unprotected steel member (°C)

$\Delta\theta_i$	temperature change at increment i (°C)
$\Delta m(\theta, \dot{\theta})$:	mass change (%)
Δt	time increment (sec)
δ	mean value of the pore size (m)
$\delta(\theta)$	pore size at temperature θ (m)
$\delta m(\theta)$	mass loss (wt%)
$\delta V(\theta)$	volume change (%)
ε_a	surface emissivity of the steel member (-)
ε_f	emissivity of the fire (-)
ε^{th}	thermal strain (-)
$\boldsymbol{\varepsilon_{T,n}(\theta)}$	vector of logarithmic thermal strains (-)
ϵ	expansion factor (-)
ϵ_n	expansion factor in n-direction (-)
$\epsilon(\theta)$	temperature-dependent expansion factor (-)
$\epsilon(\theta, \dot{\theta})$	temperature and heating rate-dependent expansion factor (-)
ϵ_i	expansion factor at increment i (-)
ϵ_{i-1}	expansion factor at increment $i-1$ (-)
ζ	weighting factor (-)
$\eta_{\mathrm{p}}(t)$	efficiency parameter (-)
θ	absolute temperature of the char (K)
θ^0	reference temperature for thermal expansion (°C)
θ^I	initial char temperature (°C)
$\dot{\theta}$	heating rate (K/s)
θ_1	temperature at heat flow entrance (K)
θ_2	temperature at heat flow exit (K)
θ_0	initial char temperature (°C)
θ_i	char temperature at increment i (°C)
θ_{i-1}	char temperature at increment $i-1$ (°C)
$\theta_{\mathrm{a,t}}$	steel plate temperature at the back side (°C)
$\theta_{\mathrm{a,\ protected}}$	temperature of the protected steel element (°C)
$\theta_{\mathrm{a,\ unprotected}}$	temperature of the unprotected steel element (°C)
θ_{gas}	temperature of the surrounding gas phase (°C)
θ_{t}	surface temperature of the coating/char (°C)
$\lambda_{\mathrm{p,t}}$	effective thermal conductivity (W/(mK))
$\lambda_p(\theta)$	thermal conductivity of the coating (W/(mK))
$\lambda_{\mathrm{rad}}(\theta)$	radiative part of heat conduction within a pore (W/(mK))
$\lambda(\theta)$	thermal conductivity of the char at temperature θ (W/(mK))
$\lambda^{air}(\theta)$	thermal conductivity of air at temperature θ (W/(mK))
$\lambda^{foam}(\theta)$	thermal conductivity of the foam structure (W/(mK))
λ^{solid}	thermal conductivity of the solid material (W/(mK))
$\xi(\theta)$	current value of the measured property at temperature θ
ξ_{i}	initial value of the measured property
ξ_{r}	residual value of the measured property

ρ_0	density at room temperature (kg/m^3)
$\rho(\theta)$	temperature-dependent density (kg/m^3)
ρ_a	density of steel (kg/m^3)
ρ_solid	density of the solid inside the two-phase material (kg/m^3)
$\rho_\mathrm{tot}(\theta)$	total density of the two-phase material (kg/m^3)
σ	Stefan-Boltzmann constant $5.67037 \cdot 10^{-8}$ (W/(m^{2}K^4))
$\tau(L)$	transmissivity of the foam structure as a function of foam thickness (-)
ϕ	configuration factor (-)
$\phi(\theta)$	porosity (-)

Abbreviations

APP	ammonium polyphosphate
DFT	dry film thickness
DSC	differential scanning calorimetry
DTG	differential thermal gravity
ETA	European Technical Assessment
EVA	ethylene vinyl acetate
FTIR	Fourier Transform Infrared Spectroscopy
GUI	graphical user interface
HRR	heat release rate
IKP	invariant kinetic parameters
LOI	limiting oxygen index test
MEL	melamine
MMT	montmorillonite
OMMT	organic-modified montmorillonite
PAL	palygorskite
PER	pentaerythritol
PP	polypropylene
PUR	polyurethane
PVA	polyvinyl alcohol
PVAc	polyvinyl acetate
SEP	sepiolite
TGA	thermogravimetric analysis
TiO_2	titanium dioxide
VOC	volatile organic compound

Contents

1 Introduction

The first chapter exemplifies the application area of intumescent coatings and highlights the motivation and objectives of the research conducted in this thesis.

Contents

1.1 Motivation

Intumescent coatings (ICs) are used whenever filigree and architecturally attractive steel structures need to fulfill fire resistance requirements. Due to their thin dry film thickness intumescent coatings combine both the maintenance of the architectural appearance of the steel structure and the required fire resistance. An example for such an application is given in Figure 1.1. Here, the intumescent coating was applied on a dissolved steel structure that was combined with a glass facade. Due to the transparency of the structure only inconspicuous fire protection materials, such as intumescent coatings, could fullfil the fire resistance requirements and remain the optical appearance of the structure unaffected at the same time.

Figure 1.1: Government building of North Rhine-Westphalia with a glass facade and a steel structure with an intumescent coating that ensures a fire resistance rating of 30 minutes (built in 2002, photo: pinkarchitektur)

At room temperature intumescent coatings remain inert and therefore can hardly be distinguished from conventional corrosion protection systems. However, intumescent coatings are designed to protect steel structures in fire due to their particular behaviour. When being exposed to high temperatures, the inert coating expands multiple times the original thickness to form a highly insulating char with low thermal conductivity that protects the underlying steel substrate from rapid heating.
Intumescent coatings are usually composed of four ingredients: an acid source, a carbon source, a blowing agent and a polymer binder (Jimenez et al. 2006*a*, Weil 2011). To increase the insulation efficiency of the coating, miscellaneous additives are additionally used.
The fire protection performance of intumescent coatings is dominated by multiple chemical and physical processes, which take place in parts simultaneously. When the surface temperature of the coating reaches a certain value during the heating phase, the binder inside the coating begins to melt resulting in a highly viscous liquid. During this time, the blowing agent decomposes by releasing gaseous products with low thermal conductivity. These non-flammable gases are trapped inside

the liquid melt to form different-sized bubbles (Camino & Costa 1986). Since the liquid melt contains polyol ester, a carbonised foam is formed when the polyol ester dehydrates during further heating (Vandersall 1971). The process of nucleation (formation of bubbles) is finally completed by the reaction stage of solidification resulting in a multicellular and heat insulating foam that acts as an insulating layer between the heat source and the underlying steel structure.
As intumescent coatings are non-standardised products, the coatings are introduced to the German market by general technical approvals (*German:* allgemeine bauaufsichtliche Zulassung, abZ), general design certifications (*German:* allgemeine Bauartgenehmigung, aBG) or European Technical Assessments (ETAs).
To receive a national or European approval, the products need to pass certain examinations that are regulated at national and European level. In Germany, the approval tests are defined in the approval principles (DIBt 1997) of the German Institute for Building Technology (*German:* Deutsches Institut für Bautechnik, DIBt). However, on the European level the approval tests are defined by the European Assessment Document EAD-50402-00-1106 (2017). In both cases the insulating efficiency of intumescent coatings is verified by small scale fire tests. Within these fire tests coated steel panels with a nominal thickness of 5 mm are exposed to the standard fire curve. To assess the insulation efficiency of the intumescent coatings, the temperature of the coated panels is measured during the fire exposure. The time at which the panel temperature reaches a mean value of 500 °C is recorded and is used for evaluation purposes.
Besides the small-scale fire tests on coated panels, additional fire tests on loaded and unloaded beams and columns are prescribed in the national and European approval principles. These tests are performed to give guidelines for the design of the dry film thickness (DFT) of intumescent coatings as a function of section factor and desired steel profile temperature. Based on the required fire resistance class, the values for the dry film thickness are given for fire resistance times of 30, 60, 90 or 120 minutes.
Except the smouldering fire according to EN-1363-2 (1999), all fire tests prescribed in the approval principles, especially those for the design of the dry film thickness, are based on the standard fire curve. Therefore, the assessment of the thermal performance of intumescent coatings is solely related to this fire scenario.
Due to the increasing use of performance-based design methods for steel structures in fire, it becomes more and more important to assess the fire protection performance of intumescent coatings in case of natural fires. As coatings are nowadays only assessed for the fire exposure according to the standard fire curve, there is a lack of scientific evidence regarding the thermal performance of intumescent coatings for fire scenarios that deviate from the standard fire. Moreover, harmonised rules (EN-1993-1-2 2010) provide already methods to design the ultimate limit state of steel structures due to natural fires although the performance of intumescent coatings in natural fires is largely unknown. As the evolution and propagation of natural fires is essentially based on the fire load and ventilation conditions inside a building, natural fire scenarios can show arbitrary regimes as well as heating and

cooling rates. Facing this fact and keeping in mind that the reaction of intumescent coatings is thermally activated, the variety of natural fires makes it even more challenging to evaluate the influence of natural fires on the fire protection performance of intumescent coatings. Nevertheless, a thorough understanding of the fire protection performance of intumescent coatings in natural fires is fundamental for a save and reliable design of coated steel structures in natural fires.

1.2 Objectives

Although intumescent coatings are evaluated and approved solely on the basis of the standard fire curve, more and more construction measures and conversions of existing buildings are realised on the basis of performance-based design methods, in which coated steel structures are designed to withstand a natural fire. However, essential knowledge regarding the deviant thermal behaviour of intumescent coatings in case of natural fires is lacking. As expert reports are not expedient in most cases due to the lack of knowledge, designers and engineers are nowadays faced with numerous problems. For example, the values for the dry film thickness of intumescent coatings given in the technical approvals deemed to be only valid for the standard fire curve. Even more, due to the unknown fire protection performance of intumescent coatings in natural fires, it is questionable if the existing method for the design of the dry film thickness is suitable in case of natural fires. Therefore, no reliable design method for the dry film thickness of intumescent coatings yet exists.
In addition, the variety of natural fires makes it quite difficult to evaluate the fire protection performance of intumescent coatings and determine the required dry film thickness experimentally with regard to the design temperature of a steel structure and its members. Therefore, suitable examination methods for the fire protection performance of intumescent coatings and reliable methods for the design of the dry film thickness are essential to handle the performance-based design of coated steel structures.
Facing this fundamental problems, the main objective of this thesis is to evaluate the thermal and mechanical performance of intumescent coatings in natural fires and, therefore, to ensure a reliable design of steel structures. The main objective of the thesis can be subdivided into the following items:

(1) Gain knowledge of the influence of various heating and cooling rates in natural fires on the fire protection performance of intumescent coatings compared to the insulating behaviour due to the standard fire.
(2) Detailed analysis of the change in expansion behaviour and morphology of intumescent coatings due to the variation in heating and cooling rates and maximum temperatures.
(3) Identification of relevant chemical and physical processes that are decisive for the heating rate-dependent behaviour of intumescent coatings.

(4) Determination of material properties on the basis of experimental investigations and development of material models for finite element simulations of the thermal behaviour of intumescent coatings in natural fires. These simulations allow for both further investigations of the fire protection performance of intumescent coatings due to the extension of the parameter range and the provision of calculation methods for engineers to evaluate the insulating performance of intumescent coatings within the performance-based design.
(5) Derivation of a suitable method for the design of the dry film thickness of intumescent coatings for heating and cooling conditions in natural fires.

All the outlined objectives have one crucial challenge in common. As natural fires can show a large range in heating and cooling rates as well as in maximum temperature, it is quite impossible to perform experimental and numerical investigations by taking all variants of natural fires into account. Therefore, systematic substitute procedures are needed to cover the spectrum of natural fires.

1.3 Structure

In order to meet the objectives and to investigate the thermal performance of intumescent coating in natural fires, a multi-stage approach will be realised in the scope of this thesis.
In the first step, the composition of intumescent coatings and their heat induced reaction mechanisms are described. Based on this, evaluation methods of the fire protection performance of intumescent coatings are discussed with regard to their transferability to natural fires. In this context, a comprehensive literature review on the thermal performance of intumescent coatings and their single ingredients is conducted. The analysis of the current state of the art is completed by the evaluation of the experimental-based design method of the dry film thickness of intumescent coatings and its applicability to natural fires.
In order to verify the validity of already existing material models and simulation methods for the heating behaviour of intumescent coatings, the latest state of research is presented and evaluated (see chapter 2).
In the next step, the literature research is followed by own experimental investigations. Besides small-scale fire tests on coated steel plates, expansion analyses, morphology analyses as well as analyses of the mass loss and heat storage capacity are performed. Due to differences in sensitivity, a solvent-borne and a waterborne intumescent coating are investigated. For both, parameters such as section factor, dry film thickness as well as fire exposure are varied. In order to cover the spectrum of natural fires, the fire exposure is replicated during the analyses by constant heating rates, natural cooling rates and varying maximum temperatures. For reasons of comparison, the small-scale fire tests and expansion analyses are also performed for a fire exposure according to the standard fire curve. As no reliable procedures exist to investigate the fire protection performance and the expansion behaviour

of intumescent coatings in natural fires, new experimental setups are developed in the scope of this thesis.
In order to evaluate the influence of shape- and stress-induced cracks in the formed char of intumescent coatings on the heating behaviour of structural members, a large-scale fire test is performed. With the help of this fire test, scale effects on the thermal performance and the morphology of intumescent coatings are also addressed (see chapter 3).
The large-scale and small-scale fire tests are used to validate three-dimensional thermomechanically coupled simulations that are developed on the basis of laboratory tests and literature review. In order to describe the high-temperature behaviour of intumescent coatings in case of natural fires, a thermal conductivity model for intumescent coatings in heating and cooling is developed. In addition, a subroutine is programmed to describe the temperature-dependent expansion behaviour of intumescent coatings with respect to changes in heating and cooling rates.
With the aim to extend the parameter range, the new developed modelling approach is used to perform parameter studies to identify the key parameters and the fire exposure that lead to fire protection performances of intumescent coatings that deviate significantly from the performance due to the standard fire. These parameters and fire exposure can be understood as thresholds for the evaluation of intumescent coatings in natural fires (see chapter 4).
In order to ensure a reliable design of coated steel structures in natural fires, in the last step, a design method is developed based on the fundamental findings of the experimental and numerical investigations. To circumvent the high effort of experimental- or simulation-based evaluation methods, a MATLAB-based calculation approach is developed that combines both a reliable calculation of the heating and cooling behaviour of coated steel structures and a performance-based design of the dry film thickness of intumescent coatings. Due to its fast and accurate operating principle, the MATLAB programme offers a great opportunity for the transfer of knowledge into practice. Nevertheless, it is worth mentioning that the new developed design approach serves as supplement to the already existing method and does not claim to replace it (see chapter 5).
With regard to the formulated motivation and objectives, the research conducted in this thesis is finally evaluated. Based on the evaluation results, conclusions are drawn and recommendations for future research and transfer services are given (see chapter 6).

2 State of the Art

The second chapter gives an overview of the latest research on intumescent coatings in natural fires and the current design approaches of steel structures in case of fire.

Contents

2.1 Introduction

The following literature review serves as a basis for the research carried out in this thesis. First, the application area, the approval procedure and the composition of intumescent coatings are explained. Subsequently, a detailed overview of the functionality and heat-induced reaction processes in intumescent coatings is given. Once a global understanding on the reaction behaviour of intumescent coatings is reached, a detailed review on experimental investigations of the fire protection performance of intumescent coatings due to fire exposures deviating from the standard fire is given. In order to understand the heating rate-dependent behaviour of intumescent coatings and their different sensitivities, a comprehensive data analysis of thermoanalytical investigations on single ingredients known in literature is performed. As numerical simulations are crucial for the detailed understanding of the thermal behaviour of intumescent coatings, the literature review is extended to material models and simulation methods that were recently developed.
With the aim to underline the discrepancy between the current practice and the state of the art, a brief overview of the design of steel structures in fire with respect to the contribution of intumescent coatings to the fire resistance is given. In this context, relevant design fires are introduced and evaluated with regard to the effect on the fire protection performance of intumescent coatings. Based on the literature review, hypotheses are formulated serving as orientation for the research that is carried out in this thesis.

2.2 Intumescent Coatings

2.2.1 Application Area

Intumescent coatings are used worldwide as fire protection materials in industry and the construction sector (see Figure 2.1, left). Due to their variable composition, intumescent coatings are not only used for steel but also for timber and concrete structures. However, steel structures are still the main application area (market share: 75 %) for intumescent coatings (see Figure 2.1, right).
According to Global Market Insights (2018) over 16,000 tons of intumescent coatings were used in the European construction sector in 2018. Worldwide, the intumescent coatings market is forecasted to grow from an estimated size of EUR 1,017 billion in 2018 to EUR 1,255 billion by 2023 according to the report of Markets & Markets Research (2019). In 2018 the APAC (Asia Pacific) states had the largest market share with 49.8 %, followed by the North American (24.3 %) and the European market (18.4 %).
Despite their thin dry film thickness intumescent coatings are able to ensure nowadays fire resistance ratings of 30 to 120 minutes. Therefore, the field of application for intumescent coatings is wide. In Germany intumescent coatings were already

used in the 1970s. A famous example for the use of intumescent coatings is the Olympia Stadium in Munich (see Figure 2.2, left). During this time the coatings were solely applied in interior areas, were based on solvents and their fire resistance rating was limited to 30 minutes. In the following two decades the solvent-borne coatings were further developed. The amount of solvents was significantly reduced and the range of colours for the topcoats was widened.

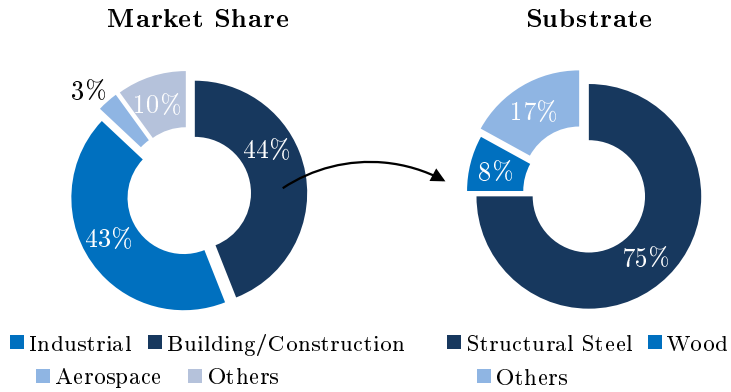

Figure 2.1: Intumescent coatings market share by application and substrate in 2018 according to Markets & Markets Research (2019)

In the 1990s waterborne intumescent coatings were developed and introduced to the German market. From this point in time, fire resistance ratings of 60 minutes were realised while the required amount of material could be reduced due to new generations of ingredients. For this reason, topcoats were no longer required for the application of intumescent coatings in interiors.
At the beginning of the 2000s a further development of the coatings took place. Through this development the fire resistance rating of solvent- and waterborne intumescent coatings was increased to 90 minutes. Therefore, projects with high demands such as the Post Tower in Bonn (see Figure 2.3, left) and the BMW World in Munich (see Figure 2.2, right) could be realised.
Due to the required drying times, solvent- and waterborne coatings are mostly applied on site by airless spraying. With the development of epoxy resin-based coatings in the following years the application process of intumescent coatings shifted to the factories. Here, the coatings are applied under controlled conditions resulting in a high level of prefabrication and product quality. As the steel elements, however, are supplied to the construction site in a coated state, high demands on the drying behaviour and the robustness of the coatings have to be met due to the transportation and the assembly on site. However, since epoxy resin-based intumescent coatings meet all these requirements, construction projects such as the Adidas Laces (see Figure 2.3, middle) and the Adidas Arena in Herzogenaurach (built in 2018) could be realised in the last years.
With the increasing development of intumescent coatings and their product classes

(see subsection 2.2.3), the application of intumescent coatings in the construction sector experienced a strong increase in the last years. In addition to office and administrative buildings, football stadiums and sports halls, intumescent coatings are now also being used in logistics halls and airport buildings such as the maintenance hangar of Lufthansa (Figure 2.2, middle) and The Squaire in Frankfurt (Figure 2.3, right). Especially the latest projects that were realised in Germany illustrate how diverse the application area of intumescent coatings is and how important these fire protection materials are for architectural structures. As shown by the examples, intumescent coatings allow indoor and outdoor use, are capable to preserve the architectural appearance of structures and allow a versatile design due to different topcoat colours. Therefore, from this perspective, there is no comparable alternative to these products.

Figure 2.2: Examples for the application of intumescent coatings. Left: Olympia Stadium Munich (built in 1971, photo: Olympiapark München GmbH), middle: Maintenance Hangar Lufthansa Frankfurt (built in 2007, photo: gmp Architekten) and right: BMW World Munich (built in 2010, photo: Getty Images)

However, the examples illustrate another fundamental aspect. In many cases of the presented projects a fully developed compartment fire cannot occur due to the design of the buildings (open spaces with low fire load). Instead of compartment fires, it is more realistic that natural fires or local fires occur. Nevertheless, national building regulations ask for fire protection requirements, e.g. fire resistance ratings of 30 to 90 minutes, which are directly linked to the standard fire curve that is deemed to describe the propagation of a fully developed compartment fire.

Figure 2.3: Examples for the application of intumescent coatings. Left: Post Tower Bonn (built in 2003, photo: Claus Boeckh), middle: Adidas Laces Herzogenaurach (built in 2011, photo: kadawittfeldarchitektur) and right: The Squaire Frankfurt (built in 2011, photo: fiylo)

As a consequence, a discrepancy between the object-specific fire scenario and the fire scenario that is assumed during the licensing procedure arises. In those cases where the object-specific fire scenarios deviate significantly from the compartment fire, steel structures can show a very different heating and load-bearing behaviour. In the meantime, regulation bodies and engineers in Europe and in Germany as well have noticed this discrepancy and offered a solution for this problem. With the help of performance-based design methods structures can be design close to the present boundary conditions and, therefore, individually. In contrast to the conventional design, the fire scenarios in the performance-based design are calculated individually on the basis of the present space dimensions, ventilation conditions and of course fire loads. Thus, performance-based design methods are based on natural fire scenarios. As long as steel structures are unprotected, the new design methods offer a great opportunity for the evaluation of the heating and load-bearing behaviour of steel structures in case of natural fires. However, if the steel structures are protected with intumescent coatings or any other fire protection material, the design methods cannot be readily applied due to the lack of knowledge regarding the thermal behaviour of the materials in natural fires and due to missing methods for the design of their required dry film thicknesses. This missing accordance between the design regulations for structures and the evaluation of fire protection materials is caused by the national and European approval procedures, as explained in the following.

2.2.2 Approval Procedures in Europe and Germany

Intumescent coatings are non-standardised products. In order to use these products in the construction sector, intumescent coatings need to be officially approved. In Germany, this is done by national regulations such as general technical approvals (*German:* allgemeine bauaufsichtliche Zulassung, abZ) or European Technical Assessments (ETAs). Since assessment documents have not the same status as approvals, ETAs are nationally incorporated in general design certifications (*German:* allgemeine Bauartgenehmigung, aBG) to introduce European products to the German market (see Figure 2.4). In this way, both national and European products can be used as fire protection materials in national construction projects. In principle, the German approval procedure distinguishes between product-related and construction-related approvals. As long as a single product is to be approved, this is done by a general technical approval or a European Technical Assessment in combination with an aBG, as already mentioned. On the other hand, if several products are combined to form a construction (*German:* Bauart), a general design certification (aBG) or a project-related design certification (vBG) is granted (see Figure 2.4). However, in the case of intumescent coatings, the approval procedure is limited to general technical approvals and European Technical Assessments.
In order to receive a general technical approval or a European Technical Assessment, intumescent coatings need to pass certain examinations that are regulated

at the national and European level. In Germany, the approval tests are defined in the approval principles (DIBt 1997) of the German Institute for Building Technology (*German:* Deutsches Institut für Bautechnik, DIBt). On the European level, however, the approval tests are defined in the European Assessment Document EAD-50402-00-1106 (2017) published by the European Organisation for Technical Assessment (EOTA). In both cases the insulating efficiency of intumescent coatings is verified by small scale fire tests. Within these fire tests coated steel panels with a nominal thickness of 5 mm are exposed to the standard fire curve according to DIN-4102-2 (1977) and EN-1363-1 (2012) respectively.

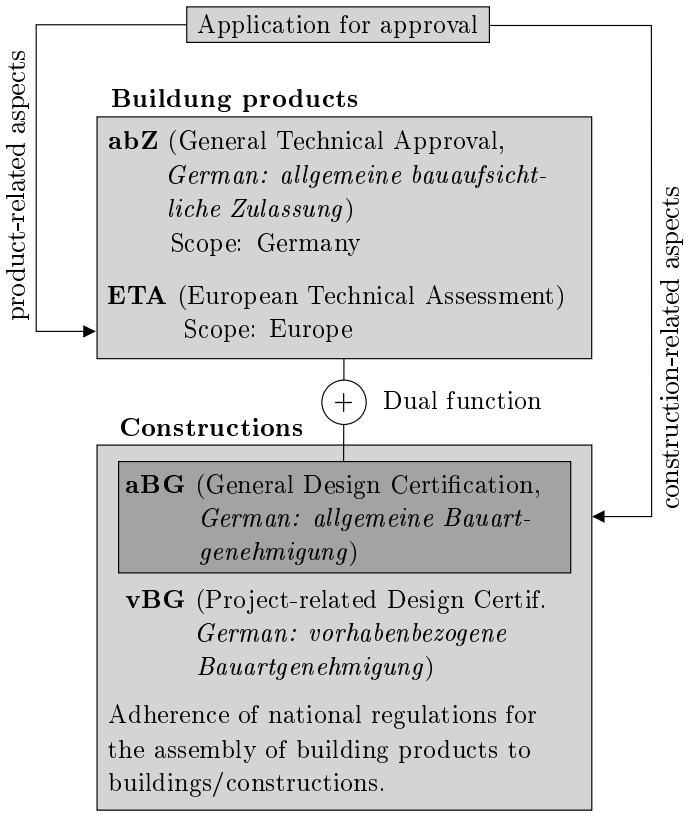

Figure 2.4: Approval procedure for building products and constructions in Germany according to DIBt (2017)

To assess the insulation efficiency of the intumescent coatings, the temperature of the coated panels is measured during the fire exposure. The time at which the panel temperature reaches a mean value of 500 °C is recorded and used for evaluation purposes. Significant differences between the national and European procedure in this context do not exist. This also applies to the prescribed fire tests on beams and columns. Here, the fire protection performance of intumescent coatings is evaluated on loaded and unloaded I-profiles and hollow sections that are exposed

to a three-sided or four-sided fire exposure according to the standard fire curve. For both the national and European approvals these tests serve as a basis for the design of the dry film thickness of intumescent coatings with respect to the required fire resistance time, the section factor (A/V) and the critical steel temperature. In national approvals the dry film thickness is only defined for a critical temperature of 500 °C. In European approvals, on the other hand, the dry film thickness is defined for a temperature range of 350 - 750 °C. This is possible due to different evaluation methods of the test results (such as the graphical approach, the differential formula analysis with variable λ, the differential formula analysis with constant λ and the numerical regression analysis) that are given in EN-13381-8 (2013).

Table 2.1: Application of intumescent coatings with respect to the profile type and mechanical loading

loading	I	□	○	●
compression	no limit	no limit	no limit	-
bending	no limit	-	-	-
tension	$\mu_{fi} \leq 0.50$	no regulation	$\mu_{fi} \leq 0.60$*	$\mu_{fi} \leq 0.65$*

* product-specific limitation of the utilisation factor according to the national approval (abZ) Z-19.11-2194

On the basis of the national and European approval tests, intumescent coatings are nowadays approved to be applied on I-profiles and hollow sections under compression and I-profiles under bending as listed in Table 2.1. For both loading situations, compression and bending, no limitations of the utilisation factor are prescribed. Although possible, square and circular hollow sections under bending are in most cases not part of national or European technical approvals due to a lack of application.
As the beam and column tests that are prescribed in the national and European approval procedures are not suitable to evaluate the influence of pure tension loads on the fire protection performance of intumescent coatings, numerical investigations were performed by Hothan (2010) on behalf of the German Institute for Building Technology. Comparing the strain state of I-profiles under bending and tension, Hothan derived a limit for the utilisation factor of I-profiles under pure tension. In order to ensure the application of intumescent coatings on I-profiles under tension, Stopp & Proschek (2011) followed the recommendation of Hothan and limited the utilisation factor to $\mu_{fi} \leq 0.50$ (see Table 2.1). Although no explicit tests are performed, intumescent coatings with a valid approval for beams and columns are also allowed to be applied on I-profiles under tension based on the investigations of Hothan. However, the application of intumescent coatings on hollow sections and solid steel bars under tension could not be enabled through this approach due to a deviant behaviour of the char that was expected.
With the introduction of the revised draft of EN-13381-10 (2018) a new test methodology for the evaluation of the fire protection performance of intumescent

coatings on solid steel bars was introduced. However, as the proposed test procedure assumes normally an unloaded condition for the steel bars, there is a disagreement between European and German approval procedures. This is due to experimental investigations of Hothan & Häßler (2015) and Häßler (2016) that were conducted in the last years. The research group found out that the stickability of their investigated coating applied on steel bars was significantly affected by mechanical loading and the curvature of the bars. Since the EN-13381-10 (2018) does not take this research findings entirely into account, Germany prohibits the application of the approval procedures given in the EN-13381-10 (2018). Nevertheless, the application of intumescent coatings on solid steel bars and circular hollow sections under tension is, however, possible in Germany, provided that all tests are performed under loading (see Table 2.1).

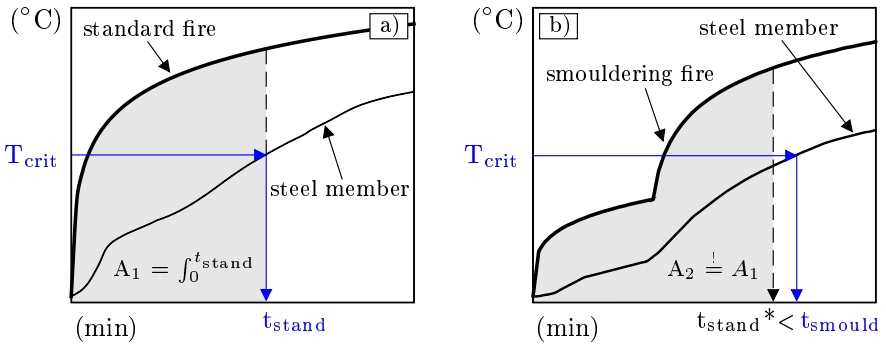

Figure 2.5: Evaluation procedure of the fire protection performance of intumescent coatings due to a smouldering fire according to DIBt (1997)

With the performed investigations additional to the already existing approval procedures, the scope of application has been significantly expanded for intumescent coatings within the last years. Nevertheless, the evaluation results and the data given in the national and European approvals are only valid for compartment fires since all approval tests are performed based on the standard fire curve.
The smouldering curve is the only fire scenario that is described in the national and European approval procedures that can be used to evaluate the effect of non-standard fires with lower temperature developments in the initial state on the fire protection performance of intumescent coatings. However, the evaluation procedure differs considerably between the national and European Guidelines. At the national level, the fire protection performance of intumescent coatings due to the smouldering fire is evaluated based on the time that is needed to reach a critical steel temperature (T_{crit}) for both the smouldering fire and the standard fire curve. Assuming that the area under the standard fire (A_1) and the smouldering fire curve (A_2) are equal, the time to reach the critical steel temperature due to the smouldering fire curve (t_{smould}) has to be greater than the equivalent time to reach the critical temperature due to the standard fire curve (t_{stand}*) as depicted

in Figure 2.5. As the areas under the fire curves ($°C \cdot min$) do not have any physical meaning such as the amount of heat (J), the suggested principle of equivalency is not appropriate and does not lead to reliable results.

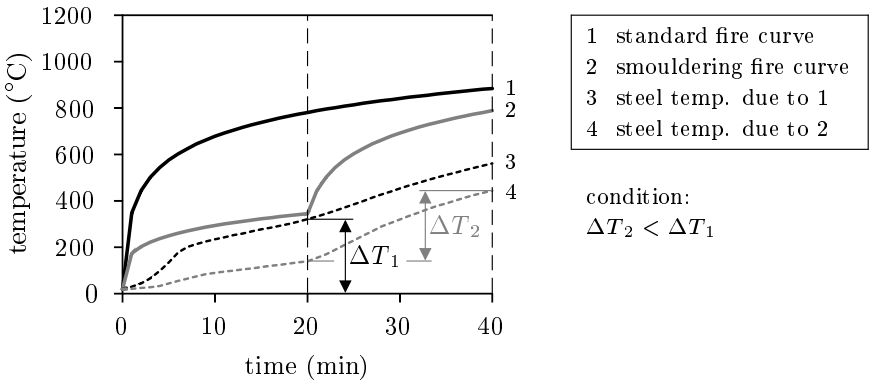

Figure 2.6: Evaluation procedure of the fire protection performance of intumescent coatings due to a smouldering fire according to EN-13381-8 (2013)

On the European level, on the other hand, a more convincing evaluation method is proposed (see Figure 2.6). Since the part of the smouldering fire curve between 20 and 40 minutes is equal to the standard fire curve in the first 20 minutes, the effect of smouldering (0 - 20 minutes) is evaluated by the comparison of the temperature increase of a coated steel panel due to the standard fire (ΔT_1) after 20 minutes and the smouldering fire curve (ΔT_2) after 40 minutes. Based on this comparison, intumescent coatings deemed to be less sensitive to smouldering if the increase in temperature due to the pre-heating by the smouldering fire (ΔT_2) is less than the temperature increase due to the standard fire curve (ΔT_1).
The evaluation methods that are based on the smouldering fire are the only methods that are given in the national and European Guidelines that deal with a non-standard fire exposure. However, these evaluation methods are not capable to assess the effect of natural fires on the fire protection performance of intumescent coatings due to the limitation to the smouldering fire curve. Since the evaluation methods are only informative and not directly prescribed in the approval procedures, both methods are only considered as indicators for the sensitivity of intumescent coatings due to smouldering fires. Therefore, a transfer of the evaluation results to natural fires and their effect on the expansion behaviour, the morphology, the thermal conductivity characteristics and the design of the dry film thickness of intumescent coatings is impossible. Taking this as a basis, national and European Guidelines do not provide any reliable evaluation method for intumescent coatings in natural fires, so far.

2.2.3 Product Classes and Layer Structure

Due to the historical development of intumescent coatings (see subsection 2.2.4) three different product classes are currently used in the construction sector: waterborne, solvent-borne and epoxy resin-based intumescent coatings. All three belong to the group of wet coatings. Despite the new development of epoxy resin-based intumescent coatings, water- and solvent-borne intumescent coatings are still mainly used in the European and German market. However, due to the steady tightening of VOC (volatile organic compound) limits for the control of air pollution, the market share of solvent-borne intumescent coatings will decrease in the future more and more.
In addition to the well established wet coatings, a new product family on the basis of the powder technology is currently under development. First investigations on the composition and the production of intumescent powder coatings were performed by Horacek (2014) and Jiao et al. (2015). Their feasability analysis proved that intumescent powder coatings can be pressed into sheets using high temperature press machines without thermal activation of the reactive components. Also the application and the curing of the intumescent powder could be demonstrated afterwards. However, more extensive investigations are required until intumescent powder coatings can be used on the industrial scale. Therefore, intumescent powder coatings are not part of this thesis. However, the powder technology represents an innovative solution for steel constructions and has to be brought into focus in the near future.

Table 2.2: Layer structure of intumescent coatings based on the product class and the environmental condition (Z_2: internal condition with low humidity, Z_1: internal condition with high humidity, Y: semi-exposed condition, X: exposed condition)

Condition	Waterborne	Solvent-borne	Epoxy resin-based
type Z_2	○ ●	○ ●	○ ●
type Z_1	○ ● ●	○ ●	○ ●
type Y	○ ● ●	○ ● ●	○ ●
type X	○ ● ●	○ ● ●	○ ● ●

Description: ○ primer, ● reactive coating, ● top-coat

Despite their diversity, all intumescent coatings that are available in the European and German market have the same layer structure. Usually, intumescent coating systems consist of three layers: a primer, a reactive coating and a topcoat. While the primer acts as a corrosion inhibitor and adhesion agent, the topcoat protects the reactive coating against environmental influences, such as ultraviolet (UV) radiation, high humidity, sprayed water etc. and allows a versatile design due to different colours. The fire protection performance, on the other hand, is solely ensured by the reactive part of the intumescent coating systems.

Since environmental conditions can be very different, a topcoat is not always required. Therefore, in Table 2.2 typical layer structures are given as a function of product class and environmental condition according to the EAD-50402-00-1106 (2017). Due to their water solubility, waterborne intumescent coatings require a topcoat when being exposed to high humidity (type Z_1) or spray water (type Y and type X). Epoxy resin-based intumescent coatings, on the other hand, are less susceptible to environmental influences and, therefore, can be used even in semi-exposed conditions (type Y) without any topcoat.

2.2.4 Historical Development and Main Ingredients

The reactive part of intumescent coating systems (here declared as intumescent coating) is basically composed of four main ingredients: an acid source, a carbon donor, a blowing agent and polymer binders (Jimenez et al. 2006*a*, Weil 2011). In order to increase the insulation efficiency of intumescent coatings, several additives are used additionally. The colouring of intumescent coatings is ensured by pigments. The schematic composition of single ingredients that are typically used for intumescent coatings is illustrated in Figure 2.7. The dashed lines between the main ingredients (acid source, carbon donor and blowing agent) represent the chemical interactions that take place during the thermal induced reaction of intumescent coatings. The solid lines, on the other hand, are used in combination with the polymer binder to illustrate its function as connecting element.

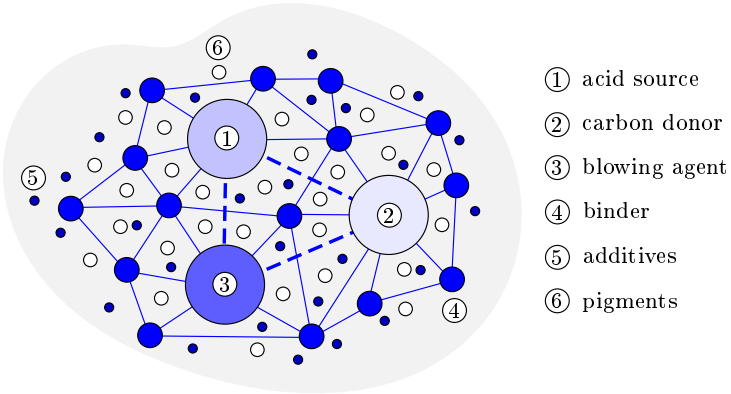

Figure 2.7: Schematic illustration of single ingredients in intumescent coatings

Intumescent coatings have undergone a great development since their invention. In addition to the ever-increasing complexity of the composition, especially the development of raw materials has contributed to a significant improvement of intumescent coatings. In order to document this development, patents of the last 70 years were analysed in terms of composition and function of main ingredients. An extract of selected patents is given in Table 2.3.

Table 2.3: Composition of essential ingredients of intumescent coatings indicated by (wt%)

Patent	Acid source	Carbon donor	Blowing agent	Binder	Pigments	Additives
Jones (1948) [1,2,a]	Mono-ammonium phosphate (60.4) Boric acid (1.8)	Starch (7.2)	Urea (13.5)	Paraformaldehyde (10.8)	Titanium-barium (3.6)	-
Nielsen (1952) [1,a]	Polyphosphorylamide (9.7)	Pentaerythritol (9.7) Resorcinol (9.7)	Urea-formaldehyde (24.3)	Paraformaldehyde (7.8)	Titanium dioxide (3.9)	-
Wilson (1955) [1-3,a]	Polyphosphorylamide (8.8)	Dipentaerythritol (15.3) Starch (31.5)	Urea-formaldehyde (26.2)	N-ethyl toluene sulfona. (2.9)	(Rutile) titanium dioxide (6.0)	-
Venable (1960) [1-3,b]	Mono-ammonium phosphate (30.0) Tris-B-chloroethyl phosphate (2.0)	Tripentaerythritol (8.0)	MEL-Formaldehyde (32.0)	Dicyandiamide (8.0) Silicone resin in toluene (12.0)	Titanium dioxide (6.0)	Bentonite clay (1.0)
Kaplan (1966) [1-3,a]	Mono-ammonium phosphate (27.8)	Pentaerythritol (10.9)	Dicyandiamide (4.9)	vinyl chloride, vinylidene chlor. (19.9)	Titanium dioxide (5.9)	Glass, asbestos fibres (4.0)
Hahn (1970) [1,a]	Ammonium phosphate (22.9)	Tripentaerythritol (3.8) Chlorinated paraffin (4.6)	Melamine (7.7) MEL-formaldehyde (1.9)	Polyvinyl acetate (15.8)	Titanium dioxide (7.7)	Cellulose ether (2.0) Potassium tripolyphosp.
Levine (1972) [2,b]	Ammonium polyphosphate (30.7)	Dipentaerythritol (9.2)	Melamine (14.5)	Vinyl-toluene/ butadiene (5.7)	Titanium dioxide (5.4)	Chlorin. natural rubber

(*table continues*)

Table 2.3: Composition of essential ingredients of intumescent coatings indicated by (wt%) (continued)

Patent	Acid source	Carbon donor	Blowing agent	Binder	Pigments	Additives
Fessler (1975) [1-4,a]	MEL pyrophosphate (21.0)	Dipentaerythritol (5.0) Chlorinated paraffin (3.0)	-	Vinyl acetate (14.0) Hydroxy ethyl cellul. (11.0)	Titanium dioxide (4.0)	Glass fibres (0.4) Potassium tripolyphosp.
Fukuba (1976) [3,a]	Ammonium polyphosphate (28.0)	Pentaerythritol (7.0)	Melamine (7.0)	Ethylene-vinyl acetate (22.0) Melamine resin (6.0)	-	Ethylcellulose (5.8)
Kasten (1981) [1-3,a]	Ammonium polyphosphate (24.8)	Dipentaerythritol (7.2) Chlorinated paraffin (3.8)	Melamine (7.6)	Vinyl acetate (21.0) Hydroxy ethyl cellul. (2.6)	Titanium dioxide (5.7)	Potassium tripolyphosp.
Ward (1985) [2,c]	Ammonium polyphosphate (2.3) Tris(2-chlorethyl) phosphate (4.4) Boric acid (10.3)	-	Melamine (1.4)	Ether bisphenol-A (17.9) Amine curing agent (36.1) Tall oil fatty acid (2.1)	-	Attapulgite clay (4.0) Amorphous silica (6.9) Wollastonite fibres
Buckingham (1994) [3,a]	Ammonium polyphosphate (13.3)	Pentaerythritol (13.3)	Melamine (15.6)	Vinyl acetate/ ethylene (20.5)	Titanium dioxide (3.1)	Zinc oxide (2.0) Mica, quartz, chlorite (9.2)

(*table continues*)

Table 2.3: Composition of essential ingredients of intumescent coatings indicated by (wt%) (continued)

Patent	Acid source	Carbon donor	Blowing agent	Binder	Pigments	Additives
Jenewein (1996) [2,c]	Ammonium polyphosphate (41.7)	-	-	Bisphenol A, epichlorohyd. (41.7) Aliphatic polyam. (16.6)	-	Carboxylic acid ester
Thewes (2001) [2,a]	-	Dipentaerythritol (4.0)	Melamine polyphosphate (29.7)	Vinyltoluene-acrylate (5.1)	Titanium dioxide (4.0)	Glass fibres, mineral fibres, kaolin, talc, alum. oxide
Duquesne (2005) [1-3,a-b]	Ammonium polyphosphate (26.0)	Dipentaerythritol (8.0)	Melamine (8.5)	Newtonian, crossl. resin (9.0) Chlorinated paraffine (9.5)	Titanium dioxide (6.0)	-
Bradford (2009) [2,c]	Boric acid (22.0) Ammonium polyphosphate (17.0)	Low viscosity polyamide (15.0)	Melamine (7.5)	Bisphenol A (10.0) Dihydroxaphosphaphenanthrene (12.0)	Titanium dioxide (0.7)	Ceramic fibres

Application on: [1]wood; [2]metal/steel; [3]plastics; [4]glass — Formulation: [a]waterborne; [b]solvent-borne; [c]epoxy resin-based

Although intumescent coatings consisted of other raw materials at the beginning of their development, a differentiation in their functionality was already made that is still valid for the main ingredients known today. The patent of Jones (1948), for example, describes a waterborne coating formulation for wood and metal substrates that already consisted of an acid source, a carbon donor, a blowing agent and a pigment (see Table 2.3). Only additives were not used at this time. The first patent that explicitly claimed to improve the performance of intumescent coatings by use of bentonite clay as synergistic additive was published by Venable (1960). With regard to their diversity and number, especially additives and binders were the main ingredients that led to a significant change in the formulation of intumescent coatings.
In the following, the most used and literature-known ingredients are presented with regard to their characteristics and their function in intumescent coatings (reaction mechanisms see subsection 2.2.5). Based on the review of the patents, the historical development of the ingredients is considered as well.

Acid Source:

The acid source is one of the main components in intumescent coatings. Besides the actual acids also their salts are used as acid donors. In former formulations boric acid (Jones 1948), mono-ammonium phosphate (Kaplan 1966) and melamine pyrophosphate (Fessler 1975) were used as acid source. However, the most widespread used acid source in intumescent coatings is ammonium polyphosphate (APP). APP (see Figure 2.8, left) is an ammonium salt of the phosphoric acid with a decomposition temperature of 150 - 350 °C. When APP is heated, it decomposes into volatile ammonia (NH_3) and meta phosphoric acid that interacts with the carbon donor in a subsequent reaction to form a carbon-containing foam, declared here as *char*, (Simon 2006). APP covers a wide range of molecular weights and, therefore, shows different performance in water solubility and thermal stability (Weil 2011). This is due to the variable number of monomer units (n) and the degree of branching (Puri & Khanna 2017). APP with shorter chains ($n < 100$) is more water sensitive and less thermal stable than APP with longer chains ($n > 1000$).

Ammonium polyphosphate (APP)

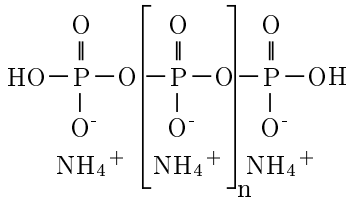

Pentaerythritol (PER)

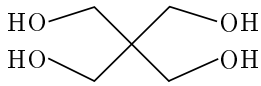

Figure 2.8: Structural formula of ammonium polyphosphate $(NH_4PO_3)_n$ and pentaerythritol $(C_5H_{12}O_4)$

In order to reduce the water solubility and to increase the thermal stability, APP

can be encapsulated on the micro scale using melamine-formaldehyde resins or other materials that help to modify the surface of APP (Wu et al. 2008). These surface passivations help to overcome the poor water resistance and low compatibility of APP with polymeric binders. Additional to the improvement of the performance, the microencapsulation acts as a char former or blowing agent (Jiang & Liu 2015).

Carbon Donor:

The closed-cell foam structure in intumescent coatings is usually formed by a carbon-rich, organic compound that is denoted as carbon donor. Due to the lack of alternatives, starch (Jones 1948) and chlorinated paraffin (Hahn 1970) were used as carbon donor in the beginning of intumescent coatings (see Table 2.3). However, in the following years the inventors realised that especially pentaerythritol (PER) and its polycondensates are best suited to form a carbon-rich foam structure in intumescent coatings. Therefore, PER is still the most commonly used carbon donor in intumescent coatings in combination with APP. PER is a tetravalent alcohol (2,2-Bis(hydroxymethyl)1,3-propanediol) with five carbon atoms (see Figure 2.8, right) and was synthesised for the first time in 1882 by Tollens & Wigand (1891). In the presence of an anorganic acid, PER undergoes an esterification, in which water and ammonia are released. This represents a preliminary reaction stage before the carbon-rich foam structure in intumescent coatings is formed.
Besides pentaerythritol, di-pentaerythritol and tri-pentaerythritol are also used in intumescent coatings. However, Andersson et al. (2007) found out that the best performance in intumescence and fire protection is achieved for coating formulations with pentaerythritol. This is due to its lower melting temperature (about 266 °C) and high ratio of OH groups that are required to react with APP. Nevertheless, Andersson et al. (2007) postulate that especially tri-pentaerythritol could possibly be applied in coating formulations for steel structures with high surface curvatures, such as tension rods. Although tri-pentaerythritol leads to a delayed and less pronounced expansion, it provides more robustness due to a higher thermal stability and delayed cracking (the temperature at which embrittlement starts is higher) of the expanded char. This behaviour is particularly important for circular cross-sections where the perimeter of the foam needs to be increased during the expansion of the coating.
The review of the patents revealed that epoxy-resin based intumescent coatings are often formulated without any carbon donor. Here, the carbon donor is substituted by the large proportion of polymer binders. Appropriate formulations are given by Ward (1985) and Jenewein (1996).

Blowing Agent:

In literature, melamine (MEL) is reported to be the most widely used blowing agent in intumescent coatings in combination with APP and PER. Melamine (see Figure 2.9, left) itself totally sublimates between 250 and 350 °C when it is heated

slowly and without any constraint of vapor (Weil 2011). However, if the vapor is constraint, such as in intumescent coatings, parts of melamine sublimate and parts undergo a condensation reaction by loosing ammonia (Costa & Camino 1988). As the gases that are produced during the sublimation (H_2O and CO_2 according to Gomez-Mares et al. (2012)) and the ammonia that is released during the condensation are trapped inside the viscous melt, the typical charred foam structure is formed. Apart from its role as blowing agent, melamine helps to provide a higher thermal stability of the carbonaceous char due to a series of reactions with APP according to the research of Taylor & Sale (1993).
In addition to MEL also melamine phosphate (see Figure 2.9, right) or melamine polyphosphate is used in intumescent coatings (Puri & Khanna 2017). Due to its OH groups melamine polyphosphate does not only act as a blowing agent but also as an acid source (Thewes 2001).

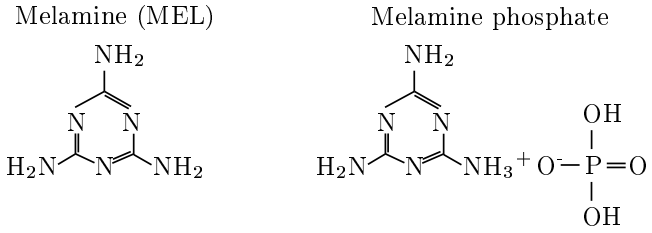

Figure 2.9: Structural formula of melamine ($C_3H_6N_6$) and melamine phosphate ($C_3H_9N_6O_4P$)

At the beginning of the development of intumescent coatings, Urea (Jones 1948), Urea-formaldehyde (Wilson 1955) and melamine-formaldehyde (Levine 1972) were used as blowing agents as well. However, the research of Camino et al. (1984) revealed that especially urea tends to reduce the intumescence in APP-PER formulations compared to MEL due to the small amount of released gases that are evolved during its decomposition. Therefore, MEL and melamine polyphosphate are preferably used as blowing agents in intumescent coatings.
Nevertheless, inventions of Jenewein (1996) and Butler (2017) showed that intumescent coatings can also be formulated without any blowing agent. Although the expansion of such coatings is than decreased due to the absence of the blowing agent, a higher robustness and char strength is achieved. However, such formulations are only found for epoxy-resin based coatings (see Table 2.3).

Polymer Binder:

At room temperature the polymer binder has the function to bind the ingredients and additives of intumescent coatings and to ensure a sufficient adhesion to the substrate. When the binder is heated, it has to change the aggregate state from solid to melted to ensure the formation of bubbles in the liquid melt. Due to

its melting behaviour and viscosity, polymer binders strongly control the expansion speed, the formation and the size of bubbles as found out by Wang & Yang (2012). However, investigations of Duquesne et al. (2005) showed that polymer binders (especially a mixture of linear and crosslinked copolymers) even synergistically interact with APP and, therefore, greatly affect the insulation efficiency of intumescent coatings.

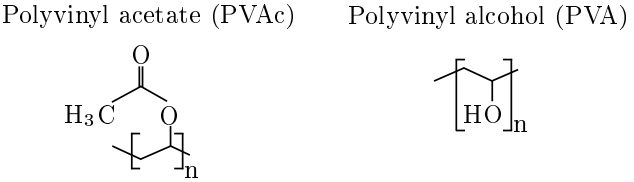

Figure 2.10: Structural formula of polyvinyl acetate $(C_4H_6O_2)_n$ and polyvinyl alcohol $(C_2H_4O)_n$

In their research of the influence of vitreous fillers on the thermal resistance of intumescent coatings, Olcese & Pagella (1999) specified formulations for each product class of intumescent coatings and make suggestions for the selection of polymer binders. For waterborne intumescent coatings Olcese & Pagella used vinyl polymers, such as polyvinyl acetate (PVAc) and polyvinyl alcohol (PVA). The melting temperature (70 - 230 °C) of the water-soluble and synthetically produced binders (see Figure 2.10) depends on the degree of polymerisation, described by the number of monomer units (n) that are included in the polymer molecule.
Other binders of waterborne intumescent coatings are combinations of vinyl acetate and ethylene (Buckingham 1994), vinyltoluene-acrylate (Thewes 2001) and paraformaldehyde (Nielsen 1952) as described by the patents in Table 2.3.
For solvent-borne intumescent coatings a polymer binder, such as polyacrylate (PA) is suggested by Olcese & Pagella (1999) and Longdon et al. (2005). Bermes (2006) and Wang et al. (2008), on the other hand, recommended to use polypropylene (PP) or polyethylene (PE) as polymer binders in intumescent coatings due to their mechanical durability and their high chemical resistance (see Figure 2.11). These recommendations are complemented by the inventions of Venable (1960) and Levine (1972) that use dicyandiamine and a combination of vinyl-toluene and butadiene, respectively as binders in solvent-borne intumescent coating formulations.
As their name already indicates, resin-based intumescent coatings are usually composed of two-component resins. As described by Gomez-Mares et al. (2012) and Gao et al. (2009) in most cases epoxy resins, such as (2,2-[(1-methylethylidene)bis(4,1-phenyleneoxymethylene)]bis-oxirane are used. Gu et al. (2007) explain in their research that also polyester resins are suitable. However, a higher thermal stability of intumescent coatings is still achieved if epoxy resin binders are used. By varying the molecular weight of the epoxy binder Wang & Yang (2012) found out that the melting temperature of the binder increases with increasing molecular weight. Due to the retarded melting and the decomposition of

the binder, the expansion of the investigated coating occurs at a later time. However, due to the higher molecular weight of the binder, the coating shows a much higher thermal stability and a reduced oxidation behaviour. Contrary to the presumption of the authors, a too high molecular weight, on the other hand, results in an irregular, uneven char and, therefore, in a reduced fire protection performance. As two-component resins show a reduced degree of cross-linking compared to solvent- or waterborne binders, the proportion of binders in epoxy resin-based intumescent coatings is significantly higher. Due to this circumstance, carbon donors are omitted since their function is taken over by the binder. Such formulations are described, for example, in the patents of Ward (1985) and Jenewein (1996).

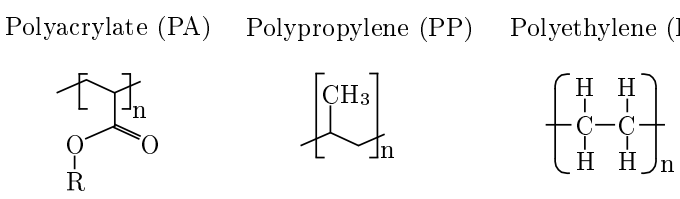

Figure 2.11: Structural formula of polyacrylate, polypropylene and polyethylene

Due to the variety of binders, not every polymer can be addressed in this thesis in detail. As solvent- and waterborne intumescent coatings are part of the experimental investigations carried out in this thesis, binders, such as polyvinyl acetate and polyacrylates will be focused predominantly to understand the thermal performance of intumescent coatings in case of natural fires.

Pigments:

Apart from their role as pure colouring elements, pigments are also used to improve the fire protection performance of intumescent coatings. In most coating formulations titanium dioxide (TiO_2) is used as a white pigment. However, Duquesne & Bourbigot (2009) found out that TiO_2 does not only act as a pigment but also as a reactant of APP to form titanium pyrophosphate. Titanium pyrophosphate is characterised by its white colouring. It becomes visible when the organic compounds of the expanded char combust at high temperatures.
According to Li et al. (2015) two types of TiO_2, rutile-type and anatase-type, are normally used in conventional intumescent coating formulations. Due to its smaller particle size, the rutile-type shows a better dispersion in coating formulations and, therefore, improves the thermal stability of intumescent coatings much more than the anatase-type. The improvement in fire-resistance is characterised by the enhanced formation of a high quality honeycomb char structure. The patent of Wilson (1955) documents that the rutile-type of titanium dioxide was already used more than 60 years ago as a white pigment in intumescent coatings.

Additives:

The term *additives* refers to compounds that are usually used to enhance the performance of intumescent coatings. Additives are not necessarily required for the

intumescence reaction. However, they are used, among others, to improve the fire protection performance and to enhance the adhesion of the char to the underlying substrate.
According to Puri & Khanna (2017) additives such as fire-retardant compounds, inorganic fillers and fibres as well as nanoparticles are used in intumescent coatings. An exemplary use of fire-retardant additives is discussed by Jimenez et al. (2006*b*). The Lille research group reports that boric acid reacts with degradation products of APP to form borophosphate. As borophosphate helps to form a hard and mechanically resistant intumescent char with enhanced adhesion to the steel substrate, the use of boric acid as a fire-retardant additive leads to a significant improvement in thermal and mechanical behaviour of intumescent coatings.
Inorganic fillers, such as aluminium hydroxide ($Al(OH)_3$), magnesium hydroxide ($Mg(OH)_2$) and TiO_2 show similar improvements in fire protection performance according to Yew et al. (2015). Basically, the use of inorganic fillers leads to the formation of thermally stable phosphate species that help to maintain the integrity of the formed char. Therefore, the fire protection lasts for a longer period compared to coating formulations without inorganic fillers (Duquesne et al. 2013).
Investigations of Olcese & Pagella (1999) revealed that also vitreous fillers help to improve the thermal insulation performance and fire resistance of intumescent coatings. In addition, better smoke emission characteristics in terms of optical density and toxicity can be achieved. In their research blends of vitreous fillers with different melting temperatures (350 - 850 °C) were tested together with refractory fillers that were incorporated in solvent- and waterborne as well as epoxy resin-based coatings.
In order to develop a high-performance intumescent polymer, Koo (1998) incorporated ceramic fibres in a waterborne coating. Duquesne et al. (2013), on the other hand, used mineral fibres with an averaged diameter of $9\mu m$ and a melting temperature >1000 °C. A chemical analysis revealed that the mineral fibres consisted of silicate fibres with a share of alkali and alkaline earth metal oxides (silicon dioxide, aluminium oxide, calcium oxide, magnesium oxide, iron(II) oxide, calcium oxide and sodium oxide).
Bodzay et al. (2011) found a way to incorporate nanoparticles, such as montmorillonite, palygorskite and sepiolite, into an intumescent coating to improve both the mechanical and the thermal stability. As described by the authors, the addition of 0.25 wt% of the mineral nano-clays was sufficient to influence the char formation significantly. However, due to the different geometry and composition of the additives, different changes in fire performance were observed. The use of palygorskite, for example, reduces the fire resistance because of the catalytic effect of ferrum (Fe) that accelerates the thermal decomposition of the char. The plate-like montmorillonite, on the other hand, improves the thermal stability of the char, but reduces at the same time the expansion. The best performance is achieved by fibrous sepiolite. Due to its low Fe content, a high-insulating char is formed on the basis of a uniform cell structure.
The use of clays as additives in intumescent coatings has a long tradition. Already

60 years ago, Venable (1960) used bentonite clay to improve the processability of his coating during the application process. In order to ensure low and stable viscosity of the coating, Hahn (1970), Fukuba (1976) and Kasten (1981), on the other hand, used potassium tripolyphosphate in their formulations.
The analysis of the patents listed in Table 2.3 reveals that the use of synergistic additives is diverse. Therefore, the properties of intumescent coatings can be adjusted specifically in the initial state and during the temperature-induced reaction.

The review on the composition of single ingredients presented in this subchapter serves as a basis for the subsequent evaluation of the heating rate-dependent behaviour of intumescent coatings and their ingredients. Since a large variety of ingredients is used for the formulation of intumescent coatings, the review does not claim to be all-encompassing and, therefore, focuses only on the main ingredients that are well known in literature. Based on this, in subsection 2.2.6 the heating behaviour of ammonium polyphosphate, pentaerythritol, melamine, titanium dioxide and selected binders will be evaluated in terms of sensitivity to varying heating rates.

2.2.5 Functionality and Reaction Processes

In order to ensure the formation of an efficient protective char, the thermal behaviour of intumescent coating ingredients needs to be attuned to each other (Jimenez et al. 2006*b*). For example, it is crucial that the blowing agent needs to decompose in a temperature range at which melting of the coating already occurs but solidification of the char not (Anderson et al. 1985). Similar dependencies also apply to the reactions of the remaining ingredients that take place before and after the release of volatile gases.
In order to examine the thermal performance of single ingredients and their interaction at high temperatures, Wang et al. (2006) performed differential scanning calorimetry (DSC) analyses. Within these analyses sample materials were heated together with an inert reference while the difference in heat that is required to increase the temperature of the sample and the reference was measured. With the help of the measured DSC curves endothermic peaks of ammonium polyphosphate, pentaerythritol and melamine were identified that can be assigned to specific reactions of each ingredient (see Figure 2.12). These results are used in the following to describe the reactions that take place in an intumescent coating based on an APP-PER-MEL formulation. The mechanism of intumescence is usually described as follows:

(1) When the surface of the coating reaches a critical temperature due to heating, the coating starts to melt and converts into a highly viscous liquid (Jimenez et al. 2006*b*). The phase change from solid to liquid is predominantly caused by the melting of the polymer binder. Electron impact mass spectroscopy

measurements performed by Ballistreri et al. (1980) show that vinyl polymers already start to melt at temperatures of 150 °C (see Figure 2.12).

(2) At temperatures of 170 - 220 °C the acid source melts. If the acid source is ammonium polyphosphate (APP), polyphosphoric acids and ammonia (NH_3) are released by decomposition due to further heating (Bradford 2009). The temperature range (260 - 380 °C) at which the decomposition reaction occurs depends on the degree of polymerisation. Both the melting reaction and the decomposition reaction of ammonium polyphosphate are represented by endothermic peaks of the DSC curve in Figure 2.12.

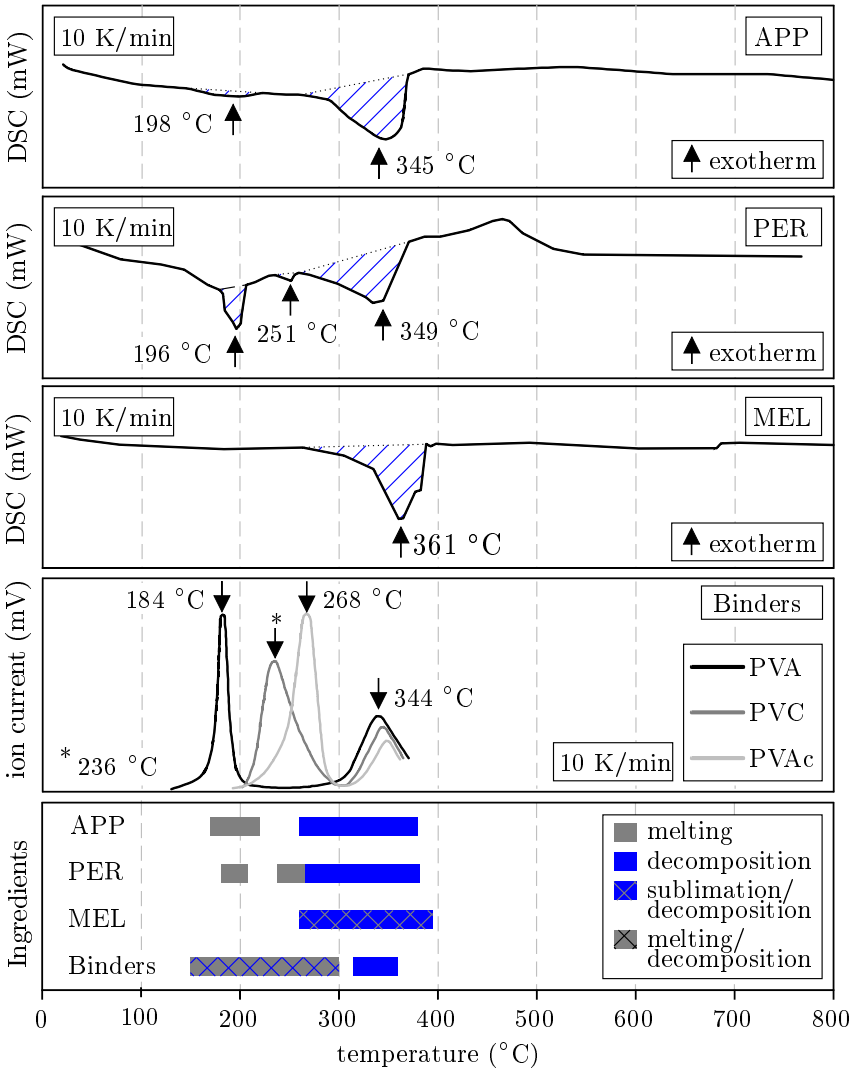

Figure 2.12: DSC curves of APP, PER and MEL acc. to Wang et al. (2006) and impact mass spectroscopy measurements of vinyl polymers acc. to Ballistreri et al. (1980)

(3) In contrast to the acid source, pentaerythritol (PER) as carbon donor melts in two reaction stages (first stage: 180 - 210 °C, second stage: 240 - 270 °C). After melting, the polyphosphoric acid that is released by the decomposition of ammonium polyphosphate reacts with pentaerythrithol to form polyphosphoric acid esters. During the decomposition of these esters (270 - 390 °C), long-chain hydrocarbon compounds are formed due to isomerisation. As a result of a subsequent cyclisation reaction, a carbon rich closed-cell foam structure is formed with the help of the blowing agent (Bradford 2009).

(4) The formation of the closed-cell foam structure is predominantly realised by the release of volatile gases and ammonia due to the sublimation and condensation reaction (260 - 395 °C) of the blowing agent (Wang et al. 2006). In most cases it is melamine (MEL). At the beginning of the reaction only few small bubbles are formed. As soon as the gas release increases, the pressure inside the bubbles increases resulting in the growth of the spherical bubbles. If the pressure inside the bubbles is high enough, the bubble walls interact with each other to form a honeycomb-like structure (Mamleev et al. 1998). During this reaction stage the solidification of the hydrocarbon compounds occurs resulting in a solid, porous structure with low thermal conductivity and, therefore, high fire protection performance (see Figure 2.13 (1)-(3)).

(5) Titanium dioxide (TiO_2) that is normally used as a white pigment in intumescent coatings reacts according to Duquesne & Bourbigot (2009) with ammonium polyphosphate to form titanium pyrophosphate. When the organic compounds of the formed char undergo a pyrolysis reaction at temperatures above 620 °C (according to Wang et al. (2006)), titanium pyrophosphate remains to form a fragile, white open-cell foam structure. As the walls of the honeycomb-like pores combust as well, the gas that is trapped inside the pores is released into atmosphere. As a consequence, the foam structure loses its fire protection performance since the heat is easily transferred through the open-cell structure (see Figure 2.13 (4)).

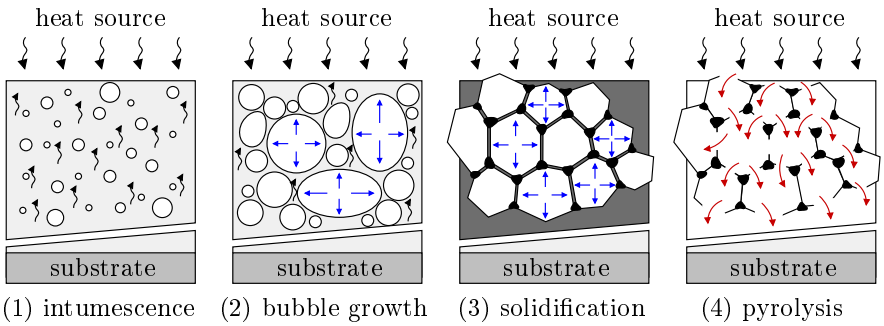

Figure 2.13: Schematic description of morphological changes in intumescent coatings due to a continuous temperature increase

The description of the literature-known reaction processes reveals that a matching

thermal behaviour of each ingredient is essential for the formation of a high insulative char. Therefore, the main ingredients, such as ammonium polyphosphate, pentaeythritol and melamine, show a nearly congruent temperature range at which they melt and decompose (see Figure 2.12).
Besides the coordinated reactions of the ingredients, the bubble and char formation is also affected by the thermal behaviour of the polymer binder. As Wang & Yang (2012) already found out, the performance of intumescent coatings is significantly affected by the melting behaviour of the binder. Therefore, it is crucial that the polymer binder melts and reduces its viscosity within a temperature range at which the reactions of the main ingredients occur. However, if the viscosity of the binder is too low, either the gases escape from the melt without beeing trapped (Jimenez et al. 2006*b*) or large bubbles and cells are formed during the decomposition process of the blowing agent. In both cases the insulation efficiency of the char is reduced either due to the uncompleted expansion or the size and fragility of the large cells and bubbles (Anderson et al. 1985). As the morphology of the char has a significant effect on the protection performance of intumescent coatings, Berlin et al. (1998) proved that the best insulation performance is given especially for small pore sizes. In order to ensure a matching melting behaviour of the binders, rheological analyses can be performed. With the help of these analyses, the viscosity of the binder is measured continuously while the sample is steadily heated. Results of such analyses are given in Figure 2.14 that were performed by Bugajny et al. (1999) and Jimenez et al. (2006*a*).

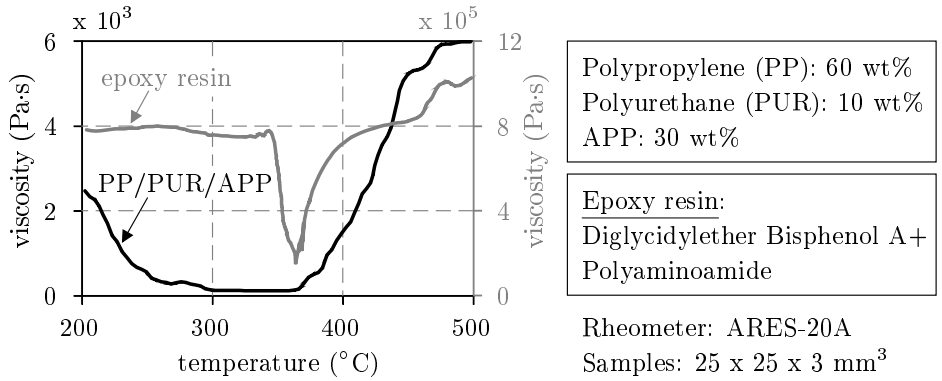

Figure 2.14: Temperature-dependent viscosity of a heat-treated PP/PUR/APP formulation acc. to Bugajny et al. (1999) at 5 K/min and an epoxy resin acc. to Jimenez et al. (2006a) at 10 K/min

Epoxy resin-based coatings normally show a reduced intumescence behaviour compared to water- or solvent-borne intumescent coatings and, therefore, require larger dry film thicknesses. This is due to the high viscosity of the epoxy binder as can be seen from the minimum values (epoxy resin: 155,800 Pa·s and PP/PUR/APP formulation: 121 Pa·s) in Figure 2.14 and the temperature range at which the binder viscosity decreases. Due to the high viscosity of the epoxy binder, the gases

that are released during the decomposition of the blowing agent are hindered to fully expand the char. As a consequence, the viscosity of the binder and of the degraded coating matrix is, among others, a critical factor for the formation of the char.

The interactive behaviour of the main ingredients makes clear, if any of the above described reactions does not proceed at the required temperature, intumescence of the coating will not occur or will be at least limited. Therefore, the temperature range at which the specified reactions of each ingredient and their interactions take place is extremely important. As a consequence, it is hypothesised that the reactions and interactions of single ingredients can be affected by temperature shifts. These temperature shifts can occur due to different heating conditions when intumescent coatings are exposed to natural fires that deviate significantly from the standard fire curve. The extent to which this hypothesis applies will be examined on the basis of the literature review on the heating rate-dependent decomposition behaviour of each ingredient (see subsection 2.2.6) and own experimental investigations (see section 3.3).

2.2.6 Heating Rate-Dependent Decomposition of Main Ingredients

In order to assess the sensitivity of intumescent coating ingredients to changes in heating rates, literature-known thermogravimetric (TG) analyses were systematically evaluated. The thermogravimetric analysis describes an analytical method that is comparable to the differential scanning calorimetry. However, instead of the heat flow, the mass change of the sample is continuously measured while the sample temperature is constantly increased.
As the published thermogravimetric analyses were carried out under different research questions, it was necessary to ensure that the analyses were carried out under comparable experimental conditions. Therefore, parameters such as the sample type and size, the atmosphere (air or nitrogen), the flow rate, the heating rate and the actuality of the investigations were compared. Only in those cases where the experimental setup was comparable, the results of the TG analyses were used to evaluate the influence of varying heating conditions on the thermal decomposition of ingredients such as ammonium polyphosphate, pentaerythritol, melamine and vinyl polymers.
It is expressly pointed out that the reviewed data presented in the following was digitised and processed and is now presented in a completely new context. Therefore, each data set is uniquely referenced by its source.

Ammonium polyphosphate (APP):

The literature-known thermogravimetric analyses of ammonium polyphosphate were performed under nitrogen (N_2) atmosphere, a flow rate of 50 - 60 cm^3/min

and a sample size of 5 - 10 mg.
As Weil (2011) already described in his review, ammonium polyphosphate covers a wide range of molecular weights and, therefore, shows different performances in thermal stability. These differences are shown in Figure 2.15 for the temperature-dependent mass loss behaviour of APP with respect to changes in monomer units. The TG curves clearly show that the thermal conversion of APP delays with increasing degree of polymerisation. However, as the DTG (differential thermal gravity) curves indicate, the decomposition of APP still proceeds in two stages, represented by the peaks in Figure 2.15 b), respectively. Taking this as a basis, the increase in monomer units leads to a shift in the reaction temperatures. This can be explained by the increase of thermal energy that is required to loosen the bonds for increasing chain lengths.

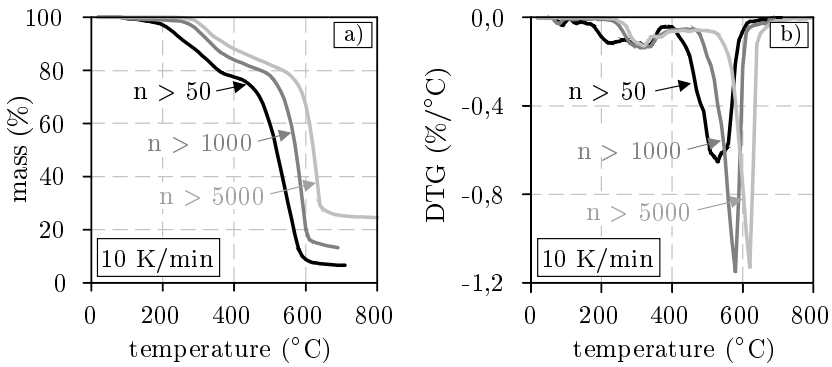

Figure 2.15: TG a) and DTG b) curves of ammonium polyphosphate (APP) under nitrogen with monomer units of n > 50 (Li et al. 2013), n > 1000 (Ge et al. 2012) and n > 5000 (Yi et al. 2013)

In order to assess the influence of different heating rates on the mass loss behaviour of APP, results of TG analyses of Ni et al. (2009), Lai et al. (2015), Zheng et al. (2014) and Deodhar et al. (2011) are compared in Figure 2.16. Here, the thermal decomposition is given for both air and nitrogen atmosphere.
In the description of the reaction processes that take place in intumescent coatings during heating (see subsection 2.2.5) it was shown that ammonium polyphosphate as acid source decomposes in a temperature range of 260 - 380 °C to form polyphosphoric acids and ammonia (NH_3). However, as the TG curves in Figure 2.16 reveal, the temperature range at which mass loss occurs changes with respect to the heating rate and the atmosphere. For example, APP undergoes a faster thermal degradation under air than under nitrogen when being heated with 10 K/min. This is clearly demonstrated by the residue and the temperature (T_{max}) at which the maximum degradation rate for reaction stages 1 and 2 (see Table 2.4) occurs. While under air the peaks of the reaction stages 1 and 2 occur at 324 and 624 °C, respectively, the mass loss under nitrogen shows a delayed behaviour due to the increase in peak temperature by 20 and 30 °C, respectively. The differential

behaviour under air and nitrogen is even more illustrated by the residual masses at, for example, reaction stage 2 (air: 25.11 wt%, nitrogen 40.71 wt%).
In addition to the differences in mass loss caused by the atmosphere, the increase in heating rate from 10 to 20 K/min leads also to changes in the decomposition behaviour of APP. Under air (see Figure 2.16 a)) the increase in heating rate results in a delayed and incomplete mass loss behaviour since a residue of 19.84 wt% remains after 700 °C. Under nitrogen, on the other hand, the mass loss is significantly accelerated when the heating rate is increased although the sample size at 20 K/min (20 mg) was twice as high as at 10 K/min. For this reason it is plausible that the reaction stages occur at the lowest temperatures (stage 1: 319 °C, stage 2: 579 °C) of all samples and reveal the highest degredation rate (R_{max}: -1.19 %/°C) at the same time (see Table 2.4).

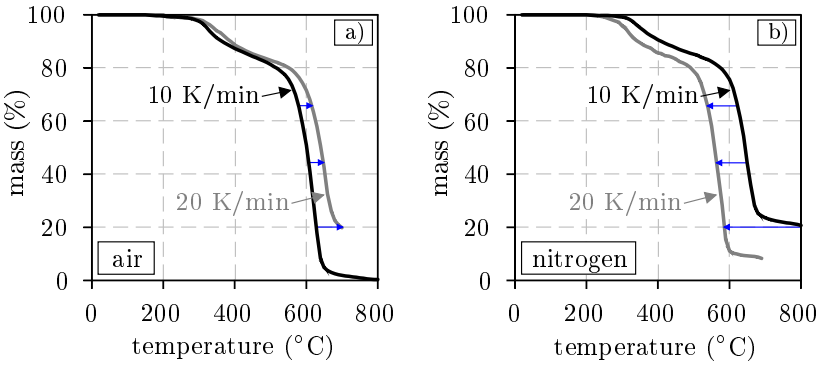

Figure 2.16: TG curves of ammonium polyphosphate (APP) under air a) at 10 K/min (Ni et al. 2009) and 20 K/min (Lai et al. 2015) and under nitrogen b) at 10 K/min (Zheng et al. 2014) and 20 K/min (Deodhar et al. 2011)

In the literature (see for example Zhang et al. (1994), Duquesne et al. (2001), Riva et al. (2003) or Dittrich et al. (2014)) the temperature-dependent degradation steps of APP are reported as follows: In the first step, which begins around 300 °C, ammonia (NH_3) and H_2O are eliminated from APP to form highly cross-linked polyphosphoric acids. While the evolution of NH_3 was proved, for example, by Dittrich et al. (2014) using Fourier Transform Infrared (FTIR) spectroscopy, the evolution of water could not be monitored since H_2O does not give a sharp IR signal as reported by Riva et al. (2003). With further heating (second degradation step) the cross-linked polyphosphoric acids start to evaporate or dehydrate to form sublimating phosphorus pentoxide (P_4O_{10}) between 450 and 650 °C.
As the literature review reveals, all sources listed above as well as Zheng et al. (2014) and Deodhar et al. (2011) assume erroneously the same degradation reactions for APP without distinguishing whether the TG analyses were performed under air or nitrogen atmosphere. Nevertheless, the results documented in Figure 2.16 and Table 2.4 show significant differences in thermal behaviour, such as

the residual mass at 700 °C (air: 1.88 wt% and nitrogen: 23.58 wt% for 10 K/min, respectively). For this reason, no convincing explanation could be found for the deviating behaviour of APP under the itert atmosphere of nitrogen in combination with increasing heating conditions. Only for the reaction under air it can be assumed that oxygen (O_2) reacts with the liberated ammonia within a redox reaction to form nitrogen monoxide (NO) and water. This intermediate reaction could explain the rapid thermal degradation of APP under air. An appropriate explanation for the reaction under nitrogen, however, is still pending.

Table 2.4: Thermal degradation data of APP under air and nitrogen (N_2) for heating rates of 10 and 20 K/min by TGA according to Ni et al. (2009), Lai et al. (2015), Zheng et al. (2014) and Deodhar et al. (2011)

	$T_{initial}$ [a]	T_{max} [b] (°C)		Residue (wt%) at			R_{max} [c]
Sample	(°C)	Stage 1	Stage 2	Stage 1	Stage 2	700 °C	(%/°C)
10 - air	160	324	624	94.81	25.11	1.88	-1.17
20 - air	201	374	649	91.41	43.87	19.84	-0.91
10 - N_2	206	344	654	95.80	40.71	23.58	-0.94
20 - N_2	227	319	579	93.24	29.43	8.29	-1.19

[a] $T_{initial}$ is the temperature at 0.1 % weight loss
[b] T_{max} is the temperature at which the maximum degradation rate occurs
[c] R_{max} is the maximum degradation rate

Pentaerythritol (PER):

The mass loss behaviour of pentaerythritol was investigated in the reviewed thermogravimetric analyses under nitrogen, air and helium atmosphere, a flow rate of 50 - 100 cm^3/min and a sample size of 5 - 10 mg.
Bradford (2009) describes in his patent that pentaerythritol as carbon donor melts already at temperatures of 180 - 210 °C and undergoes an esterification reaction with the polyphosphoric acid that is released by APP. In subsequent reactions the formed esters decompose (270 - 390 °C) and result in a carbon rich closed-cell foam structure. However, without any reactant, the thermal decomposition of pentaerythritol occurs at significantly lower temperatures, as the results of the performed TG analyses of Sakamoto et al. (1984) reveal. When being heated with 1 K/min under nitrogen atmosphere, PER entirely decomposes in a temperature range of 186 - 280 °C (see Figure 2.17 a)). An increase in heating rate up to 20 K/min, however, leads to a temperature shift (240 - 387 °C) in mass loss. As Sakamoto et al. (1984) have also carried out TG analyses for intermediate heating rates (3, 5 and 10 K/min), an almost uniform increase in temperature (T_{max}) can be observed at which the maximum degradation rate occurs (see Table 2.5). As the degradation rates are almost identical for all investigated heating rates (-2.30 to -2.50 %/°C), except for 1 K/min (-2.79 %/°C), it is assumed that the observed temperature shifts are due to thermal inertia of PER (see the residual mass at 300 °C in Table 2.5) and not due to possible changes in reaction. For this reason,

the thermal decomposition of PER takes place rapidly and independently from the heating rates in a single step.
The review of the TG analyses of Lv et al. (2005), Dahiya et al. (2012) and Sun et al. (2013) that were carried out under different atmospheres (nitrogen, helium and air) reveals that the thermal decomposition of PER takes place, in contrast to APP, independently from the fluid that surrounds it. As the results in Figure 2.17 b) show, the differences in the measured TG curves under the varying atmospheres are very small and, therefore, can be attributed to measurement tolerances. This is due to the chemical structure of PER. When heated, PER decomposes rather by dehydration than by oxidation or other combustion reactions as proposed by Lv et al. (2005). This is why, for example, oxygen does not affect the decomposition of pure PER at all.

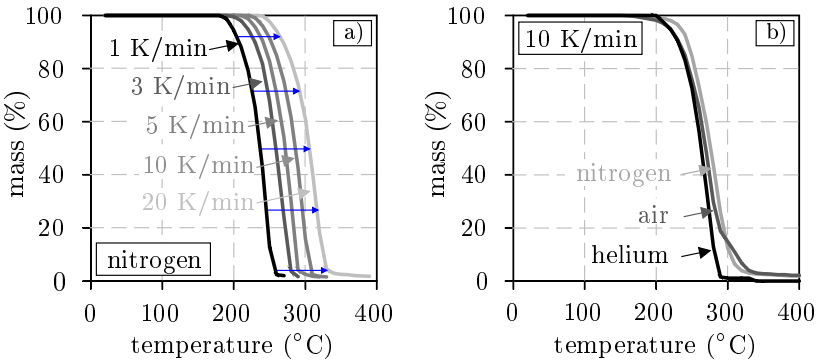

Figure 2.17: TG curves of pentaerythritol (PER) under nitrogen a) at 1, 3, 5, 10 and 20 K/min (Sakamoto et al. 1984) and at 10 K/min b) under nitrogen (Lv et al. 2005), air (Sun et al. 2013) and helium (Dahiya et al. 2012)

As explained in subsection 2.2.5, a congruent thermal behaviour of main ingredients is crucial for the formation of a highly thermal protective char. The presented studies, however, reveal that APP and PER show different sensitivities to changes in heating rates. For example, a change in heating rate from 10 to 20 K/min results for APP under air atmosphere in a temperature shift for reaction stage 1 from 324 to 374 °C (Δ 50 K, see Table 2.4), whereas the temperature (T_{max}) at which the maximum degradation rate occurs shifts for PER from 294 to 313 °C (Δ 19 K, see Table 2.5). As a consequence, the increase in heating rate leads in this case to different temperature shifts for APP and PER. Therefore, the reaction processes described in subsection 2.2.5 can be affected by the mismatch of the indiviual thermal behaviour of each ingredient that is caused by the change in heating rate. On the other hand, the shift of thermal degradation to higher temperatures means also that the ingredients are longer available for chemical reactions and interactions. However, based on the reviewed data, it cannot be finally concluded which effect is more significant. The extent to which even higher heating rates can enhance

the observed effects of shifting decomposition reactions cannot be quantified as well since adequate investigations are missing. In how far also melamine influences the reaction processes in case of changing heating rates, will be explained in the following.

Table 2.5: Thermal degradation data of PER under nitrogen (N_2) for heating rates of 1, 3, 5, 10 and 20 K/min by TGA according to Sakamoto et al. (1984)

	$T_{initial}$[a]	T_{max}[b] (°C)	Residue (wt%) at		R_{max}[c]
Sample	(°C)	Stage 1	Stage 1	300 °C	(%/°C)
1 K/min	186	242	35.97	-	-2.79
3 K/min	196	266	33.17	1.38	-2.41
5 K/min	214	280	30.35	2.52	-2.50
10 K/min	226	294	32.25	15.92	-2.49
20 K/min	240	313	34.38	61.10	-2.30

[a] $T_{initial}$ is the temperature at 0.1 % weight loss
[b] T_{max} is the temperature at which the maximum degradation rate occurs
[c] R_{max} is the maximum degradation rate

Melamine (MEL):

Costa & Camino (1988) and other researchers performed thermogravimetric analyses in which the thermal decomposition behaviour of melamine was investigated. Within these analyses samples of 10 mg size were examined using nitrogen, air and argon atmosphere with a flow rate of 30 - 90 cm^3/min. Only Derakhshesh et al. (2012) deviated from the majority of the analyses and used in their investigations a sample size of 0.6 mg. However, a very good comparability of the results is still given.
Melamine is used in intumescent coatings as blowing agent and is known to undergo sublimation and condensation reactions simultaneously (Costa & Camino 1988). Upon heating a part of MEL sublimes at the same time as the other part condensates by elimination of ammonia (Derakhshesh et al. 2012). For the condensation reaction Costa & Camino (1988) propose two different routes in which MEL decomposes to build linear branching or cyclic condensates. During this condensation, intermediates such as melam, melem and melon are formed (Ducrocq et al. 2006). When heated at atmospheric pressure, melamine does not melt, but rather sublimates (Weil & Choudhary 1995). According to Wang et al. (2006) the sublimation and condensation reactions occur between 260 and 395 °C. This temperature range can be confirmed by the reviewed thermogravimetric analyses, as described in the following.
In order to assess the influence of different heating rates on the decomposition behaviour of MEL, results of TG analyses performed by Costa & Camino (1988), Wang & Yang (2011) and Jiao et al. (2012) are compared in Figure 2.18 a). Similar to PER, MEL decomposes in one reaction stage due to heating. With the increase in heating rate (10 to 100 K/min) the decomposition reactions shift to higher tem-

peratures. While the decomposition behaviour of MEL is initiated at 196 °C for 10 K/min, the start in mass loss occurs for 100 K/min at 287 °C (see Table 2.6). This behaviour could be due to thermal inertia of the samples. It is noteworthy that the observed temperature shift between 20 and 100 K/min, however, is less pronounced than the shift for the increase in heating rate from 10 to 20 K/min (compare the distances between the graphs in Figure 2.18 a) and the degradation rate (R_{max}) in Table 2.6). Therefore, it is assumed that the influence of thermal inertia is limited to a certain scale.
Since TG curves of MEL under air atmosphere are missing for different heating rates in literature, the mass loss behaviour is therefore shown in Figure 2.18 b) for a constant heating rate of 10 K/min under nitrogen, air and argon atmosphere. As the decomposition of MEL occurs due to sublimation and condensation by elimination of ammonia, it is comprehensible that no significant differences in mass loss behaviour can be observed due to the variation in atmosphere. Although a slightly different behaviour under nitrogen occurs when reaching about 12 wt%. This is rather due to the circumstances (actuality of the investigations) under which the analyses were performed (Costa & Camino 1988) than due to the influence of atmosphere. Similar differences in TG curves have already been shown in Figure 2.18 a), although all studies were carried out under nitrogen atmosphere. As a consequence, due to the similar behaviour under different atmospheres, it can be assumed that MEL will also exhibit a similar heating rate-dependent behaviour under air, as observed under nitrogen.

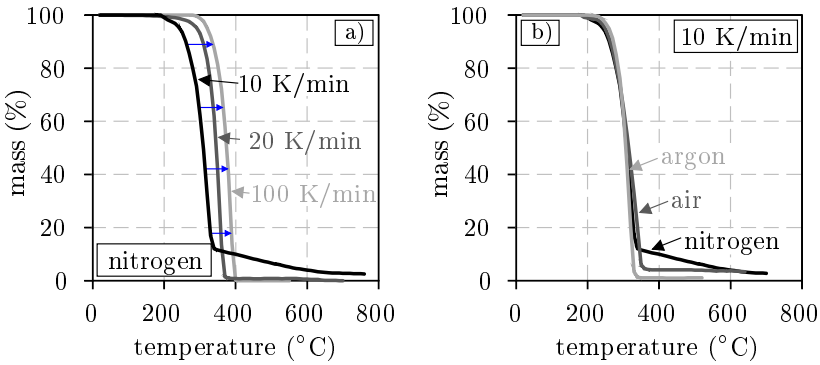

Figure 2.18: TG curves of melamine (MEL) under nitrogen a) at 10 K/min (Costa & Camino 1988), 20 K/min (Wang & Yang 2011) and 100 K/min (Jiao et al. 2012) and at 10 K/min b) under nitrogen (Costa & Camino 1988), air (Derakhshesh et al. 2012) and argon (Balabanovich 2004)

When evaluating the reviewed thermogravimetric data of APP and PER, it has already been found out that changes in heating rate lead to different temperature shifts in the decomposition reactions of the two ingredients. While APP reacts more than twice as sensitive as PER to changes in heating rate (APP: Δ 50 K,

PER: Δ 19 K), the data (T_{max}) given in Table 2.6 reveal that the sensitivity of MEL to the increase in heating rate from 10 K/min (320 °C) to 20 K/min (354 °C) lies in between (Δ 34 K). An increase from 10 to 100 K/min leads, however, to a temperature shift in the decomposition reactions of Δ 65 K. With the increase in heating rate and the resulting temperature shift, a continuous decrease in residual mass at stage 1 (reaction stage at which the maximum degradation rate occurs) and at 600 °C occurs for MEL. Since comparable literature data with such a high heating rate for APP and PER are missing, no general conclusions can be drawn on the interactive behaviour of APP, PER and MEL. Nevertheless, similar to the previous reflections, the observed heating rate-dependent behaviour of MEL provides important information to understand the fire protection performance of intumescent coatings under natural fires in general.

Table 2.6: Thermal degradation data of MEL under nitrogen (N_2) for heating rates of 10, 20, and 100 K/min by TGA according to Costa & Camino (1988), Wang & Yang (2011) and Jiao et al. (2012)

	$T_{initial}$[a]	T_{max}[b] (°C)	Residue (wt%) at		R_{max}[c]
Sample	(°C)	Stage 1	Stage 1	600 °C	(%/°C)
10 K/min	196	320	32.78	4.0	-1.62
20 K/min	227	354	31.28	0.6	-2.57
100 K/min	287	385	27.84	-	-2.28

[a] $T_{initial}$ is the temperature at 0.1 % weight loss
[b] T_{max} is the temperature at which the maximum degradation rate occurs
[c] R_{max} is the maximum degradation rate

Vinyl polymers:

A large number of polymer binders is used for intumescent coatings (see Table 2.3). For this reason, the present literature review cannot meet the requirement to be complete. As a consequence, only the binders that are mostly relevant for the work are presented in the following with regard to their thermal decomposition behaviour. As the focus lies on waterborne intumescent coatings, vinyl polymers such as polyvinyl acetate, polyvinyl alcohol and ethylene vinyl acetate will be addressed in the following.
Vinyl polymers belong to a group of polymer binders which are derived from polymerisation of vinyl monomers (Oda & Shinke 2014). Polyvinyl acetate (PVAc) and polyvinyl alcohol (PVA), for example, are made of vinyl acetate. While PVAc is made directly by polymerisation of vinyl acetate, PVA is produced by a subsequent hydrolysis of PVAc. Ethylene vinyl acetate (EVA) that is also used as a polymer binder in intumescent coatings (see Fukuba (1976) and Buckingham (1994)) consists also of a certain amount of vinyl acetate.

In order to assess the sensitivity of EVA to changes in heating rates, results of TG

analyses performed by Beyer (2001), Bonnet et al. (2012), Yen et al. (2012) and Liu et al. (2013) are compared in Figure 2.19. Here, the thermal decomposition is given for heating rates of 10 and 20 K/min as well as for different atmospheres, such as air, nitrogen and helium. In order to ensure comparability, only samples with comparable mass (9 - 15 mg), density (0.948 - 0.949 g/cm^3), melting temperature (75 - 77 °C) and melt flow index (2 - 4.5 g/10 min) were used. The melt flow index represents in this case a measure of the plastic melt viscosity and was measured with the help of a capillary rheometer.

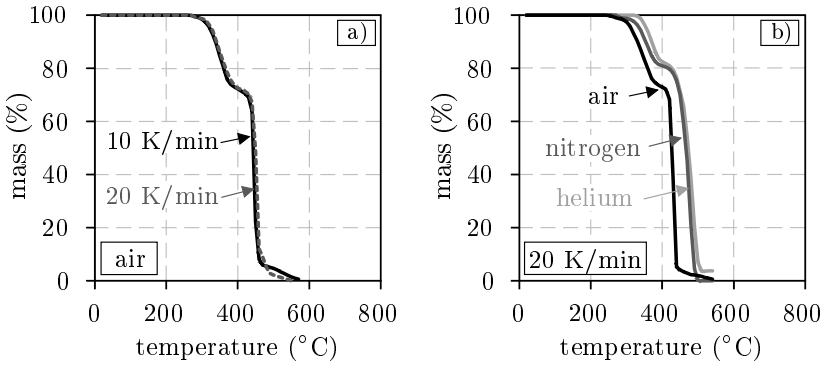

Figure 2.19: TG curves of ethylene-vinyl acetate (EVA) under air a) at 10 K/min (Bonnet et al. 2012), 20 K/min (Beyer 2001) and at 20 K/min b) under air (Yen et al. 2012), nitrogen (Liu et al. 2013) and helium (Beyer 2001)

As reported by Ballistreri et al. (1980), the decomposition of polymer binders in intumescent coatings is first initiated by melting. This phase change from solid to liquid occurs normally for vinyl polymers at temperatures of 150 °C. However, EVA starts already to melt at 75 °C but decomposes initially at 270 °C (for a vinyl acetate content of 28 wt%) under air atmosphere (see Figure 2.19 a)).
The comparison of different EVA copolymers reveals that the temperature-induced start of decomposition shifts to higher temperatures when the acetate content decreases. However, it is worth mentioning that this observed behaviour remains unaffected by changes in heating rate as shown in Figure 2.19 a). Regardless of whether the TG analyses were carried out for a vinyl acetate content of 18 wt% (see Fu & Qu (2004) and Wang et al. (2011)) or 28 wt% (see Beyer (2001) and Bonnet et al. (2012)) under air or nitrogen atmosphere, in all cases the measured TG curves are congruent for 10 and 20 K/min. Thus, it can be concluded that the thermal decomposition behaviour of EVA remains unaffected by changes in heating rate.
When heated, EVA undergoes two main degradation steps (El Hage et al. 2014). The first degradation step (270 - 400 °C) corresponds to the deacylation reaction (dissociation of acetoxy group) in which the loss of the acetic acid is initiated (Bonnet et al. 2012). The second step (400 - 550 °C) involves the thermal decomposition

of the formed unsaturated backbone either by further chain scissions (non-oxidative decomposition) or by thermal combustion (oxidative decomposition) as reported by Beyer (2001). This is the reason why the measured TG curves under nitrogen and helium (non-oxidative atmospheres) given in Figure 2.19 b) deviate from the TG curve obtained under air atmosphere.

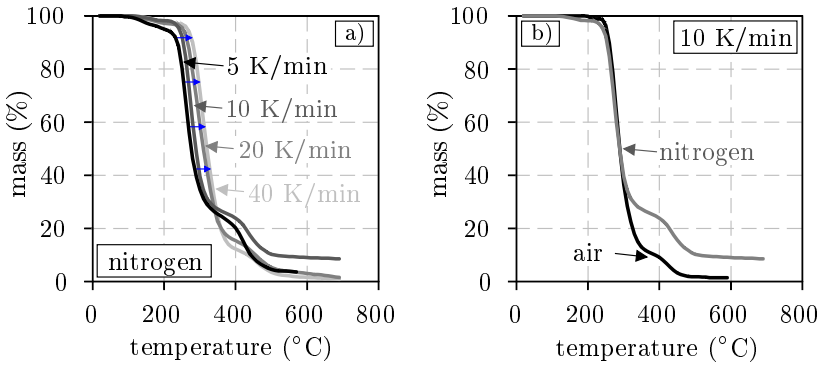

Figure 2.20: TG curves of polyvinyl alcohol (PVA) under nitrogen a) at 5, 10, 20 and 40 K/min (Dong et al. 2016) and at 10 K/min b) under air (Xu et al. 2016) and nitrogen (Dong et al. 2016)

While EVA was mainly used in the 1970s to 1990s as polymer binder in intumescent coatings, nowadays PVA and PVAc are mainly used in waterborne coatings. With regard to their heating rate-dependent behaviour, both vinyl polymers show a differentiated behaviour compared to EVA. According to the TG analyses of Dong et al. (2016) presented in Figure 2.20 a), PVA (degree of polymerisation: 1,700, degree of hydrolysis: 99 mol%) shows a low heating rate-dependence for the investigated parameter range of 5 - 40 K/min. Under air and nitrogen, however, PVA undergoes a similar decomposition behaviour until the second reaction stage (380 - 500 °C) is reached (see Figure 2.20 b)).
In literature it is accepted that the degradation of PVA occurs in two stages. While the first stage (250 - 380 °C) is dominated by the elimination of water and residual acetate groups (Cui et al. 2016), the second degradation stage is due to chain scissions and cyclisation reactions (Lu et al. 2011). Since the elimination of water and the acetate groups is a physical process, the first reaction stage is affected by thermal inertia due to the increase of the heating rate. This is the reason why the mass loss of PVA occurs at higher temperatures for increasing heating rates. However, the resulting temperature shift (Δ 16 K) of the first reaction stage due to the increase in heating rate (from 10 to 20 K/min) is less than with ammonium polyphosphate, pentaerythritol or melamine.
As already mentioned, PVA is produced by a hydrolysis reaction of PVAc, which in turn is formed by polymerisation of vinyl acetate. Since the heating rate dependence of PVA is caused by, among others, the elimination of water, it can be assumed that the degradation behaviour of PVAc is not affected by changes in

heating rates due to the absence of water and its thermal inertia. The results of TG analyses (see Figure 2.21) that were performed by Rimez et al. (2008) and Rimez et al. (2015) confirm this hypothesis. Their analyses were carried out for PVAc with a molar mass of 100,000 g/mol under air and nitrogen atmosphere. In case of air there is only a small difference between the measured TG curves at 10 and 20 K/min. This can be due to the differences in setup of the analyses since different flow rates (25 and 50 cm^3/min) were used. Under nitrogen atmosphere, however, the influence of the increase in heating rate on the degradation behaviour of PVAc is almost non-existent.

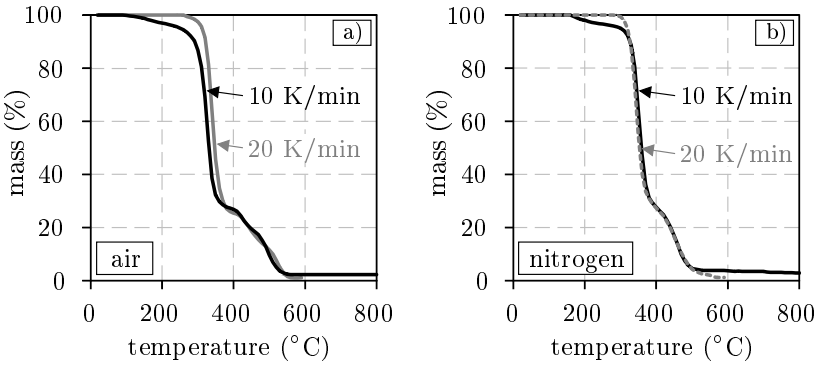

Figure 2.21: TG curves of polyvinyl acetate (PVAc) under a) air and b) nitrogen at 10 K/min (Rimez et al. 2015) and 20 K/min (Rimez et al. 2008)

The reaction stages that occur during the thermal degradation of PVAc are reported in literature to be independent of the atmosphere. Varma & Sadhir (1975), for example, suggest that the first decomposition stage (300 - 380 °C) of PVAc is caused by the loss of acetic acid. In the second stage (380 - 530 °C), the remained olefinic residue subsequently decomposes either by cyclisation, aromatic compound formation or chain scission. Thus, no reactions take place that could cause a heating rate dependence of PVAc due to thermal inertia. Therefore, it can be concluded that PVAc, similar to EVA, shows an independent thermal behaviour with regard to changes in heating rates.
Basically, all three polymer binders (EVA, PVA and PVAc) at which the literature review was focused on, show either no or only a slight heating rate-dependent behaviour compared to the rest of the main ingredients. The extent to which this deviant behaviour has an influence on the performance of intumescent coatings in natural fires will be discussed in the following.

Discussion:

In order to assess the decomposition behaviour of intumescent coatings' main ingredients under varying heating conditions, over 60 papers were systematically reviewed. From these publications, 34 data sets of performed thermogravimetric

analyses were subsequently selected and analysed with regard to their sensitivity to changes in heating rates. Within the scope of the literature review, of course, significantly more data were collected. However, only those results were used for the evaluation of the heating rate dependence of the ingredients, which were obtained under comparable conditions.
In order to compare the sensitivity of the main ingredients to changes in heating rates, the temperature shifts (ΔT) of the first degradation stage that occur due to the increase of the heating rate from 10 to 20 K/min is visualised by a bar diagram in Figure 2.22 a). Here, the temperature shifts are given for both air and nitrogen atmosphere. The data marked with (*) were originally determined under nitrogen atmosphere. However, a comparison of single TG curves that were obtained under nitrogen and air has shown a nearly congruent behaviour. Therefore, the temperature shifts (ΔT) of PER, MEL and PVA are assumed to be valid for both air and nitrogen atmosphere. This is important since the fire-induced intumescence reactions of intumescent coatings normally take place under oxidative conditions.

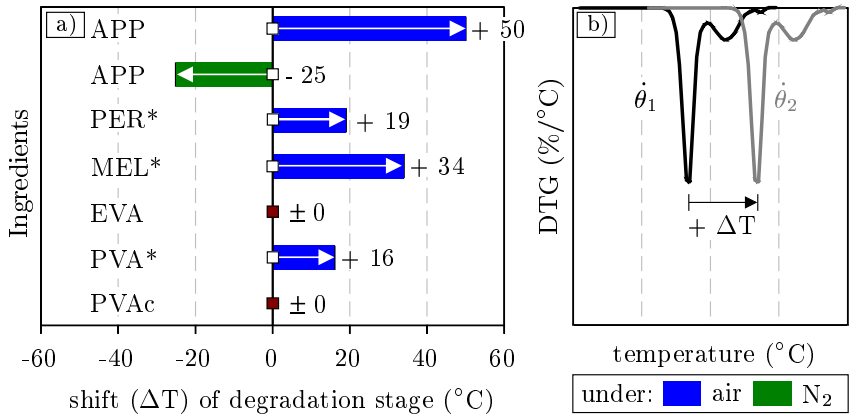

Figure 2.22: Comparison of the heating rate-dependent bahaviour of ammonium polyphosphate (APP), pentaerythritol (PER), melamine (MEL), ethylene-vinyl acetate (EVA), polyvinyl alcohol (PVA) and polyvinyl acetate (PVAc) based on the data from Figures 2.16 to 2.21: a) temperature shifts of the first degradation stage and b) definition of the temperature shift (ΔT) for the heating rates of 10 and 20 K/min ($\dot{\theta}_1$ and $\dot{\theta}_2$, respectively)

Taking into account the definition of the temperature shift (ΔT) that is graphically described in Figure 2.22 b), APP is the only ingredient that thermally decomposes faster under nitrogen due to the increased heating rate. An explanation for this behaviour could not be found in the literature and, therefore, is still pending. The reason for this is that in literature the same degradation reactions are falsely proposed for both air and nitrogen atmosphere, although significant differences in mass loss behaviour are observed for oxidative and non-oxidative conditions.

Under air atmosphere, the mass loss of the main ingredients is retarded due to the increase in heating rate and, therefore, occurs at higher temperatures. The sensitivity to changes in heating rate is especially pronounced for APP, PER and MEL, even if there are some differences between them. The polymer binders (EVA, PVA and PVAc), on the other hand, are less sensitive or even unaffected by the increase of the heating rate.
In contrast to the reviewed thermogravimetric analyses, natural fires can show significantly higher heating rates (up to 100 K/min and higher). As the majority of the presented data is limited to heating rates of maximum 20 K/min, the effect of a further increase in heating rate on the thermal degradation behaviour of the main ingredients cannot be conclusively clarified on the basis of the data that is given in literature. In addition, natural fires (see subsection 2.4.2) are characterised by a heating and a cooling phase. As the performed TG analyses were solely performed for the heating state, no information is provided by the analyses for the thermal degradation behaviour of the ingredients in the cooling phase.
In order to assess these entire facts correctly, the following should be pointed out: (1) In the diagrams shown above, only the thermal decomposition behaviour of isolated ingredients is analysed. The intumescence reaction, however, requires an interaction of all ingredients simultaneously. (2) The thermal decomposition behaviour obtained from the TG analyses and the reaction or interaction behaviour of single ingredients in intumescent coatings should not be treated as equal. For example, the ingredients may undergo a phase change from solid to liquid without being recognised in the TG curves. Differential scanning calorimetry analyses, however, can detect such physical phenomena. (3) On the basis of TG data alone, no conclusion can be drawn whether the heating rate-induced temperature shift of e.g. the decomposition of APP has a positive or negative effect on the fire protection performance of intumescent coatings. However, the fact that it was found out that the main ingredients show a differentiated behaviour due to the increase in heating rate, represents a high gain of knowledge. (4) The TG analyses were originally carried out under different aspects. Only with the compilation of the data under the aspect of heating rate dependence, a new basis of knowledge could be created. In the scope of this thesis, this data will serve as a basis for the description and identification of relevant parameters for the heating rate-dependent fire protection performance of intumescent coatings in natural fires. Since data is now available at the level of single ingredients, explanations for the heating rate-dependent behaviour of intumescent coatings can be found beyond the phenomenological observations. However, literature-known experimental investigations (see subsection 2.2.7) as well as especially own experimental (see chapter 3) and numerical investigations (see chapter 4) will complete the findings entirely.

2.2.7 Experimental Investigations of the Thermomechanical Behaviour and its Heating Rate Dependence

In literature, many experimental studies address the performance of intumescent coatings. However, in most cases, the influence of recipe optimisation or single ingredients is investigated. Only few studies have been performed to investigate the fire protection performance of intumescent coatings under different fire or heating conditions. For this reason, the studies that are relevant for this work will be presented in the following, starting with the intumescence behaviour and the morphology of intumescent coatings under varying heating conditions.

Intumescence Behaviour and Morphology:

In order to assess the affect of different heat fluxes (35 and 75 kW/m^2) on the intumescence and fire protection performance of two commercial waterborne intumescent coatings, Mesquita et al. (2009) performed cone calorimeter tests on coated steel plates (100 x 100 mm, thickness: 4 and 6 mm). The operating principle of the cone calorimeter and the influences of its setup on the results are described, among others, by Babrauskas (2016) and Schartel et al. (2005) and, therefore, are not part of this chapter. During the tests the research group monitored the steel plate temperature and the intumescence behaviour of the coatings. While the steel temperature was measured by thermocouples (type K), the intumescence data was obtained from a digital camera and a subsequent image processing technique. As the intumescence behaviour of the investigated coatings was assessed by Mesquita et al. (2009) by means of the total char thickness, the data is transferred to an expansion factor ϵ according to Equation 2.1. This allows a better comparability of the results.

$$\epsilon = \frac{t(\theta)}{t_0} \tag{2.1}$$

$t(\theta)$: char thickness at char temperature θ (mm)
t_0: dry film thickness at ambient temperature (mm)

In Figure 2.23 the calculated expansion factors and the corresponding steel plate temperatures are given as a function of time. Based on this data Mesquita et al. (2009) were able to demonstrate a clear correlation between the expansion behaviour of the coatings and the heating conditions. One of the waterborne intumescent coatings (coating B) showed a significantly higher expansion behaviour for the higher heat flux (75 kW/m^2). In addition, the authors were also able to determine higher expansion values for the lower dry film thickness (1500 μm) for both investigated heat fluxes, respectively. However, despite the higher expansion factors, a higher steel temperature was still observed for the samples with low dry film thickness (see Figure 2.23 b)). This is due to the total char thickness that was observed to be smaller for the samples with low dry film thickness.
When the steel temperatures are evaluated in terms of heat flux, the conclusion can

be drawn that the fire protection performance of the investigated coating is better for the lower heat flux. However, when interpreting the results of Mesquita et al. (2009), the following must be considered. A comparison of the results over time implies that the intumescent coating is exposed to different thermal energies. To illustrate these differences, Figure 2.24 a) shows the integrals of the two heat fluxes over time. These integrals illustrate that in case of 75 kW/m^2, more than twice as much energy is added to the intumescent coating than for 35 kW/m^2. Therefore, in order to ensure comparability, the results must be related to the same energy level (94.5 · 10^3 kJ/m^2).

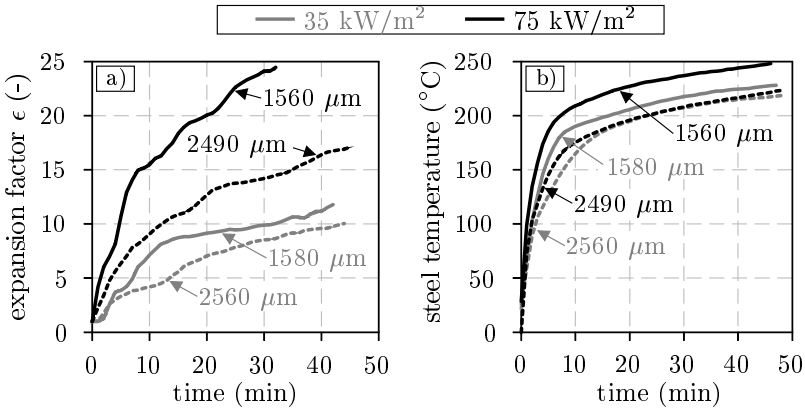

Figure 2.23: Results of cone calorimeter tests for 35 and 75 kW/m² of a waterborne intumescent coating according to Mesquita et al. (2009): a) averaged expansion factor ϵ of a four-time measurement and b) steel plate (100 x 100 x 4 mm) temperatures

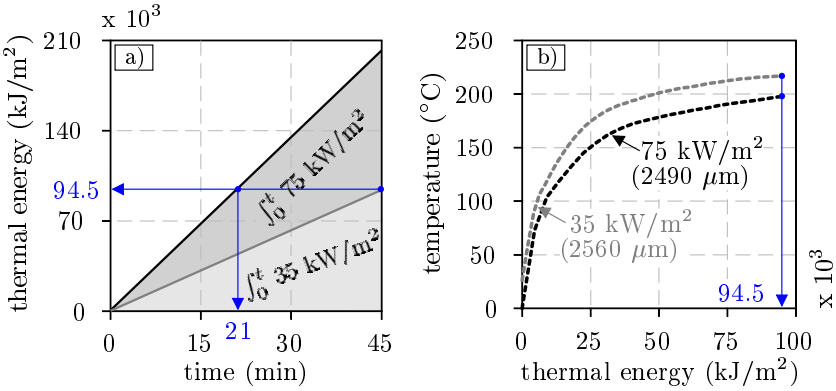

Figure 2.24: Conversion of the cone calorimeter tests of Mesquita et al. (2009): a) integral of the acting heat flux and b) steel plate (100 x 100 x 4 mm) temperatures as a function of the resulting thermal energy

This was done exemplarily for the steel plate temperature in Figure 2.24 b). Here, the transferred data reveal that the waterborne coating show a better insulation

performance for the higher heat flux as the steel temperatures are now compared at different points in time (after 21 and 45 minutes) to ensure the same energy level. Depending on the data processing and the evaluation, as a consequence, the results lead to completely different conclusions compared to Mesquita et al. (2009). To be clear, in this case, the transformation of data was performed exemplarily with nominal heat flux values. Especially for intumescent coatings, however, it is of great importance to monitor the actual heat flux. Since the distance between the heat source and the char surface changes with the expansion of the coating, the heat flux increases and, therefore, does not remain constant. However, the expansion and insulation performance of intumescent coatings should be evaluated at the same energy level. Hence, the expansion and temperature data should be assessed in case of cone calorimeter tests as a function of thermal energy and not as a function of time as it was done by Mesquita et al. (2009).
The review of other literature-known cone calorimeter tests on intumescent coatings reveal that in nearly all cases the results are evaluated as a function of time. Therefore, almost all authors disregard the influence of unequal energy levels, resulting in partially misleading conclusions. Zhang et al. (2012*b*), for example, also performed cone calorimeter tests for a waterborne intumescent coating (Firetex, Leighs Paints, UK) a few years after Mesquita et al. As the research group carried out their analyses under different heat fluxes (50 and 65 kW/m^2), steel plate thicknesses (5, 10 and 20 mm) and desired coating thicknesses (500, 1000 and 1500 μm), the parameter range of Mesquita et al. was extended. However, Zhang et al. (2012*b*) focused in their paper only on the validation of their calculation model and did not evaluate their experimental results in terms of the heating rate dependency of the investigated intumescent coating. Nonetheless, besides the documentation of the intumescence and heating behaviour of the samples, Zhang et al. (2012*b*) examined also the influence of the distance between the cone heater and the char surface on the acting heat flux. According to their measurements, the heat flux varies between 62 and 44 kW/m^2 and between 82 and 57 kW/m^2 for a distance between 15 and 80 mm and nominal heat flux values of 50 and 65 kW/m^2, respectively. In a previous paper, Wang et al. (2005) determined the heat losses that occur during a cone calorimeter measurement. The heat loss by convection, the heat radiation of the char surface and the heat storage capacity of the insulating material on the backside of the samples were identified to be the influencing variables. With the help of this data and the measured char thicknesses, the actual heat flux that is acting on the char surface can be calculated. However, since the two heat flux distributions determined by Zhang et al. (2012*b*) are almost linear and parallel to each other, it is sufficient, for purposes of comparison, to refer the results to the nominal values. For this reason, Figure 2.25 and 2.26 show the measured expansion factors and steel plate temperatures as a function of thermal energy that was calculated on the basis of the approach described in Figure 2.24. However, due to the partially strong scattering dry film thicknesses, the influence of varying heat fluxes on the expansion behaviour of the investigated coating cannot be finally evaluated on the basis of the results provided by Zhang et al. (2012*b*). In addition, the heat

fluxes of 50 and 65 kW/m^2 are very close to each other. This could be the reason why no significant differences in surface properties were observed. In addition, the authors report that most expanded chars were too fragile to examine the pore size inside the char. Only the samples formed due to the lower heat flux (50 kW/m^2) were sufficiently stable.

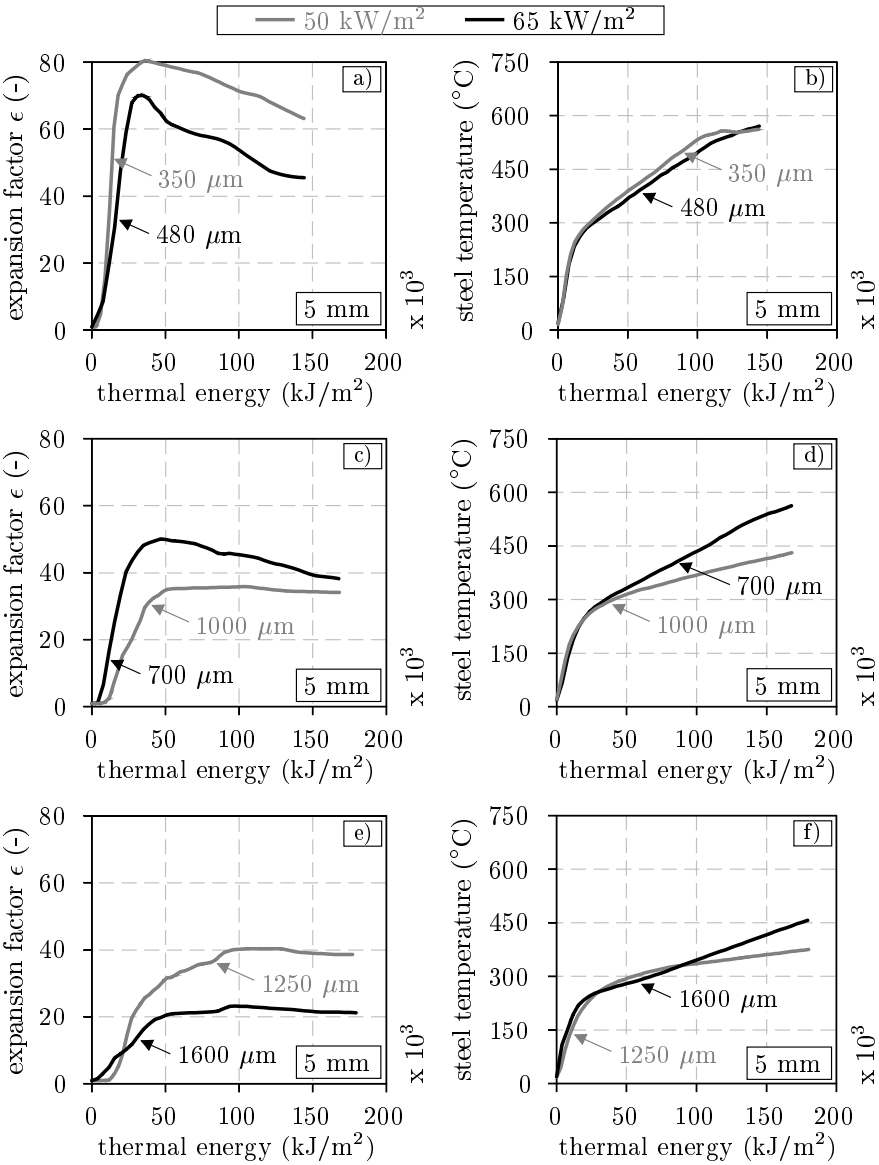

Figure 2.25: Results of cone calorimeter tests for 50 and 65 kW/m^2 of a water-borne intumescent coating according to Zhang et al. (2012b). Averaged expansion factors (a, c and e) and steel plate (100 x 100 x 5 mm) temperatures (b, d and f) for different DFTs

Here, the maximum pore size was determined to 3.5 mm, which is the same as observed at the surface of the char. Yuan & Wang (2009) investigated years before the same intumescent coating and reported a similar bubble growth.

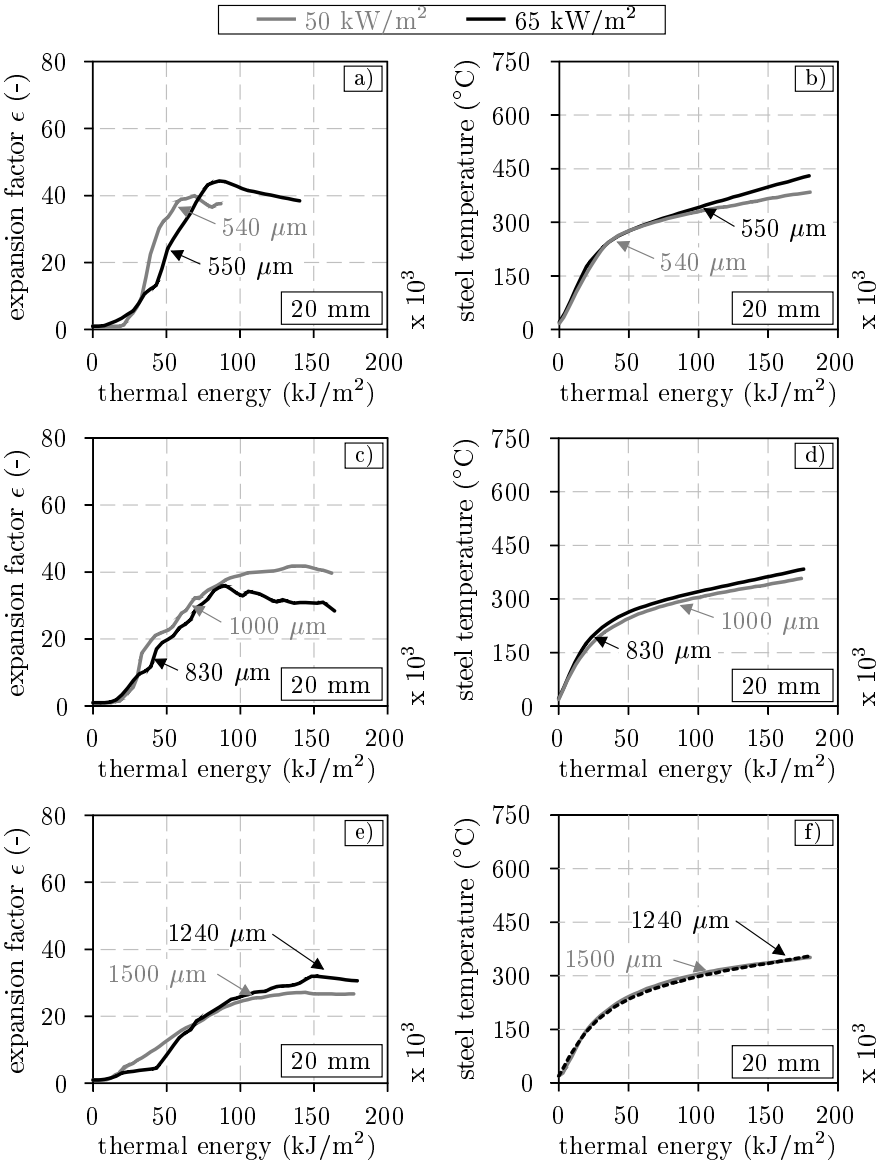

Figure 2.26: Results of cone calorimeter tests for 50 and 65 kW/m² of a waterborne intumescent coating according to Zhang et al. (2012b). Averaged expansion factors (a, c and e) and steel plate (100 x 100 x 20 mm) temperatures (b, d and f) for different DFTs

On the other hand, morphology investigations performed by Wang et al. (2015) show that changes in heating conditions have a certain influence on the quality of

the pore formation. Their research confirms that intumescent coatings show higher expansion factors when being exposed to higher heating rates and temperatures. But more important, the research group found out that their waterborne intumescent coating formed a more uniform and compact pore structure due to higher heating rates. This applies to both the surface and the interior of the formed char as documented by the photos and SEM (scanning electron microscope) micrographs in Figure 2.27.

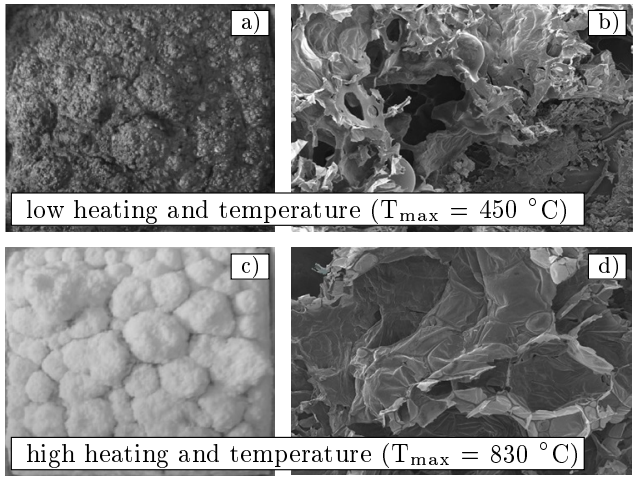

Figure 2.27: Photos of the char surface (a and c) and SEM micrographs of the interior of the char (b and d) formed by a waterborne coating under different non-standard fires according to Wang et al. (2015)

To conclude, the results of Zhang et al. (2012*b*) confirm that the extent of char expansion depends on the dry film thickness of the intumescent coating and the bulkiness of the steel structure. The largest expansion factors are measured for samples having the lowest dry film (350 μm) and steel plate thickness (5 mm). In the case of the 20 mm steel plates the bulkiness prevails, so that even different dry film thicknesses come to comparable expansion values. As a result, almost congruent steel temperatures are observed despite the difference in the acting heat fluxes, as can be seen in Figure 2.26 b), d) and f). Differences in pore structure and morphology due to changes in heat flux could not be observed since the samples could not be examined non-destructively. Investigation of Wang et al. (2015), on the other hand, show that changes in heating rate affect the morphology of intumescent coatings in a similar way as the intumescence and the heating behaviour. Basically, the morphology of intumescent coatings is sensitive to numerous factors, as described by Schartel et al. (2011). Besides the chemical interactions between the polymer, the additives and the surfactants, also the physical structure of the components (particle size, molecular weight, etc.) plays a decisive role for the formation of a uniform and highly fire resistive pore structure.

The results regarding the expansion behaviour presented above were all obtained in cone calorimeter tests. Cone calorimeter are usually designed to perform studies under constant heat fluxes. In the case of intumescent coatings, however, this is impossible due to changes in distance that occur between the cone heater and the char surface due to the intumescence process. In order to eliminate this effect, Lucherini et al. (2019) used a novel testing method to investigate the influence of varying heat fluxes and boundary conditions on the intumescence behaviour of a solvent-borne coating. The novel testing method is called H-TRIS (Heat-Transfer Rate Inducing System) and was developed at the University of Edinburgh by Maluk (2014). Originally, the method was developed to investigate the fire behaviour of high-performance concrete structures, such as heating and explosive spalling (Rickard et al. 2018, Maluk et al. 2019).
Within the test method, computer-controlled radiant panels are used. Therefore, the thermal exposure is controlled by the time-history of the incident heat flux (in a range of 10 - 200 kW/m^2), similar to the cone calorimeter. For this reason, H-TRIS and its advanced setup of the University of Queensland can be used to simulate any thermal boundary condition that is experienced by materials or structures due to the exposure to any source of heat (e.g. standard fire curve, real fire or some other thermal boundary conditions that are calculated by computational fluid dynamics models). Crucial for the testing method, however, is that the position of the radiant panels is adaptively computer-controlled (Lucherini & Maluk 2017). In this way, the distance between the radiant panels and the investigated material remains always constant, even if, for example, intumescent coatings expand.
Lucherini et al. (2019) used this method to investigate experimentally the influence of thermal conditions of steel elements on the high-temperature performance of a solvent-borne intumescent coating. For this reason, the research group examined coated steel plates (200 x 200 x 10 mm) with four different boundary conditions at the unexposed surface of the steel plates. The boundary conditions were realised by two different sample holders. Sample holder A was used to reproduce adiabatic conditions (ADC). Sample holder B, on the other hand, was used to define heat sink conditions. The heat sink was realised by a thick (20 mm) steel plate and water (20 °C) circulation. The degree of heat sink was regulated by the water flow. In this way, a heat sink with a low rate (HSC1: no water circulation), medium rate (HSC2: water flow of 0.5 L/min) and high rate (HSC3: water flow of 10 L/min) was realised. This boundary conditions were chosen by the authors to simulate different structural conditions in large space buildings. The adiabatic condition, for example, is only valid for a compartment fire, in which flash over occurs and the steel structure is fully surrounded by the hot gases. In case of large space buildings (e.g. atriums, halls, stadiums, airports, etc.) steel structures are usually exposed to localised fires (see subsection 2.4.2). While only a part of the steel structure is exposed to the fire, the surrounding components remain unaffected. Due to these boundary conditions, a temperature gradient arises between the exposed and the unexposed components. As a result, the thermal energy is conducted from the directly exposed to the unexposed components. In order to evaluated the effect

of this loss in energy on the performance of a solvent-borne intumescent coating, Lucherini et al. (2019) performed experimental investigations by using the H-TRIS testing method in combination with the new developed sample holders.

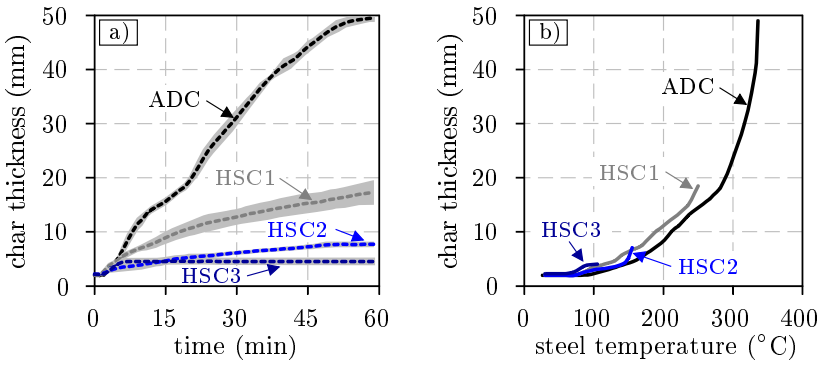

Figure 2.28: Results of small-scale fire tests acc. to Lucherini et al. (2019) using the Heat-Transfer Rate Inducing System (H-TRIS) with a heat flux of 50 kW/m². Measured char thickness of a solvent-borne intumescent coating (DFT = 1920-2300 µm) as a function of a) time and b) steel plate (200 x 200 x 10 mm) temperature under varying thermal conditions (ADC: adiabatic condition, HSC1: heat sink - low rate, HSC2: heat sink - medium rate and HSC3: heat sink - high rate) at the back of the steel plates

The intumescence behaviour of the coating was measured (at the centre of each sample) by a high-resolution video camera under a constant heat flux of 50 kW/m². The results of the char thickness measurements are given in Figure 2.28 as a function of time and steel plate temperature. Since three tests were performed for each boundary condition, the scattering of the expansion curves are represented in Figure 2.28 a) by the gray envelopes. The mean values are represented by the dashed lines.

From the mean values of the steel plate temperatures given in Figure 2.28 b) it can be seen that the boundary conditions controlled by the heat sink prevent the steel plates from heating. While under the adiabatic condition the steel plates reach a temperature of 340 °C, the samples that are influenced by the heat sink do not exceed the temperatures of 250, 150 and 100 °C, respectively. Therefore, despite the same heat flux, significantly lower char thicknesses (18, 7 and 5 mm) are finally achieved compared to the adiabatic boundary condition (50 mm). On the basis of this results, the authors conclude that the thermal conditions of steel structures control directly the intumescence behaviour of intumescent coatings. Unfortunately, Lucherini et al. (2019) do not establish a correlation between the boundary conditions within their measurements and the bulkiness of real steel structures. An extension of the investigations to further heat fluxes would also be very desirable in order to be able to evaluate the influence of other energy levels on the char formation of intumescent coatings. However, the investigations contribute

to a significant gain in knowledge. Besides the correlation between the steel temperature and the expansion ratio, the authors observed a large amount of virgin and unreacted material in the case of the heat sink tests. This behaviour is not the same as the decrease in expansion that was previously observed in literature due to reduced heating conditions. Low heating rates lead to reduced expansions, however, the intumescent coatings react entirely. The authors, on the other hand, observed that most parts of the coating remained unreacted due to the influence of the heat sink. Only the top layer directly exposed to the radiant panels expended and formed a carbonaceous layer. With regard to the evaluation of the fire protection performance, this can be classified as more positive, since in the case of a higher heat exposure, the remaining coating can expand and still protect the underlying steel component. For the heating rate-controlled expansion, on the other hand, this is not possible.

A completely different method for evaluating the expansion behaviour of intumescent coatings is presented by Gomez-Mares et al. (2012). Here, the authors used the so-called *fixed-bed tubular reactor* method to investigate an epoxy resin-based intumescent coating of Akzo Nobel. This setup (Barontini & Cozzani 2006) is formed by a stainless steel tube (length: 60 mm), in which a coating sample (thickness: 9 mm, diameter: 18 mm) is placed without a substrate. Than, the tube filled with the sample is placed in another stainless steel tube (length: 640 mm) that is located in an electric tube furnace (HST 12/300 Carbolite). In this way, a closed system is formed so that simultaneous measurements of the gas phase are possible using a Fourier-transform infrared spectroscopy (FTIR) equipment. Despite the high sample temperature of 800 °C, the investigated epoxy resin-based coating reached only a maximum expansion factor of 5.4 when heated with 10 K/min. This is due to both the high dry film thickness and the experimental setup. The arrangement of the sample within the tube creates a friction-based resistance between the expanded char and the inner surface of the tube. As a result, the expansion of the coating is significantly hindered.

In principal, the experimental setup of Gomez-Mares et al. (2012) is significantly different from other testing methods. On the one hand, the sample is arranged inside an untransparent stainless steel tube, so that a continuous monitoring of the expansion behaviour cannot be ensured. On the other hand, with this experimental setup the influence of the substrate bulkiness cannot be investigated either. In addition, the heating of the sample takes place via the inner surface of the tube and thus perpendicular to the expansion direction. For regular steel elements, however, the heating of the intumescent coating occurs normally unidirectional and parallel to the expansion direction.

A systematic analysis of the expansion behaviour of intumescent coatings at varying heating conditions was carried out by Tabeling (2014). He examined two solvent- and waterborne intumescent coatings as well as an epoxy resin-based coating of two different manufacturers. In addition to the standard fire curve, he used constant heating rates of 10, 30 and 50 K/min in a temperature range of 20 - 1000 °C for his investigations in an electric furnace (Nabertherm LE 1/11). He deter-

mined the expansion behaviour of the investigated coatings on thin steel plates (20 x 20 x 1 mm) with dry film thicknesses between 130 and 360 μm. Compared with other investigations known from the literature, the dry film thickness of the coatings was deliberately chosen to be as small as possible in order to minimise the temperature gradient within the expanded char. This was a requirement for the temperature measurement at different levels inside the formed char. In this way, Tabeling (2014) was able to determine the expansion behaviour of the investigated coatings as function of char temperature using an image-based analysis.

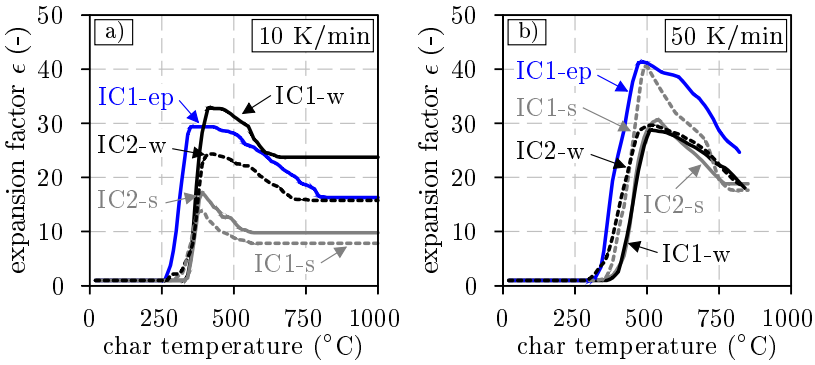

Figure 2.29: Results of expansion analyses according to Tabeling (2014) performed at a) 10 K/min and b) 50 K/min for waterborne (w), solvent-borne (s) and epoxy resin-based (ep) intumescent coatings of two manufacturers (IC1 and IC2)

The expansion factors given in Figure 2.29 as a function of char temperature and heating rate (10 and 50 K/min) confirm the results of Mesquita et al. (2009) and Lucherini et al. (2019) that the expansion behaviour of intumescent coatings basically depends on the heating conditions. However, the sensitivity to changes in heating rates vary among the different product classes. Due to the decrease of the heating rate from 50 to 10 K/min the strongest reduction of the expansion factors occurs for the solvent-borne intumescent coatings (IC1-s and IC2-s). The waterborne (IC1-w and IC2-w) and the epoxy resin-based intumescent coatings (IC1-ep) are also affected by the changes in heating rate. However, the changes are less pronounced.

In order to assess the influence of different heating conditions on the intumescence behaviour of intumescent coatings, several studies from the literature were reviewed and compared to each other. Except Zhang et al. (2012*b*), all studies report a heating rate-dependent expansion behaviour of intumescent coatings. Regardless of whether the investigations were carried out by using a cone calorimeter, radiant panels or an electric furnace, in all cases the coatings show for high heat fluxes or heating rates a more homogeneous and pronounced char formation. Few

studies, such as those of Wang et al. (2015) report that the different heating conditions do not only influence the char formation on the macroscopic but also on the microscopic level. On the basis of SEM images the research group shows that the pore structure and thus the morphology of the intumescent coatings is influenced by the heating conditions. However, explanations for these phenomenological observations on the basis of chemical or physical processes are not reported. Investigations regarding the changes in char formation and morphology during the cooling phase have also not been carried out so far.
In the approval tests (see subsection 2.2.2), intumescent coatings are tested under standard fire conditions. In order to pass these tests, the coatings are usually optimised by the manufacturers with regard to the heating regime of the standard fire curve. In the first minutes this curve is characterised by very fast heating rates of 95 K/min and higher. This could be the reason why intumescent coatings show the best expansion behaviour for higher heating conditions and a reduced char formation for lower heating rates.
To which extent the differential expansion behaviour of intumescent coatings affects their fire protection performance and which methods are currently used to assess the performance will be discussed in the following.

Fire Protection Performance:

In literature, different approaches are reported for the assessment of the fire protection performance of intumescent coatings under varying fire conditions. Most studies underline that it is rather difficult to directly measure the thermal properties of intumescent coatings such as the thermal conductivity. Therefore, the fire protection performance of intumescent coatings is generally assessed by indirect parameters. Bartholmai et al. (2003), for example, propose to use the thermal conductivity of intumescent coatings that is calculated from experimental data using the Fourier's law of heat conduction (see Equation 2.2).

$$\frac{\partial}{\partial x}\left(\lambda \cdot \frac{\partial T}{\partial x}\right) + \frac{\partial}{\partial y}\left(\lambda \cdot \frac{\partial T}{\partial y}\right) + \dot{\mathbf{w}} = \rho \cdot c \cdot \frac{\partial T}{\partial t} \tag{2.2}$$

For their calculations, the authors used a computer program called IOPT2D, which was developed at the Federal Institute for Materials Research and Testing (Müller 1989). As the program is based on the finite difference method, the thermal conductivity of the investigated coating was systematically varied until the calculated and measured sample temperatures coincided. In order to obtain the required experimental data, the research group performed cone calorimeter tests on coated steel plates (100 x 100 x 5 mm). In total, five different heat fluxes (30, 45, 60, 75 and 90 kW/m^2) were used to evaluate the influence of varying heating conditions on the fire protection performance of a waterborne intumescent coating with dry film thicknesses of 300, 600, 1000 and 1500 μm. An extract of the calculated thermal conductivity and the measured steel plate temperatures is given in Figure 2.30. The results show a clear dependence. After a certain heating, the thermal conduc-

tivity decreases rapidly due to the expansion of the coating and remains for the rest of the time nearly constant. During this time, the heating of the steel plates decreases as it is significantly affected by the insulative effect of the formed char. However, due to the variation in heat fluxes, differences in thermal conductivity and steel plate temperature are documented. According to the calculations, an increase in heat flux causes an increase in thermal conductivity which obviously correlates with the measured steel plate temperature (see Figure 2.30 b)).

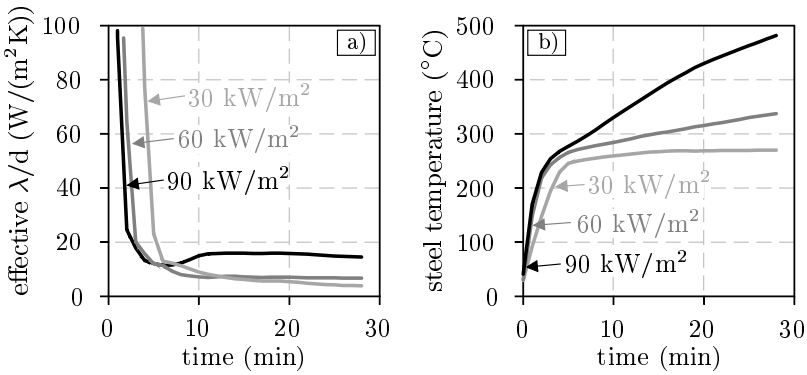

Figure 2.30: Results of cone calorimeter tests for 30, 60 and 90 kW/m² of a waterborne intumescent coating (DFT = 1000 µm) acc. to Bartholmai et al. (2003): a) effective thermal conductivity λ/d and b) steel plate (100 x 100 x 5 mm) temperatures

A similar correlation can be derived from the relationship between the thermal resistance and the heat flux that is given in Figure 2.31 a). Bartholmai et al. (2003) used the calculated thermal conductivity to compute the final thermal resistance of the waterborne coating for different dry film thicknesses. According to these calculations, especially high dry film thicknesses in combination with low heat fluxes show the highest thermal resistance. By evaluating these results, the authors ignore the fact that there is no uniform basis for the comparison of these results. Since the thermal resistances are compared at the end of each experiment, the samples are exposed to different amounts of thermal energy. The extent to which the thermal energies differ is shown in Figure 2.31 b). Therefore, in order to be able to compare the thermal resistances, it is necessary to refer them to the same energy level. This also applies to the calculated thermal conductivity and the measured steel plate temperatures in Figure 2.30.

In addition to the finite difference method, EN-13381-8 (2013) provides a simplified calculation approach to evaluate the fire protection performance of intumescent coatings. Within this approach the *effective thermal conductivity* is calculated from substrate temperatures that are measured during a fire test. In order to perform the calculations, the intumescent coatings are treated as non-reactive products with a constant material thickness. In this way, the effective thermal conductivity is

obtained from the measured substrate temperature ($\theta_{a,t}$) dependent on the section factor (A_p/V) and the heat storage capacity ($c_a \cdot \rho_a$) of the protected steel element by reverse calculation as described in Equation 2.3. Since it is rather difficult to measure the surface temperature of the char (θ_t), it is assumed to be equal to the temperature of the surrounding gas phase (θ_{gas}). If these assumptions are valid, the calculation approach should lead in the case of different thicknesses to the same results, provided that the investigated material has temperature and heating rate-independent material properties.

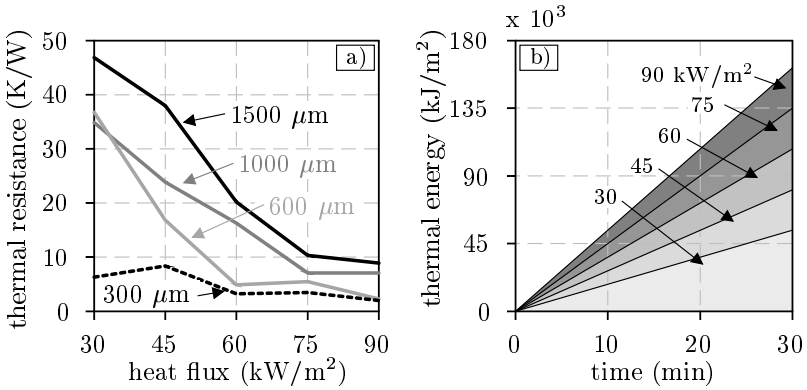

Figure 2.31: Results of cone calorimeter tests for 30, 45, 60, 75 and 90 kW/m² of a waterborne intumescent coating for different DFTs acc. to Bartholmai et al. (2003): a) final thermal resistance of the coating as a function of heat flux and b) visualisation of the resulting thermal energy due to the acting heat fluxes

$$\lambda_{p,t} = d_p \cdot \frac{V}{A_p} \cdot c_a \cdot \rho_a \cdot \frac{1}{(\theta_t - \theta_{a,t}) \cdot \Delta t} \cdot \Delta\theta_{a,t} \tag{2.3}$$

d_p:	dry film thickness (m)
V/A_p:	reciprocal of the section factor (m)
c_a:	temperature-dependent heat capacity of steel (J/(kgK))
ρ_a:	density of steel (kg/m³)
θ_t:	surface temperature of the coating/char (°C)
$\theta_{a,t}$:	substrate temperature at the back side (°C)
θ_{gas}:	temperature of the surrounding gas phase (°C)
$\Delta\theta_{a,t}$:	change of substrate temperature within the time increment Δt (°C)
Δt:	time increment (sec)

In order to evaluate the fire protection performance of a waterborne intumescent coating at different heating conditions, Wang et al. (2015) used the presented calculation approach. For the calculation of the effective thermal conductivity, the research group used results of fire tests carried out in an electric furnace for coated

steel plates (100 x 100 x 10 mm). Despite the different fire curves (maximum temperatures 450 and 830 °C, see Figure 2.27), the authors could not find a clear dependency between the effective thermal conductivity and the different heating conditions. However, a significant difference in effective thermal conductivity could be observed for different dry film thicknesses of the coating. Samples with a dry film thickness of 2000 μm showed despite the heating conditions higher char thicknesses (low heating: 28.9 mm and high heating: 30.9 mm) than the samples with a dry film thickness of 1000 μm (low heating: 17.1 mm and high heating: 22.6 mm). However, the effective thermal conductivity was twice as large for the higher dry film thickness. This is a contradiction since the steel plate temperatures for the samples with the higher dry film thickness were lower.

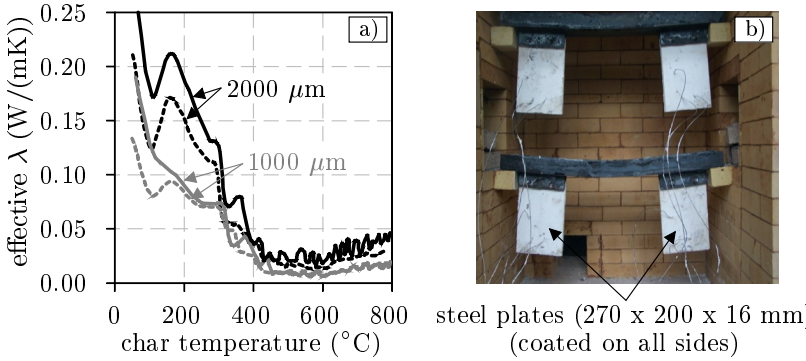

Figure 2.32: Results of standard fire tests for a waterborne intumescent coating according to Wang et al. (2013): a) effective thermal conductivity λ and b) arrangement of the test specimens inside the furnace

Similar observations were also made by Wang et al. (2013). The research group assessed the performance of their intumescent coating also on the basis of the effective thermal conductivity. The conductivity was calculated from fire tests of steel plates (270 x 200 x 16 mm) that were coated and exposed to fire from all sides. The dry film thickness was chosen, similar to Wang et al. (2015), to 1000 and 2000 μm. However, the fire exposure was based on the standard fire curve. Despite the fact that higher dry film thicknesses resulted in lower steel plate temperatures and showed higher expanded char thicknesses, the calculations of the effective thermal conductivity led to the results given in Figure 2.32. Here, the highest values for the effective thermal conductivity are also observed for higher dry film thicknesses. As the fire exposure is the same for all tests, the results can only be explained by the different dry thicknesses. A closer look at the calculation approach (see Equation 2.3) reveals that the dry film thickness is included in the equation as a linear factor. With an approximately equal quotient of the temperature change in the steel plate ($\Delta\theta_{a,t}$) and the difference between the gas and steel plate temperature (θ_t - $\theta_{a,t}$), the dry film thickness remains the only parameter that can dominate the results of the thermal conductivity calculation. This explains why both the

effective thermal conductivity values of Wang et al. (2013) and Wang et al. (2015) differ by a factor of two.
When evaluating their fire tests, Lucherini et al. (2018) also followed the calculation instructions of EN-13381-8 (2013). However, instead of the effective thermal conductivity, the research group introduced the thermal resistance $R = d_p/\lambda_p$ as a measure for the fire protection performance of intumescent coatings. In this way, the authors investigated a solvent- and a waterborne intumescent coating that were applied on both IPE400 steel profiles and steel plates (100 x 100 x 10 mm). In order to evaluate the influence of different heating conditions on the fire protection performance of the coatings, the research group performed fire tests in an electric furnace, a gas furnace and a cone calorimeter. The reference for the heating conditions was defined by the standard fire curve.

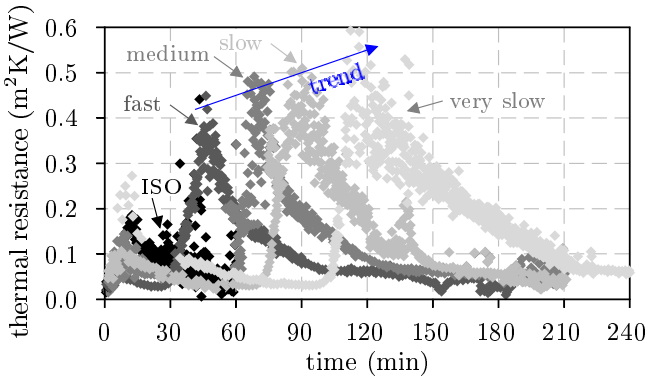

Figure 2.33: Calculated thermal resistance of a waterborne intumescent coating (DFT = 890-950 µm) for different heating conditions (ISO, fast, medium, slow and very slow) on the basis of fire tests of coated IPE400 steel profiles (four-sided fire exposure, A/V = 175 m^{-1}) according to Lucherini et al. (2018)

In Figure 2.33 the calculated thermal resistance is exemplarily shown for the waterborne coating as a function of time. The calculated values are based on the IPE400 fire tests that were performed for very slow, slow, medium and fast heating conditions as well as for the standard fire curve. The corresponding temperature-time curves are given in Figure 2.34 b).
The results show that the thermal resistance of the coating increases when the heating rates decrease. This trend is derived at least from the data points of the thermal resistance and means that the best fire protection performance is achieved for the lowest heating condition. However, the efficiency parameter $\eta_p(t)$ defined by Lucherini et al. (2018) contradicts these findings. According to the parameter, the fire protection performance of the investigated coatings increases with increasing heating rates (see Figure 2.34 a)). The solvent-borne coating, however, shows a higher sensitivity to changes in heating rate than the waterborne coating.
The research group defines the efficiency parameter according to Equation 2.4 as

the temperature difference between the unprotected and protected steel component in relation to the temperature of the unprotected component. In this way, a dimensionless parameter is obtained that becomes small with little difference between the unprotected and protected steel element. This corresponds directly to a low fire protection performance of the coating. However, it also means, that additional fire tests with unprotected steel elements need to be carried out to provide the required data for the evaluation of the fire protection performance of the coatings.

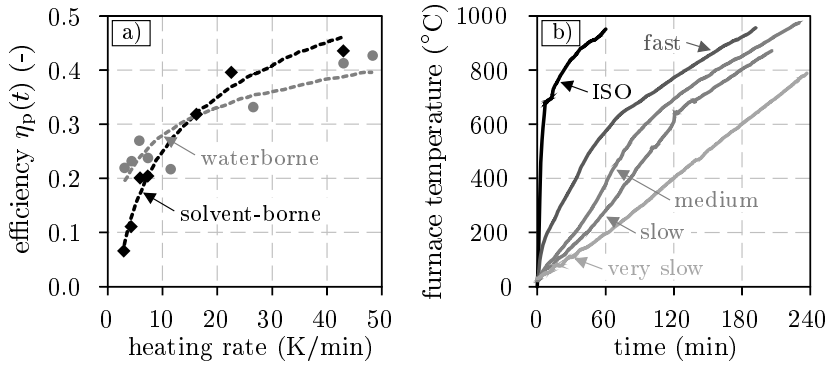

Figure 2.34: Results of fire tests according to Lucherini et al. (2018): a) thermal protection efficiency $\eta_p(t)$ (weighted temperature difference between unprotected and protected samples) of a solvent- and waterborne intumescent coating as a function of heating rate and b) corresponding furnace temperatures

$$\eta_{\mathrm{p}}(t) = \frac{\theta_{\mathrm{a,\ unprotected}} - \theta_{\mathrm{a,\ protected}}}{\theta_{\mathrm{a,\ unprotected}}} \tag{2.4}$$

$\theta_{\mathrm{a,\ unprotected}}$: temperature of the unprotected steel element (°C)
$\theta_{\mathrm{a,\ protected}}$: temperature of the protected steel element (°C)

The results of the previously presented studies have already shown that the assessment of the fire protection performance of intumescent coatings on the basis of the effective thermal conductivity, on the one hand, and the steel temperature, on the other hand, has a certain discrepancy. With the investigations of Lucherini et al. (2018), this discrepancy becomes even clearer. Depending on the choice of the assessment method, the authors come to completely different conclusions when evaluating the same experimental data. Therefore, this raises the question of which effect causes the differences and which method provides the right results? To answer this question, it is necessary to have a closer look at the assumptions that are made within the method of the *effective thermal conductivity*.
When calculating the effective thermal conductivity according to the EN-13381-8 (2013), three main assumptions are made: (1) The coatings are treated as non-reactive materials. This means, the thickness of the coatings is taken into account

only through the initial dry film thickness. Therefore, the heating and temperature-dependent behaviour of the coatings and their differential char formation that is reported in literature are not considered. (2) When calculating the temperature difference between the fire exposed and the unexposed side of the char, it is assumed that the temperature at the fire exposed surface is equal to the surrounding gas temperature. However, since the heat transfer due to convection is predominant at the beginning of the fire, in reality a significant difference between the gas temperature and the surface temperature of any material occurs as shown graphically in Figure 2.35 b). (3) The third assumption corresponds to the assignment of the calculated conductivity values to the char temperature. In this case, a mean value is calculated for the char temperature under the assumption of a linear gradient inside the formed char. Experimental investigations of several independent research groups, however, report that the temperature distribution inside the char can show a highly non-linear shape (see Figure 2.35 b)).
As can be seen, every assumption on its own deviates decisively from the real condition. Therefore, a combination of all three assumptions has an even more significant influence on the results of the calculations. However, this will be quantified in chapter 4 in more detail using numerical calculations. Nevertheless, it can already be concluded at this point that the fire protection performance of intumescent coatings should be assessed by means of the measured substrate temperature rather than by the calculated thermal conductivity. Discrepancies in data evaluation that were revealed by the literature review at least give rise to this conclusion.

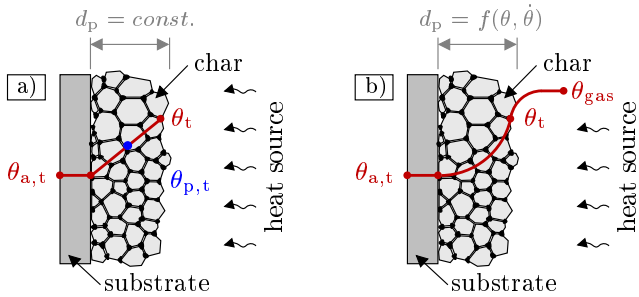

Figure 2.35: Temperature distribution within the expanded char of intumescent coatings: a) simplified assumption according to EN-13381-8 (2013) and b) actual behaviour of the char taking the heat transfer conditions between the gas phase and the char surface into account

In order to better understand the fire protection behaviour of intumescent coatings, several research groups have independently developed new experimental setups in the last years. With the help of these setups not only the substrate temperature but also the temperature development inside the formed char can be examined. The first laboratory tests in which the char temperature was measured during the intumescence process were performed by Mamleev et al. (1998) and Bourbigot et al. (1999). While Mamleev et al. investigated the heating behaviour of a fire-retardant

polymeric material (80 wt% phenol-formaldehyde resin and 20 wt% boron oxide) in a gas burner test, Bourbigot et al. used equidistantly arranged thermocouples to monitor the char temperature of a polypropylene-based intumescent coating during the limiting oxygen index test (LOI). This is a standard test method to measure the minimum oxygen concentration that is required to support candle-like combustion of plastics. In both cases, the gas burner test and the LOI test, ultra-thin thermocouples (200 μm and 250 μm) were used to minimise possible effects on the char formation. However, since the tests were performed at laboratory-scale and in parts without the control of the fire exposure, the tests are not representative for the research questions of this work.

The investigations performed by Schartel & Weiß (2010) and Wu (2011) are more relevant. Here, the temperature development inside a fire protection material was measured during cone calorimeter tests. The research subjects were epoxy nanocomposites in combination with layered silicate. In order to measure the temperature inside the formed silicate-carbonaceous char, the authors placed thermocouples (type K) at different heights horizontally within the sample holder. The insulation of the thermocouples was removed over several centimeters. This allowed the char temperature to be measured as soon as the char passed the individual levels of the thermocouples. However, due to the concentrated and horizontal arrangement of the thermocouples, an influence on the char formation could not be excluded.

Some years later Norgaard (2014) and Tabeling (2014) developed almost simultaneously and independently of each other a new setup to monitor the char temperature of intumescent coatings within a furnace test. In both cases, the thermocouples were no longer arranged in parallel but perpendicular to the test specimens (coated steel plates). Tabeling, however, positioned the thermocouples in front of the test specimens, while Norgaard arranged the thermocouples through drilled holes inside the steel plates. Instead of wire thermocouples, Norgaard used thermocouples with a shielding ceramic cover and a diameter of 1.5 mm (Norgaard et al. 2016). In this way, Norgaard was able to measure the distinctive time-temperature curves within the expanded char of a solvent-borne coating. However, in both cases, Norgaard (2014) and Tabeling (2014), the fire protection performance of the investigated coatings was only assessed for a fire exposure according to the standard fire curve. The same applies to Krüger et al. (2016). At the Federal Institute for Material Research and Testing, the experimental setup was even further developed and extended by a high-temperature-resistant endoscopic camera. This allows the expansion of the intumescent coating to be recorded while the temperature inside the expanded char is simultaneously measured. However, as the name of the electric furnace (STT Mufu$^+$) already indicates, the experimental setup has been used only for standard fire tests, so far.

For the sake of completeness, the testing methodology of Zhang et al. (2017) and Bozzoli et al. (2018) should also be mentioned. Both research groups used a similar way to arrange thermocouples inside the char of intumescent coatings as reported by Norgaard (2014). However, instead of furnace tests, the authors performed

cone calorimeter tests on coated steel plates for nominal heat flux values of 35 and 50 kW/m^2. As Zhang et al. (2017) focused in their research on synergistic additives and their influence on the fire protection performance of an epoxy resin-based coating, the research group found out with the help of the new testing methodology that especially chlorinated paraffin significantly hinders the transfer of external heat to the interior of the formed char. Bozzoli et al. (2018), on the other hand, used the experimentally obtained char temperature data to validate their finite element model for the calculation of the apparent thermal conductivity of intumescent coatings.

As the current state of research shows, there is currently no standard procedure for assessing the fire protection performance of intumescent coatings. The review of the literature-known investigations on the heating rate dependence of intumescent coatings even reveals contradictions between the provided assessment procedures. The method of the *effective thermal conductivity*, for example, comes to the conclusion that intumescent coatings show the best fire protection performance for lower heating conditions. The evaluation method based on steel temperatures, however, reveals the best fire protection performance for higher heating rates. As a consequence, systematic investigations have to be carried out in order to identify the reason for this contradiction so that in the future the fire protection performance of intumescent coatings can be properly assessed for the use in natural fires.

Mechanical Resistance:

The resistance of intumescent coatings against mechanical stresses is decisive for the fire protection performance during a fire event. A high mechanical stability of intumescent coatings prevents the formed char from cracking and, therefore, reduces the transfer of heat energy that normally penetrates through the cracks. Mechanical stresses can be caused by internal pressure (due to the release of gases), external effects due to surrounding components that prevent the intumescent coating from foaming or changes in thermal and mechanical elongation caused by the substrate to which the coatings are applied. As the differences in mechanical stresses reveal, intumescent coatings are exposed to both compressive and tensile stresses.
In order to investigate the resistance of intumescent coatings against mechanical destruction, Reshetnikov et al. (2000) compared different literature-known methods with regard to their suitability to measure the compressive strength of fully expanded chars. Besides a rotation-based measuring procedure, Reshetnikov presented two methods in which the char is loaded horizontally or vertically by a stainless steel punch. In the case of these two methods, the force that is required to destroy the char is measured and plotted as a function of deformation.
In the last two decades, one of the measuring methods has prevailed and is now used exclusively for the investigation of the compressive strength of intumescent coatings in the foamed state. In Figure 2.36 the operating principle of a rheometer is illustrated in different loading stages according to Toldy et al. (2007). A

rheometer is a device that can be used to measure the rheological properties, such as viscosity and elasticity of a non-Newtonian material (Heinz 1965). In order to perform the measurements, the samples are normally placed between two plates. When a torsional moment is applied to the upper plate, a shear stress occurs inside the investigated material. In this way, the deformation or deformation rate of the material is measured. Since the upper plate (or punch) of the rheometer is controlled in its vertical movement, the normal force applied to the sample can be arbitrarily adjusted. This adaptability is used in the case of intumescent coatings to measure the compressive strength of the char.

Figure 2.36: Mechanical destruction of an epoxy resin-based intumescent coating according to Toldy et al. (2007) using a rheometer (TA Instruments AR2000)

Studies on the compressive strength of intumescent coatings were performed, among others, by Bourbigot & Duquesne (2007) and Bodzay et al. (2011). Bourbigot & Duquesne focused their experimental study on the influence of inorganic fillers such as montmorillonite (MMT) and layered double hydroxides (LDH) on the compressive strength of the composition of ethylene-vinyl acetate (EVA), ammonium polyphosphate (APP) and polyamide 6 (PA6). Bodzay et al., on the other hand, used a typical APP/PER/MEL/TiO_2 formulation to evaluate the influence of nanoclays such as organic-modified montmorillonite (OMMT), sepiolite (SEP) and palygorskite (PAL) on the mechanical resistance of the formed chars against compression. In both cases the thickness (1 mm) and the diameter (25 mm) of the samples were identical. However, Bourbigot & Duquesne heated their samples with 100 K/min to a temperature of 400 °C, while Bodzay et al. performed their rheometer tests after reaching 500 °C (heating rate: 10 K/min). Differences also exist in the compression rate. Bourbigot & Duquesne loaded their char samples with 0.02 mm/s by moving the upper plate (punch). Bodzay et al. used a loading speed of 0.03 mm/s to set their samples under compression.
The results of both studies are given in Figure 2.37. Despite the different ways of presentation (the compressive force (N) is given as a function of gap (mm) or deformation(%)), the results qualitatively describe a similar behaviour for all samples. With decreasing gap distance between the plates or increasing deformation, a higher force needs to be applied to compress the samples. Therefore, the increase

in compressive force shows an almost exponential shape. This is due to the fact that the samples were strongly compressed. However, due to the different coating formulations, reaction stages and heating rates, significant differences in the maximum bearable load (16.0 N vs. 2.0 N) were observed. To what extent the heating rate of the samples has influenced the results cannot be conclusively clarified.
As can be seen in Figure 2.37 a), the use of inorganic fillers increases the stiffness of the intumescent char. This is due to the formation of chemical structures (rigid crystalline domains) that exhibit higher mechanical properties. However, these rigid domains are also responsible for the formation of cracks which have a negative effect on the insulation performance (Bourbigot & Duquesne 2007). Therefore, the amount of fillers in an intumescent coating formulation has to be chosen in a way that the mechanical properties are increased without causing cracking. Similar conclusions regarding the crack formation and the mechanical resistance of intumescent chars are also drawn by Jimenez et al. (2006*a*).
Bodzay et al. (2011) were able to confirm that also nanoclays such as OMMT improve the mechanical resistance of intumescent chars similar to the inorganic filler MMT (see Figure 2.37 b)). However, OMMT was observed to decrease the char thickness compared to the reference coating. Unfortunately, an explanation for this could not be given by the authors.

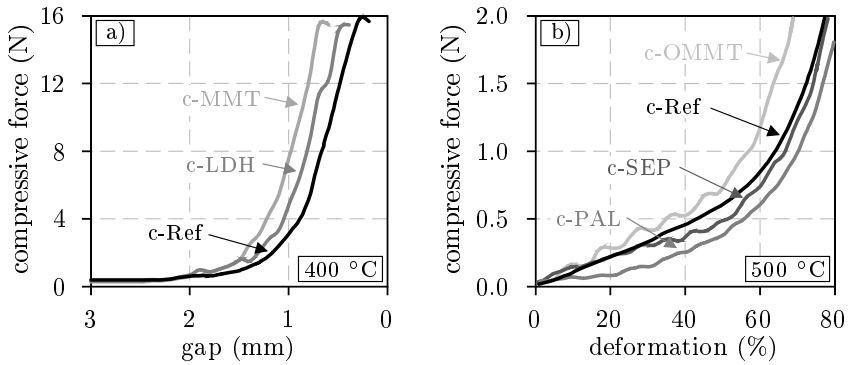

Figure 2.37: Compressive strength of a) an EVA/APP/PA6 (c-Ref) formulation with montmorillonite (c-MMT) and layered double hydroxides (c-LDH) as inorganic fillers according to Bourbigot & Duquesne (2007) and b) a solvent-borne coating (c-Ref) modified with organic-modified montmorillonite (c-OMMT), untreated sepiolite (c-SEP) and untreated palygorskite (c-PAL) according to Bodzay et al. (2011)

In contrast to the compressive strength, the tensile strength of pure intumescent coatings cannot be determined in the foamed state. For this reason, tensile strength tests are normally limited to the initial state. In this case, especially the binder is predominant for the tensile strength. Therefore, Fu & Qu (2004) performed tests to investigate the load-bearing and elongation behaviour of pure ethylene-vinyl acetate (18 wt% vinyl acetate) and compositions with different amounts of

magnesium hydroxide (MH). The tests were carried out with an elongation rate of 25 mm/min using an Instron Universal Tester. The shape of the specimens was chosen in accordance with the regulations for standard test methods for vulcanised rubber and thermoplastic elastomers (ASTM-D-412 1987).
In contrast to the compression tests, the specimens of the tensile tests have a clearly defined geometry. Therefore, the load capacity of the specimens can be expressed in *MPa*. The results of the tensile strength tests performed by Fu & Qu (2004) are given in Figure 2.38 a). Two aspects should be emphasised when evaluating the results. (1) EVA shows a highly pronounced deformation behaviour since the elongation at break reaches a value of 1650 % resulting in a tensile strength of 19.2 MPa. For comparison, carbon steel usually exhibits an elongation of 20 to 30 % at break. At elevated temperatures, the elongation is even limited to 20 % according to EN-1993-1-2 (2010). (2) If magnesium hydroxide is added to EVA, the high extensibility and tensile strength of the blends decreases (55 % MH: 144 % elongation). Similar observations were also made by Bourbigot et al. (2004), when the research group evaluated the influence of ammonium polyphosphate (APP) and polyamide 6 (PA6) on the tensile strength of EVA with a vinyl acetate content of 24 wt%. However, the authors found out that regardless of whether PA6 was added in the normal state or as a nanoparticle, the reduction in tensile strength and elongation was almost identical (see Figure 2.38 b)).

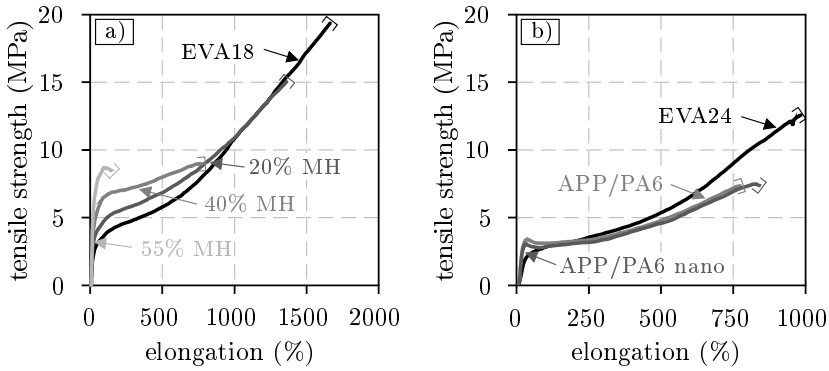

Figure 2.38: Tensile strength of a) pure ethylene-vinyl acetate (EVA18) and blends with magnesium hydroxide (MH) of 20, 40 and 55 wt% according to Fu & Qu (2004) and b) pure ethylene-vinyl acetate (EVA24) and blends with ammonium polyphosphate (APP) and polyamide (PA6) according to Bourbigot et al. (2004)

In terms of conventional intumescent coatings, the results mean that coatings in their initial state show a significantly lower extensibility compared to the pure binder. However, the elongation at break of intumescent coatings at room temperature is still higher than the elongation of carbon steel. Therefore, no cracks can occur within the virgin coating due to tensile stresses. However, as soon as the coating reacts and the char is formed, the susceptibility to cracks increases.

In order to investigate this phenomenon, Häßler (2016) performed fire tests on loaded steel tension bars that were protected by a waterborne intumescent coating. Besides the tension bar diameter and the dry film thickness of the coating, Häßler varied the tensile stress. In this way, he found out that cracking inside the formed char occurs more frequently and more pronounced if the tension bars are mechanically loaded. Depending on whether the bars were arranged horizontally or vertically, Häßler was also able to observe a certain slipping of the intumescent coating during the char formation. This was due to the melting of the coating in combination with the circular shape of the bars. During the melting phase, the viscosity of the coating decreases, resulting in a viscous liquid that starts to flow due to gravity. In this state, no tensile or compressive strength can be carried by the liquid melt. Only due to the formation of the char, again a solidification takes place that leads to the compressive strength that is documented in Figure 2.37. However, due to the prior movement of the liquid melt and internal stresses in circumferential direction, cracks inside the char are formed due to the increase in perimeter. This form of crack formation is illustrated in Figure 2.39 a). It was not only identified on tension bars by Häßler (2016) but also on circular and square hollow sections as reported by Raveglia (2008). Generally, a distinction between geometrically and mechanically induced cracking is made. The crack formation due to the increase in perimeter is a typical geometrical problem. This includes also the expansion on sharp edges, such as flanges etc., where the char is formed bidirectionally. Due to the contrary expansion, the tensile strength of the char is exceeded resulting in a typical crack that is illustrated in Figure 2.39 b).
If intumescent coatings are applied to steel members that are exposed to large bending deformations (see Figure 2.39 c)), cracks inside the char usually occur due to the exceeding of the tensile strength. In this case the crack formation is mechanically induced. This also applies to structural elements that are exposed to pure tension loads, such as steel tension bars or truss members.

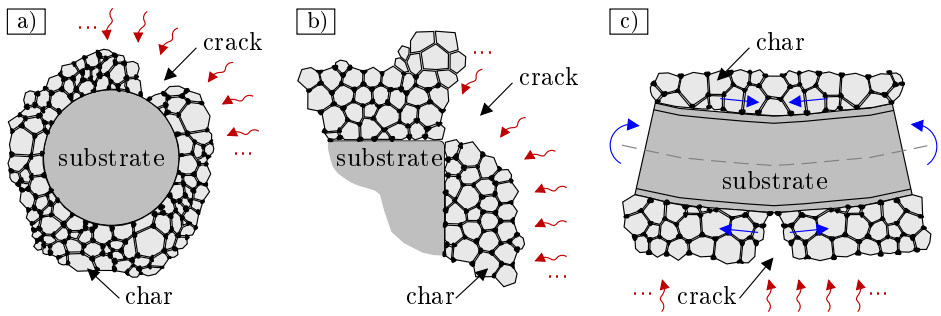

Figure 2.39: Formation of cracks inside the char: a) geometric crack due to the increase in perimeter, b) geometric crack due to a multidirectional expansion and c) stress induced crack formation due to bending

To conclude, crack formation inside the char of intumescent coatings is usually caused by gravity-induced material flow of the liquid melt or the exceeding of the

tensile strength of the char structure regardless of whether this is caused by geometry or by external mechanical stresses.
To what extent the different heating conditions have an influence on the crack formation, has not been investigated so far. The fire tests of Häßler (2016) and Raveglia (2008), for example, were exclusively performed under standard fire conditions. The influence of different heating conditions on the viscosity of intumescent coatings is also largely unknown. In literature, only few works, such as the rheological investigations of Duquesne et al. (2005), can be found dealing with this topic. In order to identify the correlation between the viscosity of intumescent coatings and the char formation, the research group performed rheometer tests on circular samples (diameter: 25 mm and thickness: 1 mm) that were heated with 10 K/min within a temperature range of 20 - 500 °C. The results of the rheological measurements are shown in Figure 2.40 for both linear (A and B) and crosslinked (D) binders and the corresponding coating formulations (c-A, c-B and c-A+D).

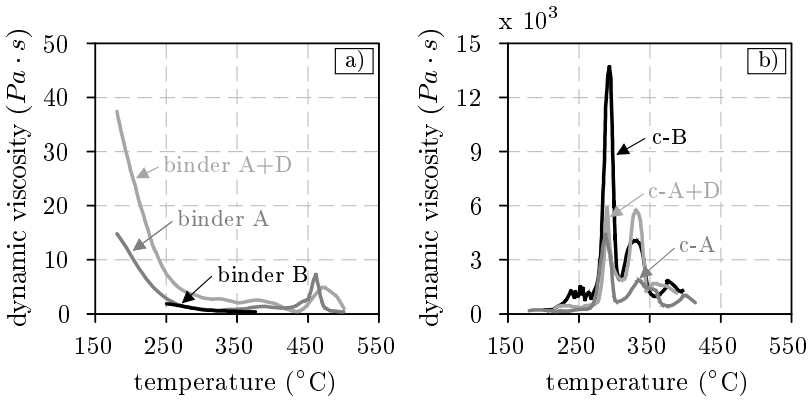

Figure 2.40: Temperature-dependent viscosity of a) different thermoplastic binders (A, B and A+D) and b) corresponding APP/DPER/MEL formulations (c-A, c-B and c-A+D) according to Duquesne et al. (2005)

Irrespective of their monomer structure, the linear and crosslinked binders show a very low viscosity (14.8 - 37.4 Pa·s at 180 °C), which decreases markedly during heating. When a crosslinked resin (D) is added to the linear binder (A), however, a slightly higher dynamic viscosity is observed. Nevertheless, no charring can be observed for any binder. Only by adding the main ingredients to the binders, a significant change in viscosity occurs resulting in maximum values of 4400, 13700 and 5870 Pa·s for the coatings c-A, c-B and c-A+D, respectively. This is due to the two-step charring process that was determined by Duquesne et al. (2005) in the temperature range of 270 - 320 °C and 320 - 350 °C as documented in Figure 2.40 b). Especially the second peak of the viscosity seems to be decisive for the char formation since Duquesne et al. found a clear correlation between the peak and the expansion of the coatings. The best char expansion, for example, was observed for the binders A+D. These binders showed the highest viscosity during

the second peak. In the other cases (c-A and c-B), in which the viscosity of the coating was lower, only half of the expanded char thickness was measured. For this reason, a clear correlation between the coating viscosity and the efficiency of char formation can be drawn. If the viscosity is too low, the released gases due to the decomposition of the blowing agent escape from the char. On the other hand, if the viscosity is sufficient, a slow diffusion of the gases occurs during the intumescence process, resulting in a uniform and closed-cell char structure. Therefore, according to these results, the char formation is significantly controlled by the viscosity and the strength of the char. To what extend the viscosity and, therefore, the char formation of intumescent coatings is affected by different heating conditions, will be assessed on the basis of own experimental investigations (see chapter 3).

Discussion:

With regard to the heating rate dependence, the viscosity of the polymer binder and the char seems to be the most decisive parameter for the formation of a uniform and high-insulative char structure. In publications, such as Camino & Costa (1986), Duquesne et al. (2005) or Jimenez et al. (2006*a*), the viscosity of the coating is reported to be one of the most important physical parameters that controls the inclusion of released gases inside the char. As the most relevant research works all report that the expansion of intumescent coatings is decreased when exposed to lower heating conditions, it is assumed that the intumescence is controlled by the amount of trapped gases inside the char. Although not proven by anyone yet, changes in viscosity due to the different heating conditions could be responsible for this. However, the review on the thermal performance of single ingredients reveals that the polymer binders are the least heating rate-dependent components. Therefore, the temperature shift that was identified for the main ingredients on the basis of the reviewed TG analyses (see subsection 2.2.6) could be also responsible for the heating rate-dependent expansion behaviour of intumescent coatings.
As reported in literature, the viscosity of intumescent coatings does not only control the char formation in terms of the morphology but also in terms of the resistance against mechanical destruction and the crack formation due to geometrical, gravitational or external effects. Therefore, if the viscosity controls the amount of gases that are trapped inside the formed char in case of different heating conditions, then the crack formation could also show a heating rate dependence.
For both, the reduced expansion and crack formation, the fire protection performance of intumescent coatings is significantly affected globally and locally. In order to assess this fire protection performance in terms of the heating rate dependence, several approaches are reported in literature. However, these approaches lead, in parts, to completely different conclusions. Therefore, especially the *effective thermal conductivity* approach according to EN-13381-8 (2013) that is widely used should be examined in more detail. The assumptions that are made within this approach require an accurate assessment in order to evaluate the suitability of this approach for the assessment of the heating rate-dependent fire protection

performance of intumescent coatings in natural fires. This will be done within the scope of the numerical investigations in chapter 4.

2.2.8 Material Models and Numerical Simulations

Numerical simulations are a useful way to supplement experimental investigations and to expand the investigated parameter range. However, such simulations are only reliable if the material models that are used in the simulations are proven to be valid to describe the complex behaviour of materials close to the reality. In the last two decades, enormous efforts have been made to develop appropriate material models for intumescent coatings. Due to the different objectives, the models were formulated at different levels of complexity. For the description of the expansion behaviour and the formation of individual bubbles, for example, highly complex models were developed on the microscopic level of chemical reactions. On the other hand, if only thermal analyses had to be carried out, the effective thermal conductivity was recalculated from cone calorimeter or standard fire tests, without considering the chemical and physical processes that take place in intumescent coatings. However, the results obtained from such calculations are restricted to the investigated parameters, such as the dry film thickness, the section factor of the steel substrate and of course the fire condition. Therefore, those results are not allowed to be extrapolated to deviant applications.
Since the material models of intumescent coatings were developed under different aspects, the models are divided into different categories within the scope of this work. However, in some cases, the models can be assigned to several categories at the same time due to their holistic formulation. In those cases, the models are assigned to the category that appears to be most relevant for the model. In the following, the most important, literature-known material models for intumescent coatings will be presented, starting with the models for the intumescence behaviour and the bubble growth.

Intumescence and Bubble Growth Models:

Together with the morphology and the thermal conductivity, the expansion ratio represents a decisive parameter for the fire protection performance of intumescent coatings. Therefore, many research groups developed mathematical models for the prediction of the expansion behaviour and char formation of intumescent coatings. A selection of some literature-known approaches is listed in Table 2.7. One of the most relevant models for the description of single bubble growth and its effect on the temperature and flow field of the viscous melt of intumescent coatings was developed by Butler et al. (1997). The physical model is based on submodels describing the hydrodynamics of the melt, the growth rate of single bubbles and the heat transfer through the porous medium. The viscous melt of the coating is assumed to be an incompressible fluid with a viscosity and a surface tension defined as input parameters. The growth rate of the bubbles is defined to be controlled by

the temperature-dependent decomposition reaction of the blowing agent and the physical properties of the released gases as well as the surrounding melt. Especially in the initial state, the bubble growth is controlled by the surface tension of the melt. Therefore, only a part of the released gases is trapped inside the bubbles. Since thermal material properties are assigned to the gas and the viscous melt, a temperature field calculation is enabled by the material model. As shown in Figure 2.41, the formation of bubbles prevent the substrate (bottom of the control volume) from faster heating. This is due to the low thermal conductivity of the bubbles and the endothermic chemical reactions (bubbles act as a heat sink), which reduce the temperature of the insulated substrate during gasification.

Table 2.7: Selection of literature-known intumescence and bubble growth models

Model	Description	Input	Output
Butler et al. (1997)	Physical model with hydrodynamics, growth rate and heat transfer submodels	Bubble nucleation, density, viscosity, thermal diffusivity, conductivity, surface tension	Bubble positions, flow and temperature field
Butler (2002)	Combustion model of bubbling thermoplastics (bubble submodels: nucleation, growth, migration, bursting, coalescence)	Density, specific heat, conductivity, activation energy, emissivity, surface tension	Bubble radius, mass loss rate, flow and temperature field
Gillet et al. (2007)	Growth model with moving boundary conditions based on Arrhenius equation	Activation energy, specific heat, conductivity, density, viscosity, pressure, porosity	Steel temperature, mass loss
Yuan & Wang (2009)	Mass loss-based intumescence formulation in combination with Fourier's law and Arrhenius equation	Maximum expansion ratio, bubble size, activation energy, conductivity, specific heat, density, mass fraction	Steel temperature, char conductivity, char thickness, mass loss rate, decomposition heat
Zhang et al. (2012*b*)	Mathematical model based on chemical kinetics (Arrhenius equation, chemical reactions) and TGA	Bubble size, amount of trapped gas, activation energy, melting temperature, mass fraction, mass loss rate	Steel temperature, char expansion, mass loss
Cirpici et al. (2016)	Intumescence model for different heating conditions based on TGA	Mass loss, viscosity, porosity, bubble size, surface tension	Expansion ratio, effective thermal conductivity, steel temperature

With the help of the model, Butler et al. (1997) were able to identify that the growth rate of the bubbles has a significant influence on the char formation (swelling) and the heat transport. The swelling and heating behaviour is affected by the migration of the bubbles towards regions of lower viscosity and surface tension caused by temperature gradients.
Since the model of Butler et al. was designed to be easily extended by further submodels, a further development of the model was undertaken some years later by Butler (2002) during a research project that was funded by the NASA Glenn Research Center. In addition to the existing submodels, formulations for the coalescence and the bursting of bubbles were introduced. In this way, the sensitivity of the pyrolysis to the bursting behaviour of the bubbles was identified. However,

Butler observed that the viscous melt of intumescent coatings tends to lose material by a fine drop spray when the viscous melt ruptures during the bursting process. Since this phenomenon was not considered within the formulation of the mass loss rate, Butler recommends to improve the submodel. According to Butler this would not only influence the description of bubble merging but also the heat and mass transfer within the melt.

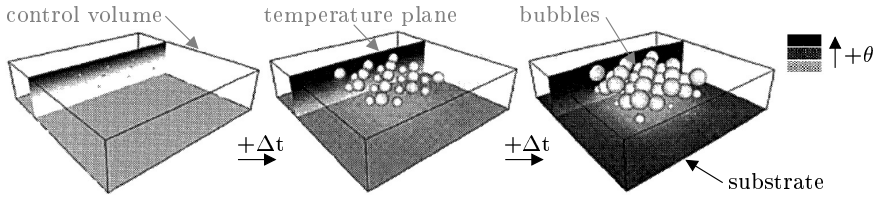

Figure 2.41: Illustration of bubble growth (arrangement of 38 bubbles in three horizontal planes) and their effect on the temperature distribution in intumescent coatings according to the model of Butler et al. (1997)

In contrast to Butler et al., Gillet et al. (2007) used a more simplified formulation for the description of the intumescent coating growth. Instead of modeling discrete bubbles, the research group distinguishes only between three main layers: (1) The steel substrate, (2) the virgin coating and (3) the growing part of the char. For each layer, boundary conditions are defined. When the gasification reaction starts, the upper boundary of the growing layer is considered to move upwards while the lower boundary follows the regression of the virgin coating layer. In addition to the moving boundaries, a transformation of the reactive layer into a char layer is considered. The regression (mass loss) of the virgin material is described by the Arrhenius equation (see Vyazovkin (2015) and Equation 2.5) and, therefore, requires activation energy data. The growth rate of the char, on the other hand, is related to the pressure of the released gases and is calculated from fluid viscosity and material permeability data. Since the research group also assigns thermal material properties to the single layers, a substrate temperature is calculated with the help of the model using the finite difference method (FDM). However, Gillet et al. (2007) report that for thick intumescent coating layers, the accuracy of the model is unsatisfactory.

Yuan & Wang (2009) developed some years later a similar material model for the description of the intumescence behaviour of intumescent coatings. In this model, the authors use a one-dimensional finite difference approach in which the coating is divided into single layers. The coating is assumed to be composed of the three main ingredients: the inorganic acid source, the blowing agent and the charring material. The temperature-dependent decomposition of the ingredients is also described by the Arrhenius equation. However, only the decomposition products of the blowing agent are assumed to be responsible for the bubble formation and the swelling of the char. It is also assumed that only the gas that is generated in each layer contributes to the swelling of this specific layer. As a consequence, if

a layer reaches its maximum expansion, it is assumed that no further growth in layer thickness occurs due to further gas release. It is rather postulated that the excess gas flows through the other layers without any contribution to their growth. As the maximum expansion ratio is considered by Yuan & Wang (2009) to be the most important parameter in their mathematical model, it is treated as an input value. The main reason for this is that at the time of publication, no reliable model existed for the prediction of the maximum expansion ratio of intumescent coatings. However, despite this limitation, the authors were able to perform a sensitivity study with their material model to evaluate the influence of the reaction kinetics, the bubble size and the maximum expansion ratio on the fire protection performance due to high radiative heat fluxes (over 150 kW/m^2).
A few years later, Zhang et al. (2012*b*) presented a further developed material model. The assumptions regarding the composition of the coating, the description of the decomposition behaviour and the one-dimensional heat and mass transport are identical to the previous model of Yuan & Wang. Only the intumescence behaviour is no longer described by the maximum expansion ratio but by the amount of gas trapped inside the char. Since a measurement of the trapped gas fraction is not possible, an estimate is made by a trial and error approach. The remaining portion of the gases is assumed to escape and contributes to the convective heat transfer at the char surface. According to their experimental findings, Zhang et al. consider also a shrinkage behaviour of the char during the degradation stage. In order to describe the initiation of the swelling and the morphology of the char, the authors define a heating rate-independent melting temperature $T_{melt} = 150\,°C$ and vary the bubble size in a range of 2.8 and 4.2 mm.
Despite the further development of the model, many input parameters are still needed to describe the intumescence behaviour of the coating. Especially the required activation energies and the mass loss behaviour presuppose that numerous thermogravimetric analyses have to be carried out at different heating rates. In the case of Zhang et al. TG analyses for 2, 10, 20 and 50 K/min were performed. Unfortunately, the results are nowhere presented.
Cirpici et al. (2016) followed the recommendations of Zhang et al. and developed a mathematical model for the swelling behaviour of intumescent coatings by using the mass loss data of TG analyses. In order to describe the bubble growth, the analytical approach of Amon & Denson (1984) is used within the model. As viscosity data is required to define the limit state of the surface tension of the bubbles, the research group relied to the temperature-dependent data of Bugajny et al. (1999) due to the lack of own investigations (see Figure 2.14). In this way, Cirpici et al. were able to calculate the heating rate-dependent expansion behaviour of a waterborne intumescent coating. In contrast to the experimental investigations (see subsection 2.2.7), the material model of Cirpici et al. (2016) postulate that the expansion behaviour of the coatings is pronounced for low heating rates. For higher heating rates, on the other hand, the expansion factor decreases significantly as shown by the expansion curves in Figure 2.42 a). For 100 K/min, for example, nearly no expansion occurs. The same applies also to the thermal conductivity. Ac-

cording to the model description, the best fire protection performance is assumed to occur for low heating rates as the lowest thermal conductivity values are obtained for 1 K/min. Unfortunately, the authors did not discuss these material data but merely used them to recalculate the fire tests of Zhang et al. (2012*b*) and Zhang et al. (2012*a*). Therefore, a final evaluation, why the material model of Cirpici et al. leads to a completely reverse material behaviour than experimentally observed, is lacking. However, to which extent this material behaviour can be explained by differences in thermal energy absorbency rather than by heating rate dependency, will be discussed during own numerical investigations in chapter 4.

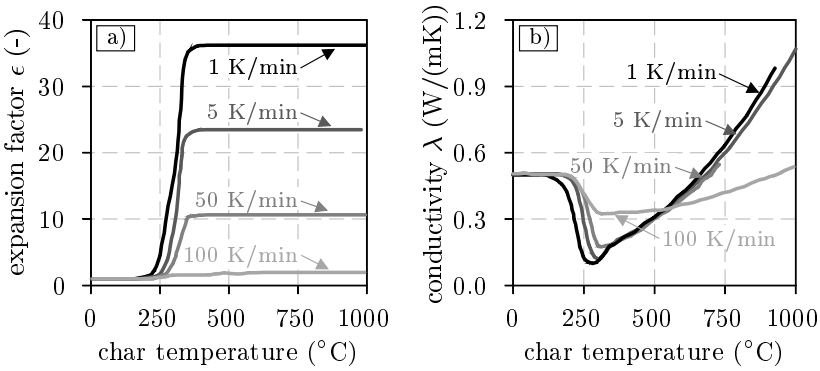

Figure 2.42: Influence of different heating rates on the a) expansion behaviour and b) apparent thermal conductivity of intumescent coatings according to the material model of Cirpici et al. (2016)

Although the presented material models show differences in complexity and objectives, most of the approaches focus on describing the expansion behaviour of intumescent coatings by decomposition reactions of single ingredients. Experimental investigations of Fateh et al. (2017) seem to confirm this assumption, as the research group found a coherence between the expansion of intumescent coatings and the mass loss rates. Their postulation that the expansion behaviour is completely independent of the heating conditions, however, needs to be verified. Basically, the heating rate dependency of the intumescence process is little treated in the literature-known models. And when treated, the approaches raise more questions than offering adequate solutions. Therefore, it can be concluded that currently no reliable material model for the description of the heating rate-dependent expansion behaviour of intumescent coatings exists so far.

Decomposition Models:

When describing the fire protection behaviour, in many cases the chemical processes that take place during the reaction of intumescent coatings are described in a simplified way. However, some models still focus on more detailed descriptions of the chemical and physical processes. Therefore, a selection of these models (see

Table 2.8) will be briefly explained in the following.
The most cited and used decomposition model of intumescent coatings was developed by Di Blasi & Branca (2001). The one-dimensional finite difference model is based on a composite system composed of three zones: the virgin, the decomposition and the char zone as shown in Figure 2.43. The decomposition zone is considered to be responsible for the chemical reactions. It is assumed to consist of three components (S_1, S_2 and S_3) with mass proportions of Y_1, Y_2 and Y_3. Each of the components degrades according to its independent reaction corresponding to melting, swelling and charring as described by Cagliostro et al. (1975). The products resulting from the reactions consist of volatile gases (V_1, V_2 and V_3) and a charred solid residue C. The rate at which the volatile gases and the char are formed is described by the temperature-dependent mass changes ($\partial m_i / \partial t$) and the reaction rate constants k_i (with i = 1, 2, 3). Since each component follows its own reaction (interactions between the components are not considered), different conservation equations are formulated. However, each equation requires kinetic parameters, such as the activation energy E_i and the pre-exponential factor A_i that both are calculated from thermogravimetric data using the Arrhenius equation (see Equation 2.5).

$$k_i = A_i \cdot e^{-\frac{E_i}{R \cdot T}} \tag{2.5}$$

k_i: reaction rate constant (1/s)
A_i: temperature-independent pre-exponential factor (1/s)
E_i: activation energy (J/mol)
R: universal gas constant (8.314 J/(K· mol))
T: absolute temperature (K)

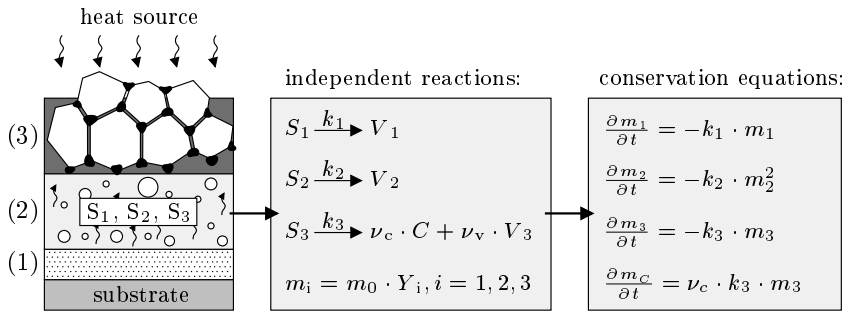

Figure 2.43: Graphical and mathematical description of the decomposition model of Di Blasi & Branca (2001) for a composite system composed of (1) the virgin material, (2) the decomposition zone (with its components S_i, masses m_i and mass fractions Y_i) and (3) the char

In order to provide a self-contained solution, Di Blasi & Branca combine the chemical reactions described above with finite difference equations for the heat and mass transport. For the calculation of the effective thermal conductivity, the authors use different approaches. Some of the approaches are based on the porosity and

the mean bubble size and will be presented below. The expansion rate is calculated from the gas volume that is released during the degradation reaction of the component S_2. However, an empirical parameter is still required to limit the maximum expansion ratio of the finite difference layers. Despite the required input data (see Table 2.8), the model is reliable and provides good approximations of experimental data. Therefore, Farkas et al. (2008) and Zhang et al. (2012*b*), for example, adopted the material model for their numerical calculations. However, in its current version, the model is unable to describe the heating rate-dependent behaviour of intumescent coatings, although thermogravimetric analyses for different heating rates could be performed to calculate the kinetic parameters. By introducing heating rate-dependent expansion factors, however, a dependency on the heating conditions could be considered within the model.

Table 2.8: Selection of literature-known decomposition models

Model	Description	Input	Output
Di Blasi & Branca (2001)	Nonsteady decomposition model on the basis of chemical reactions	Amount of trapped gas, expansion factor, pore diameter, conductivity, specific heat	Mass loss, char thickness, substrate temperature
Staggs (2003)	Heat and mass transport model according to Darcy's law	Permeability, viscosity, conductivity, specific heat capacity, emissivity, convective heat transfer coefficient	Mass flux, pressure, char temperature, failure time due to char rapture
Griffin et al. (2004)	Thermal degradation model based on invariant kinetic parameters	Activation energy, pre-exponential factor, conversion, specific heat capacity	Thermal resistance, mass loss
Lautenberger & Fernandez-Pello (2009)	Generalised pyrolysis model for combustible solids	Activation energy, pre-exponential factor, reaction order, bulk density, conductivity, specific heat capacity, emissivity	Temperature profile, coating thickness, mass loss rate, gas evolution

Another equally known material model for the decomposition of intumescent coatings was developed by Staggs (2003). Similar to the previous model, the transport of gas and heat as well as the conservation of mass are combined. The transport of the gas through the char, however, is modeled by a simplified formulation of the Navier-Stokes equation, known as Darcy's law (empirical description of the relationship between the pressure gradient ∇P and the average flow velocity $\mathbf{v}$ through a porous, regular medium). The thermal degradation of the coating is assumed to occur in a single step, once the critical temperature is reached. Due to the degradation, a fixed mass fraction r of the char and $1 - r$ of the volatile gases are formed. This implies that the gas and the molten coating cannot coexist in the same volume. Therefore, an interface between the molten coating and the volume containing the char and the gas is defined. In addition, it is assumed that no overall volume change occurs during the formation of the char. However, the volumes of the char and the molten material do change with time. As a consequence, the interface between the char and the melt moves with time. The movement of the upper

boundary of the char that represents the expansion is controlled by the pressure and the diffusion of the volatile gases inside the char volume. As Staggs (2003) already described, his model requires numerous input parameters, such as the mass fraction of the char r, the critical temperature, the thermal conductivity, density and specific heat capacity of the gas and the coating as well as the diffusivity ratio between the char and the molten coating. For this reason, Staggs endeavoured to reduce the number of parameters. However, with the help of his model the pressure at the interface between the molten material and the char as well as the time at which char rupture occurs due to over-pressure can be calculated. A heating rate dependency of the decomposition behaviour is unfortunately not included in the model.
In order to model the degradation behaviour of different intumescent coatings, Griffin et al. (2004) used the approach of invariant kinetic parameters (IKP) to calculate the required kinetic parameters. For this reason, the research group performed in the first step TG analyses and determined the mass loss behaviour of the coatings experimentally. In the second step, the experimental data was used to calculate the mass conversion $\alpha(\theta)$ as defined in Equation 2.6.

$$\alpha(\theta) = \frac{\xi_i - \xi(\theta)}{\xi_i - \xi_r} \tag{2.6}$$

$\alpha(\theta)$:	degree of conversion (-)
ξ_i:	initial value of the measured property
$\xi(\theta)$:	current value of the measured property at temperature θ
ξ_r:	residual value of the measured property

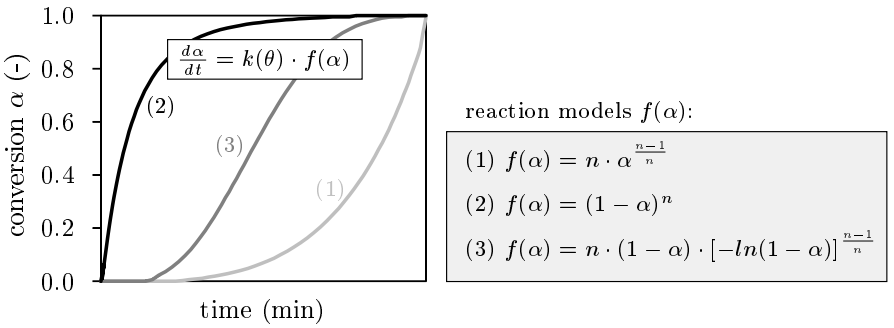

Figure 2.44: Schematic and mathematical description of the conversion behaviour of degrading materials following the (1) accelerating, (2) decelerating and (3) sigmoidal model according to Vyazovkin et al. (2011)

The degree of conversion $\alpha(\theta)$ is a dimensionless value and describes the change of a physical property. Generally, any physical property whose change is measured as a function of time can be used for the calculation of kinetic parameters. In the area of thermal analyses, for example, kinetic data are collected most commonly by measuring changes in either heat of mass using differential scanning calorimetry

and thermogravimetry, respectively (Vyazovkin et al. 2014). The change of the conversion in time ($d\alpha/dt$) is considered in the majority of kinetic methods to be a function of the temperature θ and α. The dependence of the process rate on the temperature is represented by the reaction rate constant $k(\theta)$ that is mathematically expressed by the Arrhenius equation (see Equation 2.5). The dependence on α, on the other hand, is described by the reaction model $f(\alpha)$, which can take many mathematical forms. Three of these mathematical forms (accelerating, decelerating and sigmoidal) are described in Figure 2.44. Further reaction models are defined by Vyazovkin et al. (2011). The kinetic models that were used by Griffin et al. within their investigations were adopted from Richard-Campisi et al. (1996). A total of 18 models were used to determine the kinetic parameters from TG analyses that were performed at heating rates of 10, 15, 20 and 30 K/min. Despite this enormous effort, Griffin et al. (2004) did not achieve satisfactory results. One possible explanation for this could be that the research group partly combined the reactions of melting and char formation into one. Therefore, the mass loss rate during the char degradation could not be described in a realistic manner by most of the selected reaction models. However, the fact that this is possible was proven by the model of Di Blasi & Branca (2001). Here, also single-step reactions are used, but each reaction is described by a separate conservation equation.
Per definition, the method of invariant kinetic parameters assumes that the calculated kinetic parameters are independent of the heating rate as described by Griffin et al. (2004). Therefore, it should be discussed whether this method is suitable for describing the heating rate-dependent behaviour of intumescent coatings. However, the method is very versatile. It can be used to determine kinetic parameters of combustible materials, e.g. wood, to implement pyrolysis models in computational fluid dynamics (CFD) simulations to calculate the heat release rate (HRR) as described by McGrattan et al. (2010) and Hostikka & Matala (2017). For this reason, further information for the determination of kinetic parameters (by graphical, analytical or model fitting methods) are given by the Kinetics Committee of the International Confederation for Thermal Analysis and Calorimetry (Vyazovkin et al. 2014).
The models presented above all have in common that they were developed exclusively for intumescent coatings. In order to counteract this limitation, Lautenberger & Fernandez-Pello (2009) developed a generalised pyrolysis model to simulate the gasification of condensed phase combustible materials that are composed of M chemically distinct condensed phases. The model that is named *Gpyro* can be applied to non-charring polymers, charring solids, intumescent coatings and smolder in porous media. It is based on conservation equations for the gaseous and condensed phases and implies a convective-diffusive solver in order to calculate the flux and composition of volatiles that escape from the solid phase. Due to the implementation of numerous submodels, such as for the bulk density, porosity, effective thermal conductivity, specific heat capacity and permeability, the temperature and pressure distribution inside the simulated solid can be determined. The input parameters required for the simulations are calculated from bench-scale

fire tests or thermogravimetric analyses similar to Griffin et al. (2004). An explicit consideration of heating rate-dependent material properties is not included in the model.
By comparing the simulated results with experimental data of different materials (a non-charring thermoplastic, a white pine and an intumescent coating), the authors prove the suitability of their model. In the case of the intumescent coating, the pyrolysis model is able to predict the surface temperature and the expansion ratio in a very good approximation. However, Lautenberger & Fernandez-Pello (2009) put the applicability of their model into perspective since material parameters are required that cannot be easily measured but need to be *inferred* from experimental data. Therefore, the authors claim on further research. From their point of view research should focus more on methods for estimating material properties than on more complex reaction mechanisms or the addition of new physical phenomena.
The complexity of the presented models makes it clear that numerous input parameters are needed for the description of the degradation behaviour of intumescent coatings. The modeling is made even more difficult, as some of the input parameters (such as the permeability, surface tension or the amount of trapped gases) cannot be directly determined experimentally and, therefore, have to be concluded from experimental data. Therefore, in order to provide a reliable and user-friendly modeling, the amount of required input parameters should be limited to the minimum. In addition, only such material properties should be used as input parameters, which can be clearly determined experimentally. Otherwise, a clear distinction between the model validation and the estimation of material properties is not given as postulated by Lautenberger & Fernandez-Pello (2009).

Thermal Conductivity Models:

When developing material models, the main focus lies usually on the insulating performance of the intumescent coatings. The fire protection performance is dominated by the interaction of the intumescence process, the formation of a uniform and fine pore structure and a low thermal conductivity. Especially the modelling of the thermal conductivity behaviour of intumescent coatings is difficult, since an experimental determination of the characteristic value is not possible for direct validation purposes. This is due to changes in char thickness, pore size, char structure and the transient temperature distribution inside the char. However, in order to model the thermal conductivity behaviour of intumescent chars, it is usually assumed that the char structure can be described by a two-phase system consisting of a solid and a gas phase. For this reason, already existing material models from other disciplines were adopted in the past. Based on the density of the solid (ρ_{solid}) and the total density of the material (ρ_{tot}), the content of the gas phase can be expressed by a related factor that is known as porosity ϕ (see Equation 2.7). The term *porosity* is typically used in the area of foams and soils. Here, the porosity is normally a constant and temperature-independent value. In the case of intumescent coatings, however, the porosity changes with the temperature as it is a

function of intumescence and mass loss.

$$\phi(\theta) = 1 - \frac{\rho_{tot}(\theta)}{\rho_{solid}} \tag{2.7}$$

$\phi(\theta)$:	porosity (-)
$\rho_{\mathrm{tot}}(\theta)$:	total density of the two-phase material (kg/m^3)
ρ_{solid}:	density of the solid inside the two-phase material (kg/m^3)

The simplest and best known thermal conductivity models of a composite material are referred to as *parallel* and *series* circuit. With regard to the maximum and minimum values, the two approaches represent the upper and lower limit of the thermal conductivity of a two-phase material that incorporates a certain amount of gas. In Figure 2.45 both approaches are illustrated schematically and graphically as a function of porosity. For the normalised graphic, a ratio between the thermal conductivity of the solid and the gas of $\kappa = 20$ was exemplarily chosen. Anderson et al. (1988), for example, used these two approaches to estimate the equivalent thermal conductivity of coated coupons that were exposed to a one-dimensional heat flux. However, due to the simplicity of the models the authors determined thermal conductivity values that were a factor of three compared to the experimentally determined values. In earlier studies, such as Woodside & Messmer (1961) or Curtis & Miller (1988) an intermediate approach of the upper and lower limit was used. However, these research studies focused on unconsolidated sands and fibrous cellulose particles, respectively.

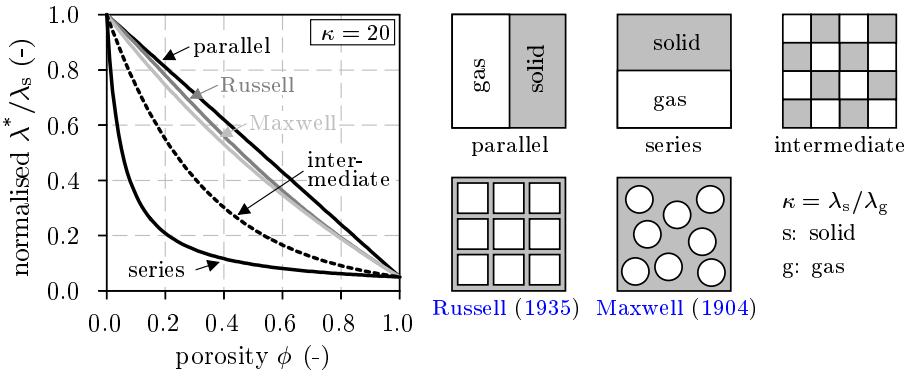

Figure 2.45: Normalised thermal conductivity of a two-phase porous material as a function of porosity for various mathematical models according to Staggs (2009) and Kang et al. (2017)

The approaches of Russell (1935) and Maxwell (1904) also come originally from other disciplines and were used to describe the conductivity behaviour of bricks and electric conductors, respectively (see Table 2.9). However, in both cases the equivalent thermal conductivity of the considered material is calculated, among other,

from the porosity, which only describes the volume of the pores but not their size. This applies to all conductivity models that are illustrated in Figure 2.45. Since only the thermal conductivity of the solid and the gas are weighted, it is clear that no other transport mechanism than only pure heat conduction is considered within the models. For illustration purposes, Figure 2.46 shows the heat transport due to conduction within the solid phase (blue arrows) and the gas phase (red curved arrows) caused by a one-dimensional heat flux. The associated mathematical equations are listed next to the graphic.

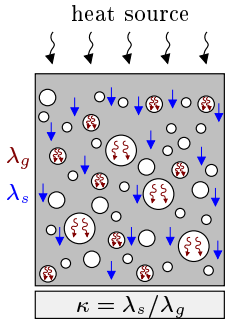

(1) $\lambda^* = \phi \cdot \lambda_g + (1-\phi) \cdot \lambda_s$ (parallel)

(2) $\lambda^* = \frac{\lambda_s \cdot \lambda_g}{\phi \cdot \lambda_s + (1-\phi) \cdot \lambda_g}$ (series)

(3) $\lambda^* = \lambda_g^{\phi} + \lambda_s^{1-\phi}$ (intermediate)

(4) $\frac{\lambda^*}{\lambda_s} = \frac{\phi^{2/3} + \kappa \cdot (1-\phi^{2/3})}{\phi^{2/3} - \phi + \kappa \cdot (1-\phi^{2/3}+\phi)}$ (Russell)

(5) $\frac{\lambda^*}{\lambda_s} = 1 + \frac{3 \cdot \phi}{(\frac{\lambda_g + 2 \cdot \lambda_s}{\lambda_g - \lambda_s}) - \phi}$ (Maxwell)

Figure 2.46: Mathematical formulations of thermal conductivity models of a two-phase porous material (solid: λ_s, gaseous: λ_g) according to Di Blasi & Branca (2001), Russell (1935) and Maxwell (1904)

In addition to pure heat conduction, radiation across the pore structure has a significant influence on the thermal conductivity at elevated temperatures. Therefore Staggs (2010) developed a finite element based approach to estimate the equivalent thermal conductivity of a fully expanded intumescent char by the use of highly segmented black and white digital images of a two-dimensional char section. In order to identify the pore structure and to distinguish between the solid and the gas phase, Staggs developed a pore finding algorithm that is illustrated in Figure 2.47. By assigning a finite element to each pixel, the pore structure of the char is replicated within the model. The effect of heat radiation is represented by Equation 2.8 in which the porosity (ϕ), the mean pore size (δ) and the char temperature (θ) are considered.

$$\lambda_{rad}(\theta) = 4 \cdot \phi \cdot \delta \cdot \sigma \cdot \theta^3 \tag{2.8}$$

$\lambda_{\mathrm{rad}}(\theta)$:	radiative part of heat conduction within a pore (W/(m·K))
ϕ:	porosity (-)
δ:	mean value of the pore size (m)
σ:	Stefan-Boltzmann constant $5.67037 \cdot 10^{-8}$ (W/(m^2·K^4))
θ:	absolute temperature of the char (K)

As the mean value of the pore size is multiplied by the porosity ($0 \leq \phi \leq 1$), a temperature-dependent pore growth is considered within the approach. In this

way a disproportional increase in thermal conductivity is described with increasing temperatures. How significant the influence of radiation inside the pores is, is illustrated in Figure 2.47. Here, the equivalent thermal conductivity of two intumescent chars (char 1 and 2) was calculated according to the finite element approach of Staggs (2010). Without considering the radiation inside the pores, only a slight increase in thermal conductivity occurs (char 1*) due to increasing temperatures. If radiation, on the other hand, is considered, the thermal conductivity increases multiple times (char 1) compared to the non-radiative approach. Significant differences in thermal conductivity are also observed due to the pore size. As the pores of char 2 were larger than of char 1, a significant higher thermal conductivity is observed due to the higher amount of heat radiation inside the larger pores.

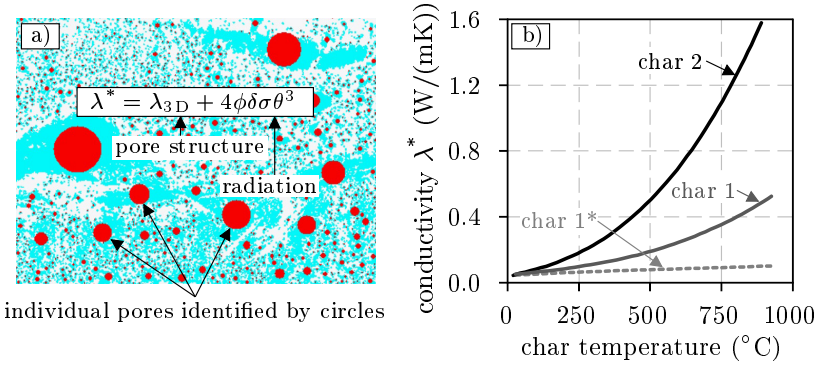

Figure 2.47: Thermal conductivity estimates of intumescent chars by direct numerical simulation according to Staggs (2010): a) Illustration of the pore finding algorithm and b) results of conductivity calculations of two different intumescent coatings with (char 1 and 2) and without (char 1) considering the radiation inside the pores*

The third heat transport mechanism that can occur inside a closed-cell foam structure is convection, represented by the curved, gray arrow in Figure 2.48 a). However, convection inside the pore structure only occurs when the pores are large enough. As soon as the cell walls of single pores degrade due to high temperatures, an open-cell foam structure is formed by the remaining cell struts (see Figure 2.48 b)). Due to this degradation process, changes in heat transport mechanism occur. Internal radiation inside the pores (represented by gray arrows), for example, does no longer occur due to the absence of the cell walls at which the radiation is normally reflected. The heat conduction along the cell walls (represented by blue arrows), therefore, is also eliminated in the case of open cells. The heat conduction due to the cell struts is still present. However, due to the absence of the cell walls, the space in which heat transmission occurs increases. As a consequence, the heat transfer through the open-cell foam structure by radiation becomes nearly unhindered in case of a single pore (continuous, red arrow). Only

through the arrangement of several, open pores, one behind the other, a reduction in radiative transmission takes place due to the decrease in permeability. However, the permeability of the foam structure is still significantly higher compared to the undegraded reaction stage and, therefore, enables also a higher convective heat transport as cell walls no longer exist to hinder the gas phase from flowing (red, curved arrows).
When describing the heat transport mechanisms in intumescent chars, the changes in pore structure (from closed to open) are not considered in the literature-known approaches yet. Most of the reviewed material models only consider the closed cell structure, such as Staggs (2010), Cirpici (2015) or Kang et al. (2017). Therefore, a suitable and self-contained material model does not exist to describe both the heat transport mechanisms in closed and open-cell char structures as described in Figure 2.48. However, Tabeling (2014) recognised within his numerical simulations the influence of open cells on the changes in thermal conductivity. Therefore, he modified his approach for closed pores that is based on the models of Di Blasi & Branca (2001) and Staggs (2010) by an artificial increase in pore diameter in order to consider the merge of adjacent pores due to the degradation of the cell walls.

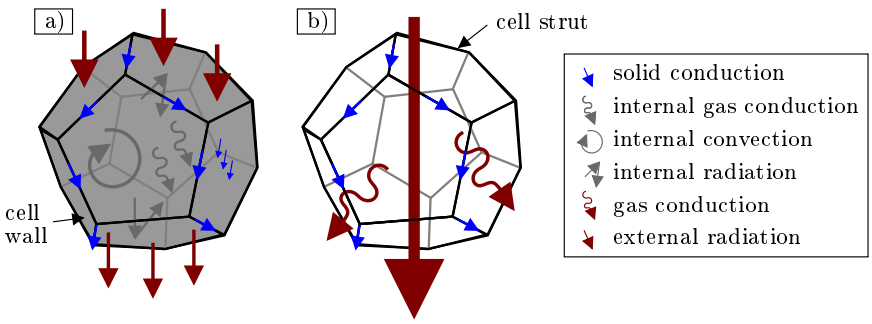

Figure 2.48: Schematic description of the heat transport mechanisms inside a single pore at the reaction stage of a) full expansion and b) cell wall degradation in analogy to Kang et al. (2017) and Mendes et al. (2014)

For other materials, such as polyurethane or metal foams, that are characterised already at room temperature by an open-cell foam structure, mathematical formulations are proposed to calculate the radiative part of the equivalent thermal conductivity. Ankang & Houde (2013), for example, developed a material model for open polyurethane foams in which the equivalent thermal conductivity is defined as the summation of the heat conduction of the solid and gas phase, the convection between the gas and solid phase, and the radiation. In order to calculate the pure solid and gas phase conduction, the cell structure of the foam is described by a simplified geometry consisting of rectangular frames with rectangular, solid struts. The radiative component of the equivalent thermal conductivity is calculated according to Equation 2.9 as a function of the temperature at the entrance (θ_1) and the exit (θ_2) of the heat flow and the extinction coefficient β. The extinction coef-

ficient describes the logarithmic transmissivity (τ) of the electromagnetic radiation that is transmitted through an open foam structure with thickness L. If the transmissivity parameter and the foam thickness are known, the extinction coefficient can be calculated according to Equation 2.10.

$$\lambda_{rad}(\theta) = \frac{4 \cdot \sigma \cdot (\theta_1^2 + \theta_2^2) \cdot (\theta_1 + \theta_2)}{3 \cdot \beta} \tag{2.9}$$

$\lambda_{\mathrm{rad}}(\theta)$:	radiative part of heat conduction (W/(m·K))
σ:	Stefan-Boltzmann constant $5.67037 \cdot 10^{-8}$ (W/(m^2·K^4))
θ_1:	temperature at heat flow entrance (K)
θ_2:	temperature at heat flow exit (K)
β:	extinction coefficient (m^{-1})

In order to determine the transmissivity of a foam structure, usually spectrometric measurements are required. However, Loretz et al. (2008) developed an image-based method to measure the transmissivity of open foams from computer tomographic scans (X-ray). An example for the determination of β is given in Figure 2.49. Here, two images of an aluminium foam with a different number of tomographic slices are shown.

$$\beta = -\frac{log(\tau(L))}{L} \tag{2.10}$$

β:	extinction coefficient (m^{-1})
$\tau(L)$:	transmissivity of the foam structure as a function of foam thickness (-)
L:	foam thickness (m)

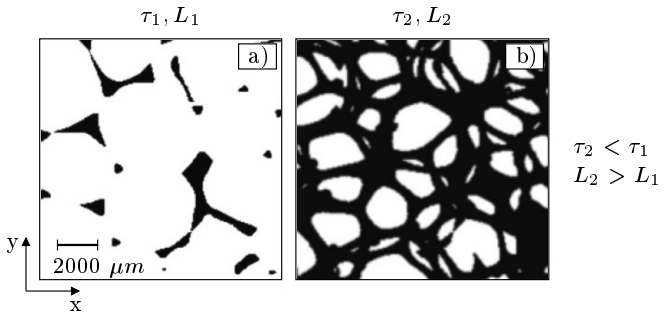

Figure 2.49: Changes in transmissivity (τ) due to the addition of aluminium foam slices in z-direction (expressed by the foam thickness L) according to Loretz et al. (2008)

The tomographic slices (each only a few microns thick) are used to project the shadow of the solid phase in the xy-plane. As soon as the number of the slices is increased, the transmissivity of the foam structure decreases ($\tau_2 < \tau_1$). After the projection of each slice, the transmissivity τ is calculated from the ratio of

the remaining white pixels divided by the total surface of the xy-segment. As the computer tomographic scans are three-dimensional, the transmissivity and the extinction coefficient can be determined virtually in all directions. In this way, an anisotropic transmissivity behaviour of open foams can be investigated. However, the effort of computer tomographic scans seems to be quite high in order to solely determine the extinction coefficient. Therefore, Mendes et al. (2014) used their computer tomographic scans not only to calculate the β coefficient for their simplified approaches but also to develop a detailed finite volume model in which the geometry of the investigated Al_2O_3 ceramic foams is defined by voxels (volume elements) obtained from the computer tomographic scans. With the help of this modelling technique, the research group performed coupled conduction-radiation heat transfer simulations in order to calculate the equivalent thermal conductivity of open-cell foams considering both the pure thermal conduction and radiation. As the simulations were performed with the help of the finite volume method (FVM), thermal conductivity properties of both the solid and the gas phase could be defined within the simulations. Convection within the porous foam structures was neglected. However, numerical approaches for the description of forced and natural convection in porous, open-cell foams are described by Liu et al. (2017) and Chiappini (2018).

Table 2.9: Selection of literature-known thermal conductivity models

Model	Description	Input	Output
Maxwell (1904)	Electric conductivity model of a random distribution of spherical solids in a continuous medium	Conductivity of the solid and medium, porosity	Conductivity of a two-phase material
Russell (1935)	Thermal conductivity model of a brick with rectangular pores	Conductivity of the solid and air, porosity	Conductivity of a brick filled with air
Loretz et al. (2008)	Model of the radiative behaviour of open-cell metallic foams	Refractive index, extinction coefficient, porosity, pore diameter	Radiative conductivity of open-cell foam structures
Staggs (2010)	Thermal conductivity model of intumescent coatings based on porosity measurements from digital images	Conductivity of the solid and air, porosity	Conductivity of a char with radiative heat flux across the pores
Ankang & Houde (2013)	Radiative conductivity model of open-cell foams based on the fractal theory	Conductivity of the solid and air, porosity, extinction coefficient, fractal dimension value	Equivalent thermal conductivity of a foam due to heat conduction and radiation
Mendes et al. (2014)	Radiative conductivity model of open-cell porous foams based on simulations	Conductivity of the solid and air, porosity, pore diameter, extinction coefficient, emissivity	Equivalent thermal conductivity of a porous foam due to heat conduction and radiation

A direct measurement of the thermal conductivity of intumescent coatings is usually difficult due to the unsteady intumescence process. Therefore, modelling approaches from other disciplines have been adapted in the past, in order to describe the heat transport mechanisms, such as thermal conduction and radiation that take place inside intumescent chars. In contrast to other porous media, such as ceramic

or metallic open-cell foams, intumescent chars change their morphology due to the increase in temperature. This applies not only for the intumescence process but also for the degradation of the cell walls due to the combustion of organic compounds. As a consequence, the heat transport mechanisms inside the intumescent chars change due to the transformation of the foam structure from closed to open-cell. However, also for this case, work from other research areas offer promising approaches (see Table 2.9) that can be applied to intumescent coatings.
With regard to different heating conditions, most of the models, e.g. the models of Staggs (2010) or Di Blasi & Branca (2001), describe the thermal conductivity of intumescent chars as a function of porosity and pore size. As the porosity and the pore size are dependent on the char temperature, the description of the equivalent thermal conductivity is also a function of temperature, even if only implicitly. However, in all cases these material models are only valid for the heating phase. For the cooling phase of a natural fire the models do not provide any solution to describe the thermal conductivity behaviour. In any case, it is clear that the thermal conductivity of the heating phase has to differ from the thermal conductivity of the cooling phase as the char formation and degradation are irreversible processes. As a consequence, new material models are required in order to describe both the changes in char morphology from closed to open-cell and the changes in heating and cooling conditions. According to this, a new material model for the thermal conductivity of intumescent chars will be presented in subsection 4.2.3.

Inverse Calculations:

As outlined by the review of the thermal conductivity models above, no material model currently exists that is able to fully describe the thermal conductivity behaviour of intumescent coatings at different morphology stages as well as heating and cooling conditions. This is, among others, due to the complexity of chemical and physical processes that take place in parts simultaneously during the reaction of the coatings. However, in order to assess the insulation behaviour of the coatings, several research groups developed mathematical approaches to recalculate the thermal resistance or the effective thermal conductivity from fire tests. The *effective thermal conductivity* approach, for example, described by Equation 2.3 is one of the most used calculation approaches and was already presented in subsection 2.2.7. This inverse calculation approach is still widely used, although it has the disadvantage that the validity of the results is strictly limited to the parameter range of the evaluated fire tests. Zhang (2012), for example, used the approach to recalculate the thermal resistance of an intumescent coating from small-scale fire tests of coated steel plates. Although he performed the tests under standard fire conditions, he used the thermal resistance values to perform probabilistic analyses on coated steel columns under natural fire exposure. Since the transfer of the fire protection performance of intumescent coatings from the standard fire to natural fires is not readily possible, the results of the performed reliability analyses must be questioned. This also applied to the approach of Li et al. (2016). Although the

inverse calculation approach is already simplified, the research group calculated an arithmetic mean from the effective thermal conductivity values that were obtained from inverse calculations. With the help of the constant thermal conductivities, Li et al. performed simplified calculations in order to predict the temperatures of coated steel plates and steel profiles. However, due to the strong simplification, a good agreement between the test data and the calculations could not be achieved, although the conductivity values were obtained from the same fire tests.

Table 2.10: Approaches for inverse calculations of the thermal conductivity

Approach	Description	Input	Output
Bartholmai & Schartel (2007)	Inverse calculation of the effective thermal conductivity from cone calorimeter tests on the basis of the FDM	Sample temperature, dry film thickness, density, specific heat capacity, convective heat transfer coefficient, emissivity	Effective thermal conductivity, thermal resistance
Zhang (2012)	Inverse calculation of the thermal resistance from standard fire tests on the basis of EN-13381-8 (2013)	Sample temperature, section factor, dry film thickness	Thermal resistance, effective thermal conductivity
Li et al. (2016)	Inverse calculation of constant effective thermal conductivity values from standard fire tests on the basis of EN-13381-8 (2013)	Sample temperature, section factor, dry film thickness	Constant effective thermal conductivity
Bozzoli et al. (2018)	Inverse heat transfer modelling of fully expanded chars using the FEM	Char temperatures at equidistant positions, density, specific heat capacity	Sample temperature, char thickness, apparent thermal conductivty

Another method for inverse calculations of material properties from experimental data (see Table 2.10) was presented by Bartholmai & Schartel (2007). With the help of the finite difference method, the two researchers solved the Fourier's law of heat conduction (detailed descriptions are given on page 54 in subsection 2.2.7) in order to recalculate the apparent thermal conductivity of their investigated intumescent coating. However, as the thermal conductivity is represented in Equation 2.2 as an input parameter, the conductivity values were systematically varied until the calculated and the measured sample temperatures coincided. Therefore, this approach represents rather an iterative procedure.

Despite the expressed criticisms, the use of inverse calculation methods should be reconsidered due to recent developments. In previous works, during fire tests only the steel temperature was measured from which the material properties of intumescent coatings could be recalculated. With the latest developments of new test setups, now possibilities are created to recalculate the apparent thermal conductivity from measured char temperatures. This is ensured by the arrangement of additional thermocouples inside the formed char. Of course, these conductivity values are also dependent on the respective parameter range. However, this special data set offers new validation opportunities. Up to now, the reliability of thermal conductivity models is usually assessed on the basis of steel temperatures and thus only indirect. With the recalculation of the apparent thermal conductivity from

equidistantly measured char temperatures, however, it is now possible to directly compare the thermal conductivity of a material model with the experimental data as requested by Lautenberger & Fernandez-Pello (2009). In order to enable these calculations, the temperature-dependent heat storage capacity ($\rho \cdot c_p$) of the examined coatings must be known. Otherwise solving Fourier's equation by finite difference or finite element methods will lead to incorrect results.

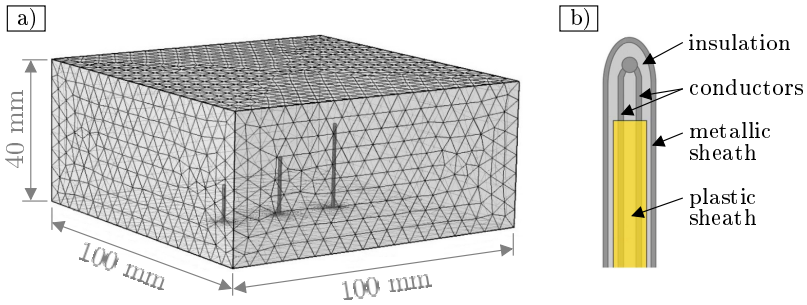

Figure 2.50: Inverse heat transfer modelling of an intumescent char layer according to Bozzoli et al. (2018): a) finite element mesh instrumented with thermocouples at different heights and b) sketch of the thermocouple structure

An example of such an approach is presented, for example, by Bozzoli et al. (2018). The research group developed a finite element based method in order to calculate the apparent thermal conductivity of a waterborne intumescent coating from temperature measurements of the growing char layer by solving the inverse heat conduction problem. As an accurate and complete solution was required, the researchers modelled not only the char in its expanded state but also the thermocouples that were placed inside it. The char thickness of the model was chosen according to the averaged thickness that was measured experimentally for coated steel plates (100 x 100 x 4 mm). In contrast to the performed cone calorimeter tests (radiative heat flux: 50 kW/m^2), the char thickness could remain constant within the finite element model since the effect of expansion was included in the measured char temperatures that were used as input parameters. In Figure 2.50 the finite element mesh of the model as well as the structure of the modelled thermocouples (type K) are given.
Following the idea of Bozzoli et al. (2018), the inverse calculation of the thermal conductivity of intumescent coatings from measured char temperatures is also possible with the help of the finite difference method. The advantage of this method is that it requires less modelling effort than the finite element method. However, reliable results can only be achieved if the measured char temperatures do not show a high degree of scattering. As a consequence, it is particularly important to arrange the thermocouples with the utmost accuracy inside the intumescent char, in order to ensure a precise temperature measurement.

Heat Transfer Models:

The idea of temperature measurements inside the intumescent char is not only used for inverse calculations of material properties but also for model validation. Due to the additional information that results from the temperature distribution, much stricter criteria for model validation exist. On the basis of experimental data it is now possible to validate the temperature development inside the char at different levels in addition to the substrate temperature and the char thickness. Therefore, researchers such as Schaumann et al. (2016), Norgaard et al. (2016) or Kang et al. (2017) performed simulations in order to predict not only the substrate temperature but also the heat transfer across the intumescent char.

Table 2.11: Selection of literature-known heat transfer models

Model	Description	Input	Output
Trelles & Lattimer (2007)	Transient thermal degradation and heat transfer model	Thermal Conductivity, specific heat capacity, density, activation energy, enthalpy, emissivity, heat transfer coefficient	Steel temperature, char temperature at different heights, mass flux
Griffin (2010)	Model for calculating the temperature profile across the intumescent char	Thermal Conductivity, specific heat, density, activation energy, expansion factor, porosity, mean diameter	Substrate temperature
Staggs et al. (2012)	Heat transfer and expansion model including radiation across the pores	Activation temperature, heat of reaction, thermal conductivity, specific heat, density, heat transfer coefficient	Substrate temperature, expansion ratio
Schaumann et al. (2016)	Three-dimensional model of a restrained coating expansion due to adjacent trapezoidal sheet sheets	Thermal Conductivity, specific heat, density, expansion factor, porosity, pore size, emissivity, heat transfer coefficient	Char expansion, substrate and char temperature
Norgaard et al. (2016)	Heat transfer calculation model with moving decomposition front across the intumescent char	Thermal Conductivity, specific heat capacity, density, heat transfer coefficient, porosity, pore diameter, activation energy, emissivity	Sample temperature, char temperature at different heights, char expansion
Kang et al. (2017)	One-dimensional heat transfer calculations with explicit expansion modelling	Thermal Conductivity, specific heat, density, emissivity, heat transfer coefficient, degree of expansion, porosity, pore size	Substrate temperature, char temperature at different heights, expansion thickness

Representative for all models, Figure 2.51 shows a typical temperature development inside a fully expanded char and a comparison with simulation results according to Norgaard et al. (2016). Since the thermocouples that are used to measure the char temperature are initially outside the char layer, only the gas temperature of the furnace is recorded in the first stage. As soon as the intumescent char passes the thermocouples during the expansion, the thermocouple temperature decreases due

to the insulation effect of the char. As the thermocouples are arranged at different heights (10 - 40 mm), a time offset in the temperature drop can be observed. This time offset continues through the remaining heating phase. As the heat transfer model of Norgaard et al. considers a moving decomposition front, it is able to describe the temperature distribution inside the char in a realistic way as the temperature curves especially at 10 and 20 mm coincide very well with the test data.
The models of Trelles & Lattimer (2007), Griffin (2010) and Staggs et al. (2012) are also able to simulate the temperature development inside intumescent coatings. However, as the new test setup to measure the temperature distribution inside the char did not exist during their time, experimental data was not available to validate their heat transfer models explicitly by char temperatures.

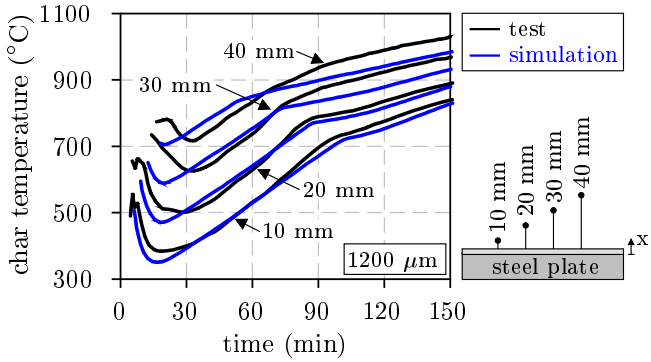

Figure 2.51: Comparison between simulated and measured char temperatures at different height levels of a solvent-borne intumescent coating applied on a steel plate (200 x 300 x 6 mm) according to Norgaard et al. (2016)

Since the heat transfer models in Table 2.11 are based on the previously presented submodels for thermal degradation, expansion and heat conduction, no further description of the models will be given here. It is rather pointed out that especially these models deal with the temperature development inside intumescent coatings. However, two models should be highlighted as they describe the expansion behaviour of the intumescent coatings explicitly. In both cases, Schaumann et al. (2016) and Kang et al. (2017), the expansion behaviour of the coatings is expressed by a logarithmic thermal strain ε_T (Hencky strain) that is calculated from the thermal elongation coefficient α_T according to Equation 2.11. The thermal elongation coefficient, on the other hand, can be calculated from the expansion factors ϵ in x-, y- and z-direction following the recommendations of Tabeling (2014) that are given in Equation 2.12.
Usually, the expansion of intumescent coatings is assumed to occur primarily perpendicular to the steel substrate. Therefore, Schaumann et al. use the expression $\alpha_{T,y}$ given in Equation 2.12 in order to describe the unidirectional expansion of their investigated coating. Kang et al., on the other hand, consider also the expansion in

transverse direction that is assumed to be 10 % of the expansion perpendicular to the substrate. However, the shrinkage of the intumescent char due to the degradation of organic compounds is not considered in the simulations. The heat transfer model of Schaumann et al. (2016) that is based on Tabeling (2014) does not only consider shrinkage but also a restrained expansion due to adjacent components such as roof panels.

$$\boldsymbol{\varepsilon_{T,n}(\theta)} = \boldsymbol{\alpha_{T,n}} \cdot \Delta\theta_i \tag{2.11}$$

$$\boldsymbol{\alpha_{T,n}} = \begin{pmatrix} \alpha_{T,x} \\ \alpha_{T,y} \\ \alpha_{T,z} \end{pmatrix} = \begin{pmatrix} \frac{ln(\epsilon_x)}{\theta_i - \theta_0} \\ \dots \\ \frac{ln(\epsilon_z)}{\theta_i - \theta_0} \end{pmatrix} \tag{2.12}$$

$\boldsymbol{\varepsilon_{T,n}(\theta)}$:	vector of logarithmic thermal strains (-)
$\boldsymbol{\alpha_{T,n}}$:	vector of thermal elongation coefficients (1/K)
$\Delta\theta_i$:	temperature change at increment i (°C)
ϵ_n:	expansion factor in n-direction (-)
n:	x, y or z-direction in Cartesian coordinates (-)
θ_i:	char temperature at increment i (°C)
θ_0:	initial char temperature (°C)

Despite their differences, especially the models of Tabeling (2014), Norgaard et al. (2016) and Kang et al. (2017) seem to be promising to describe the thermal behaviour of intumescent coatings at elevated temperatures in a realistic manner. So far, the models have only been used for a fire exposure according to the standard fire curve. Therefore, an extension to natural fires is required.

2.3 Current Design Approaches

2.3.1 Design of Steel Structures According to the Eurocode

The design of steel structures in case of fire is based on the Eurocode 3 part 1-2 (EN-1993-1-2 2010). Irrespective of the verification methods, it is generally required that the structure resists a fire exposure for a certain period of time and maintain its load-bearing capacity. However, a distinction between a standard fire and a natural fire exposure is made. In case of the standard fire (see subsection 2.4.1), the steel structure is allowed to collapse after reaching the required fire resistance time. The time during which the load-bearing capacity is ensured is classified by the mechanical resistance criterion R. In case of a natural fire the steel structure is required to withstand the whole fire exposure, including the cooling phase. A structural failure, therefore, is not allowed.
In order to verify the load-bearing capacity of the steel structure during the relevant fire exposure time t for the ultimate limit state, it shall be verified that the design value of the actions $E_{fi,d}$ is less than or equal to the design value of resistance $R_{fi,d,t}$

as described in Equation 2.13. This verification can be done by both simplified and advanced calculation methods.

$$E_{fi,d} \leq R_{fi,d,t} \tag{2.13}$$

$E_{fi,d}$: design effect of actions including effects of thermal expansion
$R_{fi,d,t}$: corresponding design resistance in the fire situation

The simplified calculation methods provided in EN-1993-1-2 (2010) allow for the design of single members under pure tension, bending and compression. A combination of the mechanical actions is also considered. However, single member analyses represent a simplification of the global structure behaviour as the interactions of the single member with other parts of the structure are replaced by boundary conditions as illustrated in Figure 2.52. These boundary conditions are assumed to remain unchanged during the fire exposure. Effects of thermal deformations are only considered for thermal gradients across the cross-section and axial or in-plane thermal expansions are neglected. This is due to the fact that member analyses are usually performed for a standard fire exposure. As an alternative to the calculations, fire tests are also permissible in EN-1993-1-2 (2010) to proof a sufficient load-bearing capacity of single members.

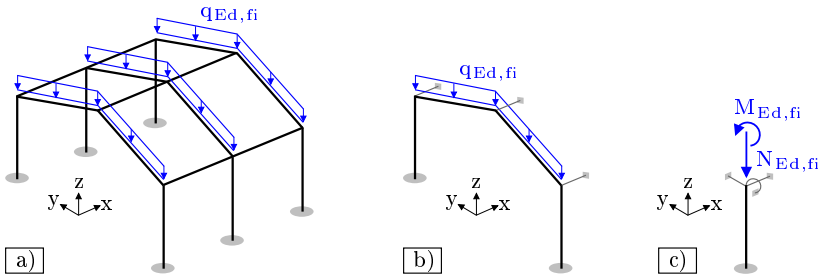

Figure 2.52: Design of steel structures according to EN-1993-1-2 (2010) enabling structural analyses of a) a global structure b) a part of a structure and c) a single member

As soon as analyses of the global structure or at least parts of the structure need to be performed (see Figure 2.52 a) and b)), the simplified calculation methods are not applicable. Therefore, advanced calculation methods are used. Advanced calculations are usually carried out when the fire resistance of a steel structure needs to be verified under a natural fire exposure. However, the calculations are also allowed to be used in association with any fire curve. In such cases, greater attention must be paid to the interaction between fire exposed and unexposed members. Therefore, in order to describe the relevant failure mode of the structure, temperature-dependent material properties and member stiffness as well as effects of thermal expansions and deformations have to be taken into account. Otherwise, the interaction between the examined members and the other parts of the

structure will not be modelled correctly.
When dealing with fire protection materials such as fire protection panels or fire resistant plasters, EN-1993-1-2 (2010) provide a simplified calculation method to calculate the temperature development of protected steel profiles. Due to its simplification, only a uniform temperature for the whole cross-section is calculated. However, when using the calculation method it is recommended to assess the material properties of the fire protection materials by means of fire tests. This is explicitly claimed for non-reactive fire protection materials that are regulated in EN-13381-4 (2013). Intumescent coatings, on the other hand, are not explicitly mentioned. A possible explanation for this could be the fact that the calculation method provided in the Eurocode 3 part 1-2 is not used for intumescent coatings as additional data is required to describe the temperature-dependent changes in char thickness. Therefore, even for standard fire conditions no calculation approach is included in the EN-1993-1-2 (2010) to determine the contribution of intumescent coatings to the fire resistance of steel members, although a respective method is provided in EN-13381-8 (2013). However, a calculation of the temperature and the load-bearing capacity of coated steel members is usually not necessary as the required fire resistance is verified by means of the dry film thickness of the coatings that is taken from the national or European technical approvals (see subsection 2.2.2) depending on the required fire resistance time and the section factor of the steel member. For natural fires, on the other hand, this procedure cannot be adopted as the values for the dry film thickness are determined exclusively under standard fire exposure. Therefore, a simplified calculation approach is required that enables both a reliable prediction of the heating behaviour of the steel members and a reliable design approach for the dry film thickness of intumescent coatings in case of any fire exposure.

2.3.2 Properties of Carbon Steel during Heating and Cooling

The temperature-dependent thermal and mechanical properties of carbon steel are regulated in EN-1993-1-2 (2010). While the thermal properties are generally formulated, the reduction factors for the mechanical properties are defined only for a certain range of steel grades. Following the definitions of EN-10025-2 (2011), the reduction factors and calculation methods provided in the Eurocode are only applicable to structural steel grades S235, S275, S355, S420 and S460. As the stress-strain relationship of carbon steel shows a dependency on the strain rate and the heating rate, the validity of the mechanical properties is limited to heating rates between 2 and 50 K/min. However, explanation of the extent to which the material properties are also valid for the cooling phase, are not given in the Eurocode.

Thermal Properties:

The thermal properties of carbon steel, such as the thermal conductivity λ_a and the specific heat capacity c_a are defined in EN-1993-1-2 (2010) as a function of temperature. While the thermal conductivity decreases linearly between 20 and 800 °C, the specific heat capacity reaches its maximum at 735 °C. This is due to demagnetisation processes that take place inside the steel. This phenomenon as well as other internal changes of carbon steel can be explained by the behaviour of pure iron according to Figure 2.53. Up to a temperature of 911 °C, iron is present as α-iron which is characterised by its cubic, body-centered grid structure. Due to this structure only 0,02 % of carbon (C) can be incorporated in α-iron. When further heated, a change in grid structure occurs resulting in γ-iron. As γ-iron has a face-centered grid structure, a significantly higher proportion of carbon (2.06 %) as alloying element can be absorbed. Prior to the grid change, at temperatures about 769 °C the iron is fully demagnetised. Both phenomena, the state of demagnetisation and the grid change, are characterised by constant temperature plateaus. During this plateaus the temperature remains constant despite a further heat input until the changes in demagnetisation or grid structure are completed. Such energy-consuming processes are responsible for the increase in specific heat capacity. This applies also to the plateaus at 1392 °C and 1534 °C that represent a further change in grid structure and the beginning of melting, respectively.

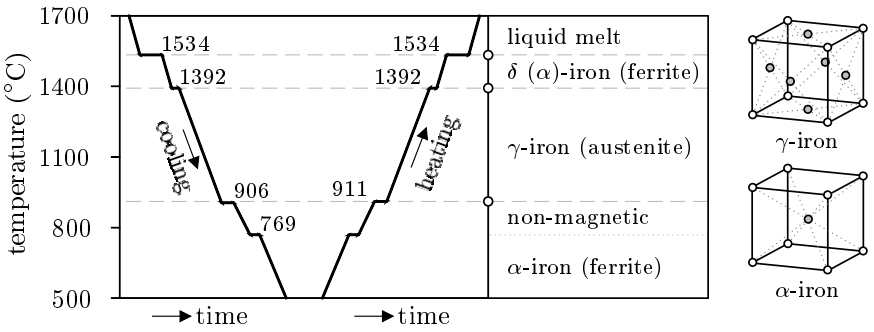

Figure 2.53: Phase transformation of the iron grid structure during cooling and heating as a function of temperature according to Petersen (2013)

As described by Petersen (2013), the changes in grid structure and demagnetisation do not only occur during the heating but also during the cooling phase. Even the temperatures at which the changes occur do not differ significantly. Therefore, it can be assumed that at least the thermal properties of carbon steel show a reversible behaviour. As a consequence, the temperature-dependent thermal conductivity and the temperature-dependent specific heat capacity of carbon steel can be defined equally for both the heating and the cooling phase.

Mechanical Properties:

The mechanical properties of carbon steel S235 to S460 given in the Eurocode are defined as temperature-dependent reduction factors for the yield strength $f_{y,\theta}$, the proportional limit $f_{p,\theta}$ and the Young's modulus $E_{a,\theta}$. However, the validity of the reduction factors is only guaranteed for heating rates between 2 and 50 K/min. Information on the application limits of these reduction factors in case of cooling or to what extent steel recovers its strength after a fire event are not given in the Eurocode. This is due to the fact that most steel structures are designed with regard to the standard fire curve. Only with the introduction of natural fires, the question regarding the mechanical behaviour of carbon steel during the cooling phase arises. However, the answer to this question is given by the experimental investigations of Qiang et al. (2012). The research group performed tensile strength tests on high strength carbon steel S460QL and S690QL after cooling down from different temperature levels in order to investigate their post-fire behaviour. The results of these investigations are given in Figure 2.54.

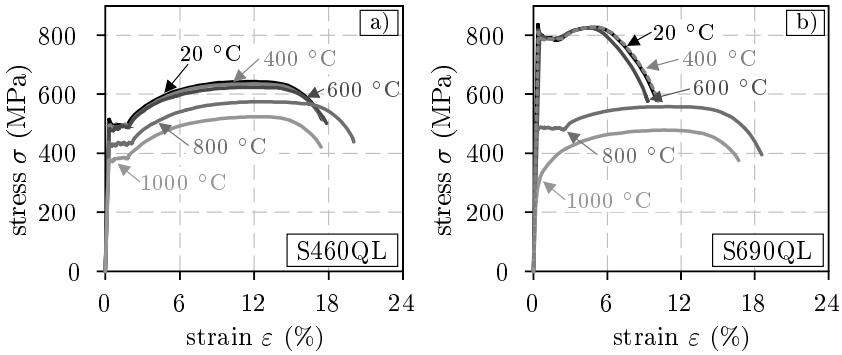

Figure 2.54: Post-fire stress-strain curves of high strength carbon steel a) S460QL and b) S690QL after cooling down according to Qiang et al. (2012)

If high strength carbon steel is not heated above 600 °C, the initial stiffness and the initial strength recover after cooling. This applies also for very high strength carbon steel, such as S960QL (Qiang et al. 2013). However, if the temperature exceeds 600 °C, high strength and very high strength carbon steel show a significant reduction in mechanical properties after cooling. Although the steel recovers its Young's modulus entirely, the yield point is no longer reached as can be seen in Figure 2.54 for both steel grades. However, this behaviour does not apply to all structural steels. Normal strength steel, such as S355 seems to totally recover its mechanical behaviour after cooling regardless of the maximum steel temperature. This can be inferred from experimental investigations of Tang et al. (2019). The researchers investigated the post-fire behaviour of the Chinese carbon steel Q345 (equivalent to S355) by tensile strength tests. In order to perform these tests, unloaded specimens were first heated up to different temperature levels (20 - 900 °C). Subsequently, the test specimens were cooled down either in air or in water. In this

way both a natural extinction of the fire event and the affect of sprinkler systems or firefighting operations were simulated. While under natural cooling the steel regains its original mechanical properties entirely, cooling with water results in an increase in strength for test specimens that were heated above 700 °C. This is due to the sudden cooling and the resulting solidification of the grid structure inside the steel that leads to the strain hardening and the reduction in ductility.
Based on the research of Qiang et al. (2012) and Tang et al. (2019), the following conclusions can be drawn. If the temperature of fire protected steel structures is limited during a natural fire to 600 °C, the stress-strain relationship that is regulated in EN-1993-1-2 (2010) for the heating phase may also be used for the cooling phase. If the stress-strain relationship after cooling correlates with the stress-strain relationship at 20 °C, this should also apply to other temperature levels during cooling, as long as the limit of 600 °C is not exceeded. However, this applies only to high and very high strength steels. For normal strength steels there is no temperature limit at all. Therefore, the mechanical properties of normal strength steel can be defined for the cooling phase without any restriction. Nevertheless, it should be pointed out that more high strength steels will be used in future. Therefore, further investigations on the mechanical behaviour is required in order to understand the intermediate states of the stress-strain relationship during cooling after reaching high temperatures ($> 600\,°C$). For this purpose, new experimental procedures should be used, in which the test specimens are first heated to a high temperature and then cooled down to the desired target temperature (e.g. 500 °C) at which the tensile strength tests are performed. With the curves already existing for the heating phase, two stress-strain relationships are provided for one temperature level in order to describe the mechanical behaviour of high strength steel during both heating and cooling.

2.4 Design Fires

2.4.1 Nominal Fire Curves

In order to provide uniform test and evaluation conditions, nominal fire curves were developed in the past. One of the most commonly used fire curves is the standard time-temperature curve according to ISO-834-1 (2010). The curve is internationally accepted to represent a fully developed cellulose fire. Therefore, the standard fire curve is used for both fire tests and the design of structural members. As shown in Figure 2.55, the curve is characterised by a fast temperature rise and the absence of a cooling phase. However, in case of small and medium-sized compartment fires, the standard fire curve shows normally a good agreement with the temperature development in reality.
When liquid fires or tunnel fires are considered, the hydrocarbon curve is usually used. This curve is characterised by an even faster temperature rise and higher temperatures as illustrated in Figure 2.55. In addition to the standard fire and

the hydrocarbon curve, a third nominal fire curve, the so-called external fire curve, is also defined in EN-1991-1-2 (2010). This curve represents a fire load to which façade elements and external structures are exposed during a compartment fire that penetrates through a building opening to the outside. Therefore, the external fire curve is used less for the design of structural elements than for the assessment of facade elements and their fire behaviour.

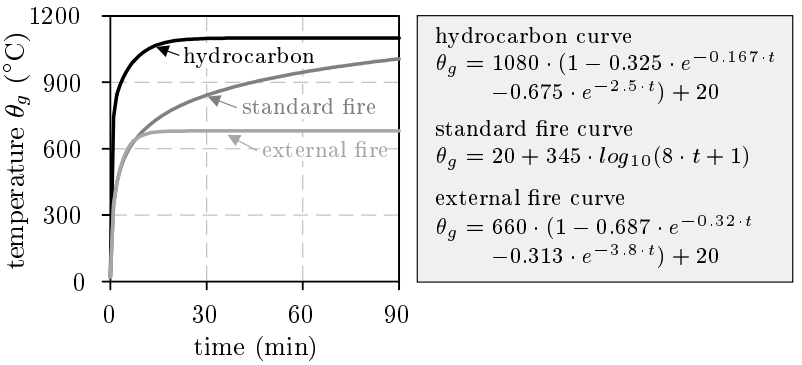

Figure 2.55: Nominal fire curves according to EN-1991-1-2 (2010)

In general, the nominal fire curves represent simplifications that cannot be considered in every application. For example, in very large fire areas or in case of local fires, the application of nominal fire curves is less useful. Therefore, for such cases natural fire models are used. Similar to the fire design of steel structures, natural fires can be calculated with the help of simplified or advanced calculation methods as described in the following.

2.4.2 Natural Fire Models

In contrast to the invariant nominal fire curves, natural fire models can be used to determine a performance-based fire exposure taking into account the most influencing input parameters for a natural fire development. These parameters are the type and the amount of the fire loads, the ventilation conditions, the geometry of the fire compartment and the thermal properties of the surrounding components. For example, Annex A of EN-1991-1-2 (2010) contains such a simplified fire model for the calculation of a fully developed natural fire. However, this simplified model has been criticised for a long time since the model does not adequately describe the real course of a natural fire. For this reason, the application of this model is prohibited in Germany. In order to provide an alternative method, Zehfuß & Hosser (2005) developed a more differentiated approach with much better agreement with experimental and numerical data. The model distinguishes between a fire load-controlled and a ventilation-controlled natural fire and describes the course of the temperature development on the basis of the heat release rate (HRR)

as shown in Figure 2.56. Due to the correlation between the heat release rate and the time-temperature curve, a natural fire is characterised by three phases, (1) the development, (2) the stationary and (3) the cooling phase. The occurrence of a flash over as well as a safety concept taking into account the annual occurrence probability of a fire and the probability of failure of automatic and manual fire fighting is also considered within the model. Since the model has proven its reliability, it is now regulated in the National Annex EN-1991-1-2/NA (2015) of Germany and replaces the parametric time-temperature curves of Eurocode 1 part 1-2. It is valid for compartments up to a height of 5 m, an area up to 400 m^2 and a proportion of ventilation openings between 12.5 and 50 % of the floor area. The fire load density is limited to 100 - 1300 MJ/m^2.

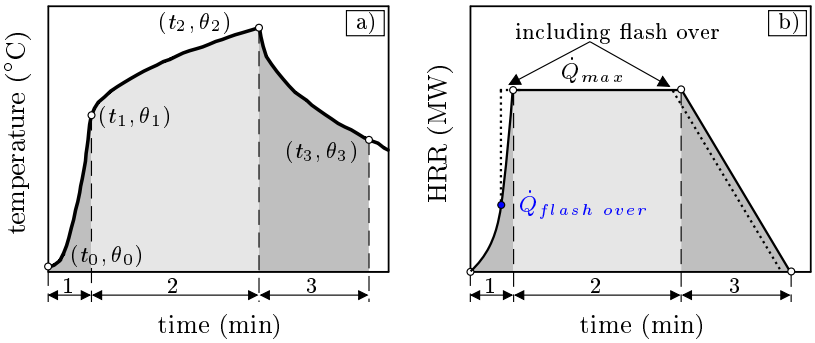

Figure 2.56: Correlation between a) the time-temperature curve and b) the heat release rate (HRR) of a natural fire (1: development phase, 2: stationary phase and 3: cooling phase) according to the simplified calculation approach of EN-1991-1-2/NA (2015)

Since the prevailing boundary conditions in a fire compartment do not always lead to a fully developed fire, EN-1991-1-2 (2010) provides in Annex C methods that can be used to describe a local fire event. Here, a distinction is made between two approaches. The first approach is based on the research of Heskestad (1983) and describes the temperature distribution along the plume axis of a local fire. The flame height is described to be dependent on the fire diameter and the heat release rate assuming that the flame does not reach the ceiling. An extension of this model (Heskestad & Delichatsios 1979) enables, in addition, the calculation of the gas temperature outside the plume axis. However, this model is not part of the Eurocode.

The second approach in the Eurocode describing a local fire event is based on Hasemi & Tokunaga (1984). This approach is usually used to calculate the flame impact on horizontal space-enclosing elements due to a local fire that reaches the ceiling. The resulting ceiling jet is described by a horizontal flame spread. The temperature development of the fire exposed ceiling is calculated according to the heat flux that results form the accumulation of the plume heat under the ceiling.

In addition to the simplified calculation models, the Eurocode 1 part 1-2 provides

also the ability to calculate the temperature evolution in a fire area using advanced calculation methods. Here, a distinction is made between one-zone models, two-zone models and field models. While the one- and two-zone models are usually based on the mass and energy balance equation, the field models incorporate additionally a partial differential equation (Navier-Stokes) in order to describe field variables, such as the velocity and the direction of the gas phase flow.

2.4.3 Travelling Fires

The current fire safety approaches are based on fires that are transient in time but stationary in their position, regardless of whether it is a local fire or a fully developed fire. However, studies on the fire development and propogation over the last two decades have shown that especially large compartment fires tend to move across the floor over a period of time. Although this form of fire propagation has not been standardised yet, numerous experimental and analytical investigations are reported in the literature. Dai et al. (2017), for example, give an overview on the so called travelling fire scenarios for the performance-based design of structures in case of moving fires. At this point it is deliberately omitted to present all the studies. However, at least one work should be highlighted as it is particularly suitable to describe the travelling fire concept. According to Rein et al. (2015) a travelling fire is characterised by a moving fire front and an inhomogeneous gas temperature distribution along the compartment as it is illustrated in Figure 2.57. The gas phase, in which the plume axis rises and leads to high gas temperatures under the ceiling, is referred to as the *near field zone*. The area in which the fire load (fuel) has already been burned and the area into which the fire spreads are referred to as the *far field zone*. Here, the gas temperatures are assumed to be much lower than in the near field zone.

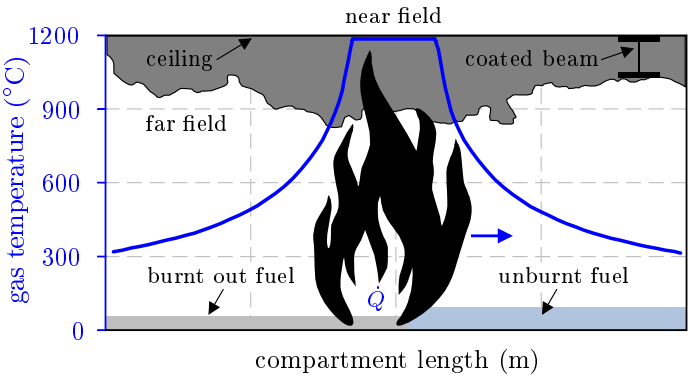

Figure 2.57: Schematic description of a travelling fire and its gas temperature distribution underneath the ceiling along the compartment length according to Rein et al. (2015)

Despite the low temperatures in the far field zone, the heat energy could already be enough to thermally activate intumescent coatings, although the actual fire front is still far away. This could be, for example, the case when a coated steel beam is located underneath the ceiling (see Figure 2.57) and the fire continues to move closer to the beam. Such a travelling fire scenario could be relevant for the design of the dry film thickness of intumescent coatings due to the premature thermal activation. Therefore, when evaluating the fire protection performance of intumescent coatings in case of natural fires, the occurrence of possible travelling fires should also be considered.

2.5 Summary and Conclusions

Intumescent coatings are non-standardised products that require an official approval in order to be used in the construction sector. During the approval procedure intumescent coatings need to pass certain examinations at the national and European level. Within these examinations the insulation efficiency of the coatings is assessed for a fire exposure according to the standard fire curve. Additional fire tests based on the smouldering curve are also possible. However, these tests are not prescribed and, therefore, serve only for orientation.
Due to the historical development of intumescent coatings, three different product classes are currently used in the construction sector: waterborne, solvent-borne and epoxy resin-based intumescent coatings. All three belong to the group of wet coatings and consist of four main ingredients: an acid source, a carbon donor, a blowing agent and polymer binders. In order to increase the insulation efficiency of the coatings, several additives are also used. The colouring is ensured by pigments such as titanium dioxide.
Intumescent coatings belong to reactive fire protection materials. When being exposed to heat, the inert coating expands multiple times the original thickness to form a highly insulating char with low thermal conductivity that protects the underlying steel structure from rapid heating. However, in order to ensure the formation of an efficient protective char, the thermal behaviour of the main ingredients need to be attuned to each other. As the reaction of intumescent coatings is thermally activated, changes in heating conditions seem to influence the chemical reactions of single ingredients. This was derived at least from a comprehensive literature review on thermogravimetric data. Especially the acid source, the carbon donor and the blowing agent seem to show a pronounced sensitivity to changes in heating rates. The polymer binders, on the other hand, are less sensitive or even unaffected by changing heating conditions.
Besides the thermogravimetric data, numerous investigations of the expansion behaviour of intumescent coatings under different heating conditions are documented in literature. Regardless of whether the investigations were performed under a cone calorimeter or in an electric furnace, the expansion behaviour of intumescent coatings basically depends on the heating conditions. However, the sensitivity

to changes in heating rates vary among the different product classes. When intumescent coatings are exposed to low heating rates, the strongest reduction of the expansion ratios (factors) occurs for solvent-borne coatings. Waterborne and epoxy resin-based coatings, on the other hand, show a less pronounced dependence on changing heating conditions. However, as already known from standard fire tests, the extend of char expansion depends also on the dry film thickness and the bulkiness of the substrate.
Cone calorimeter are usually designed to perform studies under constant heat fluxes. However, in the case of intumescent coatings this is impossible due to changes in distance between the cone heater and the char surface as soon as the coating starts to expand. In order to eliminate this effect, a novel testing method (H-TRIS) was developed, in which the position of radiant panels is adaptively computer-controlled to ensure a constant distance between the heat source and the heat exposed char surface at any time. This method promises a high reproducibility for the tests and is therefore predestined to evaluate the fire protection performance of intumescent coatings at different heating conditions. However, there is currently no standard procedure for assessing the fire protection performance of intumescent coatings. The review of the literature-known investigations on the heating rate dependence of intumescent coatings even reveals contradictions between the provided assessment procedures. The method of the *effective thermal conductivity*, for example, comes to the conclusion that intumescent coatings show the best fire protection performance for lower heating conditions. The evaluation method based on steel temperatures, however, reveals the best fire protection performance for higher heating rates. As a consequence, systematic investigations have to be carried out in order to identify the reason for this contradiction so that in the future the fire protection performance of intumescent coatings can be properly assessed for the use in natural fires.
As reported in the literature, crack formation inside the char can significantly increase the heat transport from the heat exposed char surface to the underlying substrate. Cracks inside the char are usually caused by gravity-induced material flow of the liquid melt or the exceed of the tensile char strength regardless of whether this is caused by geometry or external mechanical stresses. To what extent different heating conditions have an influence on the crack formation, has not been investigated so far. For the viscosity of the liquid melt, on the other hand, a clear influence on the heating rate-dependent char formation is identified. For example, if the viscosity is too low, the released gases due to the decomposition of the blowing agent escape from the char. If the viscosity, on the other hand, is sufficient, a slow diffusion of the gases occurs during the intumescence process, resulting in a uniform and closed-cell char structure. Therefore, according to these results, the char formation is significantly controlled by the viscosity and the char strength. To what extend the viscosity and, therefore, the char formation of intumescent coatings is affected by different heating conditions, will be assessed on the basis of own experimental investigations.
Numerical simulations are a useful way to supplement experimental investigations

and to expand the investigated parameter range. However, simulations are only reliable if the material models that are used within the simulations are proven to be valid to describe the complex behaviour of materials close to the reality. In the last two decades, enormous efforts have been made to develop appropriate material models for intumescent coatings. Due to the different objectives, the models were formulated at different levels of complexity. For the description of the expansion behaviour and the formation of individual bubbles, for example, highly complex models were developed on the microscopic level of chemical reactions. The complexity of the models, however, makes it clear that numerous input parameters are needed to describe the thermal behaviour of intumescent coatings. The modeling is made even more difficult, as some of the input parameters cannot be determined experimentally and, therefore, have to be inferred from experimental data. Therefore, in order to provide a reliable and user-friendly modelling, the amount of required input parameters should be limited to the minimum. In addition, only such material properties should be used as input parameters, which can be clearly determined experimentally. As the literature review reveals, currently no reliable material model exist to describe the heating rate-dependent expansion and thermal conductivity behaviour of intumescent coatings at different morphology stages as well as heating and cooling conditions. Therefore, new material models are required. The inverse calculation of the apparent thermal conductivity from equidistantly measured char temperatures that are ensured by new test setups could be of great help for this. As intumescent coatings are only evaluated for a fire exposure according to the standard fire curve during the approval procedure, the design of the dry film thickness that is ensured by tabulated data given in the approvals is limited to the nominal fire curve. For natural fires, these values cannot be adopted. Therefore, a simplified calculation approach is required that enables both a reliable prediction of the heating behaviour of coated steel members and a reliable design approach for the dry film thickness of intumescent coatings in case of any fire exposure since no generally valid method exists so far. When evaluating the fire protection performance of intumescent coatings in case fire, not only regular natural fires but also travelling fires should be considered. A travelling fire is characterised by a moving fire front and an inhomogeneous gas temperature distribution that can thermally activate intumescent coatings, although the actual fire front is still far away.

2.6 Hypothesis and Research Aims

The review of the current state of the art reveals numerous open questions regarding the fire protection performance of intumescent coatings and its evaluation as well as its design in case of natural fires. Therefore, in order to answer these questions the following hypothesis are formulated to be addressed in the present thesis:

(1) The intumescence behaviour and fire protection performance of intumescent coatings is dependent on the heating and cooling conditions. At high heating

rates intumescent coatings show a better insulation performance than at low heating rates. This is due to the heating rate-dependent expansion behaviour and char morphology.

(2) Intumescent coatings usually consist of four main ingredients: an acid source, a carbon donor, a blowing agent and a polymer binder. Regardless of the product class (waterborne, solvent-borne or epoxy resin-based), the acid source is normally represented by ammonium polyphosphate, the carbon donor by pentaerythritol and the blowing agent by melamine. However, despite the same ingredients, intumescent coatings show different sensitivities to changes in heating rates depending on the product class. This is due to the different polymer binders (see subsection 2.2.4) that are usually used.

(3) The viscosity of the melt and its ability to trap the gases that are released during the decomposition of the blowing agent are mainly responsible for the heating rate-dependent behaviour of intumescent coatings. As a consequence, not only the amount of trapped gases is affected by the viscosity but also the char structure and its morphology.

(4) The thermal conductivity behaviour of intumescent coatings is significantly affected by the char morphology and the mean pore size. Therefore, it is assumed that the thermal characteristics of intumescent coatings differ for the heating and cooling phase due to irreversible changes in char morphology, e.g. the change from a closed to an open-cell foam structure. This applies also to the specific heat capacity and the density. However, the effect of the heat storage capacity ($\rho \cdot c_p$) on the heating behaviour of intumescent coatings is significantly lower.

(5) For the evaluation of the fire protection performance of intumescent coatings the *effective thermal conductivity* method given in EN-13381-8 (2013) is inappropriate. Due to the assumptions made within this method, inaccurate results are obtained that can lead to misleading interpretations. The evaluation of the fire protection performance of intumescent coatings, therefore, should be done by means of measured temperatures of coated and uncoated substrates. The temperature measurement inside the char structure at equidistant intervals also provides important information on the fire protection performance of intumescent coatings and, therefore, should be considered within experimental investigations as well.

(6) Some of the material models found in the literature are suitable for further development to describe the thermal behaviour of intumescent coatings in natural fires. However, so far, there is no model that requires only few input parameters in order to describe the heating rate dependence and the differentiated thermal behaviour in heating and cooling of intumescent coatings due to changes in char morphology.

(7) In order to ensure a safe performance-based design of coated steel structures in natural fires, a reliable and science-based approach for the design of the dry film thickness of intumescent coatings is required. Currently, no method exists that is able to evaluate the influence of different heating and cooling

conditions on the heating behaviour of coated steel elements. For this reason, there is no option to calculate the required dry film thickness of intumescent coatings depending on the permissible critical temperature of a steel structure.

In order to work through the hypothesis listed above, experimental and numerical investigations are performed within the scope of this thesis. Exemplarily, a waterborne and a solvent-borne intumescent coating are used for the investigations. Small-scale as well as large-scale experimental tests are performed in order to understand the effect of varying heating and cooling conditions on the fire protection performance of the coatings. Laboratory tests on the expansion, the mass loss behaviour and the heat storage capacity are also performed. These investigations serve, among others, for the development of a holistic material model for intumescent coatings that is valid for both advanced and simplified calculations. While the advanced numerical simulations are performed in order to extend the examined parameter range, a simplified calculation method is developed in order to ensure a reliable and accurate approach for the design of the dry film thickness of intumescent coatings in case of any natural fire scenario.

3 Experimental Investigations

The third chapter deals with own experimental laboratory, small-scale and large-scale tests of the fire protection performance of a solvent- and a waterborne intumescent coating in case of various heating rates in natural fires.

Contents

3.1 Introduction

As the review of recent research reveals, intumescent coatings show different sensitivities to changes in heating conditions. In the context of the experimental investigations, therefore, two different products are exemplarily examined. Both the solvent- and the waterborne intumescent coating are produced and sold in Germany by two different manufacturers. Based on their national and European approvals the coatings are allowed to be applied on I-section beams and columns as well as on hollow sections. Depending on the dry film thickness and the section factor, the products are able to realise a fire resistance time for coated steel members up to 120 minutes.
The waterborne coating is based on a waterborne binder into which fire retardant agents, such as ammonium polyphosphate (APP) and pentaerythritol (PER) are incorporated. The intumescence reaction is ensured through the blowing agent melamine (MEL), whereas titanium dioxide (TiO_2) is used as white pigment. The whole formulation of the coating is given in Table 3.1.

Table 3.1: Ingredients of the investigated waterborne intumescent coating (technical approval: Z-200.4-15)

Ingredients	Amount (%)
Ammonium polyphosphate (APP)	20 - 30
Pentaerythritol (PER)	5 - 15
Melamine (MEL)	5 - 15
Pigment TiO_2	5 - 15
Water	15 - 25
Polymeric dispersion 50 %	15 - 25
In-can preserver	< 0.25
Dispersing agents	< 1
Thixotropic agents	< 1

For the solvent-borne coating, unfortunately, no publicly available formulation was provided by the manufacturer. However, according to the technical approval, the coating is normally used for exterior applications (X). The waterborne coating, on the other hand, is only permitted for internal conditions (Z_2 and Z_1).
In order to examine the heating rate-dependent behaviour of the coatings in case of natural fires, different experimental investigations at different scales are performed. As natural fires are characterised by a broad spectrum of time-temperature curves, the fire exposure is replicated within the investigations by constant heating rates, natural cooling rates and varying maximum temperatures. In this way the broad spectrum of natural fires is assumed to be covered.
In the first stage of the experimental investigations the mass loss behaviour and the heat storage capacity are examined under different heating and cooling conditions. This is done by simultaneous thermogravimetric (TG) and differential scanning calorimetry (DSC) analyses. In the next step, the influence of varying heating

and cooling conditions as well as maximum temperatures on the intumescence behaviour of the coatings is evaluated during digital expansion analyses. The samples that are used for the expansion analyses are also used to study the char morphology. The fire protection performance of the coatings, on the other hand, is evaluated within small-scale fire tests on coated steel plates with the help of a new developed experimental setup. In order to monitor the effects of different heating conditions on the insulation behaviour, the temperature distribution inside the char as well as the substrate temperatures are measured. Following the ideas of Lautenberger & Fernandez-Pello (2009) and Bozzoli et al. (2018), the equidistantly measured char temperatures are used to perform reverse calculations in order to determine the apparent thermal conductivity of the expanded char. For this purpose, a finite difference method is implemented in MATLAB (Release 2017a) by the author and is used as evaluation software.
In order to evaluate scale effects on the fire protection performance and the morphology of the coatings, finally a large-scale fire test is performed. As loaded and unloaded steel beams are used within the fire test, the influence of shape- and stress-induced cracks inside the char on the fire protection performance is also assessed. Due to the high effort, however, the large-scale fire test could only be carried out for one intumescent coating. Therefore, the waterborne coating was chosen as its product class becomes increasingly important in the construction sector.

3.2 TG and DSC Analyses

3.2.1 Testing Procedure

The aim of the investigations was to identify the influence of different heating conditions on the mass loss behaviour and heat storage capacity of the solvent- and waterborne intumescent coating. Therefore, coupled thermogravimetric (TG) and differential scanning calorimetry (DSC) analyses were performed using a NETZSCH STA 409 PC/PG DSC-TGA analyser. The analyser is owned by the Institute of Physical Chemistry and Electrochemistry at the Leibniz University Hannover. A limited number of experiments could be carried out. However, in order to perform differentiated analyses, different heating rates were chosen. While the waterborne coating was investigated under heating rates of 5, 10 and 20 K/min, the solvent-borne coating was heated with 10, 30 and 50 K/min. The maximum temperatures were also chosen in different ways. The waterborne coating, for example, was heated up to 1000 °C. The solvent-borne coating, on the other hand, was only heated up to 600 °C, in order to investigate also the mass loss and heat storage behaviour during a natural cooling. In both cases, the reaction gas (80 % argon (Ar) and 20 % oxygen (O_2)) was the same.
Throughout the experiments, the mass and the temperature of the samples were

continuously measured. Since the samples had only a very low mass, a high measurement accuracy was required. Therefore, the precision of the weight measurement was 20/30000 mg over the whole range of temperature (40 - 1000 °C), whereas the error of temperature measurement was ±1 °C.

3.2.2 Materials and Parameters

The samples required for the coupled TG-DSC analyses were prepared by applying the liquid coatings on a glass plate. After drying at room temperature and normal humidity for three weeks, the coatings were removed from the glass plate and were processed into a fine powder. Subsequently, the powder was filled in aluminum oxide (Al_2O_3) crucibles. Before the samples were placed inside the analyser, the initial sample mass (without the crucible) was measured. The sample masses of the waterborne (6.6 - 8.1 mg) and the solvent-borne coating (5.9 - 7.9 mg) are listed in Table 3.2 and Table 3.3, respectively.

3.2.3 Results

For each coating and heating rate two coupled TG-DSC analyses were performed. Therefore, results of 12 analyses are documented in the following. In order to differentiate between the two coatings, the results are presented separately.

Waterborne Intumescent Coating:

The results of the performed TG-DSC analyses of the waterborne coating are given in Figure 3.1 and Table 3.2. As graphically illustrated, the mass of the waterborne coating decreases for all investigated heating rates in several stages. In the first stage the mass loss is dominated by water evaporation. With further heating, the mass loss increases significantly. This behaviour correlates with the char formation and leads to the major mass loss between 200 and ca. 550 °C (see Table 3.2). Within this temperature range the sample mass changes in three stages which is discernable by sectors with constant slopes. The last stage, in which the mass decreases, is caused by the pyrolysis of organic compounds resulting in an inorganic residue with a remaining mass of 27 - 30 wt%. According to Wang et al. (2006) this residue consists of titanium dioxide and titanium pyrophosphate (TiP_2O_7). Although the differences between the measured TG curves in Figure 3.1 a) are small, the mass loss of the waterborne coating changes with heating rates. The analyses of the test data reveals that the coating degrades thermally slower when being exposed to fast heating rates. This can already be seen by comparing the masses TG-5 (95.1 and 96.5 wt%) and TG-20 (97.6 and 98.2 wt%) at 200 ° C in Table 3.2. This heating rate-dependent behaviour can be explained by the thermal inertia of the char. When the coating is exposed to high heating rates, less time remains for the char to adapt to the surrounding temperatures. This effect is

even more pronounced after the full expansion of the coating since the low thermal conductivity of the char increases the effect of thermal inertia. This is the reason why the TG curves for 5 and 20 K/min deviate most strongly from each other between 500 and 900 °C. During this temperature range the char is fully expanded and starts to degrade thermally.
As the thermogravimetric analyses were performed simultaneously to differential scanning calorimetry analyses, the results of the measured heat flow are given in Figure 3.1 b). Here, for each investigated heating rate several reactions, such as the melting of the polymer binder or the initiation of char formation are identified. To have a more precise view on the individual reactions, the results of the samples TG-5-wa-I and TG-20-wa-I are shown in Figure 3.2. Here, the reactions are illustrated by blue shaded and numbered (① - ④) areas. According to Vandersall (1971) the first reaction (①) represents the melting of the binder and the phosphate (APP). This reaction occurs for each investigated heating rate (5, 10 and 20 K/min) at nearly the same temperature (T_1: 183, 186 and 188 °C in Table 3.2). The second reaction (②) is dominated by the char formation. During this reaction the decomposed blowing agent (MEL) releases volatile products (CO_2, NH_3 and H_2O) which are trapped inside the carbon-phosphorus char (Camino & Costa 1986, Camino et al. 1989). Although the heat flow during this reaction changes with heating rates (see Figure 3.1 b)), the starting point of the reaction (represented by temperature T_2 in Table 3.2) is less affected by the changes in heating rates.

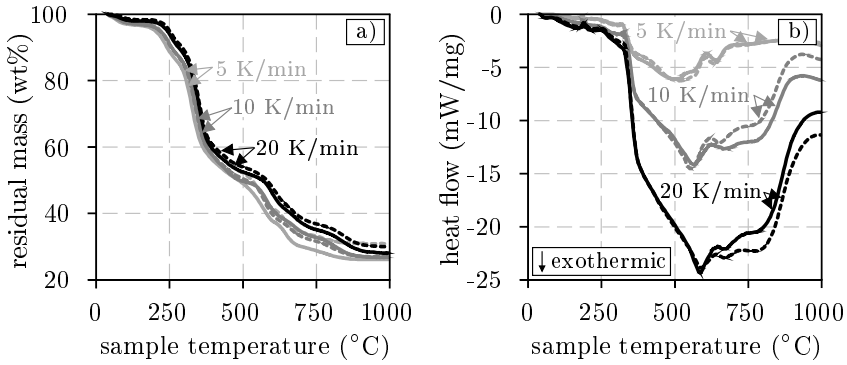

Figure 3.1: Results of the performed coupled TG-DSC analyses for the waterborne intumescent coating at heating rates of 5, 10 and 20 K/min: a) mass loss and b) heat flow behaviour

In contrast to the previous reactions, the last two reactions (③ and ④) are characterised by their exothermic peaks due to the oxidation of organic compounds and the release of carbon dioxide (Wang et al. 2006). As the heat flow inside the small sample is strongly influenced by the formed char and its low thermal conductivity, the exothermic peak for the heating rate of 5 K/min (see Figure 3.2 a)) is characterised by a narrow temperature range. This indicates that the sample heats up uniformly and therefore oxidises in a small temperature range. Faster heating rates,

on the other hand, lead to a broad endothermic peak in the heat flow curve (see Figure 3.2 b)) with a retarded thermal decomposition of the organic compounds of the char. The delay in heating and thermal decomposition is potentially the reason why reaction ③ occurs for 10 and 20 K/min in two stages whereas reaction ④ does not take place at all within the considered temperature range. The corresponding temperatures T_3 and $T_{(3)}$ (the temperature of the second peaks) of reaction ③ as well as the temperature T_4 at which reaction ④ occurs are listed in Table 3.2.

Table 3.2: Results of the performed TG-DSC analyses of the waterborne intumescent coating given by the masses (m_i), sample temperatures (T_i) and maximum heat flow (DSC_{max}) for heating rates of 5, 10 and 20 K/min

Sample ID	$m_{20\,°C}$ (mg)	$m_{200\,°C}$ (wt%)	$m_{400\,°C}$ (wt%)	$m_{600\,°C}$ (wt%)	T_1 (°C)	T_2 (°C)	T_3 (°C)	$T_{(3)/4}$ (°C)	T_{max} (°C)	DSC_{max} (mW/mg)
TG-5-wa-I	6.6	96.5	58.9	41.6	183.0	319.8	635.4	889.6	503	-6.27
TG-5-wa-II	8.1	95.1	55.7	37.8	183.4	319.2	640.8	887.4	496	-6.12
TG-10-wa-I	7.2	96.1	57.3	39.7	186.0	322.2	652.6	(760.2)	551	-14.55
TG-10-wa-II	8.0	96.0	57.4	41.2	187.2	325.0	682.6	(760.4)	565	-14.16
TG-20-wa-I	7.6	98.2	60.3	47.9	189.2	326.2	668.8	(768.8)	589	-23.89
TG-20-wa-II	7.8	97.6	59.1	46.0	188.0	326.6	668.2	(776.4)	585	-24.36

Following the graphs in Figure 3.1 b), the measured heat flow is much more influenced by the different heating rates than the observed reactions of the coating. With faster heating rates more thermal energy is required related to the time in order to undergo the chemical reactions. Hence, the heat storage capacity of the waterborne coating shows a strong heating rate-dependent behaviour resulting in high heat storage values for high heating rates. However, due to the high mass loss and the change in volume caused by the expansion, the heat capacity is assumed to have only little influence on the fire protection performance of the formed char. Nevertheless, in order to examine the heating rate-dependent behaviour of intumescent coatings, it is still of great importance to perform DSC analyses to better understand the reaction mechanisms.

Solvent-borne Intumescent Coating:

For the solvent-borne intumescent coating slightly different results are obtained from the performed TG-DSC analyses. Due to the absence of water, nearly no mass loss occurs within the first 250 °C as can be seen in Figure 3.3 a). However, the endothermic peaks representing the melting of the binder (reaction ①) are identified to occur for all heating rates in a temperature range of 182 - 188 °C. Therefore, similar to the waterborne coating, the melting of the binder takes place nearly independently of the heating rates although these are much higher. This also applies in parts to the endothermic peaks between 334 and 344 °C in Figure 3.3 b) that are assumed to represent the intumescence process of the coating (see temperature T_2 of reaction ② in Table 3.3). Due to the degradation of the blowing agent, the main mass loss of the solvent-borne coating occurs in two stages. The first degradation stage occurs between 250 and 450 °C. The second stage, on the

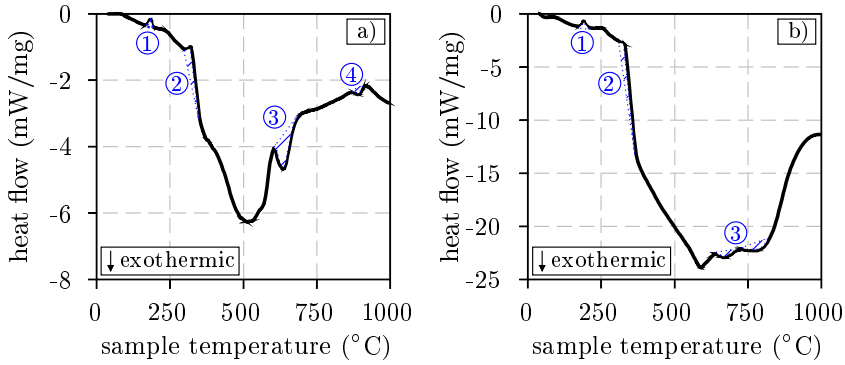

Figure 3.2: Reaction characteristics of the waterborne intumescent coating at heating rates of a) 5 K/min and b) 20 K/min (remark: the axes of the ordinates have different scales)

other hand, takes place between 450 and 600 °C. Thereafter, by the onset of cooling the mass loss stagnates. This is consistent with the hypothesis that thermally activated processes do not progress further when energy is removed.

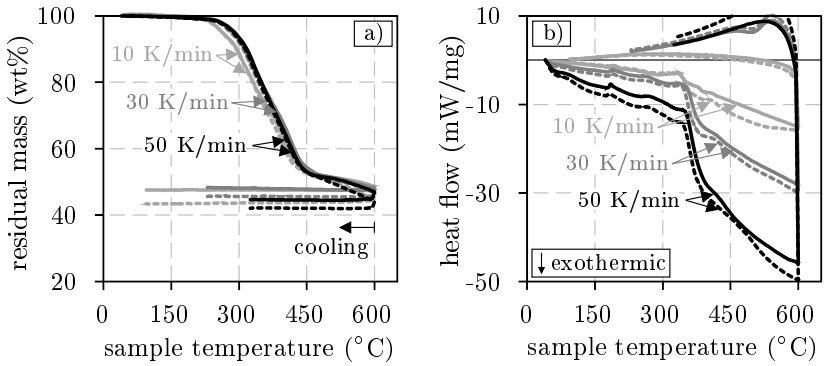

Figure 3.3: Results of the performed coupled TG-DSC analyses for the solvent-borne intumescent coating at heating rates of 10, 30 and 50 K/min: a) mass loss and b) heat flow behaviour

As the residual mass after 600 °C is between 44.0 and 48.6 wt%, the solvent-borne coating appears to be more thermally stable than the waterborne one. In addition, comparing the significantly higher heating rates of the solvent-borne coating, even a pronounced dependence of the mass loss behaviour on the heating conditions cannot be observed. This, however, does not apply to the heat storage capacity. Similar to the waterborne coating, a significant increase in heat flow occurs as the heating rate is increased. For 10 and 50 K/min, for example, heat flow values of -14.96 to -15.77 mW/mg and -45.79 to -49.65 mW/mg are observed, respectively. The temperatures, at which the reactions of melting and degradation of the blow-

ing agent occur, however, are less affected by the different heating conditions. The differences in the measured heat flow can be explained similar to the waterborne coating by thermal inertia. Especially in the foamed state, the influence of thermal inertia seems to be the greatest. This applies also during the cooling phase, when the sign of the heat flow turns from negative to positive, i.e. the heat flow changes its direction. Since more energy is added at higher heating rates (30 and 50 K/min) in relation to time, more energy is correspondingly released during the cooling phase. For the heating rate of 10 K/min, on the other hand, only a small amount of energy is released during the cooling phase as can be seen in Figure 3.3 b). The results of the performed DSC analyses thus show that the heat storage capacity of intumescent coatings depends not only on the heating, but also on the cooling rate and the previously applied amount of thermal energy.

Table 3.3: Results of the performed TG-DSC analyses of the solvent-borne intumescent coating given by the masses (m_i), sample temperatures (T_i) and the heat flow at 600 °C ($DSC_{600\,°C}$) for heating rates of 10, 30 and 50 K/min

Sample ID	$m_{20\,°C}$ (mg)	$m_{200\,°C}$ (wt%)	$m_{400\,°C}$ (wt%)	$m_{600\,°C}$ (wt%)	T_1 (°C)	T_2 (°C)	$DSC_{600\,°C}$ (mW/mg)
TG-10-s-1	5.9	99.8	62.4	48.6	188.2	333.9	-14.96
TG-10-s-2	6.6	99.6	60.2	44.8	187.8	334.2	-15.77
TG-30-s-1	7.8	99.5	64.2	46.7	186.3	338.1	-30.05
TG-30-s-2	8.3	99.6	66.9	48.0	187.9	334.1	-28.24
TG-50-s-1	7.7	99.2	64.0	44.0	181.9	343.3	-49.65
TG-50-s-2	7.9	99.2	65.0	46.9	184.9	344.2	-45.79

As the samples are cooled down after reaching 600 °C, the exothermic reactions ③ and ④ corresponding to the combustion of organic compounds are not represented within the measured DSC curves. These occur, as learned from the waterborne coating at temperatures above 630 °C. However, the temperature value may vary depending on the product as reported by Tabeling (2014).

3.2.4 Discussion

When reviewing the TG data of the main ingredients in subsection 2.2.6, it was postulated that the observed differences in heating rate dependency have an influence on the overall performance and the heating rate-dependent behaviour of intumescent coatings as a whole. While the polymer binders were nearly unaffected by changes in heating conditions, especially APP and MEL showed the greatest temperature shifts (ΔT: +50 and +34 °C) in mass loss due to the increase in heating rates (from 10 to 20 K/min). In contrast to the reviewed TG data, the present analyses were performed for a composition of several ingredients. Therefore, it is plausible that the temperature shift ΔT in mass loss, for example, for the waterborne coating was identified to be only 20 °C and, thus, in between the values of the binder and APP or MEL due to changes in heating rate from 10 to 20 K/min.

However, despite the retarded mass loss behaviour, the endothermic reactions of melting (①) and char formation (②) take place almost independently of the heating conditions and, therefore, each at almost the same temperature. This, at least, is represented by the temperatures T_1 and T_2 that were measured during the DSC analyses. As the TG and DSC analyses were performed simultaneously, a direct correlation between the data can be established. Therefore, when the TG and DSC curves are combined, the following coherence comes into focus. The char formation of intumescent coatings is dependent on two main mechanisms, e.g. the release of volatile gases due to the decomposition of the blowing agent and the ability to trap the gases inside the liquid melt. As the DSC analyses reveal, the melting reaction of both coatings occurs nearly independent from the chosen heating condition. This applies also to the temperature at which char formation occurs. However, between these two nearly constant reaction points, different amounts of mass are lost, depending on the heating rate. The mass loss in this case mainly corresponds to the decomposition of the blowing agent and the release of volatile gases. As a consequence, the change in residual mass between reaction ① and ② is equivalent to the amount of gas that escapes from the coating without being trapped inside the char. The more gases are released before the solidification of the char, the lower the char thickness will be. In order to systematically evaluate this phenomenon from the perspective of heating rate dependence, Figure 3.4 presents a calculation approach for the lost (m_{lost}) and the trapped ($m_{trapped}$) volatile gases. Here, a schematic coherence between the TG and DSC data is given by the correlation between the reactions ① and ② and the corresponding residual masses m_a and m_b. The residual mass m_c, on the other hand, corresponds to the state in which the decomposition of the blowing agent is completed. This value can be derived from the slope change of the TG curve, taking into account the temperature range in which MEL normally decomposes (see subsection 2.2.6).

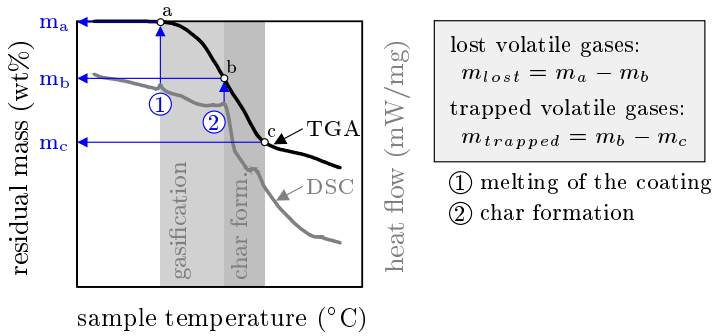

Figure 3.4: Graphical correlation between TGA and DSC data in order to determine the amount of lost and trapped gases inside the formed char

Based on the equations defined in Figure 3.4, it is possible to calculate the mass fractions corresponding to the gas release before and after the initiation of char formation. The amount of gas that is lost before the coating starts to expand, can

be correlated to the formed char thickness or the expansion factor. Normally, the amount of the trapped gas should be used for this purpose. However, as it cannot be excluded that volatile gases also escape from the char during the expansion, the actual amount of gas that is trapped inside the char is assumed to be less than the ideally calculated value $m_{trapped}$. Nevertheless, with the help of the approach, it can be clearly stated that, especially at very low heating rates, more volatile gases escape before the char is formed compared to higher heating conditions. This finding applies to both investigated coatings as documented in Table 3.4. For a heating rate of 10 K/min, for example, between 46.2 and 49.2 % of the gases are released before the initiation of char formation. At 20 K/min, on the other hand, the gas loss is only between 40.5 and 42.8 % in the case of the waterborne coating. A similar amount of lost gases is also observed for the solvent-borne coating (38.5 - 40.3 %). However, these values were determined under 50 K/min.

Table 3.4: Proportion of lost (m_{lost}) and trapped ($m_{trapped}$) volatile gases of the solvent- and waterborne coating derived from the performed TG-DSC analyses at different heating rates

Sample ID	m_a (wt%)	m_b (wt%)	m_c (wt%)	m_{lost} (wt%)	$m_{trapped}$ (wt%)	gas loss (%)
TG-5-wa-I	97.4	77.4	62.1	20.0	15.3	56.7
TG-5-wa-II	96.0	75.1	59.0	20.9	16.1	56.5
TG-10-wa-I	96.6	78.8	59.6	17.8	19.2	48.1
TG-10-wa-II	96.5	78.2	59.3	18.3	18.9	49.2
TG-20-wa-I	98.3	83.6	62.0	14.7	21.6	40.5
TG-20-wa-II	97.7	81.9	60.8	15.8	21.1	42.8
TG-10-s-I	99.8	79.3	55.4	20.5	23.9	46.2
TG-10-s-II	99.7	78.8	54.8	20.9	24.0	46.5
TG-30-s-I	99.4	81.4	54.2	18.0	27.2	39.8
TG-30-s-II	99.6	83.5	54.9	16.1	28.6	36.0
TG-50-s-I	99.3	80.8	53.4	18.5	27.4	40.3
TG-50-s-II	99.3	81.7	53.6	17.6	28.1	38.5

On the basis of the performed TG-DSC analyses and the findings about the performance of individual ingredients, an explanation for the heating rate-dependent expansion behaviour of intumescent coatings that is reported in literature could be found. As a result, intumescent coatings show lower char thicknesses at lower heating rates since more volatile gases are released between the reaction stages of melting and initiation of char formation than at higher heating conditions. The amount of the released gases, which are formed primarily due to the decomposition of the blowing agent, is lost and, therefore, is not available for the char formation. This depends in particular on the heating rate-independent mass loss behaviour of the binder and the observed temperature shift of the blowing agent. However, it cannot be excluded that due to heating rate-dependent changes in physical properties such as the viscosity of the liquid melt gases escape from the char structure also during the expansion. This amount of gas loss, of course, cannot be determined by coupled TG-DSC analyses. Therefore, other investigation methods are required.

3.3 Laboratory Expansion Tests and Morphology

3.3.1 Test Setup and Data Processing

The aim of the investigations was to evaluate the influence of different heating rates, maximum temperatures and cooling rates on the char formation behaviour of intumescent coatings. Beside the fact that the investigations themselves should provide a gain in knowledge, it was intended to use the experimental data subsequently for the development of a new material model. For this reason, the expansion tests were not performed on thick steel plates, as commonly described in literature, but on thin steel plates (0.70 mm) as recommended by Tabeling (2014), in order to minimise the influence of thermal inertia of the substrate. With the selection of such test samples it was assumed that the expansion behaviour of the coatings was dominated almost exclusively by the chosen heating conditions.
In previous investigations, the expansion behaviour of the solvent- and waterborne coating was analysed for selected heating rates (10, 30, 50 and 70 K/min) in a temperature range of 20 to 1000 °C. The results of these investigations were published accordingly for both coatings by Weisheim & Schaumann (2019). However, due to the test setup, the samples could not be removed non-destructively after the test. As a result, the samples could not be used subsequently for morphological examinations. Within the scope of the German research project IGF 19176 N (Zehfuß et al. 2018), therefore, a new experimental setup was developed. The main change to the previous setup was that the thermocouples that were used to measure the char temperature were no longer placed in front of the samples but through drilled hole (⌀ = 2.0 mm) in the samples. For this purpose, it was necessary to design a sample holder, through which the thermocouples were also arranged.

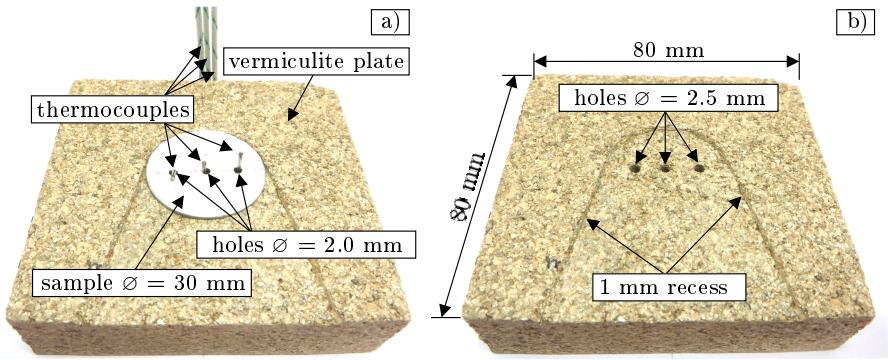

Figure 3.5: Sample holder made of a 25 mm thick vermiculite plate and thermocouple arrangement (type K at levels of 0, 3 and 6 mm) through a coated steel plate (thickness: 0.7 mm) for expansion analyses

Figure 3.5 shows the sample holder that was made from vermiculite. In addition to the drilled holes (⌀ = 2.5 mm), a 1 mm deep recess was made in the sample holder,

in order to ensure that the samples were held in their position and could be recorded from the front with an endoscope camera. The thermocouples had to be flexible, as they were bent below the sample holder by 90°. For this reason, high-temperature thermocouples of type K (wire thickness: 0.51 mm) with a glass fibre braid were used. In order to carry out the expansion analyses, the sample holder was placed together with the sample inside an electric furnace (Nabertherm LE 1/11). As the samples were arranged at the height of a peephole, an endoscope camera was placed in front of the electric furnace (see Figure 3.6). With the help of the camera, a continuous measurement of the char formation was ensured. However, as the camera was not fire-resistant, it was necessary to keep a certain distance (~ 30 mm) between the camera and the peephole and to cool the camera by a compressed air stream.

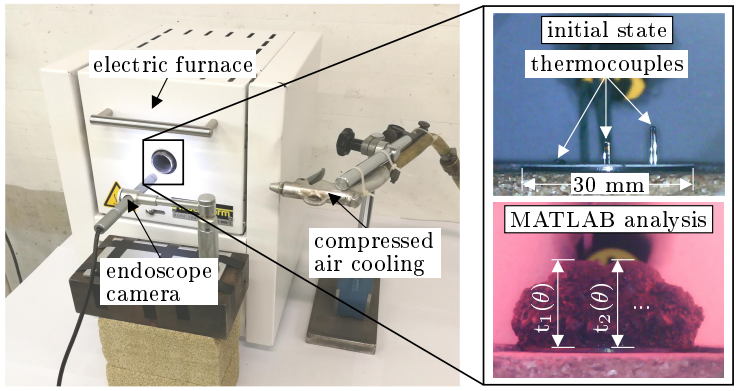

Figure 3.6: Test setup of the performed expansion analyses and illustration of the image-based char thickness measurement in MATLAB

While the samples were heated (by two heating elements at each side), a video (AVI format) was recorded with a frame rate of 5 frames per second. After the tests, the videos were read into MATLAB in order to extract individual frames. In the next step, the frames were used to measure the char thickness. For this purpose, a measuring tool was used that was developed by Neggers (2014). Since the measuring tool is based on a correlation between the real geometry size and the number of pixels, a calibration is required before the measurement. The sample diameter ($\varnothing = 30$ mm) was therefore used as reference. To make sure that the calibration was correct, the thickness of the steel plate (0.7 mm) was verified once before the measurement of the char thickness.
During the period in which the char was formed, the char thickness $t(\theta)$ was measured every 5 seconds (25 frames). As soon as the coating expanded entirely, only small changes in the char thickness were expected. Therefore, during this period the char thickness was measured only every 30 seconds (150 frames). Due to the arrangement of the thermocouples inside the expanded char (at levels of 0, 3 and 6 mm above the initial coating surface), for each measured thickness value, a tempera-

ture value was assigned. In this way, the expansion behaviour of a coating could be described not only as a function of time but especially as a function of the char temperature according to Equation 2.1. Of course, only the temperature data of the thermocouples were used to calculate the averaged char temperature, which were surrounded by the formed char at the considered point in time.

3.3.2 Sample Preparation and Parameters

In order to investigate the heating rate-dependent expansion behaviour of the coatings, circular samples with a diameter of 30 mm and a thickness of 0.7 mm were used. In contrast to Mesquita et al. (2009) and Zhang et al. (2012*b*), the thickness of the steel substrates was minimised to the lowest limit. In this way, the effect of thermal inertia of the steel plates was almost eliminated. To prepare the samples, blanks were first cut out of sheet metal (steel 1.0330 according to EN-10130 (2007)) using a nitrogen laser. After cleaning, the blanks were returned to the sheets from which they were cut out. In this way a uniform plane was formed, which was ideal for the application of the coating. However, in order to ensure a uniform coating thickness, the surface of the raw material was smoothed after the application. In total, the coating was kept for five weeks at ambient temperature and normal humidity in order to ensure complete drying. Subsequently, the circular samples were removed from the sheets. In some cases it was necessary to re-treat the edges of the samples as the coating was not always evenly detached from the sheets. In the last step, three holes with a diameter of 2.0 mm were drilled inside the samples with a distance of 8 mm to each other (see Figure 3.5 a)). Along an imaginary line, the second hole was always positioned in the centre of the sample.

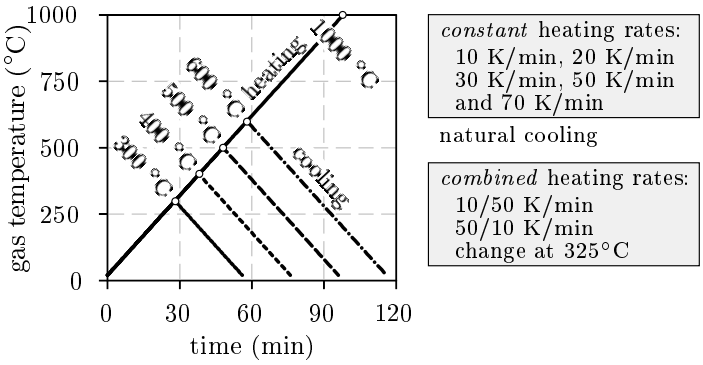

Figure 3.7: Schematic description of time-temperature curves defined for the expansion analyses at different maximum temperatures, different heating rates and natural cooling

Prior to the tests, the dry film thickness of the coating was measured for each sample at 12 points (see Figure 3.12 f)) using a digital thickness gauge (QNix 8500, Automation Dr. Nix). The mean values of the measured dry film thickness are

listed in Table 3.5. In order to evaluate the influence of different heating rates and temperature levels on the expansion behaviour of the samples, a systematic analysis had to be performed. For this reason, time-temperature curves with constant heating rates (10, 20, 30, 50, and 70 K/min) and different target temperatures (300, 400, 500 and 600 °C) were defined (see Figure 3.7). Once the desired target temperature was reached, a natural cooling phase was initiated by switching off the heating elements of the electric furnace. In this way, a broad spectrum of time-temperature curves was generated to cover the variety of natural fires.
In addition to the combination of heating and cooling, further tests were performed with pure heating (up to 1000 °C), in order to examine the high temperature behaviour of the samples and the influence of the heating sequence. For this purpose, the samples were either heated with a single constant heating rate or with two combined heating rates. In case of combined heating, the heating rate was changed as soon as the gas temperature reached 325 °C. In previous investigations (Weisheim & Schaumann 2019) it was found that the expansion of the coatings is normally triggered when this gas temperature (the sample temperature is lower) is reached. By changing the heating rate from 10 to 50 K/min and from 50 to 10 K/min it should be identified what effect a sudden change in heat input has on the char formation in its early phase. The definition of all systematic time-temperature curves with their constant and combined heating rates is described exemplarily in Figure 3.7.
In addition to the time-temperature curves described above, another four fire curves were used for the expansion analyses. In Figure 3.8 a comparison between the nominal curves and the gas temperatures realised by the electric furnace is shown. In addition to the standard fire curve and the smoulderung fire according to EN-13381-8 (2013), a natural fire curve was used, which was determined during the research project IGF 19176 N by the research partner from the Technical University Braunschweig for a small industrial building (500 m^2) with a fire load density of 300 MJ/m^2. In order to verify the hypothesis that the viscosity of the liquid melt has an influence on the loss of volatile gases and, therefore, on the intumescence process, the natural fire curve was modified by adding a smouldering phase (see Figure 3.8 d)). The temperature level of the smouldering phase (350 °C) was defined in a way that the decomposition of the blowing agent was triggered but not the formation of the char. At this point it is expressly pointed out that this modified fire curve was developed exclusively for the purpose of the experimental investigations and should by no means be used for approval tests.
In all cases, the nominal fire curves could be modeled with a good agreement by a multilinear control of the heating elements of the electric furnace. Only in the cooling phase, in which the heating elements were switched off, the furnace temperature deviates more from the natural fire curve.
For each examined time-temperature curve two tests were carried out. Therefore, for one test series 62 test samples had to be investigated. After each test, the thermocouples were carefully removed from the samples and the char morphology was investigated using a digital microscope (VHX-1000 from Keyence). Due to

the high effort it was decided to carry out the new expansion tests only for the waterborne coating. However, since results are available from previous investigations (Weisheim & Schaumann 2019) for both the solvent- and waterborne coating, sufficient data is available to verify the hypothesis that different coatings show different sensitivities to changes in heating conditions although they consist of the same main ingredients.

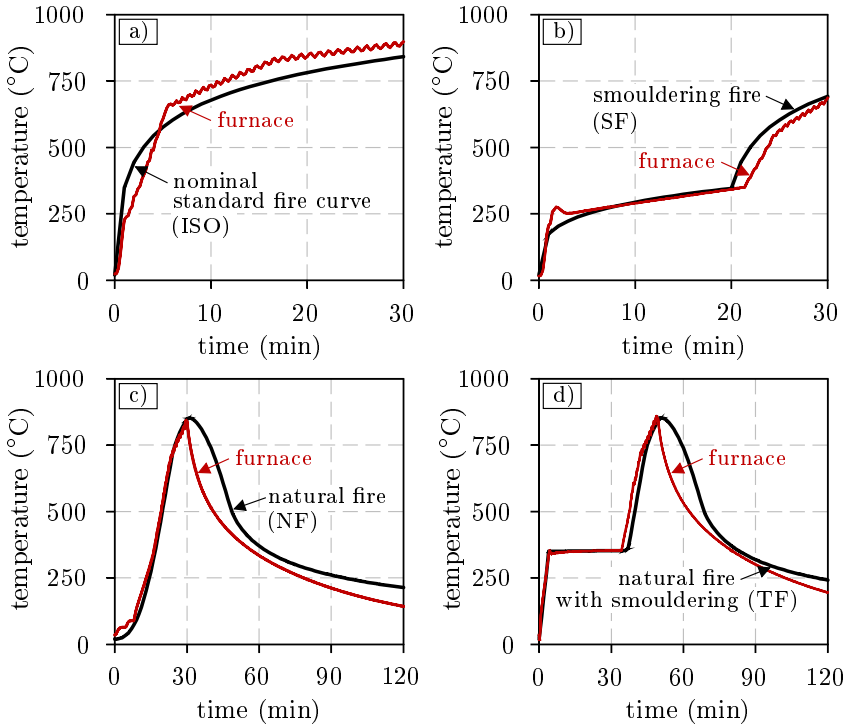

Figure 3.8: Comparison between the nominal fire curves and the fire curves realised with the electric furnace Nabertherm LE 1/11: a) standard fire curve, b) smouldering fire according to EN-13381-8 (2013), c) natural fire curve from the research project IGF 19176 N (Zehfuß et al. 2018) and d) combination of a smouldering and a natural fire (= travelling fire)

3.3.3 Results of the Expansion Tests

The results of the performed expansion tests are presented below as tabulated and graphical data. In Figure 3.9, 3.10 and 3.11 the expansion behaviour of the waterborne coating is described by the measured expansion factor ϵ in combination with the measured char temperature ($\epsilon = f(\theta)$). The change is char thickness, expressed by the expansion factor, is analysed for both the heating and the cooling phase. However, in the first step, the results of the expansion tests will be presented with the help of Table 3.5. For each sample, the dry film thickness (DFT) and the characteristic parameters for describing the expansion behaviour of the coating are

listed here. In order to identify the samples, a nomenclature is introduced consisting of the type of heating (*H*: constant heating, *ISO*: standard fire curve, *SF*: smouldering fire, *NF*: natural fire and *TF*: travelling fire), the heating rate (10, 20, 30, 50, 70 and a combination of 10/50 or 50/10), the target temperature (400, 500, 600 or 1000 °C) and the sample number (I or II). The characteristic parameters are given by $T_{initial}$, T_{max} and $T_{cool/res}$, which represent the temperatures at which the char formation is initiated, the maximum char thickness is reached and the char thickness remains unchanged during the cooling phase (index: cool) or after the pyrolysis of organic compounds at high temperatures (index: res). The corresponding expansion values are defined as ϵ_{max} and $\epsilon_{cool/res}$ as can be seen in the second and third last column of Table 3.5.

For all investigated heating rates, the temperature at which the char formation of the waterborne coating is initiated ($T_{initial}$ = 183 - 198 °C) is approximately the same. Only few samples deviate from this temperature range and show initiation temperatures of 175 °C in minimum and 204 °C in maximum. The temperature range at which the expansion maximum is reached (T_{max} = 320 - 370 °C) is also nearly the same. However, the maximum expansion factors differ clearly depending on the chosen heating rate. For example, the lowest expansion factors are observed for 10 K/min (28.83 - 32.87). As soon as the waterborne coating is exposed to higher heating rates, the expansion factors increase up to 48.74 (70 K/min). This corresponds especially for samples heated up to 1000 or at least 600 °C. If the samples are only heated up to 400 °C or less, lower expansion maxima are reached (12.31 and 20.10 at 50 K/min). This is due to the incomplete expansion reaction that occurs as soon as the heating elements of the electric furnace are switched off. This phenomenon is particularly pronounced for higher heating rates due to the thermal inertia of the samples. Note that samples that were heated up to 300 °C are not included in Table 3.5 because no char formation could be observed (only isolated bubbles were formed inside the coating). However, the samples will be used later to discuss the morphological characteristics of the coating.

In addition to the tabulated data, the expansion curves given in Figure 3.9, 3.10 and 3.11 also provide important insights into the heating rate-dependent expansion behaviour of the waterborne coating. Both the samples with constant heating rates and time-temperature curves (ISO, SF, NF and TF) show the typical expansion course. In the first period the expansion factor remains unchanged. As soon as the initiation temperature is reached, the char thickness increases rapidly. After the maximum expansion factor is reached, the char thickness decreases again. From literature (Tabeling 2014, Wang et al. 2015) it is known that the shrinkage of the char layer corresponds to the oxidation (pyrolysis) of the organic compounds inside the char. The extent to which a char layer shrinks depends on the heat exposure. In this thesis the char shrinkage ($\Delta\epsilon$) is calculated as the difference between the maximum (ϵ_{max}) and the minimum ($\epsilon_{cool/res}$) expansion factor. The results of the calculation are listed in Table 3.5.

Table 3.5: Char temperatures T_i and expansion factors ϵ_i at characteristic reaction states of the waterborne coating derived from expansion tests (initial: initiation of char formation, max: maximum char thickness, cool: final char thickness during the cooling phase, res: residual char thickness due to high temperatures and $\Delta\epsilon = \epsilon_{max} - \epsilon_{cool/res}$: change in char thickness due to shrinkage)

sample ID	DFT (μm)	$T_{initial}$ (°C)	T_{max} (°C)	$T_{cool/res}$ (°C)	ϵ_{max} (-)	$\epsilon_{cool/res}$ (-)	$\Delta\epsilon$ (-)
H10-400-I	345	198	333	156	32.04	27.09	4.95
H10-400-II	333	193	329	99	26.81	24.18	2.63
H10-500-I	328	196	337	314	33.40	29.49	3.91
H10-500-II	325	193	352	332	30.24	26.58	3.66
H10-600-I	341	192	342	245	29.62	21.84	7.78
H10-600-II	336	196	364	297	28.83	22.51	6.32
H10-1000-I	324	191	362	781	32.87	23.33	9.54
H10-1000-II	331	192	344	751	29.32	22.31	7.01
H20-400-I	322	196	311	201	39.35	34.48	4.87
H20-400-II	321	192	306	200	32.18	24.69	7.48
H20-500-I	318	202	375	429	67.53	63.38	4.15
H20-500-II	329	194	349	262	61.61	52.83	8.78
H20-600-I	313	189	335	297	69.50	53.97	15.53
H20-600-II	326	189	341	380	43.90	38.18	5.72
H20-1000-I	322	184	355	637	40.81	33.14	7.67
H20-1000-II	322	184	346	816	43.34	31.75	11.59
H30-400-I	323	198	284	106	19.94	15.35	4.58
H30-400-II	329	194	284	83	18.50	16.51	1.99
H30-500-I	315	188	360	192	42.41	40.67	1.74
H30-500-II	321	187	345	98	48.47	45.97	2.51
H30-600-I	363	180	358	286	38.38	34.55	3.83
H30-600-II	366	183	370	331	39.72	35.36	4.36
H30-1000-I	329	189	345	769	43.45	34.47	8.99
H30-1000-II	331	187	352	880	45.18	36.44	8.74
H50-400-I	360	175	263	145	12.31	8.84	3.47
H50-400-II	364	183	260	110	22.10	13.60	8.50
H50-500-I	332	185	311	150	43.70	39.42	4.28
H50-500-II	340	175	327	162	47.49	41.86	5.63
H50-600-I	332	184	355	327	38.92	35.17	3.75
H50-600-II	323	191	342	313	44.54	41.78	2.76
H50-1000-I	348	190	351	897	40.07	33.09	6.99
H50-1000-II	355	204	358	865	43.02	37.63	5.38
H70-400-I	318	192	245	147	8.87	6.62	2.24
H70-400-II	317	188	257	120	14.79	9.09	5.70
H70-500-I	330	203	295	177	41.57	37.40	4.17
H70-500-II	332	187	295	171	37.12	31.08	6.04
H70-600-I	333	180	320	-	43.02	-	-
H70-600-II	335	197	357	143	46.23	43.36	2.86
H70-1000-I	319	184	349	800	48.74	41.64	7.10
H70-1000-II	316	182	354	790	46.96	40.82	6.13
H10/50-325-I	302	196	358	880	48.36	40.33	8.03
H10/50-325-II	300	193	352	884	36.80	31.22	5.58
H50/10-325-I	379	192	370	632	45.15	31.20	13.94
H50/10-325-II	315	186	346	867	60.05	43.51	24.27

(*table continues*)

Table 3.5: Char temperatures T_i and expansion factors ϵ_i at characteristic reaction states of the waterborne coating derived from expansion tests (initial: initiation of char formation, max: maximum char thickness, cool: final char thickness during the cooling phase, res: residual char thickness due to high temperatures and $\Delta\epsilon = \epsilon_{max} - \epsilon_{cool/res}$: change in char thickness due to shrinkage) (continued)

sample ID	DFT (μm)	$T_{initial}$ (°C)	T_{max} (°C)	$T_{cool/res}$ (°C)	ϵ_{max} (-)	$\epsilon_{cool/res}$ (-)	$\Delta\epsilon$ (-)
ISO-I	325	183	364	811	47.41	38.45	8.96
ISO-II	330	180	349	839	44.56	36.40	8.16
SF-I	303	196	349	602	41.47	36.77	4.70
SF-II	304	196	355	639	34.39	28.46	5.92
NF-I	301	198	331	528	47.36	39.82	7.54
NF-II	307	188	350	569	43.52	37.10	6.42
TF-I	294	192	326	489	36.01	28.78	7.23
TF-II	284	175	349	581	52.84	44.02	8.82

A closer look at the different expansion curves reveals that for higher heating rates (50 and 70 K/min) the char layer is formed almost immediately after reaching the initiation temperature. The expansion curves show a direct transition from the initial state ($\epsilon = 1.0$) to the phase of char formation ($\epsilon > 1.0$). However, when the samples are exposed to lower heating rates (30, 20 or 10 K/min), a plateau within the transition area is formed. This plateau is characterised by an expansion factor of $\epsilon \approx 4.0$ that remains nearly constant for a certain time. Only then the coating thickness increases disproportionately. Observations of the video recordings (use AR^+) show that during this phase bubbles are formed in the liquid melt over several minutes, which burst again. Due to the bursting, volatile gases that are formed during the decomposition of the blowing agent escape from the liquid melt and are later no longer available for the formation of the char. For this reason a smaller char layer is formed. This observation correlates with the results of the coupled TG-DSC analyses (see subsection 3.2.4). For low heating rates a greater gas loss was identified than for higher heating rates. However, looking at these results, the question still arises why the excessive gas loss and the plateau in the expansion curves only occur at low heating rates? And even more, can the phenomenon of bubble bursting be explained physically?

In literature the bursting of bubbles is already addressed by Butler et al. (1997). According to the research group, the bursting is caused if the molten binder is not viscous enough. Due to the low viscosity, the surface tension of the bubbles is too low to withstand the internal inflation pressure that is caused by the release of volatile gases. Therefore, the bubble bursts and the gas is released instead of being trapped. Butler et al. describe that such behaviour can occur if the sequence and timing of chemical reactions are not coordinated. Following this idea means that the heating rate-dependent expansion behaviour of the coating is not due to the low binder viscosity itself but due to the release of volatile gases during the reaction state in which the binder viscosity is too low to trap the decomposition products of the blowing agent. At higher heating rates, the decomposition of the blowing agent

(MEL) and, therefore, the release of volatile gases shifts to higher temperatures (see Figure 2.22 a)). The polymer binder, on the other hand, is less sensitive to changes in heating rates and decomposes at nearly the same temperature regardless of the heating conditions. Therefore, if the blowing agent decomposes and releases its gases at higher temperatures due to the heating rate-dependent temperature shift, the polymer binder is already in a more advanced reaction state.

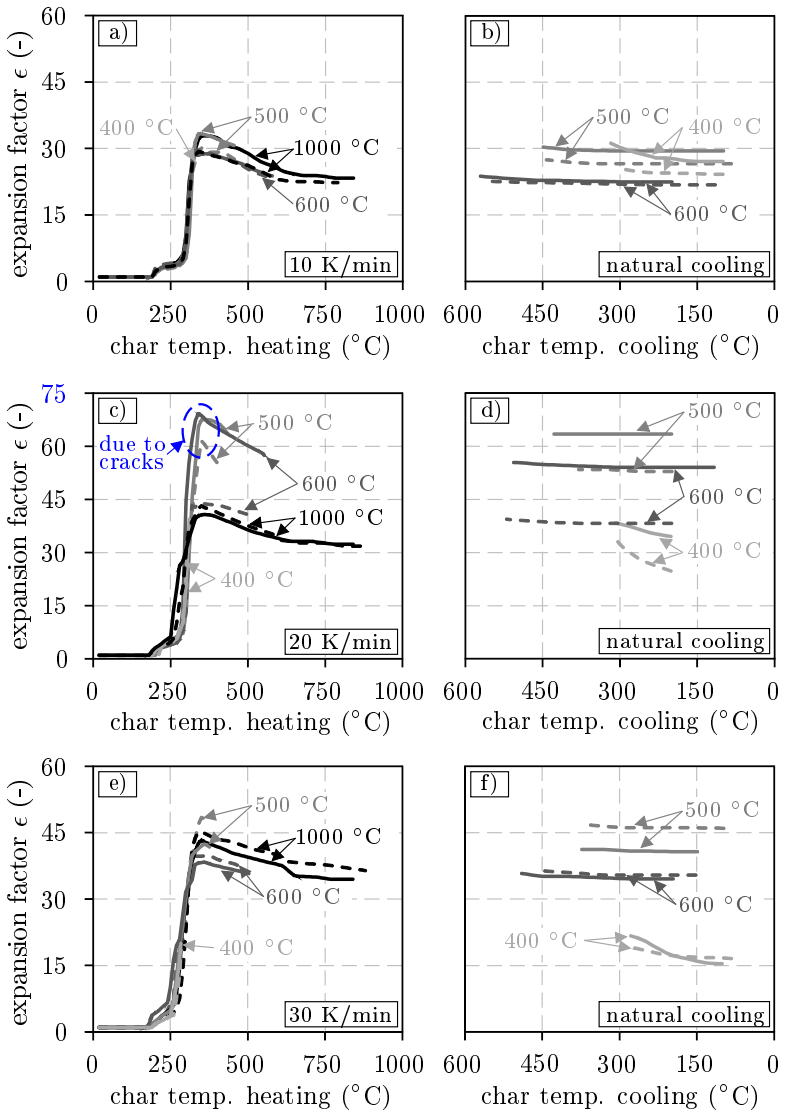

Figure 3.9: Measured expansion factors of the waterborne coating as a function of char temperature in heating and cooling at different maximum temperatures (400, 500, 600 and 1000°C) and constant heating rates of a) 10 K/min, c) 20 K/min and e) 30 K/min

According to the rheological investigations of Bugajny et al. (1999) and Jimenez

et al. (2006*a*) (see Figure 2.14), this reaction state is characterised by a higher viscosity. Due to the increase in binder viscosity, less bubbles burst and more volatile gases are trapped. This is the reason why for heating rates of 50 and 70 K/min higher char thicknesses are formed and no plateaus in the expansion curves are observed.

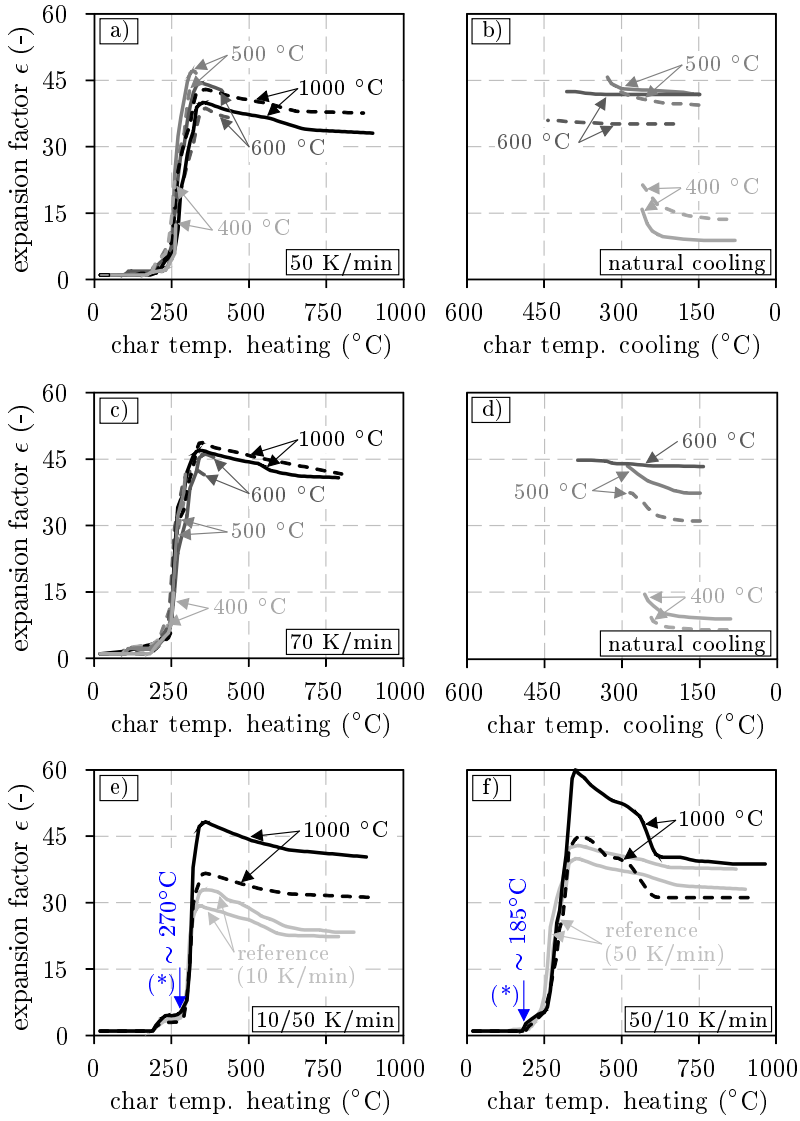

Figure 3.10: Measured expansion factors of the waterborne coating as a function of char temperature in heating and cooling for constant and combined heating rates: a) 50 K/min, c) 70 K/min, e) change from 10 to 50 K/min at 325° C and f) change from 50 to 10 K/min at 325° C. The char temperature at which the heating rate changes is marked with (*)

The samples heated with lower heating rates, on the other hand, suffer from a premature gas loss and a fragile char. As long as the char is not completely carbonised and the polymer binder is still viscous, the char structure and its single bubbles are dominated by the inflation pressure.

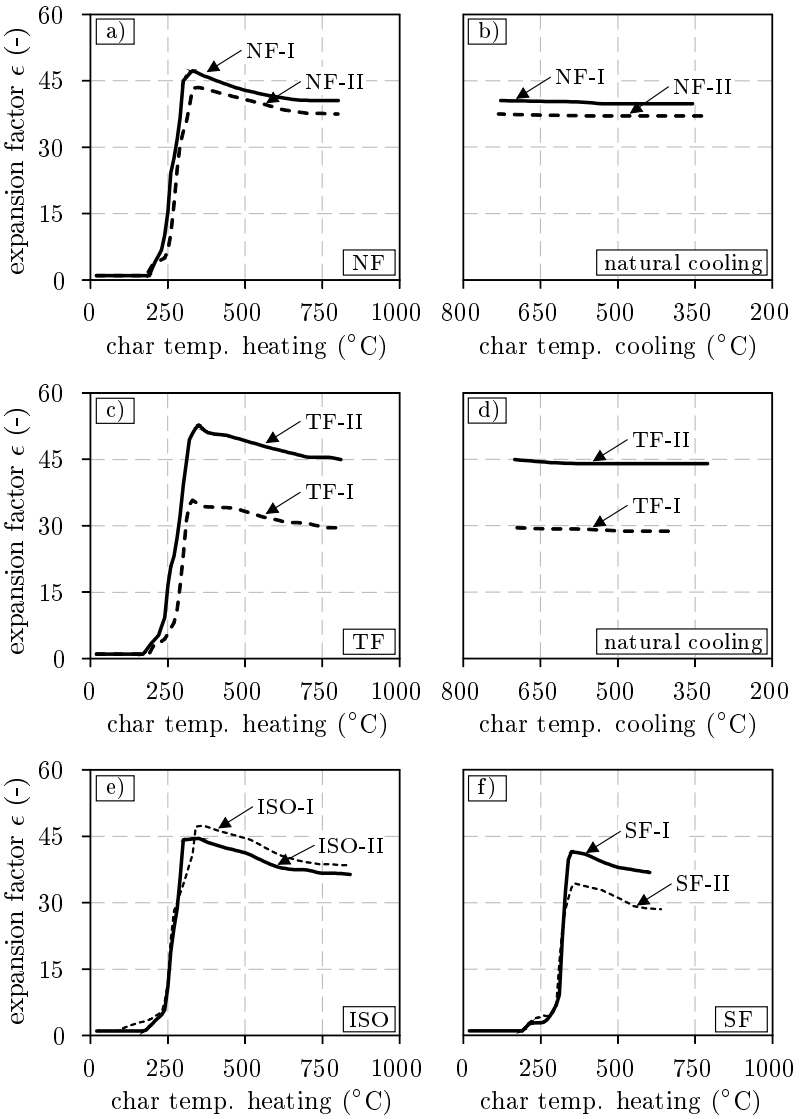

Figure 3.11: Measured expansion factors of the waterborne coating as a function of char temperature for different time-temperature curves: a) natural fire (NF) accord. to the research project IGF 19176 N (Zehfuß et al. 2018), c) generic travelling fire (TF), e) standard fire (ISO) accord. to (ISO-834-1 2010) and f) smouldering fire (SF) accord. to EN-13381-8 (2013)

Therefore, when the inflation pressure decreases due to the removal of thermal energy, the bubbles collapse. Phenomenologically, this can be observed (see Figure 3.9 and 3.10) by the sudden decrease in char thickness for samples heated up to 400 °C (all samples) and 500 °C (only for 50 and 70 K/min) during the cooling phase. Note that this behaviour should not be confused with shrinkage, where the char thickness collapses due to the combustion of organic compounds and the char structure turns white. In contrast to this, during the char thickness reduction caused by the loss of inflation pressure, the char structure remains intact and grey in colour. Only the gas escapes until the inflation pressure adjusts to atmospheric pressure. Samples heated up to 600 °C do not show this behaviour. For this reason, almost no changes in char thickness can be observed during the cooling phase. This is due to the full carbonisation of the samples. Since the char structure solidifies, it can no longer be influenced by a drop in inflation pressure. When dealing with natural fires and their cooling phases, this is an important finding for the understanding of intumescent coatings.

Besides constant heating rates with and without natural cooling, the waterborne coating was also examined under combined heating. For this purpose the heating rates 10 and 50 K/min were combined. The results of these tests are given in Figure 3.10 e) and f). For reference, the results of the constant heating rates are also shown in the diagrams (grey colour). In order to identify a correlation between the expansion curves and the state at which the heating rate changes from slow to fast or from fast to slow, the respective char temperatures are marked in the diagrams with (*). For the test samples H10/50, the char temperature is $\sim$ 270 °C when the change in heating rate occurs. Since the sample is first heated with 10 K/min, the plateau of constant char thickness is completely formed. Until the maximum expansion factor of the reference (29.32 and 32.87) is reached, the expansion curves are almost identical. However, due to the faster heating, the H10/50 samples show higher expansion values (36.80 and 48.36) in the further course. Due to the higher heating rate and the associated thermal inertia, the samples do not heat up as much as the reference. For this reason the char structure shrinks less. This can be observed on the basis of the shrinkage values ($\Delta\epsilon$) in Table 3.5 (H10/50: 5.58 and 8.03; H10-1000: 7.01 and 9.54) or the course of the expansion curves in Figure 3.10 e).

Due to the effect of thermal inertia caused by the higher heating rate, the H50/10 samples are only heated up to $\sim$ 185 °C when the rise in gas temperature changes from 50 to 10 K/min. At this reaction state only a few bubbles are formed. However, the coating seems to have been so strongly influenced by the higher heating rate that no significant stagnation in char formation occurs, although the char is subsequently heated with 10 K/min. Due to the previous heating with 50 K/min, the binder seems to be viscous enough to trap more gases in the subsequent reactions than if heated at 10 K/min alone. For this reason even higher expansion values (45.15 and 60.05) are reached than for the H50-1000 samples (40.07 and 43.02). At lower heating rates the samples are heated more homogeneously. This has a positive effect on the char formation in case of the H50/10 samples as higher

expansion factors are formed. However, the different expansion maxima observed for the two samples indicate that the char formation is very susceptible to scatter. But this does not apply to shrinkage. As shown in Figure 3.10 f), the two expansion curves run parallel after the maximum expansion factors are reached. Due to the high char thicknesses and the strong heating, the H50/10 samples shrink most ($\Delta\epsilon$ = 13.94 and 24.27). However, at temperatures higher than 630 °C almost no reduction in char thickness is discernible.

In the investigations presented so far, the samples were heated either with one constant heating rate or a combination of two. In the following, test results are presented in which the samples were exposed to different fire curves. These results are documented in Figure 3.11. The diagrams a) and b) show the expansion curves for the heating and cooling phase of the natural fire curve. For both test samples (NF-I and NF-II) the expansion is initiated at char temperatures between 188 and 198 °C. Due to the rapid increase in char thickness, maximum expansion factors of 43.52 and 47.36 are reached (T_{max} = 350 and 331 °C). These values are comparable with the H30-100 samples (see Table 3.5). However, this is not surprising since the average heating rate of the natural fire curve is about 26.9 K/min. Since the samples are heated up to 750 °C and higher, no significant changes in char thickness are observed during the cooling phase. This applies also to the results of the travelling fire (see diagrams c) and d)). However, in contrast to the natural fire, the samples TF-I and TF-II show a much greater scatter in the expansion behaviour (ϵ_{max} = 36.01 and 52.84). Contrary to expectations, it can be observed that no distinct stagnation of the char thickness occurs at the beginning of the expansion ($T_{initial}$ = 175 and 192 °C). Due to the extension of the natural fire curve by the smouldering phase, it was assumed that a distinct plateau would be formed in the expansion curves, similar to the H10 samples. However, this is not the case. The reasons for this seem to be the high heating rate (~ 77.6 K/min) and temperature (~ 350 °C) at the beginning of the smouldering phase (see Figure 3.8 d)). Although later a smouldering plateau is formed that is characterised by an extreme low heating rate of 0.1 K/min, the char formation seems to be more affected by the fast preheating in the first 4.5 minutes. Although no pronounced stagnation in the expansion curves can be observed, the different expansion behaviour and the formed char structure (see subsection 3.3.4) are clearly due to the smouldering phase.

In contrast to the generically developed travelling fire, the fire curve according to EN-13381-8 (2013) proves that a smouldering fire does not only affect the char structure but also the course of expansion. While the samples heated with the standard fire curve (see Figure 3.11 e)) reach expansion maxima of 44.56 and 47.41, the smouldering fire reduces the expansion factors of its samples to 34.39 and 41.47. Moreover, due to the lower preheating temperature (~ 250 °C), a pronounced stagnation in expansion is formed during the subsequent smouldering phase (5.3 K/min), which is comparable to the H10 samples (see Figure 3.11 f)). On the other hand, when the samples are exposed solely to the standard fire curve without any smouldering phase, the samples expand directly as soon as the initial

temperature (180 and 183 °C) is reached. This expansion behaviour is comparable in shape and value to the samples heated with 70 K/min. However, this is not surprising, since in both cases the samples are exposed to high heating rates. While the H70-1000 samples are heated constantly with 70 K/min, the samples ISO-I and ISO-II are heated between the first and the sixth minute with nearly 95 K/min (compare the red curve in Figure 3.8 a)). Only with the further course of the standard fire curve, the gas temperature flattens noticeably resulting in a high temperature level. This temperature level is the reason why the samples shrink under the influence of the standard fire curve more ($\Delta\epsilon = 8.16$ and 8.96) than the samples heated constantly with 70 K/min ($\Delta\epsilon = 6.13$ and 7.10).

To finally conclude, the results of the performed expansion tests confirm the findings given in the literature (Mesquita et al. (2009), Tabeling (2014), Wang et al. (2015), Lucherini et al. (2019) etc.) that intumescent coatings show a heating rate-dependent behaviour. Even more, the expansion tests helped to identify the reason for the heating rate dependency of the investigated waterborne coating.
All in all, the following findings could be made: (1) The initiation and the maximum temperature at which the char is formed and its maximum is reached are for all investigated heating rates (10, 20, 30, 50 and 70 K/min) nearly the same. However, the main differences in the expansion behaviour are characterised by the expansion values. The lowest expansion factors are reached for the lowest heating rates. As soon as the heating rates are increased, higher char thicknesses are formed. (2) Another characteristic of low heating rates is that the char structure is not formed immediately, but initially stagnates in the formation phase. With the help of the video recordings it could be identified that during this reaction state the bubbles formed within the liquid melt burst and release volatile gases. (3) Based on the coupled TG-DSC analyses carried out previously, the hypothesis has already been made that the coatings lose significantly more gases at low heating rates before they expand. This observation can now also be visually confirmed. (4) With the help of the evaluated TG data from literature, an explanation could also be given why this behaviour only occurs at low heating rates. The single ingredients, especially the blowing agent (MEL) and the polymer binder, show different sensitivities to changes in heating rates. While the decomposition temperature of the blowing agent shifts to higher temperature when the heating rate is increased, the temperature at which the polymer binder starts to decompose remains nearly unchanged. On the other hand, after melting, the binder must build up sufficient viscosity to trap the released gases. However, this time is missing at low heating rates because the blowing agent decomposes and releases volatile gases at lower temperatures due to its heating rate dependency. The acid source (APP) and the carbon donor (PER), which are responsible for the solidification of the char structure, also influence the gas release through their heating rate-dependent behaviour (see Figure 2.22). (5) Further investigations with combined heating rates show additionally that the order in which the samples are heated also plays an important role for the char formation. Depending on the sequence (for example, first fast,

then slow heating), high expansion values and a pronounced shrinkage behaviour are observed. (6) On the other hand, if the coating is exposed to a smouldering fire (EN-13381-8 2013), the char formation is noticeably reduced. However, the extent to which the smouldering phase influences the expansion behaviour depends on the heating rate and the maximum gas temperature.
The expansion tests carried out show how differentiated the waterborne coatings reacts to the different time-temperature curves. However, at the same time, it is noticeable that within the most thermal effects the expansion behaviour scatters to a very small extent. Only for a few samples (see especially 20 K/min in Figure 3.9) the expansion curves scatter very strongly. However, this is due to the tearing of the samples as the morphological investigations will show in the following. Since the scattering of the expansion curves is caused by the material behaviour itself and not by the test setup, it can be stated that the new test setup is very suitable to carry out reproducible expansion tests. However, due to its susceptibility to cracking, it is of great importance to examine the char structure formed in the expansion tests. For this reason, the morphology of the waterborne coating is examined and evaluated below in terms of the quality and integrity of its surface and char structure.

3.3.4 Results of the Morphology Investigations

Within the scope of the expansion analysis, a total of 62 tests were carried out. Due to this large amount, not every sample can be used for morphological examinations. For this reason, only selected samples are used below in order to evaluate the influence of different heating rates and time-temperature curves on the formation of the char structure. In Figure 3.12 a) - e) the residual chars for 600 °C are shown for different heating rates. The points at which the dry film thickness of each sample was measured before the expansion tests are shown in Figure 3.12 f).
As can be seen from the pictures, the residual chars of the samples H70, H50 and H30 are all coloured dark grey or almost black. The surfaces are irregular and formed by individual large bubbles. However, differences in the foam structures do not seem to arise for these three heating rates. This confirms the expansion behaviour observed so far, as the heating rates of 70, 50 and 30 K/min showed nearly the same expansion curves. The samples H20 and H10, on the other hand, show a completely different char formation behaviour. While the char structure heated with 20 K/min show a large crack, the residue of the H10 sample shows a highly irregular and fissured char structure. Due to its irregularity, the char structure formed at 10 K/min could not even cover the thermocouple, positioned at 6 mm. For this reason, the thermocouple was completely unprotected during the entire fire exposure. The same applies also to the underlying substrate.
The white colouring on the top of the char structure (see Figure 3.12 d) and e)) is due to oxidation. This means that due to the slow heating, higher temperatures occurred over a longer period of time, which initiated the combustion of organic

compounds. However, the high temperatures are not responsible for the fissured and cracked char structure. This is due to the low heating rates and the resulting physical properties of the binder. To be more precise, it is assumed that the char morphology is influenced by the viscosity of the liquid melt.

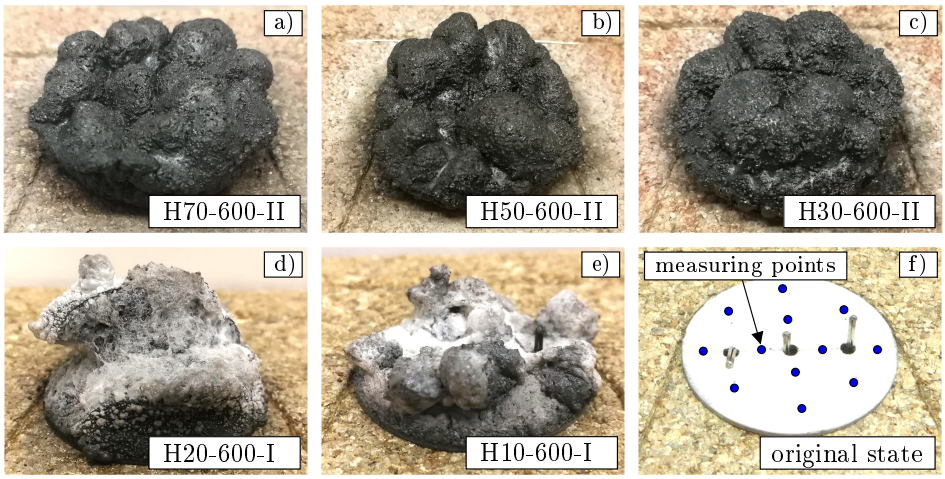

Figure 3.12: Char formation of the waterborne coating after 600 °C at constant heating rates of a) 70 K/min, b) 50 K/min, c) 30 K/min, d) 20 K/min, and e) 10 K/min. Definition of the measuring points of the dry film thickness according to f) the original state of the samples

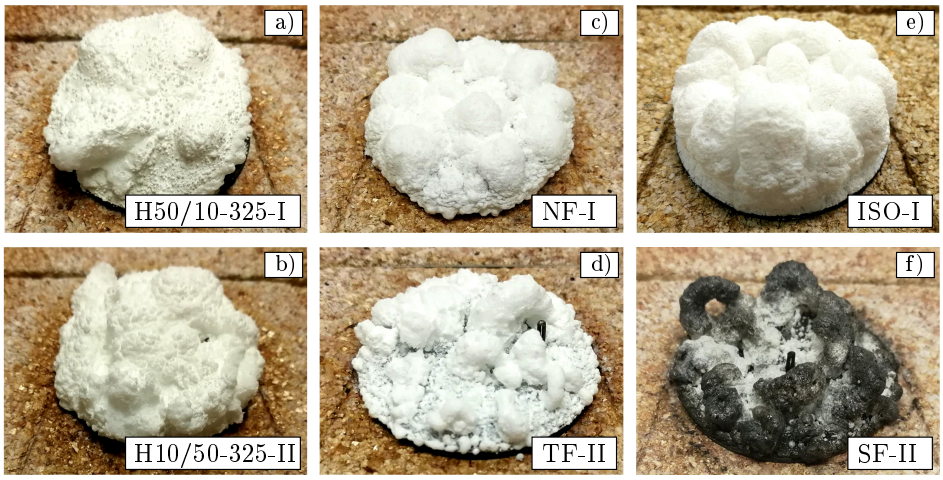

Figure 3.13: Char formation of the waterborne coating due to different time-temperature curves: a) and b) combination of 10 and 50 K/min or 50 and 10 K/min, c) natural fire, d) travelling fire, e) standard fire and f) smouldering fire

Similar observations are also made for the samples H10/50-II, TF-II (travelling fire)

and SF-II (smouldering fire according to EN 13381-8) in Figure 3.13 b), d) and f). What they all have in common is that the samples are heated at low heating rates or a smouldering phase at the very beginning. This reduced heating leads in all three cases to the formation of a strongly fissured char with reduced expansion factors. However, without the reduced heating rates (see the samples H50/10-I, NF-I or ISO-I) a completely different char morphology is formed. Except for a few bubbles, high integrity surfaces are formed as soon as the samples are not exposed to reduced heating or smouldering. Nevertheless, certain differences can also be seen here. During the natural fire (NF-I) and the standard fire (ISO-I) large bubbles are formed on the surface. In case of the H50/10-I sample, on the other hand, the bubbles seem to be very small. However, with regard to the formation of a barrier for the thermal protection of steel members all three char structures are suitable. This does not apply to the samples exposed to the travelling and the smouldering fire at all (see Figure 3.13 d) and f)). Due to the combination of both reduced expansion factors and especially the irregular char morphology, the chars do not provide a sufficient fire protection that is required to prevent steel members from fast heating.

In order to better understand how the differences in the char structures are caused, the samples heated with constant heating rates were additionally examined under the microscope (Keyence, VHX-1000). The corresponding images of the char surfaces are shown in Figure 3.14. In order to evaluate the char morphology for the entire expansion process, three different reaction stages (melting, charring and oxidation) were examined. Please note that for melting two different temperatures (300 and 400 °C) had to be used, in order to examine also the high heating rates. Therefore, the samples H10-H30 and H50-H70 are only comparable to a limited extent.

For 10 and 20 K/min (see images a) and d)) the melting of the coating is characterised by the formation of bubbles (recognisable by the elevation of the surface) and many yellowish beads that are only a few micrometres in size. It is obvious that the beads represent the molten binder. But the question arises how the binder can melt and form such beads on the surface? The image g) helps to answer this question. As can be seen from the sample H30, numerous holes are formed within the coating surface. This seems to happen before the binder melts. As soon as the melting temperature of the binder is reached and sufficient internal pressure is accumulated by the release of volatile gases, the liquid binder is pressed out through the holes. This creates the typical bead shape on the coating surface. According to this, a particularly large number of holes must have been formed in the samples H10 and H20. However, the holes are not visible, as they are covered by the beads that are formed by the molten binder. At 50 and 70 K/min (see images j) and m)) the beads are no longer visible. Since the samples are already in an advanced reaction stage due to the higher temperature (400 °C), the binder has already melted and has formed a brown film on the coating surface. Despite the entire melting of the binder, holes are still formed within the liquid melt. However, the number is significantly lower than for low heating rates.

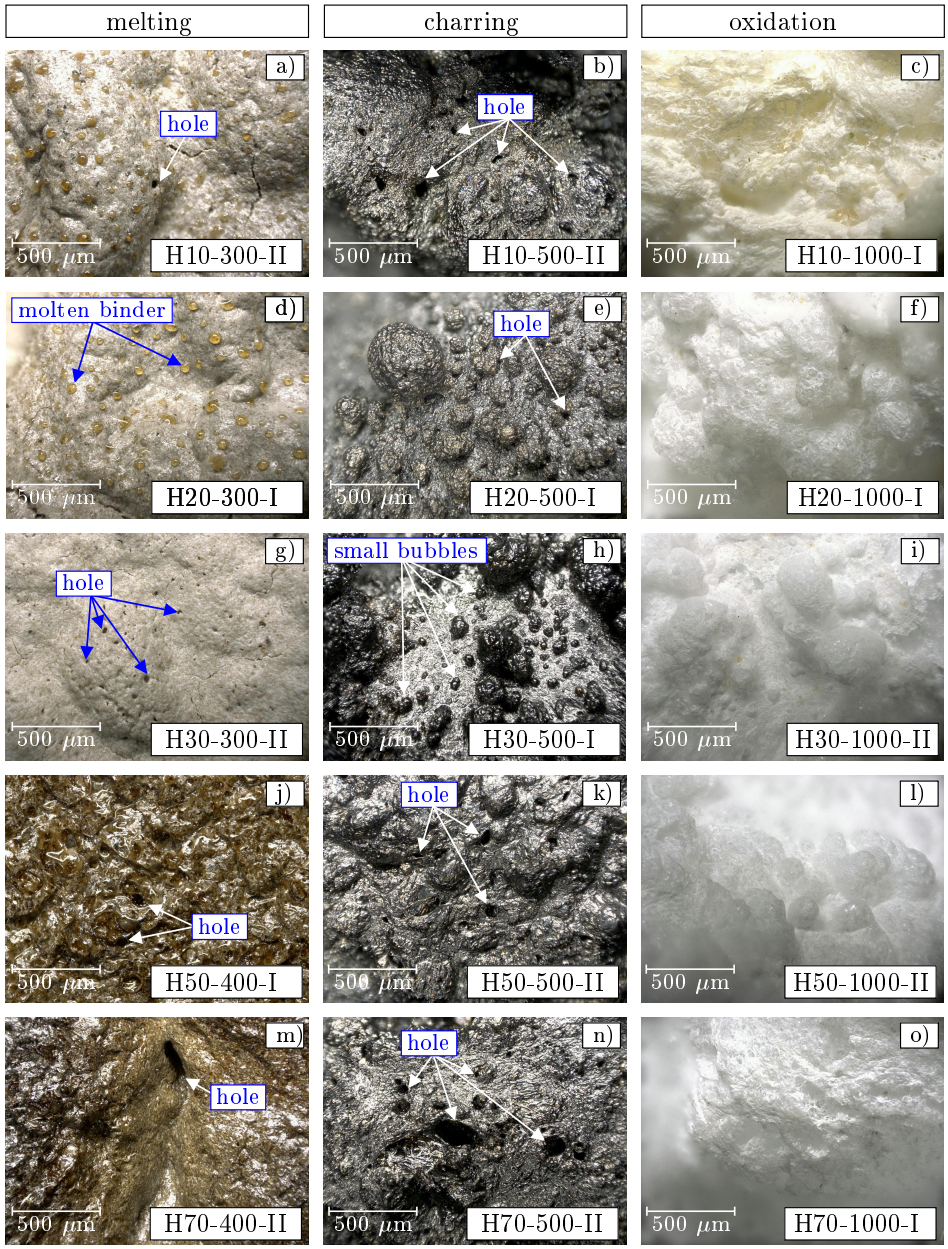

Figure 3.14: Digital microscope images of the char surfaces formed due to different heating rates (10, 20, 30, 50 and 70 K/min) and target temperatures (300, 400, 500 and 1000° C) at hundred times (100x) magnification

The microscope images of the carbonised coating (see middle column in Figure 3.14) prove that the holes formed inside the liquid melt also remain in the carbonised surface. This means that the holes formed at the very beginning of the melting

phase do not only have an influence on the release of volatile gases at the beginning of the expansion process, but also on all subsequent processes. The basis for an effective thermal protection is thus already formed during the melting phase. However, although the highest expansion values were measured for the samples H70, H50 and H30, holes inside the char surface can also be found here. In isolated places, especially for 70 K/min, large holes are formed inside the char. In contrast to this, for the lower heating rates (H10 and H20), the size of the holes seems to be smaller. The number of the holes, however, is much higher. The samples also differ in terms of microscopic surface structure. Although H10 is very fissured at the macroscopic level, the surface of the samples appears to be even at the microscopic level. The same applies also to the samples H50 and H70. H20 and H30, on the other hand, are characterised by different sized bubbles that are formed on top of the surface. Especially for H30 the combination of a partially smooth surface with small bubbles and the absence of holes is very conspicuous.
Due to the white colour, the pore structure is less visible in the phase of oxidation (see the last column in Figure 3.14). Nevertheless, a significant difference can be seen compared to the previous reaction phase. As the organic compounds burn due to the effect of high temperatures, an open-cell foam structure is formed that changes its colour from dark grey to white. The open-cell foam structure results in two aspects: (1) As the single cells are no longer closed, the thermal protection decreases. This is due to the loss of the trapped gases that are needed to form a thermal barrier in order to prevent the direct transmission of thermal radiation and convection. (2) Due to the combustion of the cell walls, only the cell struts remain, which have to support the entire foam structure. As a result, the foam structure is partially weakened to such an extent that it collapses. On the macroscopic level, this process is perceived as shrinkage.
The microscope images of the burnt foam structure reveal that especially for low heating rates (H10 and H20) a highly open-cell foam structure is formed. For the highest heating rate (H70), on the other hand, only few pores have lost their cell walls. The same applies also to the heating rates of 30 and 50 K/min, whereby many areas are found where the pore structure is almost intact (see images i) and l)).

3.3.5 Discussion

When evaluating the results of the expansion and morphological investigations, several aspects become striking. Some samples have a uniform, almost smooth surface. Other samples crack or have a completely fissured surface that cannot guarantee effective thermal protection. The following correlation also has to be considered. The samples with the smooth surface expand much more. The samples with the fissured surface expand considerably less. However, an exception are the samples heated with 20 K/min. Here the samples tear apart and increase the char thickness. However, an effective thermal protection cannot be guaranteed due to the apparent increase in char thickness, because the samples usually tear apart

horizontally. As a consequence, the heat can penetrate through the halved char structure from the side into the substrate. Thus the type of char formation (completely intact vs. fissured) is directly related to the expansion factors of the char structure. But which explanation can be found for this? And how is this behaviour related to the different heating rates?
The successive decrease in char thickness and the susceptibility of the foam structure to rupture is striking. As the heating rate decreases, the char seems to be more susceptible to cracking. For example, at 70, 50 and 30 K/min the char structure is completely intact. At 20 K/min, the foam cracks, although parts of the foam structure are still connected. At 10 K/min, on the other hand, there is no coherent char formation at all. A possible reason for this behaviour could be the interaction between the release of volatile gases by the blowing agent and the physical properties of the polymer binder during the melting phase. From the observations, it is assumed that at lower heating rates the blowing agent decomposes at lower temperatures. Due to this temperature shift towards lower temperatures, the polymer binder has to withstand the internal pressure caused by the release of volatile gases although the binder is still very liquid. For this reason, bubbles that are formed inside the liquid polymer binder burst and the volatile gases escape. When most of the gases escape, the char does not expand so much. Furthermore, due to the cracking and bursting, an inhomogeneous and fissured char structure is formed. This leads to two negative effects: (1) Formation of reduced char thicknesses and (2) formation of a heterogeneous and fissured char structure with reduced thermal protection. Therefore, it is not sufficient to examine only the expansion behaviour. The morphology of the formed char structure has to be examined as well. The pore size, for example, is a very important parameter that is later required for the numerical simulations. However, the fissured char structure is difficult to represent numerically. Here engineering assumptions have to be made.
When evaluating the fire protection performance of intumescent coatings at the European level, smouldering fire tests according to EN-13381-8 (2013) are recommended. These tests are performed by the manufacturers voluntarily in order to identify the sensitivity of their products to reduced heating due to smouldering. However, the tests are not mandatory and, therefore, rarely performed. As the results of the expansion and morphology tests show, smouldering has a significant effect on the expansion behaviour, the char formation and, therefore, on the fire protection performance. This applies for both smouldering in combination with the standard fire and the natural fire used during the national research project IGF 19176 N (Zehfuß et al. 2018). As the investigated product showed a high sensitivity to smouldering, it should be discussed whether the smouldering tests should be given more attention. This discussion should be held at least for products that will be used in the future for natural fires with moderate heat release rates. As soon as full developed fires are expected, standard fire tests that are nowadays prescribed within the approval tests are sufficient to characterise the fire protection performance of intumescent coatings.

3.4 Small-scale Fire Tests

3.4.1 Test Specimens and Sample Holder

Fire tests on coated steel plates have proven to be an established and suitable method for investigating the fire protection performance of intumescent coatings. By choosing different steel plate thicknesses, the section factor (A/V) can be varied in order to quantify the influence of the thermal inertia of the steel substrate on the fire protection performance. Currently, the state of the art shows a trend towards even smaller steel plates. In the national and European approval tests, for example, samples with dimensions of 500 x 500 x 5 mm and 300 x 200 x 5 mm are used, respectively. In research studies, smaller samples (100 x 100 x 5 mm) are usually preferred. However, all approaches have in common that only the temperature measured on the backside of the steel plates is used to assess the fire protection performance of the coatings. This also includes the assessment based on the *effective thermal conductivity* according to Equation 2.3 as it is derived from the measured substrate temperature. The development of the temperature gradient inside the expanded char, however, is also important for the evaluation of the insulating behaviour of intumescent coatings. For this reason, a new test setup was developed in which both, the steel substrate and the char temperature, are measured. Similar approaches are described by Norgaard (2014), Tabeling (2014) and the Federal Institute for Materials Research and Testing (Krüger et al. 2016). However, the test setups differ from the setup presented in this work in the arrangement and the type of thermocouples, the size of the specimens and the fire exposure since all fire tests of the research studies mentioned above were performed under the standard fire curve.

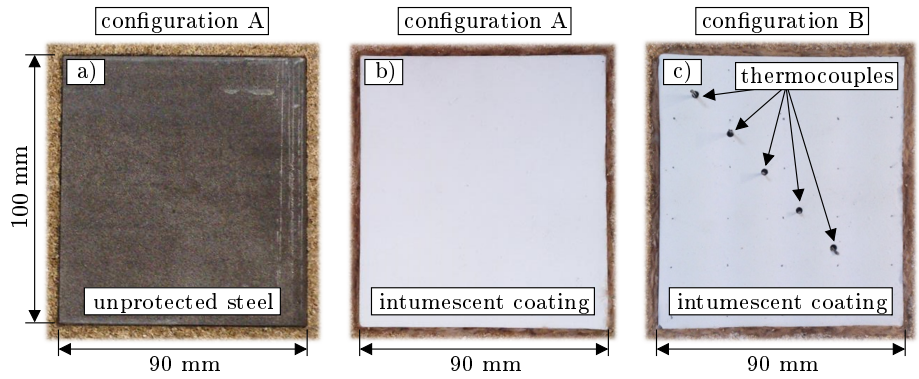

Figure 3.15: Test specimens (100 x 90 x 5 mm) used for the small-scale fire tests: a) unprotected steel plate, b) coated steel plate and c) coated steel plate with drilled holes (⌀ = 2.0 mm) equipped with thermocouples on the backside (configuration A) and levels of 0, 3, 6, 9 and 12 mm (configuration B) to measure the char temperature

In order to carry out the experimental programme, the electric furnace Nabertherm LE 1/11 was used. Since the dimensions of the furnace opening are 110 x 100 mm, the size of the test specimens (carbon steel S235JR) had to be limited to 100 x 90 mm. In this way, an unhindered expansion of the coatings could be ensured at the edges. In order to measure the temperature profile inside the expanded char, thermocouples of type K (wire thickness: 0.51 mm) were arranged at different levels (0, 3, 6, 9 and 12 mm) above the coating surface. To hinder the char formation as little as possible, it was necessary to arrange the thermocouples through the steel plates from below. For this reason circular holes with a diameter of $\varnothing = 2.0$ mm were drilled inside the samples as can be seen in Figure 3.15 c). Due to the arrangement of the thermocouples, the char temperature was measured as soon as the coatings started to expand. However, before the char formation, the coating temperature was measured by only one thermocouple (0 mm) as it was arranged directly on the surface.

Both the drilled holes inside the steel plates and the thermocouples inside the char represent disturbances for the temperature field. In order to evaluate their influence, additional fire tests were performed on coated and completely untreated steel plates (see Figure 3.15 b)). The temperature measured on the backside of these steel plates served as a reference. At the same time, the steel temperature was used to assess the fire protection performance of the coatings. This can be done, among others, by comparing the temperature of protected and unprotected test specimens. Therefore, unprotected steel plates (see Figure 3.15 a)) were also examined during the experimental programme.

In order to investigate the influence of thermal inertia on the heating rate-dependent fire protection performance, the experimental programme was based on two different steel plate thicknesses, 3 and 5 mm. The dry film thickness of the coatings, on the other hand, was chosen to fulfill a fire resistance time of 30 minutes for a section factor of 200 m^{-1}. Therefore, target thicknesses of 400 and 740 μm were defined for the solvent- and the waterborne coating, respectively. In the case of the waterborne coating, additionally a dry film thickness of 1150 μm was investigated for both 3 and 5 mm thick steel plates. Before applying the coating, the steel plates were drilled, deburred and cleaned. Subsequently, the coatings were applied directly on the steel plates without any primer. In order to ensure a uniform surface, the virgin coatings were smoothed after the application. After a drying time of five weeks at ambient temperature and normal humidity, the clogged holes inside the steel plates were drilled again. Thereafter, the coating thickness was measured for each specimen in a grid of 6 x 5 using a digital thickness gauge (QNix 8500, Automation Dr. Nix). The mean values of the measurements are listed in Table 3.6, 3.7 and 3.8. A total of 95 fire tests were carried out on coated steel plates of different thermocouple configurations. Another 18 tests were performed on unprotected steel plates in order to provide reference data for the assessment of the fire protection performance of the coatings.

To carry out the fire tests, the test specimens were placed within a sample holder (see Figure 3.16), consisting of a square (200 x 200 mm) and 50 mm thick vermi-

culite plate. A recess in the centre of the sample holder allowed to arrange the sample surface at the same level as the surface of the vermiculite plate. Due to this precisely edging of the samples, a possible heat input through gaps at the edges was prevented. At the same time, nearly adiabatic conditions on the unexposed side of the specimens were ensured. Analogous to the steel plates, holes ($\varnothing = 2.5$ mm) were drilled inside the sample holder, through which the thermocouples were arranged. Here, a distinction is made between two configurations.

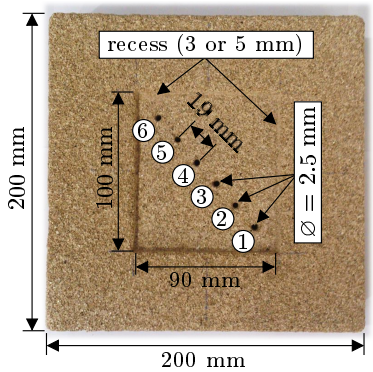

Figure 3.16: Sample holder made of a vermiculite plate (200 x 200 x 50 mm) with equidistant arranged holes for the thermocouples that are passed through the samples or welded on the backside

For configuration A two thermocouples were welded on the backside of the steel plates. One thermocouple was arranged through hole ① of the sample holder to measure the steel plate temperature near the edge (see Figure 3.16). The second thermocouple was arranged through hole ④ to ensure a temperature measurement in the centre of the sample. Configuration A was used for both the unprotected and the coated steel plates without boreholes. Configuration B, on the other hand, consisted of five thermocouples that were arranged through the sample holder (holes ② to ⑥) and the steel plates in order to measure the char temperature. In addition, a sixth thermocouple (hole ①) was welded on the backside of the steel plate to control the substrate temperature.

3.4.2 Test Setup and Parameters

In order to perform the small-scale fire tests, the sample holder was arranged together with the test specimen under the electric furnace as illustrated by the schematic description in Figure 3.17 a). The test specimens were deliberately kept in a horizontal position in order to keep the thermocouples in their place. However, it is also possible to arrange the test specimens vertically or overhead in order to assess the influence of a possible slipping of the coatings during the phase of melting and char formation. This influence was not considered within this work.

During the tests, not only the char and steel plate temperatures were measured every 0.5 seconds using a QuantumX MX1609KB (HBM GmbH), but also the furnace temperature. For this purpose, a thermocouple type K was arranged above the test specimen as documented in Figure 3.17 a). An exemplary photo documentation of a test specimen and the arrangement of thermocouples for the char temperature measurement is shown in Figure 3.17 b) and c) before and after the test.
The fire exposure was ensured by two heating elements at each side of the test specimen. In this way, a one-dimensional fire exposure of the test specimens was realised. Similar to the expansion analyses, different time-temperature curves were used to examine the fire protection performance of the coatings. In the first step, both the solvent- and the waterborne coating were exposed to time-temperature curves with constant heating rates of 10, 20, 30, 50 and 70 K/min (between 20 and 1000 °C) and to the standard fire curve. While only the 5 mm steel plates were used for the solvent-borne coating, both steel plate thicknesses (3 and 5 mm) were examined for the waterborne coating. In addition, the performance of the waterborne coating was also examined for the smouldering fire, the natural fire and the combined (travelling) fire curve that are defined in Figure 3.8.

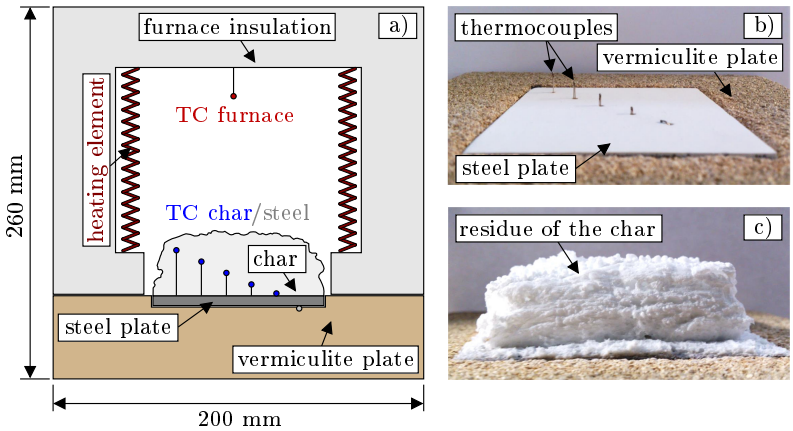

Figure 3.17: Small-scale fire tests on unprotected and coated steel plates: a) schematic description of the test setup, b) arrangement of thermocouples (0, 3, 6, 9 and 12 mm) through drilled holes in the steel plates and c) residue of an expanded char after the fire test

As inverse calculations should be performed following the ideas of Bartholmai & Schartel (2007) and Bozzoli et al. (2018), in order to recalculate the actual thermal conductivity of the coatings, some selected waterborne samples were subjected to a double heating. These samples are marked in Table 3.7 and 3.8 with (†). Of course, the data measured during the first heating of the samples already allows to perform the inverse calculations. However, the advantage of a second heating is that the thermocouples are already surrounded by the char at the beginning of the

experiment. As a result, a much smoother and more homogeneous temperature field can be measured right from the beginning of the fire exposure. Of course, the thermal conductivity values obtained from these data do not correspond to the actual behaviour of the coatings since the samples were already *thermally preloaded*. However, it is an extremely valuable approach to scientifically investigate the heating rate-dependent behaviour of the coatings.

3.4.3 Evaluation Software

In order to perform reverse calculations to determine the actual thermal conductivity of intumescent coatings from measured char temperatures, a calculation routine has been developed in MATLAB by the author. Within this routine, the Fourier's law of heat conduction according to Equation 2.2 is approximately solved using finite difference methods (FDMs). For this purpose, the derivatives u_t and u_{xx}, representing the change of a field variable u with time and space, are approximated by central difference quotients at a grid point (x_j, t_n) as described in Equation 3.1 and 3.2. Here, j represents the control variable of the space and n the control variable of the time. The remaining terms of the heat conduction equation such as the heat capacity $(\rho \cdot c_p)$ and the internal heat source $(\dot{\mathbf{w}})$ are known from the performed TG/DSC and expansion analyses or can be set to zero, respectively. For this reason, the thermal conductivity can be recalculated from the Fourier's law.

$$u_t := \frac{\partial u}{\partial t} \approx \frac{u_j^{n+1} - u_j^n}{\Delta t} \tag{3.1}$$

$$u_{xx} := \frac{\partial^2 u}{\partial x^2} \approx \frac{u_{j+1}^n - 2u_j^n + u_{j-1}^n}{(\Delta x)^2} \tag{3.2}$$

For the calculations, three different finite difference methods were implemented, the explicit Euler Method, the implicit Euler Method and the Crank-Nicolson approach. The methods differ in the approximation of the spatial derivative $\frac{\partial^2 T}{\partial x^2}$ as graphically and mathematically described in Figure 3.18. In the *explicit* finite difference method, the spatial temperature change is evaluated at the current time step n. In case of the *implicit* finite difference method the spatial temperature change is evaluated at the new time step $n + 1$. The Crank-Nicolson approach, on the other hand, represents the average of the explicit and the implicit method at the grid points (x_j, t_n) and (x_j, t_{n+1}), respectively. The main advantage of the Crank-Nicolson approach is that the finite difference calculations are unconditionally stable. This means that any time step Δt can be used to perform the calculations. The explicit method, on the other hand, is only stable if a certain threshold is not exceeded (Davis 2010).
The equations of the three mentioned finite difference methods are given in Figure 3.18. In order to illustrate the differences in the methods, a set of grid points (time vs. space) is used. With the help of the grid, it is possible to show at which points in time and space the char temperature must be known in order to calculate

the actual thermal conductivity (represented by the red point). As indicated by the red colour, the thermal conductivity is the only unknown quantity in the equations. Normally, in finite difference calculations, the material properties are known and the temperature is the quantity sought. However, due to the measurement of the char temperature at equidistant levels (Δx), the finite difference equations can be rearranged in order to calculate the thermal conductivity on the basis of the measured temperature data.

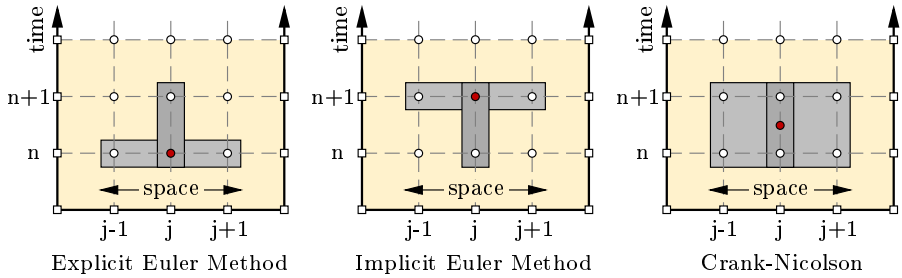

Explicit Euler Method

$$\lambda(T) \cdot \frac{T_{j+1}^{n} - 2T_{j}^{n} + T_{j-1}^{n}}{(\Delta x)^2} = \rho(T) \cdot c_p(T) \cdot \frac{T_{j}^{n+1} - T_{j}^{n}}{\Delta t}$$

Implicit Euler Method

$$\lambda(T) \cdot \frac{T_{j+1}^{n+1} - 2T_{j}^{n+1} + T_{j-1}^{n+1}}{(\Delta x)^2} = \rho(T) \cdot c_p(T) \cdot \frac{T_{j}^{n+1} - T_{j}^{n}}{\Delta t}$$

Crank-Nicolson

$$\lambda(T) \cdot \left(\frac{T_{j+1}^{n} - 2T_{j}^{n} + T_{j-1}^{n}}{(\Delta x)^2} + \frac{T_{j+1}^{n+1} - 2T_{j}^{n+1} + T_{j-1}^{n+1}}{(\Delta x)^2} \right) = \rho(T) \cdot c_p(T) \cdot 2\frac{T_{j}^{n+1} - T_{j}^{n}}{\Delta t}$$

Figure 3.18: Graphical description and mathematical formulation of finite difference methods (Explicit Euler, Implicit Euler and Crank-Nicolson) in order to solve Fourier's law of heat conduction

Because measured data are used within the calculations, certain scattering and irregularities have to be considered. The temperature scattering shown in Figure 3.19, for example, is due to the control of the heating elements of the furnace and the high measuring rate (2 Hz) of the temperature. Without any data processing, such temperature courses would lead to convergence problems during the finite difference calculations. For this reason, it was necessary to implement smoothing methods within the calculation routine. In order to allow a certain variability, the following three methods were used: (a) arithmetic mean, (b) linear regression and (c) polynominal regression. Comparative calculations have shown that especially the method of *arithmetic means* seems to be particularly suitable for data smoothing. With a sufficient number of sampling points ($n > 20$), the method is able to calculate a mean and smooth temperature curve. The *linear regression* method is also capable of calculating a smooth and mean temperature. However, this only applies to the user-defined time intervals (in this example, it is 30 seconds). In the transitions between the time intervals, temperature jumps and discontinuities

(see the red sharp-edged curve in Figure 3.19 b)) occur which cause problems in convergence. The *polynomial regression* approach, on the other hand, leads to a very continuous curve. However, since the regression curve deviate strongly from the measured values, the method also does not represent a good solution in this particular application. An increase of the polynomial degree (here $n = 50$) does not necessarily improve the approximation capability. Of course, it is conceivable to subdivide the measured data into several segments and to approximate each segments with a polynomial function. However, this would also lead to discontinuities in the transitions and, therefore, would result in convergence problems. For this reason, it was decided to use the *arithmetic mean* for the data processing. However, all methods are implemented within the calculation routine and can be used where appropriate.

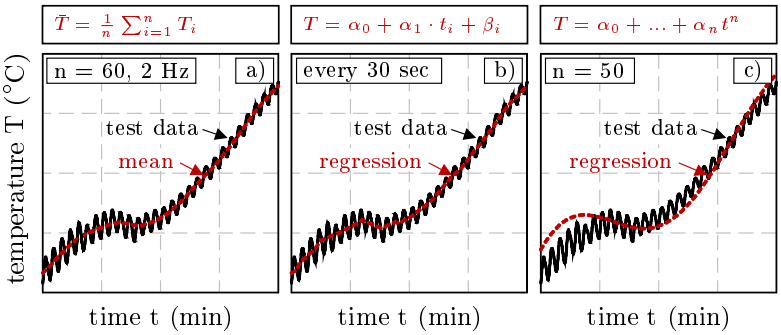

Figure 3.19: Comparison of different smoothing methods of measurement char temperature data: a) arithmetic mean, b) linear regression and c) polynominal regression

The implemented calculation routine is divided into several steps as can be seen from the flowchart in Figure 3.20. The graphical user interface (GUI) is started by executing the m-file *Control_GUI_FDM_Lambda.m*. With the help of the user interface, the entire calculations are controlled. The first step is to choose between the finite difference methods. Due to its stability, the Crank-Nicolson approach is recommended. In the next step, the measured char temperatures and the required material properties are read in during the data input. It should be noted that the data should have the same structure as indicated in the flowchart. The measured char temperatures, for example, should be arranged within a m x 6 matrix, with the time (sec) in the first column and the temperature values (°C) of the thermocouples (0, 3, 6, 9 and 12 mm) in the remaining columns. A similar structure is also prescribed for the material properties density (ρ) and specific heat capacity (c_p). However, the properties have to be arranged in pairs for each considered heating rate. In this case it is 10, 20, 30, 50 and 70 K/min.
After the data input, a decision has to be made whether the finite difference calculations should be performed with the raw data read in, or whether data smoothing should first be carried out. It this work it was decided to smooth the data using

the *arithmetic mean* method. For the recalculation of the actual thermal conductivity, char temperatures of three measuring points are required. As described in the flowchart in Figure 3.20, four data series are available for selection.

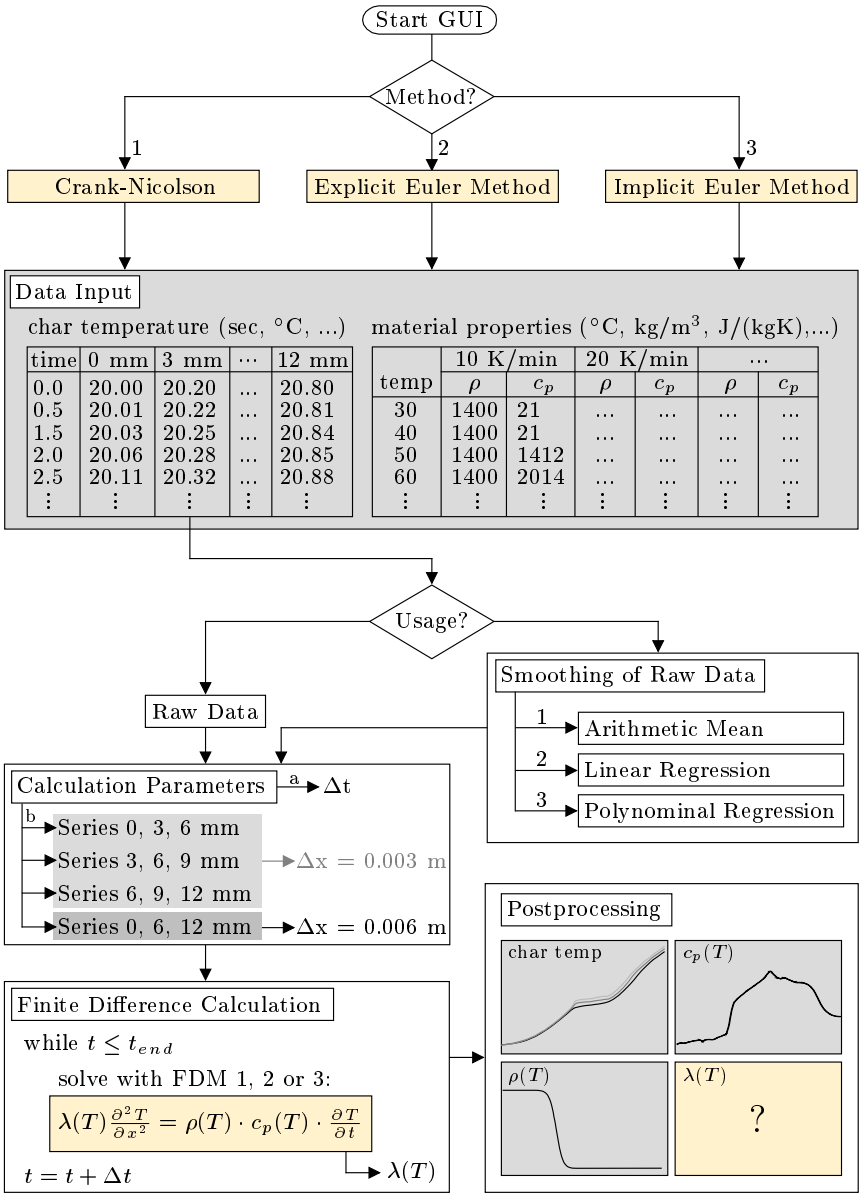

Figure 3.20: Flowchart of reverse calculations implemented in MATLAB to determine the actual thermal conductivity of intumescent coatings from char temperatures using finite difference methods

Depending on the selection of the data set, the state step size Δx is automatically set to 0.003 or 0.006 m with respect to the distance between the thermocouples that are arranged inside the char. The time step Δt, on the other hand, can be set manually. If the time step is too large and the calculations do not converge, an algorithm is implemented within the routine to reduce the time step size automatically. However, this is common within a finite difference method and will not be explained here. For more details, please refer to the source code.
After all calculation parameters have been defined, the actual calculation takes place. In order to solve Fourier's heat conduction equation, one of the previously defined finite difference methods is used. The result of the reverse calculation is the temperature-dependent actual thermal conductivity $\lambda(T)$. During the postprocessing the thermal conductivity and the input data (char temperatures, density and specific heat capacity) are graphically displayed. This is the last step of the calculation routine.

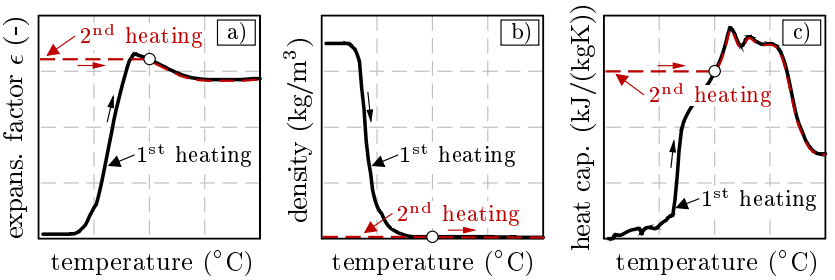

Figure 3.21: Exemplary description of the material property treatment for the reverse calculation of the actual thermal conductivity during the 2nd heating of the test specimens

Depending on whether the reverse calculations are carried out for the first or the second heating, care must be taken that the material properties change due to the irreversible reaction of the coatings. When a sample is heated up to 1000 °C for the first time, it is assumed that the temperatures at the arranged thermocouples are much lower. In terms of the expansion, for example, this means that the char has not gone through the full expansion reaction, but has come to a stagnation. In Figure 3.21 a) this point of stagnation is represented by a small white circle. During the cooling phase, it is assumed that no changes in the expansion behaviour occur. This is appropriate, since the heat source is removed in the cooling phase immediately after reaching the maximum temperature. For the second heating it is assumed that the expansion behaviour remains unchanged until the previous temperature is reached. After exceeding the temperature threshold, the expansion follows the original behaviour. The same behaviour is assumed to apply to the density and the specific heat capacity as illustrated in Figure 3.21 b) and c). The assumed behaviour of the specific heat capacity is derived from the respective state of the char. As long as the state of the char structure does not change, it is assumed that the heat storage capacity also remains unchanged. Only by

exceeding the temperature of the first heating, changes in char morphology are assumed to be initiated resulting in specific heat capacity changes. However, this assumption is not entirely correct. With the start of the second heating, energy is supplied to the char, so that certain morphology changes are already caused before reaching the temperature threshold. How strong this influence actually is can be quantified on the basis of TG and DSC analyses. However, due to the absence of available data, the assumptions presented above are taken for granted for the reverse calculations. This should be taken into account when evaluating the results of the thermal conductivity calculations. It should also be taken into account that the conductivity values should only be used to evaluate the heating rate dependency of the coatings. As true material properties the thermal conductivity values are not suitable to describe the insulation performance of intumescent coatings entirely as they are derived from measured data that originate from a double heating. On the other hand, the thermal conductivity values derived from the first heating represent property values which correspond to the real conditions. Therefore, these values can be used to better understand the performance of intumescent coatings and to develop or validate new material models.

3.4.4 Results of Performance Evaluation

The results of the performed fire tests on coated steel plates are given for the solvent- and the waterborne coating in Figure 3.22 and 3.23, respectively. In the diagrams both the steel plate temperatures of the thermocouple configuration A and B are presented. The temperatures of the test specimens with and without the arranged thermocouples inside the steel plates are compared to each other, in order to evaluate the influence of the temperature field manipulation within the char on the measured steel plate temperature. For each heating condition (constant heating with 10, 20, 30, 50 and 70 K/min and the standard fire curve) three measured time-temperature curves are plotted in one diagram. For the designation of the test specimens, a nomenclature is introduced. The first part of the nomenclature represents the heating condition. The time-temperature curves with constant heating rates are declared by an *H* followed by the value of the heating rate (*10, 20, 30, 50* or *70*). On the other hand, the standard fire, the smouldering fire, the natural fire and the travelling fire are declared by *ISO*, *SF*, *NF* and *TF*, respectively. The second part of the nomenclature (*sol* for solvent-borne or *wa* for waterborne) distinguishes between the coating type. The third part of the nomenclature (*3* or *5*) stands for the steel plate thickness (3 or 5 mm), while the Roman designations *I-V* define the number of the tests carried out. All tests performed with the thermocouple configuration A are declared by the Roman number *I*. Configuration B, on the other hand, is represented by the numbers *II, III, IV* and *V*. Using this nomenclature, all test specimens are listed in Table 3.6 to 3.8.
The measured steel plate temperatures of the solvent-borne coating in Figure 3.22 show a typical course for intumescent coatings, independent of the investigated

heating condition. In the first period, a nearly exponential increase in temperature takes place. As soon as the char formation is initiated, the temperature increase of the test specimens is slowed down. After a while, however, the temperature rises faster again. This behaviour can be observed for both thermocouple configurations. Especially for the tests performed under 20, 30 and 50 K/min almost no differences in measured steel plate temperature can be detected, regardless of whether

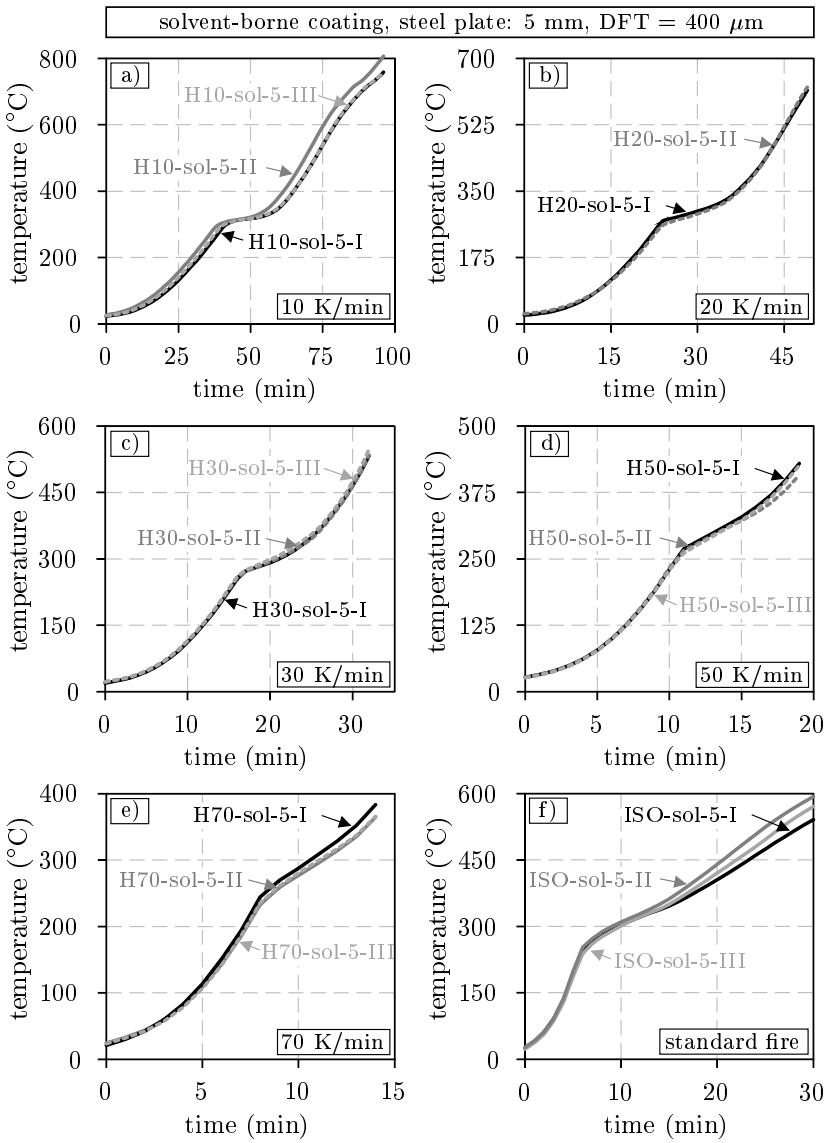

Figure 3.22: Measured steel plate (100 x 90 x 5 mm) temperatures of the solvent-borne coating for thermocouple configurations A (-I) and B (-II, -III) due to different heating conditions: a) 10 K/min, b) 20 K/min, c) 30 K/min, d) 50 K/min, e) 70 K/min and f) standard fire curve

thermocouples were arranged inside the char or not. For the constant heating rates of 10 and 70 K/min and the standard fire curve, on the other hand, at least one test specimen of the thermocouple configuration B shows slightly higher temperatures. However, this can be explained by the dry film thickness which has the lowest values of all specimens. Similar observations can also be made for the waterborne coating. In Figure 3.23 measured steel plate temperatures of the waterborne

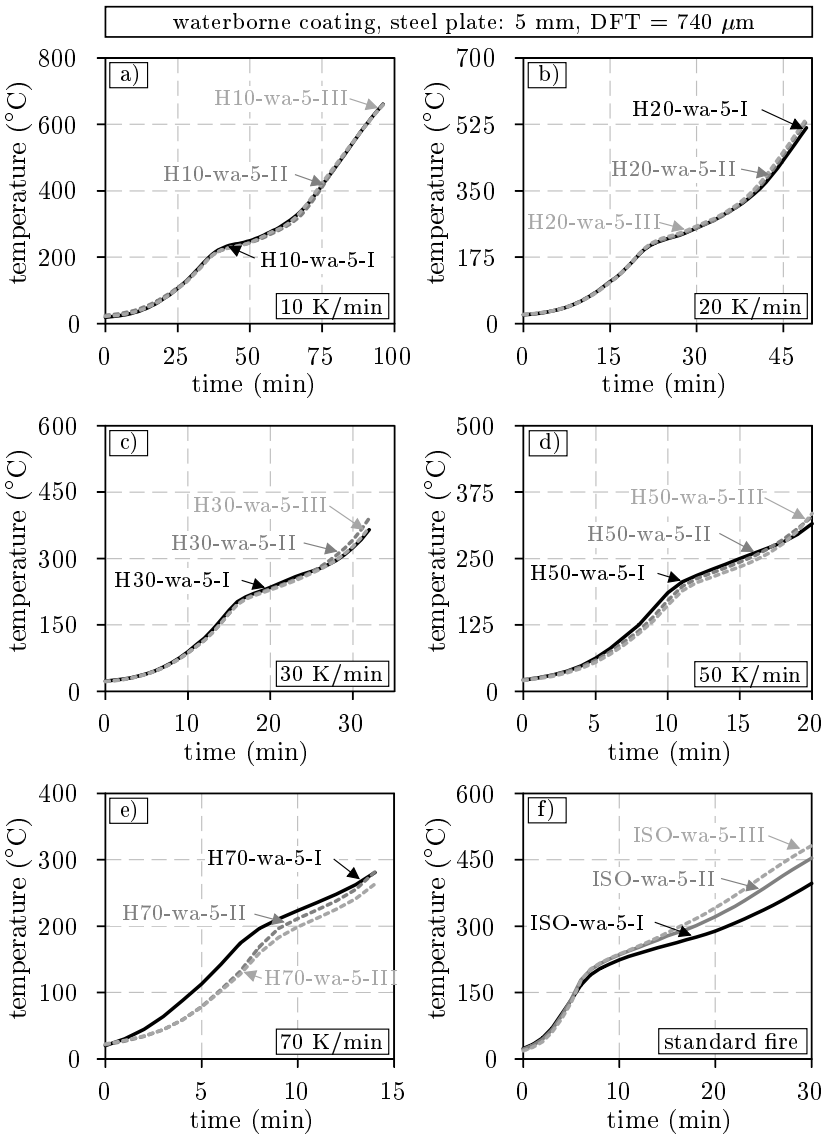

Figure 3.23: Measured steel plate (100 x 90 x 5 mm) temperatures of the waterborne coating for thermocouple configurations A (-I) and B (-II, -III) due to different heating conditions: a) 10 K/min, b) 20 K/min, c) 30 K/min, d) 50 K/min, e) 70 K/min and f) standard fire curve

test specimens (5 mm steel plates) with thermocouple configuration A (-I) and B (-II and -III) are compared to each other. Here, almost identical courses can be detected for 10, 20, 30 and 50 K/min. Only for the constant heating rate of 70 K/min and the standard fire curve differences in the measured steel plate temperatures are detected. However, these differences occur not only between the test specimens of different thermocouple configurations but also for the same configuration. Therefore, it can be assumed that other influences such as the difference in dry film thickness or the char formation near the edges (uneven expansion) are responsible for the differences. However, the observed deviations can be tolerated since they are rare (most of the tests show a high agreement in the measured steel temperatures) and due to the product-dependent behaviour. For this reason, the following two conclusions can be drawn: (1) The new developed test setup is suitable to carry out highly reproducible fire tests. (2) The arrangement of the thermocouples within the char and the drilled holes in the steel plates have no significant influence on the heating behaviour of the test specimens.

*Table 3.6: Measured dry film thickness (DFT), steel temperature at the initiation of the insulation effect ($T_{initial}$), related surface temperature (T_{surf}) temperature difference (ΔT) between the unprotected and the protected test specimen as well as final char thickness (t_{final}) and expansion factor (ϵ_{final}) of the **solvent-borne** coating for steel plates **100 x 90 x 5 mm***

Sample ID	heating cond. (-)	conf. (-)	DFT (μm)	$T_{initial}$ (°C)	T_{surf} (°C)	ΔT (°C)	t_{final} (mm)	ϵ_{final} (-)
H10-5	10 K/min	A	-	-	-	-	-	-
H10-sol-5-I	10 K/min	A	460	264	-	209	22.5	48.9
H10-sol-5-II	10 K/min	B	410	261	270	169	16.5	40.2
H10-sol-5-III	10 K/min	B	475	264	268	209	23.5	49.5
H20-5	20 K/min	A	-	-	-	-	-	-
H20-sol-5-I	20 K/min	A	538	255	-	245	26.3	48.9
H20-sol-5-II	20 K/min	B	605	245	274	247	28.8	47.6
H30-5	30 K/min	A	-	-	-	-	-	-
H30-sol-5-I	30 K/min	A	476	252	-	295	24.0	50.4
H30-sol-5-II	30 K/min	B	474	251	280	298	24.5	51.7
H30-sol-5-III	30 K/min	B	472	253	287	289	23.9	50.6
H50-5	50 K/min	A	-	-	-	-	-	-
H50-sol-5-I	50 K/min	A	410	250	-	319*	25.0	60.9
H50-sol-5-II	50 K/min	B	420	233	266	341*	26.0	61.9
H50-sol-5-III	50 K/min	B	460	229	263	323*	24.5	53.5
H70-5	70 K/min	A	-	-	-	-	-	-
H70-sol-5-I	70 K/min	A	487	231	-	326*	15.9	32.6
H70-sol-5-II	70 K/min	B	498	221	279	344*	15.0	30.1
H70-sol-5-III	70 K/min	B	500	223	270	344*	16.4	32.8
ISO-5	ISO	A	-	-	-	-	-	-
ISO-sol-5-I	ISO	A	492	207	-	364	23.5	47.8
ISO-sol-5-II	ISO	B	475	199	286	337	22.3	46.9
ISO-sol-5-III	ISO	B	530	204	282	353	21.0	39.6

* The maximum of ΔT has not been reached because the test ended before the char reacted completely. Therefore, the value corresponds to the last measured temperature difference. The real maximum value is theoretically higher.

*Table 3.7: Measured dry film thickness (DFT), steel temperature at the initiation of the insulation effect ($T_{initial}$), related surface temperature (T_{surf}) temperature difference (ΔT) between the unprotected and the protected test specimen as well as final char thickness (t_{final}) and expansion factor (ϵ_{final}) of the **waterborne** coating for steel plates **100 x 90 x 5 mm***

Sample ID	heating cond. (-)	conf. (-)	DFT (μm)	$T_{initial}$ (°C)	T_{surf} (°C)	ΔT (°C)	t_{final} (mm)	ϵ_{final} (-)
H10-wa-5-I	10 K/min	A	534	184	-	306	15.8	29.6†
H10-wa-5-II	10 K/min	B	648	181	184	316	15.5	23.9†
H10-wa-5-III	10 K/min	B	667	188	191	303	14.8	22.2†
H10-wa-5-IV	10 K/min	B	1170	180	193	391	30.0	25.6†
H10-wa-5-V	10 K/min	B	1170	174	186	408	29.5	25.2†
H20-wa-5-I	20 K/min	A	655	182	-	318	21.0	32.1†
H20-wa-5-II	20 K/min	B	604	183	194	311	20.4	33.8†
H20-wa-5-III	20 K/min	B	549	183	189	302	19.4	35.3†
H20-wa-5-IV	20 K/min	B	1212	159	177	371	39.2	32.3†
H20-wa-5-V	20 K/min	B	1214	165	185	366	40.3	33.2†
H30-wa-5-I	30 K/min	A	578	184	-	410	25.2	43.6†
H30-wa-5-II	30 K/min	B	575	176	196	408	23.8	41.4†
H30-wa-5-III	30 K/min	B	655	176	195	409	28.9	44.1†
H30-wa-5-IV	30 K/min	B	1151	162	187	427	42.8	37.2†
H30-wa-5-V	30 K/min	B	1156	161	181	434	44.2	38.2†
H50-wa-5-I	50 K/min	A	528	171	-	468*	30.3	57.4†
H50-wa-5-II	50 K/min	B	621	171	200	455*	29.2	47.0†
H50-wa-5-III	50 K/min	B	635	162	192	449*	27.9	43.9†
H50-wa-5-IV	50 K/min	B	1156	149	192	485*	37.3	32.3†
H50-wa-5-V	50 K/min	B	1162	151	200	483*	38.8	33.4†
H70-wa-5-I	70 K/min	A	578	159	-	429*	31.8	55.0†
H70-wa-5-II	70 K/min	B	601	160	216	428*	26.9	44.8†
H70-wa-5-III	70 K/min	B	624	144	213	446*	28.6	45.8†
H70-wa-5-IV	70 K/min	B	1199	134	199	452*	35.5	29.6†
H70-wa-5-V	70 K/min	B	1227	133	188	450*	35.8	29.2†
ISO-wa-5-I	ISO	A	578	134	-	479	-	-
ISO-wa-5-II	ISO	B	572	135	174	445	-	-
ISO-wa-5-III	ISO	B	703	153	204	427	29.0	41.3
ISO-wa-5-IV	ISO	B	1164	132	170	478	48.6	41.8
ISO-wa-5-V	ISO	B	1259	112	208	489	44.7	35.5
SF-5	smouldering	A	-	-	-	-	-	-
SF-wa-5-II	smouldering	B	750	190	239	248	16.1	21.5
SF-wa-5-III	smouldering	B	763	205	221	228	16.0	21.0
SF-wa-5-IV	smouldering	B	1188	197	239	238	20.5	17.3
SF-wa-5-V	smouldering	B	1203	198	232	242	21.8	18.1
NF-5	natural fire	A	-	-	-	-	-	-
NF-wa-5-II	natural fire	B	563	171	189	366	27.0	48.0
NF-wa-5-III	natural fire	B	596	172	194	367	28.8	48.3
NF-wa-5-IV	natural fire	B	1246	140	180	405	46.3	37.2
NF-wa-5-V	natural fire	B	1252	138	173	416	49.5	39.5
TF-5	travelling fire	A	-	-	-	-	-	-
TF-wa-5-II	travelling fire	B	761	245	270	363	20.5	26.9
TF-wa-5-III	travelling fire	B	812	247	263	366	18.0	22.2
TF-wa-5-IV	travelling fire	B	1222	225	260	428	35.6	29.1
TF-wa-5-V	travelling fire	B	1271	228	250	427	34.8	27.4

* The maximum of ΔT has not been reached because the test ended before the char reacted completely. Therefore, the value corresponds to the last measured temperature difference.

*Table 3.8: Measured dry film thickness (DFT), steel temperature at the initiation of the insulation effect ($T_{initial}$), related surface temperature (T_{surf}) temperature difference (ΔT) between the unprotected and the protected test specimen as well as final char thickness (t_{final}) and expansion factor (ϵ_{final}) of the **waterborne** coating for steel plates **100 x 90 x 3 mm***

Sample ID	heating cond. (-)	conf. (-)	DFT (μm)	$T_{initial}$ (°C)	T_{surf} (°C)	ΔT (°C)	t_{final} (mm)	ϵ_{final} (-)
H10-3	10 K/min	A	-	-	-	-	-	-
H10-wa-3-II	10 K/min	B	607	231	231	277	17.8	29.3†
H10-wa-3-III	10 K/min	B	634	264	257	265	22.4	35.3†
H10-wa-3-IV	10 K/min	B	1135	183	186	347	24.4	21.5†
H10-wa-3-V	10 K/min	B	1170	177	174	344	25.5	21.8†
H20-3	20 K/min	A	-	-	-	-	-	-
H20-wa-3-II	20 K/min	B	615	216	214	330	17.8	28.9†
H20-wa-3-III	20 K/min	B	616	218	210	326	19.7	32.0†
H20-wa-3-IV	20 K/min	B	1150	172	185	468	34.1	29.7†
H20-wa-3-V	20 K/min	B	1195	171	180	465	33.2	27.8†
H30-3	30 K/min	A	-	-	-	-	-	-
H30-wa-3-II	30 K/min	B	627	187	195	369	21.7	34.6†
H30-wa-3-III	30 K/min	B	628	193	192	361	22.2	35.4†
H30-wa-3-IV	30 K/min	B	1222	185	196	421	37.5	30.7†
H30-wa-3-V	30 K/min	B	1238	178	192	418	38.3	30.9†
H50-3	50 K/min	A	-	-	-	-	-	-
H50-wa-3-II	50 K/min	B	642	202	212	453*	27.0	42.1†
H50-wa-3-III	50 K/min	B	648	198	203	443*	25.6	39.5†
H50-wa-3-IV	50 K/min	B	1242	182	215	544*	39.9	32.1†
H50-wa-3-V	50 K/min	B	1258	179	205	547*	38.0	30.2†
H70-3	70 K/min	A	-	-	-	-	-	-
H70-wa-3-II	70 K/min	B	645	184	192	384*	27.3	42.3†
H70-wa-3-III	70 K/min	B	645	188	193	371*	28.1	43.6†
H70-wa-3-IV	70 K/min	B	1257	170	208	455*	33.4	26.6†
H70-wa-3-V	70 K/min	B	1266	166	208	445*	35.4	28.0†
ISO-3	ISO	A	-	-	-	-	-	-
ISO-wa-3-II	ISO	B	632	177	193	363	27.1	42.9
ISO-wa-3-III	ISO	B	637	166	185	353	28.8	45.2
ISO-wa-3-IV	ISO	B	1195	141	193	428	32.7	27.4
ISO-wa-3-V	ISO	B	1208	143	178	415	40.2	33.3
SF-3	smouldering	A	-	-	-	-	-	-
SF-wa-3-II	smouldering	B	694	204	235	280	18.6	26.8
SF-wa-3-III	smouldering	B	696	243	261	239	17.2	24.7
SF-wa-3-IV	smouldering	B	1287	227	242	279	27.5	21.4
SF-wa-3-V	smouldering	B	1292	214	230	279	27.8	21.5
NF-3	natural fire	A	-	-	-	-	-	-
NF-wa-3-II	natural fire	B	655	196	207	397	28.8	44.0
NF-wa-3-III	natural fire	B	664	175	172	336	28.0	42.2
NF-wa-3-IV	natural fire	B	1276	176	197	464	44.8	35.1
NF-wa-3-V	natural fire	B	1277	170	193	454	42.7	33.4
TF-3	travelling fire	A	-	-	-	-	-	-
TF-wa-3-II	travelling fire	B	674	264	257	339	22.9	34.0
TF-wa-3-III	travelling fire	B	676	264	272	346	21.8	32.2
TF-wa-3-IV	travelling fire	B	1223	245	259	424	41.9	34.3
TF-wa-3-V	travelling fire	B	1248	244	260	425	28.5	22.8

* The maximum of ΔT has not been reached because the test ended before the char reacted completely. Therefore, the value corresponds to the last measured temperature difference.

Therefore, it can be concluded that the proposed test method is suitable to measure the char temperatures without falsifying the steel plate temperatures. The extent to which the temperature development over the char thickness and time is affected by different heating conditions will be described in detail in subsection 3.4.5.

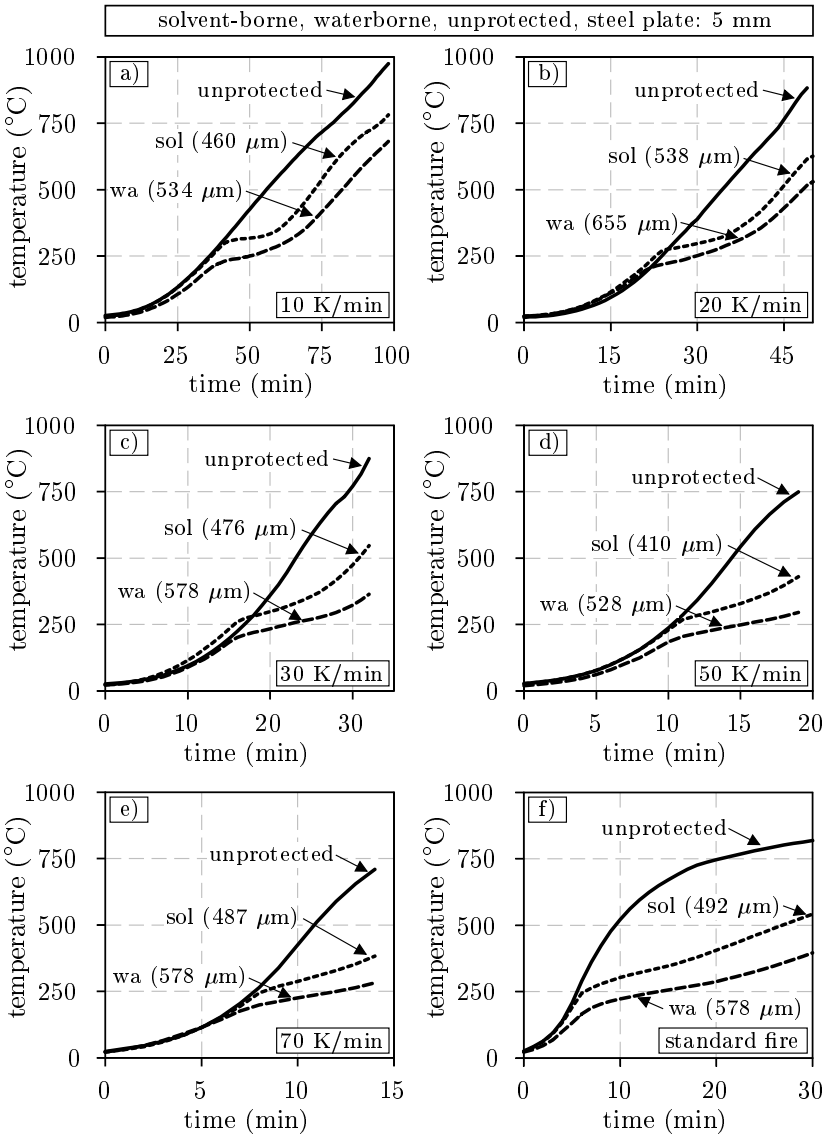

Figure 3.24: Measured temperatures of protected (solvent- and waterborne coating) and unprotected steel plates (100 x 90 x 5 mm) due to different heating conditions: a) 10 K/min, b) 20 K/min, c) 30 K/min, d) 50 K/min, e) 70 K/min and f) standard fire curve

In order to evaluate the fire protection performance of the coatings, measured tem-

peratures of coated and unprotected steel plates are compared to each other in Figure 3.24. In this way, for each heating condition (10, 20, 30, 50, 70 K/min and the standard fire curve), the temperatures of the unprotected test specimens are compared with the heating behaviour of the test specimens coated with the solvent- (sol) and the waterborne (wa) coating. For this purpose, only the steel plate temperatures of configuration A (sample ID -5-I) are used.
Although the dry film thickness of the solvent-borne coating (410 - 538 μm) was higher than the required value (400 μm) for the fire resistance time of 30 min compared to the waterborne coating (528 - 655 μm vs. the required dry film thickness of 740 μm), the temperatures of the steel plates coated with the solvent-borne product are perceptibly higher. This applies not only to the constant heating rates (see Figure 3.24 a) - e)) but also for the standard fire curve. After 30 minutes of fire exposure, for example, the temperature of the solvent-borne test specimen is 541 °C. The steel temperature of the waterborne coating, on the other hand, is only 397 °C, which is significantly lower than expected. On the basis of this comparison, it can be assumed that the design of the dry film thickness according to the technical approval of the waterborne coating is more conservative in case of flat components such as steel plates than for the solvent-borne coating. However, when evaluating the fire protection performance on edged components such as typical steel profiles, the waterborne coating may show a more expected fire protection performance (500 °C after 30 minutes) due to the formation of cracks inside the char (definition of cracks see Figure 2.39). Nevertheless, in case of the investigated steel plates, the dry film thickness of the waterborne coating appears to be too high in order to meet the fire resistance requirements, although the applied dry film thicknesses are already lower than the values specified in the technical approval. This should be taken into account when evaluating the fire protection performance in comparison to the solvent-borne coating. The higher temperatures of the solvent-borne coating are therefore not necessarily due to the poorer thermal insulation but due to the different dry film thicknesses. However, for the evaluation of the heating rate dependency, the comparison of the coatings is only of secondary importance.
In order to evaluate the heating rate-dependent behaviour of the coatings, a comparison between the unprotected and the coated test specimens has to be made. This is done by calculating the difference (ΔT) between the temperature of the unprotected ($T_{a,unprotected}$) and the protected ($T_{a,protected}$) test specimens as a function of time. The results of these calculations are given in Figure 3.25. Here, the calculated ΔT-curves are given for the 5 mm test specimens of configuration A. However, the calculations were carried out for all test specimens and are documented in the Tables 3.6 to 3.8. The ΔT values that are listed in the tables are declared as the local maximum of the temperature difference and are marked with a dot in Figure 3.25. In cases where there is no local maximum because the intumescence reaction of the coating was not complete (compare the data for 50 and 70 K/min), the maximum value of the calculated temperature difference is taken as ΔT. However, in order to identify these values during the evaluation process,

the data is marked with a (*) in the tables. This is a convention that is made in order to compare and evaluate the fire protection performance of the investigated coatings.
The courses of the calculated ΔT-curves are for both coatings nearly the same. Clear differences in the courses are only observed with regard to the different heating rates and magnitudes. As the fire protection performance of the coatings is expressed by the temperature difference, the best insulation performance is determined in case of the standard fire curve. This applies for both coatings. Basically, the higher the temperature difference between the unprotected and the protected test specimens, the better the protective effect of the intumescent coatings. Therefore, it should be pointed out that the temperature difference between the unprotected and the protected steel plates decreases with reduced heating rates. This means that the fire protection performance is reduced as soon as the heating of the test specimens is slowed down. This again applies to both products.

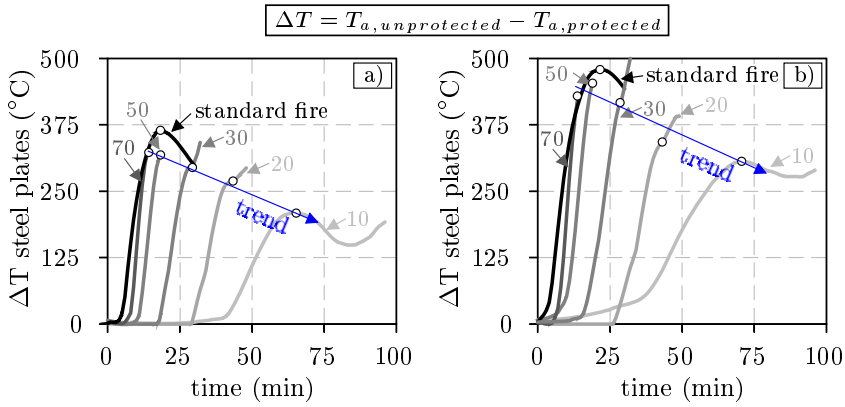

Figure 3.25: Evaluation of the fire protection performance of a) the solvent-borne and b) the waterborne coating on the basis of the temperature difference (ΔT) between the unprotected and protected steel plates (100 x 90 x 5 mm) calculated from the curves given in Figure 3.24

When evaluating the efficiency (see Equation 2.4) of a solvent- and a waterborne coating due to different heating conditions, Lucherini et al. (2018) came to the same conclusions. In addition, the authors found that their solvent-borne coating reacted more sensitively to changes in heating conditions than the waterborne coating. This cannot be confirmed with regard to the calculated temperature difference as the trend of the ΔT reduction is for both investigated coatings nearly the same. However, the question arises how the heating rate-dependent behaviour of the coatings can be explained and which influencing parameters are responsible for it? To answer this question, the measured temperatures of the coated test specimens were subjected to further evaluation. For this purpose, a time derivative was calculated for the measured steel temperature using a difference method with a time increment Δt of 15 seconds. Since the derivative of the measured temperature

represents a heating rate (°C/min), the initiation of the fire protection performance of the coatings can be identified by the changes in temperature derivation. In the same way, it is also possible to identify the point in time or the corresponding sample temperature, at which the formed char loses its insulation efficiency.
In order to visualise these reaction states, Figure 3.26 and 3.27 show the derivatives of the measured steel plate temperatures for the solvent- and the waterborne coating. The reaction states of the initial insulation and the loss of thermal protection are marked within the diagrams with a dot and a corresponding temperature value. The temperature value ($T_{initial}$), representing the initiation of the thermal protection, is determined at the time when the heating rate of the sample starts to decrease. These values were systematically determined for all test specimens and are given in the Tables 3.6 to 3.8. If the sample reaches the original value of the heating rate in the course of further heating, the sample temperature is determined again. This temperature value is then considered as the reaction state, in which the thermal protection of the formed char is lost and the sample heats up faster than before the char formation. However, for some test specimens, these values could not be determined because the tests were completed before the heating rate had reached its original value. This applies especially to heating rates higher than 30 K/min. Since the range between the identified temperatures is a measure of the thermal protection effect, it is marked in the diagrams by a crosshatching. The larger the range, the longer the fire protection performance lasts.
For both coatings, the temperature range between the initiation and the loss of fire protection increases with increasing heating rates. However, this is not only due to the ever-increasing temperature, at which the thermal protective effect is lost. This is also related to the temperature $T_{initial}$, which decreases with increasing heating rates. For example, if the solvent-borne test specimens are heated with a constant heating rate of 10 K/min, the thermal protection is initiated at 264 °C. For 70 K/min, on the other hand, the insulation effect is already triggered at 231 °C (see Figure 3.26 and Table 3.6). In the case of the standard fire curve, the initial temperature is even lower (207 °C). A similar behaviour can also be observed for the waterborne coating (see Figure 3.27). However, the values for the initiation temperature are even lower. This phenomenon can be explained by the thermal inertia of the test specimens in combination with the heating rates and the dry film thickness of the coatings. When a test specimen is heated at a low heating rate, it has more time to adapt to the furnace temperature. This has already been proven by appropriate studies of Schaumann & Weisheim (2017). On the other hand, when the heating rate is increased, the test specimen is not able to adapt to the furnace temperature due to the reduced time until the maximum temperature of 1000 °C is reached. The coating on the heat exposed side, however, starts to expand since the surface temperatures (T_{surf}) of the coating are high enough to trigger the chemical reactions. A similar behaviour was also observed by Lucherini et al. (2019) when the influence of sample cooling on the performance of a solvent-borne coating was evaluated. Nevertheless, it should be noted that increasing the heating rate also leads to a larger temperature difference between the surrounding

gas and the surface of the test specimen. This generates a larger heat flow into the test specimen, which represents an opposite effect.

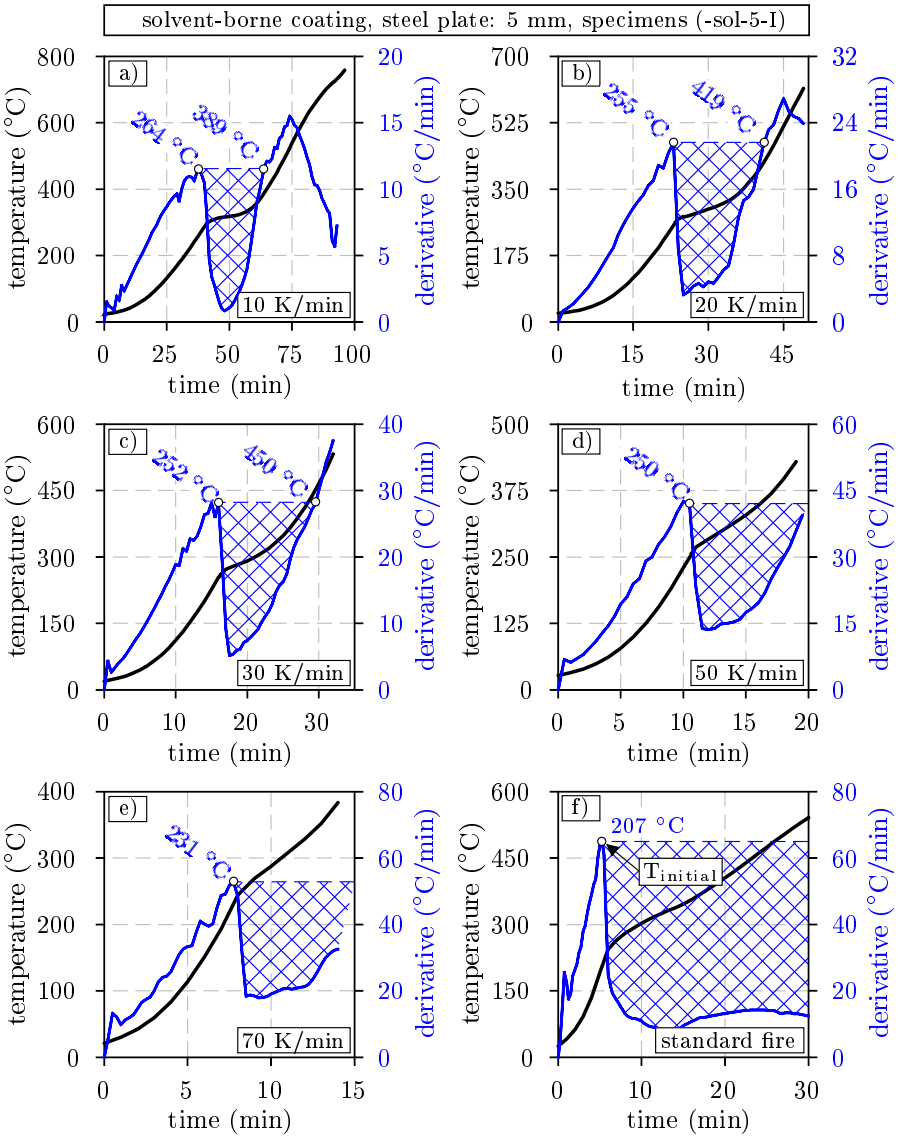

*Figure 3.26: Identification of the initiation temperature ($T_{initial}$) of the fire protection performance of the **solvent-borne** coating on the basis of the time derivative of the measured steel plate (100 x 90 x 5 mm) temperatures for different heating conditions: a) 10 K/min, b) 20 K/min, c) 30 K/min, d) 50 K/min, e) 70 K/min and f) standard fire curve*

When comparing the $T_{initial}$ values of the solvent- and the waterborne coating (compare the diagrams in Figure 3.26 and 3.27), it becomes clear that not only the

thermal inertia of the steel substrate, but also the coating composition (composition of single ingredients) itself dominates the initiation of char formation. For example, at 10 K/min the insulation effect of the waterborne coating was determined to start at 184 °C. The protective effect of the solvent-borne coating, on the other hand, starts at 264 °C and thus 80 °C later.

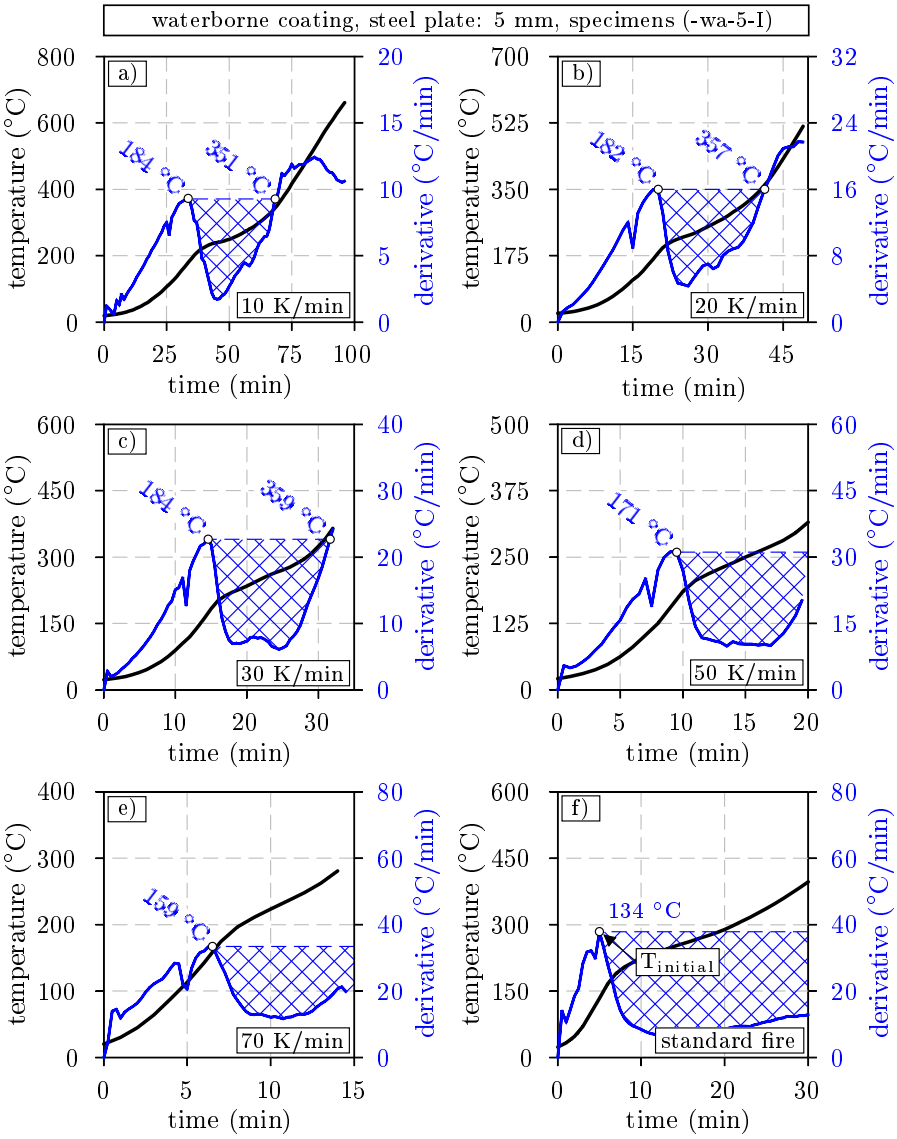

*Figure 3.27: Identification of the initiation temperature ($T_{initial}$) of the fire protection performance of the **waterborne** coating on the basis of the time derivative of the measured steel plate (100 x 90 x 5 mm) temperatures for different heating conditions: a) 10 K/min, b) 20 K/min, c) 30 K/min, d) 50 K/min, e) 70 K/min and f) standard fire curve*

Similar differences in initiation temperature of the char formation are also observed for other heating rates. With regard to the fire protection performance, a low initiation temperature is preferred. The lower the sample temperature, at which the coating starts to expand, the lower the maximum temperature during the whole fire exposure. This is, among others, the reason why the waterborne coating shows a better fire protection performance than the solvent-borne coating. However, the initiation temperature of char formation changes with steel plate and dry film thickness as illustrated in Figure 3.28. Here, the measured initiation temperatures $T_{initial}$ and the corresponding surface temperatures of the liquid melt T_{surf} (listed also in the Tables 3.6 to 3.8) are given for both coatings as a linear regression and a function of the heating rate (10, 20, 30, 50 and 70 K/min).

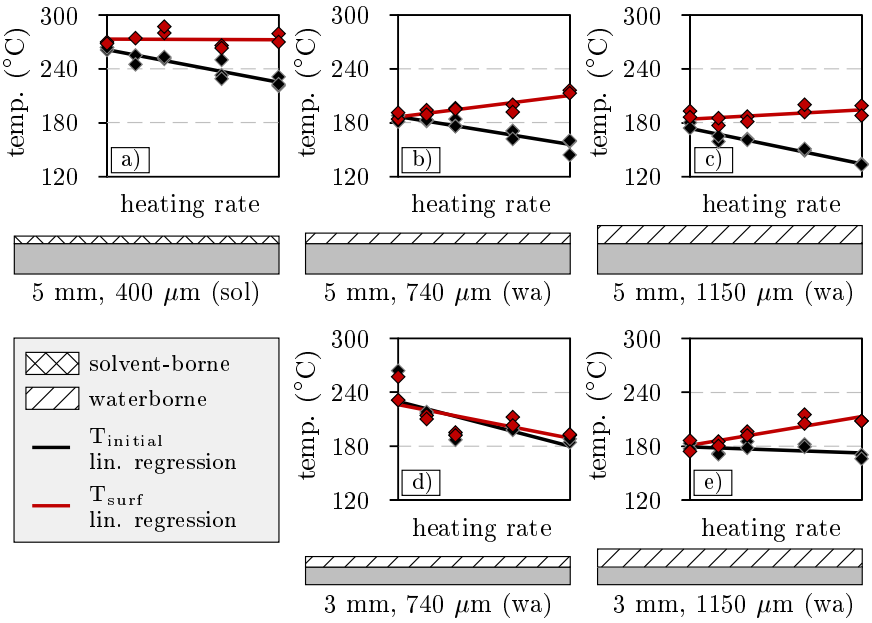

Figure 3.28: Heating rate dependency (heating rates: 10, 20, 30, 50 and 70 K/min) of the initial temperature ($T_{initial}$) of the insulation effect and the related surface temperature (T_{surf}) of the coatings with regard to changes in steel plate and coating thickness for a) the solvent- and b) - e) the waterborne coating

As only one steel plate thickness and dry film thickness were examined for the solvent-borne coating, the values for $T_{initial}$ and T_{surf} are shown in Figure 3.28 a). Here it can be seen that the initiation temperature of the solvent-borne coating decreases with increasing heating rate as it was already described in Figure 3.26. The same applies also to the waterborne coating. However, since for the waterborne coating fire tests with different steel plate thicknesses (3 and 5 mm) and different nominal dry film thicknesses (740 and 1150 µm) were carried out, it can be identified that the heating rate dependency of the initiation temperature changes

also with substrate and coating thickness. For example, in case of the waterborne coating the highest $T_{initial}$ values are observed for the lowest steel plate and dry film thicknesses as can be seen in Figure 3.28 d). Here, the 3 mm steel plates (A/V = 333 m^{-1}) that are exposed to a constant heating rate of 10 K/min are heated up to 231 °C until the char formation is triggered. However, at the same heating rate and nominal dry film thickness (740 μm), the initiation temperature of the waterborne coating is only 184 °C when being applied on 5 mm steel plates (A/V = 200 m^{-1}). This behaviour is due to the lower sample mass, which results in a faster heating and is also observed for other heating rates ($T_{initial}$ at 50 K/min: 202 °C for 3 mm and 171 °C for 5 mm) as can be seen also from the comparison of the data listed in Table 3.7 and 3.8. However, the dry film thickness of the coatings counteracts the effect of the sample bulkiness. For example, if higher coating thicknesses are applied on the 3 mm test specimens, the $T_{initial}$ values start to decrease (183 °C for 10 K/min, nominal thickness: 1150 μm). This is due to the higher values of the dry film thickness that cause a certain delay in sample heating even before char formation. Nevertheless, for higher heating rates the $T_{initial}$ values are still higher than for 5 mm steel plates and a nominal dry film thickness of 740 μm (compare Figure 3.28 b) and e)).

Besides the initiation temperatures, Figure 3.28 shows also linear regressions for the surface temperatures of the coatings that were measured with the help of thermocouples arranged at 0 mm. In contrast to the initiation temperature, which is derived from the measured steel plate temperature, the values for T_{surf} represent the actual temperature of the liquid melt, at which the char formation occurred. Therefore, it is even more remarkable that the surface temperatures behave in a different way with respect to the heating rates than the initiation temperatures. While the initiation temperatures of both coatings decrease with higher heating rates, the surface temperatures, on the other hand, increase or remain at least unchanged (in case of the solvent-borne coating). Only for the lowest steel plate (3 mm) and dry film thicknesses (740 μm) the surface temperatures show a similar behaviour to the initiation temperatures. But how can this differentiated behaviour be explained? When evaluating the behaviour of the surface temperature, it should be noted that the initiation temperature of the char formation corresponds to the steel temperature that is measured on the back side of the steel plate. The thicker the steel plate and the dry film thickness of the coating, the greater the distance and temperature difference between the two measuring points. This effect is even intensified in the case of higher heating rates, as the low thermal conductivity of the coating and the thermal inertia of the steel substrate causes a heat accumulation on the surface, which results in increased surface temperatures (see Figure 3.28 b), c) and e)). However, if both the dry film thickness of the coating and the bulkiness of the steel plate are low, the test specimen heats up more homogeneously so that almost no gradient is formed between the surface and the back side. For this reason, the two regression curves of $T_{initial}$ and T_{surf} in Figure 3.28 d) are almost identical. However, this behaviour also means that the test specimens heat up significantly more ($T_{initial}$ = 231-264 °C for 10 K/min) before the char formation is initiated.

As a result of these findings, the conclusions can be drawn that the onset of fire protection depends on several influencing parameters such as ① the composition of the intumescent coating, ② the dry film thickness, ③ the section factor of the steel substrate and ④ the type of fire exposure. Depending on the intumescent coating, the dry film thickness and the section factor, different steel temperatures result at which the expansion of the coatings is initiated. As soon as the heating rate of the test specimens is increased, the initiation temperature of the char formation decreases. However, this applies only to the initiation temperature $T_{initial}$ that is derived from the steel temperature measured on the back side of the steel plate. The surface temperature T_{surf}, on the other hand, normally increases with higher heating rates. The reasons for this are the thermal inertia of the test specimens and the low thermal conductivity of the coating, which influence both the steel and the surface temperature. Although the $T_{initial}$ values provide a first indicator for the degree of thermal protection provided by an intumescent coating, the calculated temperature differences ΔT are the most decisive values for the evaluation of the fire protection performance. For self study and comprehension, the values are graphically prepared in the Figures 3.26 and 3.27 and numerically listed in the Tables 3.6 to 3.8.

In order to create the diagrams in Figure 3.28, test results of 3 and 5 mm thick steel plates with nominal dry film thicknesses of 740 and 1150 μm of the waterborne coating were used. The time-temperature curves of these test specimens are shown in Figure 3.29 and 3.30 for the sake of completeness. Here, the same behaviour can be observed as in the tests presented before. For example, the increase in dry film thickness leads to lower steel temperatures. The differences in the measured time-temperature curves are even more pronounced for the 3 mm steel plates, as their heating behaviour is more affected by the dry thicknesses of the intumescent coating due to their lower bulkiness.

In addition to the constant heating rates and the standard fire curve, other fire scenarios were also investigated within the small-scale fire tests. These fire curves are the smouldering fire curve according to EN-13381-8 (2013), the natural fire curve from the national research project IGF 19176 N (Zehfuß et al. 2018) and a travelling fire, which was designed by the author for testing purposes. The measured temperatures of the steel plates (3 and 5 mm) that were exposed to these fire curves are given in Figure 3.31. Here, for each fire curve measured temperatures of an unprotected and two protected steel plates each coated with a nominal dry film thickness of 740 μm (-II and -III) and 1150 μm (-IV and -V) are compared in one diagram. Similar to the constant heating rates, an increase in the dry film thickness leads to lower steel temperatures and thus to a higher fire protection. However, the evaluation of the fire protection performance in terms of the heating rate dependence is much more remarkable in this context. If the $T_{initial}$ values in the Tables 3.7 and 3.8 are compared between the standard fire and the smouldering fire, it becomes clear that the test specimens heat up much more during the smouldering fire until the coating expands (standard fire: 166-177 °C vs. smouldering fire: 204-243 °C). This applies for both 3 and 5 mm steel plates. The same applies,

if a smouldering fire is added before the natural fire. The smouldering phase within the travelling fire does not only cause the $T_{initial}$ values to increase, but also the char thicknesses and the expansion values to decrease. This becomes clear when the $T_{initial}$ and ϵ_{final} values of the natural fire and the travelling fire are compared to each other.

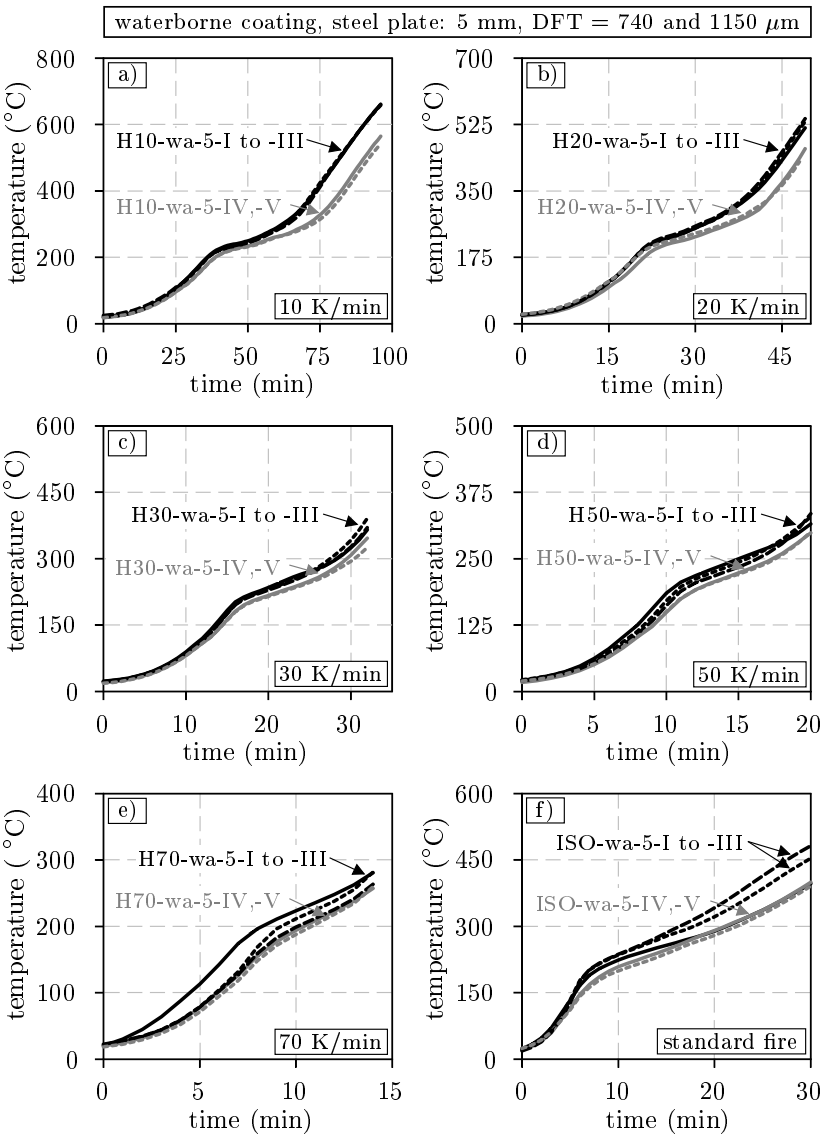

*Figure 3.29: Measured steel plate (**100 x 90 x 5 mm**) temperatures of the waterborne coating for target dry film thicknesses of 740 µm (-I to -III) and 1150 µm (-IV, -V) due to different heating conditions: a) 10 K/min, b) 20 K/min, c) 30 K/min, d) 50 K/min, e) 70 K/min and f) standard fire curve*

During the expansion analyses it could already be observed that the formation of the char structure is significantly influenced by the smouldering fire phase. This observation can also be confirmed by the small-scale fire tests as the expansion of the waterborne coating is initiated at higher steel temperatures and leads to irregular and reduced char thicknesses.

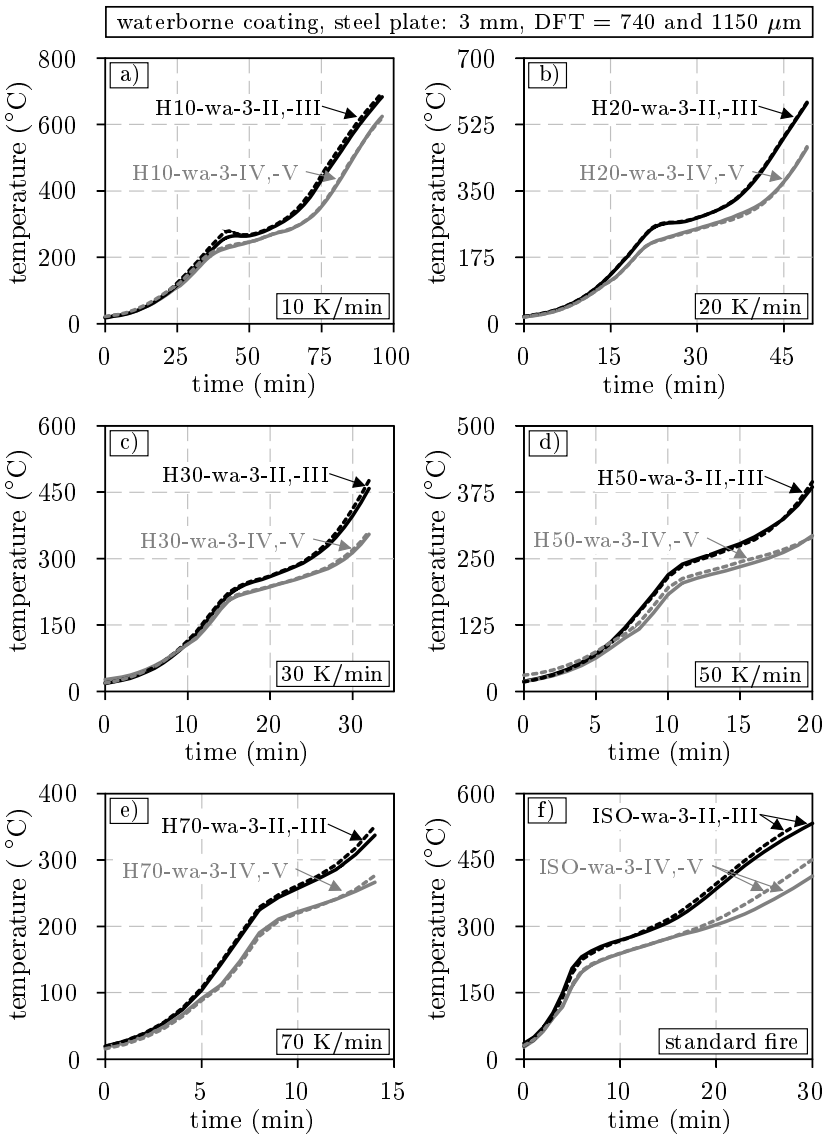

*Figure 3.30: Measured steel plate (**100 x 90 x 3 mm**) temperatures of the waterborne coating for target dry film thicknesses of 740 µm (-II, -III) and 1150 µm (-IV, -V) due to different heating conditions: a) 10 K/min, b) 20 K/min, c) 30 K/min, d) 50 K/min, e) 70 K/min and f) standard fire curve*

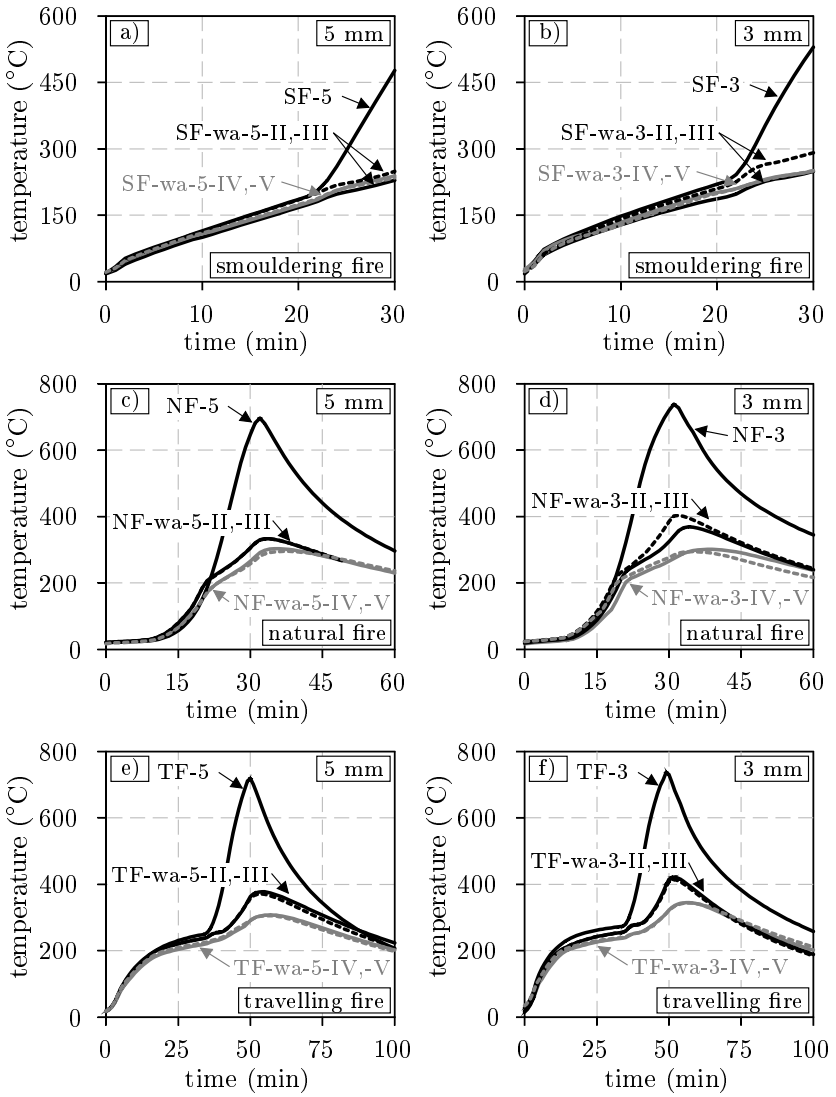

*Figure 3.31: Measured temperatures of protected (**waterborne** coating) and unprotected steel plates (3 and 5 mm) for nominal dry film thicknesses of 740 µm (-II, -III) and 1150 µm (-IV, -V) due to different heating conditions: a)-b) smouldering fire according to EN-13381-8 (2013), c)-d) natural fire according to the national research project IGF 19176 N (Zehfuß et al. 2018) and e)-f) travelling fire developed by the author*

Nevertheless, high temperatures do not occur in the investigated steel plates, since the dry film thicknesses are comparatively high and the temperatures of the acting fires only show high temperatures for a short period of time. Therefore, in order to systematically investigate the influence of smouldering on the thermal protection effect, further investigations with additional fire curves with different

smouldering fire phases and temperature peaks are required. The tests carried out here serve only as an indicator for the differentiated behaviour of the investigated coatings.

3.4.5 Results of Reverse Calculations

In order to evaluate the actual thermal conductivity of the investigated coatings with the help of the performed small-scale fire tests, reverse calculations were performed using the evaluation software that was presented in subsection 3.4.3. According to this finite-difference approach, char temperatures measured at equidistant intervals are required as input data in order to perform the reverse calculations. In the previous section, the performance of the solvent- and the waterborne coating have been evaluated so far on the basis of the measured steel plate temperatures and the char thicknesses. However, since the small-scale fire tests were performed with additional thermocouples in order to measure also the char temperatures during the char formation, Figure 3.32 and 3.33 show the results of the char temperature measurements. Due to the large amount of data, it was decided to concentrate only on the results of the waterborne coating and the 5 mm steel plates.
Figure 3.32 shows the measured char and the furnace temperatures for heating rates of 10, 20 and 30 K/min. The results of the first heating are given in the diagrams on the left side. Here, the transient expansion behaviour of the coating can already be recognised from the temperature curves measured at different heights. As soon as the waterborne coating expands, the temperature increase at the lowest thermocouple (0 mm) is the first to be slowed down. Since these thermocouples are located directly on top of the sample surface, the curves are very similar to the measured steel temperatures. As soon as the formed char reaches the thermocouples arranged further up, the temperature rise is also slowed down. Since several minutes can pass between reaching the first and the last thermocouple (12 mm), the time required for the expansion process can be estimated with the help of the measured char temperatures. In addition to the time offset, it is also noticeable that the temperature curves measured at the highest thermocouples show certain irregularities. This is due to the control of the heating elements of the furnace. However, with increasing distance to the char surface, the irregularities in the temperature curves decrease. The reason for this is the low thermal conductivity of the char, which develops a stronger insulation effect with increasing char thicknesses. Similar observations can also be made for the diagrams on the right-hand side of Figure 3.32. However, the difference here is that these char temperatures were measured during a second heating of the test specimens. Since all thermocouples are already surrounded by the char structure at the beginning of the second heating, different temperatures are already measured at the beginning of the measurements. Therefore, a temperature gradient is formed between the lowest and the highest thermocouple. The characteristics of the gradients can be derived from the distances between the measured char temperatures. The greater the distance

between the top and the bottom curve, the greater the gradient. In addition, the higher the heating rate at which the test specimens are heated, the greater the distances between the curves and thus the temperature gradients within the char structure (compare for example the diagrams in Figure 3.32 b), d) and f)). The shapes of the gradients that are formed within the char structure are shown for example in Figure 3.33 f) for the standard fire curve and in Figure 3.34 for the smouldering fire, the natural fire and the travelling fire.

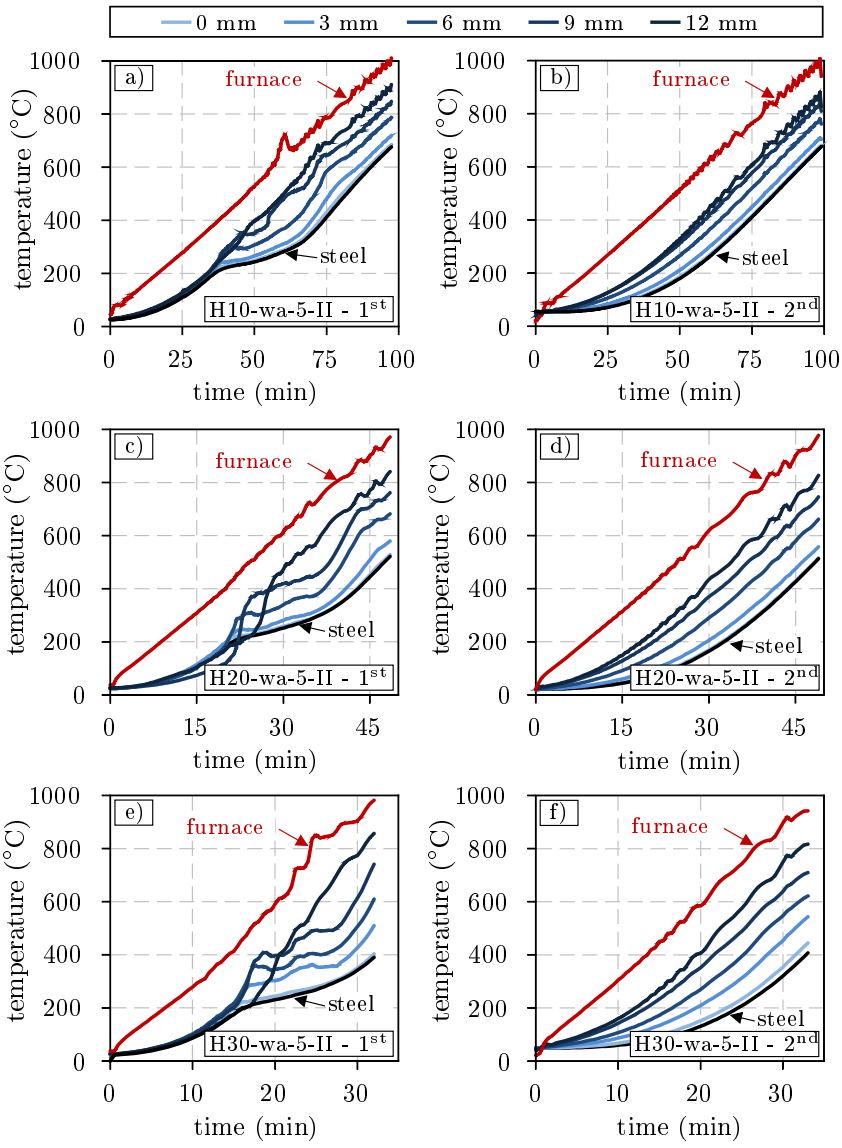

Figure 3.32: Char temperatures of the waterborne coating measured at different heights (0-12 mm) during the first and second heating of 5 mm steel plates at a)-b) 10 K/min, c)-d) 20 K/min and e)-f) 30 K/min

In these diagrams, the magnitude of the temperature gradient can be determined from the slope of the char temperature curves. The flatter the curves, the larger the gradient. The temperature gradients measured for the smouldering fire and the natural fire, for example, are similar to each other. However, the temperature gradient of the natural fire is almost linear.

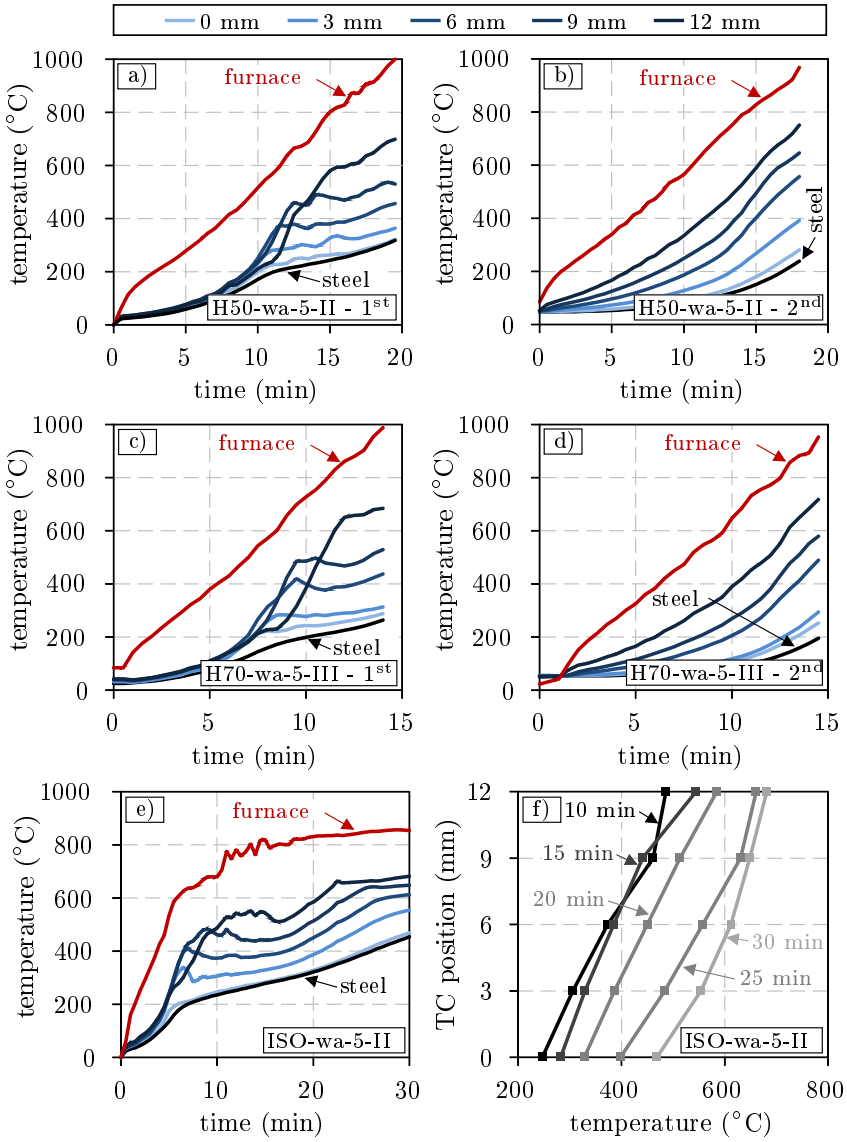

Figure 3.33: Char temperatures of the waterborne coating measured at different heights (0-12 mm) during the first and second heating of 5 mm steel plates at a)-b) 50 K/min and c)-d) 70 K/min and e) the standard fire curve. The temperature gradient within the char measured for the standard fire curve is given in figure f)

The same applies also to the temperature gradients for the standard fire curve that are given in Figure 3.33 f) for different times of fire exposure. In contrast to this, a deviating behaviour can be observed for the waterborne coating when being exposed to the travelling fire. Here, an almost linear temperature gradient is formed only between the upper char layers (thermocouples 12-3 mm).

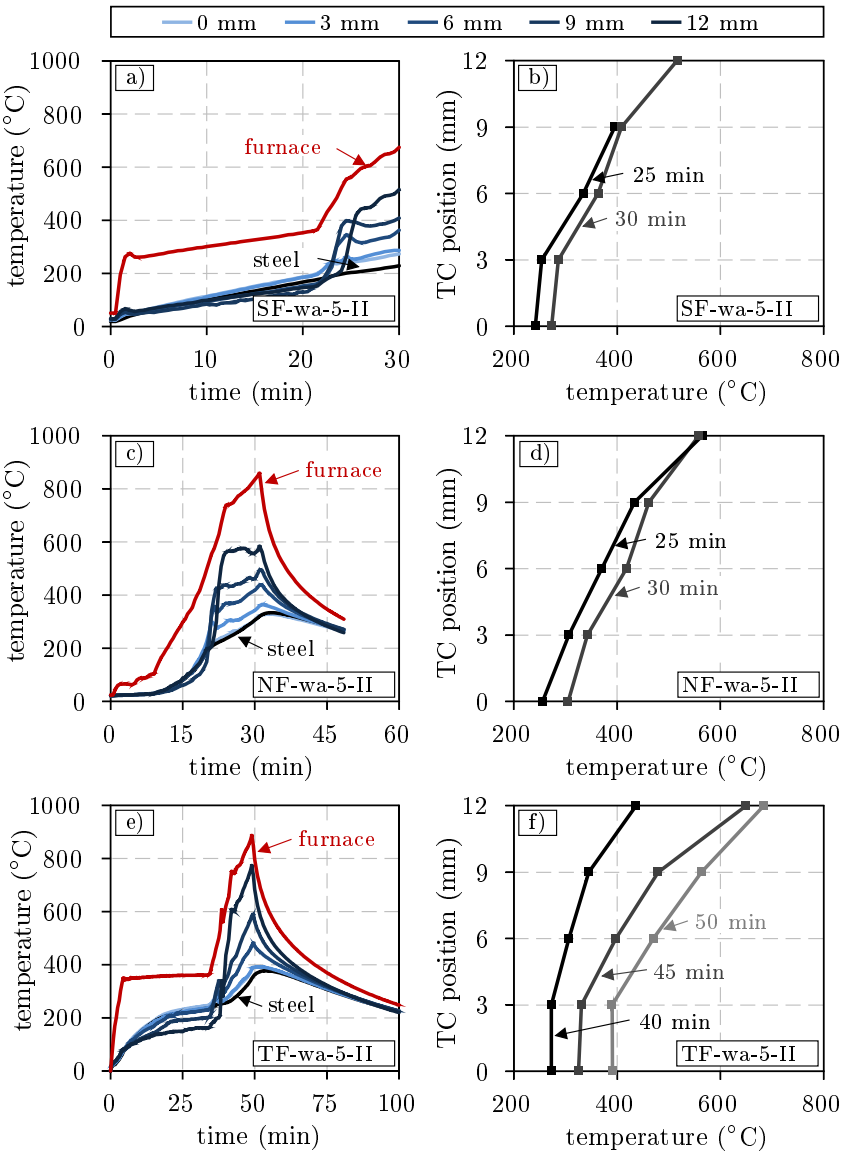

Figure 3.34: Char temperatures and temperature gradients of the waterborne coating measured at different heights (0-12 mm) during the fire exposure of 5 mm steel plates according to a)-b) the smouldering fire, c)-d) the natural fire and e)-f) the travelling fire

For the thermocouples arranged at 0 and 3 mm, on the other hand, almost identical temperatures are measured. A similar behaviour can also be observed for the smouldering fire (compare Figure 3.34 b) and f)). For this reason, the question arises how this behaviour can be explained? In order to answer this question, Figure 3.35 shows the char structures of the waterborne coating after the exposure to different fire curves. The samples were sliced in the middle in order to better evaluate the char morphology. The ruler arranged on the left side of the pictures serves as a scale.

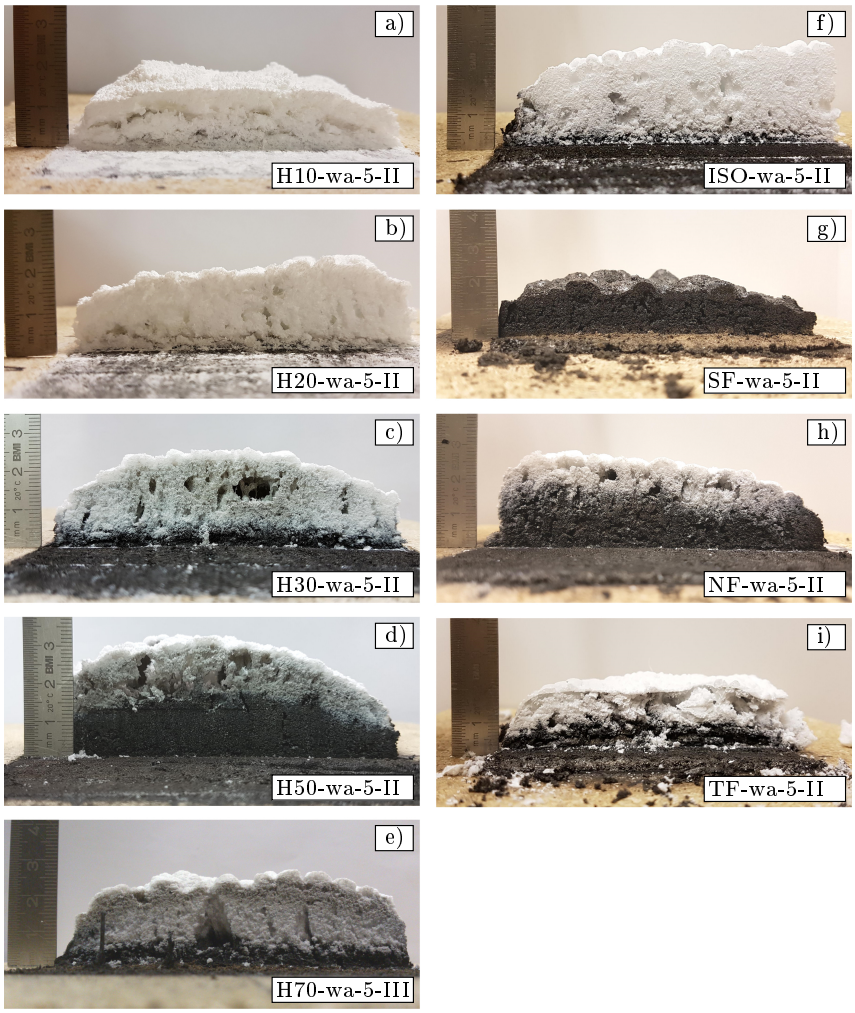

Figure 3.35: Char morphology of the waterborne coating at different heating rates and fire curves derived from 5 mm steel plates after the fire test (second heating). Summary of the test results see Table 3.7

As already observed in the expansion tests, the time-temperature curves with low heating rates and the standard fire curve lead to a white colouring of the char. The

fact that the 10 K/min samples are particularly fragile and the char morphology of the travelling fire samples is irregular was already observed in the previous investigation. However, these are not the only observations that can be made from the images. A closer look at the smouldering fire sample reveals that the lower part of the char still has a beige-brown colour. This is an indication that the coating did not react completely and was still in the reaction phase when the test stopped. In the phase where the coating is still beige in colour, the sample is viscous and has a high thermal conductivity. This could be a possible explanation for the absence of a temperature gradient between the thermocouples arranged at 0 mm and 3 mm. Due to the high thermal conductivity, the heat passed through this sample area almost unhindered. The same applies also to the travelling fire sample, although no beige coloration can be identified in the images. This is due to the fact that the sample was removed from the furnace only after the entire cooling phase has been completed. The smouldering fire sample, on the other hand, was directly removed from the furnace as soon as the fire exposure time of 30 minutes was reached. This stopped the reaction abruptly.

Verification of the MATLAB Evaluation Software:

The measured char temperatures given in Figure 3.32 and 3.33 should be used to recalculate the actual thermal conductivity of the waterborne coating using the evaluation software that was implemented in MATLAB. In order to ensure that the implementation of the finite difference method was correctly, a verification had to be carried out.

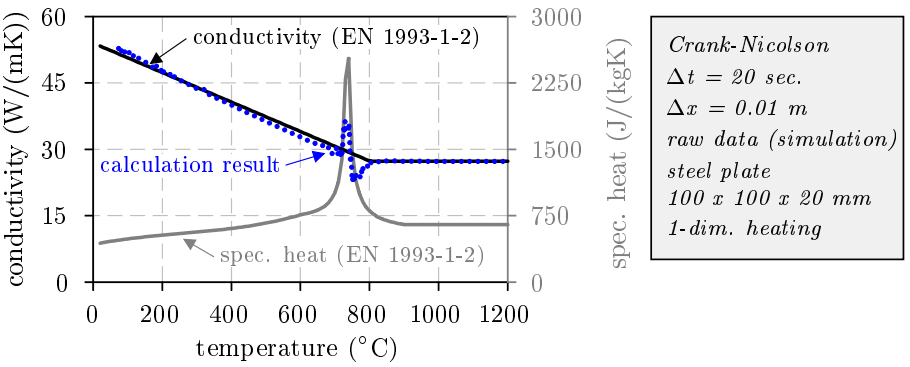

Figure 3.36: Reverse calculation of the thermal conductivity of carbon steel from a numerical simulation in order to verify the implemented MATLAB routine from subsection 3.4.3

The verification consists of a numerical simulation that was carried out in ABAQUS 2017 (HF6). An unprotected steel plate (100 x 100 x 20 mm) was subjected to one-dimensional heating while the steel temperature was measured at three different points (fire exposed surface, center and backside of the steel plate). A constant density of 7850 kg/m^3 as well as the temperature-dependent thermal conductiv-

ity and the specific heat capacity of carbon steel according to EN-1993-1-2 (2010) (see Figure 3.36) were defined as thermal material properties of the steel plate. The Crank-Nicolson method with an initial time step size of $\Delta t = 20$ sec. and a space step size of $\Delta x = 0.01$ m was used to verify the implementation. Since the temperatures that were used for the reverse calculation were results of a numerical simulation, raw data (without any smoothing method) were used. The result of the verification calculation is given in Figure 3.36 as a blue dotted curve.
The recalculated thermal conductivity of the steel plate shows a very good agreement with the nominal values. Only in the temperature range between 720 and 800 ° C a larger deviation between the two curves can be observed. This deviation is caused by the peak in the specific heat capacity as can be seen from the diagram. The finite difference equation that has to be solved (see Figure 3.18) contains the specific heat capacity in the numerator. If the values of the specific heat capacity increase more than the temperature change in space, larger values for the thermal conductivity are calculated. The same applies to the reversed case. In this way the reason for the present deviation can be explained. Therefore, the following conclusions can be drawn: ① Both the quality of the measured temperatures and the values of the specific heat capacity as well as the density have a significant influence on the results of the reverse calculation. ② The use of the Cranck-Nicolson method leads to a good agreement with the expected results. ③ The results of the performed verification prove that the finite difference method was implemented correctly and that it is suitable to recalculate the thermal conductivity of fire protection materials from measured temperature data.

Waterborne Intumescent Coating:

During the verification of the source code implementation it was already explained that in addition to the measured material temperatures, the density and the specific heat capacity of the fire protection material are required in order to recalculate the thermal conductivity. For this reason, the results of the TGA and DSC measurements and the results of the expansion analysis were used to determine the required material properties of the waterborne coating. The temperature and heating rate-dependent density, for example, was calculated with the help of Equation 3.3

$$\rho(\theta,\dot{\theta}) = \frac{m(\theta,\dot{\theta})}{V(\theta,\dot{\theta})} = \frac{m_0 \cdot \Delta m(\theta,\dot{\theta})}{A_0 \cdot t(\theta,\dot{\theta})} = \frac{m_0 \cdot \Delta m(\theta,\dot{\theta})}{A_0 \cdot t_0 \cdot \epsilon(\theta,\dot{\theta})} = \rho_0 \cdot \frac{\Delta m(\theta,\dot{\theta})}{\epsilon(\theta,\dot{\theta})} \tag{3.3}$$

ρ_0:	density at room temperature (kg/m^3)
$\Delta m(\theta,\dot{\theta})$:	mass change (%)
$\epsilon(\theta,\dot{\theta})$:	expansion factor (-)

While the mass change $\Delta m(\theta,\dot{\theta})$ was determined from the TGA measurements, the volume change of the formed char was calculated from the measured expansion values $\epsilon(\theta,\dot{\theta})$. In both cases the values are temperature and heating rate-dependent. The specific heat capacity of the waterborne coating, on the other hand, was cal-

culated from the heat flow that was measured during the DSC analysis divided by the heating rate at which the samples were heated (see Equation 3.4)

$$c_p(\theta, \dot{\theta}) = -\frac{DSC(\theta, \dot{\theta})}{\dot{\theta}} \tag{3.4}$$

$DSC(\theta, \dot{\theta})$:	heat flow (mW/mg) according to Figure 3.1 b)
$\dot{\theta}$:	heating rate (K/s)

With the help of these two equations, the density and specific heat capacity of the waterborne coating could be determined as can be seen in Figure 3.37 a)-b). Since intumescent coatings show an irreversible thermal behaviour, in the diagrams it is indicated that the material properties are only valid for the first heating. For the cooling phase, it is assumed that the density and the specific heat capacity remain constant and adopt the value that was reached at the last highest temperature. This assumption was already described in detail in subsection 3.4.3 and is assumed to be also valid for the second heating. However, since the last reached temperature of the samples differs depending on the dry film thickness and the heating rate, Figure 3.37 c)-d) and e)-f) distinguishes between a dry film thickness of 740 and 1150 μm and heating rates of 10, 20 and 30 K/min. In this way, the density and the specific heat capacity are calculated individually for each sample in order to be used during the recalculation procedure of the actual thermal conductivity. The last reached temperature that separates the constant and the variable part of the material properties during the second heating is determined from the mean value of the three lowest thermocouples (0, 3 and 6 mm) from the first heating.
With the material properties and the measured char temperatures that were presented above, the reverse calculations could be carried out for the waterborne coating. The results of the calculations are given in Figure 3.39 for the first and in Figure 3.40 for the second heating of the samples. In both cases the calculations could only be performed for 10, 20 and 30 K/min since tests with higher heating rates did not achieve sufficiently high temperatures to provide a wide temperature spectrum for the calculations.
Before the results of the reverse calculations are presented, the correlations between the input data and the calculated actual thermal conductivity are explained by means of an exemplary calculation for 10 K/min. For this reason, Figure 3.38 a) shows the calculated thermal conductivity curve of the waterborne coating together with the expansion curve that was measured during the expansion analysis. Here, it can be seen that the temperature range of the expansion coincides with the temperature range in which the thermal conductivity reaches its minimum. The further increase in thermal conductivity can also be associated with the shrinkage behaviour and the reduction of the char layer. However, the measured expansion curves are only indirectly considered within the reverse calculations. The change in volume caused by expansion leads to a significant reduction in density, which is the reason why the calculated thermal conductivity starts to decrease. Since the density changes only slightly in the further course of reaction ($> 300\,^{\circ}$C), the

results of the thermal conductivity calculation depend especially on the specific heat capacity, as the graphical relationship between Figure 3.38 a) and b) shows. For example, the rapid increase in specific heat capacity leads in the same way to an increase in thermal conductivity. In addition, the temperatures at which the maximum values of both material properties are reached are also identical.

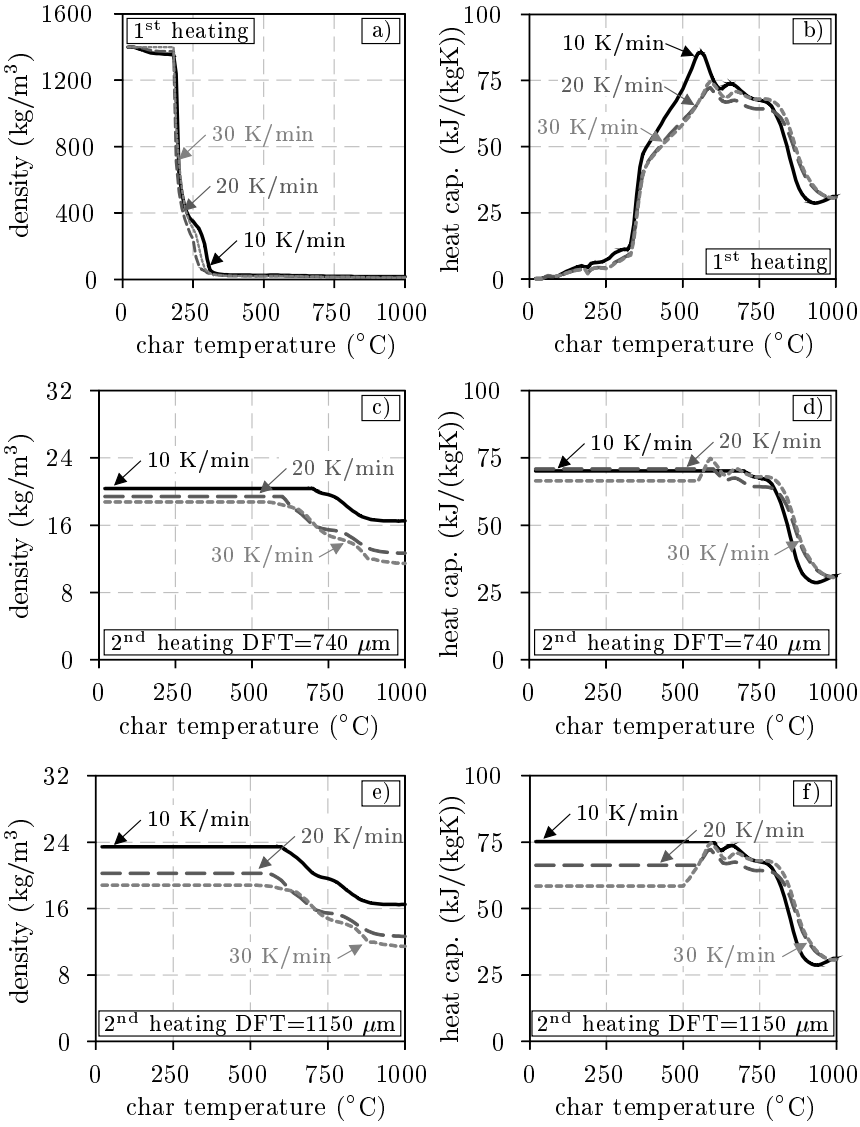

Figure 3.37: Temperature and heating rate-dependent (10, 20 and 30 K/min) density and specific heat capacity of the waterborne coating during a)-b) the first and c)-f) the second heating as a function of the dry film thickness (DFT) and char temperature

In order to put also the measured char temperatures in correlation with the actual

thermal conductivity, the temperatures were related to the mean value of the three thermocouples arranged at 0, 3 and 6 mm. As can be seen from Figure 3.38 c) the curves show an almost linear course. However, due to the approximation of the spatial derivative $\frac{\partial^2 T}{\partial x^2}$, even small changes in temperature lead to large numerical changes during the calculation of the actual thermal conductivity.
Despite the high sensitivity of the calculations, the individual thermal conductivity curves in Figure 3.39 show a very good agreement in their temperature-dependent course, regardless of whether the test specimens had a low (-II and -III) or a high dry film thickness (-IV and -V).

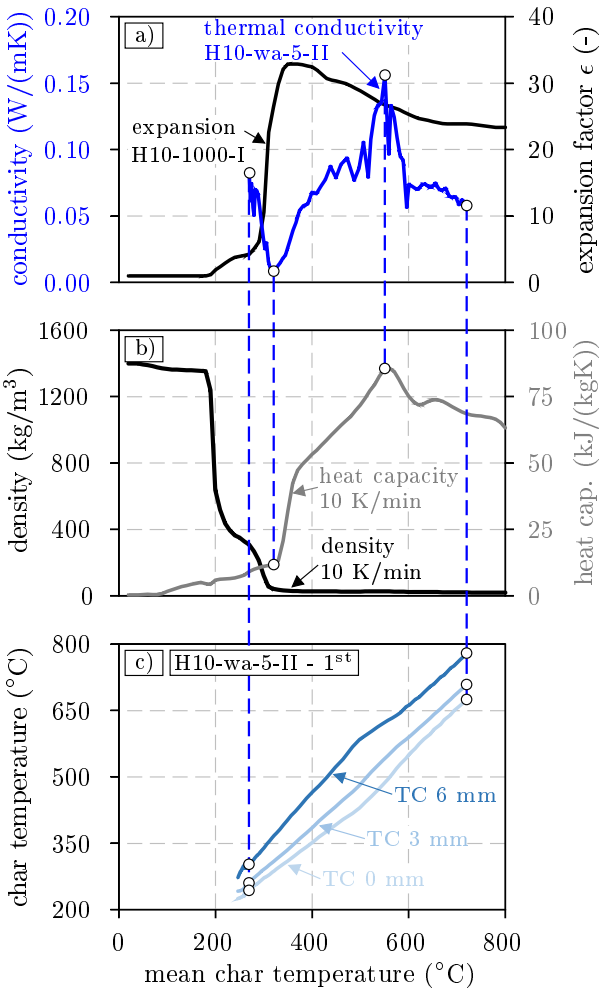

Figure 3.38: Correlation between the calculated thermal conductivity of the water-borne coating at 10 K/min and: a) the expansion curve, b) the density and specific heat capacity and c) the char temperatures measured at different thermocouple (TC) positions

This observation applies to all three evaluated heating rates. However, the results of the 20 K/min samples are particularly consistent. Larger scattering, on the other hand, is observed for 30 K/min. The curves are characterised by the fact that the thermal conductivity decreases at the beginning of the calculation and reaches its minimum at about 310-320 °C. With 0.002-0.009 W/mK the calculated minimum is many times smaller than the thermal conductivity values of

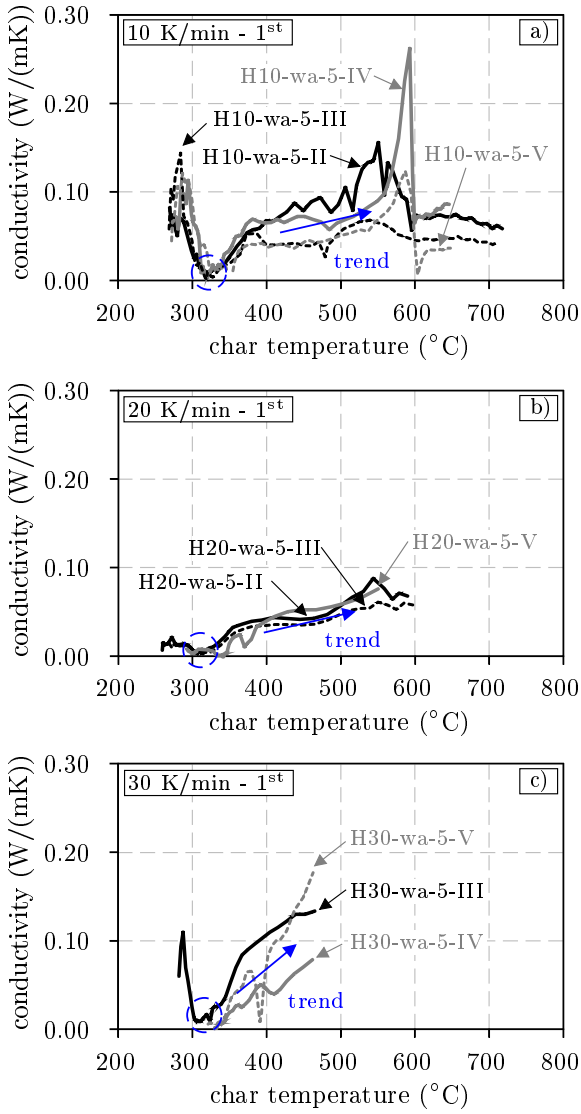

*Figure 3.39: Reverse calculation results of the thermal conductivity of the water-borne coating from char temperatures measured during small-scale fire tests (**first heating**) of coated steel plates (100 x 90 x 5 mm) at constant heating rates of a) 10 K/min, b) 20 K/min and c) 30 K/min*

air (0.044 W/mK), ammonia (0.055 W/mK) or saturated steam (0.069 W/mK) at 300 °C. This contradicts the modeling concept of Di Blasi & Branca (2001), Staggs (2010) and Tabeling (2014) that the thermal conductivity of intumescent coatings is formed by the parts of trapped gases and the char structure being weighted by the degree of porosity. According to this idea, the calculated values of the thermal conductivity should be greater than the values of the pure gases.

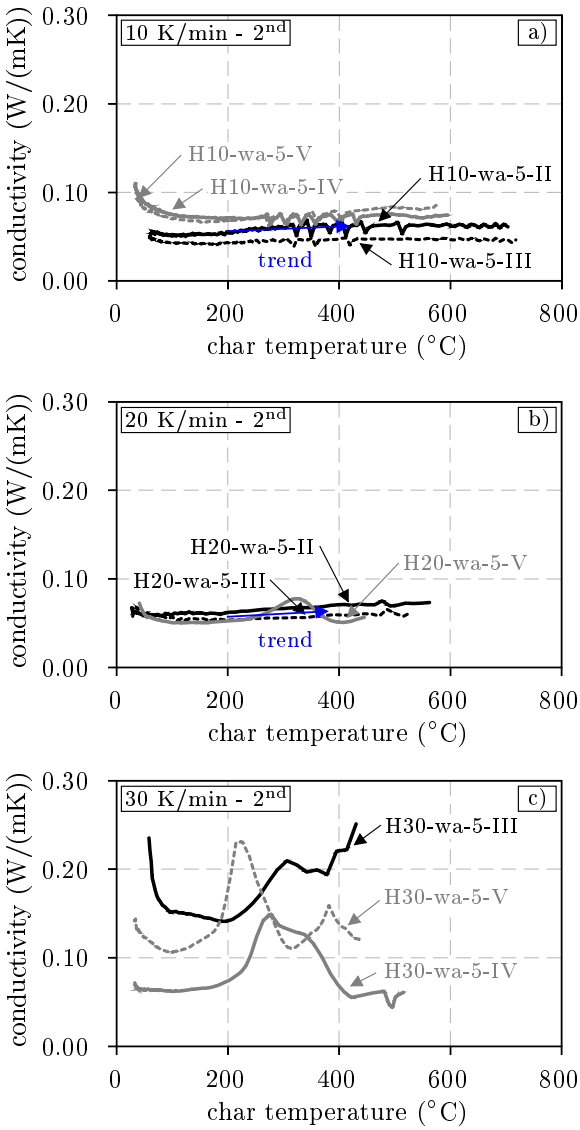

*Figure 3.40: Reverse calculation results of the thermal conductivity of the water-borne coating from char temperatures measured during small-scale fire tests (**second heating**) of coated steel plates (100 x 90 x 5 mm) at constant heating rates of a) 10 K/min, b) 20 K/min and c) 30 K/min*

Although the absolute values do not appear to be plausible, the qualitative course of the calculated thermal conductivity curves corresponds to the general idea of the fire protection behaviour of intumescent coatings. After reaching its minimum, the thermal conductivity values increase with higher temperatures. According to current knowledge, this is due to irreversible changes of the char structure from a closed to an open-cell structure. Such observations have already been made in the morphological investigations (see subsection 3.3.4) and therefore confirm this hypothesis.
As soon as the irreversible reactions are completed and an inorganic, open-cell pore structure remains at the end, no more significant changes take place in the thermal conductivity values. This can be observed, for example, in Figure 3.40 a) and b) for the 10 and 20 K/min samples that were subjected to a second heating. During the second heating, the thermocouples were already surrounded by the char structure at the beginning of the experiment. Therefore, the thermal conductivity could be recalculated from the measured temperatures starting at 50 °C. In the case of the 10 and 20 K/min samples, the thermal conductivity remained almost unchanged over the entire temperature range. The samples heated at 30 K/min, on the other hand, showed temperature-dependent changes and an even greater scattering than during the first heating (see Figure 3.40 c)).
The investigations of the char morphology (see Figure 3.35) prove that the 30 K/min samples still show a grey colouring near the steel plates. This indicates that the intumescence reaction was not fully completed after the first heating and continued during the second heating. For this reason, changes in thermal conductivity were detected during the second heating. In contrast to this, the samples heated at 10 and 20 K/min are completely white and indicate that they were already oxidised before the second heating. For this reason, the calculated thermal conductivity values remained almost unchanged and, more importantly, in the same magnitude as the values at the end of the first heating.
On the basis of these results, the following conclusions can be drawn on the results of the reverse calculations: ① The reverse calculations make it possible to qualitatively evaluate the thermal conductivity behaviour of intumescent coatings. The absolute values, which are calculated with the finite difference method, only serve as rough reference values and should therefore always be checked for plausibility. ② For the interpretation and control of the calculation results it is indispensable to examine the morphology and the reaction state of the pore structure. ③ The quality of the reverse calculation results depends strongly on the measured temperatures as well as on the density and the specific heat capacity values. For this reason all experiments should be carried out with great care to avoid falsifying the results. At least two to three tests should therefore be carried out per series in order to estimate the degree of scatter. ④ The finite difference calculations can only be performed if a temperature gradient is present in the char. For this reason, the calculations can only be performed during heating phases. For the cooling phases, suitable material models are still needed in order to describe the thermal conductivity behaviour of intumescent coatings. ⑤ When recalculating the ther-

mal conductivity of the waterborne coating from the double heated test specimens, certain assumptions were made regarding the density and the specific heat capacity. As the results of the thermal conductivity depend on these assumptions, numerical simulations will be carried out in chapter 4, in order to verify the validity of the material properties.

3.4.6 Discussion

During the evaluation of the current state of research, it was shown that no standard procedure currently exists to evaluate the fire protection performance of intumescent coatings with regard to the heating rate dependency. Normally, the method of the *effective thermal conductivity* is often used. However, this method provides more contradictory results than other methods due to the assumptions that have to be made. For this reason, new evaluation approaches were chosen for the small-scale fire tests. The evaluation of the steel plate temperatures has proven to be particularly useful. The temperature is measured as part of the approval tests and does not require much effort in the preparation of the tests. The only addition to the existing procedure is that an unprotected test specimen has to be examined as a reference. By calculating the temperature difference between the unprotected and the protected test specimen, the fire protection effect of the intumescent coatings can be determined. The higher the temperature difference, the more effective the fire protection effect. In this way it could be shown that the insulation performance of the examined solvent- and waterborne coatings increases with increasing heating rates. Figure 3.41 shows the $\Delta\ T_{max}$ values as a function of heating rate. From the graphs it can be seen that the fire protection performance increases with higher heating rates, but reaches its maximum especially for the waterborne coating at 50 K/min. With regard to the experimental procedure, this behaviour seems to be plausible. If the samples are heated up to 1000 °C at a very high heating rate, the intumescent coating cannot absorb enough energy in the short time in order to react. Therefore, the investigated heating rates were limited within the test series to 70 K/min. Similar observations were already made by Cirpici et al. (2016) in their numerical investigations. In the same way, the expansion behaviour represented by the expansion factors ϵ_{final} given in Figure 3.41 as a function of heating rate can be explained.
If the reaction properties of intumescent coatings need to be investigated in more detail, it is advisable to calculate the first derivative of the measured steel plate temperature and thus the heating rate of the test specimens. In this way, the time of expansion and the phase of effective thermal protection can be clearly determined as it was explained in subsection 3.4.4.
The evaluation software that was implemented in MATLAB goes even one step further. With the help of this software, the actual thermal conductivity of intumescent coatings can be recalculated. However, in order to perform the calculations, the char temperatures measured at equidistant intervals and the heat storage capacity

$(\rho \cdot c_p)$ must be known. Compared to the current approval tests, a significantly higher effort in test preparation is required because of the additional thermocouples that need to be arranged in the steel plates through drilled holes. On the other hand, this way of test data evaluation enables to investigate the fire protection effect of intumescent coatings at the level of material properties and represents a novelty compared to the methods that are known so far.

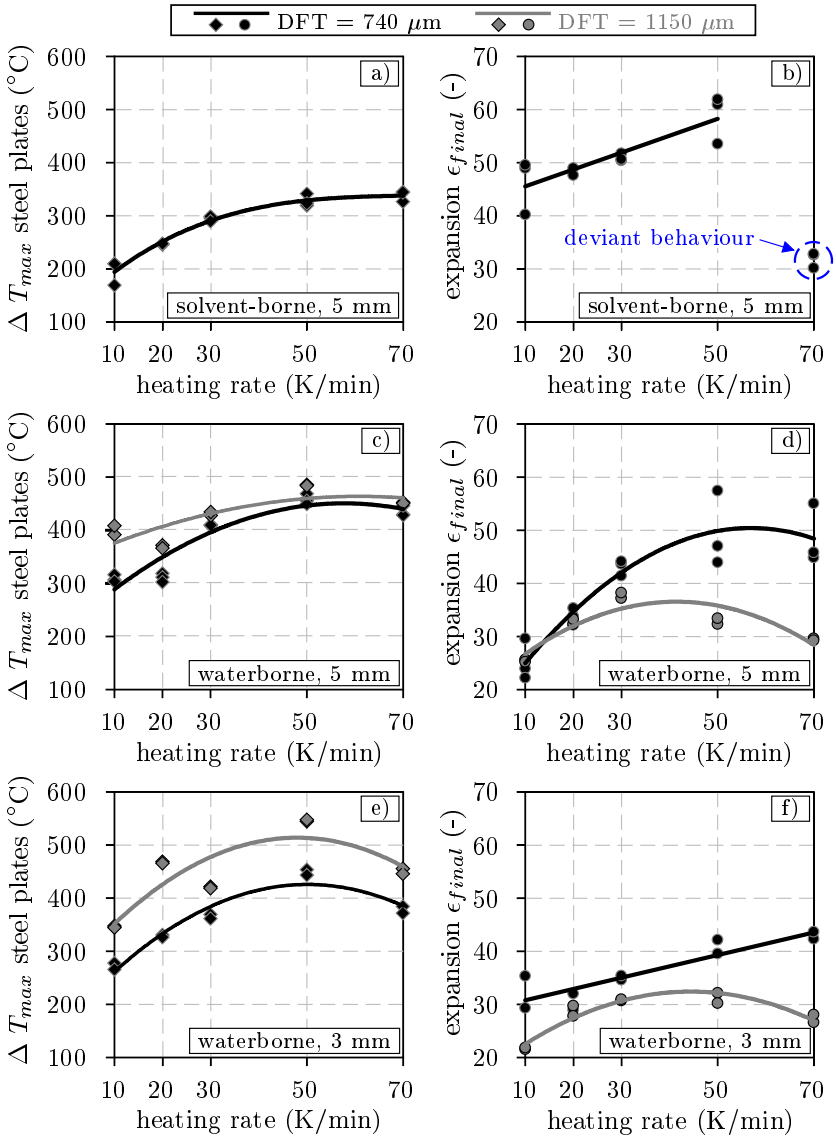

Figure 3.41: Heating rate dependency of the maximum temperature difference ($\Delta\ T_{max}$) between unprotected and protected steel plates (3 and 5 mm) and the expansion factor (ϵ_{final}) measured after the tests for a)-b) the solvent- and c)-f) the waterborne coating

3.5 Large-scale Fire Test

3.5.1 Test Specimens

Despite the numerous possibilities to examine the performance of intumescent coatings in laboratory or small-scale experiments, large-scale fire tests are essential. These tests are usually time-consuming in planning and execution and are therefore expensive. However, the tests enable to investigate the fire protection performance of intumescent coatings under geometrically and mechanically realistic conditions. By defining a specific fire scenario, assumptions are of course made which only represent a model fire based on reality. However, this is a generally accepted procedure in science.

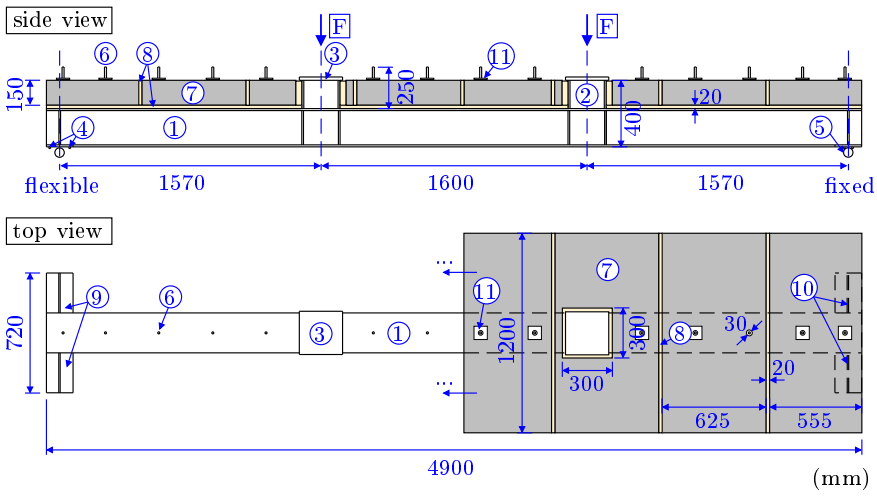

Figure 3.42: Schematic description of the loaded beam with integrated furnace cover in side and top view (length = 4.90 m, material: S235JR, dry film thickness (DFT) of the waterborne coating: 370 µm, three-sided fire exposure, mechanical loading: 60 % $M_{pl,Rd}$)

For intumescent coatings both the geometry of the protected steel profiles and the mechanical loading have a significant influence on the fire protection performance (see for example Häßler (2016)). Therefore, a large-scale fire test was carried out as part of the national research project IGF 19176 N in order to quantify the effects of scaling and loading on the insulation performance of a waterborne coating in case of a natural fire scenario. In this fire test, a total of three loaded and six unloaded

test specimens were examined. Beside the waterborne coating, a fire protection plaster and fire protection panels were investigated. As the fire protection plaster and the panels are not part of this thesis, reference is made here to the research report IGF 19176 N (Zehfuß et al. 2018).
The mechanically loaded test specimen of the waterborne coating was a steel beam HEA 240 (length: 4,900 mm, material: S235JR) with two load introduction points at one-third of the length as described in Figure 3.42. Torsionally stiff supports were formed by welding additional plates to the ends of the beam. Steel rolls were arranged under the supports to allow free rotation of the beam due to bending as well as thermal expansion due to temperature (only at the flexible support). In order to guarantee a three-sided fire exposure of the loaded beam, panels made of aerated concrete (thickness: 150 mm) were placed on the upper flange and fixed to the test specimen with threaded rods. As it was necessary to ensure sufficient smoke tightness during the test, all gaps between the concrete panels and the test specimen were filled with rock wool.
For monitoring reasons, the temperature of the loaded beam had to be measured during the fire test. For this reason, the test specimen was equipped with thermocouples type K (thickness: 0.51 mm) after sandblasting (SA 2 1/2) and before the application of the primer (dry film thickness: 75 μm). The arrangement of the thermocouples is documented in subsection 3.5.4. Data explaining the dry film thickness distribution of the waterborne coating along the test specimen are given in subsection 3.5.2.

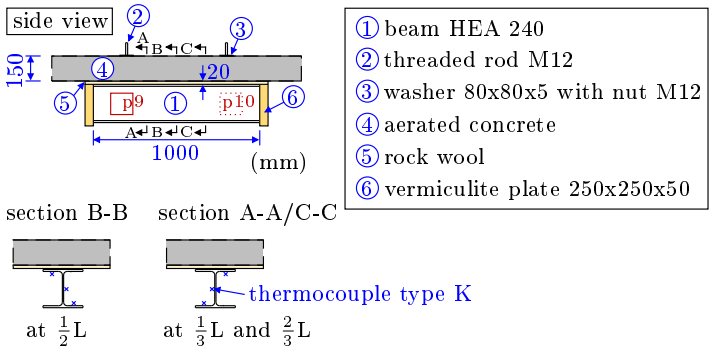

Figure 3.43: Schematic description of the unloaded reference beam with integrated furnace cover in side view (length = 1.00 m, dry film thickness (DFT) of the waterborne coating: 360 µm, three-sided fire exposure, plate thermocouples (p9 and p10) for the measurement of the gas temperature)

In addition to the loaded test specimen, an unloaded reference beam (HEA 240) with a length of 1,000 mm was investigated during the fire test (see Figure 3.43). By comparing the heating behaviour of the two test specimens, the influence of mechanical loading on the fire protection performance of the waterborne coating should be quantified. Therefore, similar to the loaded test specimen, the reference

beam was arranged below the furnace cover (aerated concrete panel) with the help of threaded rods. In order to ensure a three-sided fire exposure, the free ends of the test specimen were protected by additional vermiculite plates (thickness: 50 mm). The steel temperature of the reference beam was measured with type K thermocouples arranged in three measuring axes (A-A, B-B and C-C) as can bee seen in Figure 3.43. The gas temperature, on the other hand, was measured with plate thermocouples (p9 and p10) on both sides of the test specimen.
The third test specimen used during the large-scale fire test was an unloaded reference column (HEA 240, length: 1,000 mm). In contrast to the beams, the reference column was subjected to a four-sided fire exposure (see Figure 3.44). In order to ensure a heat flow perpendicular to the coated surface, the top and bottom of the column were protected by a vermiculite plate (thickness: 50 mm) and rock wool respectively. Following the recommendations of EN-13381-8 (2013), the steel temperature was measured 200 and 500 mm from the top of the column with the help of type K thermocouples. A total of six measuring points were arranged in each measuring axis (A-A and B-B). In this way, four flange and two web temperatures were measured in each measuring axis. At the level of the first measuring axis, the gas temperature was measured near the column using a plate thermocouple (p11). Since the column was positioned close to the furnace wall (ca. 500 mm), the gas temperature was measured right on the opposite side.

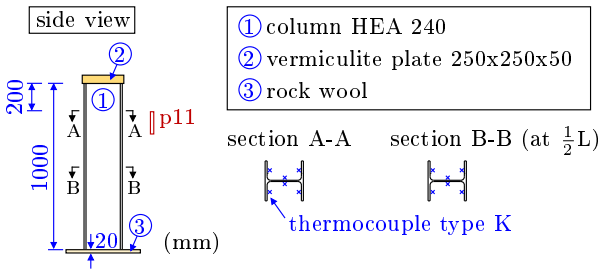

Figure 3.44: Schematic description of the unloaded reference column with a vermiculite plate on top and a rock wool cover on the bottom in side view (length = 1.00 m, dry film thickness (DFT) of the waterborne coating: 365 µm, four-sided fire exposure, plate thermocouple (p11) at the column side facing the furnace)

The arrangement of all three test specimens within the furnace is explained in subsection 3.5.3. Here, the test setup, the loading and the fire exposure are described in detail.

3.5.2 Material Properties

For the large-scale fire test, both the material properties of the structural steel and the thickness of the intumescent coating were required. For this reason, the

essential characteristics of both materials were determined prior to the test and are presented below.

Carbon Steel S235JR:

The large-scale fire test was design according to EN-13381-8 (2013). In this test standard it is recommended to load the test specimen with a maximum bending moment of 60 % of $M_{pl,Rd}$ (plastic moment resistance) at the beginning of the test (t = 0). In order to define the load utilisation factor correctly, tensile strength tests had to be performed to quantify the actual material strength of the loaded beam (S235JR). These tests were performed at the Institute of Materials Science, Leibniz University Hannover, using a universal testing machine Zwick Z250. The tests were performed according to EN-ISO-6892-1 (2009) at room temperature. The sample shape was of type B and had an initial gauge length of $L_0 = 50$ mm.
The results of the tests are given in Figure 3.45. Here three stress-strain curves are shown for both the web and the flange material. For both excess strengths are observed. With 357 - 364 MPa (average: 360 MPa), the yield strength in the web clearly exceeds the nominal properties of structural steel S235JR. In the flanges the excess strengths are slightly smaller but still between 316 and 327 MPa (average: 321 MPa). Despite the high strengths, the strains at which rupture occurs are between 25.8 and 29.9 % as it was expected (see Table 3.9). A reduced fracture strain (20.9 %) is only observed for sample *web-3*.

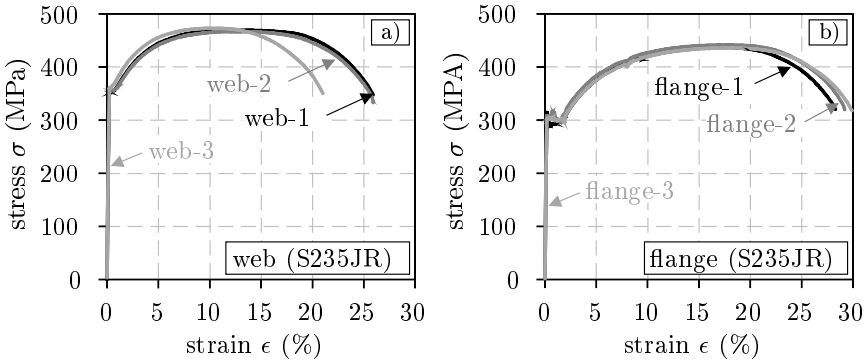

Figure 3.45: Results of the tensile strength tests performed for the loaded beam HEA 240: a) stress-strain curves of the web material and b) stress-strain curves of the flange material

A standard-compliant determination of the Young's modulus was not possible within the scope of the tensile strength tests. However, in order to evaluate the elastic behaviour of the material, the linear slope of the σ-ε-relationship was measured with a sample each for the web and the flange. For this purpose, the samples were loaded up to a maximum stress of 260 MPa. After measuring the slope, the samples were unloaded again. This procedure was performed five times for each sample. A subsequent averaging of the test data shows that the linear elastic slope

in the web is E = 210,344 MPa and in the flanges E = 211,233 MPa. Although the Young's modulus is not required for the calculation of the load-bearing capacity of the beam, it will be used later for the modelling of the material behaviour within the thermomechanically coupled simulations in section 4.5.

Table 3.9: Results of the tensile strength tests acc. to EN-ISO-6892-1 (2009) for the carbon steel (S235JR) of the loaded beam: R_{eH}: stress before the first drop in force, F_m: maximum force, R_m: tensile strength, A: strain at rupture, a_0: initial thickness, b_0: initial width and S_0: initial cross-section

Sample ID	a_0 (mm)	b_0 (mm)	S_0 (mm^2)	R_{eH} (MPa)	F_m (kN)	R_m (MPa)	A (%)
web-1	5.035	16.007	80.60	357	37.86	470	25.8
web-2	5.038	16.010	80.66	360	37.66	467	25.8
web-3	5.038	16.015	80.68	364	38.19	473	20.9
flange-1	5.041	15.381	77.54	327	33.90	437	28.2
flange-2	5.047	16.005	80.78	321	35.66	442	29.0
flange-3	5.041	15.999	80.65	316	35.17	436	29.8

Waterborne Intumescent Coating:

The dry film thickness of the waterborne coating was designed according to the national approval of the product. As the approval only regulates the thickness for a fire exposure due to the standard fire curve, a fire resistance period of 30 minutes (R30) was taken as a basis. Depending on a three-sided fire exposure and a profile factor A/V of 147 m^{-1}, the minimum value of the dry film thickness was set to 350 μm. This thickness was chosen for all three test specimens equally in order to evaluate the differences in fire exposure between beam and column (A/V = 178 m^{-1}) on their heating behaviour.
Before applying the coating, all test specimens were sandblasted (SA 2 1/2). In the next step the thermocouples (type K) were attached. Only then the test specimens were coated with the approved primer. The dry film thickness of the primer was defined by the manufacturer to 65 μm. This minimum value was maintained on average for all three test specimens (loaded beam: 69 μm, reference beam: 67 μm and reference colum: 70 μm). After the primer was dry, the waterborne intumescent coating was applied via airless spray. After drying, the dry film thickness of the coating was measured for the first time. In areas where the coating was too thick, it was planed off mechanically. This allowed the desired dry film thickness to be set very precisely. At this point it should be noted that all coating work and curing has been carried out by trained personnel of the product manufacturer. The author would like to express his gratitude for this work.
The final measurement of the dry film thickness was carried out one week before the fire test and approximately six weeks after application using a digital thickness gauge (QNix 8500, Automation Dr. Nix). The measurements were performed systematically at predefined locations. For this purpose axes were set over the length of the test specimens. The same axes were used after the fire test to measure the thickness of the formed char. Figure 3.60 shows exemplarily the measuring axes

and points (A-M) over the cross-section of the beam. Additional measuring points (N, O and P) were defined for the reference column. In this way the thickness of the loaded beam was measured in 31 axes. This corresponds to a total of 403 measuring points. Due to their reduced lengths, the measurements on the reference beam and reference column were only carried out in 7 axes (91 measuring point for the beam and 112 for the column).

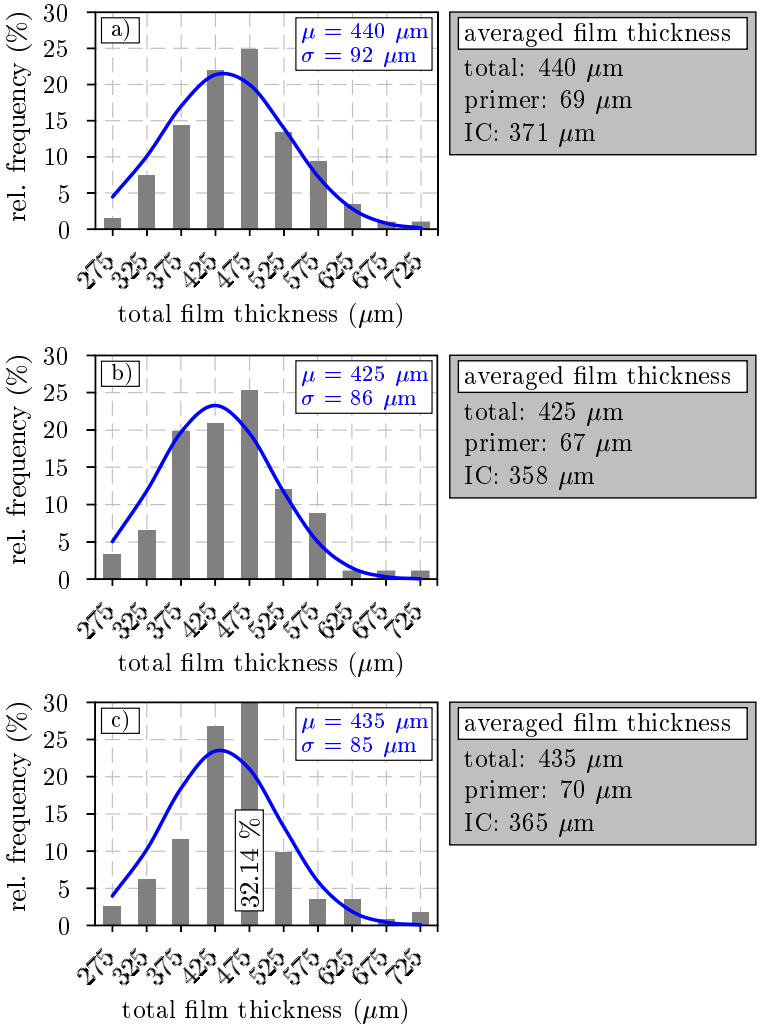

Figure 3.46: Distribution of the measured dry film thickness (primer and intumescent coating (IC)) applied on: a) the loaded beam, b) the reference beam and c) the reference column

The results of the dry film thickness measurements are given as a distribution functions in Figure 3.46. Both the mean values (μ) and the standard deviations (σ) are very similar for all three test specimens. When the primer is subtracted,

the dry film thickness of the waterborne coating applied on the loaded beam is 371 μm. With 358 and 365 μm the dry film thicknesses on the reference beam and column are slightly thinner. However, the initially defined minimum value of 350 μm is met by all three test specimens.

3.5.3 Test Setup and Fire Exposure

The large-scale fire test was carried out at the Institute of Building Materials, Concrete Construction and Fire Safety at the Technical University of Braunschweig, Germany. For this purpose the ceiling test bed *Loreley* was used. Generally, test specimens up to 10 m length can be tested here. However, in case of the large-scale fire test inner furnace dimensions of 4.0 x 5.4 m were sufficient. As can be seen in Figure 3.47 a) the loaded beams should span over the short side of the furnace and be placed on steel rolls. The steel rolls on the left side were arranged between boundary plates to form a horizontally fixed support. On the opposite side, a flexible support was realised in order to ensure free thermal elongation of the loaded beam. Three oil burners were arranged on each inside of the furnace walls perpendicular to the loaded beams in order to guarantee a sufficient heat generation. The extraction of combustion gases was provided by an air duct in the middle of the furnace.
In Figure 3.47 b) all three intumescent coating test specimens (loaded beam, reference beam and reference column) are shown together with the short columns that were tested within the large-scale fire test as well. The loaded beam and the reference column are already located at their final position. The extensions for load introduction are already attached to the loaded beam via screw connections (4 x M16, 10.9). The reference beam, on the other hand, was installed after the furnace was covered by aerated concrete panels.
Figure 3.47 c) shows the test setup from the interior of the furnace. Here, the final position of the reference beam under the aerated concrete panel can be seen. In order to provide sufficient smoke tightness during the test, additional concrete panels were placed vertically on each side of the loaded beams. Since the panels were covered with rock wool, the loaded beams were able to bend individually during the test without forming any gaps inside the furnace cover.
The state of the experimental setup, in which the furnace is already covered by concrete panels and the stabilisation structure of the load introduction points is installed is given in Figure 3.48 a). The stabilisation structure was necessary to prevent the hydraulic cylinders from tilting and the loaded beams from torsion. However, in the longitudinal direction, the beams could expand unhindered as the load introduction points were linearly guided by square pipes. Around the test specimens (the position of the loaded beam and the reference beam is marked with blue dashed lines) several monitoring devices were arranged. In order to measure the furnace temperature, plate thermocouples were installed. These thermocouples can be recognised by cylindrical rods protruding from the concrete panels.

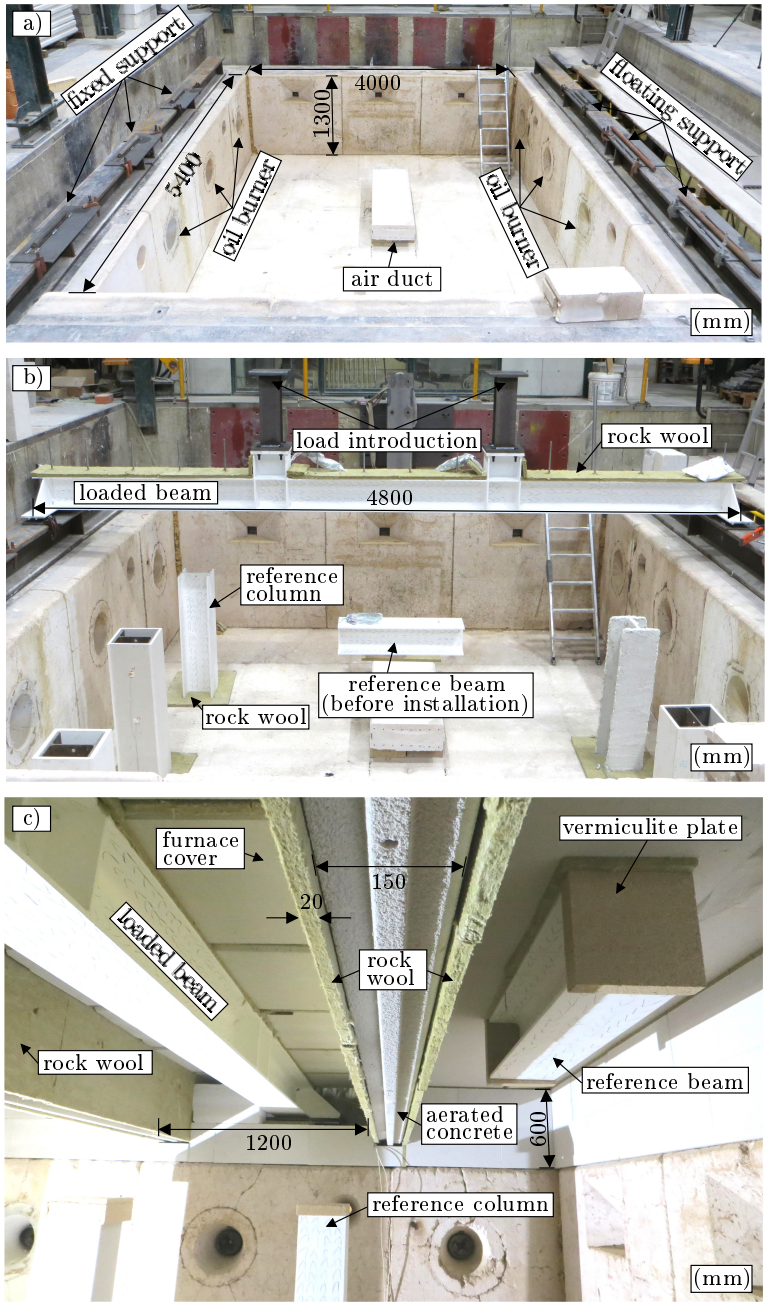

Figure 3.47: Test setup of the large-scale fire test: a) dimensions of the furnace and arrangement of the supports, b) positions of the loaded beam and reference column and c) orientation of all three test specimens inside the furnace

The deflections of the loaded beam were measured in the load introduction points using potentiometers (pot). For this purpose, threaded rods were welded to the load introduction plates (see Figure 3.48 b)), to which steel cables were attached. In this way it was possible to measure the vertical deformation of the beam on both sides of the load introduction points ($v_{I,A}, v_{I,B}$ and $v_{II,A}, v_{II,B}$).

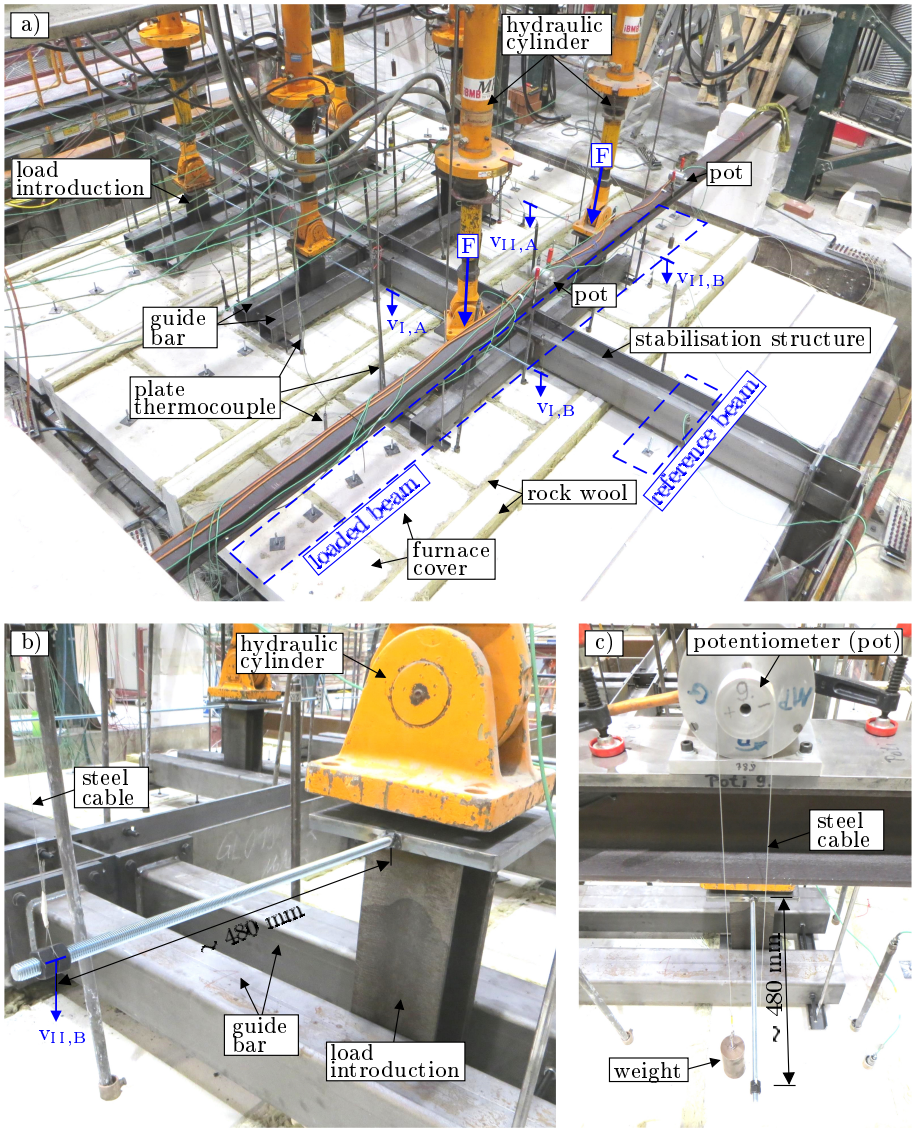

Figure 3.48: Test setup of the large-scale fire test: a) arrangement of the test specimens, the hydraulic cylinders, the potentiometers (pot) and the stabilisation structure, b) setup of the vertical displacement measurement and c) arrangement of the potentiometer including weight and steel cable

Figure 3.48 c) shows the functionality of the potentiometer. One end of the steel cable is attached to the threaded rod. The other end is attached to a weight (approx. 1.0 kg). Since the cable is wound on a thread, the potentiometer is set in rotation as soon as the test specimen pulls on the steel cable due to its vertical deformation. The weight at the other end keeps the steel cable taut.
The large-scale fire test was based on the natural fire scenario (see Figure 3.49) that was already described in subsection 3.3.2. The fire scenario is based on a simulation taking a small industrial building (500 m^2) with a fire load density of 300 MJ/m^2 into account.
Before the test specimens were exposed to the natural fire, the mechanical load had to be applied to the loaded beam. For this purpose, the pressure of the hydraulic cylinders was increased incrementally. Within each increment the load was increased by 5 kN within 10 seconds and kept constant for further 20 seconds. In this way a load of 85 kN was applied by each cylinder (see the enlargement in Figure 3.49). The load was kept constant for further 15 minutes before the oil burners were ignited and the time of fire exposure began. Until the maximum furnace temperature was reached (31 minutes), the oil burners were controlled automatically. The cooling phase was initiated by gradual throttling and shutting down of single burners. This was done manually.

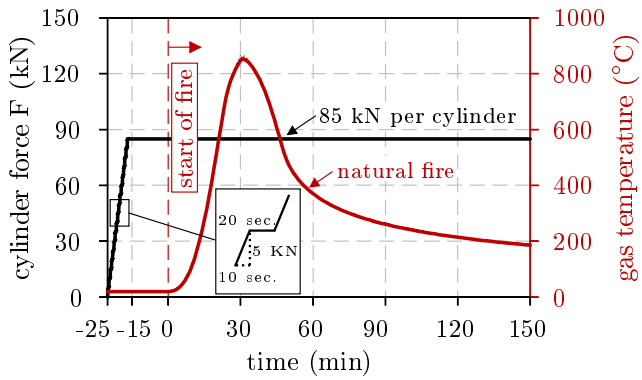

Figure 3.49: Designed cylinder force and natural fire as a function of time during the large-scale fire test

During the whole fire test the mechanical load remained constant. Based on the arrangement of the hydraulic cylinders, the applied loads corresponded to a constant bending moment in the beam of 133.5 kNm. The dead load of the beam (g_1 = 0.60 KN/m) and the dead load of the aerated concrete panels (g_2 = 1.50 KN/m) also caused a bending load. All load components together resulted in a total bending moment of $M_{Ed,fi}$ = 139.5 kNm. In relation to the cross-sectional load-bearing capacity, the loading corresponded to a utilisation factor of μ_0 = 0.57 at the beginning of the test. The plastic bending resistance of the beam $M_{pl,Rd}$ was calculated using the results of the performed tensile strength tests as illustrated in Figure 3.50.

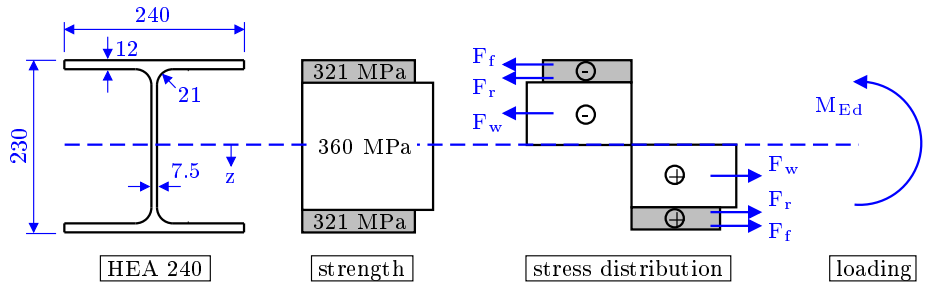

Figure 3.50: Calculation of the bending resistance $M_{pl,Rd}$ of the loaded beam (HEA 240) at room temperature in consideration of the tensile strength test results. Dimensions of the profile are given in (mm).

In order to calculate the plastic bending resistance, the nominal dimensions of the cross-section and the mean values of the measured yield strengths were used. In the first step the load components of each cross-section part, such as the flange F_f, the radius F_r and the web F_w, were calculated according to the following equations:

$$F_f = 24\ cm \cdot 1.2\ cm \cdot 32.1 \frac{kN}{cm^2} = 924.48\ kN \tag{3.5}$$

$$F_r = (2.1\ cm \cdot 2.1\ cm - \frac{\pi}{4} \cdot (2.1\ cm)^2) \cdot 32.1\ \frac{kN}{cm^2} = 30.38\ kN \tag{3.6}$$

$$F_w = \frac{20.6\ cm}{2} \cdot 0.75\ cm \cdot 36.0 \frac{kN}{cm^2} = 278.10\ kN \tag{3.7}$$

In the next step the bending resistance of the loaded beam HEA 240 was calculated as the product of the cross-sectional forces and the associated lever arms z_f, z_r and z_w, as demonstrated below:

$$M_{pl,Rd} = 2 \cdot F_f \cdot z_f + 4 \cdot F_r \cdot z_r + 2 \cdot F_w \cdot z_w = 242\ kNm \tag{3.8}$$

$z_f = 10.90\ cm$:	centroid of the flange
$z_r = 8.20 + 1.63\ cm$:	centroid of the radius
$z_w = 5.15\ cm$:	centroid of the half of the web

In contrast to EN-13381-8 (2013), the beam was not loaded with 60 % of the plastic moment capacity, but only with 57 %. The reason for the slight reduction in mechanical load was due to the fact that in addition to the beam coated with the intumescent coating, two other beams were tested simultaneously. One of the beams was clad with fire protection plaster and the other with fire protection boards. Especially fire boards tend to form cracks if they are exposed to high bending loads. For this reason, fire protection boards are normally applied to beams after the beams have been exposed to their dead loads. This ultimately corresponds to building practice. However, due to the given test setup, such a sequence was not possible. The beam first had to be clad and was then subjected

to the mechanical load. In order to find a compromise, the mechanical load was slightly reduced. However, the load was still high enough to achieve the objectives of the experiment.

3.5.4 Measurement and Test Documentation

As already mentioned in the description of the test setup, numerous parameters were measured during the fire test. The corresponding measurement setup of the loaded beam, for example, is schematically illustrated in Figure 3.51. In the side and the top view, the arrangement of the plate thermocouples is shown. A total of eight plate thermocouples were arranged at a distance of approx. 150 mm from the test specimen in order to measure the furnace temperature close to the beam.

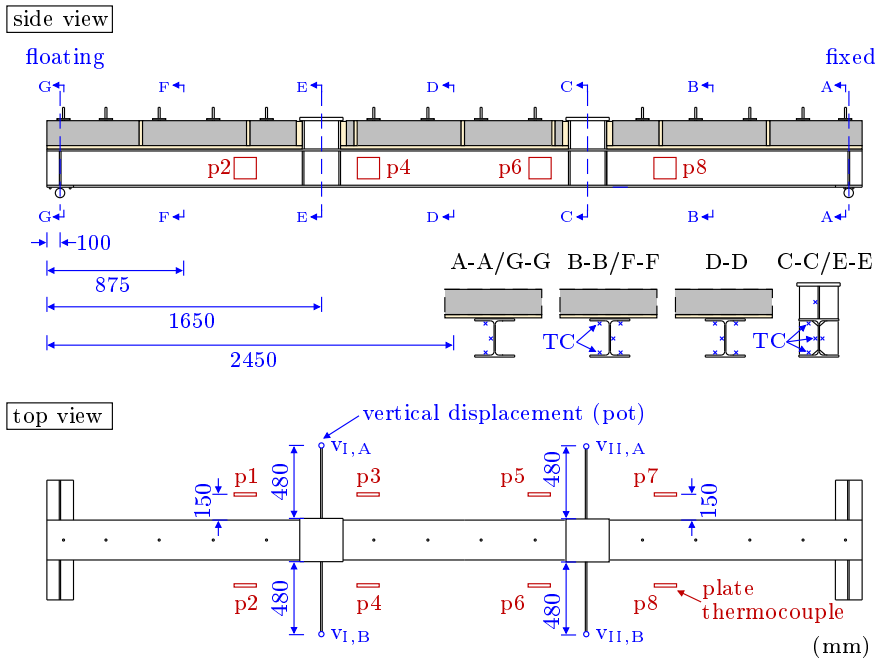

Figure 3.51: Measurement setup of the large-scale fire test: thermocouples (TC) type K for the steel temperature, plate thermocouples (p1-p8) for the gas temperature and potentiometers (pot) for the measurement of the vertical displacement of the loaded beam at the points of load application (in the top view the furnace cover is not represented)

A further 31 thermocouples (type K, wire thickness: 0.51 mm) were applied directly to the test specimen to measure the temperature of the beam during the test. The thermocouples were arranged in a total of seven measuring axes. In accordance with the specifications of EN-13381-8 (2013), the thermocouples were arranged in the middle of the web and in the quarter points of the flanges. The thermocouples

were attached to the steel beam by spot-welding. To secure the position, the thermocouples were additionally pined by welding wire brackets as can be seen in Figure 3.52. All thermocouples were led out of the beam and passed along the top flange to both ends of the test specimen. As the thermocouples were later covered by rock wool, a direct fire exposure of the thermocouples was prevent. The remaining parts of the thermocouples were coated together with the beam, first with the primer and then with the intumescent coating. For this reason, the remaining parts of the thermocouples were also fire protected.

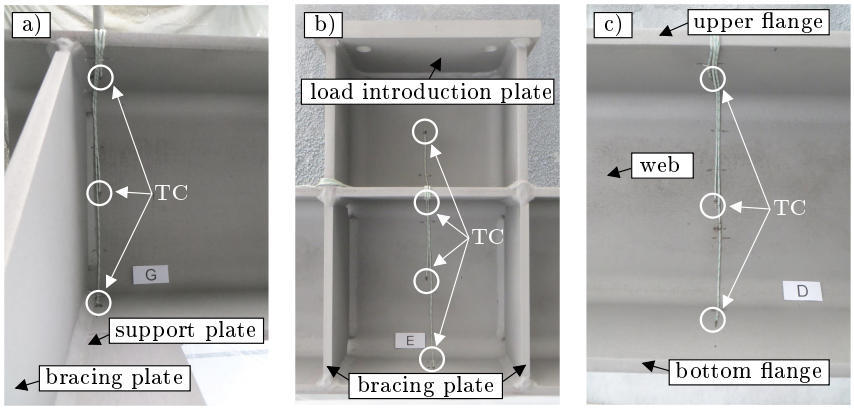

Figure 3.52: Exemplary illustration of the thermocouple application (type K, wire thickness: 0.51 mm) at the web as well as at the upper and lower flange of the loaded beam in the axes G (floating support), E (point of load introduction) and D (midfield) after sand blasting

The deflection of the beam was monitored at a total of four measuring points. For this reason, potentiometers were arranged above the test specimen at a lateral distance of 480 mm from the load introduction plate as shown in the top view of Figure 3.51. The potentiometers were connected to a measurement amplifier QuantumX MX840B in order to record the beam deflections. Since the fire test was quasi-static, it was sufficient to define a measuring rate of 5 Hz.
The furnace temperature and the steel temperatures of all test specimens were recorded via the central data processing of the test stand *Loreley*. Due to the large amount of data, the temperatures could only be recorded at a measuring rate of $\frac{1}{30}$ Hz (every 30 seconds). The laboratory tests carried out previously have shown that a measuring rate of 2 Hz is more suitable to detect the initiation of the expansion reaction based on the changes in steel temperature. However, the measuring rate of $\frac{1}{30}$ Hz was also sufficient to recognise the insulation effect of the formed char.
For the sake of completeness, it should be noted that the measurement setups for the reference beam and the column are documented in Figure 3.43 and 3.44. Since the test specimens were unloaded, only plate thermocouples and type K thermocouples were provided in order to measure the furnace and the steel temperatures.

3.5.5 Results

The results of the performed large-scale fire test are presented in the following, starting with the loaded beam. In the first step, the mechanical behaviour of the beam is discussed and the measured deflections are described. In the second step, the heating behaviour of the beam is explained, before the reaction behaviour of the intumescent coating and its morphology are discussed.

Loaded Beam HEA 240:

The correlation of the measured cylinder forces and the associated deformation of the loaded beam are shown in Figure 3.53. Since the cylinder forces were incrementally increased, an incremental increase can also be detected in the deflection of the beam. All four potentiometers recorded nearly the same deflections. For this reason, in Figure 3.53 b) and d) only the results of the measuring point $v_{I,A}$ are shown. Here it can be seen that the deformation stagnates at 18.5 mm after the full cylinder forces are applied.

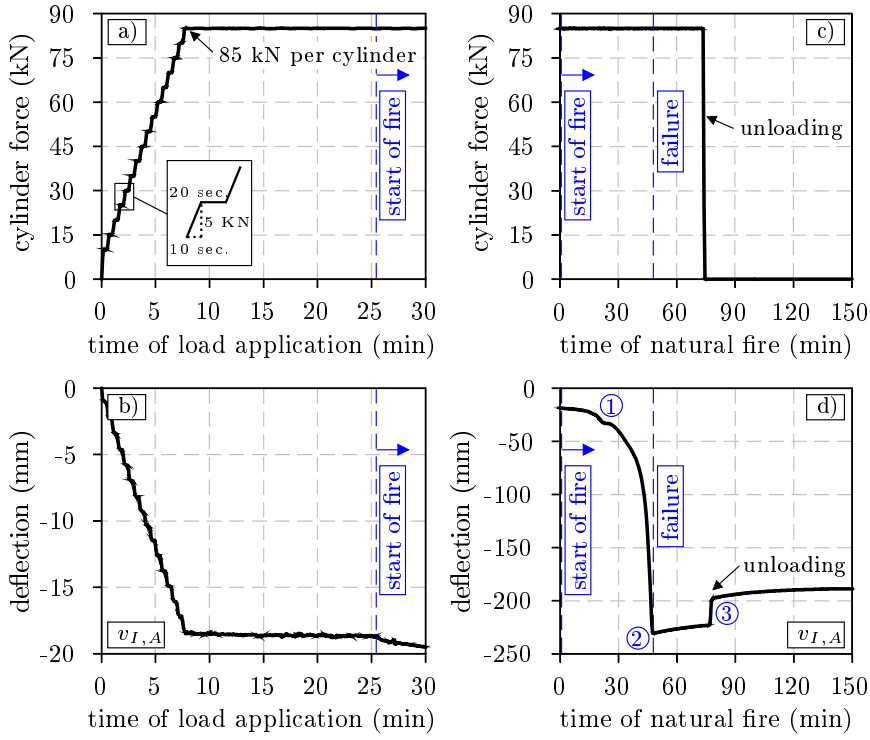

Figure 3.53: Measured cylinder forces and associated deflection of the loaded beam during load application (a-b) and natural fire exposure (c-d)

The deflection remains constant during the whole time until the oil burners are ignite and the natural fire exposure starts. From this point on the deflection starts

to increase. This is due to the thermal elongation and especially the temperature-induced curvature of the beam. In the first minutes of fire exposure, the steel temperatures are too low to cause the deflections due to the reduction of the Young's modulus. According to EN-1993-1-2 (2010), this occurs at temperatures above 100 °C. Only with increasing test duration and steel temperatures the effects of thermal elongation and stiffness reduction seem to superimpose. However, after 22 minutes of fire exposure, the deflection stagnates at 32.5 mm (see point ① in Figure 3.53 d)). At this point in time, the intumescent coating expands and develops its fire protection effect. The char formation slows down the heating of the beam, resulting in almost no increase in deflection. However, this effect lasts for only three minutes. Then, the deflection of the steel beam increases again. With every minute of the fire test, the deflection of the beam increases disproportionately until it reaches its maximum (230 mm) after 48 minutes. The high increase in deflection indicates the exceeding of the load-bearing capacity and, therefore, the failure of the loaded beam (see point ② in Figure 3.53 d)). The beam heated up to such an extent that the load-bearing capacity was exceeded due to the temperature-induced reduction in strength. In order to prevent further bending of the test specimen, the hydraulic line of the coated beam was closed. After 74 minutes the test specimen was completely unloaded, which is accompanied by the decrease in deflection to approx. 205 mm (see point ③ in Figure 3.53 d)). In the subsequent cooling phase, the deflection of the beam decreases further and reaches a value of 188 mm at the end of the test.

The different reaction stages of the waterborne coating and the deflection behaviour of the loaded beam during the fire test are illustrated in Figure 3.54. The pictures were taken by a fire room camera, which was installed in one of the furnace walls. Here, the expansion of the intumescent coating (recognised by the black colouring after 22 minutes) and the crack formation in the char perpendicular to the longitudinal axis of the beam (see picture at 32 minutes) can be seen. The white colouring of the formed char after 32 minutes indicates that the coating was already thermally decomposed. For this reason, the intumescent coating offered only a short period of effective fire protection, which led to the failure of the beam. The state of failure is impressively demonstrated by the strong deflection of the beam.

In order to better understand the mechanical behaviour of the loaded beam and the fire protection performance of the intumescent coating, the heating behaviour of the beam must be examined. Therefore, Figure 3.55 shows the steel temperatures and the corresponding furnace temperatures in the measuring axes A-A, B-B, C-C and D-D. Here, the course of the furnace temperature is divided into two parts. In the heating phase, the temperature increases almost bilinearly and reaches a maximum temperature of 818 °C in axis D-D after 31 minutes. Afterwards the cooling phase occurs. This phase also takes place in two different steps. In the first step (31 to 90 minutes), the temperature decreases rapidly. In the second step (90 to 140 minutes), the decrease in temperature slows down considerably. Although the curves of the furnace temperature show certain deviations, they almost correspond to the nominal fire curve defined in Figure 3.49.

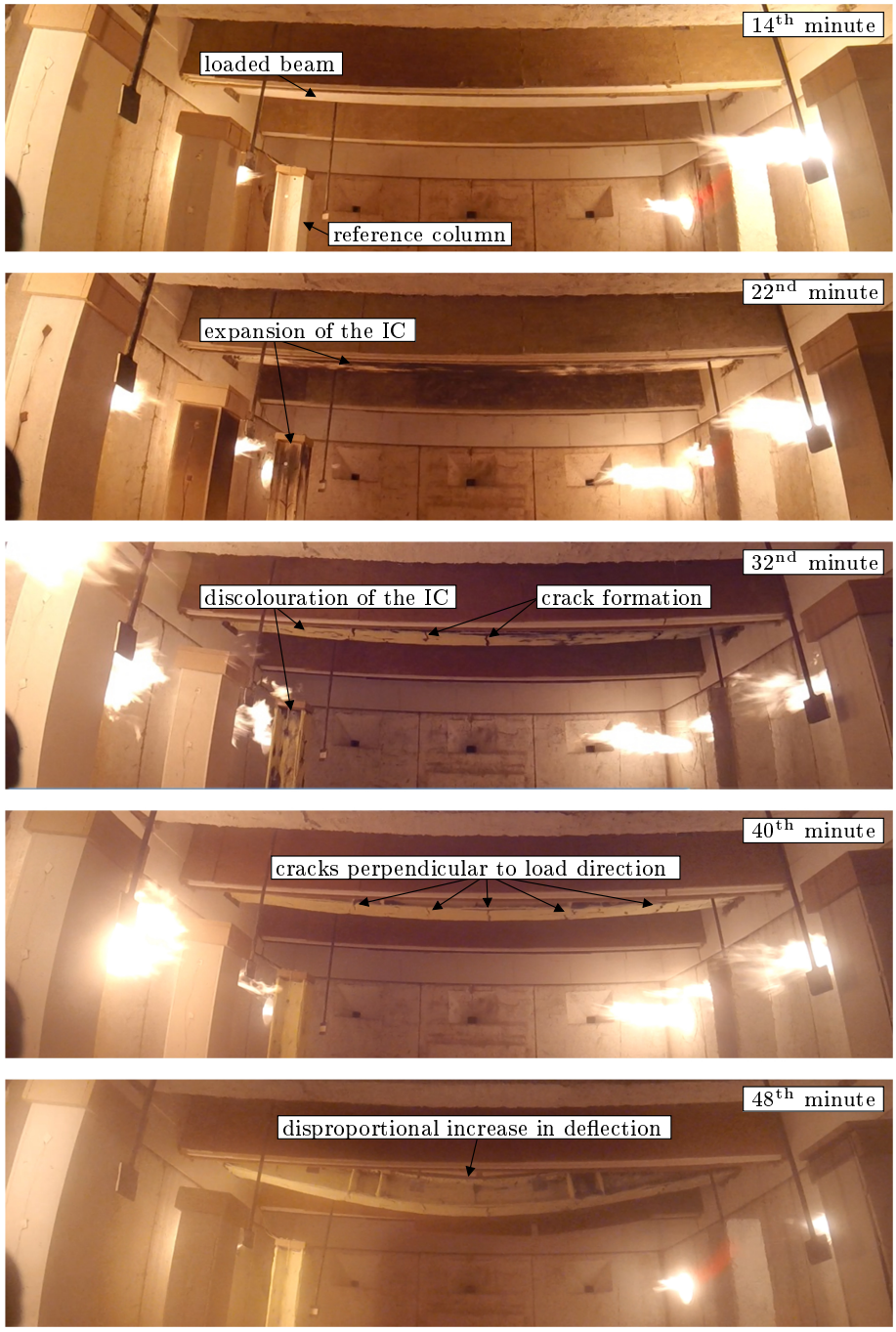

Figure 3.54: Reaction states of the waterborne intumescent coating and deflection behaviour of the loaded beam until the onset of structural failure (48^{th} minute)

Due to the course of the furnace temperature, the course of the measured steel temperatures is also divided into two parts. However, depending on the section area (bottom flange, web or upper flange) the maximum temperatures are different. On the other hand, what the steel temperatures have in common is the time offset to the furnace temperature, which is due to the thermal inertia of the test specimen. The images of the fire room camera reveal after 22 minutes that the waterborne coating had already reacted. The diagrams in Figure 3.55 show that during this time a change in temperature increase occurs. This effect is even noticeable in the upper flange of the loaded beam although its heating behaviour is significantly influenced by the furnace cover placed on top. However, in the bottom flange and in the web the effect of the reduced temperature increase due to the char formation is even more pronounced.

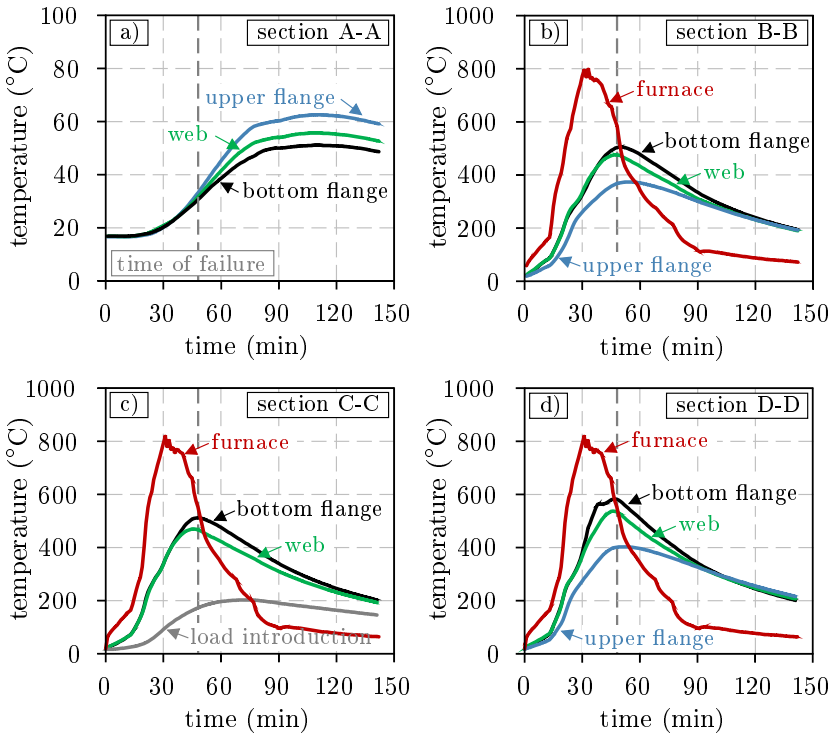

Figure 3.55: Measured steel temperatures of the loaded beam (HEA 240) in the measuring axes A-D including the furnace temperatures and the corresponding time of failure (48^{th} minute)

The thermal protection effect of the waterborne coating can be quantified in analogy to the small-scale fire tests by means of the derivation of the steel temperature over time. Figure 3.56 shows the derivation together with the corresponding steel temperature of the bottom flange in axis D-D. The course of the derivation curve shows that the reaction of the coating started after 20 minutes. At this point in time the steel temperature reached 210 °C. For comparison: the initial temperature

in the small-scale fire tests was 196 °C for the 3 mm steel plates and 172 °C for the 5 mm steel plates (see Tables 3.7 and 3.8). Considering the fact that the beam has a lower section factor (147 m^{-1}) and a lower dry film thickness (371 μm) than in the small-scale tests, this result seems to be plausible.

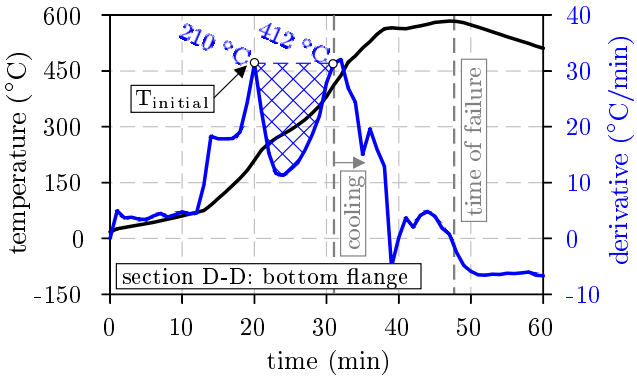

Figure 3.56: Steel temperature of the loaded beam (HEA 240) and its time derivative measured in the bottom flange of axis D-D

With the onset of char formation, the thermal protection effect of the waterborne coating also began. This is indicated by the significant decrease in heating rate. However, the period of effective fire protection lasted only 11 minutes, since the maximum heating rate of 31 K/min was reached again after 31 minutes and at a steel temperature of 412 °C. A further increase in heating rate did not occur hereafter, since the cooling phase of the natural fire began. Nevertheless, due to the thermal inertia, the test specimen continued to heat up, but only at a steadily decreasing heating rate. The maximum steel temperatures were reached after 48 minutes. Then, the steel temperatures decreased, which can be identified by the negative values of the derivative. This state was equivalent to the failure of the beam. The highest steel temperatures were measured in axis D-D in the middle of the beam (see Figure 3.55 d)). While a maximum steel temperature of 584 °C was reached in the bottom flange, the steel temperatures in the web and the upper flange were 537 and 403 °C, respectively. With increasing distance from the center of the beam towards the supports, the temperatures decreased as can be seen in Figure 3.55 c), b) and a). Therefore, a temperature gradient was present not only over the height but also over the length of the beam.
Since the measuring axis A-A was outside the furnace, the lowest steel temperatures (63 °C) were measured here. In axis C-C, the measuring point of the upper flange failed during the fire test. Therefore, the temperature of the load introduction (see Figure 3.55 c)) is shown here as an alternative. Despite the fact that the load introduction was thermally protected with rock wool, the maximum temperature still reached 203 °C. After reaching the ultimate limit state and the onset of the cooling phase, a homogenisation of the steel temperatures took place. At the end of the test, the same temperatures (205 °C) were present in all parts of the loaded

beam (upper flange, web and bottom flange), except the supports and the load introduction.

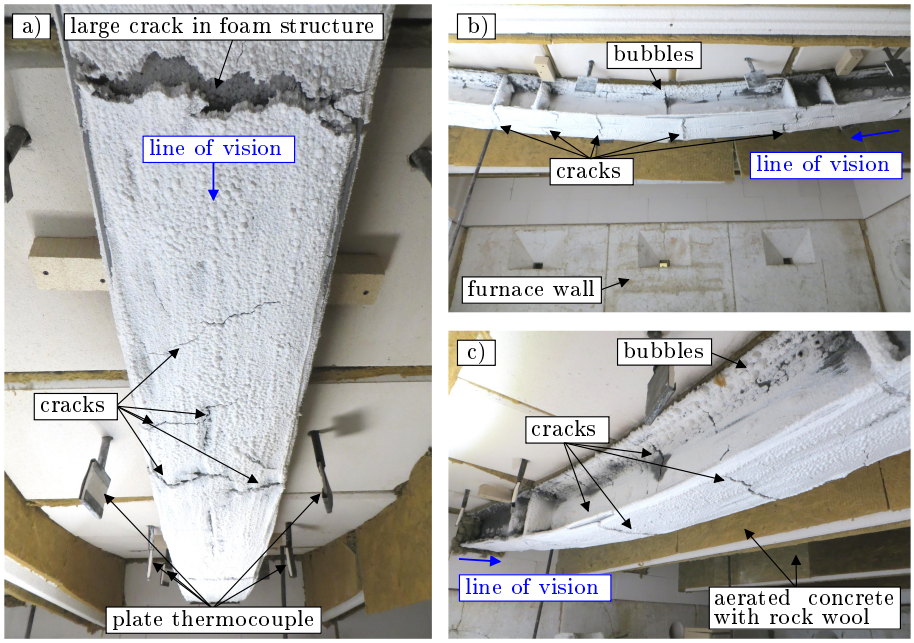

Figure 3.57: Illustration of the loaded beam (HEA 240) after the large-scale fire test from different directions

After the test setup cooled down during the night, the morphology of the formed char could be examined. The condition of the loaded beam after the fire test is shown in Figure 3.57. Here, numerous cracks of different sizes can be seen in the white char structure. These cracks are mainly located on the underside of the bottom flange and are, among others, due to the mechanically induced deflection of the beam. However, a distinction must be made between cracks that were already formed during the expansion of the coating and cracks that only occurred when the ultimate limit state of the beam was reached. For example, the large crack in the foam structure shown in Figure 3.57 a) probably occurred only towards the end of the fire test, which can be deduced from the irregular teared edges. Cracks that occur during the expansion or melting phase of intumescent coatings show filament-like crack flanks that indicate a time-dependent, viscous reaction process. A corresponding example of such a crack formation is shown in Figure 3.58 c) for the edge of the bottom flange. The reason for this crack is the convex shape of the flange edge and the limited ability of the waterborne coating to expand in transverse direction. This observed behaviour confirms the findings in literature (see Figure 2.39), even if they have only been derived from standard fire tests.
On the basis of the measured steel temperatures, it can be seen that both the geometrically and mechanically induced cracks reach a size (up to 20 mm) that

influences the thermal behaviour of the beam. This becomes particularly clear by the temperature of the bottom flange in axis D-D. Both the higher magnitude and the deviating course of time-temperature curve compared to the other measuring axes is assumed to be due to the crack formation in the middle of the beam.

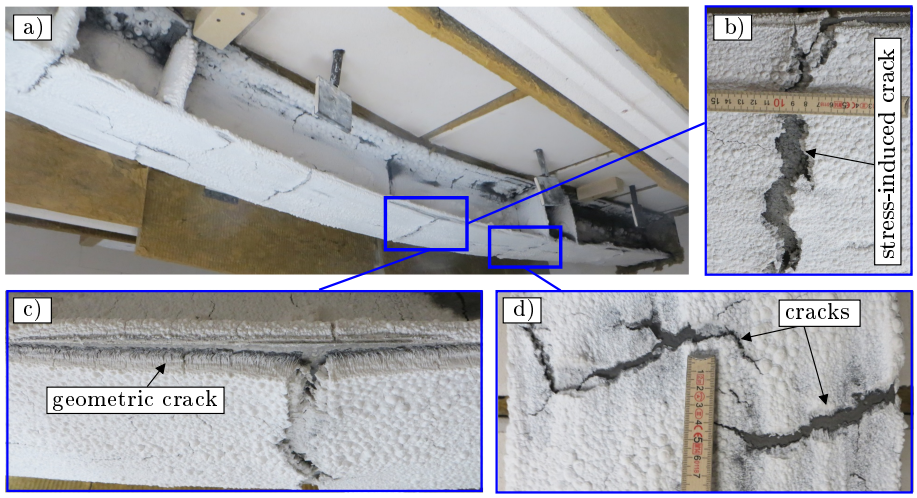

Figure 3.58: Geometrical and stress-induced cracks within the foam structure of the waterborne coating applied on the loaded beam

In addition to the cracks, bubbles several centimetres in size were also observed in the char structure. The bubbles were mainly found in the area of the supports (see Figure 3.59 a) and b)). Both closed and open bubbles could be observed here. While the closed bubbles are common for the expansion behaviour of intumescent coatings, the bubbles with holes were observed for the first time. Bubbles with subsequently closed holes could also be observed in the remaining parts of the test body (see Figure 3.59 c) and d)). In contrast to the area of the supports, however, these were significantly smaller. This type of bubble formation can possibly be explained by the viscous phase of the coating, in which individual bubbles burst and collapsed due to the low heating rate of the natural fire. After bursting the bubbles were filled again by the post-foaming char material. This, however, is an assumption and needs further systematic investigations. In this context, it must also be clarified why such a bubble formation was only observed on the upper flange and in the shadowing areas of the beam.
In addition to the documentation of the crack formation and the bubble shapes, the thickness of the formed char structure was also determined after the test by means of a measuring needle in several measuring paths along the upper and bottom flange and the web. The measured char thicknesses are plotted as bar charts in Figure 3.60 over the beam length.
As can be seen, the char thickness of the waterborne coating is more uniform in the upper and the bottom flange compared to the two sides of the web. The average

values for the upper and the bottom flange are approximately 13 and 11 mm, respectively. A similar averaged char thickness (12 mm) is also present in the web. However, this thickness is subjected to much greater fluctuations. This is due to the dry film thickness of the coating. At the upper and the bottom flange, excess material was removed with a planer. Therefore, a completely even dry film thickness was achieved. However, this could not be achieved in the area of the roll fillets and in the transition area to the web. For this reason, the dry film thickness here was comparatively uneven, which led to the striking formation of the char structure.

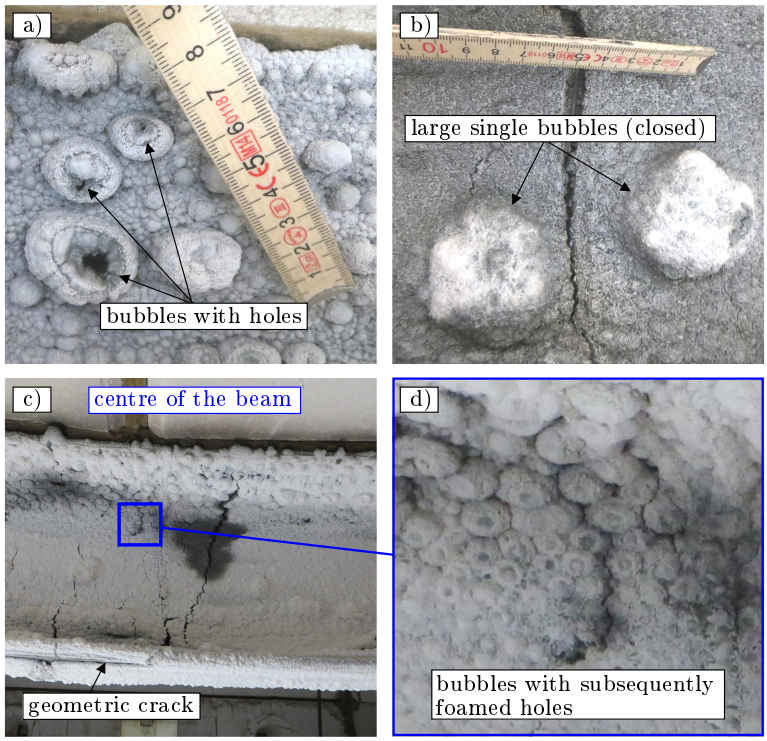

Figure 3.59: Bubbles of different shapes formed by the waterborne coating in the area of the fixed support (a-b) and the centre of the beam (c-d)

By taking into account the measured char thicknesses and the dry film thicknesses of the waterborne coating, the expansion factors of the char structure can be determined for each part of the cross section. However, since the char thicknesses were measured after the fire test and the organic components of the char structure were mostly burnt, these values do not represent the maximum expansion factors due to the expected shrinkage.
With a mean expansion factor of $\epsilon = 30.0$, the highest expansion of the waterborne coating was observed on the upper flange. The lowest expansion ($\epsilon = 24.0$), on the other hand, occurred on the bottom flange.

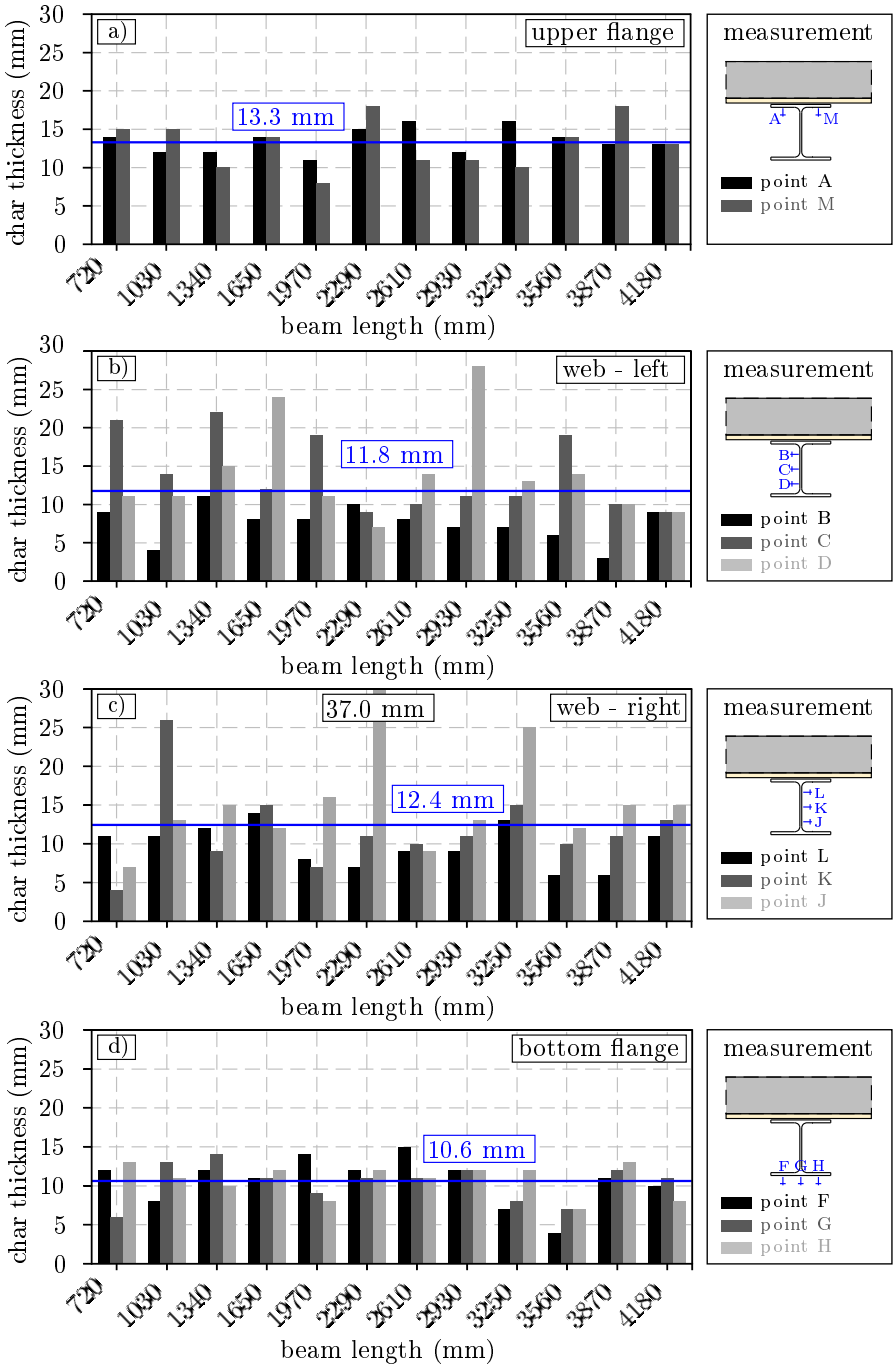

Figure 3.60: Measured char thicknesses of the waterborne coating along the loaded beam, starting at the floating support

At the web, the irregular expansion resulted in a mean expansion factor of $\epsilon = 27.5$. When comparing these values to the residual expansion factors ($\epsilon_{res} = 39.82$ and 37.10) of the test samples *NF-I* and *NF-II*, that were determined during the digital expansion analysis (see Table 3.5 and Figure 3.11), it is obvious that the expansion behaviour observed in the large-scale fire test differs from the laboratory investigations. In literature it is well known that the bulkiness of a structural component can significantly influence the expansion behaviour of intumescent coatings. Even if the natural fire curves from the laboratory tests and the large-scale fire test are comparable, the bulkiness of the loaded beam (A/V = 147 m^{-1}) leads to a reduced expansion compared to the thin steel plates (0.7 mm). Therefore, the behaviour of the waterborne coating seems to be plausible.
In the small-scale fire tests it could be demonstrated that the fire protection performance of the waterborne coating depends on the bulkiness of the substrate, on the dry film thickness and especially on the fire scenario. All these influences could be confirmed with the help of the large-scale fire test. The test also revealed that the waterborne coating tends to form cracks under the natural fire. The extent to which this crack formation is caused by mechanical stresses or other effects will be discussed on the basis of the results of the reference beam and column.

Reference Beam HEA 240:

In order to evaluate the influence of the mechanical loading on the fire protection performance of the waterborne coating and on the resulting heating behaviour of the loaded beam, an unloaded reference beam (HEA 240) with a length of 1,000 mm was additionally examined within the large-scale fire test. To ensure comparability of the fire exposure, the reference beam was placed at a distance of 1.2 m next to the loaded test specimen.
Figure 3.61 shows the results of the temperature measurement for the unloaded reference beam. Here the steel temperatures measured at the centre of the beam and at two-thirds of the beam length are shown. In both cases, almost identical temperatures are observed in the respective parts of the cross-section. Similar to the loaded beam, a temperature gradient is formed over the height of the reference beam. While the maximum steel temperature (603 °C) is located after 46 minutes in the bottom flange, the temperature in the upper flange is at the same time 460 °C. This means that the maximum steel temperature in the reference beam occurs approximately two minutes earlier than in the loaded beam. This can be seen by comparing the maximum bottom flange temperature and the grey dashed line, which represents the point in time at which the loaded beam failed. Since 20 °C higher steel temperatures were measured in the reference beam than in the loaded beam, the influence of the mechanical loading on the fire protection performance of the waterborne coating cannot be simply evaluated by comparing the temperatures of the two test specimens. However, the change in temperature development due to char formation is just as significant.
An examination of the expanded char structure provides a similar impression as

for the loaded beam. For example, numerous cracks in the char are found on the underside of the bottom flange as can be seen from Figure 3.62. On a closer look, however, it can be seen that the crack widths (max. 8 mm) are smaller and the shapes are more irregular than for the loaded beam. Here the cracks were considerably wider (up to 20 mm) and were oriented perpendicular to the beam axis. Therefore, it can be concluded that the cracks inside the char structure that were observed at the reference beam are due to the thermal behaviour of the char and the thermal elongation of the test specimen, whereas the single large cracks of the loaded beam are rather due to the mechanically induced deflection.

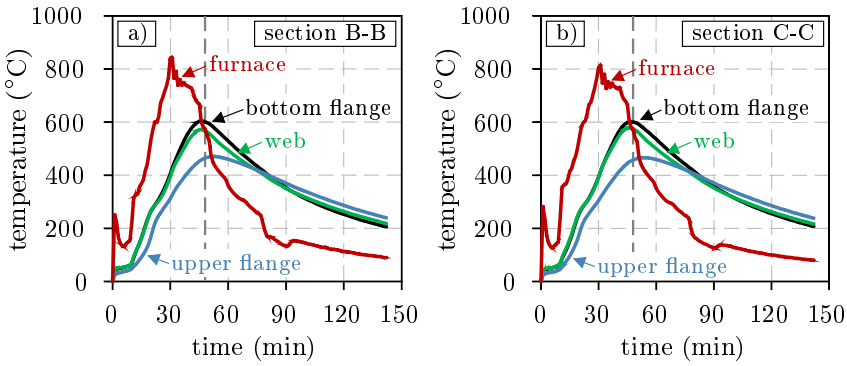

Figure 3.61: Measured steel temperatures of the reference beam (HEA 240) in the measuring axes B-B (centre of the beam) and C-C (at 2/3 of the beam length) including the furnace temperatures and the time of failure (48^{th} minute) of the loaded beam

The phenomenon of bubble formation that was observed for the loaded beam also occurred for the unloaded reference beam. Numerous small bubbles with subsequently closed holes were formed on the lower side of the upper flange. Single large bubbles, on the other hand, were formed on the upper side of the bottom flange and in the transition area to the fillets (see Figure 3.63). Since both types of bubbles occurred on the loaded beam and on the unloaded reference beam, it can be excluded that the bubble formation was influenced by the mechanical loading. It is rather plausible that the bubble formation was effected by the thermal impact. However, the natural fire scenario alone does not appear to be the reason for this, since the bubbles were not formed on the entire test specimen, but only at certain parts. The deviating behaviour of bubble formation occurred in both test specimens in areas where the thermal radiation was partially shielded. As a result, the intumescent coating had less reaction energy than already caused by the natural fire. Therefore, the combination of thermal impact and test specimen geometry seems to be the reason for the deviating bubble formation.
Similar to the loaded beam, the thickness of the formed char was also measured along the reference beam after the fire test. The results of the measurements are shown in Figure 3.64. On the basis of this data, it can be deduced that the char

structure was formed uniformly, especially at the upper and the bottom flange. Here, the average char thickness is 9 mm for the upper flange and 8 mm for the bottom flange. In the area of the web the average char thickness (11.5 mm) is slightly higher. However, compared to the loaded beam, the char thicknesses of the reference beam are approximately 2-3 mm lower. This could be the reason why slightly higher steel temperatures were measured in the reference beam, although larger cracks were formed in the char of the loaded beam.

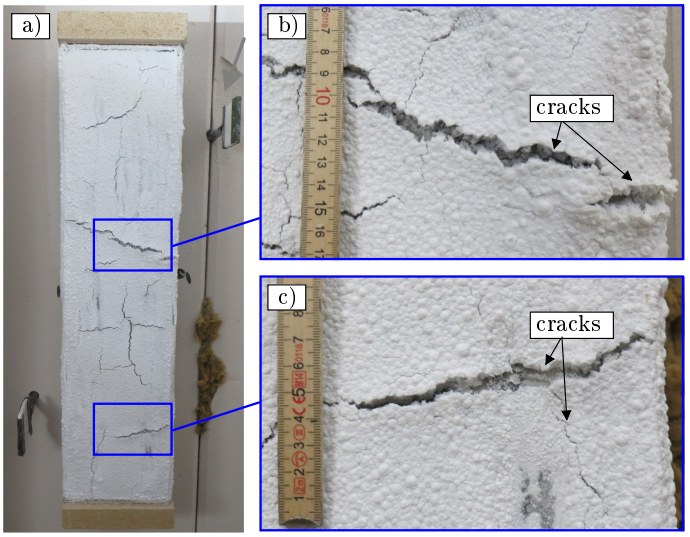

Figure 3.62: Crack formation within the waterborne coating applied on the bottom flange of the unloaded reference beam: a) bottom view of the flange and b) and c) close-ups of the cracks

On the basis of the results it can be concluded that the consideration of the unloaded reference beam, unfortunately, does not allow to finally evaluate the influence of mechanical loading on the heating behaviour of the loaded beam, since higher steel temperatures were measured in the reference beam due to lower char thicknesses. However, the comparison of the loaded and the unloaded beam allows to analyse the char and bubble formation of the waterborne coating and to distinguish between mechanically induced and temperature induced cracks in the formed char. For this reason it was very useful to investigate both test specimens during the large-scale fire test simultaneously.

Reference Column HEA 240:

In addition to the three-sided fire exposed beams, a four-sided fire exposed column (HEA 240, length 1,000 mm) was also investigated during the large-scale fire test. The aim was to quantify and evaluate the influence of the natural fire on the heating behaviour of the HEA 240 profile due to different section factors.
The results of the temperature measurement for the unloaded column are shown

in Figure 3.65. It can be seen that the heating of the column is more homogeneous compared to the beams. As expected, the four-sided fire exposure results in almost the same steel temperatures in all cross-section parts. Only in the flange, which is oriented towards the furnace wall, temperatures are about 30-40 °C lower after 32 minutes. However, this is due to the furnace temperature and the control of the oil burners. After approximately 31 minutes, the cooling phase of the natural fire was initiated by reducing the burner power. This can be seen, for example, in the size of the burner flames in Figure 3.54. Due to the reduction of the burner flames, the flange facing the furnace wall was exposed to less radiation, which caused the temperatures in the flange to rise more slowly than in the remaining cross-section parts.

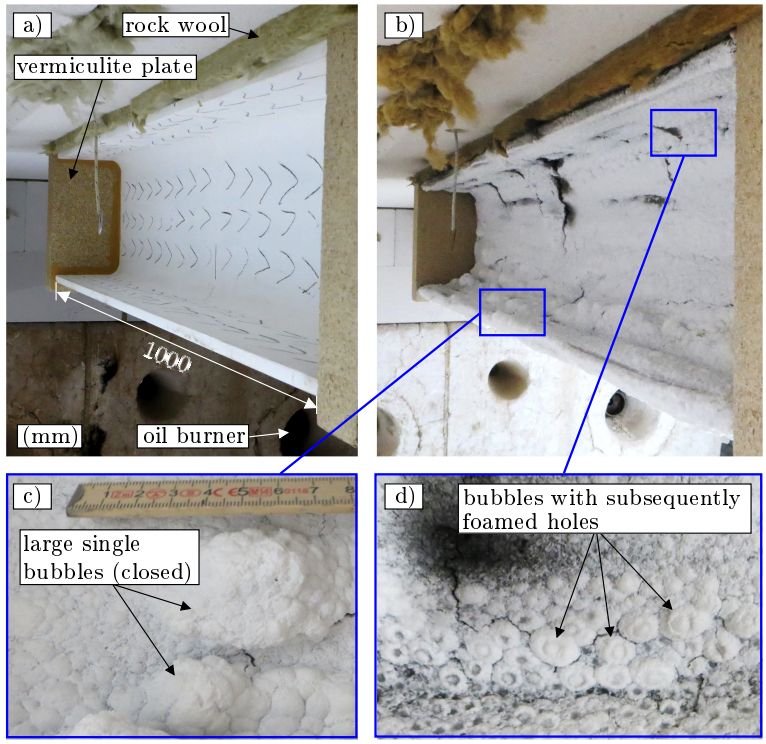

Figure 3.63: Illustration of the reference beam a) before and b) after the fire test with different bubble shapes formed at c) the bottom and d) the upper flange

The unloaded column heats up slightly more than the two beams. The maximum steel temperature is 612 °C and was measured, as expected, in the web of the upper measuring axis (see Figure 3.65 b)). The flange temperatures at this point in time (45 minutes) are 607 and 575 °C. Despite the four-sided fire exposure and the homogeneous heating, the maximum steel temperatures of the column are not significantly higher than the temperatures of the beams.

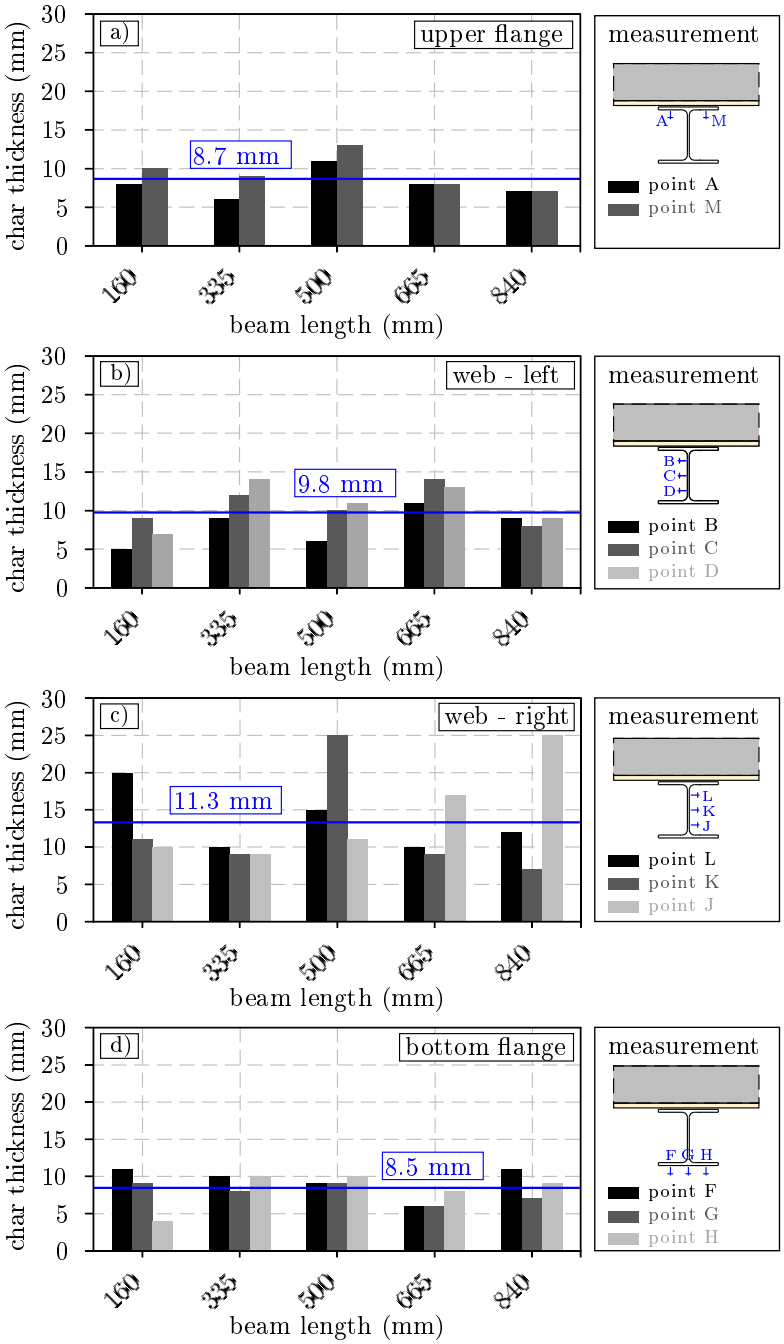

Figure 3.64: Measured char thicknesses of the waterborne coating at: a) the upper flange, b) and c) the web and d) the bottom flange along the reference beam

With regard to the crack formation, the waterborne coating showed a similar behaviour on the reference column, which was already observed for the two beams. For example, geometric cracks were formed in the char structure at the flange edges of the column (see Figure 3.66), which were already observed on the loaded beam. In addition, irregular cracks were formed on the column flange facing the furnace as can be seen in Figure 3.67. Judging by their shape and distribution, these cracks were formed only after the expansion. A possible reason for the crack formation could be the shrinkage behaviour of the char caused by the pyrolysis of the organic compounds.

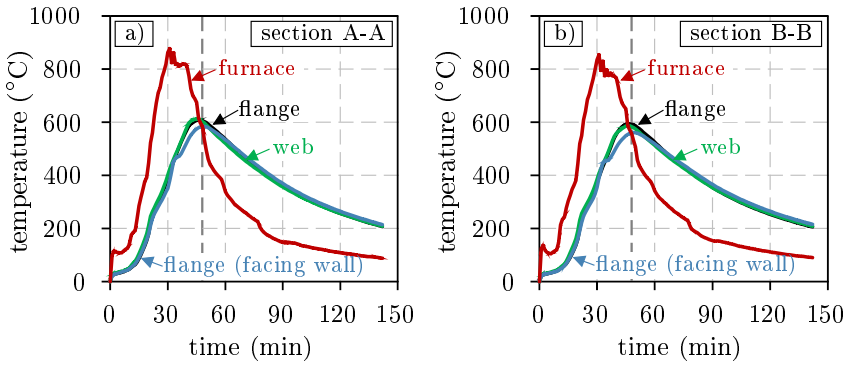

Figure 3.65: Measured steel temperatures of the reference column (HEA 240) in the measuring axes A-A (at 4/5 of the column length) and B-B (centre of the column) including the furnace temperatures and the time of failure (48^{th} minute) of the loaded beam

The large, single bubbles with holes, which were formed on the upper flanges and the roll fillets of the beams, could only be observed at the bottom of the column. However, the bubbles were formed around the entire cross-section as can be seen in Figure 3.66 a). This represents a difference compared to the previous results, but makes also clear that the bubble formation is significantly influenced by the prevailing temperatures. The lowest furnace temperatures are normally found at the bottom of the furnace. In the case of the reference column, this could have influenced the melting phase and the release of volatile gases. Since the temperatures at the bottom of the furnace were lower, the coating had more time to expand and to form large single bubbles before the char temperature was reached at which the carbonisation reaction took place. However, as soon as the internal pressure, caused by the release of volatile gases, exceeded the strength of the viscous material, several bubbles burst. As there was still enough material remaining to foam, the holes were closed again as can be seen from the close-up in Figure 3.66 c). However, in some cases the holes remained open. With regard to the insulation performance, this is a big disadvantage.
In analogy to the other two test specimens, the thickness of the formed char structure was also investigated in addition to the morphology. The results of the mea-

sured char thicknesses are given in Figure 3.68. As can be seen from the first bar diagram, the lowest char thicknesses were measured at the flange that was oriented towards the furnace. Here, the average char thickness is only 7 mm. On the flange facing the furnace wall, on the other hand, a 10 mm thick char structure was formed. With approximately 12 mm on the one side and 17 mm on the other, the highest char thicknesses were measured again in the area of the webs. Taking the measured dry film thickness of the waterborne coating into account, the lowest expansion factors ($\epsilon = 18.0$) occurred in the area of the flange facing the furnace. In combination with the cracks that were formed inside the char, these low expansion factors resulted in the middle of the reference column (l/2) in higher steel temperatures in the flange than in the web (flange: 595 °C, web: 583 °C). Through this it becomes clear how single cracks and reduced char thicknesses can influence the heating behaviour of coated steel structures.

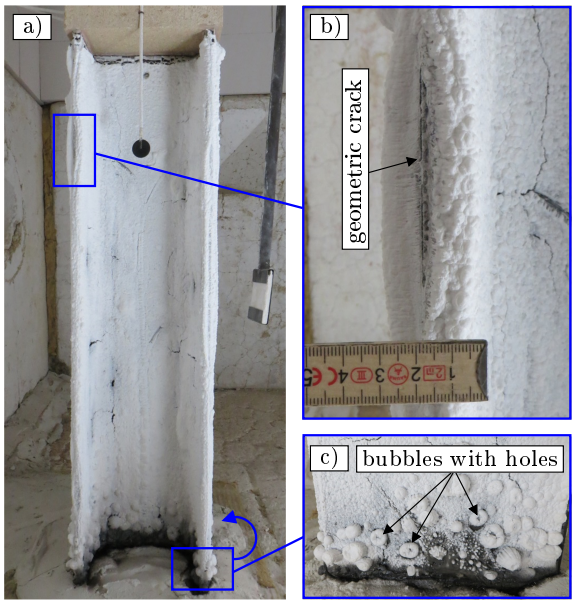

Figure 3.66: Char formation of the waterborne coating applied on the unloaded reference column: a) side view of the column, b) close-up of a geometric crack and c) bubble formation (with holes) on the flange near the furnace ground

The results obtained for the reference column show that cracks inside the char structure are formed in the same way as for the unloaded reference beam. In both cases the cracks can be attributed to the shrinkage behaviour of the char structure. However, it is assumed that the amount of cracks can be reduced by the increase of the dry film thickness of the coating. As soon as enough material is available, the cracks can be closed due to the subsequent foaming. Such a behaviour was already observed by Häßler (2016).
The formation of single, large bubbles with openings is less pronounced in the case

of the column. Here, the bubble formation appeared only in the area of the column base. However, the bubbles were not only formed in single places but around the whole cross-section.
Despite the four-sided fire exposure and similar dry film thicknesses, the maximum steel temperatures of the column are only slightly higher than the temperatures measured in the bottom flanges of the two investigated beams. With a dry film thickness of 365 μm, the waterborne coating was able to protect the four-sided fire exposed column from direct heating in the course of the investigated natural fire. The extent to which an increase in the dry film thickness of the waterborne coating leads to a greater reduction in steel temperature will be discussed within the numerical simulations in chapter 4.

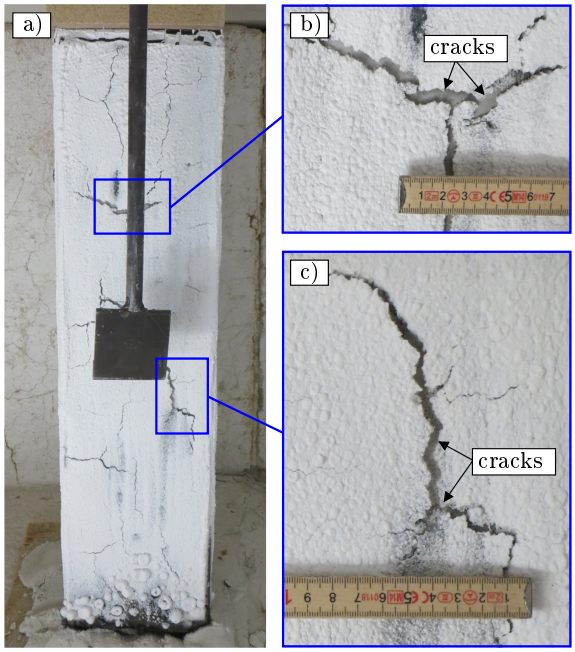

Figure 3.67: Crack formation within the waterborne coating applied on the flange of the unloaded reference column facing the furnace: a) view of the flange and b) and c) close-ups of the cracks

3.5.6 Discussion

Small-scale fire tests offer the advantage of being carried out in a large number. They are normally highly reproducible, inexpensive and allow to investigate several parameters within one test series as well as to quantify scatter. However, as small-scale fire tests are normally performed with coated steel plates, neither the geometry nor the loading situation of common steel structures are represented in a correct way. For this reason, large-scale fire tests are required in order to confirm the findings of laboratory tests or to reveal new findings.

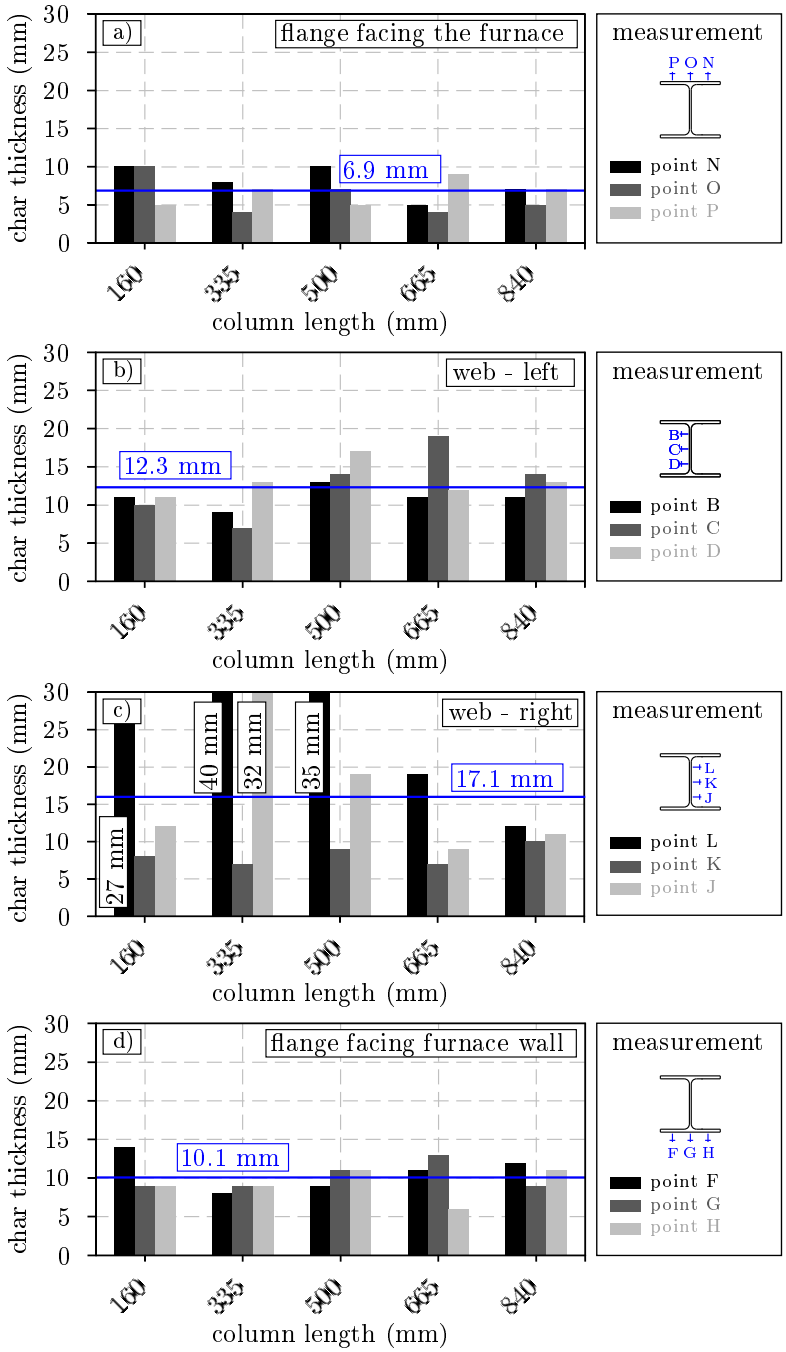

Figure 3.68: Measured char thicknesses of the waterborne coating at: a) the flange facing the furnace, b) and c) the web and d) the flange of the reference column facing the furnace wall, starting at the bottom of the column

In the case of the large-scale fire test carried out here, both aspects apply. For example, crack formation in the char structure was observed during the expansion tests, when the waterborne coating was exposed to certain heating rates (10 and 20 K/min) and fire curves (smouldering fire according to EN-13381-8 (2013) and travelling fire). However, when the samples were exposed to the natural fire according to the national research project IGF 19176 N (Zehfuß et al. 2018), no cracks appeared. In the case of the large-scale fire test, on the other hand, the waterborne coating showed a large amount of cracks, when being exposed to the same natural fire. But how can such a different behaviour occur? When evaluating the crack formation behaviour of intumescent coatings it is always of great importance to distinguish between different types of cracks. For example, the cracks that were formed along the flange edges are due to the geometry of the investigated HEA 240 profile. Since the steel plates investigated within the small-scale fire tests were only coated at one side, no geometric cracks could occur. The large cracks perpendicular to the loading direction that were found at the underside of the loaded beam, on the other hand, are due to the mechanical loading. In literature it is well known that mechanical loading leads to additional and larger cracks inside the char structure of intumescent coatings. In this case, for example, larger cracks were also measured in the loaded beam than in the unloaded reference beam or column. However, despite the absence of mechanical loading, arbitrary cracks were formed in the char of both the beam and the column. These cracks are the result of thin dry film thicknesses of the waterborne coating in combination with the shrinkage behaviour of the char. As already observed in the expansion analyses, intumescent coatings tend to shrink as soon as the organic compounds combust. The wider or longer a steel member is, on which the char shrinks, the greater the distances to the free ends. Since the char shrinkage also takes place in the transverse direction, cracks occur, if the component is too wide and the strength of the fragile char is exceeded. However, if the coating thickness is large enough, new char material can be formed and close the cracks again. In this case, the dry film thickness of the waterborne coating was only a few micrometres, so that no further char material could be formed after the formation of cracks.

During the expansion analyses, single bubbles were observed which were formed in the early stage of expansion and burst again. As soon as the waterborne coating expanded completely, these bubbles could no longer be distinguished from the rest of the char material. Only a few small holes in the surface could be detected. In the large-scale fire test such bubbles were also formed. However, these bubbles were many times larger and could still be distinguished from the rest of the char material after the fire test. In addition, the bubbles were formed in two types: ① bubbles with open holes and ② bubbles with subsequently closed holes. In both cases the bubbles were formed in areas, where lower temperatures and lower heating rates prevailed. With regard to the fire protection behaviour, this type of bubble formation has clear disadvantages compared to a homogeneously formed char structure. When the bubbles become larger, the amount of internal radiation inside the bubbles increases. This effect significantly reduces the fire protection of

the char. If the bubbles burst or become damaged, the trapped gases evaporate and the insulation effect is even further reduced. Therefore, in order to prevent this behaviour, a homogeneous char structure with small bubbles should always be formed. Even if single bubbles burst, this has only little effect on the fire protection performance of the entire char structure.
As the bubble formation and char morphology have a significant influence on the fire protection performance on intumescent coatings, it is of great importance to identify the conditions (gas temperatures, heating rates, material properties such as the viscosity, etc.), at which the two types of bubbles are formed. However, this requires a new experimental setup, in order to perform systematic analyses.

Within the European approval procedure both unloaded and loaded fire tests are prescribed, in order to assess the fire protection performance of intumescent coatings. Taking the results of the performed large-scale fire test into account, it is highly recommended to continue with this practice. Although the behaviour of intumescent coatings can be investigated in more detail within laboratory tests, parameters such as the geometry of common steel profiles and the mechanical loading cannot be represented in these tests, so far. Therefore, it is still very important to investigate the fire protection behaviour of intumescent coatings under realistic conditions and, therefore, also under mechanical loading.

3.6 Summary

In the scope of the experimental programme, a total of 12 coupled thermogravimetric (TG) and differential scanning calorimetry (DSC) analyses, 52 expansion tests, 113 small-scale fire tests on coated steel plates and one large-scale fire test of a loaded beam and two reference test specimens were performed. The objects of investigation were two different fire protection systems, a solvent- and a waterborne coating, each with a national approval.
The experimental programme started with coupled TG-DSC analyses. With the help of these analytical methods the heating rate-dependent behaviour of the intumescent coatings could be confirmed. The analyses reveal that the coatings degrade thermally slower when being exposed to faster heating rates. As the DSC analyses were performed simultaneously for each investigated heating rate, the reactions of the coatings, such as the melting of the polymer binder, the initiation of char formation, the oxidation of organic compounds and the release of carbon dioxide could be identified within the measured DSC curves.
By combining the results of the coupled TG-DSC analyses with the results from literature, an explanation for the heating rate-dependent expansion behaviour of the investigated coatings could be found. According to this, intumescent coatings show lower char thicknesses at lower heating rates since more volatile gases are released between the reaction stages of melting and initiation of char formation than at higher heating conditions. The amount of the released gases, which are

formed primarily due to the decomposition of the blowing agent, is lost and does not contribute to the char formation. This depends in particular on the heating rate-independent mass loss behaviour of the binder and the observed temperature shift of the blowing agent. However, it cannot be excluded that due to heating rate-dependent changes in viscosity of the liquid melt gases escape from the char structure also during the expansion process. In order to quantify this amount of gas, other investigation methods such as the Fourier Transform Infrared Spectroscopy (FTIR) are required.

In order to investigate the expansion behaviour of the coatings in particular, laboratory expansion test were performed. The expansion tests were not performed on thick steel plates, as commonly described in literature, but on thin steel plates (0.70 mm). In this way, the influence of thermal inertia of the substrate could be minimised. By placing the thermocouples for the temperature measurement from below through drilled holes in the steel plates, it was ensured that the char formation was influenced as little as possible by the arrangement of the thermocouples. At the same time, the newly developed test set-up allowed the test samples to be removed non-destructively from the sample holder, in order to carry out further morphological investigations. This is a crucial aspect for the evaluation of the results.

Besides the determination of the heating rate-dependent expansion curves it could be shown that the formation of the char morphology significantly depends on the examined heating rates. As the heating rate decreases, the char structure starts to crack and forms a non-coherent char. A possible reason for this behaviour could be the interaction between the release of volatile gases by the blowing agent and the physical properties of the polymer binder during the melting phase. From the observations, it is assumed that at lower heating rates the blowing agent decomposes at lower temperatures. Due to this temperature shift towards lower temperatures, the polymer binder has to withstand the internal pressure caused by the release of volatile gases although the binder is still very liquid. For this reason, bubbles that are formed inside the liquid polymer binder burst and the volatile gases escape. When most of the gases escape, the char does not expand as much. Furthermore, due to the cracking and bursting, an inhomogeneous and fissured char structure is formed. This leads to the negative effects of reduced char thicknesses and the formation of a heterogeneous and fissured char structure with a reduced thermal protection. Therefore, it is not sufficient to examine only the expansion behaviour. The morphology of the formed char structure has to be examined as well. This applies not only for the constant heating rates that were used during the investigations but also for the smouldering fire curves that were investigated. As the results of the expansion and morphology tests show, smouldering has also a significant effect on the expansion behaviour and the char formation. As the investigated product showed a high sensitivity to smouldering, it should be discussed by the approval authorities whether the smouldering tests should become mandatory for all manufacturers. This discussion should be held at least for products that will be used in the future for natural fires with moderate heat release rates.

In addition to the expansion analyses, small-scale fire tests on coated steel plates were performed within the experimental programme. With the help of these test, the heating rate-dependent fire protection performance of the solvent- and waterborne coating could be confirmed by means of the measured steel plate temperatures. Especially the temperature difference between unprotected and protected steel plates has proven to be particularly useful in order to evaluate the fire protection performance of the coatings. To which results the method of the *effective thermal conductivity* leads when evaluating the fire protection performance of intumescent coatings, will be shown in the numerical simulations in chapter 4.
If the reaction properties of intumescent coatings need to be investigated in more detail, the first derivative of the measured steel plate temperature and thus the heating rate of the test specimens can be calculated. In this way, the time and temperature of the expansion and the phase of effective thermal protection can be clearly identified.
With the help of the developed evaluation software that was implemented in MATLAB even the thermal conductivity behaviour of the coatings can be investigated. However, this way of investigation requires the equidistant measurement of char temperatures as well as the temperature and heating rate-dependent material properties (density and specific heat capacity) of the coatings. Due to the high effort in test preparation and evaluation, this method is less suitable for approval tests, but opens up new opportunities in research.
As large-scale fire tests are performed under realistic geometry and loading situations, a loaded beam exposed to the natural fire curve of the national research project IGF 19176 N (Zehfuß et al. 2018) was investigated.
Besides different types of cracks in the char structure of the waterborne coating, bubble shapes could be identified, which were not observed before in the small-scale fire tests. The bubbles were characterised by open or subsequently closed holes and were solely formed in areas of reduced heating rates or due to shading. However, despite the formation of stress-induced cracks and open bubbles, the fast heating of the loaded beam could be delayed. With a mean dry film thickness of ca. 370 μm, which was designed based on a fire resistance period of 30 minutes according to the standard fire curve, the load-bearing capacity of the three-sided fire exposed beam could be maintained for 48 minutes within the scope of the investigated natural fire. The investigations were based on a load utilisation factor of 0.57 of the plastic bending resistance.

4 Numerical Investigations

The fourth chapter introduces a material model for the investigated intumescent coating being implemented in the finite element software ABAQUS®. After validation against test data, the material model is used among others to evaluate the calculation method of the effective thermal conductivity and its ability to identify the heating rate dependency of intumescent coatings.

Contents

4.1 Introduction

Within the scope of the experimental investigations, the hypothesis could be confirmed that the examined intumescent coatings show a heating rate-dependent behaviour. At different heating rates the expansion behaviour varies in parts significantly. Consequently, it makes a difference whether the intumescent coatings heat up first at high and then at low or first at low and then at high heating rates. In addition, significant differences in the formation of the char morphology could also be determined depending on the heating rate.
In order to carry out numerical investigations, a material model for intumescent coatings is developed which is able to describe the heating rate-dependent expansion behaviour observed in the experiments. In addition, a thermal conductivity model is implemented for the first time, which is valid for both the heating and cooling phases of natural fires. The model also differentiates between a closed-cell and an open-cell foam structure. Following the idea of Lautenberger & Fernandez-Pello (2009), the number of required input parameters is reduced to a minimum to keep the complexity of the model as low as possible. In contrast to many other models (see subsection 2.2.8), the required input parameters can all be measured reliably and with proven reproducibility within experimental investigations.
After the presentation of the material model and its implementation in ABAQUS 2017 (HF6), the expansion tests from section 3.3 are simulated in a first step. By comparing the simulation results with the test data, the implementation of the expansion behaviour is examined and evaluated with regard to its quality. In a second step, the hypothesis is examined to what extent the expansion behaviour of the coatings can be composed of different heating rate-dependent expansion curves, in order to describe the char formation at any natural fire.
In order to evaluate the new material model's ability to describe the thermal insulation behaviour of intumescent coatings, the steel plate tests from section 3.4 are recalculated in the second part of the numerical investigations. With the help of the simulation results, the method of the *effective thermal conductivity* according to EN-13381-8 (2013) is examined for its suitability to assess the heating rate-dependent behaviour of intumescent coatings. The main focus of the examination is on the assumptions made within this method.
In the last part of the numerical investigations the material model is used in order to recalculate the heating behaviour of the reference beam that was examined during the large-scale fire test (see section 3.5). Subsequently, a parameter study is carried out, in which the dry film thickness of the intumescent coating is varied. In this way, the question is answered which coating thickness would have been sufficient to prevent the loaded beam from the large-scale fire test from failing.

4.2 Material Model

4.2.1 Assumptions

When evaluating their material model, Lautenberger & Fernandez-Pello (2009) come to the conclusion that their model is too complex since the required input parameters cannot be measured directly in tests but need to be inferred from experimental data. The authors therefore propose first of all to develop experimental set-ups to reliably measure the material properties of intumescent coatings before they are incorporated into material models. However, which material properties should be considered as input and which as output parameters is controversially discussed in literature. Zhang et al. (2012*b*), for example, suggested that the expansion behaviour of intumescent coatings should not be an input parameter but the result of their calculations. For this reason, the authors develop a mathematical model that predicts the expansion behaviour based on the amount of trapped gases inside the char that is calculated from TG data. However, since the fraction of trapped gases can be hardly measured in tests, an estimate is made by a trial and error approach. Therefore, this approach is not very practical, especially with regard to the heating rate dependency.
With the integration of the temperature-dependent viscosity of the polymer binder provided by Bugajny et al. (1999), Cirpici et al. (2016) developed a material model that is able to describe a heating rate-dependent expansion behaviour of intumescent coatings based on the surface tension of the formed bubbles. In contrast to all experimental observations, however, this model delivers the largest expansion values for the lowest heating rates.
Regardless of the accuracy and correctness of the models, the approaches appear to be very complex and sensitive to errors due to the large number of input parameters required (see Table 2.7). A reliable and robust model is characterised above all by its simple and verifiable nature. This simple nature can be ensured, for example, if the few input parameters used in the model can be clearly determined in experiments and be reproduced over and over again. Following this idea, a modelling approach was chosen within the scope of this thesis, in which as few input parameters as possible are used. Since the experiments were very promising, the measured expansion ratios and the pore sizes were chosen as decisive input parameters for the material model. However, the special feature of the new material model is that the expansion represents both an input and an output parameter. In addition to the formulation of the expansion behaviour, a submodel for the thermal conductivity is implemented, which distinguishes between the heating and the cooling phase of a natural fire as well as different heating rates. The new material model is based on following assumptions:

(1) **Expansion behaviour:** The expansion of the coating is one-dimensional and perpendicular to the surface of the substrate. However, an extension to a three-dimensional expansion is possible.

During the heating phase the expansion behaviour is physically described by temperature and heating rate-dependent thermal expansion coefficients $\alpha = f(\epsilon)$ that are calculated from the measured expansion factors $\epsilon = f(\theta, \dot{\theta})$. As the expansion factors were obtained from test specimens with a thin dry film thickness and thin steel plates (no influence due to thermal inertia), they are called *elementary*. Once the cooling phase occurs, the char thickness is assumed to stagnate. In this way, an irreversible expansion behaviour is described with the help of a user subroutine. The shrinkage behaviour and the resulting reduction of the char thickness that occurs at higher temperatures is taken into account automatically by the applied expansion factors.
Since the material model is implemented within a finite element programme, the elementary expansion curves are assigned to each element (in form of thermal expansion coefficients). Since a temperature gradient is formed within the char as soon as the coating is heated, each element undergoes expansion at different times. This effect is even intensified, if the dry film thickness of the coating is higher. Therefore, by superimposing the expansion behaviour of individual elements, the expansion behaviour of the entire char layer is calculated as described mathematically in Equation 4.1.

$$t(\theta) = \sum_{i=1}^{n} t_i(\theta) \qquad with\ t_i(\theta) = f(t_0, n, \theta, \alpha) \tag{4.1}$$

$t(\theta)$:	total char thickness at char temperature θ (mm)
t_i:	char thickness of a single element at char temperature θ (mm)
t_0:	dry film thickness at ambient temperature (mm)
n:	number of elements discretising the char thickness (-)
θ:	char temperature (°C)
α:	thermal expansion coefficient at char temperature θ (1/K)

The expansion of intumescent coatings takes place layer by layer. In order to describe this behaviour numerically, the dry film thickness of the coatings should be discretised with a sufficient number of elements. For this purpose, element thicknesses of 100 μm have proven to be suitable.

(2) **Thermal conductivity behaviour:** It is assumed that the thermal conductivity of intumescent coatings is primarily dominated by the porosity of the char structure and the size of the bubbles. Within the model, the porosity is calculated directly from the measured expansion factors so that no additional measurements are required. The thermal conductivity, on the other hand, is calculated according to the combined mathematical descriptions of Di Blasi & Branca (2001) and Staggs (2010). However, these descriptions are assumed to be only valid for the closed-cell foam structure. For the open-cell foam structure, the model of Ankang & Houde (2013) is used in order to describe the temperature-dependent changes in thermal conductivity. The change in pore structure from closed to open-cell is assumed to occur at char

temperatures higher than 600 ° C. The resulting change in thermal conductivity occurs abruptly.
As soon as the cooling phase occurs, it is assumed that the chemical processes within the char stop and the foam structure remains in its current state. This assumption is taken as a basis for the description of the thermal conductivity during the cooling phase.

(3) **Heat storage behaviour:** It is assumed that the heat storage capacity of intumescent coatings has a minor role for its thermal protection effect. The reason for this can be found in the particularly low density that results from the excessive increase in volume and the simultaneous mass loss during the char formation. However, in order to carry out comparative calculations, the material properties for the density and the specific heat capacity are derived from the performed coupled thermogravimetric and differential scanning calorimetry analyses. The temperature and heating rate-dependent volume change characterising the density is described with the help of the measured expansion factors.

(4) **Mechanical behaviour:** The numerical simulations focus primarily on the temperature field problem. The mechanical behaviour is only of secondary importance, except for the thermal expansion. For this reason, it is assumed that the mechanical behaviour of the coatings can be described using Hooke's law. In contrast to the research of Bodzay et al. (2011), it is assumed that this behaviour applies to both the virgin and the reacted state.

(5) **Application of the model:** The new material model is developed to be used for both finite element and finite difference calculations. For this reason, it is implemented in the finite element programme ABAQUS® as well as in a finite difference programme that was developed within the scope of this thesis using the matrix calculation software MATLAB® (see chapter 5).

4.2.2 Expansion Behaviour

Within the numerical simulations, the expansion behaviour of the intumescent coatings is treated as thermal strain. Equation 4.2 provides a mathematical description in order to calculate the thermal strain using the finite element software ABAQUS. The temperature values θ^0 and θ^I represent initial boundary conditions and are therefore known at the beginning of the calculations. The variable θ, on the other hand, represents the current temperature value at each calculation increment and is therefore one of the result values. The only unknown in the Equation 4.2 is the *thermal expansion coefficient* α, which has to be defined as a material property at the beginning of the calculations. When assuming that the values of the predefined field variables f_β and f_β^I are zero, the thermal expansion coefficient is only dependent on the temperature. As shown in Figure 4.1, the expansion coefficients can be recalculated from thermal strains, if these are given as temperature-dependent data. In case of intumescent coatings, this data is represented by the measured

expansion factors ϵ. Depending on the size of the chosen interval and the associated temperature change, different values for the expansion coefficient (here α_1 and α_2) are derived.

$$\varepsilon^{th} = \alpha(\theta, f_\beta) \cdot (\theta - \theta^0) - \alpha(\theta^I, f_\beta^I) \cdot (\theta^I - \theta^0) \tag{4.2}$$

ε^{th}:	thermal strain (-)
$\alpha(\theta, f_\beta)$:	thermal expansion coefficient (1/K)
θ:	current char temperature (°C)
θ^0:	reference temperature for the thermal expansion coefficient (°C)
θ^I:	initial char temperature (°C)
f_β:	current values of the predefined field variables (-)
f_β^I:	initial values of the predefined field variables (-)

However, since a graphical relationship between the thermal expansion coefficients and the thermal strains or the expansion factors is not sufficient to recalculate the expansion coefficients, the mathematical relationship given in Equation 4.3 can be used. The calculation rule is based on the physical coherence between the change in length dL that is related to its initial length L and the thermal expansion coefficient α within a temperature change of $d\theta$.
If the changes in length and temperature are considered to be infinitesimal, the equation can be formulated in the form of an integral. Assuming that the thermal expansion coefficient is constant within the considered intervals, the integrals can be solved according to Equation 4.3c. The change in length L_i within the expansion of intumescent coatings can be described by the expression $L_0 \cdot \epsilon_i$. In this way, the dependency between the expansion factor and the thermal expansion coefficient is found (see Equation 4.3g). However, this expression only applies to thermal expansion coefficients that are introduced into the numerical simulations as tabulated data and are related to the reference temperature θ^0.

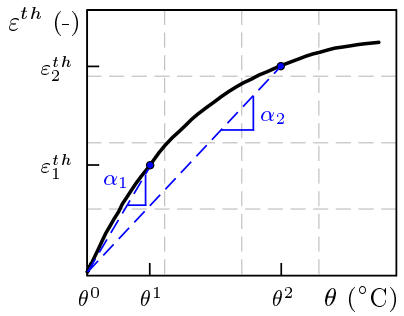

Figure 4.1: Graphical description of thermal strain computations in ABAQUS (Simulia 2016) according to Equation 4.2

If the thermal expansion coefficients have to be calculated incrementally, as it is required within the user subroutine UEXPAN, Equation 4.4 has to be used. In this case, the thermal expansion coefficients are not defined prior to the calculations,

but are calculated incrementally for each integration point (*Gauss point*) depending on the calculated temperature values at the increments i and $i-1$.

$$\frac{dL}{L} = \alpha \; d\theta \tag{4.3a}$$

$$\int_{L_0}^{L_i} \frac{1}{L} \; dL = \int_{\theta_0}^{\theta_i} \alpha \; d\theta \tag{4.3b}$$

$$[ln(L)]_{L_0}^{L_i} = \alpha \cdot [\theta]_{\theta_0}^{\theta_i} \tag{4.3c}$$

$$ln(\frac{L_i}{L_0}) = \alpha \cdot (\theta_i - \theta_0) \tag{4.3d}$$

$$ln(\frac{L_0 \cdot \epsilon_i}{L_0}) = \alpha \cdot (\theta_i - \theta_0) \tag{4.3e}$$

$$ln(\epsilon_i) = \alpha \cdot (\theta_i - \theta_0) \tag{4.3f}$$

$$\alpha = \frac{ln(\epsilon_i)}{\theta_i - \theta_0} \tag{4.3g}$$

α: thermal expansion coefficient (1/K)
ϵ_i expansion factor at char temperature θ_i (-)
θ_i: current char temperature (°C)
θ_0: reference temperature for the thermal expansion coefficient (°C)

In order to calculate the thermal expansion coefficients from the measured expansion curves, the experimental data had to be processed. Since two tests were performed for each heating rate within the expansion analysis, the data was averaged for further use. An exemplary illustration of the averaging of two expansion curves of the waterborne coating measured at 50 K/min is shown in Figure 4.2 a). The mean value functions of all investigated heating rates (10, 20, 30, 50 and 70 K/min) that were determined in the same way are shown in Figure 4.2 b). The direct comparison of the mean expansion values impressively shows the heating rate-dependent behaviour of the investigated coating.

$$\begin{aligned} \alpha_i &= \frac{ln(\epsilon_i) - ln(\epsilon_{i-1})}{\theta_i - \theta_{i-1}} \\ \alpha_i &= \frac{ln(\frac{\epsilon_i}{\epsilon_{i-1}})}{\theta_i - \theta_{i-1}} \end{aligned} \tag{4.4}$$

α_i: thermal expansion coefficient at increment i (1/K)
ϵ_i: expansion factor at increment i (-)
ϵ_{i-1}: expansion factor at increment $i-1$ (-)
θ_i: char temperature at increment i (°C)
θ_{i-1}: char temperature at increment $i-1$ (°C)

In order to describe this differential expansion behaviour within the numerical simulations, the thermal expansion coefficients were calculated from the averaged expansion curves. The calculations were performed with temperature intervals of

10 K using Equation 4.3g. The results of the calculations are shown on the right-hand side in Figure 4.3 and 4.4 respectively.
As can be seen from the diagrams, the curves of the thermal expansion coefficients differ in their shape and their maximum values, especially in the first 350 °C. While a maximum value of $1.096 \cdot 10^{-2}$ 1/K is calculated for 10 K/min at 320 °C, the maximum for 70 K/min ($1.363 \cdot 10^{-2}$ 1/K) is already reached at 275 °C. Compared to the thermal expansion coefficient of carbon steel ($1.216 \cdot 10^{-5}$ 1/K at 20 °C), the coefficients of the waterborne coating are three decimal places larger.
As the plateaus at the beginning of the expansion curves differ depending on the heating rate, the differences are also found in the thermal expansion coefficients. Especially for 10 K/min (see Figure 4.3 b)) the influence of the plateau is most conspicuous.

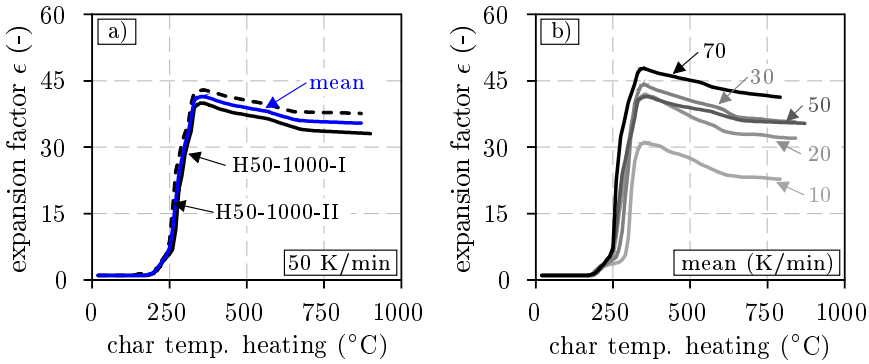

Figure 4.2: Mean values of the expansion curves of the waterborne coating: a) Exemplarily determination of the arithmetic mean for the expansion curves at 50 K/min and b) comparison of the mean curves for 10, 20, 30, 50 and 70 K/min

In ABAQUS, the thermal expansion behaviour of a material can be described in two ways; with the help of a tabular input of the thermal expansion coefficients or by means of an incremental calculation of the coefficients within the user subroutine UEXPAN. To achieve the latter, it was necessary to transfer the measured expansion curves into the user subroutine. This was done by approximating the curves with polynomial functions according to Equation 4.5 within a regression analysis and implementing the functions into the subroutine.

$$p_n(x) = a_n x^n + a_{n-1} x^{n-1} + \ldots + a_1 x + a_0 \tag{4.5}$$

Since the expansion curves could not be described as a whole with a single polynomial function, the expansion curves were divided into several sections. Each section was then approximated with a single polynomial function. The sections used to subdivide the mean expansion curves are shown in the diagrams on the left-hand side of Figure 4.3 and 4.4. The associated coefficients of the polynomial functions (a_n) are tabulated in section A.1 (Appendix A) and can be used for own

calculations.

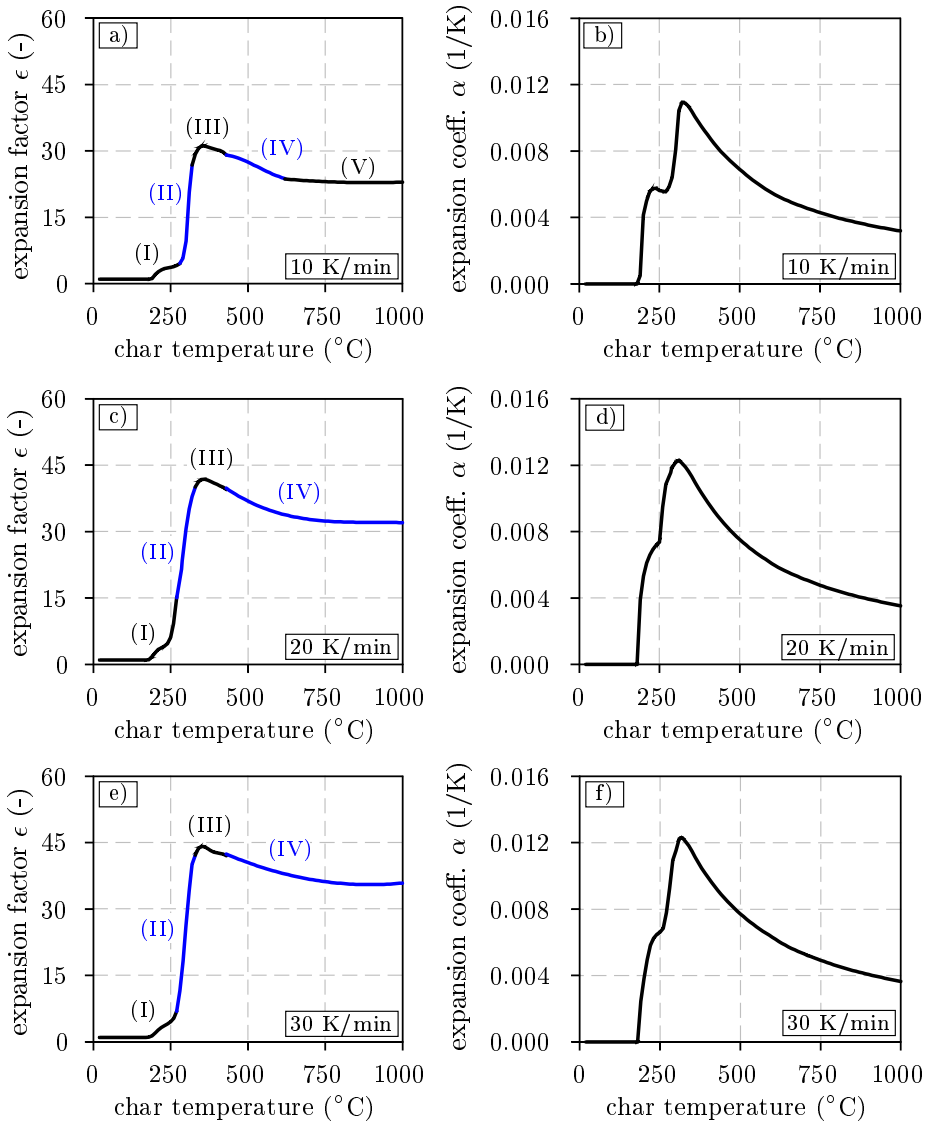

Figure 4.3: Expansion curves divided into sections (I-IV/V) and thermal expansion coefficients of the waterborne coating at 10, 20 and 30 K/min

As already described during the assumptions, the special feature of the material model is that the expansion of the coating represents both an input value and a result of the calculation. To illustrate this, Figure 4.5 schematically describes the numerical calculation of the expansion behaviour. A two-dimensional representation of a coated steel plate with thermal insulation on both sides and the back serves as an example.
As soon as the temperature of the finite elements describing the coating rises due to

heating, the top elements expand, as these are the first to reach the temperatures required for the expansion. Because of the expansion, a delay in heating occurs for the elements below. This results in a temperature gradient within the elements describing the expanding char. The gradient becomes even larger if the expansion or the dry film thickness increases. Therefore, with further heating, the temperature differences in the elements lying below each other lead to different reaction stages. While the top elements already shrink due to the high temperatures, the elements below only reach the maximum of the expansion or only start to expand due to the significantly lower temperatures (see Figure 4.5).

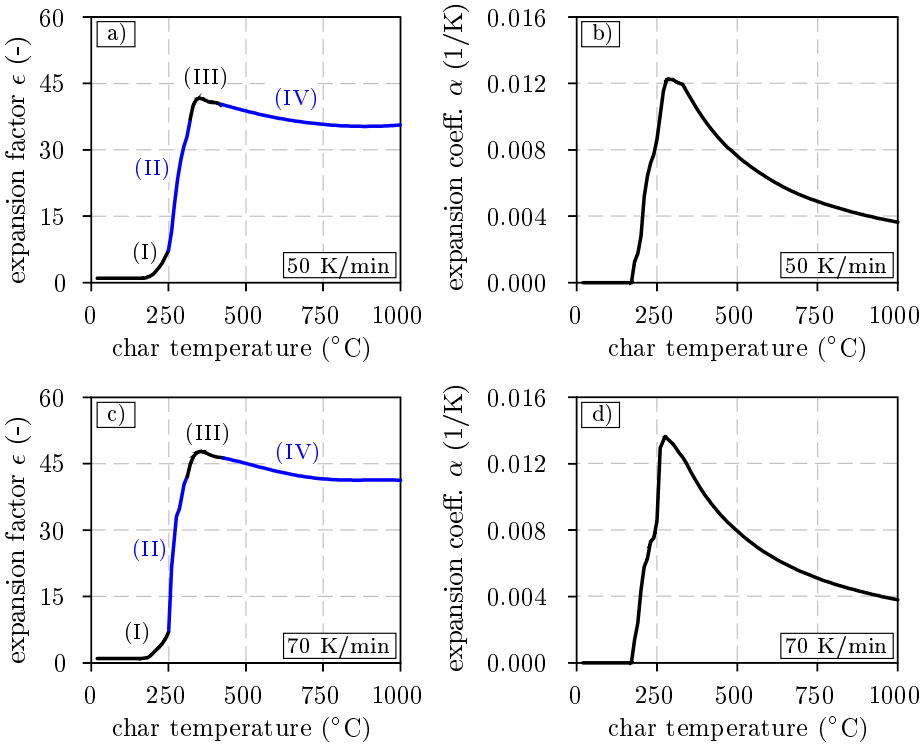

Figure 4.4: Expansion curves divided into sections (I-IV) and thermal expansion coefficients of the waterborne coating at 50 and 70 K/min

By considering the operating principles of the submodel for the expansion of intumescent coatings, the following conclusions can be drawn:

(1) Due to the different reaction states of the elements, the calculated expansion curve can never be identical to the expansion curve on which the calculations are based (input data ≠ output data).
(2) The expansion behaviour of larger dry film thicknesses can be described with the help of the expansion curves measured from thin dry film thicknesses.
(3) With the help of the user subroutine UEXPAN, the expansion curves of all

investigated heating rates can be used within a single simulation if this is required due to the different heating behaviour of individual elements.

(4) The influence of massive steel substrates on the expansion behaviour of the coatings is calculated within the modelling approach *implicitly* by affecting the temperature development within the char elements.

(5) Since the expansion of the coatings is described in layers, the approach can be used in both finite element and finite difference methods.

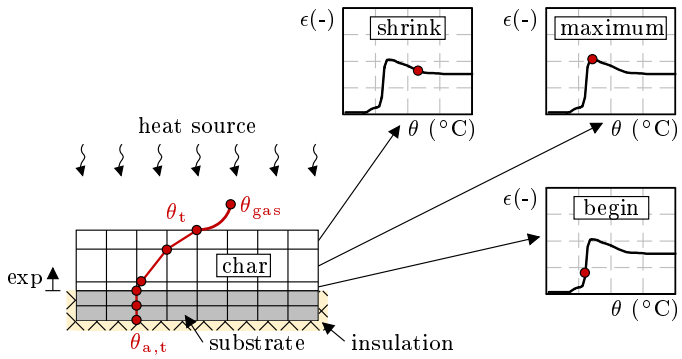

Figure 4.5: Graphical description of the submodel for the one-dimensional expansion of intumescent coatings using linear solid elements

Besides the expansion, the thermal conductivity is one of the decisive material properties controlling the fire protection performance of intumescent coatings. In the following, a material model is presented that is able to describe the thermal conductivity behaviour of coatings for both closed-cell and open-cell foam structures.

4.2.3 Thermal Conductivity Behaviour

Due to the irreversible expansion behaviour of intumescent coatings, it is assumed that the thermal conductivity of the char structure differs between the heating and the cooling phase. Because of the morphological changes in char structure at high temperatures, the heat conduction mechanisms also change, so that different modelling approaches are required to describe this behaviour. Therefore, in the following, first a material model is presented that is only suitable for the closed-cell foam structure. A model describing the thermal conductivity of the open-cell foam structure will be presented later. Both submodels follow the approach to use as few input parameters as possible.

Closed-Cell Foam Structure:

As soon as intumescent coatings start to expand, a two-phase system is formed, consisting of the gases that are released during the expansion and the char structure that traps the gases. The proportion of the released gases in relation to the total volume of the char structure is mathematically described by the porosity. In the case of intumescent coatings, the porosity can be calculated from the measured expansion factors following the idea of Tabeling (2014). The precondition for the calculation rule given in Equation 4.6 is that the area of the coating remains constant during the entire expansion. This corresponds to the assumption that the expansion is primarily one-dimensional.

$$\phi(\theta) = \frac{V^{gas}}{V^{tot}} \;\widehat{=}\; \frac{t_0 \cdot \epsilon(\theta) - t_0}{t_0 \cdot \epsilon(\theta)} = \frac{\epsilon(\theta) - 1}{\epsilon(\theta)} \tag{4.6}$$

$\phi(\theta)$: porosity of the char at temperature θ (-)
V^{gas}: volume of gas trapped inside the char (mm^3)
V^{tot}: total volume of the formed char (mm^3)
t_0: dry film thickness at ambient temperature (mm)
$\epsilon(\theta)$: expansion factor at char temperature θ (-)

Since the trapped gases show a different thermal conductivity behaviour than the solid char structure, the thermal conductivity of the two-phase system can be described by a weighting function according to Di Blasi & Branca (2001). However, in addition to pure heat conduction, the heat transport within the char structure is mainly influenced by thermal radiation, especially at higher temperatures. Therefore, the radiative part of the thermal conductivity is described by the approach of Staggs (2010) (see Equation 2.8). Both approaches together lead to the calculation rule given in Equation 4.7.

$$\lambda(\theta) = \phi(\theta) \cdot [\lambda^{air}(\theta) + 4 \cdot \sigma \cdot \theta^3 \cdot \delta(\theta)] + [1 - \phi(\theta)] \cdot \lambda^{solid} \tag{4.7}$$

$\lambda(\theta)$: thermal conductivity of the char at temperature θ (W/(mK))
$\lambda^{air}(\theta)$: thermal conductivity of air at temperature θ (W/(mK))
λ^{solid}: thermal conductivity of the solid material (W/(mK))
$\phi(\theta)$: porosity of the char at temperature θ (-)
σ: Stefan-Boltzmann constant: $5{,}67037 \cdot 10^{-8}$ W/(m^{2}K^4)
$\delta(\theta)$: pore size at temperature θ (m)
θ: absolute char temperature (K)

Within the equation, the porosity $\phi(\theta)$, the mean pore size $\delta(\theta)$ and the thermal conductivity of the trapped gases $\lambda^{air}(\theta)$ represent temperature-dependent input parameters. For the porosity, the curves given in Figure 4.6 a) are used. In order to determine the pore size, the images of the char structure obtained from the steel plate tests were used. Since the growth of the pores cannot be subjected to a continuous measurement, it is assumed that the pore growth starts with the

beginning of the expansion and reaches its maximum with the occurrence of the expansion maximum. Although the cell walls begin to burn at a temperature of 600 °C, it is assumed that the pore size remain constant after reaching the maximum. This assumption corresponds to the temperature-dependent curves given in Figure 4.6 b).

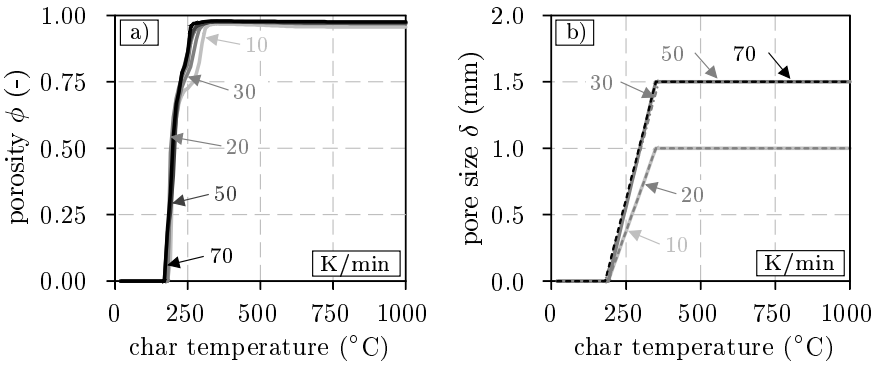

Figure 4.6: Input parameters for the calculation of the thermal conductivity of intumescent coatings: a) porosity and b) pore size. Each as a function of temperature

The thermal conductivity of the gases trapped inside the char is approximated within the model by the temperature-dependent properties of *air*. The corresponding values are given, for example, in Kabelac et al. (2013). In contrast to the gases, the thermal conductivity of the solid material is assumed to be constant due to simplification. In the case of the waterborne coating, the value was set to 1.4 W/(mK) according to own calculations. However, by carrying out additional measurements, the thermal conductivity of the solid material can also be determined experimentally. Lucherini & Maluk (2019), for example, suggest TPS (Transient Plate Source) measurements for this purpose.

The graphical representation of Equation 4.7 for the thermal conductivity of a closed-cell foam structure during heating and cooling is shown in Figure 4.7 for different heating rates. The grey marked area indicates the application area of the material formulation. Figure 4.7 a) shows the calculated thermal conductivity of the waterborne coating during the heating phase. Since the thermal conductivity is calculated indirectly via the porosity as a function of the expansion, the reduction of the thermal conductivity at 180 - 190 °C correlates with the beginning of the expansion. The minimum values of the thermal conductivity are reached at different temperatures, similar to the expansion maxima. The lowest thermal conductivity value (0.11 W/(mK)) occurs for 70 K/min. However, due to the larger pores and the associated radiation, the thermal conductivity values increase faster for 30, 50 and 70 K/min than for 20 or 10 K/min. Nevertheless, the dashed curves are beyond the application area of the material formulation as they are not able to describe the change in char morphology. Therefore, the values given for char

temperatures higher than 600 °C are not part of the material model.

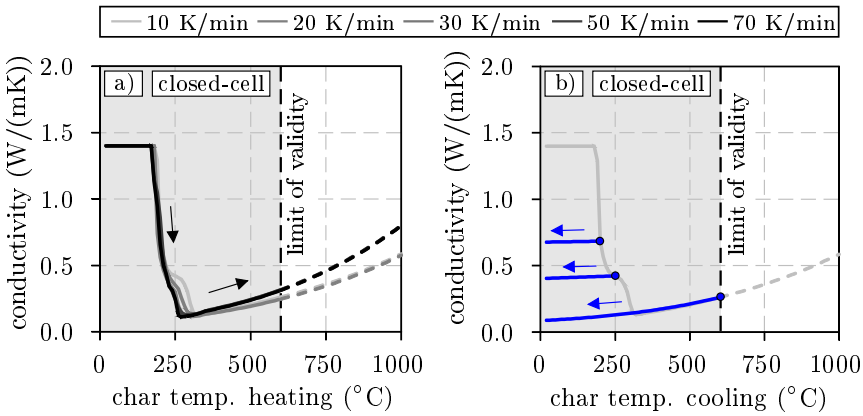

*Figure 4.7: Thermal conductivity of the **closed-cell** foam structure of the water-borne coating: a) during the heating phase for heating rates of 10, 20, 30, 50 and 70 K/min and b) during natural cooling (initial heating rate: 10 K/min)*

The calculation of the thermal conductivity during the cooling phase (see Figure 4.7 b)) is also based on Equation 4.7. However, the decisive difference to the heating phase is in the description of the porosity and the mean pore size. With the onset of the cooling phase, the values of porosity and pore size reached for the last increment are assumed to remain constant for the entire cooling phase. This takes into account the fact that the behaviour of intumescent coatings is irreversible. The thermal conductivity of the trapped gases (in this case *air*) is still described as temperature-dependent. This is the reason for the blue, descending curves given in Figure 4.7 b), which were calculated exemplarily for the onset of cooling after reaching a temperature of 200, 250 and 600 °C.

Open-Cell Foam Structure:

In order to describe the thermal conductivity behaviour of the open-cell foam structure, a material formulation is used that is normally applied for metal foams or other porous media. However, the formulation applies only for the radiative part of the thermal conductivity. Pure heat conduction of the gases and the open-cell skeleton, on the other hand, can still be described with the help of the approach of Di Blasi & Branca (2001). Both components, the pure heat conduction and the radiation, together result in the thermal conductivity of the open-cell foam structure described by Equation 4.8. Convection within the foam structure is still neglected. For the conductive part of the thermal conductivity of porous media, complex calculation rules are usually provided in literature. These usually assume a mathematically described geometry according to which the thermal conductivity components of the skeleton structure and the gases are weighted. In the course of the material formulation for the intumescent coatings, it was consciously decided not to use such

a formulation. The advantage of the calculation rule given in Equation 4.9 is that it can be used independently of the foam structure geometry.

$$\lambda(\theta) = \lambda^{foam}(\theta) + \lambda^{radiation}(\theta) \tag{4.8}$$

A description of the honeycomb geometry would possibly represent a refinement of the calculation rule, however, it would also mean additional complexity. For this reason, the thermal conductivity of the gases and the skeleton structure is also weighted in the state of the open-cell foam structure via the porosity that is calculated from the expansion factors.

$$\lambda^{foam}(\theta) = \phi(\theta) \cdot \lambda^{air}(\theta) + [1 - \phi(\theta)] \cdot \lambda^{solid} \tag{4.9}$$

$\lambda^{foam}(\theta)$:	thermal conductivity of the foam structure (W/(mK))
$\lambda^{air}(\theta)$:	thermal conductivity of air at temperature θ (W/(mK))
λ^{solid}:	thermal conductivity of the solid material (W/(mK))
$\phi(\theta)$:	porosity of the char at temperature θ (-)

For the calculation of the radiative part of the thermal conductivity, the approach of Ankang & Houde (2013) is used. As the cell walls burn at higher temperatures, the radiation does no longer take place inside the pores, but within the open-cell foam structure. How much of the heat flow passes through the foam is regulated by the permeability of the skeleton structure. In subsection 2.2.8 it was already explained that this permeability is physically described by the transmissivity $\tau(L)$. Since the transmissivity is not a fixed value, but changes with the foam thickness L, Equation 4.10 does not contain the transmissivity itself, but the extinction coefficient β. This coefficient is calculated with the help of Equation 2.10 as a function of transmissivity and foam thickness.

$$\lambda^{radiation}(\theta) = \frac{4 \cdot \sigma \cdot (\theta_1^2 + \theta_2^2) \cdot (\theta_1 + \theta_2)}{3 \cdot \beta} \tag{4.10a}$$

$$\lambda^{radiation}(\theta) = \frac{16 \cdot \sigma \cdot \theta_m^3}{3 \cdot \beta}, \quad with \quad \frac{\theta_1 + \theta_2}{2} = \theta_m \tag{4.10b}$$

$\lambda^{radiation}(\theta)$:	radiative part of the thermal conductivity (W/(mK))
σ:	Stefan-Boltzmann constant: $5{,}67037 \cdot 10^{-8}$ W/(m^{2}K^4)
θ_1 :	absolute temperature at the inlet of the heat flow (K)
θ_2 :	absolute temperature at the outlet of the heat flow (K)
θ_m :	mean char temperature (K)
β :	extinction coefficient (m^{-1})

The transmissivity itself is determined experimentally. In the case of the water-borne coating, a computed tomography (CT) measurement was carried out for this purpose. The results of the measurement are three-dimensional images of the foam structure, which can be sliced into two-dimensional layers. Depending on how

many layers are superimposed, a different transmissivity is obtained. In the case of the superimposed images shown in Figure 4.8, the transmissivity of the foam structure was calculated by relating the area of the white pixels to the entire image area. These image-based calculations were performed in MATLAB.

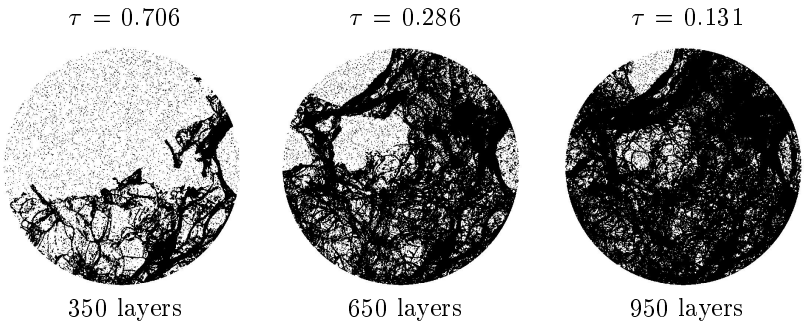

Figure 4.8: Superposition of tomographic slices (1.6 µm) of the waterborne coating heated at 70 K/min and determination of the transmissivity $\tau(L)$. Field of View (FoV): 1,610 x 1,610 µm

For a superimposition of 350 images (layer thickness: 0.56 mm), the transmissivity of the examined foam structure is approx. 70 %. By increasing the number of images, the transmissivity decreases. Therefore, at a layer thickness of approx. 1.52 mm (superposition of 950 images), the transmissivity reaches a value of 13 %. The relationship between the layer thickness and the transmissivity of the examined sample is graphically shown in Figure 4.9. Since the foam structure is irregular, the curve is non-linear. The same applies also to the extinction coefficient β, which was calculated from the measured transmissivity (see Figure 4.9).

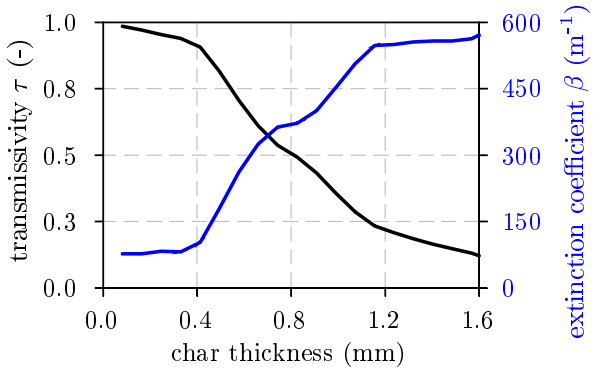

Figure 4.9: Transmissivity and extinction coefficient of the waterborne coating measured from computer tomographic scans (X-ray, see Figure 4.8) of a char heated at 70 K/min

When investigating the morphology, it was already found that smaller pores are formed at 10 and 20 K/min rather than at higher heating rates. For this reason,

it is assumed that in the case of thermal radiation, the finer foam structure leads to lower transmissivity. This assumption is taken into account by defining the extinction coefficient to 550 m^{-1} when calculating the thermal conductivity of the open-cell foam structure for 10 and 20 K/min. According to the graph in Figure 4.9, this corresponds to a transmissivity of approx. 21 %. For the higher heating rates (30, 50 and 70 K/min), on the other hand, a transmissivity value of approx. 30 % is defined. This value corresponds to an extinction coefficient of 500 m^{-1} or a layer thickness of approx. 1.0 mm. Since the coating is discretised within the numerical simulations with several elements over the dry film thickness, this assumption appears to be reasonable.

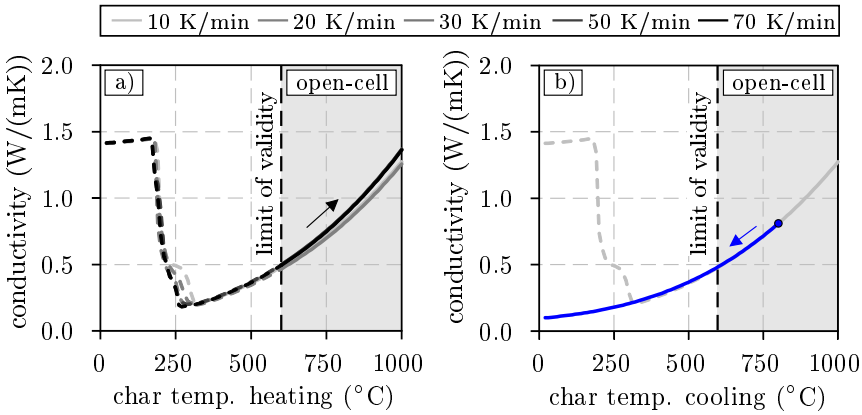

*Figure 4.10: Thermal conductivity of the **open-cell** foam structure of the water-borne coating: a) during the heating phase for heating rates of 10, 20, 30, 50 and 70 K/min and b) during natural cooling (initial heating rate: 10 K/min)*

The graphical representation of the thermal conductivity formulation for the open-cell foam structure according to Equation 4.8 is given in Figure 4.10. Similar to the closed-cell foam structure, the grey marked area indicates the application area of the material formulation. Nevertheless, the dashed lines in the white marked area are shown for the sake of completeness.
The assumption that larger pores are formed at higher heating rates results in greater transmissivity values. This is the reason why the thermal conductivity increases more for 30, 50 and 70 K/min above 600 °C. However, the differences to the lower heating rates (10 and 20 K/min) are comparatively small. Larger differences can rather be observed to the calculations of the closed-cell foam structure (see Figure 4.7 a)). The change in pore structure from closed to open-cell leads to a significant increase in thermal conductivity and thus explains the loss of fire protection at high temperatures.
Similar to the closed-cell foam structure, it is assumed for the open-cell foam structure that the porosity no longer changes with the onset of the cooling phase. In this state the thermal conductivity is primarily dominated by the temperature-

dependent behaviour of the trapped gases as can be seen from the blue curve in Figure 4.10 b).
In order to perform the numerical simulations, the thermal conductivity values of the closed-cell foam structure are used between 20 and 600 °C. However, above 600 °C, the values of the open-cell foam structure are applied. The additional differentiation between the heating and the cooling phase is made by User-Defined Fields. A detailed explanation of the implementation will be given in subsection 4.2.6.

4.2.4 Specific Heat Capacity and Mass Loss

In addition to the thermal conductivity, the heat storage behaviour of the intumescent coatings needs to be described in order to perform numerical simulations. In case of the waterborne coating the data given in Figure 4.11 is used. Both the specific heat capacity and the density are derived from experimental data. The temperature and heating rate-dependent specific heat capacity (see Figure 4.11 a)) is calculated from the measured DSC data by dividing the DSC signal with the associated heating rate as it is described in Equation 4.11.

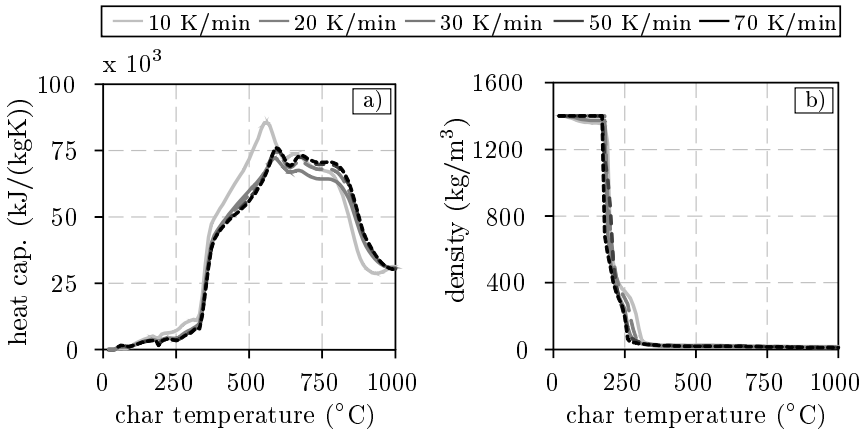

Figure 4.11: Thermal material properties of the waterborne coating at heating rates of 10, 20, 30, 50 and 70 K/min: a) specific heat capacity calculated from the DSC signals and b) density calculated from the TG and expansion data

The temperature-dependent density, on the other hand, is calculated by reducing the initial value (1.400 kg/m^3) with the mass loss data obtained from the TG analyses and the volumetric change described by the expansion factors. The corresponding calculation rule is given in Equation 4.12.
Since the coupled TG and DSC analyses were only carried out for heating rates of 5, 10 and 20 K/min (see section 3.2), the data required for 30, 50 and 70 K/min

was extrapolated. This is assumed to be sufficiently accurate, as the heat storage capacity has a minor role in the description of the fire protection behaviour.

$$c_p(\theta) = \frac{DSC\ signal}{\dot{\theta}} \tag{4.11}$$

$c_p(\theta)$:	specific heat capacity (kJ/(kgK))
$DSC\ signal$:	heat flow measured during the DSC analyses (mW/mg)
$\dot{\theta}$:	heating rate (K/s)

The temperature-dependent data for the specific heat capacity and the density given in Figure 4.11 is only valid for the heating phase. However, as it is assumed that the reaction processes of intumescent coatings stagnate as soon as the cooling phase occurs, the values of the specific heat capacity and the density reached for the last increment of the heating phase are assumed to remain constant during the entire cooling phase.

$$\rho(\theta) = \rho_0 \cdot \frac{\delta m(\theta)}{\delta V(\theta)} \quad with \quad \delta V(\theta) \mathrel{\widehat{=}} \epsilon(\theta) \tag{4.12}$$

$\rho(\theta)$:	temperature-dependent density (kg/m^3)
ρ_0:	density at room temperature (kg/m^3)
$\delta m(\theta)$:	mass loss (wt%)
$\delta V(\theta)$:	volume change (%)
$\epsilon(\theta)$:	temperature-dependent expansion factor (-)

4.2.5 Mechanical Properties

As long as the cracking behaviour of intumescent coatings is not investigated, the mechanical material properties are only of secondary importance. However, in order to perform thermomechanically coupled numerical simulations, the mechanical behaviour has to be defined. In contrast to the expansion, the description of the stiffness matrix assumes an isotropic material behaviour. Therefore, the coating is described by a constant Young's modulus of 12 MPa, independent of the temperature and the reaction stages. The value is based on the experimental investigations of Bourbigot et al. (2004) for ethylene-vinyl acetate (EVA24) blended with ammonium polyphosphate (APP) and polyamide (PA6). The corresponding stress-strain curve was already introduced in Figure 2.38 b). To prevent the temperature-dependent expansion behaviour from being falsified, the Poisson's ratio that is also required when defining a linear elastic behaviour is set to zero.

4.2.6 Implementation Approach

In order to carry out numerical simulations, the submodels and material properties described in the previous subsections are implemented in the finite element programme ABAQUS. The implementation is based on the schematic description shown in Figure 4.12. The thermal material properties (thermal conductivity λ, specific heat capacity c_p and density ρ) are introduced by tabulated data depending on the investigated heating rate. The differentiation between the heating and the cooling phase is achieved by the definition of *User-Defined Field Variables* (FV). For the description of the temperature-dependent material properties in the heating phase, the Field Variable is set to zero. In the cooling phase, on the other hand, the material properties are defined as a function of Field Variables that are unequal to zero. An irreversible behaviour is assumed for all material properties. While the thermal conductivity decreases with further cooling (see the blue dashed line in Figure 4.12 a)), the values of the specific heat capacity and the density are assumed to remain constant. In addition to the thermal material properties, the fire exposure is also defined with the help of tabulated data. In this example, a natural fire is used (see Figure 4.12 b)) that is characterised by a typical heating ($\Delta\theta > 0$) and a cooling phase ($\Delta\theta < 0$).

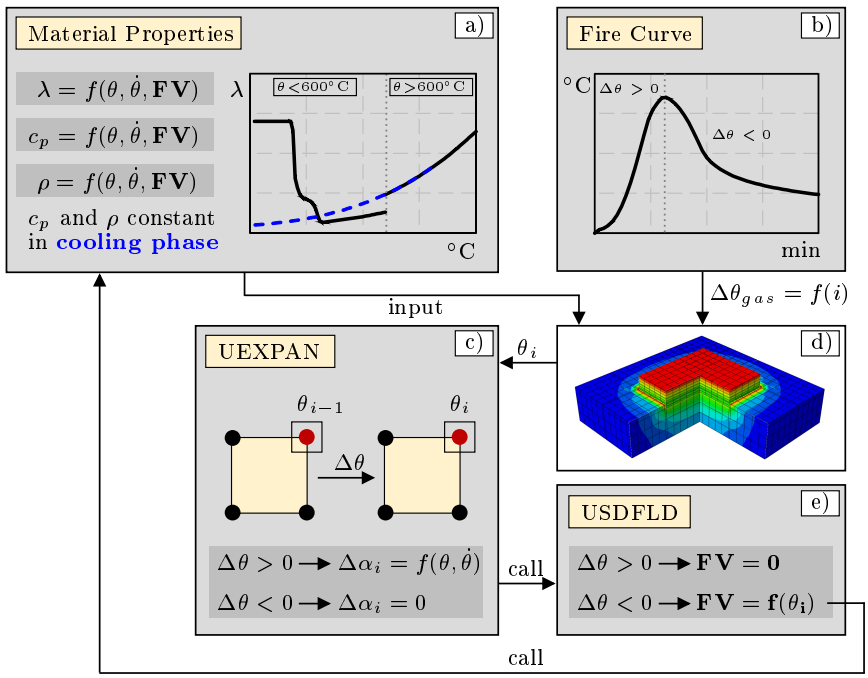

Figure 4.12: Schematic description of the material model implementation for intumescent coatings in ABAQUS using the user subroutines UEXPAN and USDFLD

The temperature and heating rate-dependent expansion behaviour of the coatings is modelled with the help of the user subroutine UEXPAN (see Figure 4.12 c)). In each increment, the temperature change between the current (i) and the previous increment ($i-1$) is calculated for each integration point. If the temperature change is positive ($\Delta\theta > 0$), the intumescent coating is subjected to heating. As a consequence, the thermal expansion coefficient α_i is calculated from the implemented expansion curves ($\epsilon = f(\theta, \dot{\theta})$) with the help of Equation 4.4. For this purpose, the heating rate ($\Delta\theta/\Delta t$) is calculated first, in order to apply the corresponding expansion curve within the calculation. However, if the temperature change at the integration point is negative, the thermal expansion coefficient α_i is set to zero and the expansion stagnates.
In a subsequent step, the user subroutine USDFLD is called (see Figure 4.12 e)). This subroutine offers the opportunity to change the thermal material properties of the intumescent char during the ongoing simulation. The changes are evoked by the control of the User-Defined Field Variables. As long as the incremental temperature change within the finite elements representing the intumescent coating is positive, the material properties defined for the heating phase are used. However, as soon as the element temperature decreases ($\Delta\theta < 0$), the Field Variable is given a different value, e.g. FV = 1. In this case, the thermal material properties, such as the thermal conductivity, the specific heat capacity and the density change into the values that are defined for the cooling phase. In this way, the varying material behaviour between the heating and cooling phase is differentiated.

4.3 Simulation of the Expansion Behaviour

4.3.1 Modelling and Parameters

In order to validate the developed material model and to verify the implementation in ABAQUS, the expansion behaviour of the waterborne coating is simulated and compared to the expansion tests from section 3.3. To perform the simulations, the finite element model given in Figure 4.13 is used. The model consists of solid elements (C3D8T: 8-node thermally coupled bricks) and represents a geometrical replication of the expansion tests that were carried out during the experimental programme. The model consists of a 25 mm thick vermiculite plate, which has a 1.0 mm deep recess. Inside the recess, a 0.7 mm thick steel plate is arranged that is coated with a waterborne coating. Except for the thermocouples and the drilled holes inside the steel plate, the model corresponds geometrically exactly to the experimental setup. Since the small-scale tests on the coated steel plates revealed that the thermocouples have a minor influence on the heating behaviour of the char, leaving out the thermocouples within the modelling approach seems to be sufficiently accurate.
During the tests, the samples were placed together with the vermiculite plates inside the electric furnace. Therefore, both the surface and the sides of the samples

and the vermiculite plates were exposed to direct heating (heating rates: 10, 20, 30, 50 and 70 K/min). Within the coupled thermomechanical analyses, this is taken into account by applying the measured furnace temperatures to both the samples and the vermiculite plates from all sides, except the bottom side. Since the tests were performed within an electric furnace, a reduced heat transfer coefficient of $\alpha_c = 15\ W/(m^2K)$ is used than it is recommended in EN-1991-1-2 (2010) for natural fires ($\alpha_c = 35\ W/(m^2K)$). The emissivity value for the coating and the vermiculite plate, on the other hand, is set to $\varepsilon = 0.8$ according to Tabeling (2014). In Figure 4.13 the application of the measured furnace temperature is symbolised with the help of the red curved arrows.
Between the interacting interfaces of the coating, the steel plate and the vermiculite plate an ideal heat transfer is defined. This is ensured by coupling the thermal degrees of freedom of the interacting nodes. While the temperature-dependent material properties for the steel plate are defined according to EN-1993-1-2 (2010), the behaviour of the vermiculite plate is described according to the manufacturer's specifications (e.g. thermal conductivity $\lambda = 0.07\ W/(mK)$, specific heat capacity $c_p = 1,050\ J/(kgK)$, density $\rho = 180\ kg/m^3$ and Young's modulus $E = 100\ MPa$). Due to limited data, the material behaviour of vermiculite is described temperature-independent.

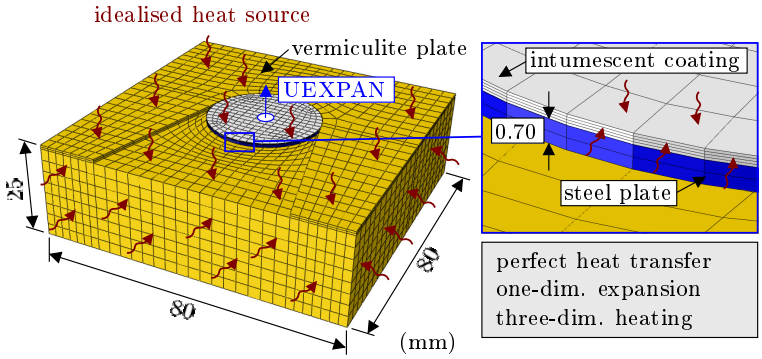

Figure 4.13: Finite element model of the expansion tests composed of a coated steel plate (0.7 mm thick, diameter: 30 mm) and a vermiculite plate (25 mm) as specimen holder

The expansion and heating behaviour of the waterborne coating is described using the developed material model that was presented in the previous section. In order to investigate the correct implementation of the user subroutine UEXPAN, the expansion behaviour of the coating is described in two ways. In a first calculation, the expansion behaviour is described with the help of the thermal expansion coefficients α, which are given in Figure 4.3 and 4.4. The input of the tabulated data into the model is done prior to the simulation. In a second calculation, the user subroutine UEXPAN is used, in order to incrementally calculate the thermal expansion coefficients α_i during the simulations using Equation 4.4. A comparison

of both simulation results provides information about the correct implementation of the user subroutine. The comparison of the simulations with the experimental results, on the other hand, helps to evaluate the accuracy of the material model. In the following, the simulation results obtained for the recalculated expansion tests are presented. Since the high-temperature behaviour is of great interest, only the tests up to 1000 °C are evaluated.

4.3.2 Results and Validation against Test Data

In order to illustrate the transient expansion behaviour of the simulated samples, Figure 4.14 shows the displacement and temperature fields of sample H30-1000-I at different points in time. Within the first minutes, the char formation of the model proves to be irregular (see Figure 4.14 a)). While at the edges the char thickness is already 6.3 mm, it is only 3.7 mm in the centre of the sample. The reason for this is the uneven heating of the sample due to the three-sided fire exposure as can be concluded from the corresponding temperature field in Figure 4.14 d). However, the effect of uneven heating on char formation decreases with further heating. After a further two minutes, the sample already shows uniform char thicknesses when reaching the maximum of expansion (13.9 mm). The same applies also to the reaction state of shrinkage (see Figure 4.14 c)). However, while the char thickness remains uniform during shrinkage (11.2 mm), the temperature field of the foam structure changes. At the end of the simulation (30 minutes), the temperature gradient within the sample is no longer as pronounced as it was after 13 minutes. This corresponds to the increase in thermal conductivity (see subsection 4.2.3), which physically describes the loss of fire protection at higher temperatures.

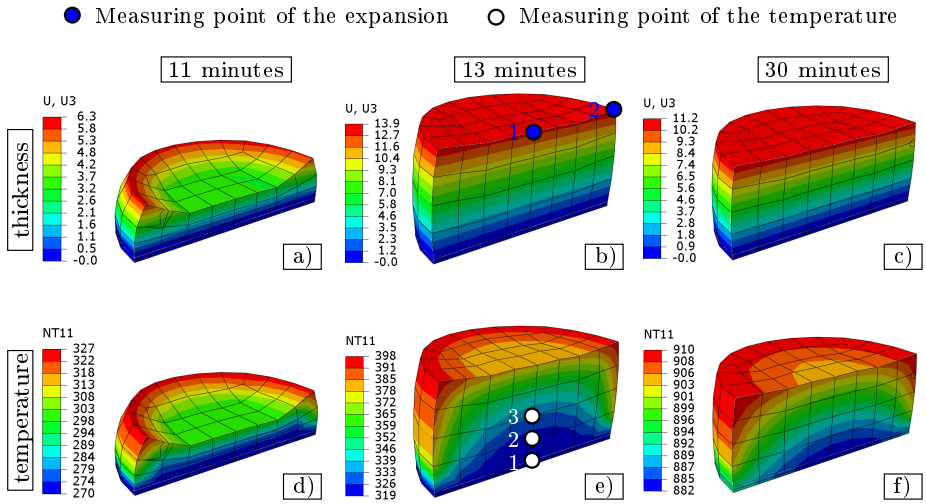

Figure 4.14: Simulated temperature and displacement fields of the sample H30-1000-I at different points in time

In order to better compare the simulation results with the test data, the char thickness and temperature developments within the models were evaluated at several points. These measuring points are defined in Figure 4.14 b) and e). As the char thicknesses and temperatures were measured at different points, the data were averaged before being plotted in Figure 4.15 and 4.16. To compare the simulated char thicknesses with the test data, the values were related to the dry film thickness, in order to determine the corresponding expansion curves.

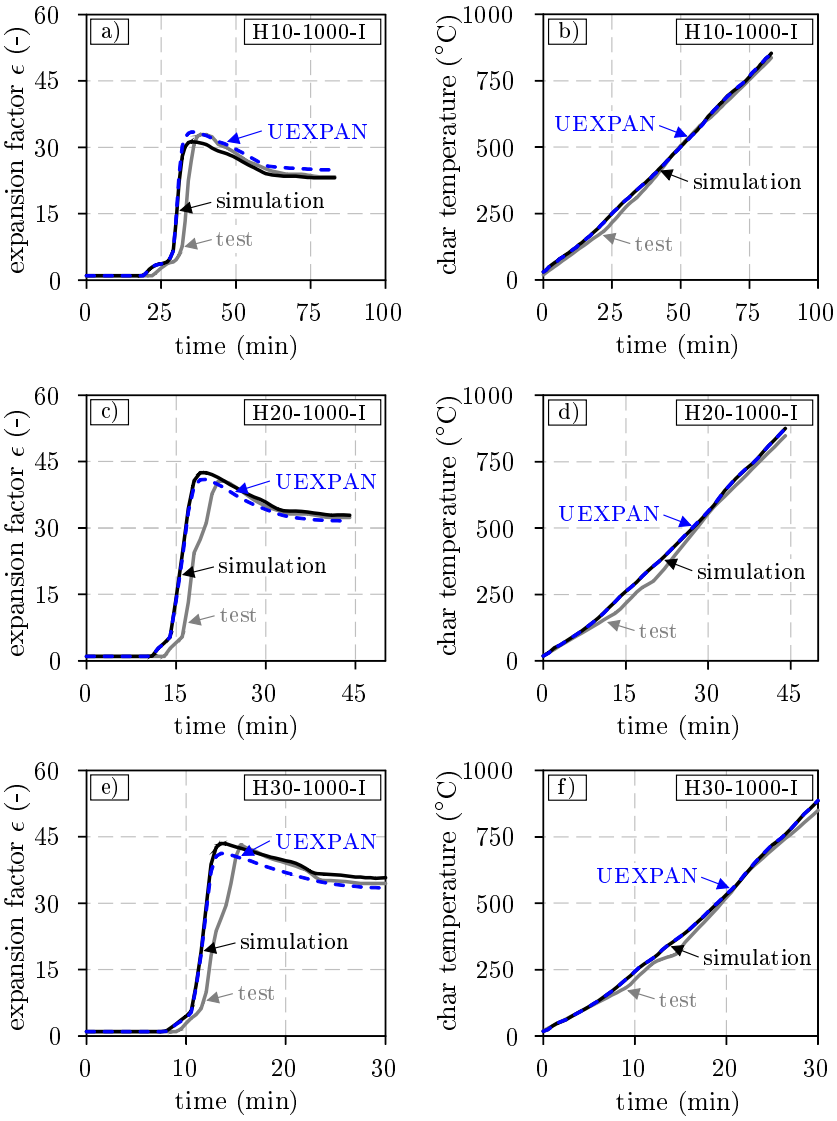

Figure 4.15: Comparison between the simulated (with and without the user subroutine UEXPAN) and measured data of the expansion tests at heating rates of 10, 20 and 30 K/min

The simulation results shown in Figure 4.15 and 4.16 are given as a function of time. The term 'simulation' within the diagrams refers to the results of the benchmark simulations. The term 'UEXPAN', on the other hand, indicates the simulations, in which the user subroutine was used. The third curve in the diagrams represents the test results and serves as a reference for the simulations.
In addition to the diagrams, the measured and simulated maximum expansion factors ϵ_{max} as well as the corresponding char temperatures T_{max} are compared with each other in Table 4.1.

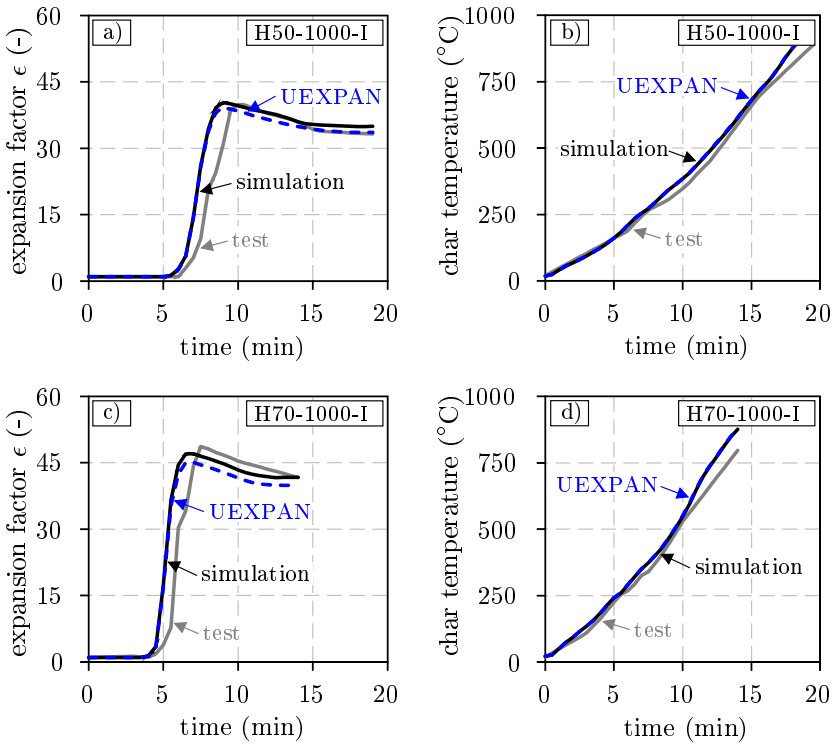

Figure 4.16: Comparison between the simulated (with and without the user subroutine UEXPAN) and measured data of the expansion tests at heating rates of 50 and 70 K/min

As can be seen from the diagrams in Figure 4.15 and 4.16, the expansion curves are almost identical for both simulations (benchmark and UEXPAN-based simulation) until the expansion maximum is reached. Only at the expansion maximum and the subsequent shrinkage certain differences ($\Delta\epsilon = 1.0 - 4.2$) occur between the simulation types. However, since the differences are small (compare the values in Table 4.1), it can be concluded that the implementation of the user subroutine UEXPAN is correct and leads to similar results as the benchmark simulations using tabulated thermal expansion data. However, when using the user subroutine UEXPAN, the following limitation has to be considered. Since the thermal expansion

coefficients α_i are calculated incrementally within the subroutine, the expansion results strongly depend on the temperature change ($\Delta\theta = \theta_i - \theta_{i-1}$) between two increments. When evaluating the results, it turned out that the temperature increments must be limited to a maximum of 5 K. Otherwise, the user subroutine will calculate larger char thicknesses than the benchmark simulations. Since the temperature increments have to be limited, this has an effect on the time required for the simulations.
The comparison between the simulated and the measured expansion curves reveals that the char formation is initiated slightly earlier within the simulations than during the tests. The same applies also to the expansion maximum ϵ_{max}. Here, similar deviations between the simulations and the test results are perceptible. The explanation for this can be found by comparing the averaged char temperatures in the diagrams on the right hand side of Figure 4.15 and 4.16. For both the benchmark and the UEXPAN-based simulations higher char temperatures are reached compared to the expansion tests. Since the expansion behaviour is modelled within the simulations as a function of temperature and higher char temperatures are reached within the simulations, the expansion starts and reaches the maximum earlier with respect to time. However, with regard to the char temperatures, on the other hand, it can be seen that especially for the heating rates of 10, 20 and 30 K/min, the temperatures (T_{max}), at which the expansion maximum is reached, are nearly the same for the simulations and the expansion tests (see Table 4.1). Only for 50 and 70 K/min, certain differences in T_{max} can be identified ($\Delta T_{max} = 7 - 19\,^{\circ}\mathrm{C}$).

Table 4.1: Comparison between the measured and simulated expansion behaviour of the waterborne coating exposed to constant heating rates of 10, 20, 30, 50 and 70 K/min (test: experimental data, sim.: benchmark simulation, UEXPAN: user subroutine-based simulation)

		ϵ_{max}			T_{max}		
sample ID	DFT (μm)	test (-)	sim. (-)	UEXPAN (-)	test (°C)	sim. (°C)	UEXPAN (°C)
H10-1000-I	324	32.87	31.31	33.50	362	351	351
H10-1000-II	331	29.32	31.34	31.96	344	349	349
H20-1000-I	322	40.81	42.61	41.03	355	348	346
H20-1000-II	322	43.34	42.25	44.17	346	347	346
H30-1000-I	329	43.45	43.52	41.28	345	343	343
H30-1000-II	331	45.18	43.28	40.58	352	342	343
H50-1000-I	348	40.07	40.29	39.25	351	343	344
H50-1000-II	355	43.02	40.39	39.39	358	341	343
H70-1000-I	319	48.74	47.19	45.23	349	336	334
H70-1000-II	316	46.96	47.63	43.39	354	335	337

Since the simulated expansion curves are almost identical to the measured expansion curves, except for the shift on the time axis, the following conclusion can be drawn. The time shift of the expansion curves is not due to the developed material model but rather due to the modelled fire exposure. If the expansion starts earlier within the simulations and the maximum expansion values are also reached earlier, but the temperatures, at which the corresponding reaction states occur, are

almost identical to the tests, this is due to stronger heating. During the expansion tests, the furnace temperature was measured in the upper part of the electric furnace. Despite the small furnace geometry, higher temperatures were present here than in the lower part of the furnace, where the samples were arranged. The fact that a certain temperature gradient developed over the furnace height can be seen from the temperatures in Figure 3.32. Here, the furnace temperatures of the steel plate tests are shown together with the char temperatures measured at different heights. Since the thermocouples did not measure the char temperatures until the expansion of the coating, the data represent furnace temperatures until the onset of expansion. As the temperatures measured close to the sample are lower than the measured furnace temperature in the upper part of the furnace, the temperatures acting on the samples are overestimated within the simulations. This finding leads to the explanation for the observed deviations between the simulated and the measured expansion curves. However, at the same time, it also means that the material model as well as the two types of simulations investigated lead to promising and reliable results.
The extent to which the UEXPAN-based simulation method can be used, in order to describe the expansion behaviour of intumescent coatings under an arbitrary fire exposure using elementary expansion curves, is discussed in the following section.

4.3.3 Combination of Elementary Expansion Curves

Based on the comparison between the numerical simulations and the experimental data, it could be shown that the developed material model is able to describe the expansion behaviour of the waterborne coating under constant heating rates with sufficient accuracy. However, natural fires are usually characterised not by only one, but by different heating rates, which sometimes also differ significantly. Therefore, the question arises to what extent the material model is also able to describe the expansion behaviour with good approximation when the waterborne coating is heated with different heating rates in sequence.
Within the scope of the expansion analysis, it was already examined to what extent the expansion behaviour of the waterborne coating changes when it is first heated at 10 and then at 50 K/min and vice versa. The expansion curves measured during these tests now serve as a basis for the validation of the numerical simulations. The approach used for these simulations is described schematically in Figure 4.17. In Figure 4.17 a) the furnace temperature and the mean value of the measured char temperature are shown exemplarily for the expansion test H10/50-325-I. The point in time at which the transition in heating from 10 to 50 K/min occurs is marked within the diagram with t^*. Up to this point, the expansion behaviour is calculated as a function of the expansion curve measured for 10 K/min. As soon as the time t^* and therefore the corresponding char temperature θ^* is exceeded, the sample is heated at higher heating rates. As a consequence, the thermal expansion

coefficients α or α_i (depending on the calculation routine) are calculated from the expansion curve for 50 K/min.
The crossover between the two expansion curves is graphically illustrated in Figure 4.17 b). Here, the blue dashed curve represents the path that is used to calculate the thermal expansion coefficients at each integration point of the model. The calculation approach can be carried out with the help of both the user subroutine UEXPAN and the user subroutine USDFLD. If the simulations are performed by means of the user subroutine USDFLD, the thermal expansion coefficients α are not calculated incrementally but are defined before the calculation as a function of Field Variables (FVs). By changing the Field Variables, the temperature-dependent thermal expansion coefficients derived from the elementary expansion curves are selected depending on the time ($t<t^*$ or $t>t^*$) at which the change in heating rates occurs. In this way, the expansion behaviour of the coating heated with different heating rates in sequence is calculated from two different expansion curves. In the case of the user subroutine UEXPAN, the calculations are performed analogously, except the fact that the thermal expansion coefficients α_i are calculated incrementally depending on the expansion curves and the incremental changes in char temperature.

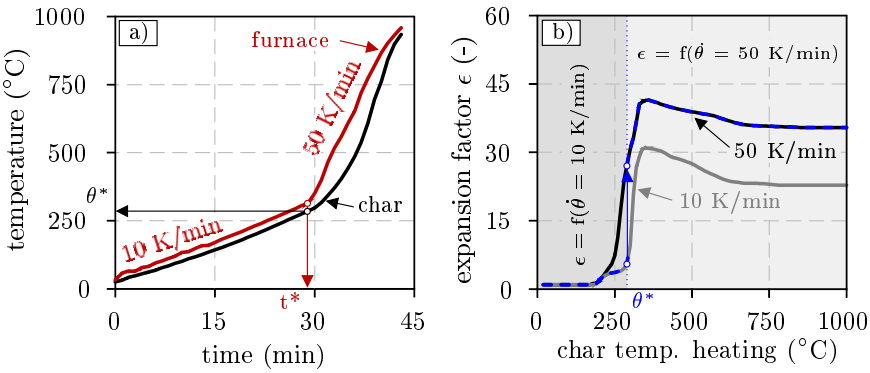

Figure 4.17: Schematic representation of the simulation approach for the expansion behaviour of the waterborne coating due to changes in heating rates: Combination of elementary expansion curves

In order to evaluate the user subroutine-based simulations, the simulation results are compared in Figure 4.18 with the experimental data and the results of the benchmark simulations. For the benchmark simulations, the measured expansion curves of the H10/50 and H50/10 tests were used as input data. In the case of the H10/50 simulations, the expansion behaviour of the samples was described using the mean value of both tests. For this reason, the expansion is underestimated for the first test ($\epsilon_{max} = 48.36$) and overestimated for the second test ($\epsilon_{max} = 36.80$) as can be seen from the expansion factors listed in Table 4.2. In the case of the H50/10 simulations, on the other hand, only the expansion curve from the expansion test H50/10-325-I was used, as the expansion of the second test was falsified

by a crack inside the char. This is the reason why the expansion values for the test H50/10-325-II (ϵ_{max} = 60.05) differ significantly from both the benchmark (ϵ_{max} = 45.35) and the user subroutine-based simulations (ϵ_{max} = 43.59).
Except for the described deviations between the simulations and the experimental data, the user subroutine-based simulations (USDFLD and UEXPAN) show a very good agreement with the benchmark simulations. This applies for both the expansion behaviour (see Figure 4.18 a) and c)) and the temperature development inside the char (see Figure 4.18 b) and d)). Only for the test H50/10-325-II (see Table 4.2) the char temperature T_{max} at which the maximum expansion is reached differ to a slightly greater extent (benchmark sim.: 362 °C, UEXPAN: 344 °C). However, for the fact that the expansion behaviour was combined from two elementary expansion curves, the deviations are tolerable.

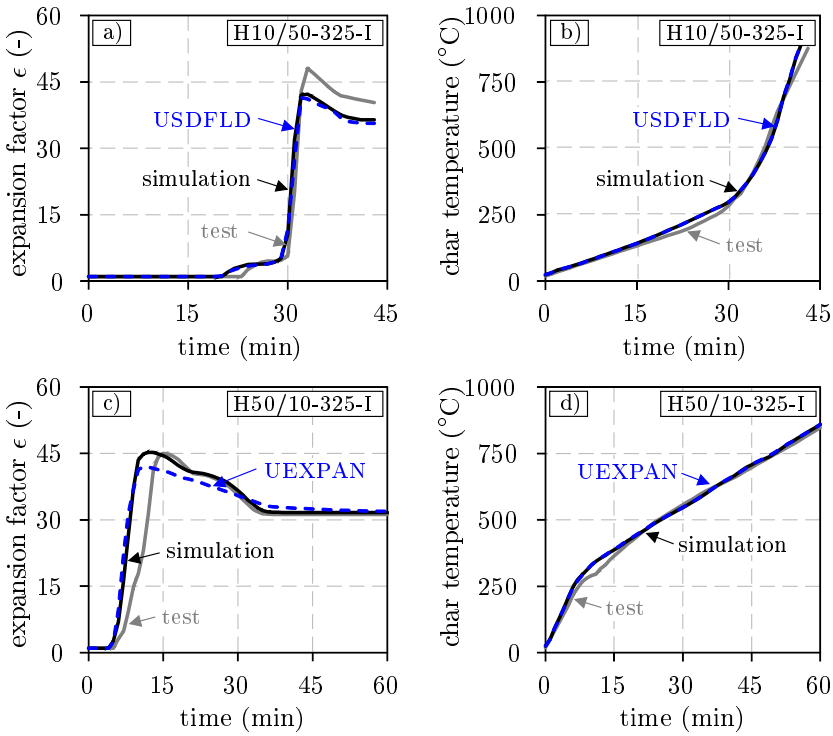

Figure 4.18: Comparison between the measured and simulated expansion curves and char temperatures of the waterborne coating exposed to heating rates of 10 and 50 K/min in sequence (USDFLD/UEXPAN: combination of elementary expansion curves according to Figure 4.17 b))

Although only four tests were recalculated, the results of the performed simulations indicate that the combination of elementary expansion curves (obtained from constant heating rates) can be used in order to describe the expansion behaviour of intumescent coatings under a sequence of different heating rates. Since natural fires can be approximated multilinearly by constant heating rates, it is obvious

that the simulation approach can also be applied to natural fires. However, such simulations are not trivial and require a high level of experience. It is therefore beneficial if experimental data are available which can be used for validation.

Table 4.2: Comparison between the measured and simulated expansion behaviour of the waterborne coating exposed to heating rates of 10 and 50 K/min in sequence (test: experimental data, sim.: benchmark simulation, USDFLD/UEXPAN: user subroutine-based simulation)

		ϵ_{max}			T_{max}		
sample ID	DFT	test	sim.	USDFLD/ UEXPAN	test	sim.	USDFLD/ UEXPAN
	(μm)	(-)	(-)	(-)	(°C)	(°C)	(°C)
H10/50-325-I	302	48.36	42.45	41.45	358	355	349
H10/50-325-II	300	36.80	42.61	41.65	352	354	349
H50/10-325-I	379	45.15	45.27	42.03	370	361	349
H50/10-325-II	315	60.05	45.35	43.59	346	362	344

4.3.4 Discussion

The numerical simulations carried out in section 4.3 were performed under several aspects. First, the new material model should be examined for its suitability to describe the heating and expansion behaviour of the investigated waterborne coating. This was achieved by validating the numerical simulations against expansion tests that were performed at constant heating rates of 10, 20, 30, 50 and 70 K/min. When evaluating the simulations, it was observed that the expansion always starts at the edges (see Figure 4.14). The reason for this is the heating of the samples, as the coating is not only heated from above but also from the side. A similar behaviour could also be observed during the expansion tests, where the initial bubble formation also occurred at the edges. However, in the further course of the expansion mostly convex surfaces were formed (see Figure 3.12 and 3.13). This is due to the surface tension of the viscous matrix and cannot be reproduced within the numerical simulations without further refinement of the material model.
In the second part of the numerical simulations, it was examined whether the expansion behaviour of the investigated coating can be simulated by the combination of two elementary expansion curves when the samples are sequentially exposed to different heating rates. Based on the obtained results, it can be concluded that the hypothesis stated at the beginning of this thesis can be confirmed. The expansion behaviour of intumescent coatings can be described with the help of elementary expansion curves (which are obtained from constant heating rates) even if the coatings are heated at different heating rates in sequence. This represents an important finding for modelling the expansion behaviour of intumescent coatings under the effect of arbitrary natural fires. However, the investigations were only carried out on two different heating rate constellations (10-50 K/min and 50-10 K/min) serving as an example. For a profound evaluation of the simulation approach, further investigations are essential.

4.4 Simulation of the Fire Protection Performance on Steel Plates

4.4.1 Modelling and Parameters

In section 4.3, the focus of the numerical simulations was on the expansion behaviour of the investigated waterborne coating. For this reason, different simulation approaches were examined and compared with each other as well as with results of the expansion tests. In this section, the focus is on the fire protection performance of the coating. Therefore, the temperature development within the steel substrate and the formed char structure are in the first place of interest.
In order to perform the numerical simulations, the finite element model given in Figure 4.19 is used. The model represents geometrically the setup of the small-scale tests that were performed during the experimental investigations and is discretised by solid elements (C3D8T: 8-node thermally coupled bricks). The model consists of coated, 3 or 5 mm thick steel plates (100 x 90 mm) that are arranged within a 50 mm thick vermiculite plate (200 x 200 mm), which serves as specimen holder. As the sides of the steel plates are protected from direct heating, a one-dimensional fire exposure to the coating surface is achieved. Similar to the simulations in section 4.3, modelling of the boreholes inside the steel plates and the thermocouples inside the char is neglected.

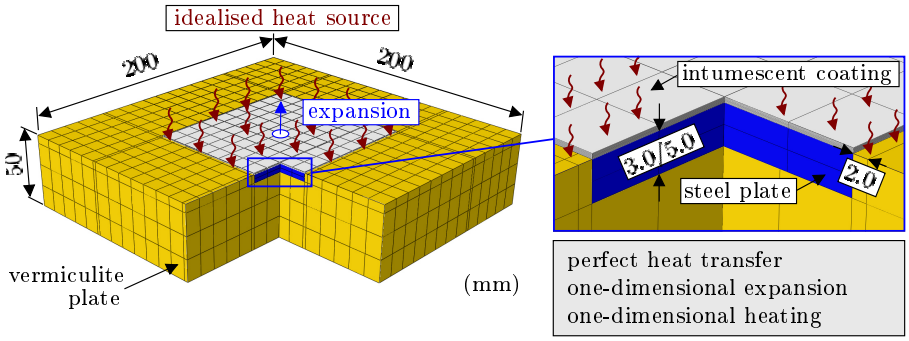

Figure 4.19: Finite element model of the small-scale fire tests composed of coated steel plates (100 x 90 x 5 mm or 100 x 90 x 3 mm) and a vermiculite plate (200 x 200 x 50 mm) used as specimen holder

Due to the arrangement of the samples in front of the electric furnace, in addition to the coating surface, a 2 mm circumferential area of the vermiculite plate is also exposed to direct heating within the numerical simulations. The thermal impact is defined according to the measured furnace temperatures and is idealised in Figure 4.19 by red curved arrows. The heat transfer due to radiation and convection is described analogously to the simulations in section 4.3. For the convective heat transfer a heat transfer coefficient of $\alpha_c = 15\ W/(m^2K)$ is used. For the radiation,

on the other hand, an emissivity value of $\varepsilon = 0.8$ is defined for both the coating surface and the vermiculite plate.
The thermal material behaviour of the coating is described on the basis of the new developed material model (see section 4.2). The thermal material properties of the steel plate are defined according to EN-1993-1-2 (2010). For the vermiculite plate, on the other hand, the material properties introduced in subsection 4.3.1 are used. The investigations in subsection 4.3.2 have shown that modelling of the expansion behaviour with the user subroutine UEXPAN and via the tabular input of thermal expansion coefficients leads to almost identical results. For this reason, the expansion of the waterborne coating in the simulations with constant heating rates is described via the input of thermal expansion coefficients. Only for the numerical simulations with a natural fire exposure, in which the samples are also exposed to a cooling phase, the expansion behaviour is described with the help of the user subroutine UEXPAN.

4.4.2 Results and Validation against Test Data

Within the scope of the experimental investigations, small-scale fire tests were carried out on unprotected steel plates. The results of these tests served as a reference to evaluate the fire protection performance of the investigated coatings. In the course of the numerical simulations, these tests were also recalculated with the aim to better evaluate the differences in heating behaviour of the coated steel plates between the simulations and the tests. Therefore, in the following section, the simulation results of the unprotected steel plates are briefly discussed with regard to their correlation with the test data.

Unprotected Steel Plates:

For the simulations of the unprotected steel plates, the numerical model described in Figure 4.19 was used. However, as the steel plates had to be exposed to direct heating, the coating on the top of the steel plates was removed. As a consequence, the emissivity value of the fire exposed surface (now steel surface) had to be changed to $\varepsilon = 0.7$ according to EN-1993-1-2 (2010).
In order to evaluate the accuracy of the numerical simulations, Figure 4.20 shows a comparison of the simulated and measured temperature-time curves of 5 mm thick steel plates at different heating conditions. The furnace temperatures forming the basis for the numerical simulations are also graphically represented in the diagrams. The best agreements between the numerical simulations and the experimental results are obtained for the highest heating rates (50 and 70 K/min). The greatest deviations ($\Delta T = 84\,^{\circ}\mathrm{C}$ and $114\,^{\circ}\mathrm{C}$), on the other hand, are observed for heating rates of 20 and 30 K/min (see Figure 4.20 b) and c)). For 10 K/min the maximum temperature difference between the simulation and the experiment is $61\,^{\circ}\mathrm{C}$. In all three cases, the measured steel plate temperatures are exceeded by the numerical simulations. The reason for this can be attributed to the fire exposure defined

within the simulations. Since the gas temperatures were measured in the upper part of the electric furnace, they are higher than the temperatures near the test specimen. Especially at low and medium heating rates, this leads to an overestimation of the simulated steel plate temperatures. At higher heating rates (50 and 70 K/min), on the other hand, the effect is less pronounced as the samples do not heat up as quickly due to thermal inertia.

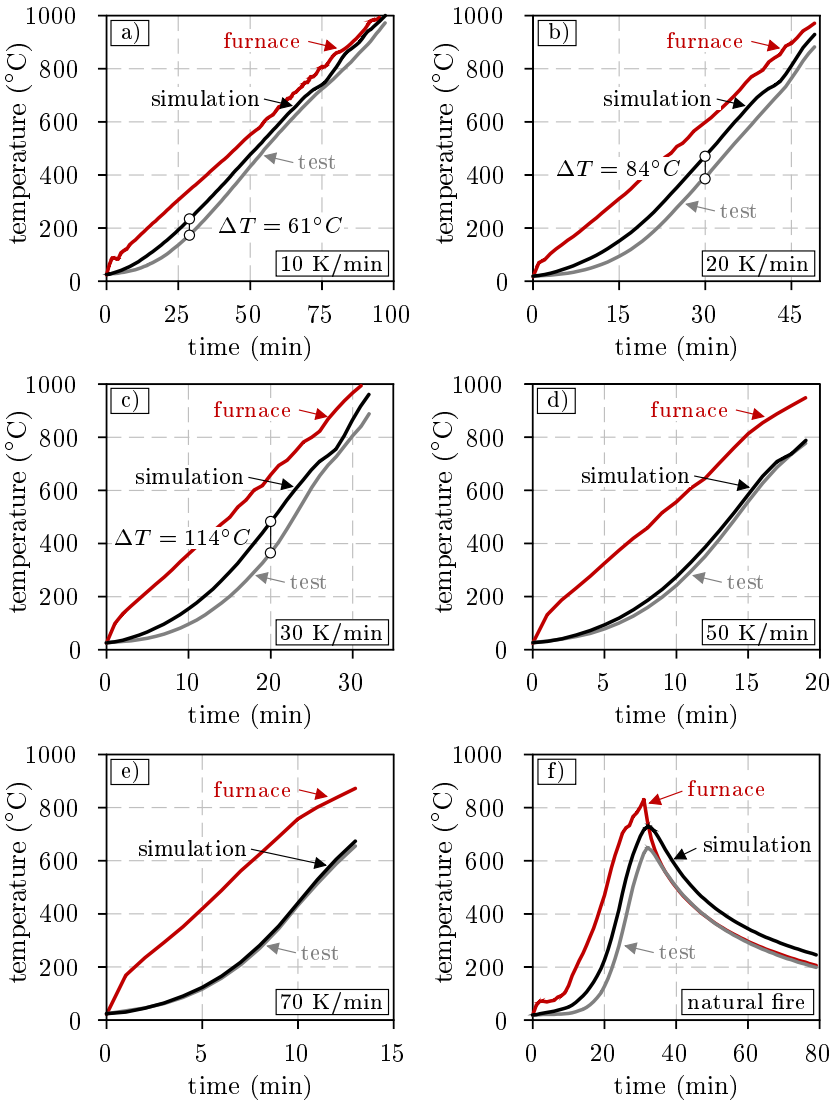

Figure 4.20: Comparison of simulated and measured temperatures of unprotected steel plates (100 x 90 x 5 mm) at heating conditions of: a) 10 K/min, b) 20 K/min, c) 30 K/min, d) 50 K/min, e) 70 K/min and f) natural fire

The simulations carried out for the 3 mm thick steel plates show a better agreement with the test results. This can be deduced from the data shown in Figure 4.21 a). Here the simulated steel plate temperatures are plotted against the test results. In this way, the simulation results can be easily compared with the test data. In order to evaluate the quality of the numerical simulations, boundary values for a deviation of +20 % and -20 % are included in the diagram.
Similar to the 5 mm steel plates, the best agreements between the simulated and measured steel plate temperatures are achieved for the highest heating rates. For the sake of completeness, the results of the 5 mm steel plates were prepared in the same way and are given in Figure 4.21 b). The comparison of both diagrams reveals that the simulated temperatures of the 5 mm steel plates are overestimated to a greater extent than for the 3 mm steel plates. However, as the differences between the simulation results and the test data are due to the higher fire load, the model used for the simulations appears to be suitable. For the evaluation of the numerical simulations of the coated steel plates, this finding provides a great assistance.

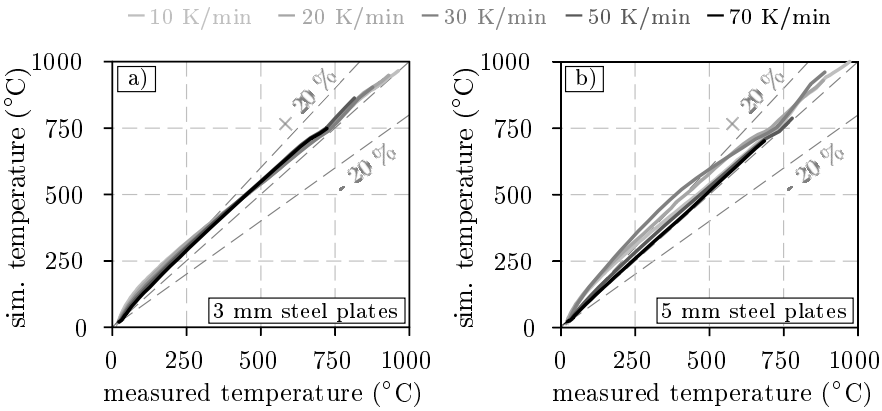

Figure 4.21: Validation of simulated temperatures of unprotected steel plates (100 x 90 mm) at constant heating rates of 10, 20, 30, 50 and 70 K/min: a) 3 mm steel plates and b) 5 mm steel plates

Constant Heating Rates:

In order to validate the thermal material model of the waterborne coating with regard to its ability to realistically describe the fire protection performance, all small-scale tests from section 3.4 were recalculated. Due to the large amount of data, the simulation results are compared with the test data with the help of the presentation form that was already used in Figure 4.21. The results are documented separately for the 3 and 5 mm thick steel plates in Figure 4.22 and 4.23. In addition to the temperature curves, the maximum steel plate temperatures T_{max} and char thicknesses t_{final} reached at the end of the simulations are compare with the test results in Table 4.3 and 4.4.

At the beginning of the simulations the steel plate temperatures from the tests are significantly overestimated. This can be seen in the diagrams of Figure 4.22 and 4.23 for both the 3 and 5 mm steel plates. However, with further heating the deviations between the simulations and the test results decrease. At the end of the simulations, in most cases the calculated steel plate temperatures show a very good agreement with the measured values from the tests.

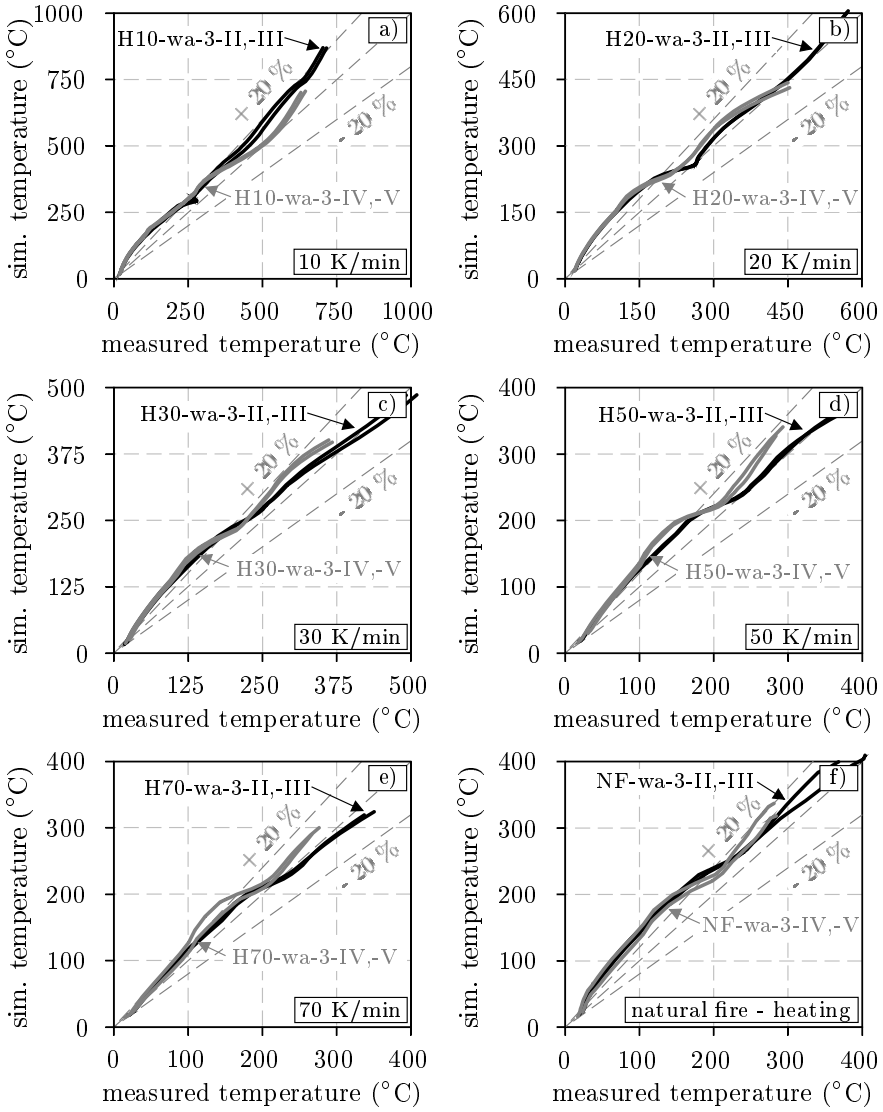

*Figure 4.22: Validation of simulated temperatures of coated steel plates (**100 x 90 x 3 mm**, waterborne coating) at heating conditions of: a) 10 K/min, b) 20 K/min, c) 30 K/min, d) 50 K/min, e) 70 K/min and f) natural fire*

Greater deviations are only observed for the heating rates of 10 K/min. Here, the steel plate temperatures are overestimated within the simulations by 154-167 °C for the 3 mm steel plates and 109-125 °C for the 5 mm steel plates (compare the values for ΔT in Table 4.3 and 4.4). However, this only applies to the test specimens with the lower dry film thicknesses. For higher dry film thicknesses, the measured steel plate temperatures are overestimated by only 61-71 °C and 42-74 °C.

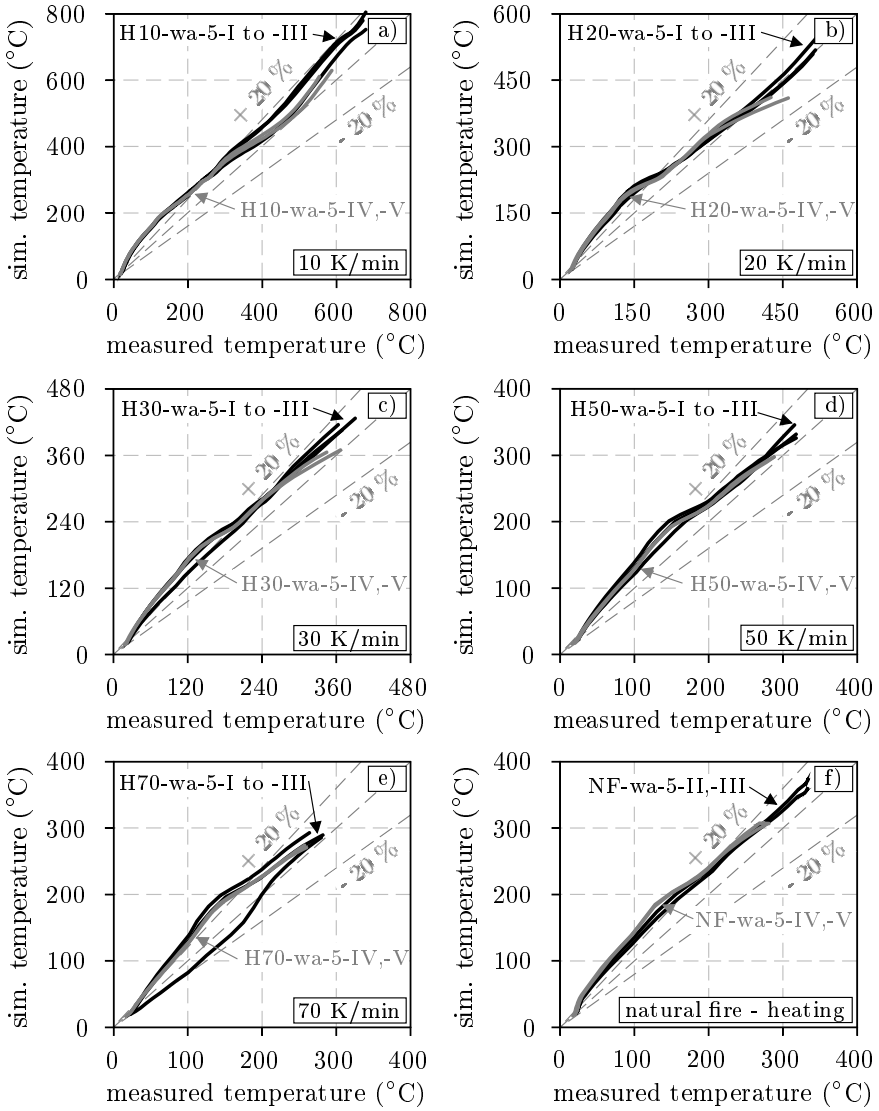

*Figure 4.23: Validation of simulated temperatures of coated steel plates (**100 x 90 x 5 mm**, waterborne coating) at heating conditions of: a) 10 K/min, b) 20 K/min, c) 30 K/min, d) 50 K/min, e) 70 K/min and f) natural fire*

For the remaining samples, the deviations between the simulated and measured steel plate temperatures are approximately +/-30 °C. As a consequence, the defined limits for tolerable deviations of +/-20 % are clearly met. The only exceptions are the tests H50-3-wa-IV and H50-3-wa-V as well as H20-5-wa-IV and H30-5-wa-I. Here, the measured steel plate temperatures are exceeded by the simulations with a maximum of 52 °C and undercut by 51 °C (see Table 4.4).

*Table 4.3: Comparison between measured and simulated steel temperatures (T_{max}) and final char thicknesses (t_{final}) of the waterborne coating for steel plates **100 x 90 x 3 mm**. Differences in steel plate temperature between simulation and test $\Delta T = T_{max,sim.} - T_{max,test}$ and differences in char thickness $\Delta t_{final} = t_{final,sim.} - t_{final,test}$*

Sample ID	heating cond. (-)	DFT (μm)	T_{max} (°C) test	sim.	ΔT (°C)	t_{final} (mm) test	sim.	Δt_{final} (mm)
H10-wa-3-II	10 K/min	607	703	870	+167	17.8	13.4	-4.4
H10-wa-3-III	10 K/min	634	715	869	+154	22.4	14.0	-8.4
H10-wa-3-IV	10 K/min	1135	644	705	+61	24.4	25.0	+0.6
H10-wa-3-V	10 K/min	1170	629	700	+71	25.5	25.6	+0.1
H20-wa-3-II	20 K/min	615	569	600	+31	17.8	19.5	+1.7
H20-wa-3-III	20 K/min	616	572	605	+33	19.7	19.4	-0.3
H20-wa-3-IV	20 K/min	1150	450	443	-7	34.1	38.7	+4.6
H20-wa-3-V	20 K/min	1195	453	432	-21	33.2	40.8	+7.6
H30-wa-3-II	30 K/min	627	492	486	-6	21.7	22.7	+1.0
H30-wa-3-III	30 K/min	628	510	486	-24	22.2	22.7	+0.5
H30-wa-3-IV	30 K/min	1222	368	397	+29	37.5	47.5	+10.0
H30-wa-3-V	30 K/min	1238	362	401	+39	38.3	47.9	+9.6
H50-wa-3-II	50 K/min	642	366	362	-4	27.0	23.9	-3.1
H50-wa-3-III	50 K/min	648	374	363	-11	25.6	23.9	-3.1
H50-wa-3-IV	50 K/min	1242	293	341	+48	39.9	43.7	+3.8
H50-wa-3-V	50 K/min	1258	284	327	+43	38.0	43.2	+5.2
H70-wa-3-II	70 K/min	645	337	319	-18	27.3	27.6	+0.3
H70-wa-3-III	70 K/min	645	351	324	-27	28.1	27.6	-0.5
H70-wa-3-IV	70 K/min	1257	266	290	+24	33.4	42.6	+9.2
H70-wa-3-V	70 K/min	1266	277	300	+23	35.4	45.1	+9.7
NF-wa-3-II	natural fire	655	368	400	+32	28.8	21.4	-7.4
NF-wa-3-III	natural fire	664	403	410	+7	28.0	21.1	-6.9
NF-wa-3-IV	natural fire	1276	301	337	+36	44.8	47.2	+2.4
NF-wa-3-V	natural fire	1277	294	318	+24	42.7	47.2	+4.5

In addition to the steel plate temperatures, during the small-scale fire tests also the char temperatures of the investigated coatings were measured using equidistantly arranged thermocouples. Therefore, these temperatures can also be used to validate the material model of the waterborne coating, similar to the investigations carried out by Norgaard et al. (2016) (see Figure 2.51).
In Figure 4.24 the simulated and measured char temperatures of the samples H10-wa-5-II and H30-wa-5-II are compared with each other. For reasons of clarity, only the curves of the thermocouples 0, 6 and 12 mm are depicted. When comparing the steel plate temperatures, it was already found that heating the coated steel plates at 10 K/min causes the simulation results to exceed the experimental data by a greater extent. This observation can also be confirmed with regard to the char

temperatures. While the simulated char temperatures at 30 K/min agree very well with the measured curves at all three measuring points (see Figure 4.24 b)), the char temperatures at 10 K/min are overestimated by the simulation. This even applies to the period prior to the onset of expansion (see Figure 4.24 a)). For this reason, it can be concluded that these deviations are not due to the material model of the coating but rather due to the increased furnace temperatures defined within the model.

*Table 4.4: Comparison between measured and simulated steel temperatures (T_{max}) and final char thicknesses (t_{final}) of the waterborne coating for steel plates **100 x 90 x 5 mm**. Differences in steel plate temperature between simulation and test $\Delta T = T_{max,sim.} - T_{max,test}$ and differences in char thickness $\Delta t_{final} = t_{final,sim.} - t_{final,test}$*

Sample ID	heating cond. (-)	DFT (μm)	T_{max} (°C) test	sim.	ΔT (°C)	t_{final} (mm) test	sim.	Δt_{final} (mm)
H10-wa-5-I	10 K/min	534	679	804	+125	15.8	11.8	-4.0
H10-wa-5-II	10 K/min	648	671	780	+109	15.5	14.2	-1.3
H10-wa-5-III	10 K/min	667	679	753	+74	14.8	14.6	-0.2
H10-wa-5-IV	10 K/min	1170	587	629	+42	30.0	25.7	-4.3
H10-wa-5-V	10 K/min	1170	554	610	+56	29.5	25.8	-3.7
H20-wa-5-I	20 K/min	655	516	518	+2	21.0	20.9	-0.1
H20-wa-5-II	20 K/min	604	511	509	-2	20.4	19.3	-1.1
H20-wa-5-III	20 K/min	549	540	573	+33	19.4	17.4	-2.0
H20-wa-5-IV	20 K/min	1212	461	410	-51	39.2	41.3	+2.1
H20-wa-5-V	20 K/min	1214	426	411	-15	40.3	41.4	+1.1
H30-wa-5-I	30 K/min	578	363	415	+52	25.2	21.1	-4.1
H30-wa-5-II	30 K/min	575	391	427	+36	23.8	21.0	-2.8
H30-wa-5-III	30 K/min	655	370	406	+36	28.9	24.0	-4.9
H30-wa-5-IV	30 K/min	1151	367	370	+3	42.8	44.2	+1.4
H30-wa-5-V	30 K/min	1156	345	366	+21	44.2	44.6	+0.4
H50-wa-5-I	50 K/min	528	316	346	+30	30.3	19.2	-11.1
H50-wa-5-II	50 K/min	621	318	332	+14	29.2	22.8	-6.4
H50-wa-5-III	50 K/min	635	318	326	+8	27.9	23.4	-4.5
H50-wa-5-IV	50 K/min	1156	288	298	+10	37.3	38.0	+0.7
H50-wa-5-V	50 K/min	1162	288	298	+10	38.8	38.2	-0.6
H70-wa-5-I	70 K/min	578	279	286	+7	31.8	24.4	-7.4
H70-wa-5-II	70 K/min	601	282	289	+7	26.9	25.3	-1.6
H70-wa-5-III	70 K/min	624	264	293	+29	28.6	26.3	-2.3
H70-wa-5-IV	70 K/min	1199	257	274	+17	35.5	38.5	+3.0
H70-wa-5-V	70 K/min	1227	260	271	+11	35.8	35.4	-0.4
NF-wa-5-II	natural fire	563	333	373	+40	27.0	19.8	-7.2
NF-wa-5-III	natural fire	596	333	360	+27	28.8	21.2	-7.6
NF-wa-5-IV	natural fire	1246	304	306	+2	46.3	44.8	-1.5
NF-wa-5-V	natural fire	1252	295	307	+12	49.5	44.9	-4.6

Except for the 10 K/min tests, the simulated char temperatures agree very well with the test data. The reason for this good agreement is due to the fact that not only the steel plate temperatures are simulated with a good approximation, but also the char thicknesses. This can be deduced from the graphical evaluation of the char formation of all simulated steel plate tests in Figure 4.25. Within the diagrams, the simulated char thicknesses are plotted analogously to the steel plate temperatures over the measured values from the tests. Since the char thicknesses

were measured after the experiments, only the final values from the simulations are used for the comparison. The simulations were performed for five different heating rates. Therefore, the differentiation of the fire exposure is achieved by five different symbols. The differentiation of the dry film thicknesses (low and high), on the other hand, is ensured by different colours.

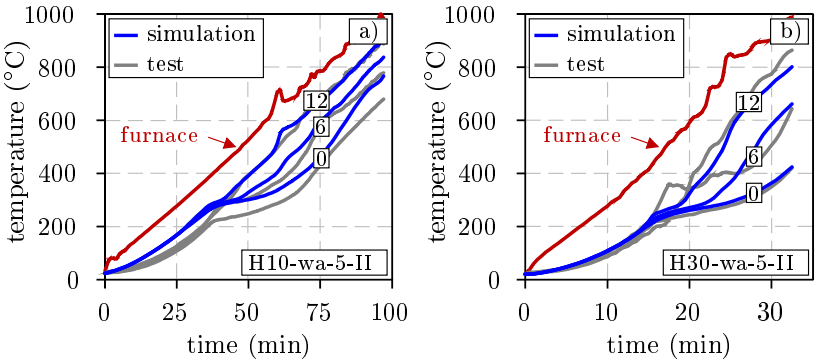

Figure 4.24: Comparison between simulated and measured char temperatures at measuring points located 0, 6 and 12 mm above the coating surface: a) sample H10-wa-5-II and b) sample H30-wa-5-II

For the 3 mm steel plates with low dry film thickness (see Figure 4.25 a)), the simulated char thicknesses agree very well with the test results. Only for 10 K/min the formed char thicknesses are undercut by 4.4 and 8.4 mm (see the values for Δt_{final} in Table 4.3). However, a heating rate dependency in the expansion behaviour can still be derived from the data points.

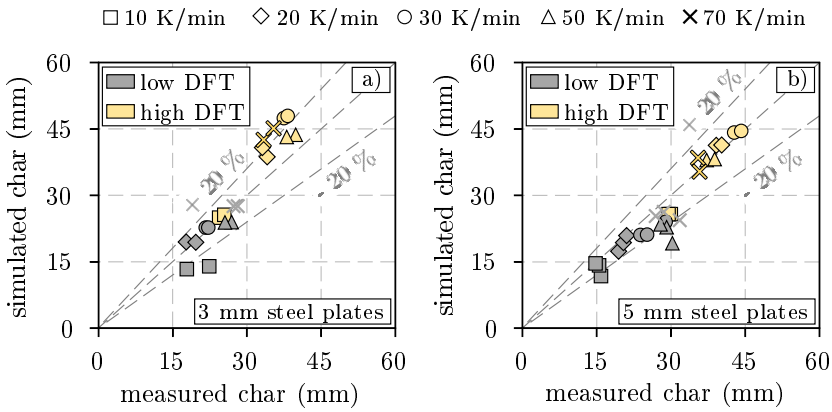

Figure 4.25: Validation of the char thickness simulation for the waterborne coating applied on 3 and 5 mm steel plates. Comparison of the simulated and measured char thickness t_{final} for constant heating rates of 10, 20, 30, 50 and 70 K/min

With increasing heating rates, higher values for the final char thickness t_{final} are reached. However, this only applies to the samples with a low dry film thickness. For higher dry film thicknesses, this finding only applies up to a heating rate of 30 K/min. For 50 and 70 K/min, lower char thicknesses are achieved, as the thermal effect does not last long enough to cause the entire coating to expand. This does not only apply for the 3 mm steel plates but also for the 5 mm steel plates (see Figure 4.25 b)). For the 3 mm steel plates in combination with the high dry film thicknesses the final char thicknesses are slightly overestimated. The simulations for the 5 mm steel plates and the high dry film thicknesses, on the other hand, agree very well with the test results. In both cases, the 3 and 5 mm steel plates, the data reveal also that the final char thicknesses for 10 K/min are significantly lower compared to the other heating rates (compare the yellow squares □ in the diagrams). This can be explained among others by the slower heating and the resulting pronounced shrinkage behaviour of the char. The reduced expansion prior to shrinkage additionally intensifies this effect.
For a more detailed comparison of the simulated and measured char thicknesses (t_{final}), please refer to Table 4.3 and 4.4.

Natural Fire:

In addition to the constant heating rates, the tests performed under the natural fire exposure were also recalculated within the numerical simulations. In contrast to the constant heating rates, the steel plates were exposed during the natural fire to both a heating and a cooling phase. For the thermal behaviour of the waterborne coating during heating and cooling, a material model was developed and presented in section 4.2. While the suitability of the material model has already been proven for the heating phase, it still needs to be verified for the cooling phase. For this reason, the results of the numerical simulations are compared with the natural fire tests in the following.
Before the results of the coated steel plates are discussed, the simulation results of the unprotected steel plates are presented first. The comparison of the simulated and measured steel plate temperatures resulting from the natural fire exposure are given in Figure 4.20 f) for the test NF-5. Similar to the other unprotected test specimens, the steel temperatures are overestimated in a range of 47-144 °C by the simulations. This applies to both the heating and cooling phase. However, compared to the tests, an error is made during the description of the cooling phase within the simulations. During the small-scale fire tests, the cooling phase was realised by switching off the heating elements of the electric furnace. As a result, both the furnace and the sample cooled down. This resulted in a temperature balance between the sample and the furnace, which is why the temperature curves of the furnace and the unprotected steel plate intersect in Figure 4.20 f). From a physical point of view, by switching off the heating elements, no further heat energy was supplied to the samples. However, with the input of the measured furnace temperatures into the simulation model, a heat input through convection and radiation is

physically described during the cooling phase. For this reason, the steel plate cools down at a lower rate in the simulation, so that the steel temperature exceeds the furnace temperature during the cooling phase. A similar behaviour was already observed during the large-scale fire test (see Figure 3.55). Here, the oil burners were only throttled. Therefore, thermal energy continued to be supplied to the test specimens. In order to avoid additional heat input during the cooling phase into the coated steel plates, the furnace temperatures measured in the tests are adjusted before the input into the simulation model. As soon as the cooling phase occurs, the furnace temperature is set to 20 °C. The results of these calculations are given in Figure 4.26 as well as in Figure 4.22 f) and 4.23 f). In addition, in Table 4.3 and 4.4 the simulated and measured steel plate temperatures T_{max} are compared with each other.

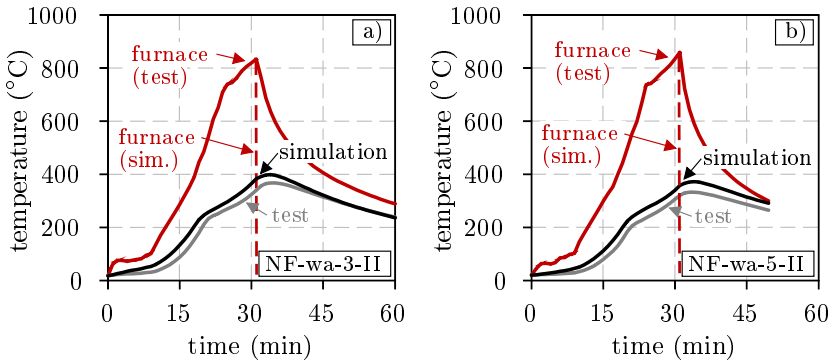

Figure 4.26: Comparison of simulated and measured steel plate temperatures of coated steel plates (100 x 90 mm) exposed to a natural fire: a) test specimen NF-wa-3-II and b) test specimen NF-wa-5-II (see Table 4.3 and 4.4)

Similar to the unprotected test specimens, the temperatures of the coated steel plates are overestimated in the simulations as can be seen from the graphs in Figure 4.26. However, with 2-40 °C, the differences between simulation and test are significantly smaller (compare the values for ΔT in Table 4.3 and 4.4). In addition to the absolute values, the course of the temperature curves is also crucial for the evaluation of the results. As can be seen from Figure 4.26, the time at which the coating starts to expand and the maximum steel plate temperature is reached agree very well between simulation and test. In the cooling phase, the temperatures also show a very good agreement. This applies for both the 3 and the 5 mm steel plates. The evaluation of the expansion behaviour, on the other hand, is more differentiated. Figure 4.27 shows the simulated char thickness development over time for all investigated small-scale tests under the natural fire exposure. In order to compare the values with each other, the measured char thicknesses are also included in the diagrams. However, as the char thicknesses were only measured after the tests, the test data are represented in the diagrams by single data points. In order to eval-

uate the influence of the transition from heating to cooling on the char thickness development, a blue dotted line is integrated in the diagrams representing the time of transition.
As can be seen from the graphs in Figure 4.27, the expansion of the simulated coating is initiated nearly at the same time for all four samples (-II, -III, -IV and -V). Differences are only observed between the two steel plate thicknesses. Due to the lower mass of the 3 mm steel plates, the expansion starts slightly earlier than for the 5 mm steel plates. While the samples with low dry film thickness (-II and -III) reached their expansion maximum and start to shrink when the heating phase turns into the cooling phase, the expansion of the samples with high dry film thickness (-IV and -V) is stopped without reaching the maximum. This corresponds to the material formulation of the waterborne coating that no changes in char thickness occur with the onset of the cooling phase. However, for the 5 mm steel plates, expansion still takes place to a certain extent after the transition from heating to cooling. This is due to the time delay in the cooling behaviour of the char. As soon as the temperature gradient inside the char reverses, the expansion stops according to the material formulation. The same applies also to the shrinkage behaviour.

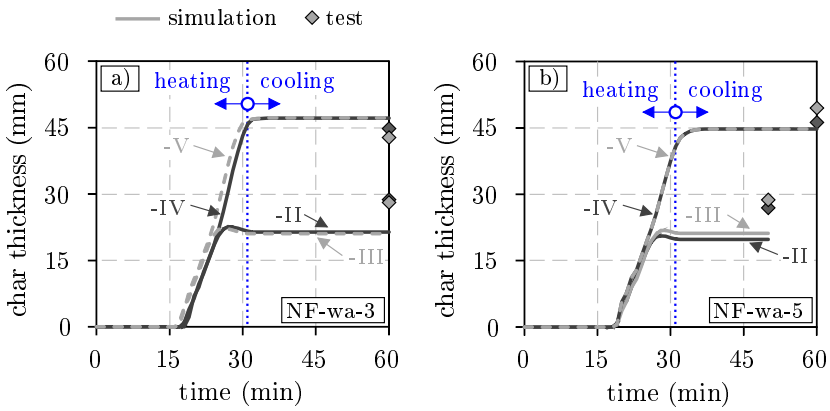

Figure 4.27: Comparison of simulated and measured char thicknesses of coated steel plates (100 x 90 mm) exposed to a natural fire: a) 3 mm steel plates and b) 5 mm steel plates (low DFT: -II, -III; high DFT: -IV, -V)

Regarding the approximation accuracy, the simulations show a very good agreement with the measured char thickness values from the tests -IV and -V. Here, the deviations are between -4.6 and +4.5 mm (compare the values for Δt_{final} in Table 4.3 and 4.4). Greater deviations, on the other hand, are observed for the tests -II and -III. For both the 3 and 5 mm steel plates, the char thickness is underestimated by 6.9 to 7.6 mm compared to the tests. A potential reason for these deviations could be the uneven expansion of the coating observed in the tests. Since the char thickness varied between 22 and 34 mm, the mean value is noticeably higher than in the simulations.
Despite the deviations, it can be stated that the application of the material model

leads to satisfying results in the case of the natural fire simulations. With the onset of the cooling phase, the irreversible expansion behaviour of the coating is correctly represented by the use of the user subroutine UEXPAN. In combination with the thermal material properties defined for the cooling phase, this enables a realistic description of the temperature development of the steel plates. However, a further evaluation of the material model will be carried out as part of the recalculation of the large-scale fire test in section 4.5. Here, a possible scale influence as well as the temperature development of the test specimens during the cooling phase will be investigated.

4.4.3 Evaluation of the Effective Thermal Conductivity

In subsection 2.2.7, experimental investigations carried out by Wang et al. (2013) and Lucherini et al. (2018) were discussed, in which the fire protection performance of their investigated coatings was analysed using the method of the *effective thermal conductivity* according to EN-13381-8 (2013). The results of both research groups revealed some inconsistencies. In the case of Wang et al. (2013), for example, the results of the effective thermal conductivity calculations indicate that test specimens with lower dry film thicknesses provide better fire protection, although the test specimens have higher temperatures and lower char thicknesses. Lucherini et al. (2018) additionally reported that their calculations of the effective thermal conductivity lead to the conclusion that the fire protection performance of their investigated coatings deteriorates with higher heating rates, although the measured steel temperatures show a contrary behaviour.
The effective thermal conductivity method is based on three main assumptions, which have already been presented in subsection 2.2.7. When discussing the experimental investigations of Wang et al. (2013) and Lucherini et al. (2018), these assumptions were identified as a possible reason for their contradictory results.
In order to investigate the calculation method and its associated assumptions, the results of the numerical simulations are used to perform comparative calculations. For the calculation of the effective thermal conductivity according to EN-13381-8 (2013), besides the dry film thickness of the coating (d_p) and the section factor (A_p/V), the steel plate temperature ($\theta_{a,t}$) and the gas temperature (θ_{gas}) are primarily required. In addition to the standard-based calculations, comparative calculations are carried out using the surface temperature of the char (θ_t) instead of the surrounding gas temperature. The char surface temperature is difficult to measure in the tests, but easy to determine in the numerical simulations. The measuring points used to determine the steel plate and char surface temperatures in the simulations are defined in Figure 4.28. Here, the results of a temperature field calculation are exemplarily shown for the test specimen H10-wa-5-V after 60 minutes of fire exposure. In addition to the measuring points, a path is marked inside the expanded char, which is used to determine the temperature gradient across the char thickness at different points in time. Within the calculation method of

the effective thermal conductivity, a linear temperature gradient inside the char structure is assumed. With the help of the simulated char temperatures measured along the defined path, this assumption can be examined.

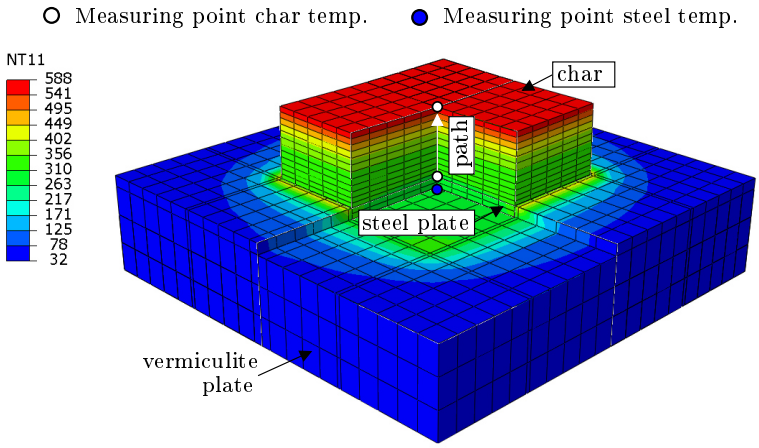

Figure 4.28: Results of the temperature field simulation for sample H10-wa-5-V after 60 minutes of fire exposure. The measuring points of the steel plate and char temperatures used for the calculation of the effective thermal conductivity are marked by blue and white circles

In order to calculate the effective thermal conductivity of the investigated water-borne coating, the steel plate temperatures and surface temperatures of the char were determined from the numerical simulations performed on the coated steel plates. Both the steel plate and char temperatures are given in Figure 4.29 and 4.30 as a function of time for a selection of test specimens representing the heating rates of 10, 20, 30, 50 and 70 K/min. The furnace temperatures, on the other hand, were taken from the small-scale fire tests and are also shown in the diagrams on the left hand side. On the right hand side of Figure 4.29 and 4.30 the results of the effective thermal conductivity calculations are depicted. As the calculations were carried out for both the furnace temperature and the actual surface temperature of the char structure, two curves are given in each diagram.
Until the expansion of the coating, the simulated surface temperature and the steel plate temperature are almost identical (see for example Figure 4.29 a)). For this reason, very high effective thermal conductivity values are calculated (see for example Figure 4.29 b)). This corresponds to an almost unhindered heating of the samples. Between the furnace temperature and the steel plate temperature, on the other hand, differences occur due to thermal inertia. Therefore, as soon as the char temperature is approximated within the calculation method by the furnace temperature, effective thermal conductivity values are calculated, which suggest a certain fire protection effect, although the coating has not yet reacted. For this reason, the results of the effective thermal conductivity calculations are falsified as soon as the surface temperature of the coating is approximated by the furnace

temperature. However, this is only valid until the onset of expansion. As soon as the coating starts to expand, the two calculated curves of the effective thermal conductivity start to converge as can be seen from the diagrams on the right hand side of Figure 4.29 and 4.30.

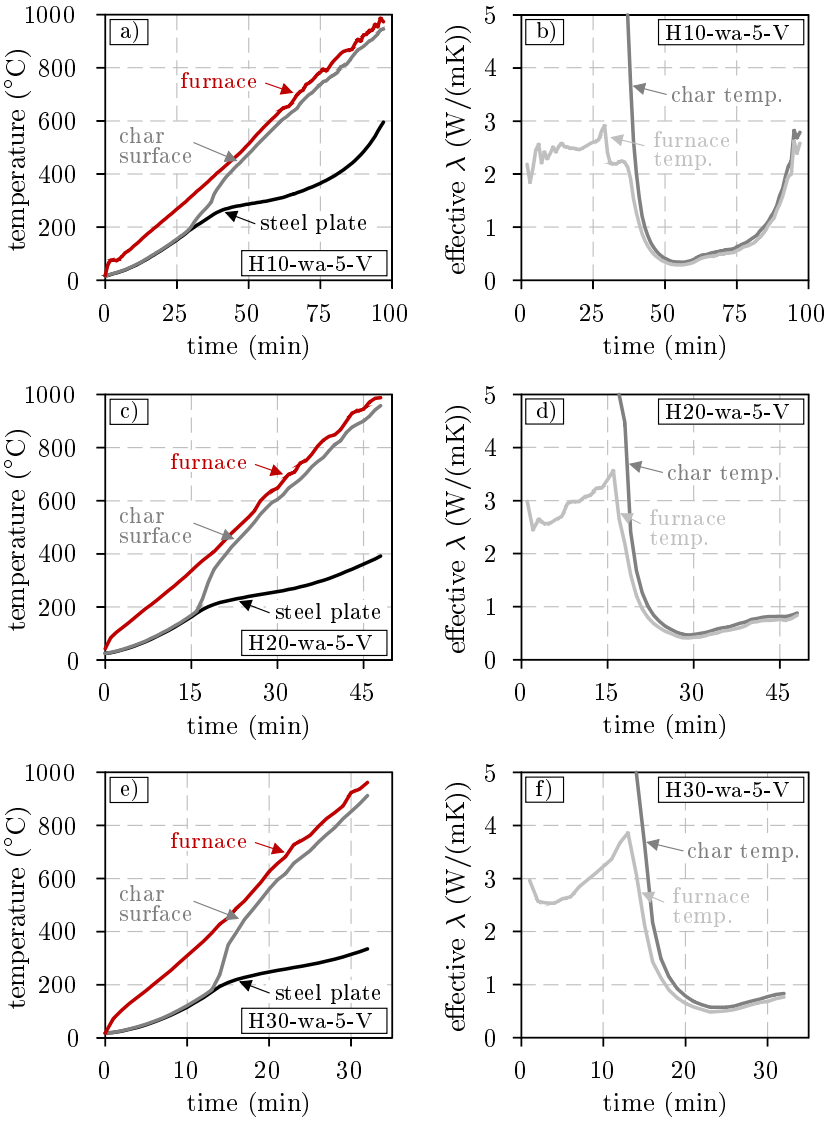

Figure 4.29: Comparison of the effective thermal conductivity calculations according to EN-13381-8 (2013) using the measured furnace and simulated char surface temperatures as input data: a) and b): test specimen H10-wa-5-V, c) and d): test specimen H20-wa-5-V, e) and f): test specimen H30-wa-5-V

The best agreement is achieved for 10 K/min. For higher hearing rates, on the other hand, a greater difference can be observed. However, regardless of whether the calculations are carried out using the furnace temperature or the char temperature, from the time of expansion onwards, the curves and therefore the values of the effective thermal conductivity are almost the same. Only for higher heating rates (see Figure 4.30 b) and d)) a small difference between the thermal conductivity values can be observed. This difference is due to the gap between the furnace temperature and the surface temperature of the char, which becomes larger with increasing heating rates (see Figure 4.30 a) and c)).

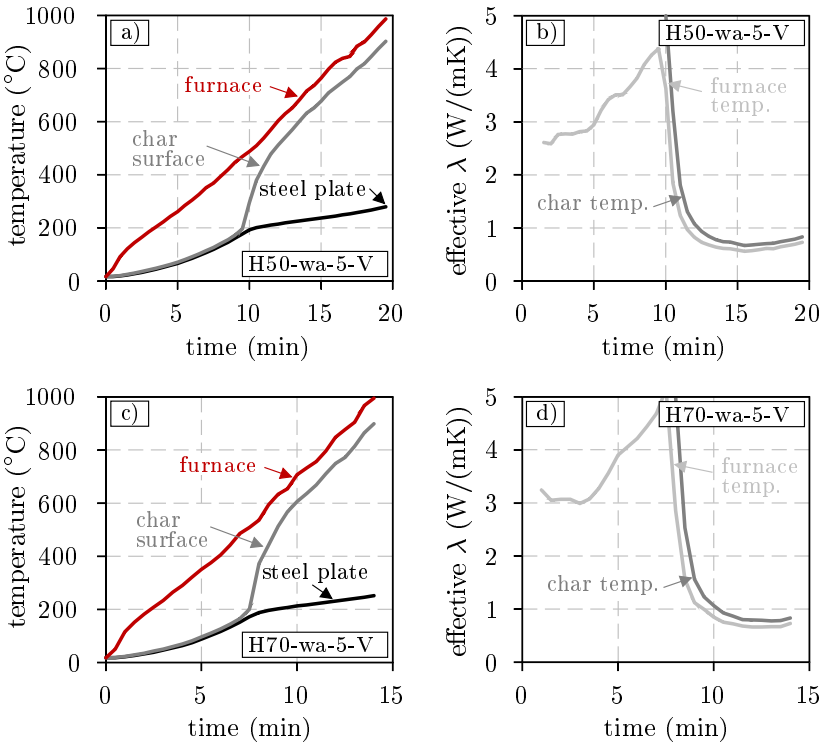

Figure 4.30: Comparison of the effective thermal conductivity calculations according to EN-13381-8 (2013) using the measured furnace and simulated char surface temperatures as input data: a) and b): test specimen H50-wa-5-V, c) and d): test specimen H70-wa-5-V

The basis for the performed calculations of the effective thermal conductivity are the results of the numerical simulations. The simulations, on the other hand, depend on the thermal material properties that were introduced in section 4.2. Here, among others, the thermal conductivity model of the waterborne coating is described. In Figure 4.7, the thermal conductivity is given as a function of char temperature for different heating rates. Between the individual curves, only small differences can be observed. However, for higher heating rates, low thermal con-

ductivity values are reached first than for lower heating rates. This behaviour is directly related to the heating rate-dependent expansion behaviour. Since the coating expands faster at higher heating rates, the char structure reaches the low thermal conductivity values earlier than for lower heating rates. This applies at least to the developed material model. When looking at the results of the effective thermal conductivity calculations, on the other hand, such correlations cannot be observed. In Figure 4.31 the effective thermal conductivities from Figure 4.29 and 4.30 are given as a function of char temperature for heating rates of 10, 20, 30, 50 and 70 K/min. The corresponding char temperatures were calculated according to EN-13381-8 (2013) as the mean value between the furnace temperature and the steel plate temperature or as the mean value between the surface temperature of the char and the steel plate temperature, depending on the calculation. Figure 4.31 a) summarises the results calculated from the furnace temperatures. The results calculated from the surface temperatures, on the other hand, are given in Figure 4.31 b).
In contrast to the material model, the lowest values of the effective thermal conductivity are calculated in both cases for 10 K/min. Even the order at which the lowest thermal conductivity values are reached first is reversed compared to the material model. Therefore, according to the calculations of the effective thermal conductivity, the waterborne coating would show the best fire protection performance at 10 K/min and the worst fire protection performance at 70 K/min. However, this clearly contradicts the experimental investigation (see Figure 3.25), where the best fire protection performance of both coatings solvent- and waterborne was identified for the highest heating rates.

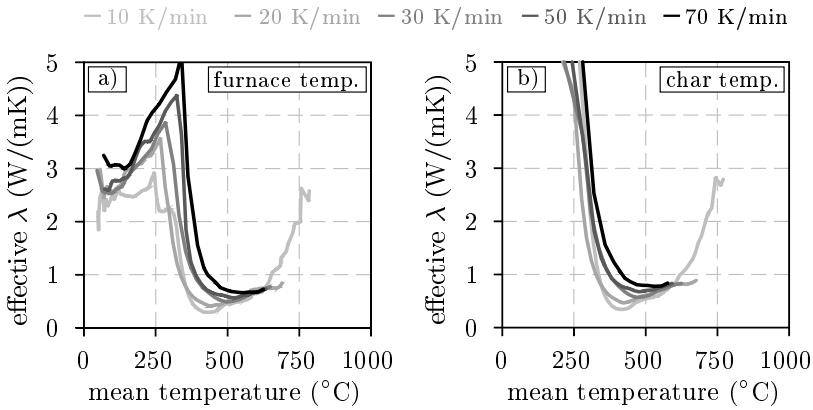

Figure 4.31: Comparison of the effective thermal conductivity calculations according to EN-13381-8 (2013) using a) measured furnace temperatures and b) simulated char surface temperatures for heating rates of 10, 20, 30, 50 and 70 K/min

In order to find an explanation for these contradictory results, it is necessary to take a closer look at the heating behaviour of the coating. Therefore, Figure 4.32 shows

the temperature development over the height of the expanded char for selected test specimens and points in time. The path defined in Figure 4.28 was used in order to determine these temperature profiles.

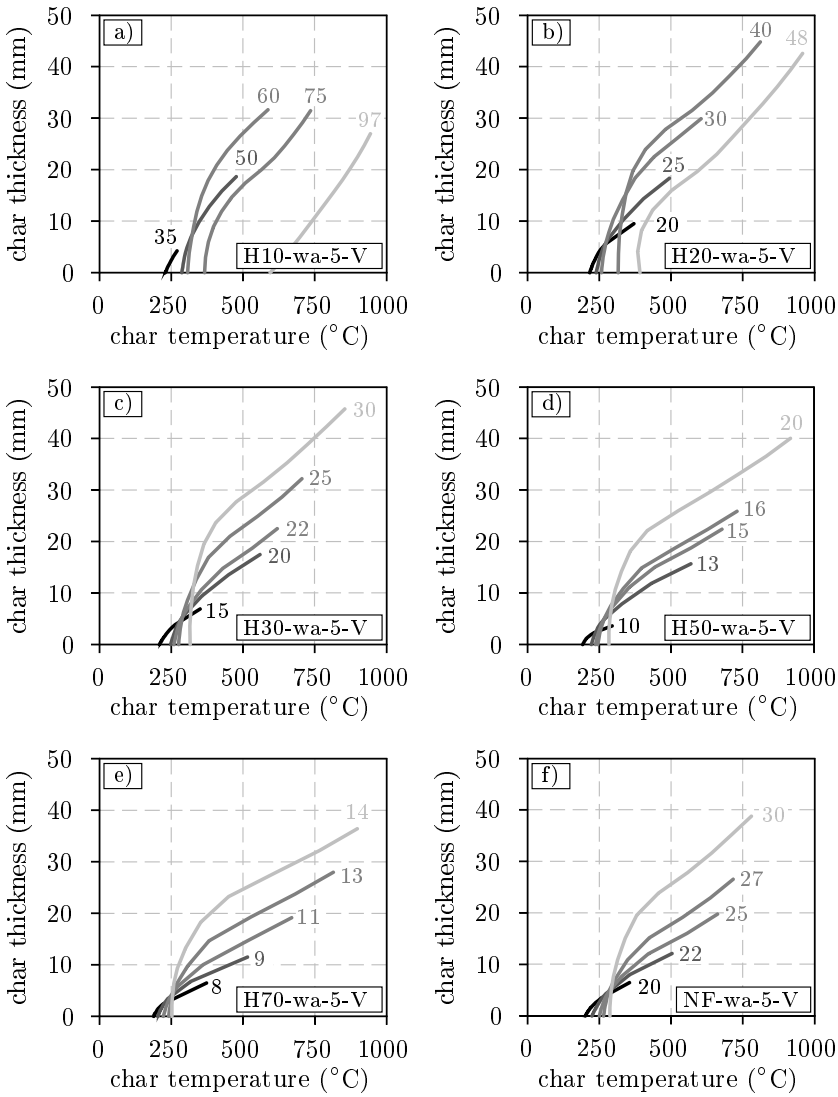

Figure 4.32: Simulated char temperatures as a function of char thickness at different points in time (min) for heating rates of a) 10 K/min, b) 20 K/min, c) 30 K/min, d) 50 K/min, e) 70 K/min and f) natural fire

As can be seen from the graphs, the temperature gradients between the top and bottom of the char increase with increasing heating rates (compare the slope of the temperature curves). At the same time, the temperature gradients show a strongly

non-linear course, especially for higher heating rates. While the temperature profiles are only slightly curved for 10 K/min (see Figure 4.32 a)), highly non-linear temperature curves are observed especially for 50 and 70 K/min (see Figure 4.32 d) and e)). However, in contrast to the actual temperature development, the method of the effective thermal conductivity assumes a linear temperature gradient within the char. The extent to which this assumption has an influence on the calculation results can be explained with the help of Figure 4.33. In order to provide a clear overview, only one temperature gradient is shown for each heating rate.

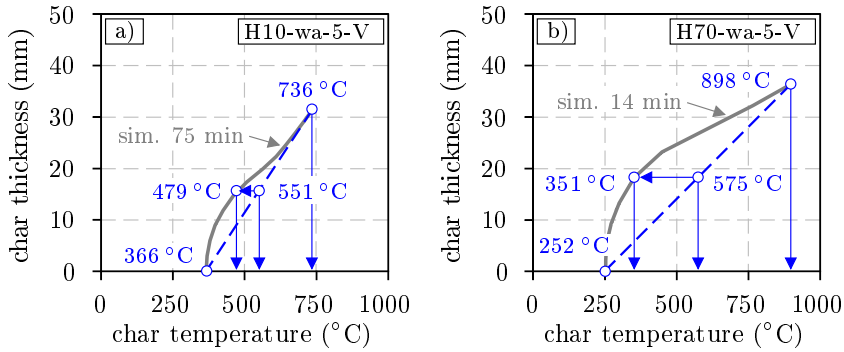

Figure 4.33: Graphical comparison between the assumption of a linear temperature gradient and the simulated temperature profile over the expanded char thickness of the waterborne coating for a) 10 K/min and b) 70 K/min

After 75 minutes of heating at a constant heating rate of 10 K/min, the temperature on the top of the expanded char is 736 °C. The temperature on the bottom, on the other hand, is 366 °C (see Figure 4.33 a)). Based on these temperature values and the calculation rule of EN-13381-8 (2013), the average temperature in the middle of the char structure has to be 551 °C. However, since the temperature gradient is non-linear, the actual temperature in the middle of the char structure is 479 °C. By assuming a linear temperature gradient, the temperature is therefore overestimated by 72 °C. For 70 K/min, this effect is even more pronounced. With a temperature of 898 °C at the top and 252 °C at the bottom, the temperature in the middle of the char structure is 575 °C when assuming a linear gradient. However, due to the non-linear course, the actual temperature within the char structure is only 351 °C (see Figure 4.33 b)). This corresponds to a difference of 224 °C between the assumption and the results of the numerical simulation. For the graphical representation of the results, this means that the value of the effective thermal conductivity calculated for the point in time of 14 minutes should not be assigned to the temperature value of 575 °C, but to 351 °C. For the comparison of the results according to Figure 4.31, this represents a serious difference. Especially because the deviation between the assumption and the simulation is significantly smaller for lower heating rates.
Based on these findings, the effective thermal conductivity curve calculated for 70 K/min must be shifted to the left on the temperature axis by several hundred degrees Celsius. In this way, the results would correspond to the expectations that

lower thermal conductivity values are reached earlier at higher heating rates than at lower. As a consequence, this would confirm the findings from the small-scale tests that both investigated coatings show the best fire protection performance at higher heating rates.
As a conclusion, it can be summarised that the assumptions made within the method of the *effective thermal conductivity* lead to deviations in the results that cannot be neglected or at least need to be considered. This applies for both the assumption of the linear temperature gradient and the approximation of the char temperature by the furnace temperature. For this reason, the method proposed in EN-13381-8 (2013) is considered to be unsuitable for the comparison of the fire protection performance of intumescent coatings at different heating rates.

4.4.4 Discussion

In section 4.4, the focus of the numerical simulations was on the thermal behaviour of the waterborne coating. For this reason, the small-scale fire tests performed on coated steel plates, which were presented in section 3.4, were recalculated using a three-dimensional, thermomechanically coupled finite element model. In order to validate the numerical simulations, the steel plate and char temperatures as well as the final thicknesses of the expanded char were used. Apart from a few exceptions, the numerical simulations showed a very good agreement with the test results. This applies to both the simulations with constant heating rates and the natural fire. Based on these findings, the numerical results confirm the correctness and accuracy of the developed material model and the applied simulation method.
In section 2.6, the hypothesis was formulated that the fire protection performance of intumescent coatings is decisively dominated by the morphology and the pore structure of the char. For this reason, it was assumed that the thermal properties of intumescent coatings differ due to irreversible reactions in the heating and cooling phase. Based on this hypothesis, the material model from section 4.2 was developed and applied in the numerical simulations. With the validation of the simulation model, now the proposed hypothesis could be indirectly confirmed.
For the comparison of the fire protection performance of intumescent coatings at different heating rates, the effective thermal conductivity method according to EN-13381-8 (2013) has often been used in the literature. Within this method, assumptions are made that have already been identified in subsection 2.2.7 as a possible reason for misinterpretations of experimental results. With the help of the validated simulation models, this hypothesis could now be examined and confirmed. The assumption of a linear temperature gradient within the expanded char structure proved to be particularly decisive. With the help of the numerical simulations, it could be shown that the temperature development within the char structure is highly non-linear. The degree of non-linearity even increases with higher heating rates. In this way, an explanation could be found why the results of the effective thermal conductivity method contradict the measured sample temperatures when

evaluating the fire protection performance of intumescent coatings. Since the effective thermal conductivity method is used in EN-13381-8 (2013) to determine design tables for the dry film thickness of intumescent coatings, these findings need to be carefully evaluated.
The method of the effective thermal conductivity primarily underestimates the fire protection performance of intumescent coatings at higher heating rates. For a comparison of the protection effect at different heating rates, the method is therefore unsuitable in its current form. For the design of the dry film thickness, on the other hand, the method does not represent any safety risks. Since the approval tests are carried out under the standard fire curve with its strong temperature rise at the beginning of the test, the fire protection performance is also underestimated due to the reasons already mentioned. However, it should be kept in mind that the temperature gradients within the char structure are not only affected by the fire curves, but also by the char thicknesses. This is the reason why different effective thermal conductivity curves are calculated for two different dry film thicknesses, although the test specimens are exposed to the same fire curve (see Figure 2.32).

4.5 Simulation of the Fire Protection Performance on H-profiles

4.5.1 Modelling and Parameters

In section 4.3 and section 4.4 numerical simulations were performed, in order to validate the new developed material model from section 4.2. For this reason, the expansion and heating behaviour of the waterborne coating was investigated and compared with the experimental investigations from section 3.3 and section 3.4. In both cases, the performance of the coating was investigated on a small scale. However, when the coating is applied on larger components, such as beams and columns, bigger pores can be formed within the char structure. This can have a direct influence on the morphology of the char and the fire protection performance of the coating. In order to investigate such influence, the reference beam from the large-scale fire test (see section 3.5) was recalculated using the finite element software ABAQUS 2017 (HF6).
In order to investigate the influence of the natural fire scenario on the fire protection performance of the waterborne coating applied on H-profiles, a two-dimensional finite element model of the reference beam (HEA 240) was set up using shell elements (CPE4T). A three-dimensional model could also have been used. However, to reduce the calculation time, it was decided to use a two-dimensional model.
The three-sided fire exposed beam was modelled with a 600 mm wide and 150 mm thick furnace cover (made of aerated concrete) on the top of the upper flange (see Figure 4.34). The coating was modelled circumferentially on the remaining

surface of the H-section with a DFT of 360 μm. Between the profile and the furnace cover as well as between the profile and the coating a perfect heat transfer was assumed. The fire exposure was applied circumferentially on the coating surface and the bottom of the furnace cover within a thermomechanically coupled analysis. For this purpose, the measured furnace temperature was implemented using an emissivity value of $\epsilon = 0.8$ for the coating and $\epsilon = 0.7$ for the aerated concrete. Following the recommendations of EN-1991-1-2 (2010) the heat transfer coefficient α_c was set to 35 $W/(m^2K)$. This represents a difference compared to the recalculations of the small-scale fire tests. The reason for this is that in the large-scale fire test the furnace was heated with oil burners. Therefore, higher convection is expected.

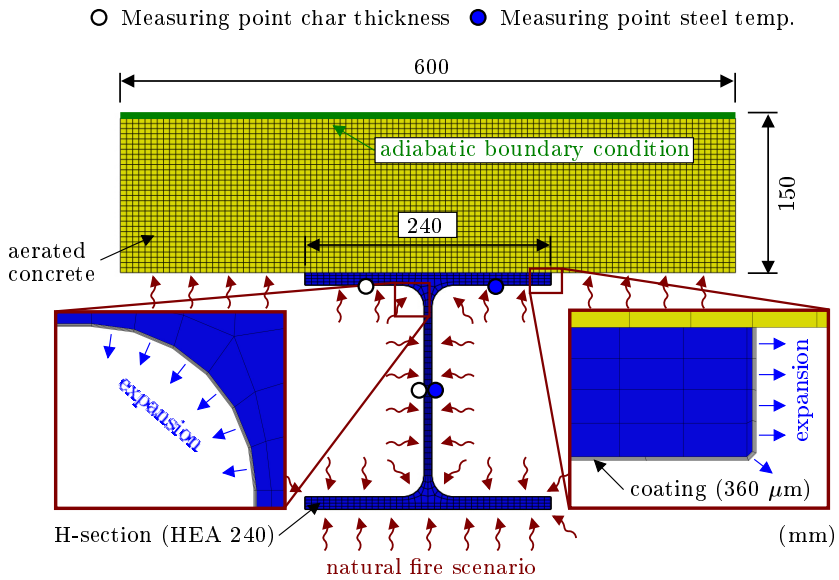

Figure 4.34: Finite element model of the coated reference beam (HEA 240) exposed to a three-sided natural fire scenario

The thermal behaviour of the steel profile was modelled using the temperature-dependent material properties given in EN-1993-1-2 (2010). The thermal material properties of the aerated concrete, on the other hand, were described according to EN-1996-1-2 (2011) for a density of $\rho = 550\ kg/m^3$ (see Figure 4.35). To simulate a heating rate-dependent behaviour of the waterborne coating, the material properties presented in section 4.2 were used. The values for the density, the thermal conductivity and the specific heat capacity were implemented as a function of temperature. For the cooling phase, additional field variables (FV) were introduced to describe the temperature-dependent material properties also in the cooling phase. In this way, the thermal material properties were changed as soon as the temperature inside each coating element decreased ($\Delta\theta < 0$). For this purpose, the user subroutine USDFLD was applied. Additionally, the user subroutine UEXPAN was

used to implement the heating rate-dependent expansion curves of the coating. For the simulation of the reference beam, the expansion curve measured for 30 K/min was used, since the average heating rate of the investigated natural fire is approximately in this range. In this way, a strict orthogonal expansion behaviour was modelled. This applies also to the concave and convex part of the H-profile as can bee seen from the details in Figure 4.34. Based on the incremental change in char temperature ($\Delta\theta = \theta_i - \theta_{i-1}$) the expansion of the coating was calculated by the thermal expansion coefficient α_i using the implemented expansion factors $\varepsilon = f(\theta, \dot{\theta})$. In this way, the coating thickness changed with temperature or remained unchanged when the expansion coefficient was set to $\alpha_i = 0$ during the cooling phase.

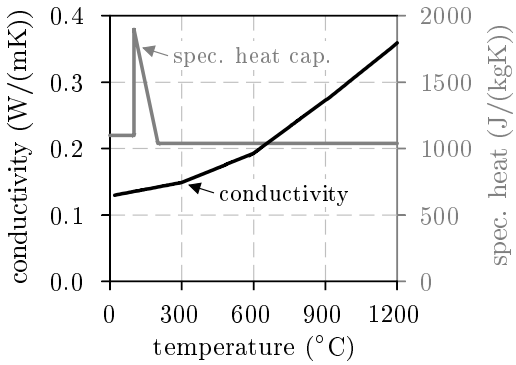

Figure 4.35: Temperature-dependent conductivity and specific heat capacity of aerated concrete ($\rho = 550\ kg/m^3$) according to EN-1996-1-2 (2011)

4.5.2 Results and Validation against Test Data

In the following, the results of the numerical simulations performed for the reference beam from the large-scale fire test are presented. To illustrate the temperature development inside the coated H-profile and the expanded char, the simulated temperature fields of the three-sided fire exposed reference beam are shown in Figure 4.36. In order to save space, only the half of the simulated model is depicted. The start of expansion occurs in the simulation after 14 minutes on the web and the edges of the flanges. At this point in time the web reaches a temperature of 184 °C, whereas the outer layer of the coating exhibits a surface temperature of 186 °C. With further progress in the simulation, the coating is exposed to higher surface temperatures and reaches a maximum value of 806 °C after 31 minutes. At this point in time the char thickness expands maximally resulting in a high temperature gradient inside the char (see Figure 4.36 b)). Due to this insulation effect, the temperature inside the web is only 415 °C. Although the dry film thickness of the coating is only 360 μm, the expanded coating is able to prevent the reference beam from fast heating. When the cooling phase of the natural fire scenario occurs, the expanded char thickness remains unchanged. This is due to the implemented

behaviour in the user subroutine UEXPAN. Since the coating has still low conductivity values, the expanded coating prevents the steel profile from fast cooling. This effect can be seen from the inverted temperature gradient inside the expanded coating after 90 minutes (see Figure 4.36 c)). With 348 °C the steel profile has a 161 °C higher temperature than the outer surface of the coating (187 °C).

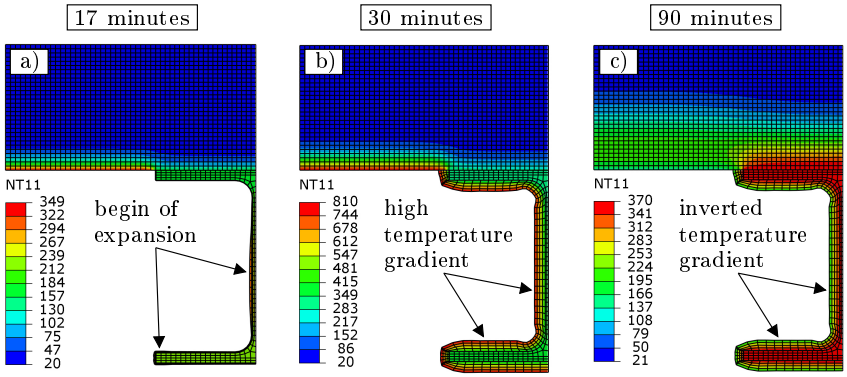

Figure 4.36: Simulated temperature fields of the coated reference beam (HEA 240, DFT = 360 µm) at different points in time

In order to evaluate the accuracy of the numerical simulations, the results of the reference beam are compared to the test data. In Figure 4.37 the simulated and measured steel temperatures as well as the simulated and measured char thicknesses are compared to each other. Both the temperatures in the heating and cooling phase are in great accordance with the test data. Only the maximum steel temperatures of the top flange and the web (470 and 572 °C, respectively) are overestimated by 34-38 °C within the simulation.The temperatures of the bottom flange, on the other hand, are almost the same (see Figure 4.37 c)). The change in temperature during the expansion of the coating is more distinctive in the simulation than in the test. However, the point in time at which the expansion of the coating occurs coincides very well with the temperature development inside the steel profile.

As the temperature development inside the reference beam is effected by the furnace cover, the expansion of the coating takes place with a slight delay between the web and the top flange (see Figure 4.37 d)). Due to the faster heating of the web, the expansion starts here first. However, at the end of the simulation the char thicknesses reach in both cases a value of approximately 12 mm. For the web, this represents a very good agreement with the measured char thickness. For the top flange, on the other hand, the test results (mean char thickness: 8 mm) are overestimated by approximately 4 mm. In the test, the expansion of the coating was stronger influenced by the thermal inertia of the aerated concrete than in the simulation.

In addition to the reference beam, a four-sided fire exposed reference column was also examined in the large-scale fire test. However, the simulations of the column

are not presented in this thesis, but can be found in Weisheim et al. (2018).

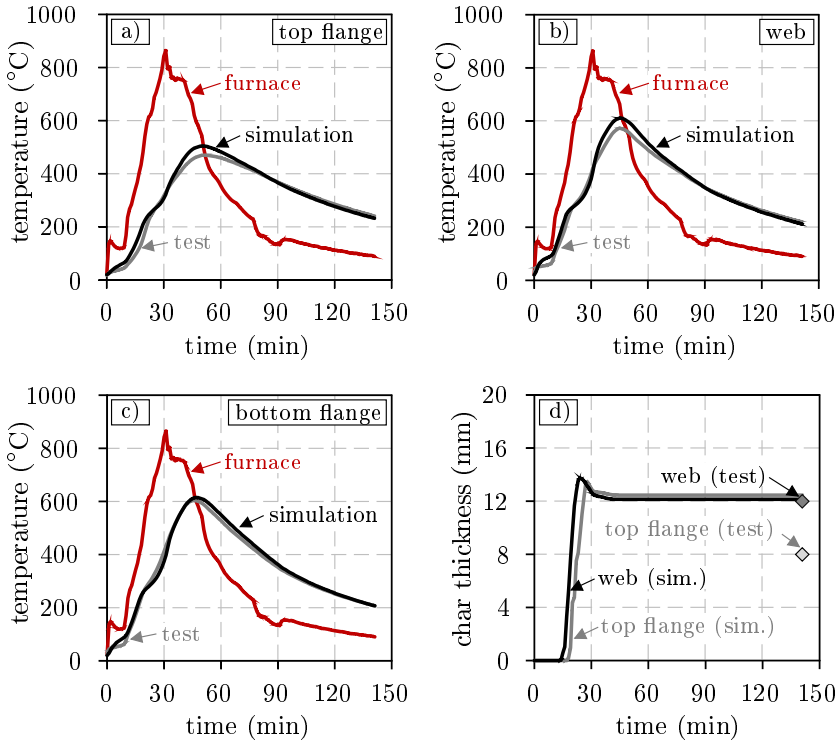

Figure 4.37: Comparison between the simulated and measured steel temperatures and char thicknesses of the reference beam (HEA 240, DFT = 360 µm). Steel temperatures of the a) top flange, b) web and c) bottom flange as well as d) char thicknesses measured at the top flange and the web

4.5.3 Parameter Study

The numerical simulation performed for the reference beam shows a very good agreement with the test results. For this reason, additional simulations were carried out. Within the scope of these simulations, the dry film thickness of the waterborne coating was varied. Besides an unprotected section, dry film thicknesses between 200 and 950 µm were applied. The aim of the parameter study was to quantify the influence of the dry film thickness on the heating behaviour of the three-sided fire exposed beam during the investigated natural fire scenario.
The results of the parameter study are shown in Figure 4.38. The simulated temperature-time curves in Figure 4.38 a) reveal that the dry film thickness of the waterborne coating significantly influences the temperature development of the reference beam in both the heating and the cooling phase. With increasing dry film thicknesses, the maximum profile temperatures occur at a later point in time.

In this way, higher dry film thicknesses slow down not only the heating but also the cooling of the profile. In contrast to this, the heating and cooling of the unprotected profile takes place almost congruently with the furnace temperature.
Despite the low dry film thickness, the waterborne coating is able to reduce the heating of the three-sided fire exposed reference beam during the natural fire scenario. According to the simulations, a dry film thickness of 950 μm reduces the maximum web temperature by approx. 347 °C compared to the unprotected profile (unprotected: 789 °C, 950 μm: 442 °C, see Table 4.5).

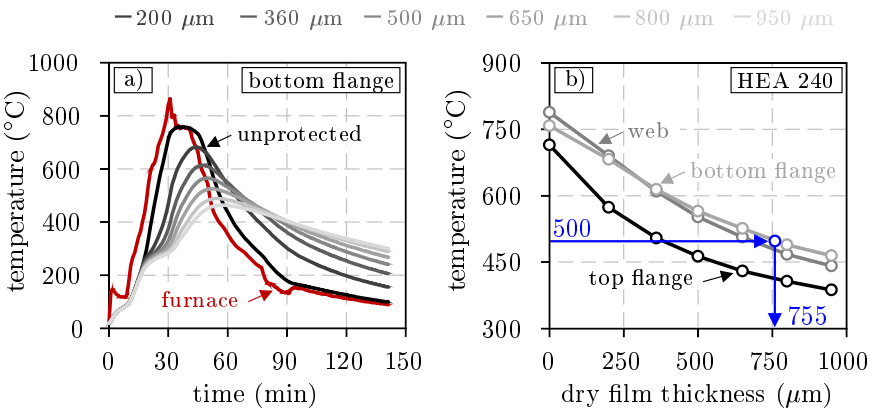

Figure 4.38: Results of the parameter study: a) Temperature-time curves of the bottom flange of the reference beam HEA 240 for different dry film thicknesses of the waterborne coating and b) steel temperatures of the reference beam as a function of dry film thickness

In the large-scale fire test, the loaded beam failed after 48 minutes. At the time of failure, the maximum steel temperature was 584 °C. This temperature was located in the bottom flange. With the help of the simulations carried out within the parameter study, a relationship between the dry film thickness and the maximum steel temperature can be determined. This relationship can now be used to design the dry film thickness of the waterborne coating in order to prevent the loaded beam from failing. Figure 4.38 b) shows the relationship between the dry film thickness and the steel temperature for the top and the bottom flange as well as the web of the reference beam. Essential for the design of the dry film thickness is the temperature of the bottom flange. According to the calculated design curve, a dry film thickness of 755 μm is required to limit the maximum steel temperature at 500 °C. Compared to the performed large-scale fire test (370 μm), this corresponds to more than a doubling of the dry film thickness. However, in order to limit the maximum steel temperature at 584 °C (failure temperature of the beam), only a dry film thickness of approx. 460 μm would be necessary.
For an experienced calculation engineer, the numerical simulations offer a possibility to design the dry film thickness of intumescent coatings on the basis of few calculations. In this way, the dry film thickness can be determined object-oriented

for a specific component, a specific coating product and a specific natural fire curve. However, a requirement for this procedure is the correct determination of the material properties of the coating as well as the validation of the simulation model on at least one natural fire test.

Table 4.5: Results of the parameter study: Maximum steel temperatures of the reference beam HEA 240 under natural fire exposure and different dry film thicknesses of the waterborne coating

DFT (μm)	top flange (°C)	web (°C)	bottom flange (°C)
0	714	789	758
200	574	690	682
360	505	610	614
500	463	552	565
650	430	507	526
800	407	468	489
950	387	442	464

4.5.4 Discussion

The new developed material model for intumescent coatings, which was presented in section 4.2, is based on input parameters that were derived from small-scale fire tests. One of the input parameters besides the measured expansion curves is the pore size, which describes the morphology of the char. Both the expansion curves and the pore size are used, among others, to calculate the thermal conductivity of the coating. With the help of the recalculations of the small-scale fire tests, which were performed on coated steel plates, it could already be shown that the developed material model is suitable to describe the heating rate-dependent behaviour of the waterborne coating close to reality. However, in order to prove that the model can also be used on large scales, the reference beam from the large-scale fire test was recalculated. The heating behaviour of the reference column was also recalculated. The results can be found in Weisheim et al. (2018).
For both the reference beam and the reference column, the heating behaviour could be recalculated in great accordance with the test results. Based on these results, the following conclusions can be drawn: ① The material model derived from small-scale fire tests can be transferred and applied on structural elements at larger scales. A potential scale influence is not apparent. At the same time, it also means that the size of the small-scale test specimens is sufficient to investigate the expansion behaviour and the morphology in order to use these as input parameters for the material model. ② The user subroutine-based description of the expansion behaviour and the thermal material properties are suitable to describe the irreversible behaviour of the coating in heating and cooling. ③ For the calculation of the temperature field it is not enough to carry out a pure thermal analysis. Thermomechanically coupled analyses have to be carried out in order to calculate the expansion of the coating and its influence on the temperature field.

4.6 Summary

The aim of the numerical investigations was to develop a material model, which is able to describe the heating rate-dependent and irreversible behaviour of intumescent coatings in case of natural fires. The model should be as simple as possible and should be based on only few input parameters. For this reason, only the expansion curves and the pore size were used as the main input parameters to calculate the temperature and heating rate-dependent thermal conductivity. For the closed-cell and the open-cell foam structure, separate submodels were used. A differentiation between the heating and cooling phases was also undertaken. The temperature-dependent density and specific heat capacity were derived from coupled TG-DSC analyses. The description of the expansion behaviour was achieved by the implementation of a user subroutine.
For the validation of the material model, both the expansion tests and the steel plate tests from section 3.3 and section 3.4 were recalculated. It could be shown that the user subroutine UEXPAN is not only suitable to realistically describe the expansion behaviour of the investigated coating at constant heating rates, but also at a combination of two different heating rates. This represents an important finding since the new developed material model should be used to describe the expansion behaviour of intumescent coatings under any natural fire exposure.
Besides the expansion behaviour, it was also possible to recalculate the heating behaviour and the associated fire protection performance of the investigated coating close to reality. Due to the very good agreement with the test results, the numerical simulations were used to assess the validity of the assumptions made in the *effective thermal conductivity* method according to EN-13381-8 (2013). The assumption of a linear temperature gradient across the char thickness was identified as the greatest simplification and possible misinterpretation when evaluating the fire protection performance of intumescent coating with the method of the effective thermal conductivity. Based on the numerical simulations, it could be shown that the temperature gradient is usually highly non-linear, especially for large dry film thicknesses and high heating rates. Similar observations could already be made during the experimental investigations in section 3.4. Based on these findings, it is recommended to evaluate the fire protection performance of intumescent coatings not with the help of the effective thermal conductivity, but with the help of the steel temperature and the temperature difference between unprotected and protected steel members.
In addition to the small-scale fire tests, the reference beam from the large-scale fire test was also recalculated during the numerical investigations. With the successful validation, it could be shown that the new developed material model, which was derived from small-scale tests, can also be applied to larger scales. Therefore, a parameter study was performed to determine the dry film thickness of the waterborne coating that would have prevent the loaded beam from the large-scale fire test from failing. However, the numerical simulations are quite complex and require a high

level of expertise. For the calculation of the required dry film thickness in natural fires, therefore, the numerical simulations are rather unsuitable. However, this applies only to the finite element method and not to the new developed material model itself.

5 Design Approach

Based on MATLAB calculations an approach for the design of the dry film thickness of intumescent coatings in case of natural fires is presented in chapter five.

Contents

5.1 Introduction

The investigations in subsection 4.5.3 have shown that numerical simulations are suitable to calculate the required dry film thickness of intumescent coatings in order to provide sufficient fire protection in case of natural fires. However, due to their complexity, the numerical simulations are quite time-consuming compared to simplified calculations and require a high level of expertise. For this reason, the use of the simulations presented in chapter 4 should rather be seen in the field of research, since the majority of calculation engineers do not have the possibility to carry out numerical simulations in practice.
As the approval procedures at national and European level do not yet provide any design approach for the dry film thickness in natural fires, the fire protection performance of intumescent coatings is currently assessed on the basis of expert reports. In Germany, the design of the fire resistance of structural elements according to the natural fire concept represents a deviation from the Model Building Regulation (*German: Musterbauordnung, MBO*). For this reason, the verifications have to be carried out by specialised planning engineers and reviewed by independent experts. In this context, it is conceivable that the design of the dry film thickness of intumescent coatings might also be carried out and assessed in a similar way. In order to enable such a procedure in the future, a calculation method was developed on the basis of the research findings from chapter 3 and chapter 4. The method enables easier handling compared to the finite element simulations. It is based on the new developed material model and was implemented in MATLAB.

5.2 Calculation Method

When complex processes are described in physics, the *similarity theory* is often used. With the help of the theory, a physical process is traced back to a model that is less complex than the reality (Trossin 1999). In the same way, a similarity relationship between a complex and a more simplified model can be established. For this purpose, the complex model is treated like the actual physical process. In the case of the numerical simulations, this assumption is permissible since the simulation models showed a good agreement with the experimental results. Therefore, in terms of the similarity theory, a simplified model can be derived from the numerical simulations in order to calculate the dry film thickness of intumescent coatings in natural fires.
The central aspect of the performed simulations was the correct calculation of the temperature field and the associated expansion behaviour of the coating. A simplified approach for the calculation of the temperature development in steel members is already given in EN-1993-1-2 (2010). However, the calculation method is only suitable for non-reactive fire protection products.
Until the reaction of the coating, the steel members can be approximately treated as unprotected. The fire protection effect only appears with the expansion of the

coating. However, the calculation approach given in EN-1993-1-2 (2010) cannot be applied without adjustments since the char thickness of the coating changes with temperature and time. In addition, the approach describes a pure heat transfer problem. Heat transfer mechanisms due to convection and radiation are not considered. When investigating the method of the *effective thermal conductivity*, it was already shown that setting the surface temperature of the coating equal to the gas temperature represents a strong simplification, especially at the beginning of the calculations. For this reason, the temperature calculation is carried out within the new developed approach in two steps. In the first step, the temperature increase $\Delta\theta_a$ in the steel member is calculated according to Equation 5.1. This equation corresponds to the calculation of an unprotected steel member according to EN-1993-1-2 (2010) in combination with EN-1991-1-2 (2010) and takes into account the heat transfer mechanisms due to convection and radiation.

$$\Delta\theta_a = k_{sh} \cdot \frac{A_m/V}{c_a \cdot \rho_a} \cdot \left[\alpha_c \cdot (\theta_g - \theta_a) + \phi \cdot \varepsilon_a \cdot \varepsilon_f \cdot \sigma \cdot \langle (\theta_g + 273)^4 - (\theta_a + 273)^4 \rangle\right] \cdot \Delta t \quad (5.1)$$

$\Delta\theta_a$:	temperature increase of the unprotected steel member (°C)
k_{sh}:	correction factor for the shadow effect (-)
A_m/V:	section factor of the unprotected steel member (m^{-1})
c_a:	specific heat capacity of steel (J/(kg·K))
ρ_a:	density of steel (kg/m^3)
α_c:	convective heat transfer coefficient ($W/(m^2 \cdot K)$)
θ_g:	gas temperature near the steel member (°C)
θ_a:	surface temperature of the steel member (°C)
ϕ:	configuration factor (-)
ε_a:	surface emissivity of the steel member (-)
ε_f:	emissivity of the fire (-)
σ:	Stefan-Boltzmann constant $5.67037 \cdot 10^{-8}$ ($W/(m^2 \cdot K^4)$)
Δt:	time interval (sec.)

Besides the heat transfer coefficient α_c, the calculation depends on the emissivity ε_a of the member surface and the section factor A_m/V. At the beginning of the calculation, the coating has almost no influence on the heating, but it has an influence on the surface properties of the steel member. Therefore, the emissivity of the steel member is not set to $\varepsilon_a = 0.7$, as usually used for unprotected steel members, but to $\varepsilon_a = 0.8$ analogue to the numerical simulations.
The first calculation step is valid until the temperature is reached, at which the coating starts to expand. After that, in the second calculation step, the temperature increase in the steel member is calculated according to Equation 5.2. Although the equation corresponds in its basic form to the approach given in EN-1993-1-2 (2010), it has been modified for the application to intumescent coatings. Within the incremental (Δt) calculation, both the thermal conductivity $\lambda_p(\theta)$ and the char thickness $t_p(\theta)$ of the intumescent coating are described as a function of temperature. In contrast to the first calculation step, the section factor $A_p(\theta)/V$ is also

defined as a function of temperature. With the expansion of the coating, the fire exposed surface (A_p) increases. As a result, more energy is introduced into the steel member. In order to illustrate this effect graphically, two steel profiles are shown in Figure 5.1, one profile with and one profile without an intumescent coating. While the section factor A_m/V of the unprotected profile remains constant (see Figure 5.1 a)), the section factor $A_p(\theta)/V$ of the coated steel profile (see Figure 5.1 b)) changes with char thickness $t_p(\theta)$.

$$\Delta\theta_a = \frac{\lambda_p(\theta)}{t_p(\theta)} \cdot \frac{A_p(\theta)/V}{c_a \cdot \rho_a} \cdot (\theta_g - \theta_a) \cdot \Delta t \tag{5.2}$$

$\Delta\theta_a$:	temperature increase of the protected steel member (°C)
$\lambda_p(\theta)$:	thermal conductivity of the coating (W/(m·K))
$t_p(\theta)$:	char thickness of the coating (m)
$A_p(\theta)/V$:	section factor of the protected steel member (m^{-1})
c_a:	specific heat capacity of steel (J/(kg·K))
ρ_a:	density of steel (kg/m^3)
θ_g:	gas temperature near the steel member (°C)
θ_a:	surface temperature of the steel member (°C)
Δt:	time interval (sec.)

In order to calculate the temperature-dependent changes in char thickness, the expansion curves from subsection 4.2.2 are used. However, the expansion of the coating is not calculated for the entire dry film thickness t_0, but for single layers similar to the discretisation in the numerical simulations.

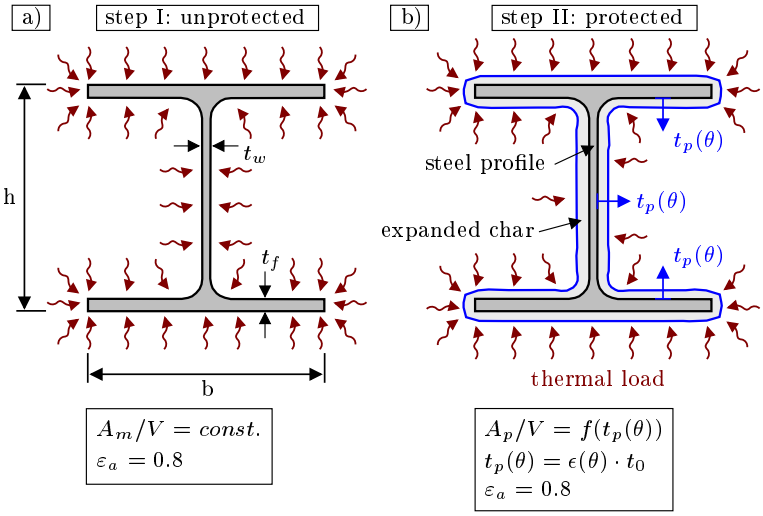

Figure 5.1: Graphical description of the section factor calculation when treating the steel profile as a) unprotected or b) protected

Figure 5.2 illustrates the division of the char structure into n individual layers. With the help of the temperature distribution inside the char structure both the temperature and the associated expansion factor $\epsilon_i(\theta)$ are calculated for each individual layer. Based on the numerical simulations, it could be shown that the temperature gradient inside the char structure is highly non-linear. For this reason, a bilinear gradient is assumed within the simplified calculation. The degree of non-linearity is controlled with the help of the weighting factor ζ. With $\zeta = 0.50$, for example, a linear gradient between the coating surface (θ_g) and the steel member (θ_a) is established. Depending on the dry film thickness and the heating rate, the weighting factor can vary between 0.20 and 0.50. With the help of the temperature gradient, for each single layer the temperature-dependent char thickness $t_i(\theta)$ is calculated. The sum of all single layers corresponds to the total char thickness $t_p(\theta)$, which is used in Equation 5.2.

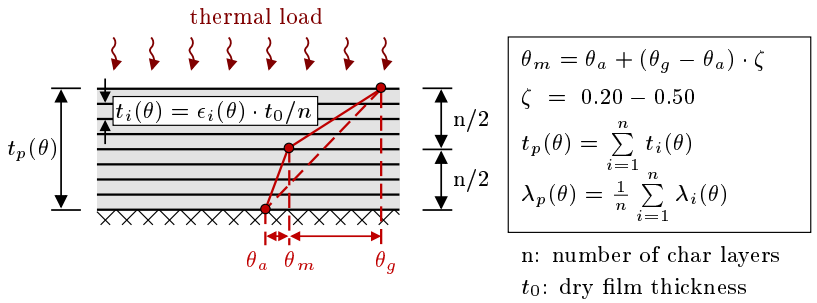

Figure 5.2: Graphical description of the layer-based calculation of the char thickness $t_p(\theta)$ and mean thermal conductivity $\lambda_p(\theta)$ using a bilinear temperature gradient inside the char

In the same way, the temperature-dependent thermal conductivity $\lambda_i(\theta)$ is calculated for each individual layer and is subsequently averaged (see Figure 5.2). The physical model for the thermal conductivity corresponds to the approach from subsection 4.2.3. Only the temperature-dependent development of the pore size slightly deviates. In order to reduce the complexity of the simplified calculation approach, the influence of the open-cell foam structure on the thermal conductivity is not described with the help of a separate submodel according to Ankang & Houde (2013), but with an artificial enlargement of the pore size. This approach goes back to Tabeling (2014) and leads to comparably good results.
In order to ensure a user-friendly application, a graphical user interface (GUI) was implemented for the calculation approach. Figure 5.3 shows the corresponding flowchart. Within the calculation method, the user has the possibility to select a steel profile from a database or to specify its geometry individually (see *GUI_SteelProfile*). In addition to conventional steel profiles, steel plates can also be defined. While a three- or a four-sided fire exposure can be applied on the steel profiles, the steel plates are only heated from one side. In *GUI_IntumescentCoating*, the product type of the coating, the dry film thickness and the initial thermal

conductivity at 20 °C have to be defined by the user. The temperature-dependent description of the pore size, on the other hand, is achieved by the definition of sampling point. In the case that no data exist, default settings are provided. Currently, only the material properties of the waterborne coating are implemented. However, it is possible to extend the properties to other products at any time.

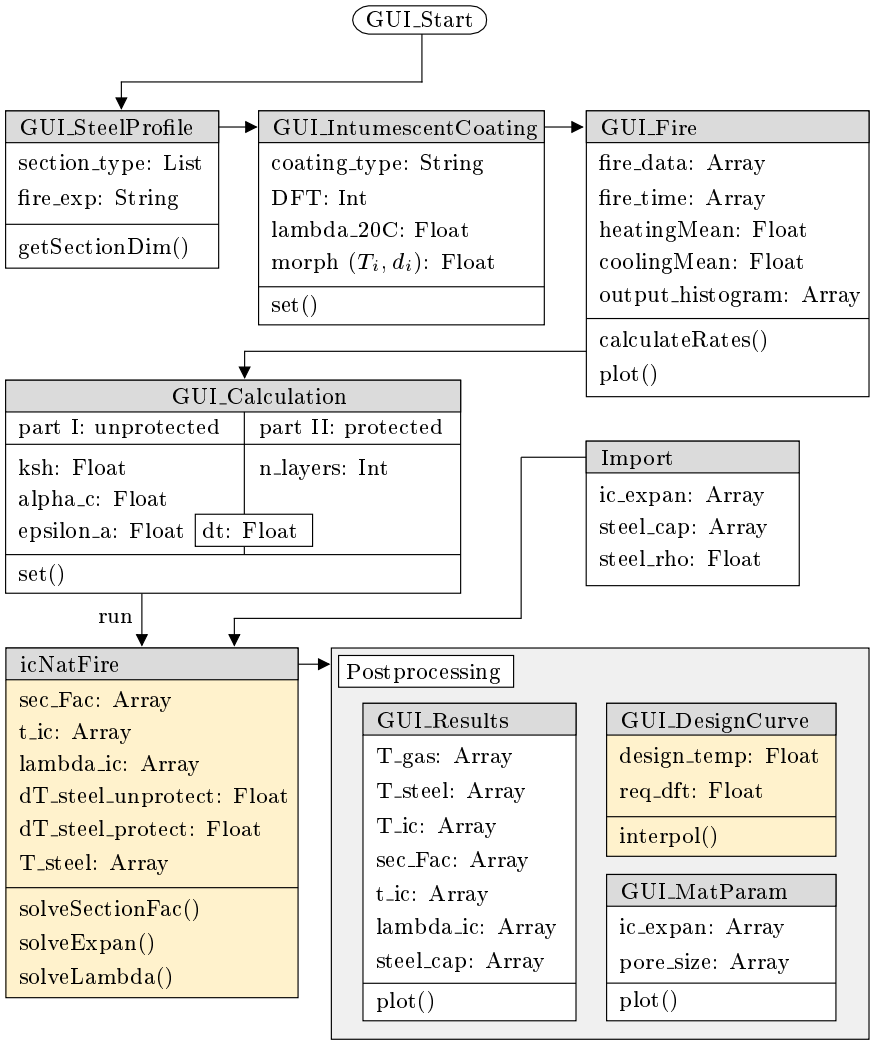

Figure 5.3: Flowchart of the graphical user interface (GUI) for the calculation of the steel member temperature and the dry film thickness of intumescent coatings in case of natural fires implemented in MATLAB

With the help of a browser function in *GUI_Fire*, the user can read in the natural fire curve that should be used for the simplified calculation. For this purpose, the fire curve has to be defined previously in column notation (sec., °C) using Excel or any other data processing software.

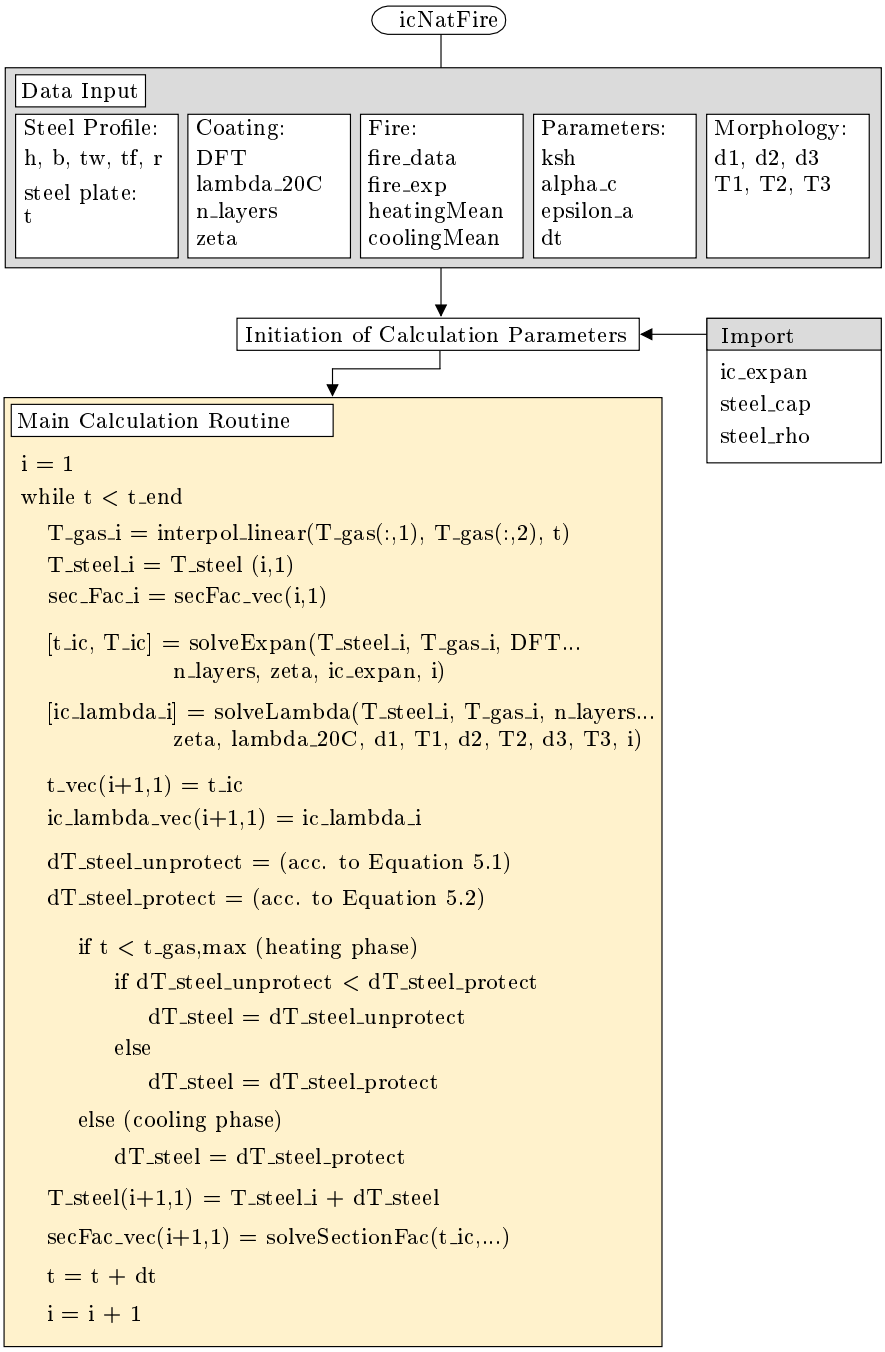

Figure 5.4: Flowchart of the routine icNatFire implemented in MATLAB for the simplified calculation of a coated steel member and its temperature during a natural fire exposure

After the import, the user-defined fire curve is visualised via a plot command. At the same time, a computational evaluation is carried out, in which the average heating and cooling rates are calculated. At a later point in time, the mean value of the heating rate is used to select the heating rate-dependent expansion curve, on which the calculation should be based on.
The calculation parameters are defined in *GUI_Calculation*. Here, the two calculation rules from Equation 5.1 and 5.2 are listed. The user has the possibility to define the heat transfer coefficient α_c, the emissivity of the coated steel member ε_a, the number of layers n to discretise the coating, as well as the time step size Δt. The actual calculation is carried out by running the script *icNatFire.m*. Depending on the previously defined profile, the dry film thickness, the fire curve and the imported expansion curve, the steel temperature of the profile and the expansion behaviour of the coating are calculated. A schematic extract of the calculation routine implemented in *icNatFire.m* is given in Figure 5.4. The incremental calculation is carried out until the last time value (t_end) of the natural fire curve is reached. The differentiation between the heating and cooling phase is based on the time (t_gas,max), at which the maximum fire temperature is reached. However, despite the decreasing fire temperature, heating of the expanded char and the steel profile usually continues due to thermal inertia. Therefore, in *solveExpan()*, *solveLambda()* and *solveSectionFac()*, the incremental change in temperature is checked for each layer. Only when the temperature decreases compared to the previous increment, the expansion is stopped. The thermal conductivity, on the other hand, decreases during the cooling phase, as already described in subsection 4.2.3.
The calculated results are graphically displayed in *GUI_Results* together with the essential calculation parameters. Both the results and the calculation parameters can be saved in Excel files. The same applies to the material parameters that are calculated in the background, such as the thermal conductivity of the coating, which can be accessed via *GUI_MatParam*.
In addition to the single calculation of the steel temperature, a multiple calculation can be performed to generate a design curve for the dry film thickness of the coating under the investigated natural fire scenario. For this purpose, several calculations with different dry film thicknesses are performed. The range in which the dry film thickness varies is fixed, but can be modified in the source code if required. At the end of the calculations, a curve is generated for the maximum steel temperature as a function of the dry film thickness. The design curve and the corresponding temperature-time curves can be accessed via *GUI_DesignCurve* and saved for further use. Further information on the user interface can be found in section A.2.

5.3 Validation against Test Data

In order to evaluate the simplified calculation method and its ability to describe the fire protection performance of the investigated coating, all small-scale fire tests from

section 3.4 were recalculated. The MATLAB calculations were performed using the expansion curves from subsection 4.2.2. Based on the results of the numerical simulations, the degree of temperature non-linearity within the char structure was set to $\zeta = 0.40$ for 10 K/min and $\zeta = 0.30$ for the rest of the heating rates. The emissivity ($\varepsilon_a = 0.8$) and the heat transfer coefficient ($\alpha_c = 15\ W/(m^2K)$) were defined analogue to the numerical simulations presented in section 4.4.

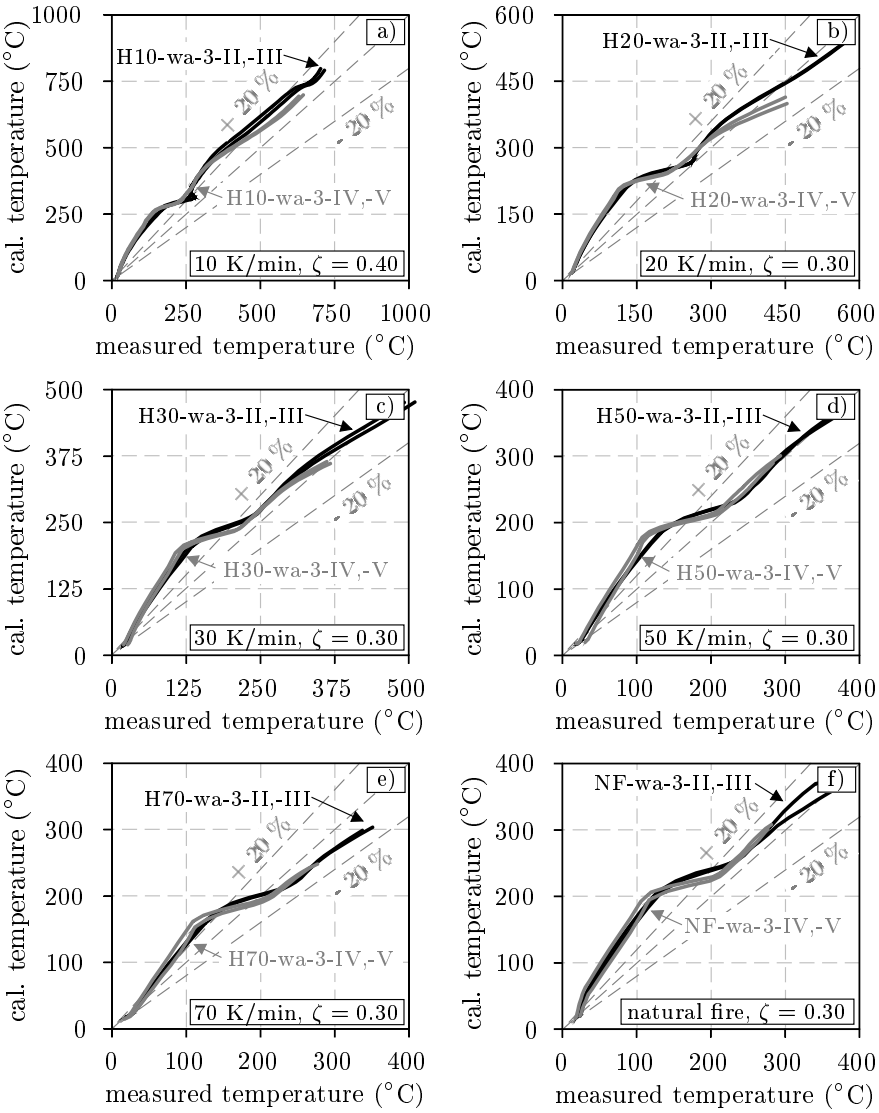

*Figure 5.5: Comparison of the simplified calculated and measured steel plate temperatures (**100 x 90 x 3 mm**, waterborne coating) at heating conditions of: a) 10 K/min, b) 20 K/min, c) 30 K/min, d) 50 K/min, e) 70 K/min and f) natural fire*

The results of the simplified calculations are documented separately for the 3 and 5 mm steel plates in Figure 5.5 and 5.6. In both Figures, the calculated steel plate temperatures are related to the measured temperatures from the tests. In this way, the differences between the results are graphically illustrated.

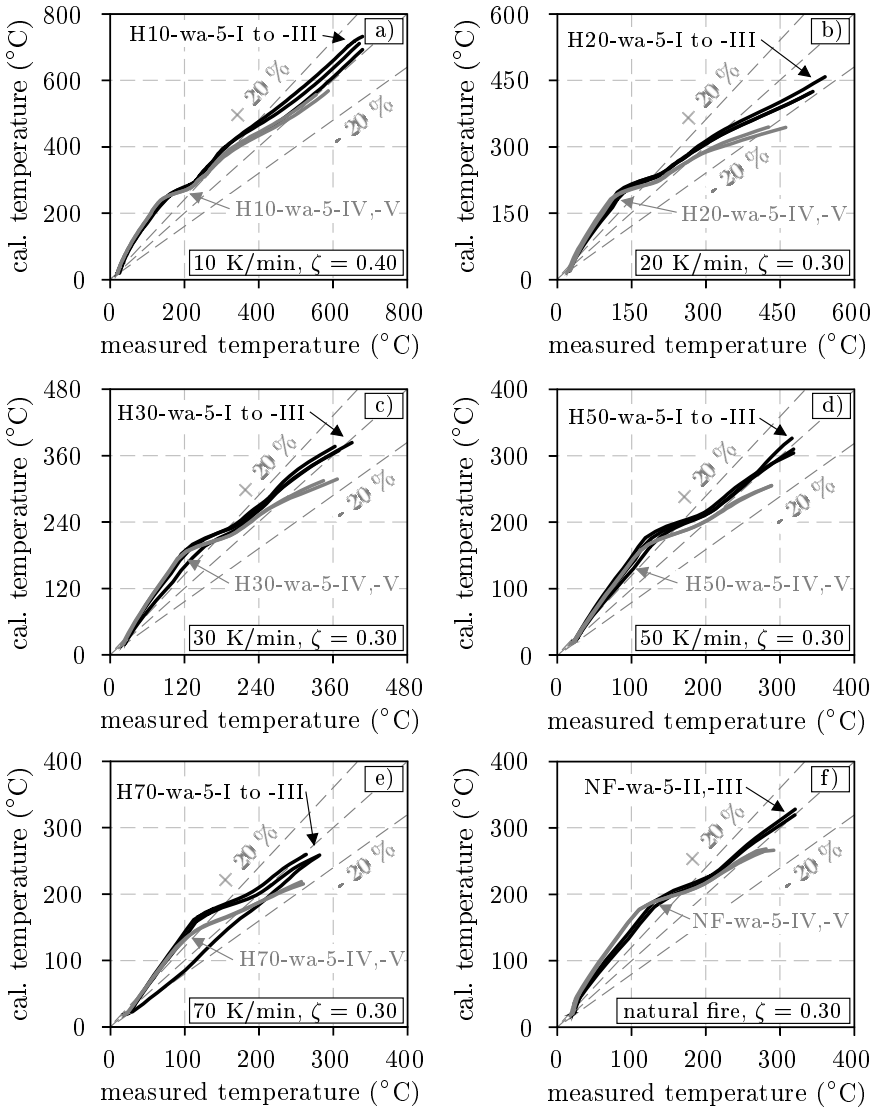

*Figure 5.6: Comparison of the simplified calculated and measured steel plate temperatures (**100 x 90 x 5 mm**, waterborne coating) at heating conditions of: a) 10 K/min, b) 20 K/min, c) 30 K/min, d) 50 K/min, e) 70 K/min and f) natural fire*

For both the 3 and 5 mm steel plates, significantly higher steel plate temperatures are calculated until the onset of expansion compared to the temperatures measured

in the tests (see for example Figure 5.5 a)). Within the simplified calculations the steel plates are assumed to be unprotected until the expansion of the coating. This could be the reason for the different heating behaviour between the calculations and the tests. However, similar observations could also be made for the numerical simulations (see Figure 4.22 and 4.23), although the coating already provided a fire protection effect at the beginning of the simulation. In the numerical simulations, the high furnace temperatures were identified to be the reason for the increased steel temperatures. Therefore, this effect could also play an important role in the simplified calculations.
As soon as the coating starts to expand, the calculation results align with the measured steel plate temperatures as can be seen for example in Figure 5.5 c) and d). However, not all calculations show such a good agreement with the experimental results. The greatest deviations occur for the tests H70-wa-3 and the H20-wa-5 (see Figure 5.5 e) and Figure 5.6 b)). While the steel plate temperatures of the H70-wa-3 tests are underestimated by approximately 23-47 °C, the H20-wa-5 calculations show the highest underestimations with 82-91 °C. However, in both cases the limits for tolerable deviations of +/-20 % are still met.

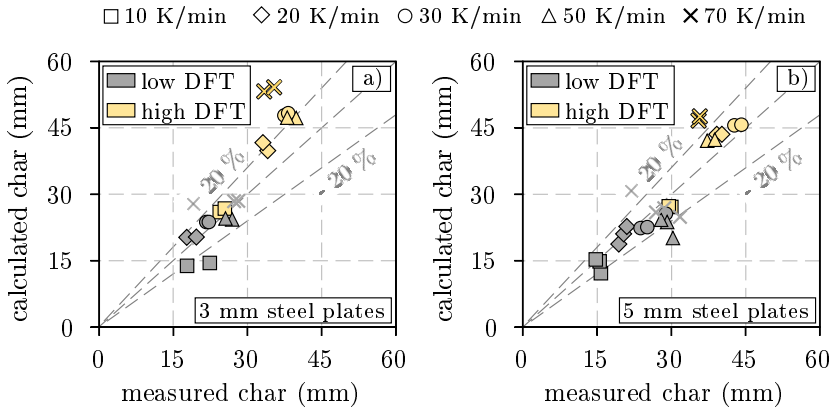

Figure 5.7: Validation of the char thickness calculation for the waterborne coating applied on 3 and 5 mm steel plates. Comparison of the calculated and measured char thickness t_{final} for constant heating rates of 10, 20, 30, 50 and 70 K/min

The reasons for the deviating behaviour of the two test series seem to be different. The lower temperatures of the H70-wa-3 calculations can be explained, for example, by the calculated char thicknesses. In Figure 5.7, the calculated char thicknesses are plotted against the measured char thicknesses t_{final} (see Table 3.7 and 3.8). From the diagram in Figure 5.7 a) it can be seen that especially for 70 K/min larger char thicknesses are calculated (42.6 and 45.1 mm) compared to the tests (33.4 and 35.4 mm). However, this only applies to the samples with high dry film thicknesses. For the lower dry film thicknesses a very good agreement with the test results is achieved. Similar observations can also be made for the 5 mm steel

plates in combination with the heating rate of 70 K/min, although the measured char thicknesses are less overestimated (see Figure 5.7 b)).
For the H20-wa-5 tests, no significantly higher char thicknesses are calculated compared to the tests. Therefore, a too high char thickness cannot be the reason for the underestimation of the steel plate temperatures. The reason seems to be rather the calculation of the thermal conductivity. As already explained during the introduction of the material model, the thermal conductivity of the coating is not only calculated as a function of expansion but also as a function of morphology. The morphology, on the other hand, is described with the help of the pore size. The pore sizes given in Figure 4.6 b) were used to perform the simplified calculations. In order to describe the effect of the open-cell foam structure on the thermal conductivity, the pore sizes were artificially increased from 1.0 to 2.0 mm (for 10 and 20 K/min) and from 1.5 to 3.0 mm (for 30, 50 and 70 K/min) at higher temperatures. In the case of the H20-wa-5 calculations, however, the increase in pore size does not seem to be sufficient to describe the fire protection performance of the waterborne coating close to reality. However, in order to maintain the consistency of the calculations and to ensure comparability with the numerical simulations, no adjustment of the parameters took place. In this way, the possibility to compare the simplified calculated expansion behaviour with the numerical simulations was preserved. By comparing the results from Figure 4.25 and 5.7, it can be seen that both the numerical simulations and the simplified calculations show a slight tendency to overestimate the char thickness for higher dry film thicknesses. At the same time, however, the char thicknesses of the test specimens H10-wa-3-II, H10-wa-3-III and H50-wa-5-I are similarly underestimated in both the numerical simulations and the simplified calculations. With regard to the intended similarity between the numerical simulations and the simplified method, these results represent an important finding.
Based on the similar results, it can be concluded that the developed calculation method can adequately replace the numerical simulations and, at the same time, provides a suitable method to calculate the heating behaviour of coated steel members in good agreement with test results. The extent to which the simplified calculation method can be used to design the dry film thickness of intumescent coatings in natural fires will be discussed in the following.

5.4 Application Example

During the numerical investigations, the three-sided fire exposed reference beam HEA 240 from the large-scale fire test was examined within a parameter study (see subsection 4.5.3). The dry film thickness of the coating was varied and a correlation function between the dry film thickness and the profile temperatures was established. Since this correlation function can be used to design the dry film thickness of the coating by interpolation, this idea was adopted for the MATLAB-based calculation method. However, in the first step, the experimental results of

the reference beam were recalculated, in order to verify the validity of the input parameters (expansion curve for 30 K/min, pore size: 1.5/3.0 mm and $\zeta = 0.30$), which were used for the recalculation of the small-scale fire tests in section 5.3. Figure 5.8 shows the results of the recalculations. As can be seen from Figure 5.8 a), the calculated top flange temperature shows a very good agreement with the test results. However, in relation to the entire cross-section, the calculated temperature represents an underestimation of the heating behaviour. In contrast to the numerical simulations, with the simplified calculation method only one temperature for the entire cross-section is calculated. Temperature gradients that result from the three-sided fire exposure cannot be reproduced. Therefore, the temperatures calculated for the top flange correspond at the same time to the web and the bottom flange. However, this contradicts the test results, as higher temperatures were measured for the web and the bottom flange. In order to avoid an underestimation of the heating behaviour, the pore size of the open-cell foam structure had to be increased from 3 to 13 mm resulting in higher thermal conductivity values. As can be seen from Figure 5.8 b), the adjustment resulted in very good agreement between the calculated and measured bottom flange temperatures.

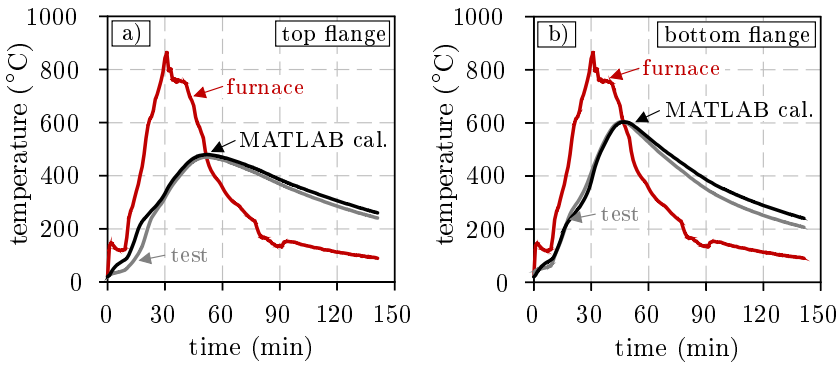

Figure 5.8: Comparison between the simplified calculated and measured steel temperatures of the reference beam (HEA 240, DFT = 360 µm) at a) the top flange (pore size: 1.5 mm/3.0 mm) and b) the bottom flange (pore size: 1.5 mm/13.0 mm)

In addition to the steel temperatures, Figure 5.9 shows the corresponding char temperatures and char thicknesses of the layers (n = 8) that were used to discretise the coating. Based on the temperature differences between the first four layers and the last four layers, the bilinear temperature gradient ($\zeta = 0.30$) within the char structure can be qualitatively identified (see Figure 5.9 a)). Due to the temperature gradient, the expansion of the layers takes place one after the other as can be seen from Figure 5.9 b). At this point it should be emphasised that although this is only a simplified calculation, the method is able to calculate the expansion behaviour in the same way as in the numerical simulations.
Since the section factor is calculated as a function of char thickness, the factor in-

creases from initially 147 to 157 m^{-1} (see Figure 5.9 b)). In this way, the calculation takes into account the increase of the fire exposed surface due to the expansion of the coating and the increase of thermal energy that is transferred into the reference beam.

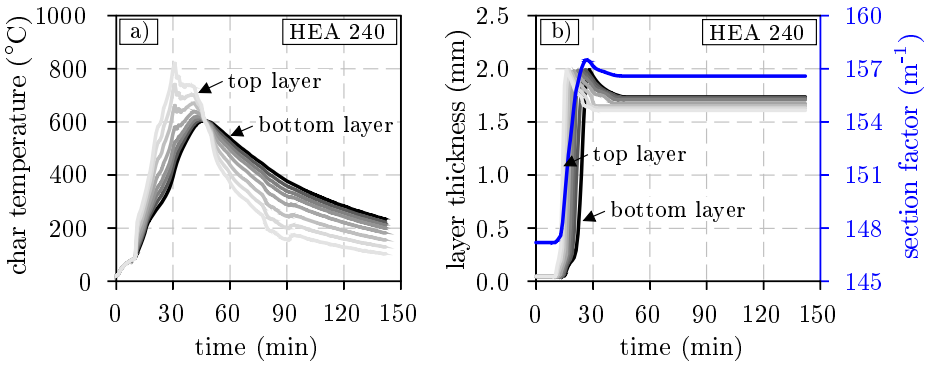

Figure 5.9: Results of the simplified calculation for the reference beam (HEA 240, DFT = 360 µm, pore size: 1.5 mm/13.0 mm): a) Char layer temperatures and b) char layer thicknesses together with the section factor

Based on the successful validation, a parameter study was performed, in which the dry film thickness of the coating was varied analogously to subsection 4.5.3. The calculated temperature-time curves are shown in Figure 5.10 a). Figure 5.10 b), on the other hand, presents the correlation functions between the steel temperature and the dry film thickness that were derived from the MATLAB and Abaqus calculations.

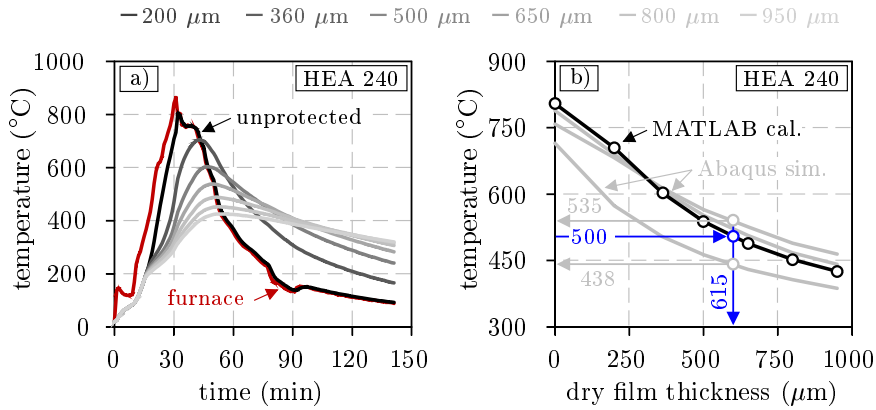

Figure 5.10: Results of the design calculations: a) Temperature-time curves of the reference beam HEA 240 for different dry film thicknesses of the waterborne coating and b) steel temperatures of the reference beam as a function of dry film thickness derived from MATLAB and Abaqus calculations

The correlation function can be used to determine the dry film thickness of the coating with regard to the member temperature. In the case of the reference beam, for example, a dry film thickness of 615 μm is required according to the simplified calculation to limit the temperature at 500 °C. According to the numerical simulations, this dry film thickness would lead to a steel temperature of 535 °C in the bottom flange and 438 °C in the top flange, if the temperature gradient due to the three-sided fire exposure is taken into account (see Figure 5.10 b)).
At the time of failure, the maximum bottom flange temperature of the loaded beam in the large-scale fire test was 584 °C. According to the simplified calculation a dry film thickness of 410 μm is required to limit this temperature. With the help of the numerical simulations, on the other hand, a required dry film thickness of 460 μm was calculated (see subsection 4.5.3). Therefore, in both cases, only a slight increase in dry film thickness is required compared to the fire test (370 μm) to prevent the loaded beam from failure.

5.5 Discussion

During the recalculations of the small-scale fire tests, a trend could already be identified that the material properties adopted from the numerical simulations need to be slightly adjusted, if the results of the simplified calculations should also agree very well with the test results. This applies especially to calculations with higher dry film thicknesses. With increasing dry film thicknesses, the fire protection performance of the coating seems to be overestimated. This is due to the calculation of the thermal conductivity $\lambda_p(\theta)$. Within the simplified calculation method, the thermal conductivity $\lambda_i(\theta)$ is calculated separately for each layer. However, in Equation 5.2 the average of the thermal conductivity is used to calculate the incremental change in steel temperature. Compared to the numerical simulations, this represents a simplification. The extent to which the simplification has an influence on the calculation results is directly related to the dry film thickness of the coating. This can be explained, for example, with the help of the calculated correlation functions in Figure 5.10 b). While up to 360 μm the simplified calculated temperatures agree very well with the simulated temperatures of the bottom flange, lower section temperatures are calculated compared to the numerical simulations when the dry film thickness increases. This is the reason why the dry film thickness of the coating is calculated to 615 μm at 500 °C and not to 755 μm as in the numerical simulations (see subsection 4.5.3).
In EN-13381-8 (2013), a correction factor k_i is derived from the temperatures of loaded and unloaded test specimens when calculating the dry film thickness of the investigated coating. It is conceivable that the temperatures calculated with the simplified method are corrected in a similar way. However, this requires comparative calculations between the numerical simulations and the simplified method in order to calculate correction factors depending on the section factor and the dry film thickness.

With the MATLAB calculation method, an approach was developed to perform simplified temperature calculations and to design the dry film thickness of intumescent coatings in natural fires. Based on the validation calculations and the application example, it could be shown that the developed method leads to reliable results when used thoroughly. Nevertheless, users must be aware that the accuracy of the results depends on the input parameters. Therefore, it is recommended to perform comparative calculations and plausibility checks before each application.

6 Summary and Outlook

Chapter six includes a summary of the gain of knowledge achieved in the present thesis as well as essential perspective on future research and transfer services.

Contents

6.1 Summary

Intumescent coatings are usually used whenever filigree and architecturally appealing steel structures have to maintain their appearance while meeting fire resistance requirements. As intumescent coatings belong to non-standardised products, the coatings are introduced to the German market by general technical approvals, general design certifications or European Technical Assessments. To receive a national or European approval, the products need to pass experimental examinations. Except the smouldering fire, all fire tests prescribed in the approval principles, especially those for the design of the dry film thickness, are based on the standard fire curve. Therefore, the assessment of the thermal performance of intumescent coatings is solely related to this fire scenario.
However, due to the increasing use of performance-based design methods for steel structures, it becomes more and more important to assess the fire protection performance of intumescent coatings in case of natural fires. Harmonised rules provide already methods to design the ultimate limit state of steel structures due to natural fires although the performance of intumescent coatings in natural fires is largely unknown. As the evolution and propagation of natural fires is essentially based on the fire load and ventilation conditions inside a building, natural fire scenarios can show arbitrary regimes as well as heating and cooling rates. Facing this fact and keeping in mind that the reaction of intumescent coatings is thermally activated, the variety of natural fires makes it even more challenging to evaluate the influence of natural fires on the fire protection performance of intumescent coatings. However, a thorough understanding of the fire protection performance of intumescent coatings in natural fires is fundamental for a save and reliable design of coated steel structures. Therefore, the main objective of this thesis was to evaluate the thermal performance of intumescent coatings in natural fires and to identify the most relevant parameters for the description of the temperature and heating rate-dependent behaviour of intumescent coatings.

In order to achieve the objective, in the first step, a comprehensive literature review was conducted. Based on patents and publications of the last 70 years, the most frequently used ingredients of intumescent coatings were identified. Subsequently, a systematic evaluation of the thermogravimetric (TG) analyses known from literature was carried out. With the help of the analyses, it could be revealed that the main ingredients of intumescent coatings show different sensitivities to changes in heating rates under air atmosphere. While the mass loss of ammonium polyphosphate (APP), pentaerythritol (PER) and melamine (MEL) is retarded due to the increase in heating rate, the decomposition temperatures of the polymer binders remain nearly unchanged. At higher heating rates, this behaviour is beneficial since the binder provides sufficient viscosity to trap the released gases and to form a stable char structure. However, at lower heating rates, APP, PER and MEL react earlier with respect to the binder. As a consequence, most of the gases escape

without being trapped inside the molten binder due to its low viscosity. This has a significant influence on both the expansion behaviour and the char morphology.
In a further literature review, an overview of experimental investigations was given, in which the fire protection performance of intumescent coatings is investigated under varying thermal loads. In contrast to this thesis, in most literature-known studies the samples are subjected to constant heat fluxes and compared to each other. However, a comparability of these results is not given, since the measured steel temperatures are not compared with each other in terms of the transferred thermal energy, but in terms of time. For the same time and different heat fluxes, however, different thermal energies are introduced into the samples. This is fundamental for the evaluation of the fire protection performance of intumescent coatings and was therefore highlighted during the literature review. The same also applied to the method of the *effective thermal conductivity*. This method is also used in literature to evaluate the fire protection performance of intumescent coatings at different fire loads, although the results of the evaluations are falsified by the assumptions the method is based on. This could be shown with the help of the numerical simulations that were performed in this thesis.
However, before conducting own numerical investigations, the literature was reviewed again. Now, the focus of the literature review was on intumescence and bubble growth models as well as on decomposition and thermal conductivity models. It could be shown that no model exists in the literature that is able to describe the heating rate-dependent and differentiated thermal behaviour of intumescent coatings due to changes in char morphology in heating and cooling of natural fires. However, some of the models showed high potential for further development and were therefore refined and linked together.

After the literature review, own experimental investigations were performed in order to investigate the heating rate-dependent behaviour of a solvent- and a water-borne coating. With the help of coupled TG-DSC analyses and expansion analyses at constant heating rates of 10, 20, 30, 50 and 70 K/min it could be confirmed that the expansion behaviour and the char morphology of intumescent coatings are significantly influenced by the changes in heating rate and the bubble bursting at the surface. Especially for lower heating rates and smouldering fires, the bursting of bubbles and the release of volatile gases reduces not only the expansion, but impairs also the formation of a uniform char structure. This became particularly evident during the morphological investigations. As a result, the fire protection performance of intumescent coatings at lower heating rates is not only affected by the reduced expansion but also by the irregular and fissured char structure.
In order to evaluate the fire protection performance of the investigated coatings with regard to the heating behaviour, a total of 113 small-scale fire tests on coated steel plates were performed. Besides the dry film thickness and the type of coating, the steel plate thickness was also varied. For the tests, a new developed test setup was used to measure both the steel plate temperature and the temperature development inside the expanded char using equidistantly arranged thermocouples.

In contrast to the studies in literature, the fire protection performance was not evaluated with the help of the effective thermal conductivity but by comparing measured temperatures of unprotected and protected steel plates. For this purpose, additional unprotected reference samples are needed. This slightly increases the experimental effort. However, it enables an accurate evaluation of the fire protection performance of intumescent coatings, especially under varying heating conditions. The best fire protection performance was observed for high heating rates. On the other hand, a reduction in heating rate showed a significant influence on the thermal performance, especially for the solvent-borne coating.
As large-scale fire tests are performed under realistic geometry and loading situations, a loaded beam exposed to a selected natural fire was investigated at the end of the experimental programme. Besides different types of cracks in the char structure, bubble shapes could be identified, which were not observed before in the small-scale fire tests. The bubbles were characterised by open or subsequently closed holes and were solely formed in areas of reduced heating rates or due to shading. However, despite the formation of stress-induced cracks and open bubbles, the fast heating of the loaded beam could be delayed. With a mean dry film thickness of ca. 370 μm, the load-bearing capacity of the three-sided fire exposed beam could be maintained for 48 minutes within the scope of the investigated natural fire. In addition to the loaded beam, an unloaded beam was also examined during the large-scale fire test. Although the results did not clearly reveal the influence of stress-induced cracks in the char structure on the heating behaviour, it is highly recommended to carry out tests on both loaded and unloaded test specimens in the future.

In order to better understand the temperature and heating rate-dependent behaviour of intumescent coatings and to identify the most relevant parameters describing the behaviour, numerical investigations were performed using the finite element software ABAQUS. For this purpose, a material model was developed, which uses only the expansion curves and the pore size as the main input parameters to describe the temperature and heating rate-dependent thermal conductivity. As the char morphology has a significant influence on the thermal conductivity, separate submodels were introduced for the closed-cell and the open-cell foam structure. A differentiation between heating and cooling was also undertaken. In order to describe the heating rate-dependent expansion behaviour, a user subroutine-based description was implementation. The temperature-dependent density and specific heat capacity, on the other hand, were derived from the performed coupled TG-DSC analyses.
For the validation of the material model, both the expansion tests and the steel plate tests from the experimental programme were recalculated. It could be shown that the implemented user subroutine is suitable to realistically describe the expansion behaviour of the investigated coating. In addition to the expansion behaviour, it could also be shown that the heating behaviour and the associated fire protection performance of the investigated coating can also be recalculated close to reality

with the help of the new developed submodels for the thermal conductivity.
Due to the very good agreement between the simulation results and the experimental data, a parameter study was performed for the reference beam from the large-scale fire test. Within the study, the dry film thickness of the waterborne coating was varied. In this way, a correlation function between the dry film thickness and the maximum steel temperature was derived. With the help of this correlation function, it was possible to determine the dry film thickness of the waterborne coating that would have prevent the failure of the loaded beam from the large-scale fire test.

Based on the idea of the correlation function, a MATLAB-based calculation approach was developed, which enables the design of the dry film thickness of intumescent coatings in natural fires. The design method is based on the incremental calculation of the temperature change in coated steel members that is given in EN-1993-1-2 (2010) and was modified for the application to intumescent coatings. Compared to the numerical simulations, the MATLAB-based calculation method enables fast calculations. For this reason, correlation functions can be calculated much faster for the design of the dry film thickness for any natural fire scenario.
Within the MATLAB-based calculation method, the expansion behaviour of intumescent coatings is calculated layer by layer. The thermal conductivity is also described analogue to the numerical simulations as a function of the expansion curves and the pore size. For this reason, despite its simplicity, the method provides similar results as the numerical simulations. This could be demonstrated within the validation of the calculation method.

With the findings of this thesis, a contribution to a safe and reliable performance-based design of coated steel members is made. For the first time, a method for the design of the dry film thickness of intumescent coatings in natural fires is provided. Although only two products were investigated in this thesis, the new developed experimental methods can be used in future to build up a database for the material properties of intumescent coatings available on the market. Together with the material properties and the calculation methods presented in this work, whether numerical or simplified, the performance of intumescent coatings can be calculated in the future with moderate effort.

6.2 Outlook

The investigations carried out within the scope of this thesis have already contributed to a significant gain in knowledge regarding the heating rate-dependent behaviour of intumescent coatings. Besides the new developed test setup for the investigation of the expansion behaviour and the method for the evaluation of the fire protection performance, especially the new developed material model as well as the MATLAB-based calculation method represent an enormous value for research

and practice. The material model, for example, offers the opportunity to design intumescent coatings in a way that is object-oriented and individual, but most of all safe and resource-saving. However, in order to use the material model and the MATLAB-based calculation method for the design of intumescent coatings in natural fires, the following steps are required:

(1) When performing the simplified calculation for the incremental temperature change $\Delta\theta_a$ of a coated steel member, the thermal conductivity of the intumescent coating calculated for each layer is averaged. Compared to the numerical simulations, this represents a simplification that leads to an overestimation of the fire protection performance, especially for higher dry film thicknesses. In order to avoid the overestimation, an adjustment of the calculation method should be made. Instead of the averaged thermal conductivity $\lambda_p(\theta)$, a temperature change $\Delta\theta_i$ for each layer should be calculated with the corresponding thermal conductivity $\lambda_i(\theta)$. The change in steel member temperature $\Delta\theta_a$ would then correspond to the summation of the temperature changes of all char layers. In this way, the fire protection performance is not overestimated for higher dry film thicknesses and the temperatures of the coated steel members are calculated close to reality.

(2) To ensure that the method presented in section 5.2 can be used for the design of the dry film thickness of intumescent coatings and for the calculation of the steel temperatures, it should be integrated in EN-1993-1-2 (2010) by extending the existing method to the application of intumescent coatings. In this way, the calculation method could be applied universally without the need for any expert report.

(3) However, the application of the calculation method requires that the product-dependent material properties of the intumescent coatings, such as the expansion behaviour and the char morphology, are known. Within the scope of this thesis, an experimental setup was developed that can be used to determine these properties. With the help of this test setup the manufacturers could carry out additional tests as part of a new approval procedure, in order to include the required material properties in the approval documents. In this way, every manufacturer at national and European level would provide the calculation engineers with the required material properties and, at the same time, would prove the performance of their products in natural fires.

(4) Both the numerical simulations and the simplified calculations in this thesis focused on the realistic description of the fire protection performance as well as on the heating and expansion behaviour of intumescent coatings. However, in the performance-based design, besides heating, especially the deformation behaviour and the load-bearing capacity of the investigated steel members play a decisive role. For this reason, sequencially coupled numerical simulations were performed for the loaded beam from the large-scale fire test, in order to compare the heating, the load-bearing and the deflection behaviour with the test results. However, in order to limit the size of this thesis, the

results of the calculations have not been presented here. Nevertheless, the results will be published separately in the near future.

(5) During the large-scale fire test, cracks were observed in the expanded char structure of both the loaded and unloaded test specimens. It is known from the literature that these cracks can have a negative influence on the fire protection performance of intumescent coatings. In order to describe the heating behaviour of intumescent coatings within numerical simulations as close to reality as possible, the developed material model should be extended by a subroutine-based approach taking the effect of the stress-induced crack formation and the unhindered heating of the underlying steel substrate into account.

A Appendix

The appendix chapter includes data that is part of the doctoral thesis

Contents

A.1 Expansion Behaviour of the Waterborne Coating

Polynomial functions can be used in order to mathematically reproduce the measured expansion curves of the intumescent coatings. These functions are required to describe the expansion behaviour of the waterborne coating within the user subroutine UEXPAN. The coefficients of the polynomial functions used for the numerical simulations are listed in tables below.

Table A.1: Polynomial coefficients describing the heating rate-dependent expansion behaviour of the waterborne coating at 10 K/min between 190 and 430 °C

	I (190-280 °C)	II (280-320 °C)	III (320-430 °C)
a_0	-155.869011655003	3164366.74094427	-6961.64815468306
a_1	0.0	0.0	0.0
a_2	0.0	0.0	0.0
a_3	0.0	-0.00000152999999583828	0.0
a_4	0.0	0.002226583327217	-0.000000313082750585764
a_5	0.0000107148407148399	-1.29478999640704	0.000485034641289187
a_6	-0.007850932400932	376.098540612334	-0.281487864221679
a_7	1.93107187257175	-54571.069545438	72.5064808022468

Table A.2: Polynomial coefficients describing the heating rate-dependent expansion behaviour of the waterborne coating at 10 K/min between 430 and 1000 °C

	IV (430-620 °C)	V (620-1000 °C)
a_0	-67.4841408811738	31.5207563404225
a_1	0.0	0.0
a_2	0.0	0.0
a_3	0.0	0.0
a_4	0.0	0.0
a_5	0.000000730606645265577	0.0
a_6	-0.00117435550047	0.000109398477177681
a_7	0.594315137802017	-0.01956668285744

Table A.3: Polynomial coefficients describing the heating rate-dependent expansion behaviour of the waterborne coating at 20 K/min between 180 and 330 °C

	I (180-270 °C)	II (270-330 °C)
a_0	1703.12263984619	42763.866855438
a_1	0.0	0.0
a_2	9.43327505822094E-07	0.0000049377510580248
a_3	-0.000785744949490031	-0.006058853620412
a_4	0.244011698716282	2.77871828663082
a_5	-33.4214403649406	-564.082060163048

Table A.4: Polynomial coefficients describing the heating rate-dependent expansion behaviour of the waterborne coating at 20 K/min between 330 and 1000 °C

	III (330-430 °C)	IV (430-1000 °C)
a_0	-4647.64657345952	84.2653768140447
a_1	0.0	0.0
a_2	-1.94930069931597E-07	0.0
a_3	0.000307604895107248	-6.92051849083278E-08
a_4	-0.181897290211145	0.000188781204383467
a_5	47.7383863639819	-0.171826681857015

Table A.5: Polynomial coefficients describing the heating rate-dependent expansion behaviour of the waterborne coating at 30 K/min between 180 and 330 °C

	I (180-270 °C)	II (270-330 °C)
a_0	980.054038454295	-6844.82801044953
a_1	0.0	0.0
a_2	4.45949883447072E-07	-1.67424242446357E-06
a_3	-0.000390471056718502	0.001750757576024
a_4	0.127466564684449	-0.672026515271368
a_5	-18.3323593627296	112.1479502404

Table A.6: Polynomial coefficients describing the heating rate-dependent expansion behaviour of the waterborne coating at 30 K/min between 330 and 1000 °C

	III (330-430 °C)	IV (430-1000 °C)
a_0	-8633.26519820893	61.1146520304268
a_1	0.0	0.0
a_2	-3.78496503499945E-07	0.0
a_3	0.000591214063719355	0.0
a_4	-0.345552476693018	0.0000319612041500596
a_5	89.5403622773867	-0.057207244257634

Table A.7: Polynomial coefficients describing the heating rate-dependent expansion behaviour of the waterborne coating at 50 K/min between 170 and 320 °C

	I (170-250 °C)	II (250-320 °C)
a_0	29.2035627705632	27687.6855956069
a_1	0.0	0.0
a_2	0.0	4.28219696975144E-06
a_3	0.0	-0.004891199495012
a_4	0.000972186147186156	2.08659678033003
a_5	-0.331034848484853	-393.580415769949

Table A.8: Polynomial coefficients describing the heating rate-dependent expansion behaviour of the waterborne coating at 50 K/min between 320 and 1000 °C

	III (320-420 °C)	IV (420-1000 °C)
a_0	-11920.6663169584	52.6492726861349
a_1	0.0	0.0
a_2	-5.69930069926933E-07	0.0
a_3	0.000869961149956511	2.40855890226731E-09
a_4	-0.497172027969461	0.0000177574793224471
a_5	126.053902485772	-0.037201004248604

Table A.9: Polynomial coefficients describing the heating rate-dependent expansion behaviour of the waterborne coating at 70 K/min between 170 and 310 °C

	I (170-250 °C)	II (250-310 °C)
a_0	825.462929290034	1114580.41866132
a_1	0.0	-6.8142838914283E-07
a_2	4.52505827504407E-07	0.000948560529029695
a_3	-0.000375517353016139	-0.527039398344033
a_4	0.116826544288657	146.092119300055
a_5	-16.0807419709371	-20200.7877645998

Table A.10: Polynomial coefficients describing the heating rate-dependent expansion behaviour of the waterborne coating at 70 K/min between 310 and 1000 °C

	III (310-430 °C)	IV (430-1000 °C)
a_0	-4236.68184322091	23.6228331437625
a_1	0.0	0.0
a_2	-1.7788461538792E-07	-1.68342599037333E-10
a_3	0.000281488927743887	4.79764730824573E-07
a_4	-0.166621896855928	-0.000475523834061536
a_5	43.7033908182063	0.181727530765935

A.2 Graphical User Interface of the Design Method

In the following, the graphical user interface (GUI) of the design method is documented that was implemented in MATLAB. The method was developed to calculate the temperature development of coated steel members and for the design of the required dry film thickness of intumescent coatings in case of natural fires.

Figure A.1: Initial screen of the graphical user interface

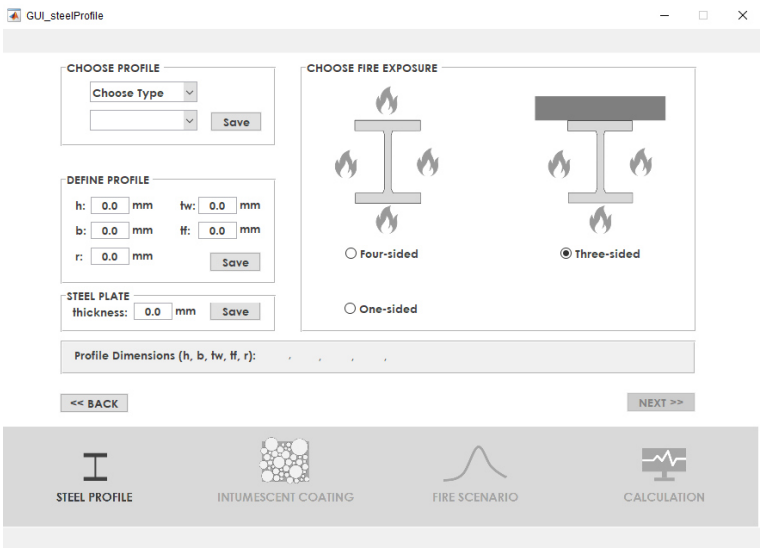

Figure A.2: Graphical user interface for the definition of the steel member and the fire exposure

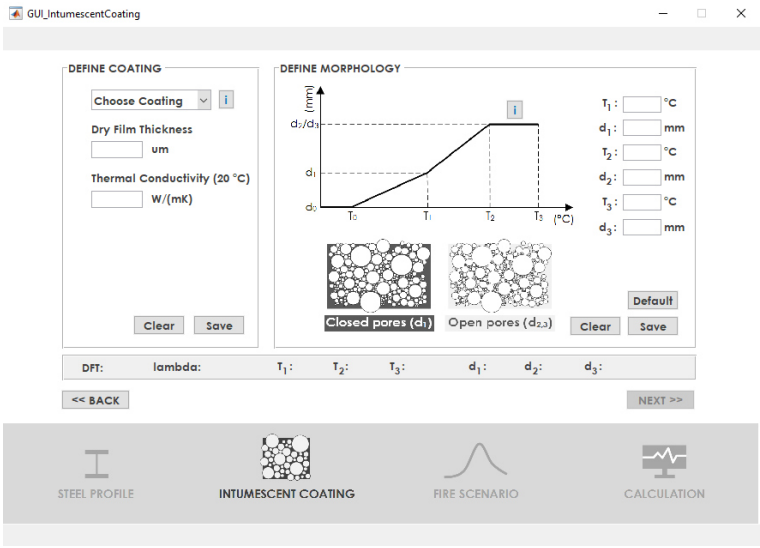

Figure A.3: Graphical user interface for the definition of the dry film thickness, the conductivity and the morphology of the intumescent coating

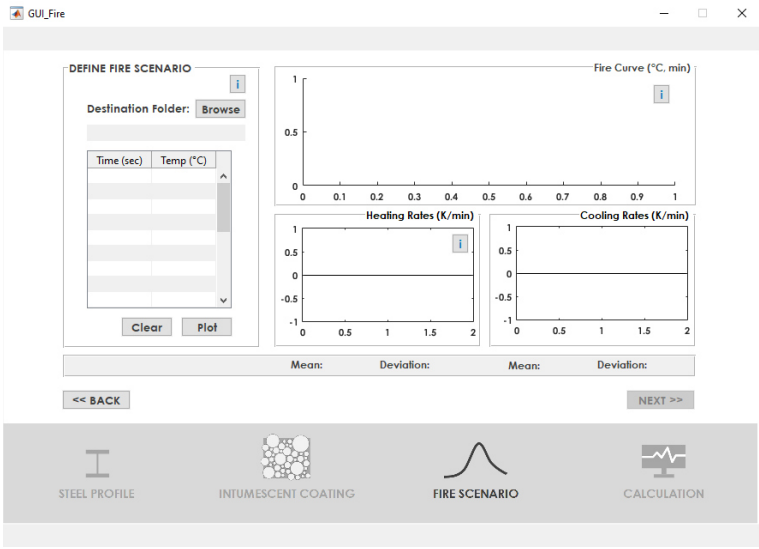

Figure A.4: Graphical user interface for the definition of the natural fire curve and the calculation of the average heating and cooling rate

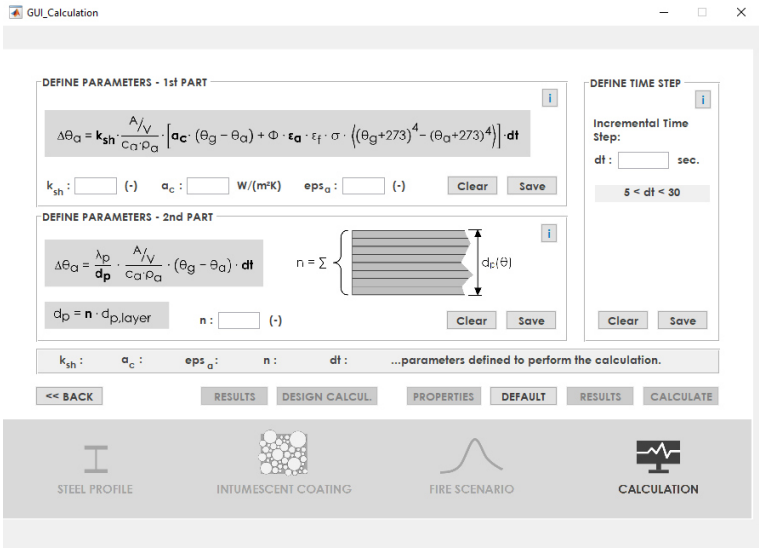

Figure A.5: Graphical user interface for the definition of the calculation parameters, such as the heat transfer coefficient, the emissivity of the coated steel member, the number of layers to discretise the coating and the time step size

B Bibliography

Please note that all non-English publications are listed with their original title and a corresponding English title. In those cases where no English title was given in the publication, the title was translated to the best of the author's knowledge.

Amon, M. & Denson, C. D. (1984), 'A Study of the Dynamics of Foam Growth: Analysis of the Growth of Closely Spaced Spherical Bubbles', *Polymer Engineering and Science* **Vol. 24**(13), pp. 1026–1034.

Anderson, C. E., Dziuk, J. & Mallow, W. (1985), 'Intumescent Reaction Mechanism', *Journal of Fire Sciences* **Vol. 3**, pp. 161–194.

Anderson, C., Ketchum, D. E. & Mountain, W. P. (1988), 'Thermal Conductivity of Intumescent Chars', *Journal of Fire Science* **Vol. 6**, pp. 390–410.

Andersson, A., Lundmark, S. & Maurer, F. H. J. (2007), 'Evaluation and Characterization of Ammoniumpolyphosphate-Pentaerythritol-Based Systems for Intumescent Coatings', *Journal of Applied Polymer Science* **Vol. 104**, pp. 748–753.

Ankang, K. & Houde, H. (2013), 'Effective Thermal Conductivity of Open Cell Polyurethane Foam Based on the Fractal Theory', *Advances in Materials Science and Engineering* **Article ID 125267**.

ASTM-D-412 (1987), Standard Test Methods for Vulcanized Rubber and Thermoplastic Elastomers - Tension, Technical report, American Society for Testing and Materials.

Babrauskas, V. (2016), *SFPE Handbook of Fire Protection Engineering*, fifth edn, Society of Fire Protection Engineers, chapter 28: The Cone Calorimeter, pp. 952–980.

Balabanovich, A. (2004), 'The effect of melamine on the combustion and thermal decomposition behaviour of poly(butylene terephthalate)', *Polymer Degradation and Stability* **Vol. 84**, pp. 451–458.

Ballistreri, A., Foti, S., Montaudo, G. & Scamporrino, E. (1980), 'Evolution of Aromatic Compounds in the Thermal Decomposition of Vinyl Polymers', *Journal of Polymer Science* **Vol. 18**, pp. 1147–1153.

Barontini, F. & Cozzani, V. (2006), 'Formation of hydrogen bromide and organobrominated compounds in the thermal degradation of electronic boards', *Journal of Analytical and Applied Pyrolysis* **Vol. 77**(1), pp. 41–55.

Bartholmai, M. & Schartel, B. (2007), 'Assessing the performance of intumescent coatings using benchscaled cone calorimeter and finite difference simulations', *Fire and Materials* **Vol. 31**, pp. 187–205.

Bartholmai, M., Schriever, R. & Schartel, B. (2003), 'Influence of external heat flux and coating thickness on the thermal insulation properties of two different intumescent coatings using cone calorimeter and numerical analysis', *Fire and Materials* **Vol. 27**, pp. 151–162.

Berlin, A., Khalturinskij, N., Reshetnikov, I. & Yablokova, M. (1998), *Fire Retardancy of Polymers - The Use of Intumescence*, The Royal Society of Chemistry, chapter Some Aspects of Mechanical Stability of Intumescent Chars, pp. 104–112.

Bermes, B. (2006), Simulation der Gasblasenentwicklung von im Brandfall aufgeschäumten Materialien (*engl.* Simulation of bubble formation in foamed materials due to fire), Dissertation, Bergische Universität Wuppertal.

Beyer, G. (2001), 'Flame Retardant Properties of EVA-nanocomposites and Improvements by Combination of Nanofillers with Aluminium Trihydrate', *Fire and Materials* **Vol. 25**, pp. 193–197.

Bodzay, B., Bocz, K., Barkai, Z. & Marosi, G. (2011), 'Influence of rheological additives on char formation and fire resistance of intumescent coatings', *Polymer Degradation and Stability* **Vol. 96**, pp. 355–362.

Bonnet, J., Bounor-Legaré, V., Boisson, F., Melis, F., Camino, G. & Cassagnau, P. (2012), 'Phosphorus based organiceinorganic hybrid materials prepared by reactive processing for EVA fire retardancy', *Polymer Degradation and Stability* **Vol. 97**, pp. 513–522.

Bourbigot, S. & Duquesne, S. (2007), 'Fire retardant polymers: recent developments and opportunities', *Journal of Materials Chemistry* **Vol. 17**, pp. 2283–2300.

Bourbigot, S., Duquesne, S. & Leroy, J.-M. (1999), 'Modeling of Heat Transfer of a Polypropylene-Based Intumescent System during Combustion', *Journal of Fire Science* **Vol. 17**, pp. 42–56.

Bourbigot, S., Le Bras, M., Duquesne, S. & Rochery, M. (2004), 'Recent Advances for Intumescent Polymers', *Macromolecular Materials and Engineering* **Vol. 289**, pp. 499–511.

Bozzoli, F., Mocerino, A., Rainieri, S. & Vocale, P. (2018), 'Inverse heat transfer modeling applied to the estimation of the apparent thermal conductivity of an intumescent fire retardant paint', *Experimental Thermal and Fluid Science* **Vol. 90**, pp. 143–152.

Bradford, S. J. (2009), Intumescent coating composition, GB Patent No. 2 451 233 A, UK Intellectual Property Office.

Buckingham, M. R. (1994), INTUMESCENT FIRE PROTECTIVE COATINGS, WO Patent No. 94/17142, World Intellectual Property Organisation.

Bugajny, M., Le Bras, M. & Bourbigot, S. (1999), 'Short Communication: New Approach to the Dynamic Properties of an Intumescent Material', *Fire and Materials* **Vol. 23**, pp. 49–51.

Butler, K., Baum, H. & Kashiwagi, T. (1997), Three-dimensional Modeling of Intumescent Behaviour in Fires, *in* I. A. for Fire Safety Science, ed., 'Fire Safety Science - Proceedings of the Fifth International Symposium', pp. 523–534.

Butler, K. M. (2002), A Numerical Model for Combustion of Bubbling Thermoplastic Materials in Microgravity, Technical Report NISTIR 6894, National Institute of Standards and Technology.

Butler, R. (2017), INTUMESCENT COATING COMPOSITION, European Patent No. 3 022 265 B1, European Patent Office.

Cagliostro, D. E., Riccitiello, S. R., Clark, K. J. & Shimizu, A. B. (1975), 'Intumescent Coating Modeling for thermal protection', *Journal of Fire and Flammability* **Vol. 6**, pp. 205–221.

Camino, G. & Costa, L. (1986), 'Mechanism of intumescence in fire retardant polymers', *Reviews in Inorganic Chemistry* **Vol. 8**(1, 2), pp. 69–100.

Camino, G., Costa, L. & Martinasso, G. (1989), 'Intumescent Fire-retardant Systems', *Polymer Degradation and Stability* **Vol. 23**, pp. 359–376.

Camino, G., Costa, L. & Trossarelli, L. (1984), 'Study of the mechanism of intumescence in fire retardant polymers: Part III - Effect of urea on the ammonium polyphosphate-pentaerythritol system', *Polymer Degradation and Stability* **Vol. 7**(4), pp. 221–229.

Chiappini, D. (2018), 'Numerical simulation of natural convection in open-cells metal foams', *International Journal of Heat and Mass Transfer* **Vol. 117**, pp. 524–537.

Cirpici, B. K. (2015), Simulating the Expansion Process of Intumescent Coating Fire Protection, PhD thesis, University of Manchester, School of Mechanical, Aerospace and Civil Engineering.

Cirpici, B., Wang, Y. C. & Rogers, B. (2016), 'Assessment of the thermal conductivity of intumescent coatings in fire', *Fire Safety Journal* **Vol. 81**, pp. 74–84.

Costa, L. & Camino, G. (1988), 'Thermal Behaviour of Melamine', *Journal of Thermal Analysis* **Vol. 34**, pp. 423–429.

Cui, S., Li, L. & Wang, Q. (2016), 'Enhancing glass transition temperature and mechanical properties of poly (propylene carbonate) by intermacromolecular complexation with poly (vinyl alcohol)', *Composites Science and Technology* **Vol. 127**, pp. 177–184.

Curtis, L. J. & Miller, Dennis, J. (1988), 'Transport Model with Radiative Heat Transfer for Rapid Cellulose Pyrolysis', *Industrial & Engineering Chemistry Research* **Vol. 27**, pp. 1775–1783.

Dahiya, J., Rathi, S., Bockhorn, H., Haußmann, M. & Kandola, B. (2012), 'The combined effect of organic phoshphinate/ammonium polyphosphate and pentaerythritol on thermal and fire properties of polyamide 6-clay nanocomposites', *Polymer Degradation and Stability* **Vol. 97**, pp. 1458–1465.

Dai, X., Welch, S. & Usmani, A. (2017), 'A critical review of "travelling fire" scenarios for performance-based structural engineering', *Fire Safety Journal* **Vol. 91**, pp. 568–578.

Davis, M. (2010), Finite Difference Methods - MSc Course in Mathematics and Finance, Script, Imperial College London.
URL: *http://wwwf.imperial.ac.uk/ mdavis/*

Deodhar, S., Shanmuganathan, K., Fan, Q., Wilkie, C., Costache, M., Dembsey, N. & Patra, P. (2011), 'Calcium Carbonate and Ammonium Polyphosphate-Based Flame Retardant Composition for Polypropylene', *Journal of Applied Polymer Science* **Vol. 120**, pp. 1866–1873.

Derakhshesh, Z., Khorasani, M., Akhlaghi, S., Keyvani, B. & Alvani, A. A. S. (2012), 'Design and optimization of an intumescent flame retardant coating using thermal degradation kinetics and Taguchi's experimental design', *Polymer International* **Vol. 61**, pp. 926–933.

Di Blasi, C. & Branca, C. (2001), 'Mathematical Model for the Nonsteady Decomposition of Intumescent Coatings', *Journal of the American Institute of Chemical Engineers* **Vol. 47**(10), pp. 2359–2370.

DIBt (1997), Zulassungsgrundsätze für reaktive Brandschutzsysteme auf Stahlbauteilen (*engl.* Approval principles for intumescent coatings on steel elements), DIBt Mitteilung, pp. 95-107, Ernst & Sohn Verlag.

DIBt (2017), Information zu neuen Bescheidtypen (*engl.* Information on new Technical Approvals), DIBt Mitteilung, Referat ZD 5, Berlin.

DIN-4102-2 (1977), Brandverhalten von Baustoffen und Bauteilen - Bauteile, Begriffe, Anforderungen und Prüfungen (*engl.* Fire Behaviour of Building Materials and Building Components - Building Components, Definitions, Requirements and Tests), DIN, Deutsches Institut für Normung e.V., Berlin.

Dittrich, B., Wartig, K.-A., Mülhaupt, R. & Schartel, B. (2014), 'Flame-Retardancy Properties of Intumescent Ammonium Poly(Phosphate) and Mineral Filler Magnesium Hydroxide in Combination with Graphene', *Polymers* **Vol. 6**, pp. 2875–2895.

Dong, S.-S., Wu, F., Chen, L., Wang, Y.-Z. & Chen, S.-C. (2016), 'Preparation and characterization of Poly(vinyl alcohol)/graphene nanocomposite with enhanced thermal stability using PEtVIm-Br as stabilizer and compatibilizer', *Polymer Degradation and Stability* **Vol. 131**, pp. 42–52.

Ducrocq, P., Duquesne, S., Magnet, S., Bourbigot, S. & Delobel, R. (2006), 'Interactions between chlorinated paraffins and melamine in intumescent paint - investing a way to suppress chlorinated paraffins from the formulations', *Progress in Organic Coatings* **Vol. 57**, pp. 430–438.

Duquesne, S. (2005), Polymer binder for intumescent coatings, European Patent No. 1 431 353 B1, European Patent Office.

Duquesne, S., Bachelet, P., Bellayer, S., Bourbigot, S. & Mertens, W. (2013), 'Influence of inorganic fillers on the fire protection of intumescent coatings', *Journal of Fire Science* pp. pp. 1–18.

Duquesne, S. & Bourbigot, S. (2009), *Fire Retardancy of Polymeric Materials*, second edn, Wilkie, C. and Morgan, A., chapter Char Formation and Characterization, pp. 239–260.

Duquesne, S., Le Bras, M., Bourbigot, S., Delobel, R., Camino, G., Eling, B., Lindsay, C., Roels, T. & Vezin, H. (2001), 'Mechanism of Fire Retardancy of Polyurethanes Using Ammonium Polyphosphate', *Journal of Applied Polymer Science* **Vol. 82**, pp. 3262–3274.

Duquesne, S., Magnet, S., Jama, C. & Delobel, R. (2005), 'Thermoplastic resins for thin film intumescent coatings - towards a better understanding of their effect on intumescence efficiency', *Polymer Degradation and Stability* **Vol. 88**, pp. 63–69.

EAD-50402-00-1106 (2017), Fire Protective Products - Reactive Coatings for Fire Protection of Steel Elements, EOTA, European Organisation for Technical Assessment, Brussels.

El Hage, R., Viretto, A., Sonnier, R., Ferry, L. & Lopez-Cuesta, J.-M. (2014), 'Flame retardancy of ethylene vinyl acetate (EVA) using new aluminum-based fillers', *Polymer Degradation and Stability* **Vol. 108**, pp. 56–67.

EN-10025-2 (2011), Hot rolled products of structural steels - Part 2: Technical delivery conditions for non-alloy structural steels, CEN, European Committee for Standardization, Brussels.

EN-10130 (2007), Cold rolled low carbon steel flat products for cold forming - Technical delivery conditions, CEN, European Committee for Standardization, Brussels.

EN-13381-10 (2018), Test methods for determining the contribution to the fire resistance of structural members - Part 10: Applied protection to solid steel bars in tension, CEN, European Committee for Standardization, Brussels.

EN-13381-4 (2013), Test methods for determining the contribution to the fire resistance of structural members - Part 4: Applied passive protection to steel members, CEN, European Committee for Standardization, Brussels.

EN-13381-8 (2013), Test methods for determining the contribution to the fire resistance of structural members - Part 8: Applied reactive protection to steel members, CEN, European Committee for Standardization, Brussels.

EN-1363-1 (2012), Fire resistance tests - Part 1: General Requirements, CEN, European Committee for Standardization, Brussels.

EN-1363-2 (1999), Fire resistance tests - Part 2: Alternative and additional procedures, CEN, European Committee for Standardization, Brussels.

EN-1991-1-2 (2010), Eurocode 1: Actions on structures - Part 1-2: General actions - Actions on structures exposed to fire, CEN, European Committee for Standardization, Brussels.

EN-1991-1-2/NA (2015), National Annex - Nationally determined parameters - Eurocode 1: Actions on structures - Part 1-2: General actions - Actions on structures exposed to fire, CEN, European Committee for Standardization, Brussels.

EN-1993-1-2 (2010), Eurocode 3: Design of steel structures - Part 1-2: General rules - Structural fire design, CEN, European Committee for Standardization, Brussels.

EN-1996-1-2 (2011), Eurocode 6: Design of masonry structures - Part 1-2: General rules - Structural fire design, CEN, European Committee for Standardization, Brussels.

EN-ISO-6892-1 (2009), Metallic materials - Tensile testing - Part 1: Method of test at room temperature, CEN, European Committee for Standardization, Brussels.

Farkas, E., Meszena, Z. G., Toldy, A., Matkó, S., Marosföi, B. B. & Marosi, G. (2008), 'Modelling of transport processes in a developing char', *Polymer Degradation and Stability* **Vol. 93**, pp. 1205–1213.

Fateh, T., Guillaume, E. & Joseph, P. (2017), 'An experimental study of the thermal performance of a novel intumescent fire protection coating', *Fire Safety Journal* **Vol. 92**, pp. 132–141.

Fessler, R. G. (1975), INTUMESCENT COATING COMPOSITIONS CONTAINING CRYSTALLINE MELAMINE PYROPHOSPHATE, US Patent No. 3,914,193, United States Patent Office.

Fu, M. & Qu, B. (2004), 'Synergistic flame retardant mechanism of fumed silica in ethylene-vinyl acetate/magnesium hydroxide blends', *Polymer Degradation and Stability* **Vol. 85**, pp. 633–639.

Fukuba, K. (1976), INTUMESCENT FIRE-RETARDANT COATING COMPOSITIONS CONTAINING AMIDE-POLYPHOSPHATES, US Patent No. 3,969,291, United States Patent Office.

Gao, M., Wu, W. & Yan, Y. (2009), 'Thermal Degradation and Flame Retardancy of Epoxy Resins Containing Intumescent Flame Retardant', *Journal of Thermal Analysis and Calorimetry* **Vol. 95**(2), pp. 605–608.

Ge, L.-L., Duan, H.-J., Zhang, X.-G., Chen, C., Tang, J.-H. & Li, Z.-M. (2012), 'Synergistic Effect of Ammonium Polyphosphate and Expandable Graphite on Flame-Retardant Properties of Acrylonitrile-Butadiene-Styrene', *Journal of Applied Polymer Science* **Vol. 126**, pp. 1337–1343.

Gillet, M., Autrique, L. & Perez, L. (2007), 'Mathematical model for intumescent coatings growth: application to fire retardant systems evaluation', *Journal of Physics D: Applied Physics* **Vol. 40**, pp. 883–899.

Global Market Insights, I. (2018), Intumescent Coatings Market Size, Technical report, Delaware, USA.
URL: *https://www.gminsights.com/industry-analysis/intumescent-coatings-market*

Gomez-Mares, M., Tugnoli, A., Landucci, G., Barontini, F. & Cozzani, V. (2012), 'Behavior of intumescent epoxy resins in fireproofing applications', *Journal of Analytical and Applied Pyrolysis* **Vol. 97**, pp. 99–108.
URL: *http://dx.doi.org/10.1016/j.jaap.2012.05.010*

Griffin, G. J. (2010), 'The Modeling of Heat Transfer across Intumescent Polymer Coatings', *Journal of Fire Sciences* **Vol. 28**, pp. 249–277.

Griffin, G. J., Bicknell, A. D. & Brown, T. J. (2004), 'Studies on the Effect of Atmospheric Oxygen Content on the Thermal Resistance of Intumescent, Fire-Retardant Coatings', *Journal of Fire Sciences* **Vol. 23**, pp. 303–328.

Gu, J.-w., Zhang, G.-c., Dong, S.-l., Zhang, G.-y. & Kong, J. (2007), 'Study on preparation and fire-retardant mechanism analysis of intumescent flame-retardant coatings', *Surface & Coatings Technology* **Vol. 201**, pp. 7835–7841.

Häßler, D. (2016), Verhalten reaktiver Brandschutzsysteme auf kreisförmigen Zuggliedern aus Blank und Baustahl (*engl.* Behaviour of intumescent coatings on circular steel tension bars made of cold-drawn and structural steel), Dissertation, Federal Institute for Materials Research and Testing, Berlin. Band 149.

Hahn, F. J. (1970), INTUMESCENT COATING COMPOSITIONS, US Patent No. 3,513,114, United States Patent Office.

Hasemi, Y. & Tokunaga, T. (1984), 'Flame Geometry Effects on the Buoyant Plumes from Turbulent Diffusion Flames', *Fire Science and Technology* **Vol. 4**(1), pp. 15–26.

Heinz, W. (1965), *Rheologie und Rheometrie mit Rotationsviskosimetern (engl. Rheology and Rheometry with Rotational Viscometers)*, Gebrüder Haake KG, Berlin.

Heskestad, G. (1983), 'Virtual Origins of Fire Plumes', *Fire Safety Journal* **Vol. 5**, pp. 109–114.

Heskestad, G. & Delichatsios, M. (1979), The initial convective flow in fire, *in* '17th International Symposium on Combustion', Vol. 17, pp. 1113–1123.

Horacek, H. (2014), 'Preparation and Fire Test of Intumescent Powder Coatings', *Open Access Library Journal* **Vol. 1 (e564)**(pp. 1-15).

Hostikka, S. & Matala, A. (2017), 'Pyrolysis Model for Predicting the Heat Release Rate of Birch Wood', *Combustion Science and Technology* **Vol. 189**(8), pp. 1373–1393.

Hothan, S. (2010), Numerische Voruntersuchungen zur Anwendung von reaktiven Brandschutzsystemen auf zugbeanspruchten Stahlbauteilen (*engl.* Preliminary numerical investigations of the application of intumescent coatings on steel components under tension), BAM, Federal Institute for Materials Research and Testing, Berlin.

Hothan, S. & Häßler, D. (2015), Numerische und versuchstechnische Untersuchungen zur Anwendung von reaktiven Brandschutzsystemen auf Zuggliedern aus Stahl (*engl.* Numerical and experimental investigations of the application of intumescent coatings on steel bars under tension), Research Report, Federal Institute for Materials Research and Testing, Berlin. Fraunhofer IRB Verlag. ISBN 978-3-8167-9444-8.

ISO-834-1 (2010), Fire-resistance tests - Elements of building construction - Part 1: General requirements, ISO, International Organization for Standardization.

Jenewein, E. (1996), Flammwidrige Überzugsmasse (*engl.* Flame-Retardant Coating Mass), European Patent No. 0 735 119 A1, European Patent Office.

Jiang, Z. & Liu, G. (2015), 'Microencapsulation of ammonium polyphosphate with melamine-formaldehyde-tris(2-hydroxyethyl) isocyanurate resin and its flame retardancy in polypropylene', *The Royal Society of Chemistry* **Vol. 5**, pp. 88445–88455.

Jiao, C., Zhao, X., Song, W. & Chen, X. (2015), 'Synergistic flame retardant and smoke suppression effects of ferrous powder with ammonium polyphosphate in thermoplastic polyurethane composites', *Journal of Thermal Analysis and Calorimetry* **Vol. 3**(6), pp. 1173–1181.

Jiao, M., Zhang, W., Xu, Y., Wei, T., Chen, C., Liu, F. & Yang, S. (2012), 'Urea as a New and Cheap Nitrogen Source for the Synthesis of Metal Nitride Clusterfullerenes: The Role of Decomposed Products on the Selectivity of Fullerenes', *Chemistry - A European Journal* **Vol. 18**, pp. 2666–2673.

Jimenez, M., Duquesne, S. & Bourbigot, S. (2006*a*), 'Characterization of the performance of an intumescent fire protective coating', *Surface & Coatings Technology* **Vol. 201**, pp. 979–987.

Jimenez, M., Duquesne, S. & Bourbigot, S. (2006*b*), 'Intumescent fire protective coating: Toward a better understanding of their mechanism of action', *Thermochimica Acta* **Vol. 449**, pp. 16–26.

Jones, G. (1948), FIRE-RETARDANT COMPOSITION AND PROCESS, US Patent No. 2,452,054, United States Patent Office.

Kabelac, S., Kind, M., Martin, H., Mewes, D., Schaber, K. & Stephan, P. (2013), *VDI-Wärmeatlas, VDI-Gesellschaft Verfahrenstechnik und Chemieingenieurwesen (engl. VDI Heat Atlas)*, 11th edn, Springer Vieweg.

Kang, S., Choi, S. & Choi, J. Y. (2017), 'Coupled thermo-physical behaviour of an inorganic intumescent system in cone calorimeter testing', *Journal of Fire Science* **Vol. 35**(3), pp. 207–234.

Kaplan, B. B. (1966), FIRE-RETARDANT COATING COMPOSITION, US Patent No. 3,284,216, United States Patent Office.

Kasten, N. H. (1981), INTUMESCENT FIRE RETARDANT COATING COMPOSITIONS, US Patent No. 4,247,435, United States Patent Office.

Koo, J. H. (1998), 'Thermal Characterization of a Ceramic Intumescent Material', *Fire Technology* **Vol. 34**(1), pp. 59–71.

Krüger , S., Gluth, G. J. G., Watolla, M.-B., Morys, M., Häßler, D. & Schartel, B. (2016), 'Neue Wege: Reaktive Brandschutzbeschichtungen fürExtrembedingungen (*engl.* New ways: Reactive fire protection coatings for extreme conditions)', *Bautechnik* **Vol. 93**(8), pp. 531–542.

Lai, X., Yin, C., Li, H. & Zeng, X. (2015), 'Synergistic Effect Between Silicone-Containing Macromolecular Charring Agent and Ammonium Polyphosphate in Flame Retardant Polypropylene', *Journal of Applied Polymer Science* pp. 1–10.

Lautenberger, C. & Fernandez-Pello, C. (2009), 'Generalized pyrolysis model for combustible solids', *Fire Safety Journal* **Vol. 44**, pp. 819–839.

Levine, D. (1972), FIRE RETARDANT INTUMESCENT PAINT, US Patent No. 3,654,190, United States Patent Office.

Li, G.-Q., Han, J., Lou, G.-B. & Wang, Y. C. (2016), 'Predicting intumescent coating protected steel temperature in fire using constant thermal conductivity', *Thin-Walled Structures* **Vol. 98**, pp. 177–184.

Li, H., Hu, Z., Zhang, S., Gu, X., Wang, H., Jiang, P. & Zhao, Q. (2015), 'Effects of titanium dioxide on the flammability and char formation of water-based coatings containing intumescent flame retardants', *Progress in Organic Coatings* **Vol. 78**, pp. 318–324.

Li, X., Yan, T., Hu, X., Wang, K. & Fu, Q. (2013), 'Synergistic Effects of Polyethylene Glycol and Ammonium Polyphosphate on Intumescent Flame-Retardant Polypropylene', *Polymer Engineering and Science* **Vol. 53**(2), pp. 410–416.

Liu, H., Yu, Q. N., Qu, Z. G. & Yang, R. Z. (2017), 'Simulation and analytical validation of forced convection inside opencell metal foams', *International Journal of Thermal Sciences* **Vol. 111**, pp. 234–245.

Liu, Y., Zhang, Y., Cao, Z. & Fang, Z. (2013), 'Synthesis and performance of three flame retardant additives containing diethyl phosphite/phenyl phosphonic moieties', *Fire Safety Journal* **Vol. 61**, pp. 185–192.

Longdon, P. J., Houyoux, C., Zhao, B. & Chico, B. (2005), Development of alternative technologies for off-site applied intumescent coatings, Technical Report ISBN 92-894-9165-5, Office for Official Publications of the European Communities, Luxembourg.

Loretz, M., Maire, E. & Baillis, D. (2008), 'Analytical Modelling of the Radiative Properties of Metallic Foams: Contribution of X-Ray Tomography', *Advanced Engineering Materials* **Vol. 10**(4), pp. 352–360.

Lu, H., Wilkie, C., Ding, M. & Song, L. (2011), 'Thermal properties and flammability performance of poly (vinyl alcohol)/a-zirconium phosphate nanocomposites', *Polymer Degradation and Stability* **Vol. 96**, pp. 885–891.

Lucherini, A., Giuliani, L. & Jomaas, G. (2018), 'Experimental study of the performance of intumescent coatings exposed to standard and non-standard fire conditions', *Fire Safety Journal* **Vol. 95**, pp. 42–50.

Lucherini, A. & Maluk, C. (2017), Novel Test Method for Studying the Fire Performance of Thin Intumescent Coatings, *in* E. Nigro & A. Bilotta, eds, 'Proceedings of the 2nd International Fire Safety Symposium (IFireSS)', Doppiavoce, Naples, Italy, pp. 565–572.

Lucherini, A. & Maluk, C. (2019), 'Assessing the onset of swelling for thin intumescent coatings under a range of heating conditions', *Fire Safety Journal* **Vol. 106**, pp. 1–12.

Lucherini, A., Torero, J. & Maluk, C. (2019), Effects of thermal conditions of steel on the fire performance of thin intumescent coatings, *in* 'Proceedings of 15th International Conference and Exhibition of Fire Science and Engineering (Interflam)', Royal Holloway College, London, UK.

Lv, P., Wang, Z., Hu, K. & Fan, W. (2005), 'Flammability and thermal degradation of flame retarded polypropylene composites containing melamine phosphate and pentaerythritol derivatives', *Polymer Degradation and Stability* **Vol. 90**, pp. 523–534.

Maluk, C. (2014), Development and application of a novel test method for studying the fire behaviour of CFRP prestressed concrete structural elements, PhD thesis, University of Edinburgh.

Maluk, C., Bisby, L., Krajcovoc, M. & Torero, J. L. (2019), 'A Heat-Transfer Rate Inducing System (H-TRIS) Test Method', *Fire Safety Journal* **Vol. 105**, pp. 307–319.

Mamleev, V. S., Bekturov, E. A. & Gibov, K. M. (1998), 'Dynamics of Intumescence of Fire-Retardant Polymeric Materials', *Journal of Applied Polymer Science* **Vol. 70**, pp. 1523–1542.

Markets & Markets Research, L. (2019), Intumescent Coatings Market - Global Forecast to 2023, Technical report, Pune, India.
URL: *https://www.marketsandmarkets.com/Market-Reports/intumescent-coating-market-151067477.html*

Maxwell, J. C. (1904), *A Treatise on Electricity and Magnetism*, 3rd edn, Oxford University Press.

McGrattan, K. B., McDermott, R. J., Mell, W. E., Forney, G. P., Floyd, J. E. & Hostikka, S. A. (2010), Modeling the Burning of Complicated Objects Using Lagrangian Particles, *in* 'Proceedings of the 2010 Interflam Conference', Nottingham, pp. 339–356.

Mendes, M. A. A., Talukdar, P., Ray, S. & Trimis, D. (2014), 'Detailed and simplified models for evaluation of effective thermal conductivity of open-cell porous foams at high temperatures in presence of thermal radiation', *International Journal of Heat and Mass Transfer* **Vol. 68**, pp. 612–624.

Mesquita, L. M. R., Piloto, P. A. G., Vaz, M. A. P. & Pinto, T. M. G. (2009), Decomposition of Intumescent Coatings: Comparison Between Numerical Method and Experimental Results, *in* F. Wald, P. Kallerova & J. Chlouba, eds, 'Proceedings of International Conference Application of Structural Fire Engineering', Czech Technical University in Prague, Prague, Czech Republic, pp. 140 – 145.

Müller, R. (1989), Ein numerisches Verfahren zur simultanen Bestimmung thermischer Stoffeigenschaften oder Größen aus Versuchen. Anwendung auf das Heissdraht-Parallelverfahren und auf Versuche an Hausschornsteinen (*engl.* A numerical method for the simultaneous determination of thermal properties from experiments. Application to the hot wire parallel method and to tests on house chimneys), PhD thesis, Technical University Clausthal, Clausthal.

Neggers, J. (2014), 'Jann5s Measuretool - Interactive tool allowing the measurement of distances, radii, and angles in images', *MathWorks - File Exchange, version 2.1.0.0* .
URL: *https://www.mathworks.com/matlabcentral/fileexchange/25964-jann5s-measuretool*

Ni, J., Song, L., Hu, Y., Zhang, P. & Xing, W. (2009), 'Preparation and characterization of microencapsulated ammonium polyphosphate with polyurethane shell by in situ polymerization and its flame retardance in polyurethane', *Polymers for Advanced Technologies* **Vol. 20**, pp. 999–1005.

Nielsen, M. L. (1952), FIRE RETARDING COATING COMPOSITION COMPOSED OF ANTROGEN-PHOSPHORUS COMPOUND WITH AN ALDEHYDE RESIN AND POLY-HYDROXY ALCOHOL, US Patent No. 2,596,939, United States Patent Office.

Norgaard, K. P. (2014), Investigation of an Intumescent Coating System in Pilot and Laboratory-scale Furnaces, PhD thesis, Technical University of Denmark - Department of Chemical and Biochemical Engineering.

Norgaard, K. P., Dam-Johansen, K. & Kiil, S. (2016), 'Engineering Model for Intumescent Coating Behavior in a Pilot-Scale Gas-Fired Furnace', *Journal of the American Institute of Chemical Engineers* **Vol. 62**(11), pp. 3947–3962.

Oda, Y. & Shinke, Y. (2014), 'Vinyl Polymers', *Encyclopedia of Polymeric Nanomaterials* pp. 1–6.

Olcese, T. & Pagella, C. (1999), 'Vitreous fillers in intumescent coatings', *Progress in Organic Coatings* **Vol. 36**(4), pp. 231–241.

Petersen, C. (2013), *Stahlbau - Grundlagen der Berechnung und baulichen Ausbildung von Stahlbauten (engl. Steel construction - Fundamentals of calculation and structural design of steel structures)*, forth edn, Springer Vieweg.

Puri, R. G. & Khanna, A. S. (2017), 'Intumescent coatings: A review on recent progress', *Journal of Coatings Technology and Research* **14**((1)), pp. 1–20.

Qiang, X., Bijlaard, F. S. K. & Kolstein, H. (2012), 'Post-fire mechanical properties of high strength structural steels S460 and S690', *Engineering Structures* **Vol. 35**, pp. 1–10.

Qiang, X., Bijlaard, F. S. K. & Kolstein, H. (2013), 'Post-fire performance of very high strength steel S960', *Journal of Constructional Steel Research* **Vol. 80**, pp. 235–242.

Raveglia, E. (2008), Grundlagen der Bemessung von intumeszierenden Brandschutzsystemen im Stahlbau (*engl.* Fundamentals of the Design of Intumescent Fire Protection Systems in Steel Construction), PhD thesis, ETH ZÜRICH.

Rein, G., Rackauskaite, E., Hamel, C. & Law, A. (2015), 'Improved Formulation of Travelling Fires and Application to Concrete and Steel Structures', *Structures* **Vol 3**, pp. 250–260.

Reshetnikov, I. S., Garashchenko, A. N. & Strakhov, V. L. (2000), 'Experimental Investigation into Mechanical Destruction of Intumescent Chars', *Polymers for Advanced Technologies* **Vol. 11**, pp. 392–397.

Richard-Campisi, L., Bourbigot, S., Le Bras, M. & Delobel, R. (1996), 'Thermal behaviour of cotton-modacrylic fibre blends: kinetic study using the invariant kinetic parameters method', *Thermochimica Acta* **Vol. 275**, pp. 37–49.

Rickard, I., Bisby, L. & Deeny, S. (2018), 'Explosive spalling of concrete in fire: novel testing to mitigate design risk', *The Structural Engineer* **Vol. 96**(1), pp. 42–47.

Rimez, B., Rahier, H., Biesemans, M., Bourbigot, S. & Van Mele, B. (2015), 'Flame retardancy and degradation mechanism of poly(vinyl acetate) in combination with intumescent flame retardants: I. Ammonium poly(phosphate)', *Polymer Degradation and Stability* **Vol. 121**, pp. 321–330.

Rimez, B., Rahier, H., Van Assche, G., Artoos, T. & Van Mele, B. (2008), 'The thermal degradation of poly(vinyl acetate) and poly(ethylene-co-vinyl acetate), Part II: Modelling the degradation kinetics', *Polymer Degradation and Stability* **Vol. 93**, pp. 1222–1230.

Riva, A., Camino, G., Fomperie, L. & Amigouet, P. (2003), 'Fire retardant mechanism in intumescent ethylene vinyl acetate compositions', *Polymer Degradation and Stability* **Vol. 82**, pp. 341–346.

Russell, H. W. (1935), Principles of Heat Flow in Porous Insulators, *in* A. C. Society, ed., 'Symposium on Heat Transfer through Refractories and Insulation in Industrial Furnaces', Cincinnati, Ohio.

Sakamoto, R., Kamimoto, M., Takahashi, Y., Abe, Y., Kanari, K. & Ozawa, T. (1984), 'Investigation of Latent Heat-Thermal Energy Storage Materials. III. Thermoanalytical Evaluation of Pentaerythritol', *Thermochimica Acta* **Vol. 77**, pp. 241–249.

Schartel, B., Bartholmai, M. & Knoll, U. (2005), 'Some comments on the use of cone calorimeter data', *Polymer Degradation and Stability* **Vol. 88**, pp. 540–547.

Schartel, B. & Weiß, A. (2010), 'Temperature inside burning polymer specimens: Pyrolysis zone and shielding', *Fire and Materials* **Vol. 34**, pp. 217–235.

Schartel, B., Weiß, A., Sturm, H., Kleemeier, M., Hartwig, A., Vogt, C. & Fischer, R. X. (2011), 'Layered silicate epoxy nanocomposites: formation of the inorganic-carbonaceous fire protection layer', *Polymers for Advanced Technologies* **Vol. 22**, pp. 1581–1592.

Schaumann, P., Tabeling, F. & Weisheim, W. (2016), 'Numerical simulation of the heating behaviour of steel profiles with intumescent coating adjacent to trapezoidal steel sheets in fire', *Journal of Structural Fire Engineering* **Vol. 7**(2), pp. 158–167.

Schaumann, P. & Weisheim, W. (2017), Effect of Heating Rates in Natural Fires on the Thermal Performance of a Solvent-borne Intumescent Coating, *in* E. Nigro & A. Bilotta, eds, 'Proceedings of the 2nd International Fire Safety Symposium (IFireSS)', Doppiavoce, Naples, Italy, pp. 373–380.

Simon, S. (2006), Untersuchungen zur systematischen Entwicklung von intumeszierenden Hochleistungsbrandschutzbeschichtungen (*engl.* Investigations on the systematic development of intumescent high performance coatings), PhD thesis, Technical University Braunschweig, Germany.

Simulia (2016), *Abaqus Analysis User's Guide - Computation of thermal strains - Chapter 26.1.2.* **URL:** *http://130.149.89.49:2080/v2016/books/usb/default.htm*

Staggs, J. E. J. (2003), 'Heat and mass transport in developing chars', *Polymer Degradation and Stability* **Vol. 82**, pp. 297–307.

Staggs, J. E. J. (2009), *Fire Retardancy of Polymers: New Strategies and Mechanisms*, Royal Society of Chemistry, chapter 14: Porosity Estimates of Intumescent Chars by Image Analysis, pp. 209–224.

Staggs, J. E. J. (2010), 'Thermal conductivity estimates of intumescent chars by direct numerical simulation', *Fire Safety Journal* **Vol. 45**, pp. 228–237.

Staggs, J. E. J., Crewe, R. J. & Butler, R. (2012), 'A theoretical and experimental investigation of intumescent behaviour in protective coatings for structural steel', *Chemical Engineering Science* **Vol. 71**, pp. 239–251.

Stopp, V. & Proschek, P. (2011), Reaktive Brandschutzsysteme auf Stahlbauteilen mit reiner Zugbeanspruchung (*engl.* Intumescent coatings applied on steel components under pure tension load), DIBt Mitteilung 42, H. 6, pp. 190-191, German Institute for Building Technology, Berlin.

Sun, L., Qu, Y. & Li, S. (2013), 'Co-microencapsulate of ammonium polyphosphate and pentaerythritol in intumescent flame-retardant coatings', *Journal of Thermal Analysis and Calorimetry* **Vol. 111**, pp. 1099–1106.

Tabeling, F. (2014), Zum Hochtemperaturverhalten dämmschichtbildender Brandschutzsysteme auf Stahlbauteilen (*engl.* High temperature behaviour of intumescent fire coatings on steel elements), PhD thesis, Leibniz University Hannover.

Tang, Z., Wei, T., Ma, Y. & Chen, L. (2019), 'Residual Strength of Steel Structures After Fire Events Considering Material Damages', *Arabian Journal for Science and Engineering* **Vol. 44**, pp. 5075–5088.

Taylor, A. P. & Sale, F. R. (1993), 'Thermoanalytical Studies of Intumescent Systsms', *Makromol. Chem., Macromol. Symp.* **Vol. 74**, pp. 85–93.

Thewes, V. (2001), FLAME-RETARDANT COATING, US Patent No. 2001/0027226 A1, United States Patent Office.

Toldy, A., Anna, P., Csontos, I., Szabó, A. & Marosi, G. (2007), 'Intrinsically flame retardant epoxy resin - Fire performance and background - Part I', *Polymer Degradation and Stability* **Vol. 92**, pp. 2223–2230.

Tollens, B. & Wigand, P. (1891), *Über den Penta-Erythrit, einen aus Formaldehyd und Acetaldehyd synthetisch hergestellten vierwertigen Alkohol (engl. About the penta-erythritol, a tetravalent alcohol synthesized from formaldehyde and acetaldehyde)*, Justus Liebigs Annalen der Chemie, pp. 316-340.

Trelles, J. & Lattimer, B. Y. (2007), 'Modelling thermal degradation of composite materials', *Fire and Materials* **Vol. 31**, pp. 147–171.

Trossin, H.-J. (1999), Nutzung der Ähnlichkeitstheorie zur Modellbildung in der Produktionstechnik (*engl.* Use of the similarity theory for modelling in production engineering), Technical report, Institute for Machine Tools and Industrial Management, Technical University of Munich.

Vandersall, H. L. (1971), 'Intumescent Coating Systems, Their Development and Chemistry', *Journal of Fire and Flammability* **Vol. 2**, pp. 97–140.

Varma, I. K. & Sadhir, R. K. (1975), 'Thermal Analysis of Poly(vinyl alcohol) and Poly(vinyl acetate) Fractions', *Die Angewandte Makromolekulare Chemie* **Vol. 46**, pp. 1–10.

Venable, J. M. (1960), FIRE-RETARDANT COATING COMPOSITION, US Patent No. 2,956,037, United States Patent Office.

Vyazovkin, S. (2015), *Isoconversional Kinetics of Thermally Stimulated Processes*, Springer International Publishing Switzerland.

Vyazovkin, S., Burnham, A. K., Criado, J. M., Perez-Maqueda, L. A., Popescu, C. & Sbirrazzuoli, N. (2011), 'ICTAC Kinetics Committee recommendations for performing kinetic computations on thermal analysis data', *Thermochimica Acta* **Vol. 520**, pp. 1–19.

Vyazovkin, S., Chrissafis, K., Di Lorenzo, M. L., Koga, N., Pijolat, M., Roduit, B., Sbirrazzuoli, N. & Sunol, J. J. (2014), 'ICTAC Kinetics Committee recommendations for collecting experimental thermal analysis data for kinetic computations', *Thermochimica Acta* **Vol. 590**, pp. 1–23.

Wang, D.-Y., Liu, Y., Ge, X.-G., Wang, Y.-Z., Stec, A., Biswas, B., Hull, T. R. & Price, D. (2008), 'Effect of metal chelates on the ignition and early flaming behaviour of intumescent fire-retarded polyethylene systems', *Polymer Degradation and Stability* **Vol. 93**, pp. 1024–1030.

Wang, G. & Yang, J. (2011), 'Thermal degradation study of fire resistive coating containing melamine polyphosphate and dipentaerythritol', *Progress in Organic Coatings* **Vol. 72**, pp. 605–611.

Wang, G. & Yang, J. (2012), 'Influences of molecular weight of epoxy binder on fire protection of waterborne intumescent fire resistive coating', *Surface & Coatings Technology* **Vol. 206**, pp. 2146–2151.

Wang, L., Dong, Y., Zhang, D., Zhang, C. & Zhang, C. (2015), 'Experimental Study of Heat Transfer in Intumescent Coatings Exposed to Non-Standard Furnace Curves', *Fire Technology* **Vol. 51**, pp. 627–643.

Wang, L. L., Wang, Y. C. & Li, G. Q. (2013), 'Experimental study of hydrothermal aging effects on insulative properties of intumescent coating for steelel ements', *Fire Safety Journal* **Vol. 55**, pp. 168–181.

Wang, X., Rathore, R., Songtipya, P., Jimenez-Gasco, M., Manias, E. & Wilkie, C. A. (2011), 'EVA-layered double hydroxide (nano)composites: Mechanism of fire retardancy', *Polymer Degradation and Stability* **Vol. 96**, pp. 301–313.

Wang, Y., Göransson, U., Holmstedt, G. & Omrane, A. (2005), A Model for Prediction of Temperature in Steel Structure Protected by Intumescent Coating, based on Tests in the Cone Calorimeter, *in* D. Gottuk & B. Lattimer, eds, 'Proceedings of the Eighth International Symposium on Fire Safety Science', International Association for Fire Safety Science, Tsinghua University, Beijing, China, pp. 235–246.

Wang, Z., Han, E. & Ke, W. (2006), 'Effect of nanoparticles on the improvement in fire-resistant and anti-ageing properties of flame-retardant coating', *Surface & Coatings Technology* **Vol. 200**, pp. 5706–5716.

Ward, T. A. (1985), FIRE PROTECTIVE INTUMESCENT MASTIC COMPOSITION AND METHOD EMPLOYING SAME, US Patent No. 4,529,467, United States Patent Office.

Weil, E. D. (2011), 'Fire-Protective and Flame-Retardant Coatings - A State-of-the-Art Review', *Journal of Fire Sciences* **Vol. 29**(3), pp. 259–296.

Weil, E. D. & Choudhary, V. (1995), 'Flame-Retarding Plastics and Elastomers with Melamine', *Journal of Fire Science* **Vol. 13**, pp. 104–126.

Weisheim, W. & Schaumann, P. (2019), 'Aktuelle Forschung und Verwendbarkeit von reaktiven Brandschutzsystemen im Stahlbau (*engl.* Latest research and usability of intumescent coatings in steel construction)', *Stahlbau* **88**(1), 11–21.

Weisheim, W., Schaumann, P., Sander, L. & Zehfuß, J. (2018), Numerical Model for the Fire Protection Performance of Intumescent Coatings Exposed to Natural Fires., *in* 'Proceedings of the 10th International Conference on Structures in Fire (SiF '18), Belfast, United Kingdom.', pp. 225 – 232.

Wilson, I. V. (1955), FIRE-RETARDANT COMPOSITIONS, US Patent No. 2,702,283, United States Patent Office.

Woodside, W. & Messmer, J. H. (1961), 'Thermal Conductivity of Porous Media. I. Unconsolidated Sands', *Journal of Applied Physics* **Vol. 32**(9), pp. 1688–1699.

Wu, G. M. (2011), Quantitative Assessment and Optimization of Flame Retardancy by the Shielding Effect in Epoxy Nanocomposites, PhD thesis, Federal Institute for Materials Research and Testing (BAM).

Wu, K., Wang, Z. & Liang, H. (2008), 'Microencapsulation of Ammonium Polyphosphate: Preparation, Characterization, and Its Flame Retardance in Polypropylene', *Polymer Composites* pp. 854–860.

Xu, L., Lei, C., Xu, R., Zhang, X. & Zhang, F. (2016), 'Hybridization of a-zirconium phosphate with hexachlorocyclotriphosphazene and its application in the flame retardant poly(vinyl alcohol) composites', *Polymer Degradation and Stability* **Vol. 133**, pp. 378–388.

Yen, Y.-Y., Wang, H.-T. & Guo, W.-J. (2012), 'Synergistic flame retardant effect of metal hydroxide and nanoclay in EVA composites', *Polymer Degradation and Stability* **Vol. 97**, pp. 863–869.

Yew, M. C., Ramli Sulong, N. H., Yew, M. K., Amalina, M. A. & Johan, M. R. (2015), 'Influences of flame-retardant fillers on fire protection and mechanical properties of intumescent coatings', *Progress in Organic Coatings* **Vol. 78**, pp. 59–66.

Yi, J., Liu, Y., Pan, D. & Cai, X. (2013), 'Synthesis, Thermal Degradation, and Flame Retardancy of a Novel Charring Agent Aliphatic - Aromatic Polyamide for Intumescent Flame Retardant Polypropylene', *Journal of Applied Polymer Science* pp. 1061–1068.

Yuan, J. F. & Wang, Y. C. (2009), *Fire Retardancy of Polymers: New Strategies and Mechanisms*, Hull, R. R. and Kandola, B. K., chapter 15: Efficient Modelling of Temperatures in Steel Plates Protected by Intumescent Coating in Fire, pp. 225–239.

Zehfuß, J. & Hosser, D. (2005), 'Vereinfachtes Naturbrandmodell fürdie Brandschutzbemessung von Bauteilen und Tragwerken (*engl.*Simplified natural fire model for the fire safety of components and structures)', *Bauphysik* **Vol. 27**(2), pp. 79–86.

Zehfuß , J., Schaumann, P., Sander, L. & Weisheim, W. (2018), Prüfverfahren für thermische Materialkennwerte von Brandschutzbekleidungen und reaktiven Brandschutzsystemen für die Bemessung von Stahltragwerken bei Naturbränden (*engl.* Test methods for thermal material properties of fire protection materials and intumescent coatings for the design of steel structures exposed to natural fires) IGF-Vorhaben 19176 N, Technical report, Deutscher Ausschuß für Stahlbau e.V. (DASt).

Zhang, C. (2012), Reliability of Steel Columns Protected by Intumescent Coatings Subjected to Natural Fires, PhD thesis, Tongji University, Shanghai, China.

Zhang, F., Sun, Y. & Cheng, Y. (2017), 'Study on Heat Transfer in Intumescent Fire Retardant Epoxy Coatings During Combustion', *Journal of Macromolecular Science* **Vol. 56**(8), pp. 608–622.

Zhang, J., Horrocks, A. & Hall, M. (1994), 'The Flammability of Polyacrylonitrile and its Copolymers IV. The Flame Retardant Mechanism of Ammonium Polyphosphate', *Fire and Materials* **Vol. 18**, pp. 307–312.

Zhang, Y., Wang, Y. C., Bailey, C. G. & Taylor, A. P. (2012*a*), 'Global modelling of fire protection performance of an intumescent coating under different furnace fire conditions', *Journal of Fire Science* **Vol. 31**(1), pp. 51–72.

Zhang, Y., Wang, Y. C., Bailey, C. G. & Taylor, A. P. (2012*b*), 'Global modelling of fire protection performance of intumescent coating under different cone calorimeter heating conditions', *Fire Safety Journal* **Vol. 50**, pp. 51–62.

Zheng, Z., Yan, J., Sun, H., Cheng, Z., Li, W., Wang, H. & Cui, X. (2014), 'Preparation and characterization of microencapsulated ammonium polyphosphate and its synergistic flame-retarded polyurethane rigid foams with expandable graphite', *Polymer International* **Vol. 63**, pp. 84–92.

List of Figures

List of Tables

INTUMESCENT COATINGS ON STEEL STRUCTURES EXPOSED TO NATURAL FIRES

Intumescent coatings are used whenever filigree and architecturally attractive steel structures need to fulfill fire resistance requirements. Due to their thin dry film thickness intumescent coatings combine both the maintenance of the architectural appearance of the steel structure and the required fire resistance.
When being exposed to high temperatures, the inert coating expands multiple times the original thickness to form a highly insulating char with low thermal conductivity that protects the underlying steel substrate from rapid heating.

Due to the increasing use of performance-based design methods for steel structures in fire, it becomes more and more important to assess the fire protection performance of intumescent coatings in case of natural fires. As coatings are nowadays only assessed for the ISO standard fire curve during the approval procedure, there is a lack of scientific evidence regarding the thermo-mechanical performance of intumescent coatings for fire scenarios that deviate from the standard fire.
Therefore, the main objective of this thesis is to evaluate the thermal performance of intumescent coatings in natural fires and to identify the relevant parameters for the description of the temperature and heating rate-dependent behaviour of intumescent coatings.

Target group:
The present thesis is addressed to scientists, material researchers, fire and calculation engineers, developers and manufacturers of intumescent coatings as well as to standardisation bodies and building authorities.

Author:
Dipl.-Ing. *Waldemar Weisheim* was research associate at the Institute for Steel Construction at the Leibniz University Hannover from 2013 to 2019.

Hannover, 2022